Gas Dynamics Laboratory
Department of Mechanical and
Industrial Engineering
University of Illinois at
Urbana-Champaign
Urbana, IL 61801

FINAL TECHNICAL REPORT

Fluid Dynamic Mechanisms and Interactions within Separated Flows

J. C. Dutton and A. L. Addy

August 1998

REPORT DOCUMENTATION PAGE	Form Approved OMB NO. 0704-0188

Public reporting burden for this collection of information is estimated to average 1 hour per response, including the time for reviewing instructions, searching existing data sources, gathering and maintaining the data needed, and completing and reviewing the collection of information. Send comment regarding this burden estimates or any other aspect of this collection of information, including suggestions for reducing this burden, to Washington Headquarters Services, Directorate for information Operations and Reports, 1215 Jefferson Davis Highway, Suite 1204, Arlington, VA 22202-4302, and to the Office of Management and Budget, Paperwork Reduction Project (0704-0188), Washington, DC 20503.

1. AGENCY USE ONLY (Leave blank)	2. REPORT DATE 31 August 1998	3. REPORT TYPE AND DATES COVERED Final

4. TITLE AND SUBTITLE

Fluid Dynamic Mechanisms and Interactions within Separated Flows

5. FUNDING NUMBERS

DAAH04-93-G-0226

6. AUTHOR(S)

J. C. Dutton and A. L. Addy

7. PERFORMING ORGANIZATION NAMES(S) AND ADDRESS(ES)

Department of Mechanical and Industrial Engineering
University of Illinois at Urbana-Champaign
1206 West Green Street
Urbana, IL 61801

8. PERFORMING ORGANIZATION REPORT NUMBER

9. SPONSORING / MONITORING AGENCY NAME(S) AND ADDRESS(ES)

U.S. Army Research Office
P.O. Box 12211
Research Triangle Park,, NC 27709-2211

10. SPONSORING / MONITORING AGENCY REPORT NUMBER

ARO 30941.16-EG

11. SUPPLEMENTARY NOTES

The views, opinions and/or findings contained in this report are those of the author(s) and should not be construed as an official Department of the Army position, policy or decision, unless so designated by other documentation.

12a. DISTRIBUTION / AVAILABILITY STATEMENT

Approved for public release; distribution unlimited.

12b. DISTRIBUTION CODE

13. ABSTRACT (Maximum 200 words)

The experimental results of this grant consist of detailed laser Doppler velocimeter (LDV), particle image velocimeter (PIV), and high-speed wall pressure measurements made in axisymmetric and planar, subsonic and supersonic flows with embedded separated regions. The LDV experiments have yielded high quality, well documented mean velocity and turbulence data for a variety of high-speed separated flows, including the near-wake regions behind a cylindrical afterbody, an axisymmetric afterbody with a boattail, and a cylindrical afterbody with base bleed in supersonic flow. The PIV experiments have studied the effect of a base cavity in a two-dimensional, subsonic base flow and the mechanism of drag reduction for this configuration. Another experimental study has considered the interaction occurring when a supersonic stream is separated by means of a second stream impinging the first at an angle (plume-induced separation). High-speed wall pressure measurements made beneath the unsteady separation shock wave and conditionally analyzed mean velocity and turbulence data in the interaction region have been obtained for this configuration. The results of these studies have been carefully documented in a series of journal articles, conference proceedings papers, and theses. The full text of the papers and thesis abstracts are included as appendices of this report.

14. SUBJECT TERMS

separated flow	shock wave/boundary layer interaction
base flow	laser Doppler velocimetry
supersonic flow	particle image velocimetry

15. NUMBER IF PAGES

484

16. PRICE CODE

17. SECURITY CLASSIFICATION OR REPORT	18. SECURITY CLASSIFICATION OF THIS PAGE	19. SECURITY CLASSIFICATION OF ABSTRACT	20. LIMITATION OF ABSTRACT
UNCLASSIFIED	UNCLASSIFIED	UNCLASSIFIED	UL

NSN 7540-01-280-5500

Standard Form 298 (Rev. 2-89)
Prescribed by ANSI Std. 239-18
298-102

FLUID DYNAMIC MECHANISMS AND INTERACTIONS WITHIN SEPARATED FLOWS

Final Technical Report

by

J. C. Dutton[*]

A. L. Addy[**]

August 1998

---

[*]   W. Grafton and Lillian B. Wilkins Professor of Mechanical Engineering

[**] Professor Emeritus of Mechanical Engineering

ABSTRACT

The significant results of a research effort investigating the fundamental fluid dynamic mechanisms and interactions within high-speed separated flows are presented in detail. The results have been obtained through primary emphasis on experimental investigations of missile and projectile base flow-related configurations. The objectives of the research program focus on understanding the component mechanisms and interactions which establish and maintain high-speed separated flow regions.

The experimental results consist of detailed laser Doppler velocimeter (LDV), particle image velocimeter (PIV), and high-speed wall pressure measurements made in axisymmetric and planar, subsonic and supersonic flows with embedded separated regions. The LDV experiments have yielded high quality, well documented mean velocity and turbulence data for a variety of high-speed separated flows, including the near-wake regions behind a cylindrical afterbody, an axisymmetric afterbody with a boattail, and a cylindrical afterbody with base bleed in supersonic flow. The PIV experiments have studied the effect of a base cavity in a two-dimensional, subsonic base flow and the mechanism of drag reduction for this configuration. Another experimental study has considered the interaction occurring when a supersonic stream is separated by means of a second stream impinging the first at an angle (plume-induced separation). High-speed wall pressure measurements made beneath the unsteady separation shock wave and conditionally analyzed mean velocity and turbulence data in the interaction region have been obtained for this configuration. The results of these studies have been carefully documented in a series of journal articles, conference proceedings papers, and theses. The full text of the papers and thesis abstracts are included as appendices of this report.

TABLE OF CONTENTS

APPENDIX A.1   AN INVESTIGATION OF LDV VELOCITY BIAS
CORRECTION TECHNIQUES FOR HIGH-SPEED
SEPARATED FLOWS

APPENDIX A.2   SUPERSONIC BASE FLOW EXPERIMENTS IN THE NEAR
WAKE OF A CYLINDRICAL AFTERBODY

APPENDIX A.3   SUPERSONIC NEAR-WAKE AFTERBODY BOATTAILING
EFFECTS ON AXISYMMETRIC BODIES

APPENDIX A.4   EFFECT OF A RAPID EXPANSION ON THE
DEVELOPMENT OF COMPRESSIBLE FREE SHEAR
LAYERS

APPENDIX A.5   STUDY OF SUBSONIC BASE CAVITY FLOWFIELD
STRUCTURE USING PARTICLE IMAGE VELOCIMETRY

APPENDIX A.6   BASE-BLEED EXPERIMENTS WITH A CYLINDRICAL
AFTERBODY IN SUPERSONIC FLOW

APPENDIX A.7   VELOCITY AND TURBULENCE MEASUREMENTS IN A
SUPERSONIC BASE FLOW WITH MASS BLEED

APPENDIX A.8   THE TURBULENCE STRUCTURE OF A REATTACHING
AXISYMMETRIC COMPRESSIBLE FREE SHEAR LAYER

APPENDIX A.9   TIME-SERIES ANALYSES OF WALL PRESSURE
FLUCTUATIONS IN PLUME-INDUCED SEPARATED
FLOWFIELDS

APPENDIX A.10 A METHOD FOR SEPARATING SHOCK WAVE MOTION
AND TURBULENCE IN LDV MEASUREMENTS

APPENDIX A.11 VELOCITY MEASUREMENTS IN A SHOCK-SEPARATED
FREE SHEAR LAYER

APPENDIX A.12 CONDITIONAL ANALYSIS OF WALL PRESSURE
FLUCTUATION MEASUREMENTS MADE IN PLUME-
INDUCED SEPARATED FLOWFIELDS

I. INTRODUCTION

A. PROBLEM STATEMENT

This report describes an ongoing research effort funded by the U.S. Army Research Office to investigate the fundamental fluid dynamic mechanisms and interactions within high-speed separated flows. The overall effort has concentrated on detailed experimental investigations aimed at gaining a more insightful understanding of the fundamental fluid dynamic mechanisms existing in the near-wake region of these flows. The investigations of separated flow problems have been focused on missile and projectile afterbody and base flows and on the interactions between the base and body flows.

Professors J. C. Dutton and A. L. Addy and their graduate students at the University of Illinois at Urbana–Champaign have conducted this series of experiments on two–dimensional and axisymmetric base flow configurations utilizing a number of diagnostic techniques. These include: schlieren and shadowgraph photography, surface streakline visualization, mean and fluctuating pressure measurements, two-component laser Doppler velocimeter (LDV) measurements, and particle image velocimeter (PIV) measurements. This information concerning the mean and fluctuating characteristics of the flowfields in and around the embedded separated flow regions has been used to characterize base flows at both subsonic and supersonic speeds.

The purpose of this final technical report is to collect and present, in their entirety or by summary and reference, the research findings for the near-wake base flow problem and related problems that have been investigated under the research sponsorship of the U.S. Army Research Office through Grant Number DAAH04–93–G–0226. The Technical Monitor for this research has been Dr. Thomas L. Doligalski, Chief, Fluid Dynamics Branch, Engineering and Environmental Sciences Division. The authors of this report and their graduate student researchers are deeply indebted to Dr. Doligalski for his support and technical comments and suggestions during the course of these studies. The research group is also indebted to Dr. Robert E. Singleton, Director,

Engineering and Environmental Sciences Division, for his long-term interest and support of this research program.

In all cases, where the experimental efforts have yielded significant or new results, the information has been presented at professional meetings and/or published in the archival literature by the individual researchers. This final report highlights this work and includes copies of the appropriate publications for completeness. In the case of master's and doctoral degree theses, which are generally quite long and detailed, a summary of the theses is provided and the appropriate reference to the full document is given. In most cases, the conference and/or archival publications are based upon the detailed work reported in these theses.

B. FINAL TECHNICAL REPORT ORGANIZATION

The overall organization of this report details the major accomplishments of the research group during the four-year period of ARO sponsorship (with an additional no-cost extension year). Each research investigation is described briefly, and the associated published literature is included in an appendix. The inclusion of a copy of each publication is intended to ease the burden on the reader in obtaining symposium proceedings and other publications which tend to be difficult to obtain.

The relatively brief "text" of this final technical report has been outlined and organized to provide quick reference to a particular topic of interest. Most of the research results have been made available through organized meetings and publications of the American Institute of Aeronautics and Astronautics (AIAA). In those instances when a detailed paper is available, only a brief description is given and the reader is referred to the appropriate appendix for further details.

After the summary of research results, the next three sections of the report provide lists concerning several administrative matters related to the subject research grant. These include the journal articles published, conference proceedings papers, graduate student theses, list of reportable inventions, faculty and graduate student participants, and advanced degrees earned.

2

The strong commitment of our research group toward developing an understanding of the base flow problem is evidenced by the multi-year development and assembly of advanced experimental equipment that will provide well-documented data for the ongoing analytical and computational work of other researchers. Although this final technical report summarizes our recent four-year effort, our research group is continuing to investigate the base flow problem and anticipates further significant contributions to the understanding of the fundamental mechanisms and interactions within high-speed separated flows.

II. SUMMARY OF RESULTS

This section summarizes the results of our ongoing research program concerned with fluid dynamic mechanisms and interactions occurring in high-speed separated flows. In each section below, the most important results are abstracted from the journal articles, conference proceedings papers, and graduate student theses that have been completed under the support of this research grant.

A.1 AN INVESTIGATION OF LDV VELOCITY BIAS CORRECTION TECHNIQUES FOR HIGH-SPEED SEPARATED FLOWS

An experimental study of the effects of velocity bias in single realization laser Doppler velocimetry measurements in a high-speed, separated flow environment is reported. The objective of the study is to determine a post-facto correction method which reduces velocity bias *after* individual realization data have been obtained. Data are presented for five velocity bias correction schemes: inverse velocity magnitude weighting, interarrival time weighting, sample and hold weighting, residence time weighting, and the velocity-data rate correlation method. These data were compared to a reference measurement (saturable detector sampling scheme); the results show that the interarrival time weighting method compares favorably with the reference measurement under the present conditions.

The complete text of this journal paper may be found in Appendix A.1.

A.2 SUPERSONIC BASE FLOW EXPERIMENTS IN THE NEAR WAKE OF A CYLINDRICAL AFTERBODY

The near wake of a circular cylinder aligned with a uniform Mach 2.5 flow has been experimentally investigated in a wind tunnel designed solely for this purpose. Mean static pressure measurements were used to assess the radial dependence of the base pressure and the mean pressure field approaching separation. In addition, two-component laser Doppler velocimeter (LDV) measurements were obtained throughout the near wake including the large separated region

downstream of the base. The primary objective of the research was to gain a better understanding of the complex fluid dynamic processes found in supersonic base flowfields including separation, shear layer development, reattachment along the axis of symmetry, and subsequent development of the wake. Results indicate relatively large reverse velocities and uniform turbulence intensity levels in the separated region. The separated shear layer is characterized by high turbulence levels with a strong peak in the inner, subsonic region which eventually decays through reattachment as the wake develops. A global maximum in turbulent kinetic energy and Reynolds shear stress is found upstream of the reattachment point, which is in contrast to data from the reattachment of a supersonic shear layer onto a solid wall.

The complete text of this journal paper may be found in Appendix A.2.

A.3 SUPERSONIC NEAR-WAKE AFTERBODY BOATTAILING EFFECTS ON AXISYMMETRIC BODIES

An experimental investigation of the near-wake flowfield downstream of a conical boattailed afterbody in supersonic flow is presented. The afterbody investigated is typical of those for conventional boattailed missiles and projectiles in unpowered flight. Flow visualization, mean static pressure measurements, and three-component laser Doppler velocimeter data have been obtained throughout the near wake of the body. The effects of afterbody boattailing on the physics of the near-wake flow are determined by comparing the present data with similar data obtained on a cylindrical afterbody. Results indicate that a net afterbody drag reduction of 21% is achieved with the current boattailed afterbody for a freestream Mach number of 2.46. The shear-layer growth rate, and therefore mass entrainment from the recirculation region behind the base, is shown to be significantly reduced by afterbody boattailing due to the reduction in turbulence levels throughout the near wake as compared to the cylindrical afterbody.

The complete text of this journal paper may be found in Appendix A.3.

A.4   EFFECT OF A RAPID EXPANSION ON THE DEVELOPMENT OF COMPRESSIBLE FREE SHEAR LAYERS

Detailed mean velocity and turbulence data have been obtained with a laser Doppler velocimeter for two axisymmetric shear layers downstream of rapid expansions of different strengths. A comparison of the data in the near field (immediately downstream of separation) and far field (shear layer approaching similarity) is presented, and the fluid dynamic effects of the rapid expansion are ascertained for each regime. In general, the rapid expansion was found to distort the initial mean velocity and turbulence fields in the shear layer in a manner similar to that in rapidly expanded, attached supersonic boundary layers; namely, two distinct regions were found in the initial shear layer: an outer region, where the turbulent fluctuations are quenched primarily due to mean compressibility effects (bulk dilatation), and an inner region, where turbulence activity is magnified due to the interaction of organized large-scale structures in the shear layer with low-speed fluid at the inner edge. With increasing strength of the rapid expansion, the effects in both regions become more pronounced, especially in the inner region, where turbulent fluctuations and mass entrainment rates are greatly magnified. Farther downstream, the turbulence activity of the large-scale eddies remains elevated, due to the rapid expansion, even though the relative distribution of the turbulence energy between the Reynolds stress components (structure of the turbulence) is independent of expansion strength.

The complete text of this journal paper may be found in Appendix A.4.

A.5   STUDY OF SUBSONIC BASE CAVITY FLOWFIELD STRUCTURE USING PARTICLE IMAGE VELOCIMETRY

A new particle image velocimetry system has been used to study the near-wake structure of a two-dimensional base in subsonic flow to determine the fluid dynamic mechanisms of observed drag reduction in the presence of a base cavity. Experiments were done over a range of freestream Mach numbers up to 0.8, including local flowfield velocities over 300 m/s. Effects of the base cavity on the von Kármán vortex street wake were found to be related to the expansion and diffusion of vortices near the cavity, although the effects are of small magnitude and no significant

change in the vortex formation location or path was observed. The base cavity effects are also less significant at higher freestream velocities due to the formation of vortices further downstream from the base. The base cavity drag reduction was found to be mainly due to the displacement of the base surface to a location upstream of the low-pressure wake vortices, with only a slight modification in the vortex street itself.

The complete text of this journal paper may be found in Appendix A.5.

A.6 BASE-BLEED EXPERIMENTS WITH A CYLINDRICAL AFTERBODY IN SUPERSONIC FLOW

The effect of base bleed on the near-wake flowfield of a cylindrical afterbody in a Mach 2.5 flow with a unit Reynolds number of 45×10^6 m^{-1} has been investigated. This study is aimed at better understanding the complex fluid-dynamic interactions occurring in the near wake due to base bleed and is motivated by the lack of detailed velocity and turbulence data in this flowfield. The experimental techniques used include static pressure measurements along the afterbody and base plane, schlieren and shadowgraph photography, and centerline traverses in the near wake using two-component laser Doppler velocimetry. Results indicate relatively uniform radial pressure profiles across the base plane. With increasing bleed flow rate, the average base pressure is found to increase initially, attain a peak value near an injection parameter of I = 0.0148, and then decrease with further increase in I. The optimum bleed condition near I = 0.0148 is also characterized by a weak corner expansion, a minimum value of the free-shear-layer angle, and the near-disappearance of the recirculation region (reverse velocity) along the centerline of the near wake.

The complete text of this journal paper may be found in Appendix A.6.

A.7 VELOCITY AND TURBULENCE MEASUREMENTS IN A SUPERSONIC BASE FLOW WITH MASS BLEED

Two-component laser Doppler velocimetry was used to obtain detailed mean velocity and turbulence measurements in the near wake of a cylindrical afterbody with base bleed in a Mach 2.5

flow. The bleed flow provides at least some of the fluid required for shear layer entrainment and shields the base annulus from the outer shear layer and the primary recirculation region, leading to an increase in base pressure. There is an overall reduction in turbulence levels throughout the base bleed flowfields relative to the near-wake flowfields of blunt-based and boattailed afterbodies. With increasing bleed, the formation of a strong bleed jet shear layer and secondary recirculation region near the base annulus offsets the benefits of base bleed, leading to a drop in the base pressure. The net benefits of base bleed are maximized at the optimum bleed condition, which corresponds to the highest base pressure, the disappearance of the primary recirculation region, and the lowest turbulence levels in the near-wake flowfield. Increased benefits from base bleed could be achieved by injecting the bleed fluid at the lowest possible velocity through the use of larger bleed orifices, porous bases, or bleed orifices located along the outer base annulus.

The complete text of this journal paper may be found in Appendix A.7.

A.8 THE TURBULENCE STRUCTURE OF A REATTACHING AXISYMMETRIC COMPRESSIBLE FREE SHEAR LAYER

The reattachment of a supersonic, axisymmetric shear layer downstream of a blunt-based afterbody is studied. Of primary interest are the effects of the "extra" strain rates, such as bulk compression, concave streamline curvature, and lateral streamline convergence associated with shear layer reattachment on the structure of the turbulence field. Experimental turbulence data obtained throughout the reattachment region with a two-component laser Doppler velocimeter are presented. In general, the axisymmetric compliant boundary reattachment process is shown to be different in character compared to the planar solid wall case. Most notably, significant reductions in the Reynolds stresses occur through the reattachment region due to the dominating effect of lateral streamline convergence as the flow approaches the axis. Similar to the planar solid wall case, however, a reduction in the mean turbulent transport toward the axis in the reattachment region was found, which suggests a radial containment of the large-scale eddies near the axis of symmetry. The reattachment process was also seen to have profound effects on the large-scale

8

structures in the shear layer, primarily through reduced structural organization as indicated by instantaneous shear angle histograms.

The complete text of this journal paper may be found in Appendix A.8.

A.9 TIME-SERIES ANALYSES OF WALL PRESSURE FLUCTUATIONS IN PLUME-INDUCED SEPARATED FLOWFIELDS

The separation shock wave motion in a plume-induced, boundary layer separated flowfield was studied experimentally. The statistical properties of the shock wave motion were determined over the intermittent region using time-series analyses of wall static pressure fluctuation measurements. The standard deviation of the pressure fluctuations, nondimensionalized by the local mean pressure, reached a maximum of 0.22 near the middle of the intermittent region. The ratio of the maximum standard deviation of the pressure fluctuations over the intermittent region to the mean pressure difference across the intermittent region was calculated to be 0.43 for this flowfield. Both of these quantities demonstrate that the unsteady pressure loading caused by the shock wave motion has essentially the same magnitude in plume-induced separated flowfields as in flowfields produced by solid boundary protuberances.

The complete text of this journal paper may be found in Appendix A.9.

A.10 A METHOD FOR SEPARATING SHOCK WAVE MOTION AND TURBULENCE IN LDV MEASUREMENTS

Two-component laser Doppler velocimetry (LDV) measurements were made in a planar, two-dimensional flow containing an unsteady oblique shock wave formed by the convergence of two supersonic streams past a thick plate. High-speed wall pressure measurements locate the shock wave and, consequently, allow separation of the effects of shock wave motion from the turbulence fluctuations in the LDV measurements of the shock-separated free shear layer. In the current flow, isolating the large-scale changes in the position of the shock from the turbulence primarily reduces the experimental scatter rather than significantly changing the shapes or

9

magnitudes of the turbulent stress profiles. Changes in the direction of shock motion do not significantly affect the mean velocity, but do affect the turbulent stresses.

The complete text of this journal paper may be found in Appendix A.10.

A.11 VELOCITY MEASUREMENTS IN A SHOCK-SEPARATED FREE SHEAR LAYER

Two-component laser Doppler velocimetry (LDV) measurements were made in a planar, shock-separated free shear layer formed by the convergence of two supersonic streams past a thick plate. High-speed wall pressure measurements locate the unsteady shock wave formed by this interaction and, consequently, allow separation of the effects of shock motion from the turbulence fluctuations in the velocity measurements of the shear layer. Shock-induced separation dramatically increases the normal stresses and shear stress. The shock-separated shear layer displays a positive shear stress region between separation and reattachment. Reattachment produces a shift in turbulent kinetic energy from the streamwise component to the transverse component. The region of shock motion has a relatively constant width irrespective of distance from the wall.

The complete text of this journal paper may be found in Appendix A.11.

A.12 CONDITIONAL ANALYSIS OF WALL PRESSURE FLUCTUATION MEASUREMENTS MADE IN PLUME-INDUCED SEPARATED FLOWFIELDS

The separation process in plume-induced, boundary layer separated flowfields was found to be unsteady. Two in-situ, fast-response pressure transducers were used to make individually and simultaneously sampled wall pressure fluctuation measurements over the intermittent region of separation shock wave motion. A conditional analysis technique was applied to the pressure-time histories, and statistical methods were then used to analyze the period, frequency, and velocity ensembles of the shock motion. The mean frequencies of this motion ranged between 1300 and 1500 Hz over the intermittent region, and the most probable shock wave frequencies occurred between 1 and 4 kHz over this region. The maximum zero-crossing frequency of the shock wave

10

motion was approximately 500-600 Hz. The mean (approximately 3.5% of the freestream velocity) and most probable (approximately 6% of the freestream velocity) shock wave velocities in either direction were found to be essentially constant over the intermittent region. These results are compared to those for shock wave–boundary layer interactions caused by solid protruberances.

The complete text of this journal paper may be found in Appendix A.12.

A.13 SUPERSONIC BASE FLOW EXPERIMENTS IN THE NEAR-WAKE OF A CYLINDRICAL AFTERBODY

The near-wake of a circular cylinder aligned with a uniform Mach 2.5 flow has been experimentally investigated in a wind tunnel designed solely for this purpose. Mean static pressure measurements were used to assess the radial dependence of the base pressure and the mean pressure field approaching separation. In addition, two-component laser Doppler velocimeter (LDV) measurements were obtained throughout the near-wake including the large separated region downstream of the base. The primary objective of the research was to gain a better understanding of the complex fluid dynamic processes found in supersonic base flowfields including separation, shear layer development, reattachment along the axis of symmetry, and subsequent development of the wake. Results indicate relatively large reverse velocities and uniform turbulence intensity levels in the separated region. The separated shear layer is characterized by high turbulence levels with a strong peak in the inner, subsonic region which eventually decays through reattachment as the wake develops. A global maximum in turbulent kinetic energy and Reynolds shear stress is found upstream of the reattachment point which is in contrast to data from the reattachment of a supersonic shear layer onto a solid wall.

The complete text of this conference paper may be found in Appendix A.13.

A.14 STUDY OF THE NEAR-WAKE STRUCTURE OF A SUBSONIC BASE CAVITY FLOWFIELD USING PIV

A new particle image velocimetry (PIV) system has been used to study the near-wake structure of a two-dimensional base in subsonic flow in order to determine the fluid dynamic

mechanisms of observed drag reduction in the presence of a base cavity. Experiments were done over a range of freestream Mach numbers up to 0.8, including local flowfield velocities over 300 m/s. Effects of the base cavity on the von Kármán vortex street wake were found to be related to the expansion and diffusion of vortices near the cavity, although the effects are of small magnitude and no significant change in the vortex formation location or path was observed. The base cavity effects are also less significant at higher freestream velocities due to the formation of vortices further downstream from the base. The base cavity drag reduction was found to be mainly due to the displacement of the base surface to a location upstream of the low-pressure wake vortices, with only a slight modification in the vortex street itself.

The complete text of this conference paper may be found in Appendix A.14.

A.15 EFFECTS OF AFTERBODY BOATTAILING ON THE NEAR-WAKE OF AXISYMMETRIC BODIES IN SUPERSONIC FLOW

An experimental investigation of the near-wake flowfield downstream of a conical boattailed afterbody in supersonic flow is presented. The afterbody investigated is typical of those for conventional boattailed missiles and projectiles in unpowered flight. Flow visualization, mean static pressure measurements, and three-component laser Doppler velocimeter data have been obtained throughout the near-wake of the body. The effects of afterbody boattailing on the physics of the near-wake flow are determined by comparing the present data with similar data obtained on a cylindrical afterbody. Results indicate that a net afterbody drag reduction of 21% is achieved with the current boattailed afterbody for an approach Mach number of 2.46. The shear layer growth rate, and therefore mass entrainment from the recirculation region behind the base, is shown to be significantly reduced by afterbody boattailing due to the reduction in turbulence levels throughout the near-wake as compared to the cylindrical afterbody.

The complete text of this conference paper may be found in Appendix A.15.

A.16 EFFECT OF A RAPID EXPANSION ON THE DEVELOPMENT OF COMPRESSIBLE FREE SHEAR LAYERS

Detailed mean velocity and turbulence data have been obtained with a laser Doppler velocimeter for two axisymmetric shear layers downstream of rapid expansions of different strengths. A comparison of the data in the near-field (immediately downstream of separation) and far-field (shear layer approaching self-similarity) is presented, and the fluid dynamic effects of the rapid expansion are ascertained for each regime. In general, the rapid expansion was found to distort the initial mean velocity and turbulence fields in the shear layer such that two distinct regions were evident: an outer region where the turbulent fluctuations are quenched by the expansion, and an inner region where turbulence levels are magnified by the expansion. For the streamwise Reynolds normal stress and primary Reynolds shear stress, the magnitude of the peak turbulence levels increased with increasing strength of the expansion; the transverse normal stress field, however, was only mildly affected by the expansion. Further downstream after the shear layer mean velocity distributions become self-similar, elevated turbulence levels for the more strongly expanded case persist although the relative distribution of turbulence energy between the Reynolds stress components appears unaffected by the strength of the rapid expansion.

The complete text of this conference paper may be found in Appendix A.16.

A.17 BASE BLEED EXPERIMENTS WITH A CYLINDRICAL AFTERBODY IN SUPERSONIC FLOW

The effect of base bleed on the near-wake flowfield of a cylindrical afterbody aligned with a Mach 2.5 flow has been investigated. This study is aimed at better understanding the complex fluid dynamic interactions occurring in the near-wake due to base bleed and is motivated by the lack of detailed velocity and turbulence data in this flowfield. The experimental techniques used include static pressure measurements along the afterbody and the base plane, schlieren and shadowgraph photography, and centerline traverses using two-component laser Doppler velocimetry (LDV). Results indicate relatively uniform radial pressure profiles across the base plane. With increasing bleed flow rate (quantified by the injection parameter, I), the average base

13

pressure is found to increase initially, attain a peak value near I = 0.0148, and then decrease with further increase in I. The optimum bleed condition near I = 0.0148 is also characterized by a weak corner expansion, a minimum value of the free shear layer angle, and the near-disappearance of the recirculation region (reverse velocity) along the centerline of the near-wake.

The complete text of this conference paper may be found in Appendix A.17.

A.18 RECENT PROGRESS ON HIGH-SPEED SEPARATED BASE FLOWS

Recent work in the area of high-speed separated flows is reviewed with particular emphasis on problems related to missile and projectile afterbody and base flows. A brief summary is first given of the current state-of-the-art in base flow numerical predictions and previous experimental studies. This is followed by discussions of our recent experimental work in this area. The particular experiments described are: detailed mean velocity and turbulence measurements for a cylindrical afterbody in Mach 2.5 flow, a similar study for a five degree boattailed afterbody that explains the associated drag reduction effects, initial pressure and velocity measurements quantifying the effects of base bleed in supersonic base flow, a particle image velocimetry study that has delineated the mechanisms of base drag reduction for a planar bluff body with a base cavity in subsonic flow, and Mie scattering visualizations of large-scale turbulent structures in the shear layers and trailing wake of a two-dimensional, supersonic base flow.

The complete text of this conference paper may be found in Appendix A.18.

A.19 THE TURBULENCE STRUCTURE OF A REATTACHING AXISYMMETRIC SUPERSONIC FREE SHEAR LAYER

The reattachment of a supersonic, axisymmetric shear layer downstream of a blunt based afterbody is studied. Of primary interest are the effects of the "extra" strain rates, such as bulk compression, concave streamline curvature, and lateral streamline convergence associated with shear layer reattachment, on the structure of the turbulence field. Experimental turbulence data obtained throughout the reattachment region with a two-component laser Doppler velocimeter are presented. In general, the compliant boundary reattachment process is shown to be different in

14

character compared to the solid wall case. Most notably, significant reductions in the Reynolds stresses occur through the reattachment region due to the dominating effect of lateral streamline convergence as the flow approaches the axis. Similar to the solid wall case, however, a reduction in the mean turbulent transport toward the axis in the reattachment region was found, which suggests a radial containment of the large scale eddies near the axis of symmetry. The reattachment process was also seen to have profound effects on the large scale structures in the shear layer primarily through reduced structural organization as indicated by the instantaneous velocity fluctuations.

The complete text of this conference paper may be found in Appendix A.19.

A.20 VELOCITY AND TURBULENCE MEASUREMENTS IN A SUPERSONIC BASE FLOW WITH MASS BLEED

Two-component laser Doppler velocimetry was used to obtain detailed mean velocity and turbulence measurements in the near-wake of a cylindrical afterbody with base bleed in a Mach 2.5 flow. The bleed flow provides at least some of the fluid required for shear layer entrainment and shields the base annulus from the outer shear layer and the primary recirculation region, leading to an increase in base pressure. There is an overall reduction in turbulence levels throughout the base bleed flowfields relative to the near-wake flowfields of blunt-based and boattailed afterbodies. With increasing bleed, the formation of a strong bleed jet shear layer and secondary recirculation region near the base annulus offsets the benefits of base bleed, leading to a drop in the base pressure. The net benefits of base bleed are maximized at the optimum bleed condition, which corresponds to the highest base pressure, the disappearance of the primary recirculation region, and the lowest turbulence levels in the near-wake flowfield. Increased benefits from base bleed could be achieved by injecting the bleed fluid at the lowest possible velocity through the use of larger bleed orifices, porous bases, or bleed orifices located along the outer base annulus.

The complete text of this conference paper may be found in Appendix A.20.

A.21 A METHOD FOR SEPARATING SHOCK WAVE MOTION AND TURBULENCE IN LDV MEASUREMENTS

Two-component laser Doppler velocimetry (LDV) measurements were made in a planar, two-dimensional flow containing an unsteady oblique shock wave formed by the convergence of two supersonic streams past a thick plate. Wall pressure measurements have been used to locate the shock wave and consequently separate the shock wave motion from the turbulence fluctuations in the LDV measurements of the shock-separated free shear layer. The primary result of isolating the large-scale changes in the position of the shock from the turbulence is a reduction in the experimental scatter rather than significant changes in the shape or magnitudes of the turbulent stress profiles. The overall effects of the changes in shock position on the turbulence were found to be small and do not significantly change the overall trends in the turbulence data. Velocity data were also analyzed to determine the effect of changes in the direction of shock motion rather than shock position. Shock motion direction was found to have a greater effect on the turbulence measurements than shock position. Like changes in the shock position, changes in the direction of shock motion did not significantly change the mean velocity. However, changes in the direction of the shock may either increase or decrease the turbulent stresses depending on the portion of the shear layer in question.

The complete text of this conference paper may be found in Appendix A.21.

A.22 VELOCITY MEASUREMENTS IN A SHOCK-SEPARATED FREE SHEAR LAYER

Two-component laser Doppler velocimetry (LDV) measurements were made in a planar, shock-separated free shear layer formed by the convergence of two supersonic streams past a thick plate. High-speed wall pressure measurements locate the unsteady shock wave formed by this interaction and, consequently, allow separation of the effects of shock motion from the turbulence fluctuations in the velocity measurements of the shear layer. Shock-induced separation dramatically increases the normal stresses and shear stress. The shock-separated shear layer displays a positive shear stress region between separation and reattachment. Reattachment

produces a shift in turbulent kinetic energy from the streamwise component to the transverse component. The region of shock motion has a relatively constant width irrespective of distance from the wall.

The complete text of this conference paper may be found in Appendix A.22.

A.23 AN EXPERIMENTAL INVESTIGATION OF SUPERSONIC AXISYMMETRIC BASE FLOWS INCLUDING THE EFFECTS OF AFTERBODY BOATTAILING

An experimental investigation of the near-wake flowfield downstream of blunt-based axisymmetric bodies in supersonic flow has been conducted. Using a blowdown-type wind tunnel designed specifically for this purpose, experiments were conducted at a nominal approach Mach number of 2.5 and a unit Reynolds number of 51 (10^6) per meter. Two different axisymmetric afterbodies were examined in the study: a circular cylinder was used as a baseline configuration, and a conical boattailed afterbody with a boattail angle of five degrees and a boattail length of one afterbody radius was used to investigate the effects of afterbody boattailing on the fluid dynamic processes in the near-wake. Neither afterbody contained a central jet so that the base flowfield in unpowered, supersonic flight was simulated. The primary objective of the research program was to enhance the understanding of the fluid dynamic processes inherent to axisymmetric base flows by obtaining and analyzing detailed, non-intrusive experimental data including flow visualization photographs, static pressure measurements, and mean velocity and turbulence data throughout the near-wake. Of special significance in the current research is the detailed turbulence information obtained with laser Doppler velocimetry (LDV) since these data are virtually nonexistent in supersonic base flows and provide new insight into the physics of these complex flows. In addition, the present data form a substantial data base which can be used to advance and improve theoretical and numerical base flow modeling techniques.

The static pressure measurements on the base and afterbody of each model indicate a relatively constant pressure across the base with the addition of the boattail resulting in a decrease in the base drag coefficient of 16% from the baseline cylindrical afterbody. The net afterbody drag

coefficient (boattail + base contributions) was reduced by 21% which shows the usefulness of afterbody boattailing as a practical method to reduce afterbody drag in supersonic, axisymmetric flow. The mean velocity and turbulence fields in the near-wake of each afterbody were investigated with LDV. In general, the near-wake flowfield can be characterized by large turbulence levels in the separated shear layer, relatively large reverse velocities in the recirculation region, and gradual recompression/realignment processes as the shear layer converges on the axis of symmetry. The shear layer development was found to be dependent on the conditions immediately downstream of the base corner separation point (upstream history effect). Furthermore, the centered expansion at the base corner reduced the turbulence levels in the outer region of the shear layer relative to the approach boundary layer but enhanced the mixing and entrainment along the fluid-fluid interface between the shear layer and the recirculating region which results in large turbulence levels along the inner edge of the shear layer. The shear layer growth rate is initially large due to substantial mass entrainment from the recirculation region near the inner edge, but further downstream, a self-similar state is reached where growth rates are significantly reduced. In general, the effects of afterbody boattailing on the near-wake flowfield include a weaker expansion at the base corner separation point (less distortion of the shear layer and reduced turbulence production near the inner edge), reduced turbulence intensity and Reynolds shear stress levels throughout the near-wake (reduced mass entrainment along the length of the shear layer resulting in a higher base pressure), and a mean velocity field which is qualitatively similar to that of the cylindrical afterbody.

The complete manuscript of this thesis is available from the authors of this report.

A.24 AN EXPERIMENTAL INVESTIGATION OF UNSTEADY SEPARATION SHOCK WAVE MOTION IN A PLUME-INDUCED, SEPARATED FLOWFIELD

An experimental investigation of the unsteady separation shock wave motion in plume-induced, boundary layer separated (PIBLS) flowfields has been conducted. The PIBLS flowfields were created in a blowdown-type wind tunnel designed specifically to produce PIBLS in a planar,

18

two-stream, supersonic flow. In this unique wind tunnel, separation of the freestream boundary layer upstream of the base plane was accomplished by utilizing an angle-induced separation geometry in the wind tunnel design in addition to operating the wind tunnel at jet-to-freestream static pressure ratios (JSPRs) greater than unity. In essence, the wind tunnel design consisted of a Mach 1.5 inner-jet flow angled at 40 degrees with respect to a Mach 2.5 freestream flow in the presence of a 0.5-inch thick base height. By throttling the stagnation pressure of the inner-jet flow, PIBLS flowfields, with nominal separation point locations ranging from two (JSPR≈1.7) to six (JSPR≈2.3) or more boundary layer thicknesses upstream of the base plane, were produced in the wind tunnel. The separation process associated with all of these PIBLS flowfields was observed by flow visualization techniques to be unsteady, and the separation shock wave that accompanied the separation process was found to exhibit large-scale (on the order of the incoming boundary layer thickness) motion in the streamwise direction.

The primary objective of the current research program was to understand the unsteady characteristics of the separation shock wave motion present in the PIBLS flowfields by obtaining and analyzing detailed, non-intrusive experimental data including flow visualization photographs, surface flow visualization patterns, mean static pressure measurements, and instantaneous pressure fluctuation measurements throughout the region of shock wave motion (called the intermittent region). Since the vast majority of the statistical properties of the shock wave motion were computed from the fast-response pressure transducer measurements, the instantaneous pressure fluctuation measurements were of primary importance in the study. In recent years, similar measurements have been used to characterize the unsteady separation shock wave motion in shock wave/boundary layer interactions (SWBLIs) produced by solid boundary protuberances (i.e., compression ramps, circular cylinders, sharp- and blunt-edged fins, etc.). However, such data are virtually nonexistent in a plume-induced interaction and, therefore, the current data are quite unique.

From standard time series and conditional analysis methods applied to the pressure fluctuation measurements, the statistical properties of the shock wave motion were determined over

the intermittent region. In general, most (70% to 80%) of the energy contained in the pressure fluctuations caused by the shock wave motion was distributed over the frequency range below 1 kHz, the mean frequency of the shock wave motion ranged between 1.3-1.5 kHz, and the most probable shock wave frequency occurred between approximately 1-4 kHz over the intermittent region. The mean shock wave velocities, when normalized by the freestream velocity, were found to be 0.034-0.035 over the intermittent region in the PIBLS flowfields. In general, the length scale of the intermittent region increased as the JSPR increased, varying from 0.32-0.37 inches (2.6δ to 3.0δ) at a JSPR of 1.95 to 0.68-0.69 inches (5.4δ to 5.5δ) at a JSPR of 2.41. The maximum zero-crossing frequency (the average number of shock wave crossings per second) of the shock wave motion was approximately 500-600 Hz, depending upon the JSPR, and occurred near the middle of the intermittent region.

The shock wave motion was found to be responsible for producing large pressure fluctuations over the intermittent region in these PIBLS flowfields. The standard deviation of the pressure fluctuations, when nondimensionalized by the local mean pressure, reached a maximum value of 0.22 near the middle of the intermittent region. The strength of the unsteady shock wave motion, determined as the ratio of the maximum standard deviation of the pressure fluctuations over the intermittent region to the mean pressure difference across the intermittent region, was calculated to be 0.43 for the current PIBLS flowfields. Both of these quantities demonstrate that the unsteady pressure loading caused by the shock wave motion has essentially the same magnitude in plume-induced separated flowfields as in SWBLI flowfields produced by solid boundary protuberances.

The complete manuscript of this thesis is available from the authors of this report.

A.25 AN EXPERIMENTAL INVESTIGATION OF THE EFFECTS OF BASE BLEED IN AXISYMMETRIC SUPERSONIC FLOW

Base bleed is a technique wherein a small quantity of fluid is injected into the base region of a projectile to reduce the base drag. The effects of base bleed on the near-wake flowfield of a

cylindrical afterbody in a Mach 2.5 flow have been investigated in the present study. This experimental study is aimed at better understanding the complex fluid dynamic interactions occurring in the near-wake due to base bleed and is motivated by the lack of detailed velocity and turbulence data in this flowfield. The experimental techniques used include static pressure measurements, schlieren and shadowgraph photography, and two-component laser Doppler velocimetry (LDV). The comprehensive LDV mean velocity and turbulence measurements obtained during this study provide valuable insight into the physics of the base bleed mechanism and constitute a benchmark data set to aid analytical and computational efforts in modeling and predicting supersonic base flows.

Static pressure measurements show that with increasing bleed flow rate, the average base pressure increases initially, attains a peak value near an injection parameter of $I = 0.0148$, and then decreases with further increase in I. The peak base pressure ratio at the optimum bleed condition is 18.5% higher than the blunt base case and 5.7% higher than for a 5 degree boattailed afterbody. Axial LDV traverses show peaks in turbulent kinetic energy along the centerline at the forward and rear stagnation point locations. Centerline measurements also indicate the near-disappearance of the primary recirculation region near the optimum bleed condition. Detailed mean velocity and turbulence data were obtained in the entire near-wake flowfield for three different bleed cases corresponding to low bleed, slightly pre-optimal bleed, and slightly post-optimal bleed conditions. These measurements indicate that the bleed flow provides at least some of the fluid required for shear layer entrainment and shields the base annulus from the outer shear layer and the primary recirculation region, leading to an increase in base pressure. There is an overall reduction in turbulence levels throughout the base bleed flowfields relative to the near-wake flowfields of blunt-based and boattailed afterbodies. With increasing bleed, the formation of a strong bleed jet shear layer and secondary recirculation region near the base annulus offsets the benefits of base bleed, leading to a drop in the base pressure. At all bleed conditions, the Reynolds normal stress distribution is highly anisotropic with the axial component dominating the near-wake turbulence field. The net benefits of base bleed are maximized at the optimum bleed condition, which

corresponds to the highest base pressure, the disappearance of the primary recirculation region, and the lowest turbulence and entrainment levels in the near-wake flowfield.

The complete manuscript of this thesis is available from the authors of this report.

A.26 CONDITIONALLY ANALYZED MEAN VELOCITY AND TURBULENCE MEASUREMENTS IN A PLUME-INDUCED BOUNDARY LAYER SEPARATED FLOWFIELD

A supersonic plume-induced boundary layer separated (PIBLS) flowfield occurs when an underexpanded exhaust plume obstructs the flow around a rocket causing an oblique shock wave to form on the afterbody. The shock oscillates randomly in the streamwise direction causing an unsteady boundary layer separation that complicates prediction and measurement of PIBLS flowfields. This study provides the first turbulence measurements in a PIBLS flowfield and, consequently, the first benchmark data for evaluating future computational models for such flows.

Conditionally analyzed two-component laser Doppler velocimetry (LDV) measurements were made in a planar, two-dimensional PIBLS flow containing an unsteady oblique shock wave formed by the convergence of two supersonic streams past a thick plate. High-speed wall pressure measurements were used to locate the shock wave and, consequently, allow separation of the effects of shock wave motion from the turbulence fluctuations in the velocity measurements of a shock-separated free shear layer. It was found that isolating the large-scale changes in the shock position from the turbulence reduces the experimental scatter rather than substantially changing the shapes or magnitudes of the turbulent stress profiles. Changes in shock motion direction, however, do significantly alter the turbulent stresses. This is the first direct evidence of the effects of changes in shock wave position on turbulence amplification.

The shock-induced separation process was found to dramatically increase the streamwise and transverse Reynolds normal stresses (which both peak near reattachment), the primary shear stress, and the normal stress anisotropy. The shock-separated shear layer consists of only a single layer with a large initial growth rate followed by a much smaller growth rate, instead of the two layers found in rapidly expanded shear layers. The large-scale structures in the shock-separated

22

shear layer span the shear layer width and exhibit a uniform transverse size. These structures display positive and negative shear stresses on their upper and lower edges, respectively, and are greatly altered by reattachment. All turbulent stresses decrease and the normal stress isotropy increases in the developing wake.

The complete manuscript of this thesis is available from the authors of this report.

III. LIST OF PUBLICATIONS

A substantial number of journal articles, conference proceedings papers, and graduate student theses have reported the results of this research effort. The following is a list of those publications.

A. JOURNAL ARTICLES

Herrin, J. L. and Dutton, J. C., "An Investigation of LDV Velocity Bias Correction Techniques for High-Speed Separated Flows," *Experiments in Fluids*, Vol. 15, No. 4/5, pp. 354-363, 1993.

Herrin, J. L. and Dutton, J. C., "Supersonic Base Flow Experiments in the Near-Wake of a Cylindrical Afterbody," *AIAA Journal*, Vol. 32, No. 1, pp. 77-83, Jan. 1994.

Herrin, J. L. and Dutton, J. C., "Supersonic Near-Wake Afterbody Boattailing Effects on Axisymmetric Bodies," *Journal of Spacecraft and Rockets*, Vol. 31, No. 6, pp. 1021-1028, Nov.-Dec. 1994.

Herrin, J. L. and Dutton, J. C., "Effect of a Rapid Expansion on the Development of Compressible Free Shear Layers," *Physics of Fluids*, Vol. 7, No. 1, pp. 159-171, Jan. 1995.

Molezzi, M. J. and Dutton, J. C., "Study of Subsonic Base Cavity Flowfield Structure Using Particle Image Velocimetry," *AIAA Journal*, Vol. 33, No. 2, pp. 201-209, Feb. 1995.

Mathur, T. and Dutton, J. C., "Base-Bleed Experiments with a Cylindrical Afterbody in Supersonic Flow," *Journal of Spacecraft and Rockets*, Vol. 33, No. 1, pp. 30-37, Jan.-Feb. 1996.

Mathur, T. and Dutton, J. C., "Velocity and Turbulence Measurements in a Supersonic Base Flow with Mass Bleed," *AIAA Journal*, Vol. 34, No. 6, pp. 1153-1159, June 1996.

Herrin, J. L. and Dutton, J. C., "The Turbulence Structure of a Reattaching Axisymmetric Compressible Free Shear Layer," *Physics of Fluids*, Vol. 9, No. 11, pp. 3502-3512, Nov. 1997.

Shaw, R. J., Dutton, J. C., and Addy, A. L., "Time-Series Analyses of Wall Pressure Fluctuations in Plume-Induced Separated Flowfields," accepted for publication in *AIAA Journal*.

Palko, C. W. and Dutton, J. C., "A Method for Separating Shock Wave Motion and Turbulence in LDV Measurements," accepted for publication in *Experiments in Fluids*.

Palko, C. W. and Dutton, J. C., "Velocity Measurements in a Shock-Separated Free Shear Layer," submitted for publication in *AIAA Journal*.

Shaw, R. J., Dutton, J. C., and Addy, A. L., "Conditional Analysis of Wall Pressure Fluctuation Measurements Made in Plume-Induced Separated Flowfields," submitted for publication in *AIAA Journal*.

B. CONFERENCE PROCEEDINGS PAPERS

Herrin, J. L. and Dutton, J. C., "Supersonic Base Flow Experiments in the Near-Wake of a Cylindrical Afterbody," AIAA Paper No. 93-2924, presented at the *24th AIAA Fluid Dynamics Conference*, Orlando, Florida, July 1993.

Molezzi, M. J. and Dutton, J. C., "Study of the Near-Wake Structure of a Subsonic Base Cavity Flowfield Using PIV," AIAA Paper No. 93-3040, presented at the *24th AIAA Fluid Dynamics Conference*, Orlando, Florida, July 1993.

Herrin, J. L. and Dutton, J. C., "Effects of Afterbody Boattailing on the Near-Wake of Axisymmetric Bodies in Supersonic Flow," AIAA Paper No. 94-0029, presented at the *32nd AIAA Aerospace Sciences Meeting*, Reno, Nevada, Jan. 1994.

Herrin, J. L. and Dutton, J. C., "Effect of a Rapid Expansion on the Development of Compressible Free Shear Layers," AIAA Paper No. 94-2229, presented at the *25th AIAA Fluid Dynamics Conference*, Colorado Springs, Colorado, June 1994.

Mathur, T. and Dutton, J. C. "Base Bleed Experiments with a Cylindrical Afterbody in Supersonic Flow," AIAA Paper No. 95-0062, presented at the *33rd AIAA Aerospace Sciences Meeting*, Reno, Nevada, Jan. 1995.

Dutton, J. C., Herrin, J. L., Molezzi, M. J., Mathur, T., and Smith, K. M., "Recent Progress on High-Speed Separated Base Flows," AIAA Paper No. 95-0472, presented at the *33rd AIAA Aerospace Sciences Meeting*, Reno, Nevada, Jan. 1995.

Herrin, J. L. and Dutton, J. C., "The Turbulence Structure of a Reattaching Axisymmetric Supersonic Free Shear Layer," AIAA Paper No. 95-2250, presented at the *26th AIAA Fluid Dynamics Conference*, San Diego, California, June 1995.

Mathur, T. and Dutton, J. C. "Velocity and Turbulence Measurements in a Supersonic Base Flow with Mass Bleed," AIAA Paper No. 96-0456, presented at the *34th AIAA Aerospace Sciences Meeting*, Reno, Nevada, Jan. 1996.

Palko, C. W. and Dutton, J. C., "A Method for Separating Shock Wave Motion and Turbulence in LDV Measurements," AIAA Paper No. 97-1919, presented at the *28th AIAA Fluid Dynamics Conference*, Snowmass, Colorado, June-July 1997.

Palko, C. W. and Dutton, J. C., "Velocity Measurements in a Shock-Separated Free Shear Layer," AIAA Paper No. 98-0698, presented at the *36th AIAA Aerospace Sciences Meeting*, Reno, Nevada, Jan. 1998.

C. THESES

Herrin, J. L., "An Experimental Investigation of Supersonic Axisymmetric Base Flows Including the Effects of Afterbody Boattailing," Ph.D. Thesis, Department of Mechanical and Industrial Engineering, University of Illinois at Urbana-Champaign, July 1993.

Shaw, R. J. "An Experimental Investigation of Unsteady Separation Shock Wave Motion in a Plume-Induced, Separated Flowfield," Ph.D. Thesis, Department of Mechanical and Industrial Engineering, University of Illinois at Urbana-Champaign, Aug. 1995.

Mathur, T., "An Experimental Investigation of the Effects of Base Bleed in Axisymmetric Supersonic Flow," Ph.D. Thesis, Department of Mechanical and Industrial Engineering, University of Illinois at Urbana-Champaign, July 1996.

Palko, C. W., "Conditionally Analyzed Mean Velocity and Turbulence Measurements in a Plume-Induced Boundary Layer Separated Flowfield," Ph.D. Thesis, Department of Mechanical and Industrial Engineering, University of Illinois at Urbana-Champaign, Oct. 1997.

IV. LIST OF REPORTABLE INVENTIONS

There were no inventions developed under the support of this grant.

V. LIST OF PARTICIPATING SCIENTIFIC PERSONNEL
AND ADVANCED DEGREES EARNED

Following are lists of the faculty and graduate student scientific personnel who have contributed to this research effort and the graduate degrees that have been earned in conjunction with this project.

A. FACULTY

J. C. Dutton
Principal Investigator
Professor of Mechanical Engineering

A. L. Addy
Co-Principal Investigator
Professor and Head of Mechanical Engineering

B. GRADUATE STUDENTS

C. J. Bourdon
B.S. 1996
M.S. Candidate

T. Mathur
M.S. 1990
Ph.D. 1996

C. W. Palko
B.S. 1993
Ph.D. 1997

J. L. Herrin
M.S. 1991
Ph.D. 1993

M. G. Olsen
M.S. 1995
Ph.D. Candidate

R. J. Shaw
M.S. 1986
Ph.D. 1995

C. ADVANCED DEGREES EARNED

J. L. Herrin
Ph.D., July 1993

T. Mathur
Ph.D., July 1996

R. J. Shaw
Ph.D., August 1995

C. W. Palko
Ph.D., October 1997

APPENDIX A.1

AN INVESTIGATION OF LDV VELOCITY BIAS CORRECTION TECHNIQUES FOR HIGH-SPEED SEPARATED FLOWS

by

J. L. Herrin and J. C. Dutton

An investigation of LDV velocity bias correction techniques for high-speed separated flows

J. L. Herrin, J. C. Dutton

Department of Mechanical and Industrial Engineering, University of Illinois at Urbana-Champaign, Urbana, IL 61801, USA

Abstract. An experimental study of the effects of velocity bias in single realization laser Doppler velocimetry measurements in a high-speed, separated flow environment is reported. The objective of the study is to determine a post-facto correction method which reduces velocity bias *after* individual realization data have been obtained. Data are presented for five velocity bias correction schemes: inverse velocity magnitude weighting, interarrival time weighting, sample and hold weighting, residence time weighting, and the velocity-data rate correlation method. These data were compared to a reference measurement (saturable detector sampling scheme); the results show that the interarrival time weighting method compares favorably with the reference measurement under the present conditions.

1 Introduction

Laser Doppler velocimetry (LDV) has become a popular experimental tool to measure the velocity filed in a variety of fluid dynamic environments. Due to its non-intrusive nature and ability to discriminate flow direction, LDV is well-suited for applications involving large regions of flow separation. The current study is part of an experimental program investigating the separated, near-wake flowfield behind a body of revolution immersed in a supersonic freestream. Characterizing the mean and turbulent velocity fields downstream of the base surface with a two-component LDV system, including the large separated region immediately downstream of the base, has been the focus of the research; hence, a detailed investigation of the accuracy of LDV measurements in this flow environment is necessary. The present paper describes an experimental study which examines the effects of velocity bias on LDV data in high-speed, separated flows and compares traditional methods to correct for this bias.

When individual realization LDV measurements are made in turbulent flows, a velocity bias caused by the correlation between the data sampling process and the magnitude of the instantaneous velocity exists. McLaughlin and Tiederman (1973) first recognized this bias and

Correspondence to: J. C. Dutton

showed that its magnitude was proportional to the square of the local turbulence intensity. This result can be used in a qualitative sense to determine if and when the effects of velocity bias are appreciable. In supersonic base flows, turbulence intensities are generally large in the separated shear layer, especially near the point of reattachment (Amatucci et al. 1992). The magnitude of velocity bias present in individual realization data taken in this region can, therefore, be significant.

Several techniques to eliminate the velocity bias have been proposed, and most fall into two general categories: post-facto correction methods and sampling methods. Techniques in the former category generate correction factors for the individual realizations that are used in computing the mean flowfield quantities. The following equation is used to calculate the ensemble-averaged value of the arbitary velocity statistic x:

$$\langle x \rangle = \frac{\sum_i x_i w_i}{\sum_i w_i} \tag{1}$$

where w is a weighting factor and the summations are taken over the entire ensemble ($w_i \equiv 1$ corresponds to the totally biased, individual realization case). Several forms of the weighting factor have been proposed including the inverse velocity magnitude (McLaughlin and Tiederman 1973), particle interarrival time (Hoesel and Rodi 1977), and particle residence time (Buchhave and George 1978). The second category of techniques to eliminate velocity bias are methods which attempt to reconstruct a time series with the same statistics as that of the turbulent flow. Commonly used methods which fit into this category include the controlled processor (Erdmann and Tropea 1981), saturable detector (Edwards 1978), and sample and hold processor (Dimotakis 1976). While the controlled processor and saturable detector are sampling techniques which utilize only a fraction of the LDV data available, the sample and hold processor reconstructs a time series

using the entire data ensemble which makes it attractive for high-speed flow applications with limited wind tunnel run times.

The task of deciding which method best eliminates the effects of velocity bias can be difficult considering the several conflicting recommendations in the literature. This is especially true in high-speed flow applications where only limited experimental verification of velocity bias effects exists (e.g., Petrie et al. 1988). Differences between high-speed and low-speed flows which can have significant effects on velocity bias include flow time scales, seed particle concentrations, and compressibility effects. In addition, another important constraint on choosing a velocity bias correction method for high-speed flows can be the limited run time of conventional blowdown-type wind tunnels. Typical wind tunnel run times and relatively sparse seed densities generally preclude the use of sampling methods to correct for velocity bias in high-speed flows. Hence, a post-facto correction method (Eq. 1), which can be used with the entire data ensemble to reduce the effects of velocity bias *after* data acquisition has been completed, is desired.

In the present study, an objective comparison of the different correction methods for velocity bias is made. The main motivation of the research is to determine experimentally which post-facto correction methods are best suited for high-speed, separated flow applications with typical seed concentrations and turbulence intensity levels. In addition, obtaining experimental data concerning the effects of velocity bias on mean velocities, turbulence intensities, and the Reynolds shear stress in high-speed, separated flow will add to the current understanding of the problem in this flow environment.

2 Experimental apparatus

The experiments described herein were conducted in a blowdown-type wind tunnel located in the Gas Dynamics Laboratory at the University of Illinois. As previously mentioned, this wind tunnel is being used to study the supersonic, axisymmetric base flow problem. A schematic diagram showing the general features of the near-wake behind a circular cylinder (verified by schlieren photography in the present case) is shown in Fig. 1. As the turbulent boundary layer separates from the afterbody, a free shear layer is formed which separates the outer inviscid flow from the recirculation region immediately behind the base. The shear layer undergoes a recompression-realignment process to satisfy the symmetry condition, and a wake develops downstream of the rear stagnation point.

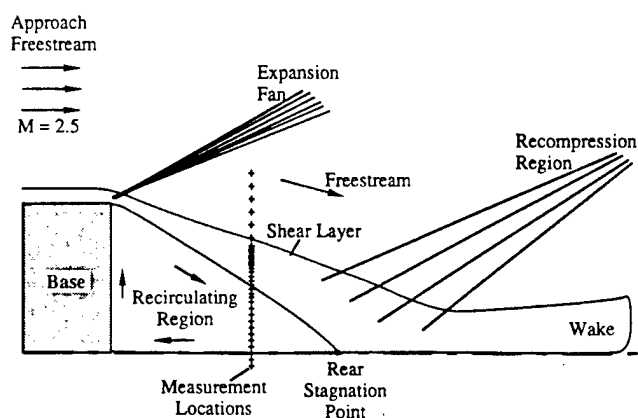Two-component LDV data have been acquired throughout the near-wake; however, the detailed velocity bias study presented herein will consider only one representative traverse across the shear layer. The location of the traverse (shown in Fig. 1) is at a downstream distance of $x/R = 1.6$ from the base plane where R is the radius of the afterbody ($R = 31.75$ mm). The LDV data obtained at this location contain several attributes commonly found in high-speed separated flows, including large variations in mean velocity ($+605$ m/s in the freestream to -160 m/s along the centerline) and large turbulent fluctuations (local turbulence intensities up to 400%). Due to the relatively large data ensembles required to obtain the reference measurements (saturable detector scheme) in the present experiments, twenty wind tunnel blowdowns were required to obtain the entire traverse of LDV data.

The LDV system employed was a TSI Inc. two-component unit with conventional optics and Bragg cell frequency shifting (40 MHz) to eliminate fringe blindness and discriminate flow direction. The LDV measurement volume was approximately 120 μm in diameter and 700 μm in length with a nominal fringe spacing of 10.5 μm. Doppler frequencies were measured with a TSI Inc. IFA-750 autocorrelation processor which was completely integrated with a Gateway 2000 486-33 personal computer for automated data acquisition. Use of the IFA-750 in the present experiments provided measurements of the interarrival time and the particle residence time with each velocity measurement. Seed particles were generated by a conventional siz-jet atomizer filled with silicone oil which has been shown (Bloomberg 1989) to produce mean particle diameters of 0.8 μm. The effective Stokes number at the measurement location was approximately 0.15 which was sufficiently small to avoid any significant particle lag effects.

Fig. 1. Schematic diagram of supersonic, axisymmetric base flow-field

3 Experimental technique

In order to make an objective comparison between different velocity bias correction techniques, it is necessary to

establish a reference measurement. Once the reference is established, different post-facto correction techniques are applied to the same raw data ensembles as used in the reference data. Subsequently, a simple side-by-side comparison of the results obtained with different correction techniques to the reference is performed in order to investigate the effects of velocity bias in the current flow environment. In the sections that follow, the reference measurement will be described and the five post-facto correction schemes to be examined will be discussed.

3.1 Reference measurement

Establishing a reference measurement for LDV data in high-speed, separated flows has been the primary problem in identifying the effects of velocity bias under these conditions. Hot-wire anemometry, a useful tool in attached flows with relatively low turbulence levels, cannot be used accurately in high-speed separated flows due to its intrusive nature and unreliability at high turbulence intensity levels. In the current study, the saturable detector sampling technique is used as the reference measurement. A description of the technique and a discussion of its applicability to the present measurements are presented below.

The saturable detector scheme is shown in Fig. 2. During data acquisition, the detector is disabled for a period T_s after a measurement is recorded, thus introducing a dead time in the acquisition process when no measurements are possible. In practice, most individual realization systems are saturable detectors with small T_s such that nearly every particle crossing occurs while the processor is enabled. The saturable detector has been used successfully by a number of researchers to minimize the effects of velocity bias in low-speed flows (Stevenson et al. 1982, Adams and Eaton 1985, Craig et al. 1986).

The saturable detector scheme belongs to the general class of sampling techniques known as controlled proces-

- Valid Particle Crossings
- Data Accepted by Saturable Detector
- Processor Disabled

Fig. 2. Sampling procedure of the saturable detector (after Edwards 1987)

sors. These techniques can remove the dependence of sampling rate on flow velocity and, therefore, provide unbiased LDV data. It has been established (Edwards and Jensen 1983, Gould et al. 1989, Winter et al. 1991) that the success of controlled processors in eliminating velocity bias effects is dependent on the relative magnitudes of three time scales: the local integral time scale of the flow (T_u), the LDV measurement time scale (T_m), and the controlled processor sampling time scale (T_s). In this context, the integral time scale of the flow describes the "persistence" time of the energy-containing turbulent eddies; the measurement time scale is merely the inverse of the mean data rate. For an LDV system with high integral scale data densities $(T_u/T_m \gg 1)$, several authors (Gould et al. 1989, Winter et al. 1991, Tummers et al. 1992) have suggested that the following two criteria must be met in order for a controlled processor to produce bias-free results:

$$T_s/T_m \gtrsim 5 \quad \text{and} \quad T_u/T_m \gtrsim 5 \tag{2}$$

In the current study, the integral time scale of the flow was estimated from the results of Gaviglio et al. (1977) who used hot-wire anemometry to measure values of approximately $T_u = 2 \, \mu s$ in a similar supersonic, axisymmetric base flow experiment. This value is also approximately equal to the shear layer eddy rollover time $(b/\Delta U)$ calculated using the current conditions. The measurement time scale is dependent on the signal-to-noise ratio of the Doppler signal, the LDV processor capabilities, and the seed concentration in the flow. Mean coincident data rates ranged from 3000–10000 samples per second in the present experiments, yielding an average measurement time scale of approximately $T_m = 150 \, \mu s$. The sampling time scale T_s was varied experimentally from 0.1–10 times the measurement time scale.

A comparison of the relative time scales (with $T_s = 10 T_m$) indicates that $T_s/T_u \approx 750$ which approaches the definition of the one-shot processor $(T_s/T_u \to \infty)$ as given by Erdmann and Tropea (1981, 1984). These authors showed analytically that the one-shot processor was capable of eliminating the effects of velocity bias as the integral scale data density, T_u/T_m, approaches zero. In the current study, $T_u/T_m \approx 0.01$ which, according to the results of Erdmann and Tropea (1981, 1984), seems to justify the use of the saturable detector scheme as a means to reduce velocity bias in this case. Note that the present conditions are far different from those established for bias-free sampling in the high data density case (Eq. 2). Several authors have cast doubt on the conclusions of Erdmann and Tropea (1981, 1984) for one-shot processors (Edwards and Jensen 1983, Edwards 1987, Winter et al. 1991) suggesting that, instead of eliminating the velocity bias at very low data densities, the one-shot processor approaches the totally biased individual realization case. The large discrepancy between these results must be
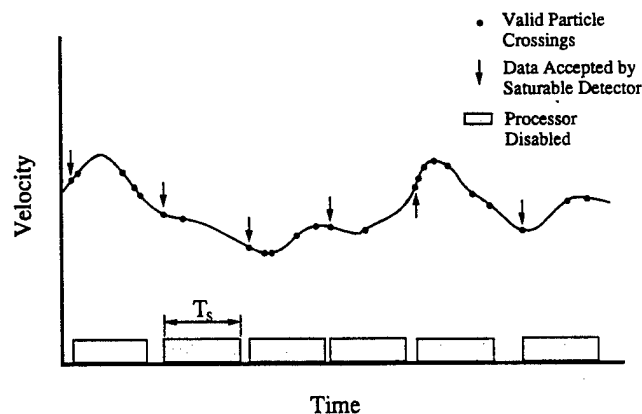
resolved by experimental means; however, to the authors' knowledge, no experimental data at the very low data densities of the present study have been obtained previously.

The saturable detector scheme in the present case was implemented in software by processing relatively large data sets (20,000–25,000 realizations per ensemble) with various sampling time scales, T_s. The dependence of the mean velocities, turbulence intensities, and Reynolds shear stress on the normalized sample interval, T_s/T_m, was investigated by altering (in software) the value of T_s starting at very small values to simulate the totally biased individual realization case and increasing until $T_s/T_m \approx 10$. Figure 3 is a plot of the mean axial velocity, axial root-mean-square (rms) velocity fluctuation, and Reynolds shear stress as a function of the normalized sample interval at a location near the inner edge of the shear layer where the local turbulence intensity is approximately 138%. This plot is representative of the results obtained throughout the regions of large turbulence intensity in the shear layer (i.e., regions where velocity bias effects should be largest) and are similar to the ones shown by Stevenson et al. (1982) and Craig et al. (1986). As Fig. 3 indicates, all three velocity statistics are dependent on the normalized sample interval for $T_s/T_m < 5$ and reach constant values (indicated by the * subscript) at larger normalized sample intervals. This trend has also been observed by Winter et al. (1991) and Tummers et al. (1992) who point out that, although the asymptotic behavior at large T_s/T_m indicates a *reduction* in velocity bias, it does not by itself guarantee the total *elimination* of velocity bias unless $T_u/T_m \gtrsim 5$ (i.e., high data density case). In the present case, the constant values for $T_s/T_m > 5$ differ from those of the individual realization case $(T_s/T_m \rightarrow 0)$ which suggests that the saturable detector does indeed reduce velocity bias in this low data density environment, in agreement with the findings of Winter et al. (1991) and

Tummers et al. (1992). Therefore, it is believed that the data obtained using the saturable detector scheme and $T_s/T_m > 5$ can be used as a reference for comparison with post-facto correction methods.

3.2 Post-facto correction methods

A brief review of the five post-facto correction methods that are compared in this paper will now be presented. Along with identification of the velocity bias problem, McLaughlin and Tiederman (1973) also provided the first velocity bias correction method: the inverse velocity magnitude correction. In the nomenclature of Eq. 1,

$$w_i = |V_i|^{-1} \tag{3}$$

where V_i is the velocity magnitude of the ith realization. This correction method was originally derived for incompressible, one-dimensional flows but has been used significantly in a wide variety of fluid dynamic environments (e.g., Amatucci et al. 1992, Abu-Hijleh and Samimy 1989). Oftentimes, a direct measurement of the total velocity vector is not possible so that assumptions must be made concerning the contributions from any unmeasured components. Nakayama (1985) and Petrie et al. (1988) suggest methods to estimate the third component of velocity in a two-component LDV data set. The effects of the three-dimensional correction, however, were shown to be significant only when both measured mean velocity components were negligible. In the present case, either the axial or radial mean velocity was always significant such that a three-dimensional correction was not necessary.

Weighting each velocity realization with the particle residence time in the LDV measurement volume, $w_i = \tau_i$, has also been suggested as a method to correct for the effects of velocity bias (Hoesel and Rodi 1977, Buchhave and George 1978). This method is founded on the inverse relationship between particle residence time and velocity. The performance of residence time weighting should be independent of the number of components measured but degrades as velocity magnitudes increase due to hardware accuracy and resolution limitations of the residence time measurement. Residence time weighting is the most difficult of the five post-facto correction methods to implement in practice due to the difficulties in making accurate measurements of τ_i.

Barnett and Bentley (1974) concluded that weighting the individual velocity realizations by the interarrival time between successive particles was a viable method to remove any velocity bias effects. That is, $w_i = t_i - t_{i-1}$ where t_i is the absolute time of arrival for particle i. Barnett and Bentley (1974) also suggested that long time delays relative to the characteristic time of the turbulent fluctuations (i.e., $T_m/T_u \gg 1$) destroy any correlation between instantaneous velocity and sampling rate. As
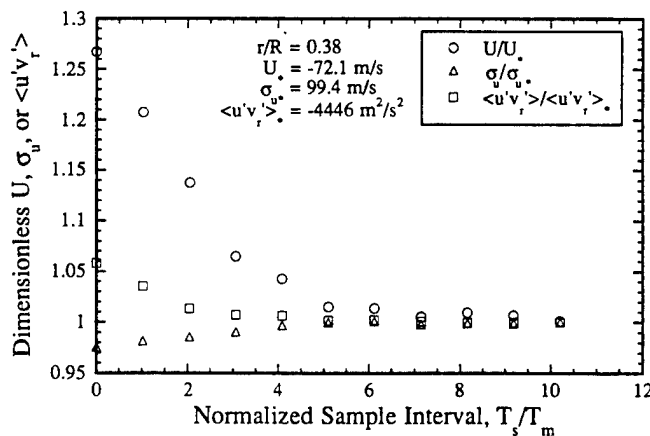

Fig. 3. Dependence of mean axial velocity, axial rms velocity fluctuation, and Reynolds shear stress on T_s/T_m

previously mentioned, this hypothesis has still not been adequately investigated for high-speed separated flows. A variation on the interarrival time weighting method is the sample and hold technique (Dimotakis 1976, Adrian and Yao 1987) which weights the individual realizations by $w_i = t_{i+1} - t_i$. Although Winter et al. (1991) suggested that the interarrival time weighting and sample and hold weighting methods should yield the same results at all data densities, they will both be investigated and compared in the present experiments.

The last velocity bias correction method that will be investigated is the velocity-data rate correlation method described by Meyers (1988). Using this technique, the persistence time of the flow and the correlation coefficient between the instantaneous velocity and data acquisition rate are estimated from individual realization LDV measurements. The LDV data ensemble is subsequently sampled once during each persistence period of the flow to yield a new ensemble of statistically independent measurements. To correct for velocity bias effects, the sampled data are normalized by the average number of LDV realizations following a sampled velocity within an average persistence interval. This technique is actually a mix between sampling and correction techniques, but since it can be applied after data acquisition to any ensemble of individual realization LDV data, it is a feasible correction technique for high-speed flow applications with limited wind tunnel run times.

4 Results

In order to document the effects of velocity bias at different locations across the shear layer, the reference data (saturable detector) are compared to the unweighted individual realization data in Fig. 4. The velocity bias effects on the mean axial velocity (Fig. 4a) follow the expected trend with mean velocities from the individual realization case being consistently higher than the reference data in the high turbulence intensity regions of the shear layer (near $r/R = 0.5$). In the outer freestream flow, the velocity bias is negligible as expected. Note that as the mean axial velocity changes sign entering the recirculation region, the velocity bias acts to increase the *magnitude* of the reversed velocity. At the $U = 0$ location, the effects of velocity bias are negligible due to the symmetry of the velocity histogram about the origin and the competing effects from positive and negative realizations (Adams and Eaton 1985). The mean radial velocity component (V_r) in the shear layer was also affected by velocity bias in a manner similar to the mean axial velocity with the magnitudes of the individual realization data generally exceeding the reference values.

The effects of velocity bias on the axial rms velocity fluctuation (σ_u) and Reynolds shear stress ($\langle u'v'_r \rangle$) are
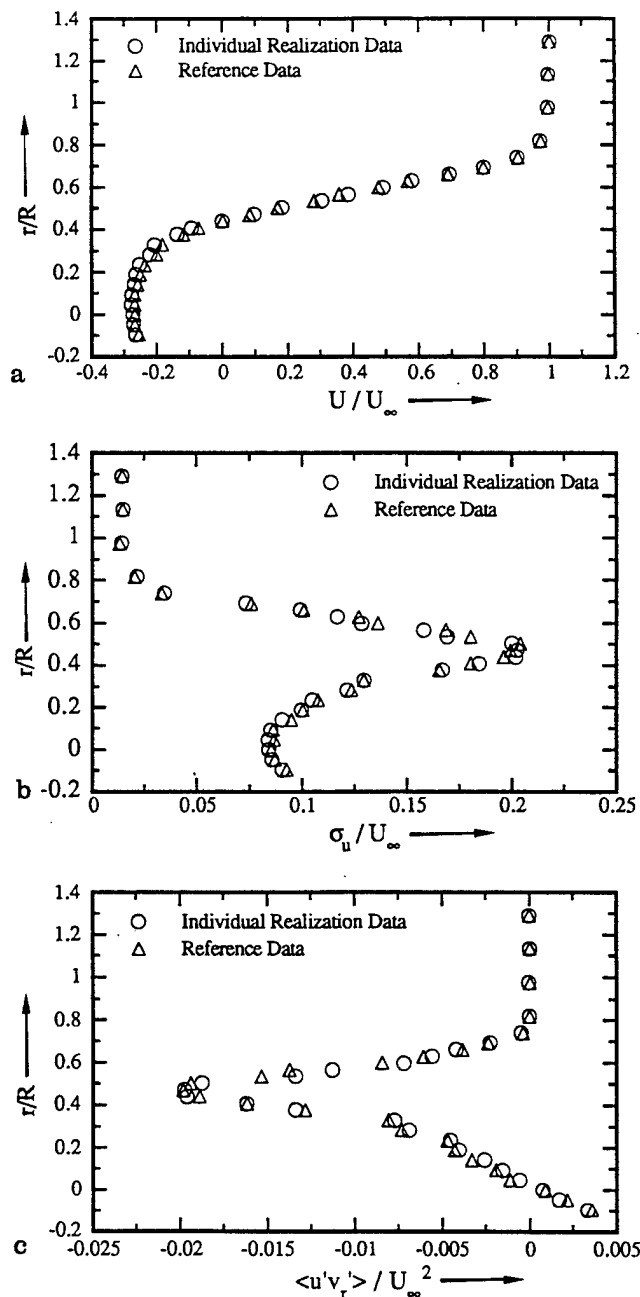

Fig. 4a–c. Comparison of reference data to individual realization data: a mean axial velocity; b axial rms velocity fluctuation; c Reynolds shear stress

shown in Figs. 4b and 4c, respectively. Note that a *global* definition of turbulence intensity (σ_u/U_∞) is used in Fig. 4b instead of the typical *local* definition (σ_u/U) to isolate the effects of velocity bias on the rms velocity fluctuation alone. As is typical of separated shear layers, a strong peak in the turbulence intensity and shear stress exists where intense turbulent mixing and energy exchange dominate the flow. In the present case, the peak values occur relatively near the $U = 0$ location such that

velocity bias effects do not distort the magnitudes of the local maxima. However, the effects of velocity bias are significant in the regions of the shear layer where the mean velocity is moderate and turbulence intensity is large (e.g., $r/R \approx 0.55$). Velocity bias tends to decrease the magnitudes of both the turbulence intensity and shear stress independent of the direction of the local mean velocity. In addition, velocity bias effects in the separated region are reduced compared to those in the outer part of the shear layer even though local turbulence intensities are similar. The radial rms velocity fluctuation (σ_{V_r}) was also determined and exhibited trends similar to those shown in Fig. 4b for the axial component. The differences between the saturable detector and individual realization data once again suggest the ability of the sampling method to reduce velocity bias effects in agreement with the findings of Winter et al. (1991) and Tummers et al. (1992).

The same raw data ensembles that were processed in software using the saturable detector scheme were also processed with the different post-facto correction techniques discussed above. A comparison of the results obtained with each correction technique will now be presented. Figure 5 shows the reference mean axial velocity profile along with the data from the five post-facto correction methods (in this and subsequent figures, the comparison between the five correction methods is shown on two separate plots for clarity). As shown in Fig. 5a, the inverse velocity magnitude weighting factor tends to overcorrect (in comparison to the reference data) for the effects of velocity bias both above and below the $U = 0$ location in the shear layer. This may be due, in part, to the three-dimensional nature of the flow as well as non-uniform seeding effects. The interarrival time weighting, sample and hold weighting, and velocity-data rate correlation methods all compare favorably with the reference measurement whenever $U > 0$, but in the recirculation region, the interarrival time weighting is superior. In general, the residence time weighting factor tends to overcorrect the data in comparison to the reference measurement across the entire traverse although to a lesser degree than the inverse velocity magnitude technique. All five post-facto correction techniques yield similar results in regions of the flow where velocity bias effects are negligible such as the freestream and $U = 0$ locations.

As Fig. 4 indicates, the effects of velocity bias are not limited to the mean velocity, but are quite important in accurately determining the turbulence moments as well. Figure 6 is a plot of the axial turbulence intensity profile as determined by the reference measurement and the five post-facto correction methods. The differences in performance of each correction technique become more evident here, with the profile significantly distorted by the inverse velocity magnitude and residence time weighting methods. A translation of the peak turbulence intensity location radially outward is a result of both of these
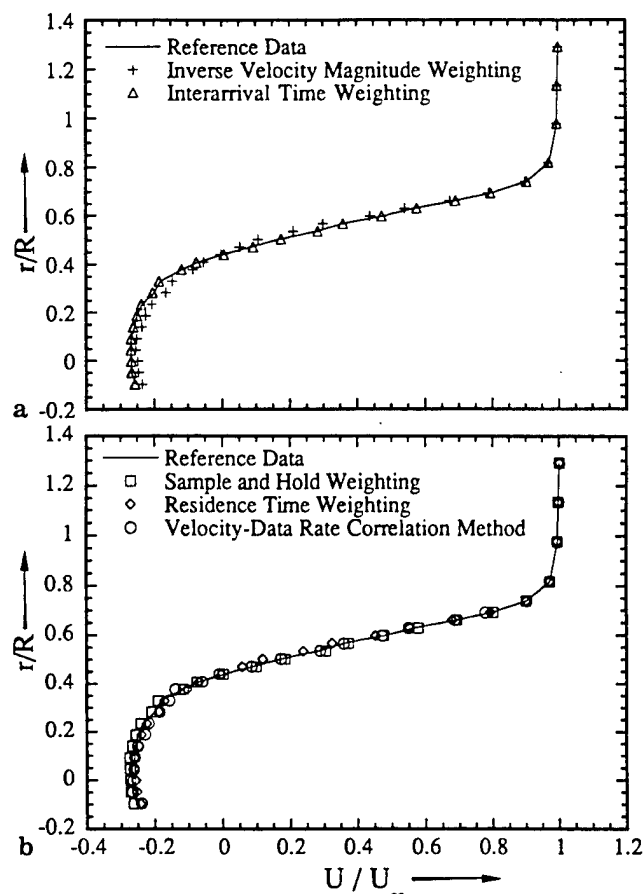

Fig. 5a, b. Comparison of post-facto correction methods with reference data for mean axial velocity: a inverse velocity magnitude and interarrival time weightings; b sample and hold weighting, residence time weighting, and velocity-data rate correlation method

methods, and turbulence intensity values vary considerably from the reference data across the shear layer. As in the mean velocity, the interarrival time and sample and hold weighted turbulence intensity distributions agree quite well with the reference data. The velocity-data rate correlation method also agrees with the reference data throughout most of the profile; however, the profile becomes distorted near the peak turbulence intensity location. A similar comparison was also done for the radial turbulence intensity with each correction method behaving in a similar manner as that indicating in Fig. 6.

A comparison of the Reynolds shear stress profiles as calculated by the five post-facto correction methods is shown in Fig. 7. Again, the differences between methods are significantly more apparent than in the mean velocity. Much like in the turbulence intensity, the inverse velocity magnitude correction significantly distorts the form of the shear stress profile and yields a peak magnitude that is reduced from the reference measurement. The interarrival time weighting closely follows the reference data throughout the entire profile. The sample and hold weighting method also agrees reasonably well with the reference
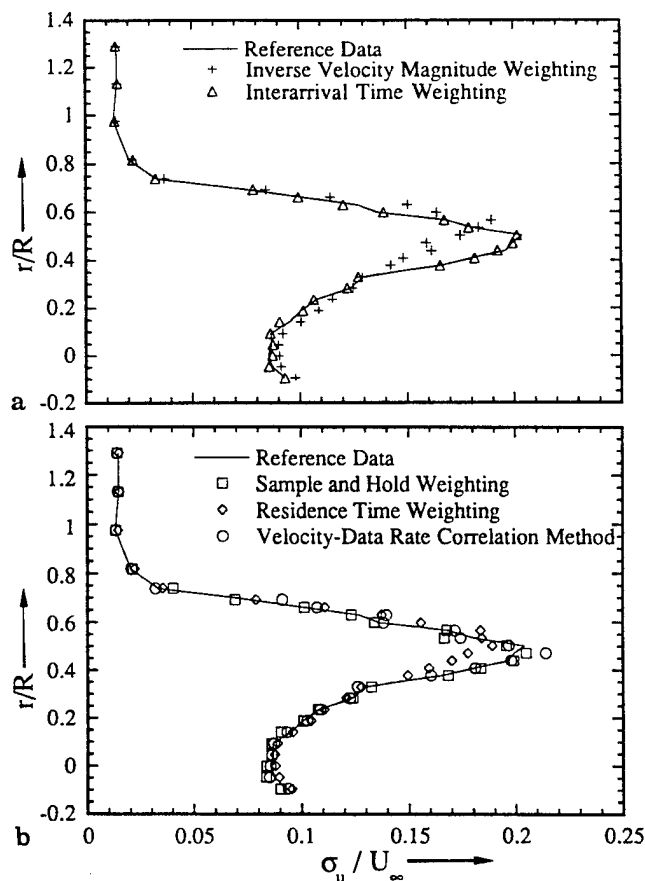
Fig. 6a, b. Comparison of post-facto correction methods with reference data for axial rms velocity fluctuation: a inverse velocity magnitude and interarrival time weightings; b sample and hold weighting, residence time weighting, and velocity-data rate correlation method
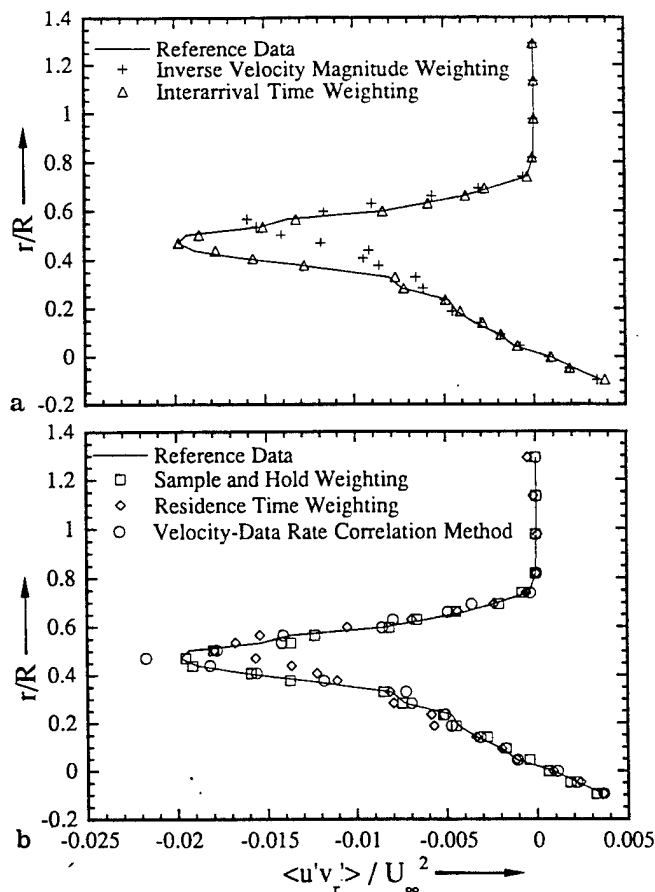

Fig. 7a, b. Comparison of post-facto correction methods with reference data for Reynolds shear stress: a inverse velocity magnitude and interarrival time weightings; b sample and hold weighting, residence time weighting, and velocity-data rate correlation method

measurement throughout most of the profile. The residence time weighted profile exhibits a peak which is displaced outward from the actual peak location and shear stress values which differ significantly from the reference data in the high turbulence intensity region of the traverse. Also, the velocity-data rate correlation method yields a peak shear stress value which is 10% larger in magnitude than the reference value, although most of the profile agrees well with the reference data.

In addition to comparing the respective profiles of mean velocity, turbulence intensity, and shear stress from each correction method, a measure of the agreement of each technique with the reference can be made by summing the differences between the corrected data and the reference data across the entire profile. The rms difference for each correction method is calculated by the following equation:

$$\text{rms difference} = \sqrt{\frac{\sum_{j} (x_j - X_j)^2}{N}} \qquad (4)$$

where x is any mean or turbulence statistic (e.g., U or $\langle u'v'_r \rangle$), X is the reference value of x at location j, and N is the number of measurement locations across the traverse. Figure 8 shows the rms differences for the mean velocities, turbulence intensities, and Reynolds shear stress (note the different scales between the two plots). In this figure, each rms difference is normalized by the maximum reference value of the statistic for the entire traverse in order to show the sensitivity of each statistic to velocity bias correction methods. Figure 8, clearly indicates that the interarrival time weighting method provides the best agreement with the reference in the present experiments. Agreement between the saturable detector scheme at $T_s/T_m > 5$ (reference technique) and the interarrival time weighting method has also been found in several previous velocity bias investigations at higher integral scale data densities (Adams and Eaton 1985, Loseke and Gould 1991, Winter et al. 1991). As expected, the sample and hold weighting technique provides results which are nearly equal to those of the interarrival time weighting method (Winter et al. 1991). On the other hand, the inverse
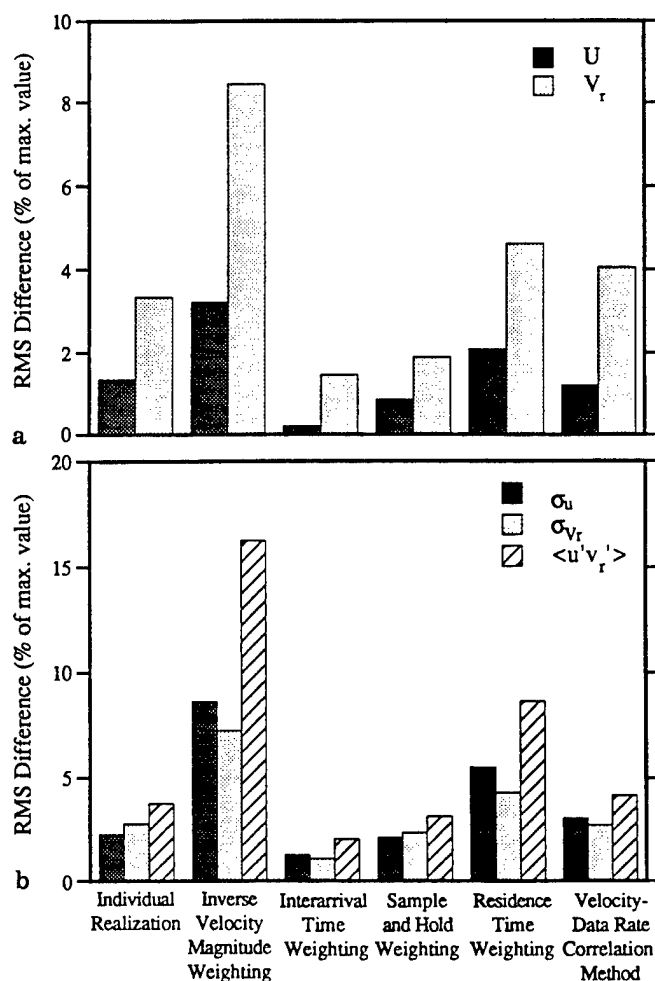
Fig. 8a, b. Rms differences across entire profile: a mean velocities; b turbulence quantities

velocity magnitude and residence time weighting methods produce mean and turbulence statistics that are in significant disagreement with the reference data. The sensitivity of the turbulence statistics (particularly the Reynolds shear stress) and radial mean velocity to the effects of velocity bias are clearly shown. The quantity which is generally used to demonstrate velocity bias effects, the mean streamwise velocity, is the least sensitive to the various correction methods, which may account for the large discrepancies in the literature as to the superior correction method for a particular flow environment.

5 Discussion

As the previous results indicate, choosing an adequate velocity bias correction method can have a large effect on the accuracy of mean velocities and turbulence statistics obtained with individual realization LDV systems. Use of a post-facto correction technique is generally necessary in supersonic, blowdown-type wind tunnels due to limited

wind tunnel run times. In the high-speed, separated flow environment of the present study, the interarrival time weighting method has been shown to agree closely with the reference saturable detector method which reduces velocity bias. In a similar velocity bias study in a low-speed (20 m/s) separated flow with comparable turbulence intensities, Loseke and Gould (1991) also showed that the interarrival time weighting method can reduce velocity bias as long as Bragg cell bias (Meyers and Clemmons 1978) is non-existent. The IFA-750 signal processor used in the present experiments ensures a single measurement for each Doppler burst using a burst centering procedure, thus eliminating any bias due to the Bragg cell frequency shifter. A brief summary of some of the important experimental aspects which may have contributed to the performance of each post-facto correction technique examined here will be presented below.

The inverse velocity magnitude weighting factor was shown to be unreliable throughout the middle region of the shear layer where turbulence intensities are large. This conclusion was also reached by Hoesel and Rodi (1977) and other authors who stated that this method is restricted to low turbulence intensity environments. In addition, the effects of compressibility may cause erroneous results using this method since the rate at which particles cross the measurement volume is proportional to the mass flux (ρV) which, for compressible flows, can be significantly different than the dependence on velocity (volume flux) alone. Lastly, the effects of non-uniform seeding, which was undoubtedly present in the current experiments due to the role of large scale turbulent structures in particle entrainment and transport, can cause additional errors in velocity bias correction by the inverse velocity magnitude technique.

The main problem encountered when implementing the residence time weighting scheme for velocity bias correction is the resolution and accuracy of the residence time measurement. In the IFA-750 processor, the residence time measurement is made with a resolution of 32 ns which, for many flow applications, may be sufficient. However, in high-speed flows the large instantaneous velocities and the small measurement volume dimensions which are necessary for adequate spatial resolution combine to make particle residence times very small. For example, in the present experiments freestream velocities as high as 605 m/s were measured with a measurement volume diameter of 120 μm which yields a particle residence time of 198 ns. In turn, this results in a worst-case residence time uncertainty due to measurement resolution of ±16%. In addition, the residence time measurement is user-dependent since the start and end of a Doppler burst are determined by a threshold level which is set by the user. The combination of these effects makes the residence time weighting technique difficult to implement accurately in high-speed flows.

The interarrival time weighting method was shown to be reliable in reducing velocity bias in the present high-speed, separated flow. Figure 9 shows representative velocity histograms from the inner edge of the shear layer generated with uncorrected individual realization data and the same data after interarrival time weighting. The bias toward higher velocity magnitudes, clearly present in the unweighted data, appears to be corrected by the interarrival time weighting (i.e., the corrected histogram is normally distributed). Of course, when implementing the interarrival time method, an accurate technique to measure the time-between-data (tbd) must be used. In the present experiments, an absolute time stamp with 1 μs resolution was output with each velocity realization, such that the tbd was determined by differencing successive time stamps. Therefore, the uncertainty due to resolution of the tbd measurement was constant for each realization in the ensemble, as opposed to typical counter-type processors which yield tbd measurements with varying resolutions, thereby causing error accumulation throughout the ensemble. Of course, the previous comments regarding the implementation of the interarrival time weighting method also directly apply to the sample and hold weighting technique.

The present results suggest that the concept of the velocity-data rate correlation method in low data density environments must be altered from its original form (Meyers 1988). The calculated persistence time, which is an important part of the debiasing scheme, must differ from the integral time scale of the flow (as defined in the original version of this method) in the low data density case since $T_m \gg T_u$. Although Tummers et al. (1992) sugges-
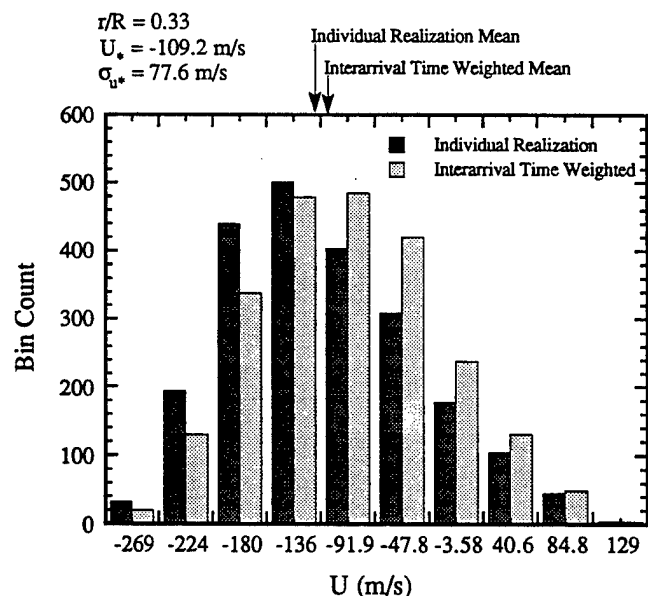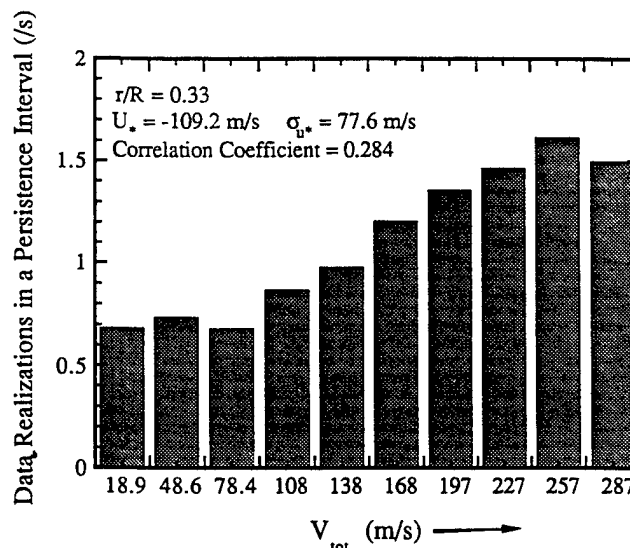

Fig. 10. Example of velocity-data rate correlation plot

ted that the use of this method was restricted to cases involving high data densities, the present investigation revealed that it was capable of detecting the velocity bias in low data density environments. Figure 10 is a typical velocity-data rate correlation histogram generated with data from the inner edge of the shear layer which shows the dependence of the data rate on the total velocity. Note that in the central region of the histogram where most of the realizations occur, the data rate dependence is almost linear as suggested by McLaughlin and Tiederman (1973). In the present investigation, the calculated correlation coefficient between velocity and data rate varied from approximately zero in the freestream to a peak value of 0.29 near the inner edge of the shear layer ($r/R = 0.35$). The magnitudes of the correlation coefficient are similar to those measured by Tummers et al. (1992) in a low-speed wake flow. The correlation coefficient was found to be a reliable indicator of the degree of velocity bias present at any spatial location.

Acknowledgements

References

Abu-Hijleh, B.; Samimy, M. 1989: An experimental study of a reattaching supersonic shear layer. AIAA Paper 89-1801, presented at the AIAA 27th Aerospace Sciences Meeting, Reno, Nevada

Adams, E. W.; Eaton, J. K. 1985: An LDA study of the backward-facing step flow, including the effects of velocity bias. Int. Symp. on Laser Anemometry, New York, ASME FED 33, 255-264

Fig. 9. Effect of velocity bias correction on shape of velocity histogram

Adrian, R. J.; Yao, C. S. 1987: Power spectra of fluid velocities measured by laser Doppler velocimetry. Exp. Fluids 5, 17–28

Amatucci, V. A.; Dutton, J. C.; Kuntz, D. W.; Addy, A. L. 1992: Two-stream, supersonic, wake flowfield behind a thick base, part I: general features. AIAA J. 30, 2039–2046

Barnett, D. O.; Bentley, H. T. III 1974: Statistical bias of individual realization laser velocimeters. Proc. 2nd Int. Workshop on Laser Velocimetry, Vol. 1, Purdue University, pp. 428–444

Bloomberg, J. E. 1989: An investigation of particle dynamics effects related to LDV measurements in compressible flows. M.S. Thesis, University of Illinois at Urbana-Champaign, Department of Mechanical and Industrial Engineering

Buchhave, P.; George, W. K. Jr. 1978: Bias corrections in turbulence measurements by the laser Doppler anemometer. Presented at the 3rd Int. Workshop on Laser Velocimetry, Purdue University, pp. 110–119

Craig, R. R.; Nejad, A. S.; Hahn, E. Y.; Schwartzkopf, K. G. 1986: Approach for obtaining unbiased laser Doppler velocimetry data in highly turbulent flows. J. Prop. Power 2, 541–545

Dimotakis, P. E. 1976: Single scattering particle laser Doppler measurements of turbulence. AGARD CP-193

Edwards, R. V. 1978: How real are particle bias errors. Proc. 3rd Int. Workshop on Laser Velocimetry, Purdue University, pp. 79–85

Edwards, R. V.; Jensen, A. S. 1983: Particle-sampling statistics in laser anemometers: sample-and-hold systems and saturable systems. J. Fluid Mech. 133, 397–411

Edwards, R. V. 1987: Report of the special panel on statistical particle bias problems in laser anemometry. ASME Trans.: J. Fluids Eng. 109, 89–93

Erdmann, J. C.; Tropea, C. D. 1981: Turbulence-induced statistical bias in laser anemometry. Proc. 7th Symp. on Turbulence, University of Missouri-Rolla, pp. 129–138

Erdmann, J. C.; Tropea, C. D. 1984: Statistical bias of the velocity distribution function in laser anemometry. Proc. Int. Symp. on Applications of Laser Doppler Anemometry to Fluid Mechanics, Lisbon, Portugal, pp. 393–403

Gaviglio, J.; Dussauge, J. P.; Debieve, J. F.; Favre, A. 1977: Behaviour of a turbulent flow strongly out of equilibrium at supersonic speeds. Phys. Fluids 20, 179–192

Gould, R. D.; Stevenson, W. H.; Thompson, H. D. 1989: Parametric study of statistical bias in laser Doppler velocimetry. AIAA J. 27, 1140–1142

Hoesel, W.; Rodi, W. 1977: New biasing elimination method for laser Doppler velocimetry counter processing. Rev. Sci. Instr. 48, 910–919

Loseke, K. W.; Gould, R. D. 1991: A comparison of velocity bias correction techniques in laser Doppler velocimetry. Proc. ASME Fluid Measurement and Instrumentation Forum, FED-Vol. 108, pp. 63–68

McLaughlin, D. K.; Tiederman, W. G. 1973: Biasing correction for individual realization of laser anemometer measurements in turbulent flows. Phys. Fluids 16, 2082–2088

Meyers, J. F. 1988: Laser velocimeter data acquisition and real time processing using a microcomputer. Presented at the 4th Int. Symp. on Applications of Laser Anemometry to Fluid Mechanics, Lisbon, Portugal

Meyers, J. F.; Clemmons, J. I., Jr 1978: Processing laser velocimeter high-speed burst counter data. Proc. 3rd Int. Workshop on Laser Velocimetry, Purdue University, pp. 300–313

Nakayama, A. 1985: Measurements of separating boundary layer and wake of an airfoil using laser Doppler velocimetry. AIAA Paper 85–0181, presented at the AIAA 23rd Aerospace Sciences Meeting, Reno, Nevada

Petrie, H. L.; Samimy, M.; Addy, A. L. 1988: Laser Doppler velocity bias in separated turbulent flows. Exp. Fluids 6, 80–88

Stevenson, W. H.; Thompson, H. D.; Roesler, T. C. 1982: Direct measurement of laser velocimeter bias errors in a turbulent flow. AIAA J. 20, 1720–1723

Tummers, M. J.; Absil, L. H. J.; Passchier, D. M. 1992: An experimental investigation of velocity bias in a turbulent flow. Presented at the 6th Int. Symp. on Applications of Laser Techniques to Fluid Mechanics, Lisbon, Portugal

Winter, A. R.; Graham, L. J. W.; Bremhorst, K. 1991: Velocity bias associated with laser Doppler anemometer controlled processors. ASME Trans.: J. Fluids Eng. 113, 250–255

APPENDIX A.2

SUPERSONIC BASE FLOW EXPERIMENTS IN THE NEAR WAKE OF A
CYLINDRICAL AFTERBODY

by

J. L. Herrin and J. C. Dutton

Supersonic Base Flow Experiments in the Near Wake of a Cylindrical Afterbody

J. L. Herrin* and J. C. Dutton†

University of Illinois at Urbana-Champaign, Urbana, Illinois 61801

The near wake of a circular cylinder aligned with a uniform Mach 2.5 flow has been experimentally investigated in a wind tunnel designed solely for this purpose. Mean static pressure measurements were used to assess the radial dependence of the base pressure and the mean pressure field approaching separation. In addition, two-component laser Doppler velocimeter (LDV) measurements were obtained throughout the near wake including the large separated region downstream of the base. The primary objective of the research was to gain a better understanding of the complex fluid dynamic processes found in supersonic base flowfields including separation, shear layer development, reattachment along the axis of symmetry, and subsequent development of the wake. Results indicate relatively large reverse velocities and uniform turbulence intensity levels in the separated region. The separated shear layer is characterized by high turbulence levels with a strong peak in the inner, subsonic region which eventually decays through reattachment as the wake develops. A global maximum in turbulent kinetic energy and Reynolds shear stress is found upstream of the reattachment point, which is in contrast to data from the reattachment of a supersonic shear layer onto a solid wall.

Nomenclature

C_f = skin friction coefficient
C_p = dimensionless pressure coefficient
H = compressible shape factor, δ^*/θ
M = Mach number
k = turbulent kinetic energy
P = pressure
P_k = production of k
R = base radius
r = radial coordinate
S = location of reattachment point
t = tangential coordinate
U = mean axial velocity
u_τ = friction velocity
V_r = mean radial velocity
V_t = mean tangential velocity
x = axial coordinate
y = vertical distance, $r-R$
γ = ratio of specific heats
δ = boundary-layer thickness
δ^* = displacement thickness
θ = momentum thickness
ν_w = kinematic viscosity at wall
Π = wake strength parameter
σ = root-mean-square value
$< >$ = ensemble-averaged value

Subscripts
base = condition at base
u = axial component
v_r = radial component
v_t = tangential component
1 = condition at nozzle exit

Superscript
$( )'$ = fluctuating value

Introduction

THE low pressures that act in the base region of bodies of revolution in supersonic flight can cause significant amounts of drag.[1] For this reason, practical methods such as boattailing, base bleed, and base burning have been developed to increase the base pressure on aerodynamic vehicles such as missiles, rockets, and projectiles. To further enhance vehicle performance, however, a more complete understanding of the complex fluid dynamic processes that occur in base flowfields is necessary. Past experimental efforts have provided an adequate description of the overall flowfield structure and some parametric trends, but very little detailed quantitative data exists, especially for supersonic flows. In fact, a comprehensive survey of the available experimental data on axisymmetric base flows was recently undertaken by GARTEUR Action Group AG09.[2] After an exhaustive search, the group concluded that no accurate, well-documented experimental data existed for the near-wake flowfield in supersonic, axisymmetric flow. Reliable turbulence information in the base region is especially scarce which presents a problem in validating numerical predictions of these flowfields (see Refs. 3–5). Clearly, the practical importance of increasing the understanding of axisymmetric base flowfields lies in the ability to someday control the near-wake flow interactions such that base drag can be reduced and vehicle stability and control can be enhanced.

A schematic diagram of the mean flowfield structure in the near wake of a cylindrical afterbody aligned with a supersonic flow is shown in Fig. 1. The supersonic afterbody freestream flow undergoes a strong expansion centered at the base corner as the turbulent boundary layer separates geometrically from the body. A free shear layer is formed which separates the outer inviscid flow from a relatively large recirculation region immediately downstream of the base. The intense turbulent mixing and energy exchange that characterize the free shear layer are important in determining the flowfield properties throughout the near wake including the recirculation region. As the free shear layer approaches the axis of symmetry, a recompression process occurs which eventually realigns the flowfield with the axis. A rear stagnation point, where the mean velocity vanishes, is located on the centerline and separates the recirculation region from the wake which develops downstream.

The early theoretical model for turbulent base flows developed by Korst[6] prompted several experimental investigations which at-
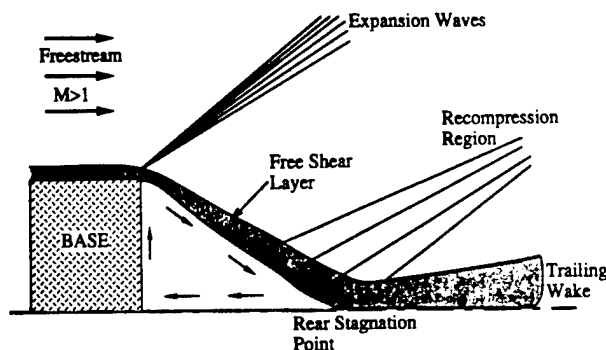
Fig. 1   Supersonic, axisymmetric base flow schematic.

tempted to gather the empirical information necessary to complete the theory.[7-10] However, many experimental problems, including improper model mounting, probe interference effects, and lack of flowfield symmetry, hampered these efforts which resulted in data of questionable accuracy. These experimental difficulties stem primarily from the axisymmetric geometry of the body as well as the sensitivity of the separated region downstream of the base to wind-tunnel interference effects.[11] Perhaps the most comprehensive previous study of supersonic power-off base flows was undertaken by Gaviglio et al.[12] using a hot-wire anemometer. The overall inviscid flow structure and downstream wake properties were determined; however, the recirculation region directly behind the base was not investigated due to possible probe interference effects which limits the utility of the data. Neale et al.[13] investigated the mean velocity field behind a circular cylinder with a pitot-static probe but, again, bypassed the separated region. Clearly, accurate experimental measurements in the recirculation region downstream of the base require nonintrusive diagnostic techniques. Laser Doppler velocimetry (LDV) is a nonintrusive velocity measurement tool well-suited for such flows. Delery[14] used LDV to successfully document the near wake of a subsonic, axisymmetric base flowfield. Detailed mean velocity and turbulence data were gathered throughout the near wake and provide a good data base for the subsonic case. Amatucci et al.[15] made similar LDV measurements in a supersonic, two-stream flowfield with a two-dimensional base that modeled the power-on case; however, the effects of the more practical axisymmetric configuration were not investigated. Heltsley et al.[16] used LDV to investigate the flowfield downstream of a transonic, axisymmetric, power-on base flow but encountered experimental problems throughout the measurements.

In the current study, experiments were conducted to document the entire near-wake flowfield structure behind a cylindrical afterbody immersed in a supersonic flow. Detailed LDV measurements were made to obtain a better understanding of the fluid dynamic processes throughout the near wake including separation, shear layer growth and development, reattachment, and wake redevelopment. To the authors' knowledge, these data also provide the first detailed investigation of the mean and turbulent velocity fields inside the recirculation region in a supersonic base flow. In addition, the data provided herein will aid both analytical and numerical modelers of supersonic, axisymmetric base flows.

Experimental Facility and Instrumentation

Wind Tunnel Facility

The experiments were conducted in a supersonic, blowdown-type wind tunnel designed solely for the study of axisymmetric base flows. Figure 2 is a schematic diagram of the axisymmetric wind-tunnel facility which is located in the University of Illinois Gas Dynamics Laboratory. Dry, compressed air passes from the stagnation chamber through a flow conditioning module consisting of screens and honeycomb (used to dampen any large-scale disturbances generated in the air supply process and to minimize freestream turbulence levels) and finally to the converging-diverging supply nozzle. The pressure and temperature in the stagnation

chamber were consistently maintained at 515 ± 2.8 kPa and 294 ± 3 K, respectively. The nozzle takes an annular shape due to the central sting which supports the base model from upstream to prevent any interference with the near-wake flowfield. The cylindrical afterbody used in the present experiments is 63.5 mm in diameter and is attached by internal threads to the sting. Physical supports for the sting are located outside the rear of the stagnation chamber and inside the wind tunnel at the flow conditioning module. The sting supports are of sufficient rigidity such that sting vibration due to flowfield fluctuations was negligible. The nominal design Mach number and unit Reynolds number at the nozzle exit are 2.5 and 52 (10^6) per meter, respectively.

Proper centering of the afterbody/base within the nozzle is critical in obtaining axisymmetric flow in the near wake. In these experiments, custom-designed wind-tunnel adjusting blocks were used to adjust the relative position between the sting and nozzle until an axisymmetric flow was obtained. Oil-streak visualization performed on the base was used effectively to examine the sting/nozzle alignment and was found to be a very sensitive indicator of the symmetry of the near-wake flowfield. Micrometer measurements at the nozzle exit indicated a maximum afterbody misalignment of 0.13 mm from the physical nozzle centerline.

Experimental Methods

Conventional schlieren and shadowgraph photography were used to investigate the qualitative structure of the near-wake flowfield. The photographs were of only moderate quality due to the axisymmetric nature of the flow, but they were used successfully to confirm the flowfield structure shown in Fig. 1 and to determine a proper operating condition that eliminated any wind-tunnel interference effects.

Mean static pressure measurements were made at several locations on the base and afterbody surfaces using a Pressure Systems Inc. digital pressure transmitter (DPT 6400-T). There were 19 pressure taps (0.64 mm in diameter) located symmetrically across the base at radial intervals of 3.18 mm. Along the afterbody, two sets of diametrically opposed pressure taps (0.64 mm in diameter) were located starting 2.38 mm upstream of the base corner with each tap separated axially by 3.18 mm and a total of five taps in each set. In addition to the afterbody pressure taps, total pressure and temperature probes were mounted in the stagnation chamber.

The focus of this investigation involved the implementation of a two-component LDV system for measuring the near-wake velocity field. Artificial seed particles were generated by a TSI Inc. six-jet atomizer filled with 50 cp silicone oil. The droplets were injected into the flow upstream of the facility nozzle to avoid disturbing the flowfield with the injection process. In previous experiments with the same seeding apparatus, Bloomberg[17] deduced a mean droplet diameter of 0.8 μm and showed mean particle relaxation distances
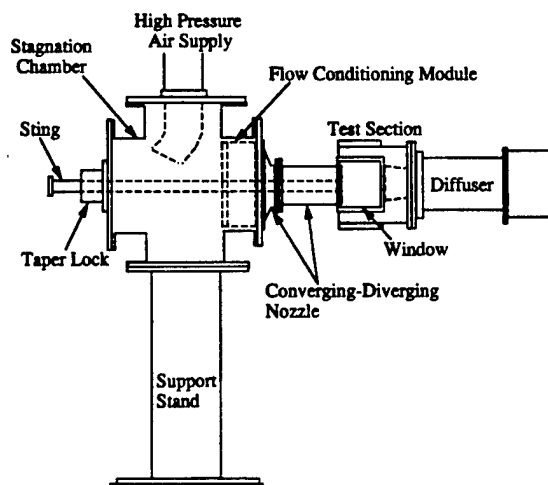

Fig. 2   Schematic diagram of axisymmetric wind tunnel.

of approximately 2 mm downstream of an oblique shock wave generated by a 15-deg compression corner in a Mach 2.6 flow. The maximum velocity gradients in the present experiments (near boundary-layer separation) are significantly weaker than for the oblique shock in Bloomberg's work; however, to ensure negligible particle lag in the current experiments, no data are presented within the first 5 mm downstream of the base corner separation point. In the separated shear layer, the Stokes number for this seeding configuration is estimated to be 0.15 which Samimy and Lele[18] have shown yields root-mean-square slip velocities (difference in velocity between the particle and the local fluid element) of approximately 1.5%.

The LDV measurement volume used in these experiments was 120 μm in diameter and had a fringe spacing of approximately 10.3 μm. A 20-deg off-axis, forward-scatter receiving optics configuration was used to reduce the effective measurement volume length to 0.70 mm. Bragg cells were used in each component to frequency shift one of the beams 40 MHz against the mean flow direction to discriminate reverse velocities. In addition, the two orthogonal fringe patterns were rotated to ±45 deg relative to the wind-tunnel axis to reduce fringe blindness. To measure accurately the Doppler frequencies in this demanding flow, a TSI Inc. IFA-750 autocorrelation processor was used. Data were gathered from the processor by a Gateway 2000 486-33 personal computer where further processing and analysis were performed. Positioning of the LDV measurement volume throughout the near-wake flowfield was accomplished using a three-axis, computer-controlled traversing table with a positioning resolution of 0.75 μm.

The LDV measurement locations were concentrated in the regions of high velocity gradients including the approach boundary layer, separated shear layer, developing wake, and also near the reattachment point. Radial traverses were completed at 21 axial stations throughout the near wake with approximately 30 spatial locations per traverse. In addition, an axial traverse along the model centerline was performed to show the development of the centerline mean velocity and turbulence intensities. During each radial traverse, three or four locations below the axis of symmetry were measured to check the symmetry of the flow. In all cases, the measured wake centerline (defined as the location where $<u'v_r'> = 0$) was within 2 mm of the geometric model centerline. Approximately 4000 instantaneous velocity realizations were gathered at each spatial location and probability density functions (pdfs) of each velocity component were calculated. The pdfs generally resembled a Gaussian profile except near the inner edge of the shear layer (near $U = 0$) where bimodal peaks in each pdf consistently occurred. The bimodal pdfs most likely indicate the presence of large-scale structures on the inner edge of the shear layer which play an important role in the entrainment of fluid from the recirculation region. The effects of velocity bias on the LDV data were accounted for by weighting each velocity realization with the interarrival time between realizations.[19]
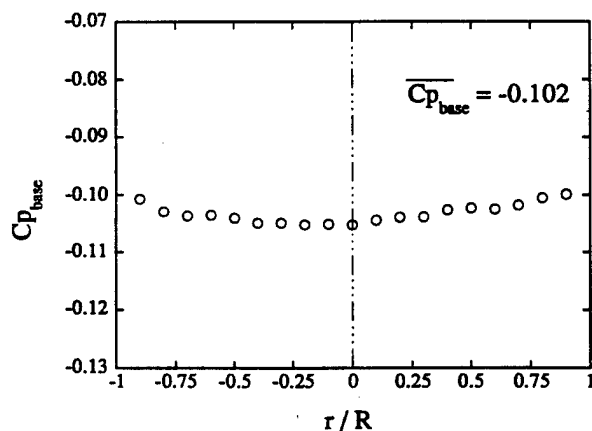
With the current two-component LDV arrangement, both the horizontal and vertical components of velocity were measured. In two-dimensional flows, this generally allows direct measurement of the streamwise and transverse velocities, but no measurement of the spanwise component. In the current axisymmetric flow, by using the same LDV configuration and making measurements independently in both the horizontal and vertical planes which pass through the axis of symmetry, all three mean and rms velocities have been measured. In addition, the axial-radial $(u'v_r')$ and axial-tangential $(u'v_t')$ Reynolds shear stresses have been directly measured. An error analysis including the uncertainties associated with velocity biasing, fringe biasing, velocity gradient biasing, finite ensemble size, processor resolution, optical misalignment, and fringe spacing determination has been completed. The estimated *worst-case* uncertainty in the mean velocity measurements is 1.2% of U_1 and, in the rms velocity fluctuations, 2.3% of U_1, where U_1 is the freestream velocity just prior to separation.

Results

Pressure Measurements

Static pressure measurements along the afterbody were used to assess the uniformity of the nozzle exit flow as well as any upstream influence of the separation process. As expected, the pressure field approaching the base corner was relatively uniform and takes a value consistent with an isentropically expanded Mach 2.44 flow. No upstream influence from the base corner separation was evident in the data.

Pressure measurements have also been made at 19 locations on the base to assess the radial distribution of the mean static pressure. Figure 3 shows the dimensionless base pressure coefficient at each location, defined as

$$C_{P_{base}} = \frac{2\left[(P_{base}/P_1) - 1\right]}{\gamma M_1^2} \tag{1}$$

where P is the static pressure. The pressure is shown to be relatively constant across the base (note the expanded vertical scale) with a slight increase toward larger radii where the maximum pressure measured was 3.9% higher than the pressure at the center of the base. Similar base pressure profiles were observed by Reid and Hastings[8] for a cylindrical afterbody in a Mach 2.0 flow with a maximum rise in pressure of approximately 3% across the base. An area-weighted average of the current data across the base was performed to determine an average base pressure coefficient of -0.102.

Flowfield Velocity Measurements

Approach Flow Measurements

The boundary layer approaching the base corner separation point was measured at three axial stations upstream of the base. Figure 4 is a plot of the boundary layer profile obtained 1 mm upstream of the base corner along with a curve fit by Sun and Childs[20] for compressible, turbulent boundary layers. The boundary-layer properties derived from the curve fit are also shown in Fig. 4. The values for the dimensionless properties (H, Π, and C_f) are typical of those found in equilibrium, compressible, turbulent boundary layers.[21] To determine the integral properties, the mean density profile through the boundary layer was determined using the ideal gas equation of state and the assumptions of negligible radial pressure gradient, adiabatic wall, and a recovery factor of 0.89 as suggested by Kays and Crawford.[22] The freestream Mach number across the nozzle exit was measured by LDV to be 2.46 ± 1% (the corresponding approach velocity was $U_1 = 567$ m/s). Also, measured freestream turbulence intensities in the approach flow were less than 1%.

Centerline Measurements

The LDV measurements along the model centerline were taken in 5-mm increments from the base to the end of the viewing window in the test section. A plot of the mean axial velocity along the
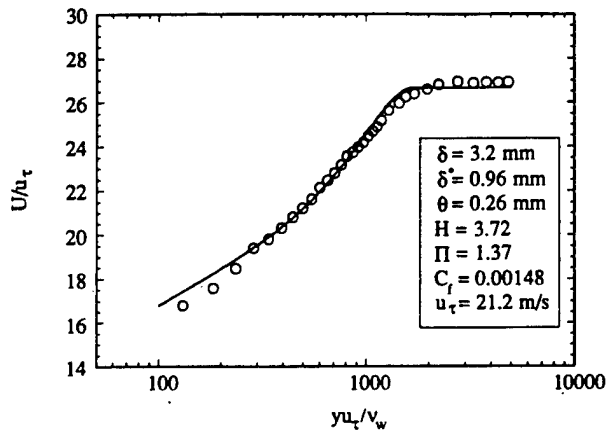

Fig. 3 Base pressure profile.

Fig. 4 Sun and Childs[20] curve fit of afterbody boundary-layer upstream of base corner.
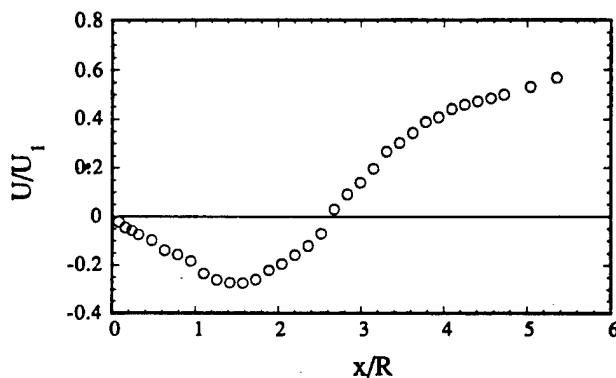

Fig. 5 Mean axial velocity along model centerline.

model centerline is shown in Fig. 5. The origin of the cylindrical coordinate system has been arbitrarily set at the center of the base with all axial distances positive downstream. The axial location where the data cross the $U = 0$ line clearly defines the rear stagnation point S since the other two measured velocity components are negligible along the centerline; this occurs at $x/R = 2.65$. The maximum reverse velocity occurs at $x/R \approx 1.5$ and takes a value of approximately 27% of the approach freestream velocity. In a similar experiment using LDV in subsonic flow (Mach 0.85) behind a circular cylinder, Delery[14] found the rear stagnation point located at 3.06 base radii downstream and a maximum reverse velocity of approximately 30% of the local freestream value located at $x/R = 1.8$. It is interesting to note that for both the supersonic and subsonic cases, the maximum reverse velocity occurs at a location approximately 57% of the distance from the base to the reattachment point. Merz et al.[23] found that for all Mach numbers from 0.1 to 0.9, the maximum reverse velocity was 35–40% of the freestream velocity and occurred at a distance 60% of the length to reattachment. The degree of wake redevelopment in the present experiments is indicated in Fig. 5 by the maximum positive centerline velocity which takes the value of 57% of the approach velocity ($M \approx 1.05$) at the farthest downstream station.

Near-Wake Mean Velocity Measurements

The mean velocity vector field in the near wake is shown in Fig. 6. In this and subsequent figures, the vertical axis has been expanded by 42% compared to the horizontal axis to more clearly show the features of the flowfield (the axial-to-radial aspect ratio of the actual LDV measurement grid is 4.27:1). To place the experimental data on a uniform grid for the vectors shown in Fig. 6, a simple linear interpolation in both x and r between the unequally spaced data was completed. The velocity vectors show clearly the

dominance of the axial velocity on the overall mean velocity field. The turning of the mean flow through the base corner expansion fan, the relatively low-speed recirculation region, and the realignment of the mean flow with the axis downstream of reattachment (S) are clearly shown.

A contour plot of the Mach number distribution throughout the near wake is shown in Fig. 7. The steep velocity gradients through the initial portion of the shear layer are clearly evident in the figure. The spreading of the contour lines farther downstream is indicative of the growth of the shear layer prior to reattachment and, also, the wake development downstream. Note that the flow along the axis reaccelerates to sonic velocity at approximately five base radii downstream which is similar to the measurements of Neale et al.[13] in a Mach 3 base flowfield where the sonic point was located at $x/R = 5.1$. The maximum Mach number of the reverse flow is 0.48 and is located on the centerline at approximately $x/R = 1.5$. The gradual recompression of the outer flow is indicated by the decreasing Mach number contours in the upper right of the figure.

The mean radial velocity contours are shown in Fig. 8. The small values relative to the mean axial approach velocity once again show the dominance of the axial velocity in the near-wake flowfield. The closely spaced contours emanating from the base corner mark the turning of the mean flow through the expansion fan. As the outer inviscid flow approaches the axis of symmetry, the radial velocity continues to increase in magnitude, due to the axisymmetric effect, to a peak value of 22% of the mean approach velocity at a location approximately two base radii downstream. The location of flowfield realignment with the axis of symmetry appears to depend on whether the flow is supersonic or subsonic. The realignment process in the outer flow is shown in the upper right of Fig. 8 by the contour lines of decreasing magnitude and the relatively uniform flow region downstream of the last contour. However, closer to the axis of symmetry, a much slower realignment of the subsonic inner flow occurs, such that the mean radial velocity is appreciable out to $x/R = 4.5$. The mean tangential (swirl) velocity was also directly measured with the LDV system, and as expected, the magnitudes were negligible compared to the other two components.

Near-Wake Turbulence Measurements

The root-mean-square fluctuation velocities were directly measured in all three coordinate directions and will be presented in the form of turbulence intensities, σ/U_1. Figure 9 shows the axial tur-
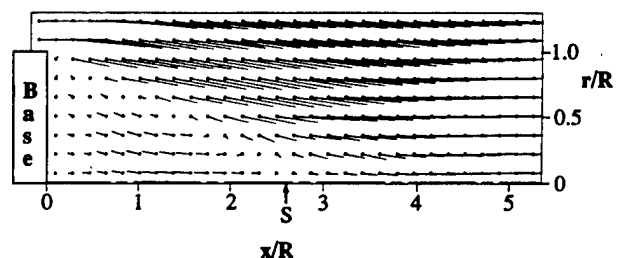

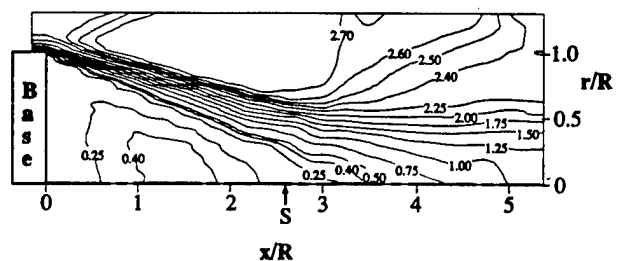Fig. 6 Mean velocity vector field throughout near wake.

Fig. 7 Mach number contours.

bulence intensity contours throughout the near wake. The large increase in turbulent fluctuations from the outer freestream to the values in the shear layer and wake are apparent. A peak axial rms velocity fluctuation of 22% of the mean approach velocity occurs at a location 83% of the axial distance from the base to reattachment. Upstream of reattachment at any axial station, the radial location of the maximum axial turbulence intensity lies in the subsonic region of the shear layer. In contrast, Amatucci et al.[15] found peak levels of turbulence intensity near the sonic line in a two-dimensional, two-stream base flow. Throughout the recirculation region in the current study, the axial turbulence intensity is relatively constant except very close to the base where it is attenuated. Farther downstream as the shear layer transforms into a wake, the overall level of turbulent fluctuations diminishes, and a well-defined peak in the axial turbulence intensity profiles is no longer discernible.

Contours of constant radial turbulence intensity are shown in Fig. 10. The general trends follow closely those of the axial turbulence intensity, but the overall fluctuation levels are smaller. The peak radial velocity fluctuation is 15.6% of U_1 and occurs at roughly the same location as the peak axial fluctuation. The recirculation region contains a greater variation in radial turbulence intensity than axial turbulence intensity with a steady increase from the base to the reattachment point (not including the base effects at $x/R < 0.5$). The turbulence relaxation beyond reattachment is fairly slow with a uniform radial turbulence intensity across the inner portion of the wake as it develops.

The tangential turbulence intensity represents fluctuations from the mean swirl velocity which, as mentioned previously, is negligible for axisymmetric flows. Figure 11 is a plot showing the tangential turbulence intensity throughout the near wake. The overall level of fluctuations in the tangential direction is reduced compared to the axial turbulence intensity and is generally smaller than the radial fluctuations. The peak value of the tangential velocity fluctuations is 13.5% of U_1 and occurs near the shear layer reattachment point at $x/R = 2.65$. The greatest variation in tangential turbulence intensity occurs at the outer edges of the shear layer and wake, and the radial profiles do not exhibit the sharp peaks evident in the axial and radial turbulence intensities.

The ratio of the turbulence intensity contributions from each component gives a relative indication of the anisotropy in the normal stress field. In the current flow, the axial turbulence intensity dominates with peak values approximately 30–50% higher than
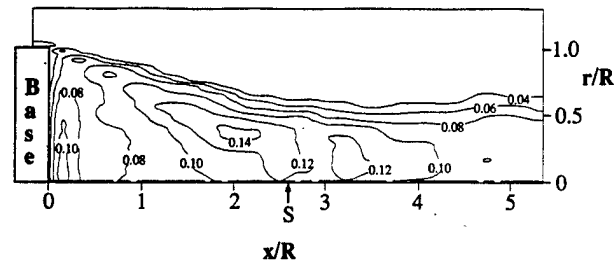

Fig. 8 Mean radial velocity contours, V_r/U_1.

Fig. 9 Axial turbulence intensity contours, σ_u/U_1.

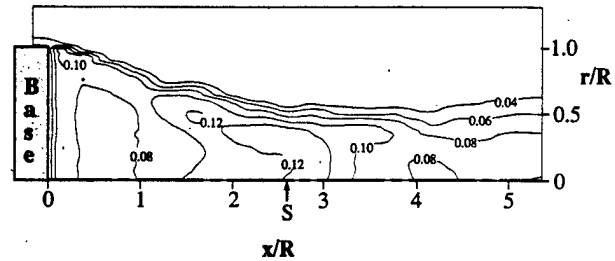Fig. 10 Radial turbulence intensity contours, σ_{v_r}/U_1.

Fig. 11 Tangential turbulence intensity contours, σ_{v_t}/U_1.

the peak radial fluctuations and 60–70% higher than the peak tangential fluctuations in the shear layer where anisotropy is largest. The relative ordering of the peak turbulence intensity magnitudes (axial-radial-tangential) found in the current base flow experiments can be contrasted with the recent data from Gruber et al.[24] for a two-dimensional, compressible, constant-pressure mixing layer. In their study, the magnitude of the spanwise component of turbulence intensity exceeded the contribution from the transverse component by approximately 20% in the peak intensity region of the shear layer, probably due to the three-dimensional nature of the large-scale structures in the planar, compressible mixing layer. In axisymmetric flow, the tendency of the structures to grow asymmetrically (in the tangential direction) is most likely dampened by the more stringent axisymmetric conditions imposed by the mean flowfield. In incompressible, constant-pressure mixing layers, the spanwise component of turbulence intensity has been shown to be approximately equal to the transverse turbulence intensity.[25]

An important turbulence quantity often used to describe the overall level of turbulent fluctuations is the turbulent kinetic energy defined as

$$k = \frac{1}{2}\left(\sigma_u^2 + \sigma_{v_r}^2 + \sigma_{v_t}^2\right) \qquad (2)$$

In these experiments, all three mean square fluctuations (normal stresses) have been directly measured. Figure 12 is a plot of the turbulent kinetic energy as measured throughout the near wake. Since the axial turbulence fluctuation levels dominate the flowfield, the contours of turbulent kinetic energy appear relatively similar to those of the axial turbulence intensity (Fig. 9). The turbulent kinetic energy grows rapidly after separation as the shear layer grows. Prior to reattachment, however, a maximum is reached and a subsequent decay to the relatively constant values in the wake occurs. Again, the sharp peaks in turbulent kinetic energy radial profiles occurring in the shear layer are nonexistent in the wake farther downstream. In the recirculation region, the level of turbulent kinetic energy is reduced by the lack of turbulence production due to small mean velocity gradients. The maximum turbulent kinetic energy measured in the near wake was 4.4% of U_1^2 and occurred at $x/R = 2.2$, or somewhat upstream of reattachment.

In the current experiments, both the axial-radial ($<u'v_r'>$) and axial-tangential ($<u'v_t'>$) Reynolds shear stresses have been measured directly. As expected, the axial-radial shear stress dominates the axial-tangential stress which is negligible throughout the near
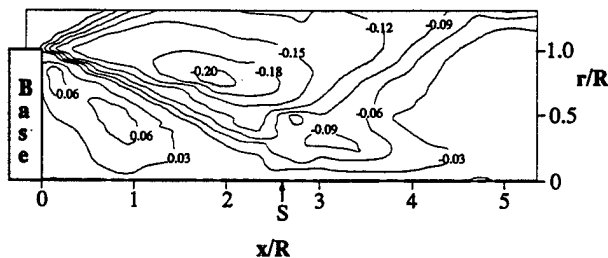
wake. Figure 13 is a plot showing the axial-radial shear stress distribution downstream of the base. The shear stress peaks in the shear layer upstream of reattachment in approximately the same location as the peak in turbulent kinetic energy. Abu-Hijleh and Samimy[26] used LDV to investigate a supersonic shear layer reattaching onto a wall and found peak values of turbulent kinetic energy and Reynolds stress *downstream* of the reattachment location. The difference in the locations for the peak turbulence quantities between these experiments may possibly be attributed to the differences between solid wall and compliant surface reattachment.

The production of turbulent kinetic energy, defined as

$$P_k = -<u_i'u_j'> \frac{\partial U_i}{\partial x_j}$$ (3)

provides a measure of the amount of kinetic energy transferred from the mean flow to the turbulence field. Investigating the distribution of P_k throughout the near wake provides insight into the structure of the turbulence field as well as establishing the role of turbulence production in different regions of the flow. In axisymmetric flow, only four of the nine production terms are nonzero which leaves the following expression for P_k:

$$P_k = -\sigma_u^2 \frac{\partial U}{\partial x} -<u'v_r'>\left(\frac{\partial U}{\partial r} + \frac{\partial V_r}{\partial x}\right) - \sigma_{v_r}^2 \frac{\partial V_r}{\partial r}$$ (4)

which is plotted in Fig. 14 (to avoid clutter, only a reference contour label is shown; all other contours are equally spaced with values increasing by 0.02). Strong turbulence production is seen to occur immediately downstream of the separation point on the inner edge of the shear layer. This is not surprising as the mean velocity gradients are very large in this region. As the shear layer develops, the mean velocity gradients decrease but the Reynolds stresses increase (Figs. 9–13) such that the total production remains significant up to the reattachment point. Downstream of reattachment, however, the Reynolds stresses and mean velocity gradients both decrease rapidly resulting in a diminished level of turbulence production.

Since the total production of turbulent kinetic energy is merely the sum of the production terms for each Reynolds normal stress,
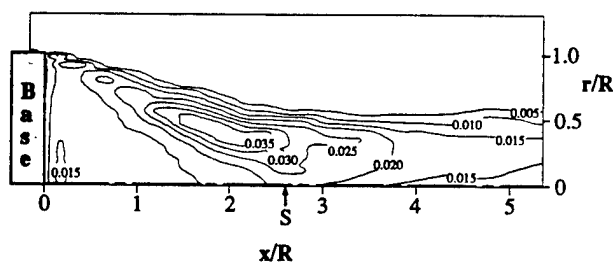

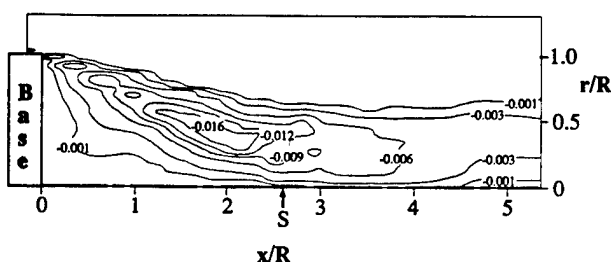**Fig. 12   Turbulent kinetic energy contours, k/U_1^2.**

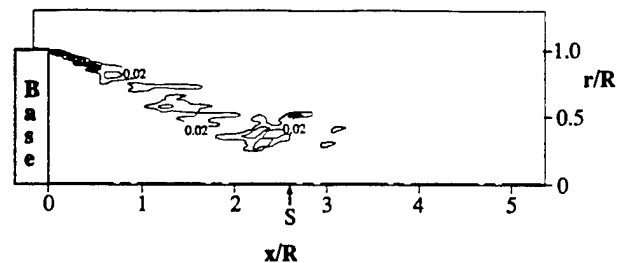**Fig. 13   Reynolds shear stress contours, $<u'v_r'>/U_1^2$.**

Fig. 14   Turbulence production contours, $P_k \cdot R/U_1^3$.

separating the total production expression into its individual components yields

$$P_k = P_u + P_{v_r} + P_{v_t}$$ (5)

where the individual production terms for each Reynolds normal stress are

$$P_u = -\sigma_u^2 \frac{\partial U}{\partial x} -<u'v_r'> \frac{\partial U}{\partial r}$$ (6)

$$P_{v_r} = -\sigma_{v_r}^2 \frac{\partial V_r}{\partial r} -<u'v_r'> \frac{\partial V_r}{\partial x}$$ (7)

$$P_{v_t} = 0$$ (8)

From the current experiments, the relative magnitudes of each term indicate that $P_u \gg P_{v_r} > P_{v_t}$. Consequently, the majority of the energy exchange between the mean flow and the turbulence field occurs through the axial component of the Reynolds normal stress. On the other hand, the radial and tangential components must receive their kinetic energy from other sources such as pressure-velocity interactions or momentum transport by turbulent velocity fluctuations. Therefore, the relative ordering of the Reynolds normal stresses ($\sigma_u^2 > \sigma_{v_r}^2 > \sigma_{v_t}^2$) is consistent with the amount of turbulence production that each component receives from the mean flow.

Summary and Conclusions

The turbulent near wake of a circular cylinder aligned with a supersonic flow has been investigated using nonintrusive measurement techniques. The main objective of these experiments is to increase the understanding of the complex fluid dynamic phenomena that occur in supersonic base flowfields by the use of detailed quantitative data gathered throughout the near wake. Specifically, afterbody and base pressure distributions, mean velocities, turbulence intensities, and Reynolds shear stresses have been obtained; these data have been tabularized on a floppy disk which is available from the authors. As a result of data analysis, the following conclusions concerning the near-wake flowfield can be made:

1) The mean static pressure profile across the base is relatively uniform with an average base pressure coefficient of -0.102.

2) The maximum reverse velocity along the wake centerline reached 27% of the mean approach velocity, or Mach 0.48, and occurs approximately 57% of the distance from the base to the reattachment point (located at $x/R = 2.65$). Along the centerline, the axial and radial turbulence intensities peak near the reattachment point and decay as the wake develops downstream.

3) The recirculating flow is generally characterized by small mean velocity gradients and relatively uniform turbulence intensities.

4) The separated shear layer is found to contain steep radial velocity gradients and sharp peaks in turbulence intensity in the subsonic region. Beyond reattachment, the sharp peaks decay toward nearly uniform turbulence intensities across the redeveloping wake.

5) Peak values of turbulent kinetic energy and axial-radial shear stress are located in the subsonic region of the shear layer upstream of reattachment. This is in contrast to earlier results on compressible shear layer reattachment onto a solid surface which indicate peak levels at or downstream of the reattachment point. The production of turbulent kinetic energy peaks immediately downstream of separation along the inner edge of the shear layer.

Acknowledgment

References

[1]Rollstin, L., "Measurement of Inflight Base Pressure on an Artillery-Fired Projectile," AIAA Paper 87-2427, Aug. 1987.

[2]Delery, J., and Wagner, B., "Results of GARTEUR Action Group AG09 on Flow Past Missile Afterbodies," *Proceedings of the AGARD/FDP Symposium on Missile Aerodynamics*, Friedrichshafen, Germany, April, 1990.

[3]Peace, A. J., "Turbulent Flow Predictions for Afterbody/Nozzle Geometries Including Base Effects," *Journal of Propulsion and Power*, Vol. 7, No. 3, 1991, pp. 396–403.

[4]Sahu, J., "Supersonic Flow Over Cylindrical Afterbodies with Base Bleed," AIAA Paper 86-0487, Jan. 1986.

[5]Wilmoth, R. G., and Putnam, L. E., "Subsonic/Transonic Prediction Capabilities for Nozzle/Afterbody Configurations," AIAA Paper 84-0192, Jan. 1984.

[6]Korst, H. H., "A Theory for Base Pressures in Transonic and Supersonic Flow," *Journal of Applied Mechanics*, Vol. 23, No. 4, 1956, pp. 593–600.

[7]Zumwalt, G. W., "Analytical and Experimental Study of Axially-Symmetric Supersonic Base Pressure Problem," Ph.D. Thesis, Dept. of Mechanical Engineering, Univ. of Illinois at Urbana-Champaign, Urbana, IL, 1959.

[8]Reid, J., and Hastings, R. C., "Experiments on the Axi-Symmetric Flow Over Afterbodies and Bases at M = 2.0," Royal Aircraft Establishment, RAE Rept. Aero. 2628, Farnborough, England, UK, 1959.

[9]Badrinarayanan, M. A., "An Experimental Investigation of Base Flows at Supersonic Speeds," *Journal of the Royal Aeronautical Society*, Vol. 65, July 1961, pp. 475–482.

[10]Demetriades, A., "Mean-Flow Measurements in·an Axisymmetric Compressible Wake," *AIAA Journal*, Vol. 6, No. 3, 1968, pp. 432–439.

[11]Hawkins, R., and Trevett, E., "Changes in the Flow at the Base of a Bluff Body Due to a Disturbance in its Wake," AGARD Rept. 539, May 1966.

[12]Gaviglio, J., Dussauge, J. P., Debieve, J. F., and Favre, A., "Behavior of a Turbulent Flow Strongly Out of Equilibrium at Supersonic Speeds," *Physics of Fluids*, Vol. 20, No. 10, 1977, pp. 179–192.

[13]Neale, D. H., Hubbartt, J. E., Strahle, W. C., and Wilson, W. W., "Effects of External Compression on an Axisymmetric Turbulent Near Wake," *AIAA Journal*, Vol. 16, No. 9, 1978, pp. 940–947.

[14]Delery, J., "ONERA Research on Afterbody Viscid/Inviscid Interaction with Special Emphasis on Base Flows," *Proceedings of the Symposium on Rocket/Plume Fluid Dynamic Interactions, Vol. III—Flow Fields*, Univ. of Texas at Austin, Austin, TX, 1983; also Fluid Dynamics Labs. Rept. 83-104, April 1983.

[15]Amatucci, V. A., Dutton, J. C., Kuntz, D. W., and Addy, A. L., "Two-Stream, Supersonic, Wake Flowfield Behind a Thick Base, Part I: General Features," *AIAA Journal*, Vol. 30, No. 8, 1992, pp. 2039–2046.

[16]Heltsley, F. L., Walker, B. J., and Nichols, R. H., "Transonic Nozzle-Afterbody Flow Field Measurements Using a Laser Doppler Velocimeter," AGARD CP-348, Sept. 1983.

[17]Bloomberg, J. E., "An Investigation of Particle Dynamics Effects Related to LDV Measurements in Compressible Flows," M.S. Thesis, Dept. of Mechanical and Industrial Engineering, Univ. of Illinois at Urbana-Champaign, Urbana, IL, 1989.

[18]Samimy, M., and Lele, S. K., "Motion of Particles with Inertia in a Compressible Free Shear Layer," *Physics of Fluids A*, Vol. 3, No. 8, 1991, pp. 1915–1923.

[19]Herrin, J. L., and Dutton, J. C., "An Investigation of LDV Velocity Bias Correction Techniques for High-Speed Separated Flows," *Experiments in Fluids*, Vol. 15, No. 4–5, pp. 353–363.

[20]Sun, C. C., and Childs, M. E., "A Modified Wall Wake Velocity Profile for Turbulent Compressible Boundary Layers," *Journal of Aircraft*, Vol. 10, No. 6, 1973, pp. 381–383.

[21]Fernholz, H. H., and Finley, P. J., "A Critical Commentary on Mean Flow Data for Two-Dimensional Compressible Turbulent Boundary Layers," AGARDograph No. 253, May 1980.

[22]Kays, W. M., and Crawford, M. E., "The Turbulent Boundary Layer for a Gas with Variable Properties," *Convective Heat and Mass Transfer*, 2nd ed., McGraw-Hill, New York, 1980, pp. 305–309.

[23]Merz, R. A., Page, R. H., and Przirembel, C. E. G., "Subsonic Axisymmetric Near-Wake Studies," *AIAA Journal*, Vol. 16, No. 7, 1978, pp. 656–662.

[24]Gruber, M. R., Messersmith, N. L., and Dutton, J. C., "Three-Dimensional Velocity Field in a Compressible Mixing Layer," *AIAA Journal*, Vol. 31, No. 11, pp. 2061–2067.

[25]Bell, J. H., and Mehta, R. D., "Interaction of a Streamwise Vortex with a Turbulent Mixing Layer," *Physics of Fluids A*, Vol. 2, No. 11, 1990, pp. 2011–2023.

[26]Abu-Hijleh, B., and Samimy, M., "An Experimental Study of a Reattaching Supersonic Shear Layer," AIAA Paper 89-1801, June 1989.

APPENDIX A.3

SUPERSONIC NEAR-WAKE AFTERBODY BOATTAILING EFFECTS ON AXISYMMETRIC BODIES

by

J. L. Herrin and J. C. Dutton

Supersonic Near-Wake Afterbody Boattailing Effects on Axisymmetric Bodies

J. L. Herrin* and J. C. Dutton†

University of Illinois at Urbana–Champaign, Urbana, Illinois 61801

An experimental investigation of the near-wake flowfield downstream of a conical boattailed afterbody in supersonic flow is presented. The afterbody investigated is typical of those for conventional boattailed missiles and projectiles in unpowered flight. Flow visualization, mean static pressure measurements, and three-component laser Doppler velocimeter data have been obtained throughout the near wake of the body. The effects of afterbody boattailing on the physics of the near-wake flow are determined by comparing the present data with similar data obtained on a cylindrical afterbody. Results indicate that a net afterbody drag reduction of 21% is achieved with the current boattailed afterbody for a freestream Mach number of 2.46. The shear-layer growth rate, and therefore mass entrainment from the recirculation region behind the base, is shown to be significantly reduced by afterbody boattailing due to the reduction in turbulence levels throughout the near wake as compared to the cylindrical afterbody.

Nomenclature

C_D = dimensionless drag coefficient
C_f = skin-friction coefficient
C_p = dimensionless pressure coefficient
d = hole diameter, mm
H = compressible shape factor, δ^*/θ
k = turbulent kinetic energy, m^2/s^2
M = Mach number
R_0 = afterbody radius upstream of boattail, mm
r = radial coordinate, mm
S = distance to shear-layer reattachment, mm
U = mean axial velocity, m/s
u_τ = friction velocity, m/s
u' = instantaneous axial-velocity fluctuation, m/s
V_r = mean radial velocity, m/s
v = instantaneous velocity, m/s
v_r' = instantaneous radial-velocity fluctuation, m/s
v_t' = instantaneous tangential-velocity fluctuation, m/s
x = axial coordinate, mm
y = distance perpendicular to local afterbody surface, mm
β = afterbody surface angle relative to horizontal, deg
δ = boundary-layer thickness, mm
δ^* = boundary-layer displacement thickness, mm
θ = boundary-layer momentum thickness, mm
ν_w = kinematic viscosity at wall, m^2/s
Π = boundary-layer wake strength parameter
σ = root-mean-square value
$\langle\ \rangle$ = ensemble-averaged value
$(\ \ )$ = area-weighted average value

Subscripts

b = boattailed afterbody
base = condition at base
c = cylindrical afterbody

net = sum of boattail and base contributions
u = axial component
v_r = radial component
v_t = tangential component
1 = approach conditions to the afterbody

Introduction

MODERN missiles and projectiles can suffer significant amounts of drag during transonic and supersonic flight due to the low pressure acting on the rear of the body. Generally termed base drag, the pressure-area force acting on the base of a typical flight vehicle can make up a substantial portion of the total drag in many instances, especially for missiles or projectiles in unpowered flight, where a high-pressure propulsive jet is absent.[1] In fact, the base drag on the Space Shuttle Columbia has been shown to be approximately 50% of the total orbiter drag during re-entry.[2] Throughout the last three decades, several methods to reduce base drag have been developed, including afterbody boattailing, base bleed, base cavities, and base burning. The simplest of these to implement in practice is afterbody boattailing, which generally involves only a slight modification to the afterbody surface angle, the payoff being a higher base pressure (reduced afterbody drag). Reference 3 has shown that conical boattails (constant afterbody surface angle β prior to separation) can reduce the net afterbody drag by up to 30% from that on a cylindrical afterbody ($\beta = 0$ deg) in unpowered, supersonic flight. Although the global benefits (i.e., drag reduction) of afterbody boattailing have been well established for different boattail angles, Mach numbers, and Reynolds numbers (e.g., Refs. 4–7), detailed studies of the fluid-dynamic effects in the near wake due to afterbody boattailing have not previously been conducted. An increased understanding of the flow physics in the base region is essential as new methods are developed to further reduce net afterbody drag on practical flight vehicles.

The near-wake flowfield of an axisymmetric, boattailed afterbody in a uniform supersonic flow is sketched in Fig. 1. Several complicated fluid-dynamic phenomena exist in the flowfield, including the rapid expansion of the turbulent boundary layer at the body-boattail junction, geometric boundary-layer separation at the base corner, growth of the compressible shear layer, and reattachment along the axis of symmetry. Obviously, the effects on the near wake of adding a boattail to a cylindrical afterbody stem from the change in initial conditions at the base-corner separation point, which include a higher freestream Mach number, nonzero local flow angle, and nonzero pressure gradient due to the axisymmetric compression effect on the boattail as the flow approaches the axis of symmetry. In addition, the presence of the boattail alters the state of the turbulent

Fig. 1   Schematic diagram of mean flowfield downstream of boattailed afterbody.

Fig. 2   Diagram of pressure-tap locations and coordinate origin for boattail model.

boundary layer by the rapid expansion at the body-boattail junction and by the adverse pressure gradient on the boattail surface. As will be shown in this paper, the outer inviscid flow over the boattail can be adequately predicted by the axisymmetric method of characteristics; however, the boundary-layer development along the boattail up to the separation point is much more difficult to predict. In addition, the mean and turbulent characteristics of the boundary layer at separation play an important role in determining the initial structure of the separated shear layer and, therefore, the turbulent mixing and mass entrainment rates in the near wake.

Several authors have shown that rapid expansions (such as those at the body-boattail junction and base corner) can significantly distort the mean and turbulence characteristics of an attached turbulent boundary layer. Reference 8 found a significant distortion in the mean-velocity profiles downstream of a variety of centered expansions in supersonic flow. This reference noted the possibility that the distorted postexpansion boundary layer could have a significant effect on the separation characteristics, shear-layer growth rates, and reattachment processes for boattailed afterbodies, the effect being greater for larger boattail angles. It has also been established that rapid expansions reduce the turbulence levels in compressible boundary layers.[9,10] Reference 11 recently used filtered Rayleigh scattering to show that the strong dilatation effect associated with the rapid expansion of a compressible boundary layer increases the scale of the turbulent structures present in the approach boundary layer. In addition, the small-scale turbulence near the wall was shown to recover more quickly from the effects of the expansion than the relatively large-scale motion in the outer region of the boundary layer. The effect of the strong expansion at the body-boattail junction on the afterbody boundary layer and, hence, on the initial conditions to the near-wake flowfield has generally been ignored in previous investigations of boattailed afterbody flowfields.

The primary objective of the present research is to investigate the fluid-dynamic effects of afterbody boattailing on axisymmetric bodies in supersonic flow in an effort to shed new light on the mechanisms associated with the increase in base pressure (reduced afterbody drag) relative to the cylindrical afterbody case. To this end, schlieren and shadowgraph photography, static pressure measurements, and three-component laser Doppler velocimetry (LDV) data have been obtained throughout the near wakes of both a cylindrical afterbody and a boattailed afterbody. The data obtained downstream of the cylindrical afterbody have been presented elsewhere.[12] In this paper measurements with the boattailed afterbody are presented and comparisons with the cylindrical afterbody case are made to determine the fluid-dynamic effects of adding a conical boattail to a cylindrical afterbody. In addition, a complete documentation of the mean velocity and turbulence fields throughout the near wake of a boattailed afterbody will provide a valuable data base to which analytical and numerical modelers of base flows can compare solutions.

Experimental Facility and Instrumentation

The experiments described herein were conducted in the axisymmetric wind-tunnel facility at the University of Illinois Gas Dynamics Laboratory. A detailed description of the axisymmetric wind tunnel and its use for the study of supersonic, axisymmetric afterbody flows has been given in Ref. 12. The mean freestream Mach
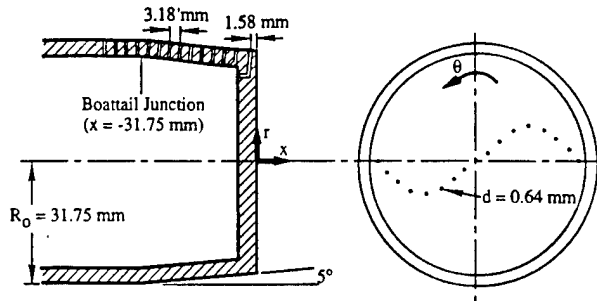
number is 2.46, the unit Reynolds number is 52×10^6 m^{-1}, and the measured freestream turbulence intensity is less than 1%. Physical support for the afterbody is provided by a cylindrical sting of radius 31.75 mm that extends upstream through the nozzle in order to avoid any flow disturbances in the near wake. The boattail chosen for the present study has a conical shape with an angle relative to the horizontal of 5 deg and an axial length of 31.75 mm (0.5 caliber). Reference 13 has shown that the optimal boattail shape (i.e., shape yielding minimum afterbody drag) is essentially conical at moderate supersonic Mach numbers for typical boattail lengths. In addition, the boattail angle chosen is near the optimal angle given in Ref. 3 for minimum total afterbody drag at Mach 2.5.

Conventional schlieren and shadowgraph photography were used to investigate the overall structure of the near-wake flowfield. These photographs were of only moderate quality because of the axisymmetric nature of the flow, but they were used successfully to confirm the mean flowfield sketched in Fig. 1. Surface oil-streak visualization on the base surface was used to document the symmetry of the near-wake flowfield. By combining motor oil (10W-30) with a black pigment and then applying it to the base in small drops, an oil-streak pattern was observed during a wind-tunnel blowdown and was found to be a very sensitive indicator of flow symmetry at the base.

Mean static pressure measurements were made on the afterbody and base surfaces with a Pressure Systems Inc. digital pressure transmitter (DPT 6400-T). Seventeen taps (0.64 mm in diameter) were located symmetrically across the base at radial intervals of 3.18 mm in order to assess the radial dependence of the time-averaged base pressure. In addition, 14 taps (0.64 mm in diameter) were located on the afterbody surface to document the mean static pressure field approaching and along the boattail. The afterbody taps were separated axially by 3.18 mm in such a way that four taps were located upstream of the body-boattail junction and ten taps were located axially along the boattail. Figure 2 is a schematic diagram showing the pressure-tap locations on the afterbody and base surfaces.

The primary experimental tool used in the current study was a two-component LDV system with frequency shifting, which was used to measure the near-wake velocity field. The optical arrangement and system setup are identical to that used in the cylindrical afterbody case.[12] The measurement-volume diameter and length are approximately 120 and 700 μm, respectively. Data were obtained in two perpendicular planes (horizontal and vertical), each intersecting the axis of symmetry. In the vertical plane, the two-component LDV system measures axial and radial velocities, while in the horizontal plane, the system measures axial and tangential velocities. Hence, two independent planes of LDV data in the near wake were obtained, from which three mean velocities, three Reynolds normal stresses (σ_u^2, $\sigma_{v_r}^2$, and $\sigma_{v_t}^2$), and two of three Reynolds shear stresses ($\langle u'v_r' \rangle$ and $\langle u'v_t' \rangle$) were determined. The LDV measurement grid consisted of approximately 1300 spatial locations concentrated in regions of large velocity gradients (e.g., the separated shear layer). An error analysis of the LDV data acquisition procedure was used to estimate a worst-case uncertainty in the mean velocity of 1.2% of U_1 and in the root-mean-square velocity fluctuation of 2.3% of U_1, where $U_1 = 567$ m/s is the mean freestream velocity approaching the afterbody.

Results

Pressure Measurements

The static pressure distribution along the boattailed afterbody is shown in Fig. 3 along with a method-of-characteristics solution for irrotational, axisymmetric flow. The sharp decrease in pressure through the expansion at the body-boattail junction $(x/R_0 = -1.0)$ is clearly evident. The experimental data are shown to relax gradually to the predicted pressure field downstream of the expansion so that near the base corner $(x/R_0 = 0.0)$ the agreement between experiment and computation is quite good. The experimental pressure distribution shown in Fig. 3 was numerically integrated along the boattail using a trapezoidal rule to determine an area-averaged boattail drag coefficient of 0.056. For comparison, the integrated-method-of-characteristics profile yields an average boattail drag coefficient of 0.061, which is slightly higher than the experimental result because of the rapid drop in pressure predicted at the body-boattail junction.

The measured static pressure distribution across the base of the boattailed afterbody is shown in Fig. 4 along with similar data obtained for the cylindrical afterbody.[12] In general, the two profiles are very similar, showing a slight increase in base pressure with increasing radius; however, the overall magnitudes of the pressure coefficient are substantially lower on the boattailed afterbody (reduced afterbody drag). The pressures at the outer edge of the base may be higher than at the center on account of the severe streamline curvature that undoubtedly occurs near this region. As the low-speed fluid flowing radially outward at the base becomes entrained by the high-speed shear layer near the base corner, a change in flow direction in excess of 90 deg results; for this reason, the static pressure imposed near the base corner should be increased over the pressure at the center of the base.

The base pressure distributions shown in Fig. 4 were numerically integrated using a trapezoidal rule to obtain area-averaged base drag coefficients of 0.086 and 0.102 for the boattailed and cylindrical afterbodies, respectively. When examining the benefits of afterbody boattailing relative to a cylindrical afterbody, the net afterbody drag coefficients (boattail + base) must be compared. For the present boattailed afterbody, the net afterbody drag coefficient was determined to be 0.081. For the cylindrical afterbody, the only contribution to the net afterbody form drag is from the base,
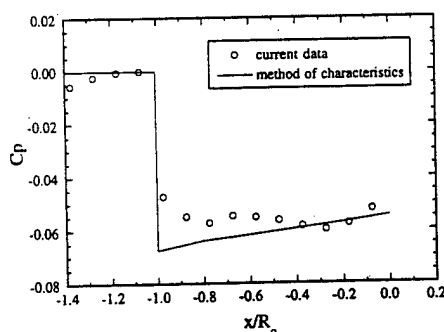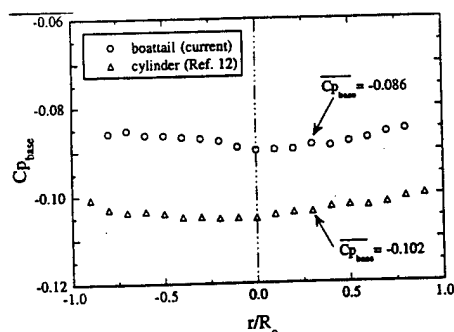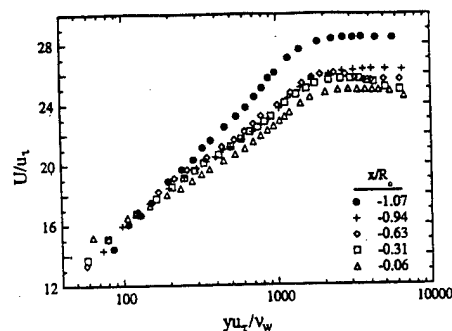

Fig. 5 Bounday-layer profiles perpendicular to boattail surface (body-boattail junction located at $x/R_0 = -1.00$).

$C_{Dnet} = C_{Dbase} = 0.102$. A comparison of the net afterbody drag coefficients for each afterbody shows a 21% reduction in drag due to afterbody boattailing. This result compares well with the data of Ref. 5, which showed a drag reduction of 25% with a similar geometry and flow conditions. From the data presented above, it is obvious that afterbody boattailing is an effective method to reduce net afterbody drag on axisymmetric bodies in supersonic flight. The fluid-dynamic effects associated with the drag reduction (increase in base pressure) have been investigated in the current study with detailed LDV measurements throughout the near-wake flowfield. These measurements are described below.

Velocity Measurements

Approach Flowfield

Mean-velocity and turbulence data have been obtained upstream of the base corner along thirteen traverses normal to the afterbody surface. These data are used to fully document the approach conditions to the near-wake flowfield as well as to determine the effects of the centered expansion at the body-boattail junction on the characteristics of the turbulent boundary layer immediately upstream of separation. The mean streamwise velocity profiles at five axial locations upstream of the base corner are plotted in conventional wall coordinates in Fig. 5 (data from only five of the thirteen traverses are shown in the figure to avoid overcrowding). By comparing the data obtained upstream of the body-boattail junction (represented by the filled symbols in the figure) with those obtained at successive axial locations along the boattail, the expansion at the body-boattail junction is shown to reduce the outer wake of the original undisturbed boundary layer and to cause a gradual reduction in the slope of the log region. Relaxation of the mean velocity downstream of the body-boattail junction appears quite rapid initially, but the general shape of the profiles appears to be slowly evolving even at the last axial station prior to separation at the base corner $(x/R_0 = -0.06)$. These results are similar to those given by Ref. 9, which showed that the boundary layer downstream of a sudden expansion recovers quickly at first, with significant changes in the mean profile occurring within the first 10 boundary-layer thicknesses downstream of the expansion (this distance corresponds to the length of the boattail in the present case); a complete recovery of the mean velocity and turbulence profiles across the boundary layer generally requires a substantially longer distance.

The mean boundary layer velocity profile immediately upstream of the base corner $(x/R_0 = -0.06)$ is shown in Fig. 6 with a curve fit for compressible, turbulent boundary layers given in Ref. 14. The integral boundary-layer properties as determined from the curve fit are important initial conditions to the near-wake flowfield and therefore are also included in the figure. The good agreement between the experimental data and the curve fit suggests that the boundary layer has nearly recovered (in the mean-velocity sense) from the expansion at the body-boattail junction and is approximately in equilibrium prior to separation (note that this "new" equilibrium state is different than that existing upstream of the body-boattail junction). In the present case, the boundary-layer thickness is approximately 15% of the base radius, so that axisymmetric effects on the boundary layer due to lateral surface curvature are generally quite weak. The values shown in Fig. 6 for the shape factor, wake strength parameter, and skin-friction coefficient fall within the ranges established by previ-
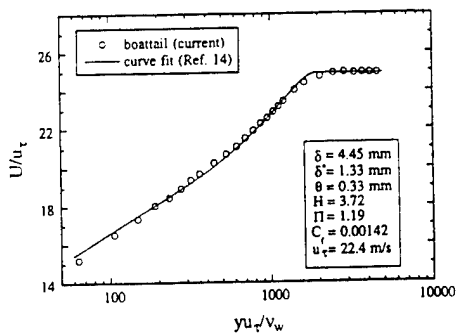

Fig. 3 Boattail pressure distribution.

Fig. 4 Base pressure distributions for boattailed and cylindrical afterbodies.

Fig. 6   Mean bounday-layer profile immediately upstream of base corner $(x/R_0 = -0.06)$.

Fig. 8   Mean axial velocity along centerline: comparison between boattailed and cylindrical afterbodies.

Fig. 7   Effect of expansion at body-boattail junction on streamwise rms velocity fluctuation.

Fig. 9   Turbulent kinetic energy distributions along centerline: comparison between boattailed and cylindrical afterbodies.
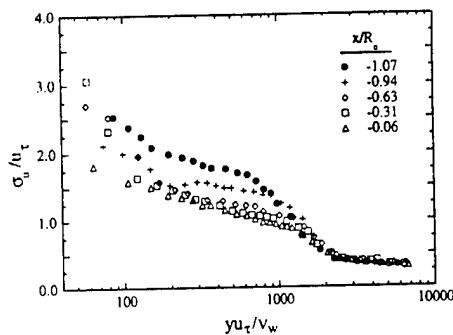
ous investigators for equilibrium, compressible, turbulent boundary layers.[15] The freestream Mach number and unit Reynolds number immediately upstream of the base corner are 2.61 and 47×10^6 m^{-1}, respectively.

Although the mean velocity in the boundary layer recovers fairly quickly from the expansion at the body-boattail junction, previous experiments have shown that the turbulence properties generally recover much more slowly.[9,10] Figure 7 is a plot of the nondimensional streamwise root-mean-square (rms) velocity fluctuation (σ_u/u_τ) distribution at five axial stations along the afterbody (again, for clarity only a few traverses are shown). A significant distortion in the streamwise rms velocity fluctuation profile occurs through the sudden expansion at the body-boattail junction with an overall reduction in the magnitude of the turbulence fluctuations (as characterized by σ_u). The collapse of the data obtained at the last two axial stations upstream of the base corner seems to indicate that a "new" equilibrium state of reduced turbulence levels has been reached prior to separation. Although not shown here for conciseness, the transverse rms velocity fluctuation profiles and the primary Reynolds shear stress profiles also exhibited a significant decrease in magnitude through the expansion at the body-boattail junction.

As indicated above, the expansion at the body-boattail junction distorts both the mean velocity and turbulence quantities in the afterbody boundary layer, so that the initial conditions for the near-wake flowfield are changed considerably from those in the cylindrical afterbody case. The implications of these changes in the approach boundary-layer characteristics for the mean velocity, turbulence intensity, and Reynolds shear stress fields in the near wake of the afterbody are discussed in the following section.

Centerline Measurements

As part of the detailed documentation of the near-wake flowfield, an axial traverse on the centerline of the afterbody was completed. The LDV data were obtained in axial increments of $\Delta x/R_0 = 0.157$ from the base to the end of the test-section window (approximately $x/R_0 = 5.4$). The mean axial velocity distribution along the centerline is shown in Fig. 8 along with similar data obtained downstream of the cylindrical afterbody.[12] The rear stagnation point (reattachment location) is defined as the location where the mean axial velocity along the centerline vanishes. Note that the mean shear-layer
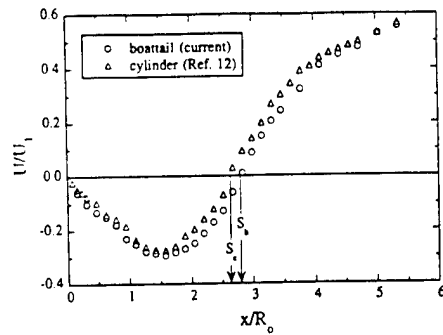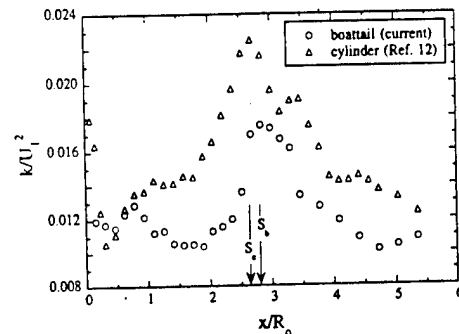
reattachment location moves downstream when the boattail is added to the cylindrical afterbody $(S_b/R_0 = 2.81$ and $S_c/R_0 = 2.65)$. This trend is consistent with the higher base pressure on the boattailed afterbody, which results in a shallower initial shear-layer angle. The mean reattachment location for both afterbodies is in general agreement with the pitot-probe measurements from Ref. 16, which found $S/R_0 = 2.9$ in a Mach 3 flow over a cylindrical afterbody. The peak reverse velocity in the separated region behind the base is approximately 29% of U_1 for the current boattailed afterbody, which is only slightly larger than that measured for the cylindrical afterbody (27% of U_1). These results are very similar to those given by Ref. 17 for a subsonic, power-off base flowfield, which supports the hypothesis of Ref. 18 that a similarity relationship may exist for the mean axial velocity along the centerline of axisymmetric bodies. In addition, the similarities in the mean axial velocity distributions at different approach Mach numbers suggest that compressibility effects are negligible in determining the mean structure of the recirculation region.

In addition to the mean axial velocity, the axial and radial rms velocity fluctuations were also determined along the centerline of each afterbody. In order to compare the overall turbulence fluctuation levels along the centerline, the turbulent kinetic energy was calculated using the following relation:

$$k = \tfrac{1}{2}\left(\sigma_u^2 + \sigma_{v_r}^2 + \sigma_{v_t}^2\right) \tag{1}$$

where $\sigma_{v_t}^2$ was set equal to $\sigma_{v_r}^2$ along the centerline. This assumption is supported by data obtained throughout the near wake, where all three components of the Reynolds normal stress were directly measured. The turbulent kinetic energy distributions along the centerline of the cylindrical[12] and boattailed afterbodies are compared in Fig. 9. Contrary to the mean axial velocity profiles shown in Fig. 8, the effect of afterbody boattailing on the centerline turbulent kinetic energy is substantial. Although both centerline distributions peak near the reattachment point as the shear layer converges on the axis, the turbulent kinetic energy is significantly reduced in the boattailed afterbody case (peak value is reduced by approximately 22%). This result suggests that the turbulence mechanisms in the near wake, and particularly in the reattaching shear layer, are attenuated by afterbody boattailing. This result stems, in part, from
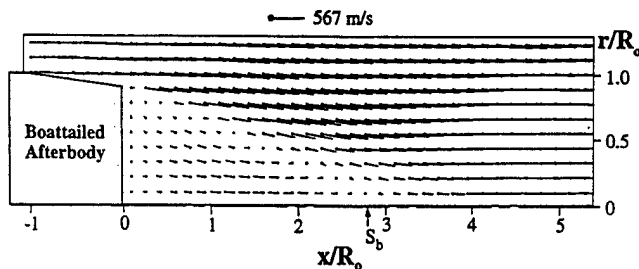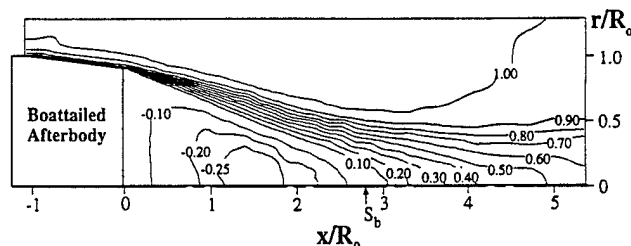
Fig. 10 Mean-velocity vector field.

Fig. 12 Mean radial velocity field—V_r/U_1.

Fig. 11 Mean axial-velocity field—U/U_1.

the reduced turbulence levels in the separating boundary layer for the boattailed afterbody case. The effects of afterbody boattailing on the mean-velocity and turbulence properties throughout the near wake are discussed in more detail in the next two sections.

Near-Wake Mean-Velocity Measurements

The mean-velocity vector field throughout the near wake of the current boattailed afterbody is shown in Fig. 10. Note that in this and subsequent figures the vertical axis has been expanded by 46% compared to the horizontal axis in order to show more clearly the important features of the flowfield. To enhance the presentation of the mean-velocity field, the uniformly spaced velocity vectors shown in Fig. 10 have been generated by a linear interpolation in both x and r of the unequally spaced LDV data. The mean-velocity vector field in Fig. 10 shows qualitatively many of the features of the near-wake flowfield shown previously in Fig. 1. The freestream flow is shown to undergo a series of deflections due to the expansions at the body-boattail junction and base corner, followed by the recompression shock wave system in the near wake, which realigns the flowfield with the axis of symmetry. The general shape of the recirculation region behind the base is also clearly shown in the figure. The location of the mean reattachment point is labeled along the horizontal axis; it provides a useful marker for the relative location of many important features of the near-wake flowfield.

A contour plot of U/U_1 in the near wake is shown in Fig. 11. The growth of the shear layer downstream of the base corner is shown by the diverging contour lines, which initially are spaced very closely together, indicating large mean axial-velocity gradients in the shear layer immediately downstream of separation. It is interesting to note that the contour levels at the inner edge of the shear layer diverge rapidly from the base corner, while those at the outer edge (contour levels 0.8–1.0) diverge slowly with downstream distance. This result suggests that a two-layer description of the initial shear-layer development (suggested in Ref. 8 for attached boundary layers downstream of a rapid expansion) may be appropriate where an inner layer of high turbulence levels and large mass entrainment rates grows rapidly within an outer layer of lower turbulence levels and relatively slow development. As suggested in Fig. 11, the inner layer eventually overtakes the outer layer and consumes a majority of the overall shear layer width. The recovery of the mean-axial-velocity profile downstream of reattachment is seen to be fairly rapid; however, at the far downstream extent of the present measurements, a velocity defect of approximately 42% still exists, which indicates that full recovery of the mean axial velocity in the wake does not occur within 5 base radii. Reference 19 found that the wake in their two-dimensional base flow fully recovered (velocity defect vanished) at a downstream distance of 4.7 base heights
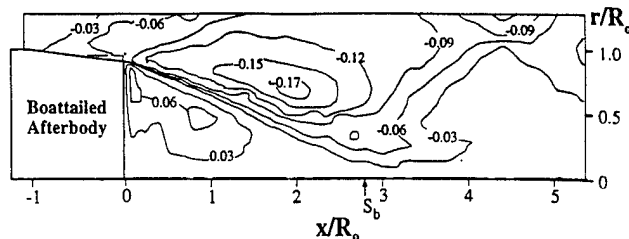
(equivalent to 9.4 base radii in the present case). Although full wake recovery was not achieved in the present case, the mean flow at the last axial station surveyed was found to be entirely supersonic, so that disturbances generated further downstream by the wind-tunnel geometry have no effect on the near-wake flowfield of interest.

In addition to the mean axial velocity, the mean radial velocity was also determined from the three-component LDV data; contours of V_r/U_1 are shown throughout the near wake in Fig. 12. The location of the rapid expansions at the body-boattail junction and base corner are now more clearly shown by decreasing contour levels (more negative radial velocity); the expansions appear to be well centered at these locations. Beyond the base-corner expansion fan, the mean radial velocity continues to increase in magnitude, due to axisymmetric effects, to a peak value of $0.18U_1$ at about two afterbody radii downstream. The gradual realignment of the freestream flow is shown on the right in Fig. 12 by the increasing contour levels, and the realignment appears even slower in the inner region of the shear layer, as evidenced by the persistence of a mean-radial-velocity "finger" at the lower right in the figure. This realignment pattern was also found in the cylindrical afterbody case[12] and is important in multicomponent modeling of these flowfields, as the recompression criterion provides the closure condition to the entire near-wake solution.[20] The mean-radial-velocity contours in Fig. 12 also show the acceleration of the low-speed fluid flowing radially outward (positive V_r) at the base as it becomes entrained into the shear layer near the base corner. Note the rapid change of flow direction (change in sign of the mean radial velocity) near the base corner, which, as mentioned earlier, may be responsible for the rising base pressure with increasing radius from the base center. Lastly, the increasing contour levels at the upper right in Fig. 12 mark the location of a compression wave generated by the reflection of the body-boattail junction expansion fan from a shear layer at the outer periphery of the test section. This region of the flow is entirely supersonic, so that interference with the near-wake flowfield of interest does not occur.

By comparing the mean-velocity field discussed above with that obtained downstream of a cylindrical afterbody,[12] it is found that the overall structure of the mean flowfield in these cases is qualitatively similar. However, one important difference that exists due to afterbody boattailing is a reduction in the mean shear-layer growth rate of approximately 20% from that in the cylindrical afterbody case. The growth rate of the shear layer is directly linked to the amount of mass entrainment from the recirculation region and therefore directly affects the base pressure. The reduction in shear-layer growth for the boattailed afterbody is consistent with the measured higher base pressure than for a cylindrical afterbody (16% higher in the present case) and is an important factor in determining the overall effectiveness of afterbody boattailing in reducing base drag.

Near-Wake Turbulence Measurements

In the present experiments, five of the six components of the kinematic Reynolds stress tensor have been directly measured. In this section, the primary results of these turbulence measurements will be presented. Figure 13 is a contour plot of the axial turbulence intensity throughout the near-wake flowfield. The increase in the axial turbulence intensity from the relatively low levels in the freestream marks the outer edge of the shear layer. A peak value of approximately 0.203 occurs in the subsonic portion of the shear layer, approximately 2 afterbody radii downstream of the base corner, and
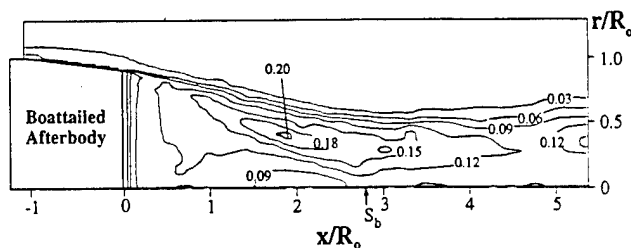
Fig. 13   Axial turbulence intensity contours—σ_u/U_1.
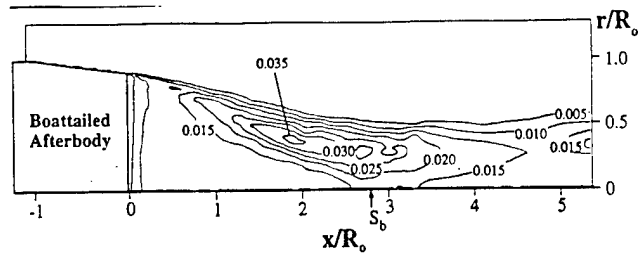
Fig. 15   Turbulent kinetic energy contours—k/U_1^2.
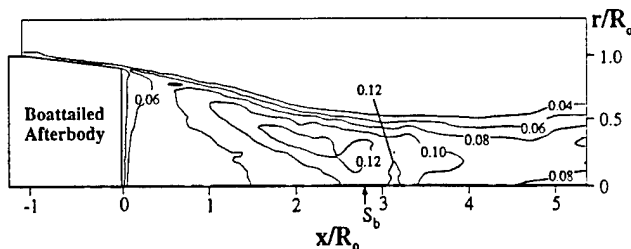
Fig. 14   Radial turbulence intensity contours—σ_{v_r}/U_1.
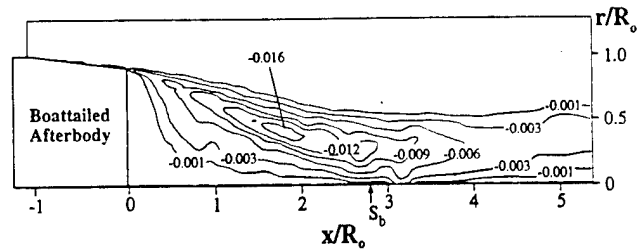
Fig. 16   Reynolds shear stress contours—$\langle u'v_r'\rangle/U_1^2$.

represents a reduction from the peak level in the cylindrical after-body case[12] of nearly 8%. In fact, throughout the shear-layer and wake regions of the boattailed afterbody near wake, the axial turbulence intensity is reduced from the cylindrical afterbody case. This is most likely a result of the reduced turbulence levels in the boundary layer upstream of the base corner. In addition, the reduced strength of the base-corner expansion fan in the boattailed afterbody case results in less distortion of the mean-velocity profiles and reduced turbulence production in the initial portions of the shear layer.[21] The axial turbulence intensity decays through the reattachment region in the present case, which is in contrast to data obtained for a compressible shear layer reattaching onto a solid wall, where it has been shown[22,23] that the axial turbulence intensity peaks downstream of the reattachment point. These differences in the locations for the peak axial turbulence intensity may be attributed to the difference in the boundary condition between the two cases. In the solid-wall case, the velocity constraint at the wall ($v = 0$) holds in an instantaneous sense, so that the mean velocity and rms velocity fluctuations both must vanish at the wall. However, in the compliant-surface reattachment of the present case, the velocity constraint at the fictitious surface requires that the mean transverse velocity vanish but not the instantaneous transverse velocity, so that a nonzero transverse rms velocity fluctuation exists. The axial turbulence intensity also peaked upstream of the reattachment point for the cylindrical afterbody case.[12] Interestingly, peak turbulence intensities have also been shown to occur upstream of reattachment for subsonic shear layers reattaching onto a solid wall.[24]

In addition to the axial turbulence intensity, the radial and tangential turbulence intensities were also determined from the LDV data; the radial turbulence intensity contours are shown in Fig. 14. The qualitative trends are similar to those of the axial turbulence intensity, with relatively large values in the shear layer that decay through the reattachment region into the downstream wake. A peak radial value of 0.129 occurs slightly upstream of reattachment and represents a 17% decrease from the peak value measured in the cylindrical afterbody case.[12] Note that the overall magnitudes of the radial turbulence intensity are smaller than those of the axial component, with a typical anisotropy, σ_u/σ_{v_r}, of 1.6–2.0 in the shear layer. Throughout the recirculation region, the radial turbulence intensity remains fairly uniform at levels reduced from those in the shear layer. The tangential turbulence intensity distribution is similar to that shown in Fig. 14 for the radial turbulence intensity, with a peak value of 0.133 occurring near the reattachment point. The addition of the boattail caused little change in the peak tangential turbulence intensity (1.4% reduction), even though the other two turbulence intensity components were significantly reduced. Throughout the shear layer, a radial-to-tangential anisotropy ratio ($\sigma_{v_r}/\sigma_{v_t}$) of ap-

proximately unity is maintained; thus, the magnitude ordering of the Reynolds normal stresses in the present case is $\sigma_u > \sigma_{v_r} \sim \sigma_{v_t}$, which indicates the preferential orientation of the turbulence field in the axial direction.

Utilizing the three turbulence intensity distributions measured in the present study, the turbulent kinetic energy [see Eq. (1)] has been determined and is shown in Fig. 15. As mentioned above, the axial turbulence intensity dominates the turbulence field, so the turbulent kinetic energy contours shown in Fig. 15 appear similar to those of the axial turbulence intensity shown in Fig. 13. The peak value of $k/U_1^2 = 0.0359$ occurs upstream of reattachment in the subsonic region of the shear layer. This global maximum in turbulent kinetic energy is significantly smaller than the value given in Ref. 19, where a peak turbulent kinetic energy of 0.07 was found near reattachment in the two-dimensional base flow study. The significant difference between these two values is most likely a result of the much weaker base-corner expansion fan in the present case, which results in less turbulence production immediately downstream of separation. In fact, Ref. 25 reports a measured peak turbulent kinetic energy of approximately 0.042 in the reattachment region of a supersonic shear layer that had been separated at constant pressure from a backstep (i.e., no expansion at the separation point). The peak value in the present case also represents an 18% reduction from the peak turbulent kinetic energy measured in the cylindrical afterbody case.[12] The measured reduction in turbulence levels in the shear layer results in less mass entrainment from the recirculation region for the boattailed afterbody case, which, as mentioned previously, is consistent with the reduction in measured shear-layer growth rate (approximately 20%) and increased base pressure. In the recirculation region behind the base, the turbulent kinetic energy is fairly uniform at values significantly smaller than those in the shear layer.

In addition to the turbulence intensity components presented above, the axial-radial and axial-tangential Reynolds shear stresses have been measured directly. The measured axial-radial shear stress was larger than the measured axial-tangential shear stress by approximately an order of magnitude in the high-turbulence regions of the shear layer. Contours of the dimensionless axial-radial shear stress are shown in Fig. 16. As in the axial turbulence intensity contours shown previously, the peak dimensionless shear stress magnitude occurs upstream of reattachment and takes a value of 0.0175, which represents an 8% decrease from the peak value measured in the cylindrical afterbody case.[12] In addition, the peak shear stress measured in the current study is significantly smaller than that measured in Ref. 19 in the two-dimensional base flow study. Throughout the recirculation region, the shear stress magnitudes are small, indicating the absence of any significant large-scale turbulence in the separation bubble downstream of the base. The locus of peak shear

Table 1 Comparison of peak values of turbulence quantities

Quantity	Cylindrical afterbody	Boattailed afterbody	Difference, %
σ_u/U_1	0.220	0.203	−7.7
σ_{v_r}/U_1	0.156	0.129	−17.3
σ_{v_t}/U_1	0.135	0.133	−1.4
k/U_1^2	0.0440	0.0359	−18.4
$-\langle u'v_r'\rangle/U_1^2$	0.0190	0.0175	−7.9

stress magnitudes at each axial station in the near wake consistently lies in the subsonic region of the shear layer, which indicates the importance of large-scale turbulent structures in the entrainment of fluid from the recirculation region.

In general, the effect of afterbody boattailing is to reduce the overall turbulence levels throughout the near-wake flowfield relative to a cylindrical afterbody. Table 1 presents a summary of the peak values of the primary turbulence quantities obtained for the current boattailed afterbody and those obtained previously for the cylindrical afterbody.[12] The addition of the boattail is shown to significantly reduce both the axial and radial turbulence intensities, with the strongest effect occurring in the radial component. In addition, the turbulent kinetic energy and Reynolds shear stress are reduced by afterbody boattailing. From an analysis of the turbulence production in the near wake of both the cylindrical and boattailed afterbodies,[21] the decrease in near-wake turbulence for the boattailed afterbody is found to be due, in part, to the reduced strength of the base-corner expansion fan, which directly affects the mean-velocity gradient (and therefore turbulence production) in the initial portion of the shear layer. Of course, the reduced turbulence in the boattailed afterbody boundary layer also plays a role in the overall reduction in turbulence in the near wake of the boattailed afterbody. The practical significance of the reduced turbulence in the present case is the substantial reduction in mass entrainment from the recirculation region (shear-layer growth rate reduced by approximately 20%), which directly implies a higher base pressure.

Conclusions

An experimental investigation of the near-wake flowfield behind a conical boattailed afterbody in supersonic flow has been presented. The primary objectives of this study are to investigate the fluid-dynamic effects of afterbody boattailing and how they relate to the increase in base pressure on conventional unpowered missiles and projectiles in supersonic flight. The experimental procedure followed during the investigation was to obtain detailed nonintrusive experimental data on a simplified configuration (i.e., without afterbody control fins) both with and without a boattail. The data include flow visualization photographs, measurements of the mean static pressure on the afterbody and base, and three-component LDV measurements throughout the near wake. A second objective of this study was to provide experimental data of sufficient detail and quality that could be used in numerical validation studies. Toward this end, the entire set of data presented in this paper has been tabulated in an easily readable format and is available on disk from the authors. From the data presented herein, the following conclusions can be drawn:

1) Afterbody boattailing is an effective means of decreasing the net afterbody drag on unpowered missiles and projectiles in supersonic flight. In the present case, the addition of a conical boattail resulted in a net afterbody drag reduction of 21% from a cylindrical afterbody at the same approach Mach number and Reynolds number.

2) The rapid expansion at the body-boattail junction in supersonic flow can significantly alter the mean velocity and turbulence distributions in the afterbody boundary layer. In addition to a reduction of the outer wake component of the mean boundary-layer velocity profile, the rapid expansion causes a decrease in the turbulence intensity and Reynolds shear stress throughout the boundary layer, which, if the boattail length is sufficiently short, can result in substantial changes in the boundary-layer conditions at separation.

3) The mean velocity in the near wake of unpowered axisymmetric bodies is qualitatively unaffected by afterbody boattailing. The most significant quantitative effect of boattailing is a reduction in the

mean shear-layer growth rate (approximately 20% in the present case), which is a result of reduced mass entrainment rates from the recirculation region behind the base. Obviously, this mechanism has direct influence on the base pressure and therefore is an important effect of afterbody boattailing in supersonic flow.

4) Turbulence levels in the separated shear layer are significantly reduced (e.g., 18% reduction in the turbulent kinetic energy) by afterbody boattailing due to the diminished fluctuations in the boundary layer at separation and to the reduced strength of the expansion fan at the base corner, which reduces turbulence production in the initial portion of the shear layer. In general, the axial Reynolds normal stress dominates the near-wake turbulence field, with the radial and tangential normal stresses being approximately equal. Strong peaks in the axial Reynolds normal stress and Reynolds shear stress occur in the subsonic region of the shear layer at an axial location upstream of the reattachment point.

Acknowledgments

References

[1] Rollstin, L., "Measurement of Inflight Base Pressure on an Artillery-Fired Projectile," AIAA Paper 87-2427, Aug. 1987.

[2] Phillips, W. P., Compton, H. R., and Findlay, J. T., "Base Drag Determination for STS Flights 1–5," AIAA Paper 83-2719, Nov. 1983.

[3] Addy, A. L., and White, R. A., "Optimization of Drag Minimums Including Effects of Flow Separation," *ASME Transactions: Journal of Engineering for Industry*, Vol. 95, No. 1, 1973, pp. 360–364.

[4] Reid, J., and Hastings, R. C., "Experiments on the Axi-Symmetric Flow over Afterbodies and Bases at $M = 2.0$," Royal Aircraft Establishment, RAE Rept. Aero. 2628, Farnborough, England, UK, 1959.

[5] Rubin, D. V., Brazzel, C. E., and Henderson, J. H., "The Effects of Jet Plume and Boattail Geometry on Base and Afterbody Pressures of a Body of Revolution at Mach Numbers of 2.0 to 3.5," U.S. Army Missile Command, RD-TR-70-5, Redstone Arsenal, AL, April 1970.

[6] Agrell, J., and White, R. A., "An Experimental Investigation of Supersonic Axisymmetric Flow over Boattails Containing a Centered Propulsive Jet," The Aeronautical Research Institute of Sweden (FFA), TN AU-913, Dec. 1974.

[7] Viswanath, P. R., and Narasimha, R., "Two-Dimensional Boat-Tailed Bases in Supersonic Flow," *The Aeronautical Quarterly*, Vol. 25, No. 3, 1974, pp. 210–224.

[8] Hampton, L. P., and White, R. A., "The Effect of Sudden Expansions and Compressions on Turbulent Boundary Layer Momentum Thickness in Supersonic Flow," American Society of Mechanical Engineers, Paper 86-WA/FE-11, Dec. 1986.

[9] Dussauge, J. P., and Gaviglio, J., "The Rapid Expansion of a Supersonic Turbulent Flow: Role of Bulk Dilatation," *Journal of Fluid Mechanics*, Vol. 174, Jan. 1987, pp. 81–112.

[10] Smith, D. R., and Smits, A. J., "The Rapid Expansion of a Turbulent Boundary Layer in a Supersonic Flow," *Journal of Theoretical and Computational Fluid Dynamics*, Vol. 2, Nos. 5/6, 1991, pp. 319–328.

[11] Arnette, S. A., Samimy, M., and Elliott, G. S., "The Effect of Expansion on the Large Scale Structure of a Compressible Turbulent Boundary Layer," AIAA Paper 93-2991, July 1993.

[12] Herrin, J. L., and Dutton, J. C., "Supersonic Base Flow Experiments in the Near Wake of a Cylindrical Afterbody," *AIAA Journal*, Vol. 32, No. 1, 1994, pp. 77–83.

[13] Maise, G., "Wave Drag of Optimum and Other Boattails," *Journal of Aircraft*, Vol. 7, No. 5, 1970, pp. 477–478.

[14] Sun, C. C., and Childs, M. E., "A Modified Wall Wake Velocity Profile for Turbulent Compressible Boundary Layers," *Journal of Aircraft*, Vol. 10, No. 6, 1973, pp. 381–383.

[15] Fernholz, H. H., and Finley, P. J., "A Critical Commentary on Mean Flow Data for Two-Dimensional Compressible Turbulent Boundary Layers," AGARDograph No. 253, AGARD, May 1980.

[16] Neale, D. H., Hubbartt, J. E., Strahle, W. C., and Wilson, W. W., "Effects of External Compression on an Axisymmetric Turbulent Near Wake," *AIAA Journal*, Vol. 16, No. 9, 1978, pp. 940–947.

[17] Delery, J., "ONERA Research on Afterbody Viscid/Inviscid Interaction with Special Emphasis on Base Flows," *Proceedings of the Symposium on Rocket/Plume Fluid Dynamic Interactions, Vol. III—Flow Fields*, Univ. of Texas at Austin, Austin, TX, 1983; also Fluid Dynamics Labs. Rept. 83-104, April 1983.

[18] Merz, R. A., Page, R. H., and Przirembel, C. E. G., "Subsonic Axisymmetric Near-Wake Studies," *AIAA Journal*, Vol. 16, No. 7, 1978, pp. 656–662.

[19]Amatucci, V. A., Dutton, J. C., Kuntz, D. W., and Addy, A. L., "Two-Stream, Supersonic, Wake Flowfield behind a Thick Base, Part I: General Features," *AIAA Journal*, Vol. 30, No. 8, 1992, pp. 2039–2046.

[20]Korst, H. H., "Axisymmetric Wakes in Supersonic Unpowered Missile Flight," *Proceedings of the Symposium on Rocket/Plume Fluid Dynamic Interactions, Vol. III—Flow Fields*, Univ. of Texas at Austin, Austin, TX, 1983; also Fluid Dynamics Labs. Rept. 83-104, April 1983.

[21]Herrin, J. L., "An Experimental Investigation of Supersonic Axisymmetric Base Flows Including the Effects of Afterbody Boattailing," Ph.D. Thesis, Univ. of Illinois at Urbana–Champaign, July 1993.

[22]Hayakawa, K., Smits, A. J., and Bogdonoff, S. M., "Turbulence Measurements in a Compressible Reattaching Shear Layer," *AIAA Journal*, Vol. 22, No. 7, 1984, pp. 889–895.

[23]Abu-Hijleh, B., and Samimy, M., "An Experimental Study of a Reattaching Supersonic Shear Layer," AIAA Paper 89-1801, June 1989.

[24]Eaton, J. K., and Johnston, J. P., "A Review of Research on Subsonic Turbulent Flow Reattachment," *AIAA Journal*, Vol. 19, No. 9, 1981, pp. 1093–1100.

[25]Samimy, M., Petrie, H. L., and Addy, A. L., "A Study of Compressible Turbulent Reattaching Free Shear Layers," *AIAA Journal*, Vol. 24, No. 2, 1986, pp. 261–267.

APPENDIX A.4

EFFECT OF A RAPID EXPANSION ON THE DEVELOPMENT OF COMPRESSIBLE FREE SHEAR LAYERS

by

J. L. Herrin and J. C. Dutton

Effect of a rapid expansion on the development of compressible free shear layers

J. L. Herrin
Flow Modeling and Control Branch, NASA Langley Research Center, Hampton, Virginia 23681

J. C. Dutton
Department of Mechanical and Industrial Engineering, University of Illinois at Urbana–Champaign, Urbana, Illinois 61801

Detailed mean velocity and turbulence data have been obtained with a laser Doppler velocimeter for two axisymmetric shear layers downstream of rapid expansions of different strengths. A comparison of the data in the near field (immediately downstream of separation) and far field (shear layer approaching self-similarity) is presented, and the fluid dynamic effects of the rapid expansion are ascertained for each regime. In general, the rapid expansion was found to distort the initial mean velocity and turbulence fields in the shear layer, in a manner similar to that in rapidly expanded, attached supersonic boundary layers; namely, two distinct regions were found in the initial shear layer: an outer region, where the turbulent fluctuations are quenched primarily due to mean compressibility effects (bulk dilatation), and an inner region, where turbulence activity is magnified due to the interaction of organized large-scale structures in the shear layer with low-speed fluid at the inner edge. With increasing strength of the rapid expansion, the effects in both regions become more pronounced, especially in the inner region, where turbulent fluctuations and mass entrainment rates are greatly magnified. Farther downstream, the turbulence activity of the large-scale eddies remains elevated, due to the rapid expansion, even though the relative distribution of the turbulence energy between the Reynolds stress components (structure of the turbulence) is independent of expansion strength. © *1995 American Institute of Physics.*

I. INTRODUCTION

The development of compressible free shear layers has received considerable attention in the scientific community over the past several years. Driven by the desire to design a practical supersonic combustion engine (i.e., scramjet), most research efforts have focused on documenting the growth rate and mixing of fully developed, two-stream mixing layers for a variety of free-stream conditions from the incompressible to compressible regimes.[1-3] The primary result of this research is that the shear layer growth rate, db/dx, and turbulence levels decrease significantly with increasing compressibility. Generally, the degree of compressibility is described in terms of either the convective Mach number (M_c) or the relative Mach number (M_r) of the mixing layer (for two streams with identical specific heat ratios, $M_r = 2M_c$). However, there appears to be growing skepticism as to the universality of these correlation parameters for all mixing layer scenarios. Viegas and Rubesin[4] show quite clearly the significant scatter in the measured shear layer growth rates obtained by different researchers at identical convective (or relative) Mach numbers. These authors suggest that the Mach numbers of each individual stream may impact the shear layer growth rate, even though the convective Mach number (calculated from the velocity difference across the shear layer) remains fixed. The recent data of Bunyajitradu-lya and Papamoschou[5] seem to support this claim. However, an additional problem, which is often overlooked when comparing shear layer data, is the effect of the initial conditions at the shear layer origin on the fully developed shear layer characteristics. As pointed out by Bradshaw[6] and others for incompressible mixing layers, the initial conditions can have a dramatic effect on shear layer development, and, in general, can affect the mean velocity and turbulence statistics of the shear layer in its fully developed state. As a result, quantitative comparisons between experiments conducted at different sites (and, therefore, under different conditions) can be quite difficult.

Mehta and Westphal[7] discuss the significant sensitivity of the incompressible shear layer to small changes in its initial conditions (e.g., approach boundary layer state and thickness) and wind tunnel operating conditions (e.g., free-stream turbulence levels), which, in practice, can be very difficult to control. In a later study of incompressible plane mixing layers with different velocity ratios, Mehta[8] showed conclusively that the interaction between the developing shear layer and the wake generated by the splitter plate strongly affected the distance required for the shear layer to achieve self-similarity, with turbulence properties developing more slowly than the mean velocity. In fact, Mehta[8] showed that, in most cases, the shear layer growth rate is approximately linear almost from the start of development, which shows the importance of utilizing the spatial independence of the more slowly developing turbulence properties as a criterion for determining the achievement of self-similarity. Also, in many practical situations, the streamwise distance available for shear layer growth is insufficient for the shear layer to reach fully developed conditions. In these cases, the shear layer development immediately downstream of boundary layer separation has increased importance.

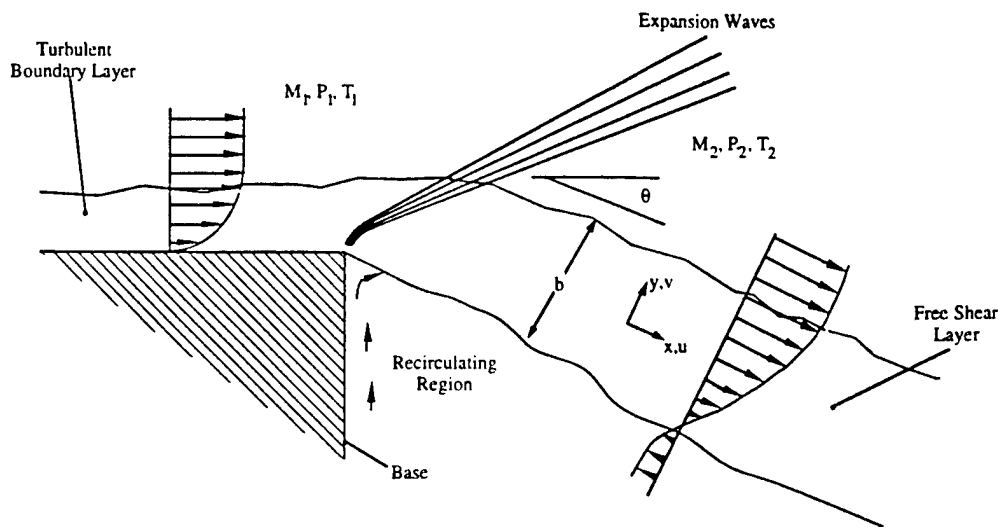Although little information is available in the initial de-

FIG. 1. Sketch of the mean flow field near the shear layer origin.

velopment region of rapidly expanded compressible free shear layers (as discussed below), a considerable amount of research has been presented on the effects of rapid expansions on attached, supersonic turbulent boundary layers. Dawson and Samimy[9] and Arnette et al.[10] used fast-response pressure measurements and filtered Rayleigh scattering, respectively, to show that rapid expansions quench the small-scale turbulence in supersonic, turbulent boundary layers while enhancing the turbulence energy in the large-scale structures (i.e., a reverse energy cascade from high to low wave numbers). Dussauge and Gaviglio[11] showed that the bulk dilatation associated with a rapid expansion is primarily responsible for an observed decrease in the Reynolds stresses, especially near the wall where small-scale turbulence dominates. To a lesser degree, stabilizing streamline curvature also contributes to a decrease in the Reynolds stresses. Downstream of the rapid expansion, a new wall layer with increasing turbulence levels was found, which grows with downstream distance within an outer layer of essentially frozen turbulence activity; eventually, the inner layer consumes the outer layer, forming a "new" boundary layer with properties that may differ considerably from those upstream of the expansion. Hampton and White[12] also proposed a two-layer structure for the recovering boundary layer downstream of rapid expansions.

In addition to providing benchmark data on the effect of rapid expansions on turbulent boundary layers, Dussauge and Gaviglio[11] also used rapid distortion approximations (RDAs) to the Reynolds stress transport equations to compute the evolution of the Reynolds stresses through the expansion. The RDAs neglect the effects of turbulence diffusion and dissipation through the expansion, while retaining the turbulence production and pressure terms in the governing equations. Comparison to experimental data was generally good. Smith and Smits[13] also used RDAs to compute the Reynolds stresses through a rapidly expanded turbulent boundary layer in supersonic flow. The expected decrease in the individual Reynolds stress components through the expansion was accurately predicted by this method, even

though the conditions for validity of the RDAs were not strictly satisfied across the entire boundary layer. As will be discussed below, many of the same effects described for rapidly expanded attached boundary layers will also be important for boundary layers that separate through a rapid expansion.

The effects of a rapid expansion on the mean velocity and turbulence properties of a developing free shear layer were investigated by Samimy et al.[14,15] and Petrie et al.[16] using laser Doppler velocimetry (LDV). By comparing the development of a shear layer separated at constant pressure to that of a shear layer that was rapidly expanded at its origin (shear layer inclination angle, $\theta = 15.4°$), the effects of the rapid expansion on the far field mean velocity and Reynolds stress distributions were deduced. These authors found that the rapidly expanded shear layer had higher peak Reynolds stress values and a stronger normal stress anisotropy $(\sigma_u/\sigma_v)^2$ throughout the majority of the shear layer development. Unfortunately, detailed LDV data were not obtained immediately downstream of the expansion due to inadequate seeding in this region. Peace[17] points out the need for detailed Reynolds stress measurements immediately downstream of boundary layer separation in order to enhance the current computational capabilities for massively separated afterbody flow fields.

The objective of the present paper is to study the development of axisymmetric, compressible free shear layers that are formed by separation of a turbulent boundary layer through a rapid expansion (see Fig. 1). The flow conditions in the present experiments are representative of those in the base region of a typical missile or projectile in unpowered supersonic flight. The focus of the investigation will be the shear layer development immediately downstream of separation, which plays an important role in determining the mass entrainment rates and subsequent growth of the shear layer. It is the interaction of the shear layer with the recirculation region behind the base (Fig. 1) that directly affects the mean pressure acting on the base surface (i.e., base drag). Included in this study are extensive LDV measurements made imme-

diately upstream and downstream of the rapid expansion. In addition to the near-interaction region, the approach of the shear layer to self-similarity will be documented to determine the long-term effect of the rapid expansion on the mean and turbulence structure of the shear layer. The effect of the shear layer development on the entire near-wake flow field of typical, unpowered projectiles has been presented earlier in two companion papers.[18,19]

II. EXPERIMENTAL FACILITY AND EXPERIMENTAL METHODS

The experiments described herein were conducted in the axisymmetric wind tunnel facility in the University of Illinois Gas Dynamics Laboratory. Specifically designed for the study of axisymmetric afterbody flows, the wind tunnel has several unique features, which ensure uniform, axisymmetric flow in the test section; a detailed description of the wind tunnel facility and its operational characteristics can be found in Ref. 20. Two different axisymmetric afterbodies were used in the present investigation: a circular cylinder and a conical boat-tailed afterbody (surface angle = 5°). For the cylindrical afterbody, the approach boundary layer separated from the base corner through a rapid expansion with a mean turning angle (θ) of approximately 9°. The rapid expansion at the corner of the boat-tailed afterbody was considerably weaker, with a mean turning angle of approximately 2°. Additional details concerning the approach boundary layer properties will be given below.

The primary diagnostic tool used in these investigations was a two-component LDV with frequency shifting; this system is capable of measuring the relatively high turbulence intensity levels and reversed velocity realizations present in the current separated flow fields. The measurement volume diameter and length were approximately 120 and 700 μm, respectively. The LDV data were obtained along radial traverses at several locations (approximately 15–20) along the shear layer axis. To eliminate any effects of the shear layer reattachment region for the present comparisons, only data obtained in the relatively constant pressure region of shear layer development will be presented. The onset of the adverse pressure gradient associated with reattachment is estimated from the data of Amatucci et al.[21] to occur near x = 65 mm for both afterbodies studied herein. The LDV data have been corrected for velocity bias using the interarrival time weighting method, which has been shown[22] to be an effective technique in the present flow fields; no correction for fringe bias was necessary.[20] An error analysis of the LDV data reduction procedure was used to estimate a worst-case uncertainty in the mean velocity of 1.2% of U_1 and in the RMS velocity fluctuation of 2.3% of U_1, where U_1 = 567 m/s is the mean free-stream velocity approaching the cylindrical afterbody.

In the current study, silicone oil droplets produced with a conventional six-jet atomizer were used as the laser light scattering media. In a previous experiment with the same seeding apparatus, Bloomberg[23] tested the tracking ability of these particles by measuring their response downstream of an oblique shock wave generated by a 15° compression corner in a Mach 2.6 flow. He found mean relaxation distances of

TABLE I. Summary of approach boundary layer and free-stream properties.

	Case 1	Case 2
M_1	2.61	2.46
M_2	2.71	2.85
Re_θ	15 700	13 700
δ (mm)	4.5	3.2
δ^* (mm)	1.33	0.98
θ (mm)	0.33	0.26
H	3.98	3.73
Π	1.19	1.37
C_f	0.001 42	0.001 48
u_τ (m/s)	22.4	21.2
θ (deg)	2	9

approximately 2 mm downstream of the shock and an estimated mean droplet diameter of 0.8 μm. Of course, the mean velocity gradient through the rapid expansion in the present experiments (maximum turning angle of 9°) is considerably weaker than the shock wave in Bloomberg's experiment. The response of the droplets to turbulent fluctuations in the shear layer was estimated with the results of Samimy and Lele.[24] Using the conditions immediately downstream of separation, the worst-case Stokes number in the present flow fields is approximately 0.6, which yields a maximum RMS error, due to particle lag of approximately 6%. As the shear layer grows, however, the local Stokes number will decrease, such that at x = 31 mm downstream of separation, the RMS error due to particle lag is only 1.7%. Farther downstream, the particle lag error continues to diminish.

III. RESULTS

A comparison of the mean velocity and turbulence fields downstream of the two afterbodies will now be presented. In both cases, the boundary layer approaching the separation point was fully turbulent, as determined by measured turbulence intensity levels and by the good agreement of the mean velocity profile with a compressible turbulent boundary layer curve fit.[18,19] The pertinent properties of the approach boundary layer for each case are given in Table I. Note that the afterbody flow fields to be compared have been labeled case 1 and case 2 for mean turning angles of θ = 2° and θ = 9° through the rapid expansion, respectively. This convention will be used for convenience throughout the remainder of the paper. The computed average relative Mach number of the developing shear layer is approximately 2.6 (M_c = 1.3) for each case. This relatively high value implies that compressibility undoubtedly has a significant impact on development of the current free shear layers.[1–3]

A. Initial shear layer structure

1. Mean velocity

In this section, the initial development of the shear layer immediately downstream of the separation point will be presented for both cases. Figure 2 shows the development of the nondimensional mean streamwise velocity, U/U_1, for each case, where U_1 is the mean free-stream velocity approaching the separation point (U_1 = 583 m/s for case 1 and 567 m/s for case 2). The magnitude of the plotted variable for each
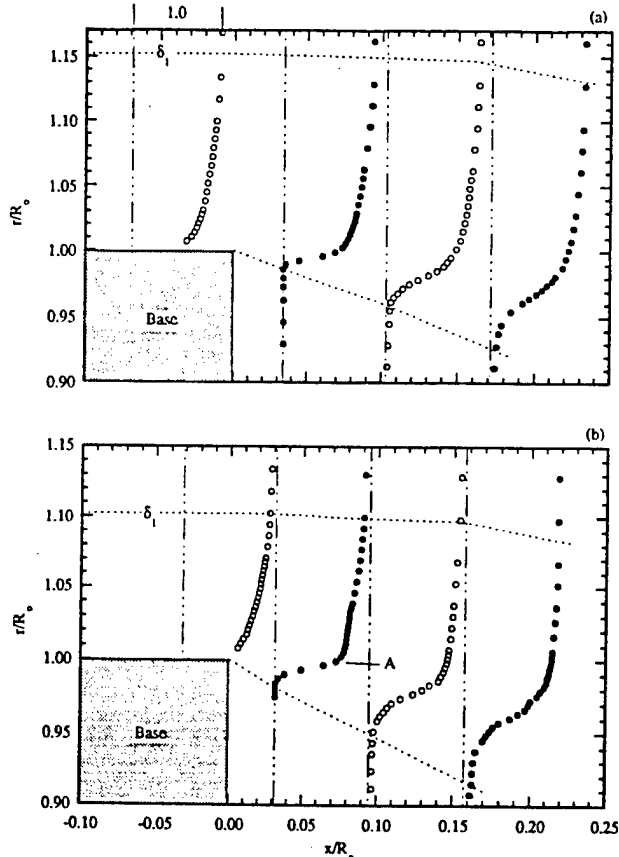
Phys. Fluids, Vol. 7, No. 1, January 1995

J. L. Herrin and J. C. Dutton   161

FIG. 2. Mean streamwise velocity profiles near separation, U/U_1: (a) case 1, (b) case 2.

case is shown by the scale at the upper left of the figure. In addition, lines denoting the approximate inner ($U \approx 0.01 \ \Delta U$) and outer ($U \approx 0.99 \ \Delta U$) edges of the shear layer are shown in the figure. The axial (x) and radial (r) location of each data point have been nondimensionalized by the radius of the base at separation ($R_0 = 28.97$ mm for case 1 and 31.75 mm for case 2), and the axial station for each data profile is shown by the dashed line to the left of that profile. It should be pointed out that the statistical data shown downstream of separation are relative to the classical shear layer coordinates (x, y, as shown in Fig. 1). In the present case, a mean shear layer angle relative to the approach flow was determined for each case by arithmetically averaging the local flow angles at the physical center of the shear layer at each axial location. Once determined, the mean angles were used to rotate the velocity data (obtained in wind tunnel coordinates) to local shear layer coordinates, so that the mean streamwise velocity, U, shown in Fig. 2, is parallel to the direction of mean shear layer growth.

The transition from the typical turbulent boundary layer mean velocity profile upstream of separation to an error function-type shear layer profile is shown to occur rather smoothly (and rapidly) for case 1 [Fig. 2(a)]. Immediately downstream of separation for case 2, however, the mean streamwise velocity profile appears to develop a "kink," where the mean velocity gradient changes abruptly [labeled as point A in Fig. 2(b)]. The discontinuity in the profile slope is similar to that found in rapidly expanded boundary

layers[11,12] and most likely represents the interface between an overexpanded viscous sublayer and an outer boundary layer remnant, which has reduced turbulence activity due to the rapid expansion (to be discussed in more detail below). Since the local strength of the expansion decreases with distance from the wall (i.e., the expansion is centered at the base corner), fluid parcels near the wall experience a more sudden expansion than those farther away from the wall, which results in a more pronounced disturbance of the mean velocity field at the inner edge of the shear layer. By comparing the mean streamwise velocity profiles between the two cases, it is obvious that the stronger expansion does indeed cause a more pronounced slope discontinuity in the mean velocity profile immediately downstream of separation. The enhanced "kink" in the case 2 profile also leads to a larger peak mean velocity gradient as expansion strength increases, such that, for only moderate changes in the shear stress, an increase in the primary turbulent kinetic energy production term, $\langle u'v' \rangle \partial U/\partial y$, occurs. As will be shown, the increase in turbulence production immediately downstream of separation for case 2 results in higher turbulence levels farther downstream as the shear layer develops.

2. Reynolds stresses

In addition to the mean velocity profiles near the separation point, the kinematic streamwise (σ_u^2/U_1^2) and transverse (σ_v^2/U_1^2) Reynolds normal stresses and the primary Reynolds shear stress ($\langle u'v' \rangle/U_1^2$) have also been determined from the LDV data ensembles. Figure 3 shows a comparison of the dimensionless streamwise kinematic Reynolds stress profiles near the separation point for each case. Two rather obvious effects of the rapid expansion are shown in the figure: the decrease in the streamwise turbulent fluctuations over the middle portion of the shear layer as compared to the boundary layer and the large increase in the turbulence levels at the inner edge of the shear layer at the interface of the rapidly expanded boundary layer and the low-speed recirculating fluid immediately downstream of the base. In the more strongly expanded shear layer of case 2 [Fig. 3(b)], both effects are amplified relative to case 1. Recent evidence[11,13] suggests that the decrease in the Reynolds stresses in the outer part of the shear layer is primarily a result of the bulk dilatation associated with the flow through the rapid expansion, which becomes more severe as expansion strength increases. The stabilizing streamline curvature associated with the expansion has also been shown[11,13] to cause a decrease in the Reynolds stresses. The increase in turbulence activity at the inner edge of the shear layer is most likely a result of significant mass entrainment from the low-speed recirculation region by large-scale eddies, the effect of which is initially limited to a very narrow portion of the shear layer. The location of the sharp peak in the profiles immediately downstream of separation coincides approximately with the location of the peak mean velocity gradient (see Fig. 2). Note also that the majority of the streamwise evolution downstream of separation occurs within the sharply-peaked region of the profile with the remaining portion of the expanded boundary layer merely convecting downstream relatively unchanged from its initial profile (the
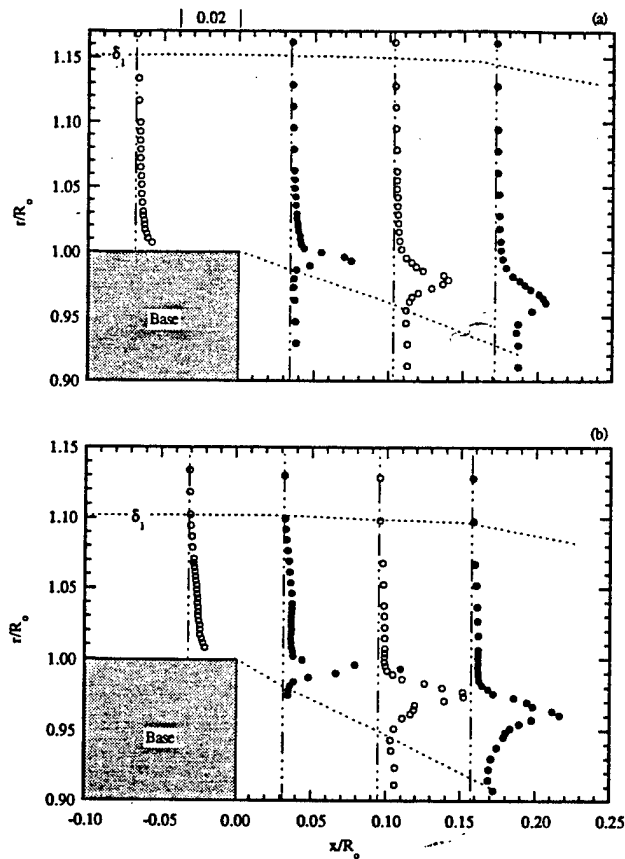
J. L. Herrin and J. C. Dutton

FIG. 3. Streamwise Reynolds normal stress profiles near separation, $(\sigma_u/U_1)^2$: (a) case 1, (b) case 2.

FIG. 4. Transverse Reynolds normal stress profiles near separation, $(\sigma_v/U_1)^2$: (a) case 1, (b) case 2.

turbulence field is essentially "frozen"). The data shown in Fig. 3 can be contrasted with the rapidly expanded boundary layer data presented by Dussauge and Gaviglio,[11] and also to similar data obtained by Smith and Smits,[13] both of which show decreases in the longitudinal Reynolds normal stress across the entire boundary layer profile through the rapid expansion. Of course, it is important to recognize the different post-expansion boundary conditions in the present case (compliant boundary at the inner edge of the shear layer) relative to the rapid expansion of a turbulent boundary layer that remains attached to a solid wall. In fact, even the weakly expanded boundary layer shown in Fig. 3(a) produces a substantial increase in σ_u^2/U_1^2 relative to the approaching solid wall boundary layer.

The effect of the rapid expansion on the transverse Reynolds normal stress, σ_v^2/U_1^2, is shown in Fig. 4. Relative to the striking changes through the rapid expansion of the streamwise normal stress profiles shown in Fig. 3, the transverse normal stress is only moderately affected by the expansion. Although a peak does appear in the profiles immediately downstream of separation, the magnitude is relatively unchanged from the peak value upstream of separation for both case 1 and case 2. This suggests that the time scale associated with the rapid expansion is small enough, such that significant turbulence reorganization (component redistribution from streamwise to transverse) does not occur for some distance downstream. Hence, the peak transverse normal stress, which depends intimately on the pressure–strain
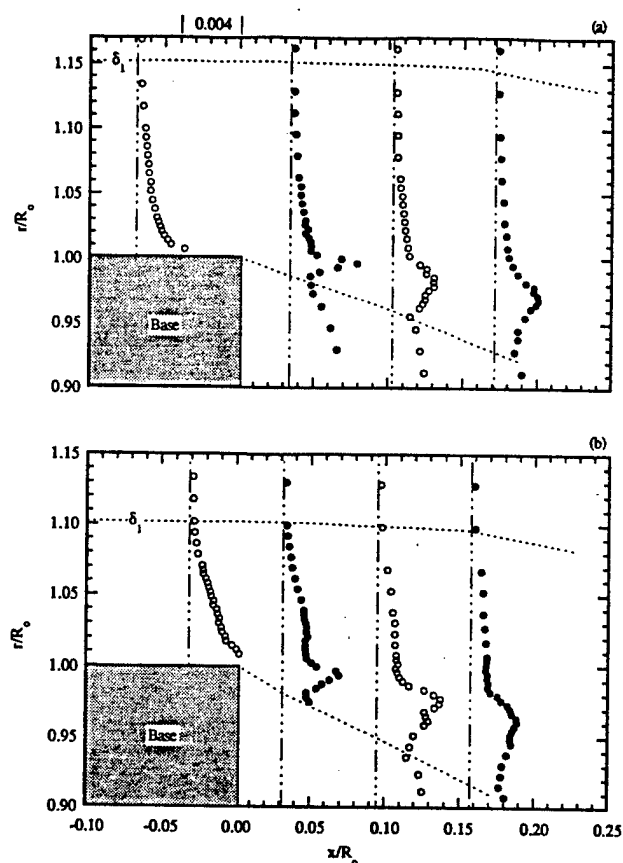
and turbulent diffusion reorganization mechanisms, is not immediately affected by the expansion. In the middle of the shear layer, the bulk dilatation associated with the rapid expansion again causes a decrease in the transverse normal stress when compared to similar regions in the approach boundary layer. By comparing the relative scales used to plot the turbulence data in Figs. 3 and 4, it is obvious that the streamwise Reynolds normal stress far exceeds the transverse component in the peak turbulence region of the shear layer immediately downstream of separation. This point is shown more clearly in Fig. 5, where the normal stress anisotropy (σ_u^2/σ_v^2) profiles near the separation point are shown. As for the peak streamwise normal stress, the peak normal stress anisotropy is approximately a factor of 2 larger for case 2 than for the weakly expanded shear layer of case 1. This distortion in the normal stress anisotropy downstream of the rapid expansion shows clearly the nonequilibrium nature of the post-expansion turbulence field and its strong dependence on the strength of the expansion. Disregarding the strong peak in the anisotropy profiles near the inner edge of the shear layer, it appears that the rapid expansion has little effect on the anisotropy profile across the remainder of the shear layer when compared to the approach boundary layer. This suggests that turbulence attenuation in each component, and not turbulence reorganization between the components, occurs across the majority of the expansion. This result is consistent with the calculations of Smith and Smits,[13] who predicted little change in the normal stress anisotropy ratio of

Phys. Fluids, Vol. 7, No. 1, January 1995
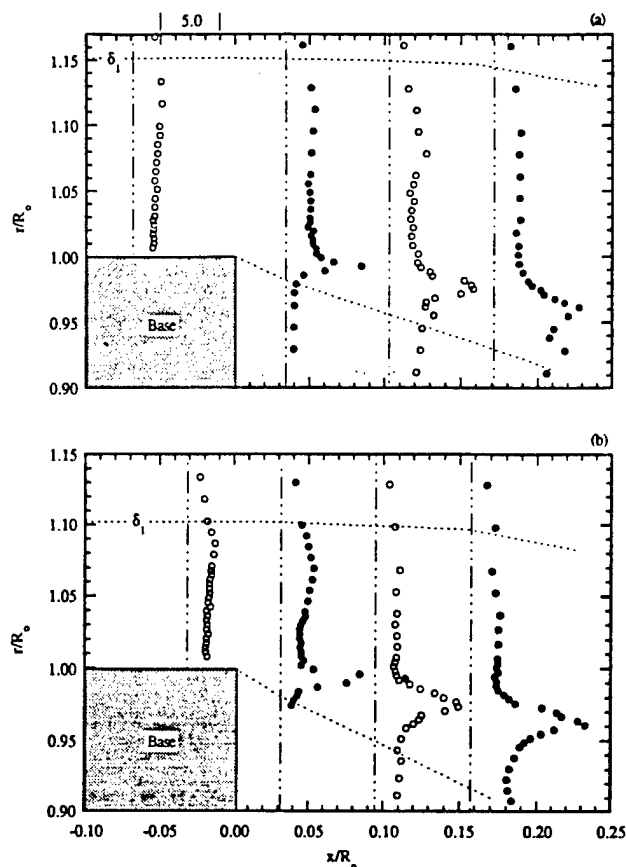
J. L. Herrin and J. C. Dutton   163

FIG. 5. Normal stress anisotropy profiles near separation, $(\sigma_u/\sigma_v)^2$: (a) case 1, (b) case 2.

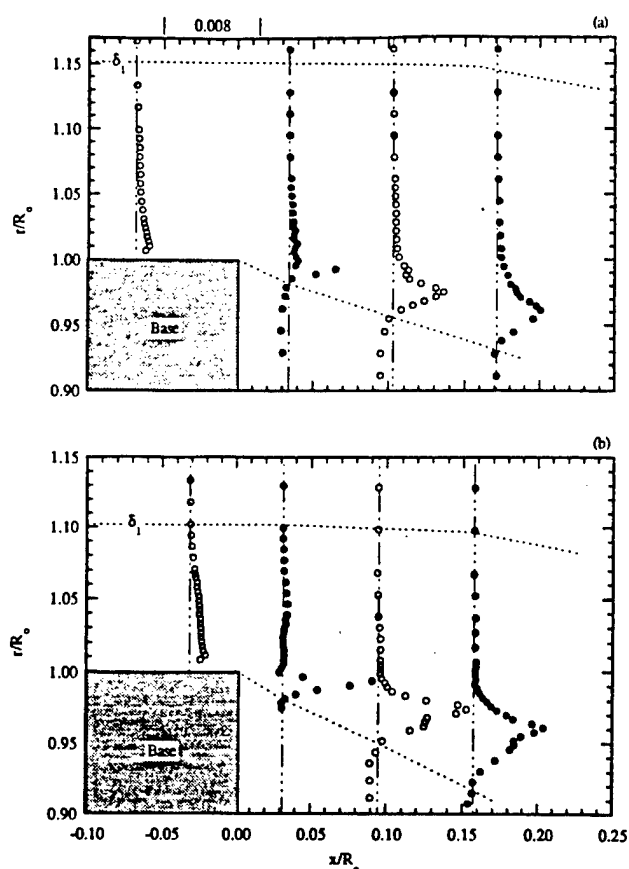FIG. 6. Primary Reynolds shear stress profiles near separation, $-\langle u'v'\rangle/U_1^2$: (a) case 1, (b) case 2.

a rapidly expanded boundary layer using RDAs.

Profiles of the primary Reynolds shear stress, $-\langle u'v'\rangle/U_1^2$, near the separation point are plotted in Fig. 6 for both cases. The effect of the rapid expansion is shown to be similar to that shown in Fig. 3 for the streamwise normal stress, namely, a reduction in the stress level over the majority of the shear layer width (primarily a bulk dilatation effect) with a sharp peak at the inner edge, where the separating boundary layer interfaces with the low-speed recirculating fluid behind the base. It is reasonable to expect large shear stress magnitudes at the inner edge of the shear layer, as large-scale organized motions are the primary source of mass entrainment from the low-speed fluid behind the base. As mentioned above, the compliant boundary at the inner edge of the shear layer, which does not restrict the motion of these large-scale eddies, results in significant increases in the magnitudes of the Reynolds stresses when compared to rapidly expanded, supersonic boundary layers along a solid wall.[11,13] When compared to the streamwise normal stress profiles in Fig. 3, the shear stress appears to be more strongly affected by the expansion, as evidenced by the complete absence of any shear stress across the majority of the profile. In fact, the turbulence structure parameter, a_1 $= -\langle u'v'\rangle/k$, was found to decrease across the majority of the shear layer with increasing expansion strength. The destruction of the shear stress through the expansion in the outer part of the expanded boundary layer implies negligible turbulence production in the outer part of the initial shear

layer, which, as mentioned previously, results in a "frozen" turbulence field that changes very little with downstream distance. Of course, in the region of the strong shear stress peak, a totally different picture of the flow is found. Large-scale structures, which contribute significantly to the Reynolds shear stress, actively entrain low-speed fluid at the inner edge of the shear layer, with this interaction being augmented by the rapid expansion. The peak shear stress occurs approximately at the same location as the peak mean velocity gradient, which, immediately downstream of separation, is quite large; hence, the primary production term for turbulent kinetic energy, $\langle u'v'\rangle\partial U/\partial y$, also reaches a strong peak at this point. The normal and shear stress profiles broaden rapidly with downstream distance as the turbulence energy is transferred from the streamwise component (primary extractor of turbulence energy from the mean flow) to the transverse and tangential components through pressure–strain and turbulent diffusion processes.

3. Quadrant decomposition analysis

In order to provide a more detailed description of the structure of the Reynolds stress field immediately downstream of separation, the individual LDV velocity realizations for both cases were analyzed using the quadrant decomposition technique.[25-27] The instantaneous velocity fluctuations (u', v') were determined for the entire ensemble of LDV data at a given spatial location and then plotted against each other, as shown in Fig. 7. For all cases
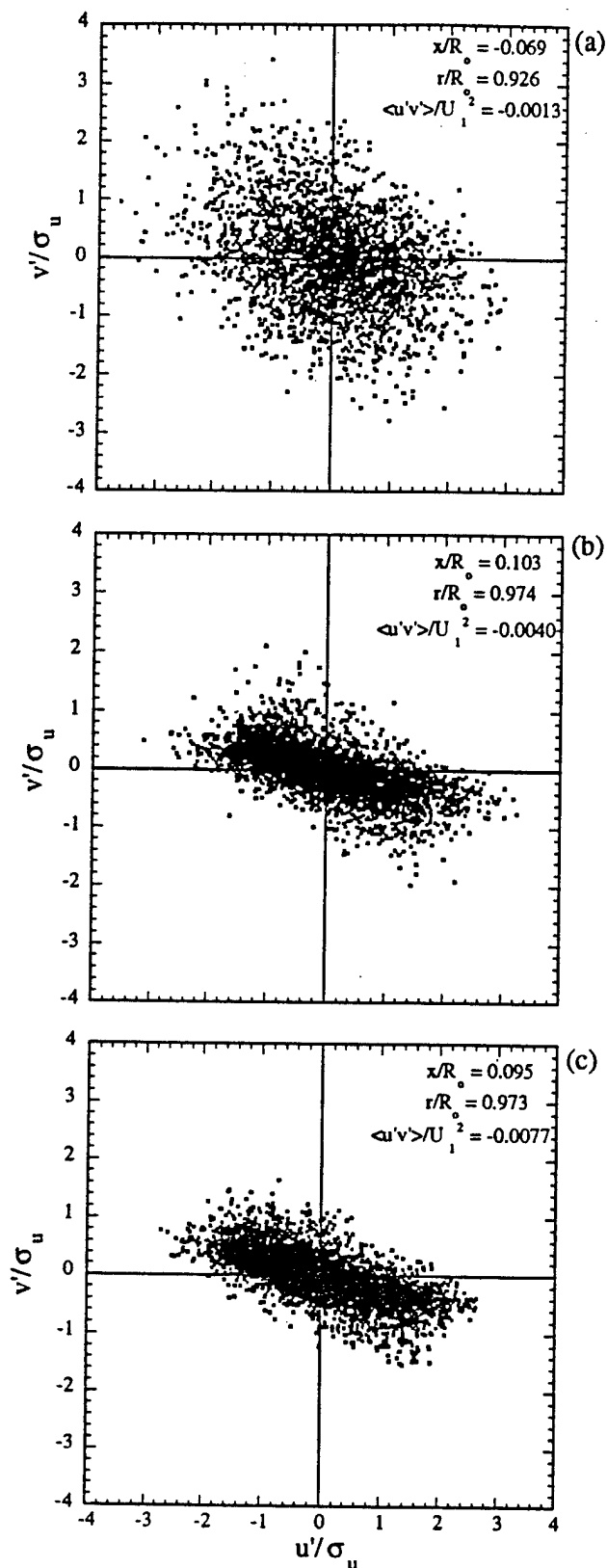
J. L. Herrin and J. C. Dutton

FIG. 7. Shear stress quadrant decomposition near separation: (a) approach boundary layer case 1; (b) downstream of separation case 1; (c) downstream of separation case 2.

shown, the velocity fluctuations are nondimensionalized by the local streamwise root-mean-square velocity fluctuation, σ_u. In this manner, the decomposition provides a comparison of the typical turbulence structure upstream of separation

[Fig. 7(a), case 1 shown, although case 2 results are similar] to that immediately downstream of separation for case 1 [Fig. 7(b)] and case 2 [Fig. 7(c)]. The data ensembles shown in Fig. 7 correspond with the peak shear stress location in each case, with the actual (x,r) position of the data given at the upper right of each figure, along with the ensemble-averaged shear stress value. Notice that, in general, the distribution of the turbulence energy (i.e., turbulence structure) at the peak shear stress locations changes significantly from the attached boundary layer to the separated shear layer. The quadrant decomposition in the boundary layer [Fig. 7(a)] displays a wide array of velocity fluctuations with no strong preferential orientation. This is in sharp contrast to the velocity fluctuations shown in Figs. 7(b) and 7(c) immediately downstream of separation for case 1 and case 2, respectively. In the separated shear layers, the velocity fluctuations tend to become more organized and strongly aligned along a preferential stress direction. Since coherent, large-scale turbulent structures are the most significant contributor to the Reynolds shear stress, it follows from Fig. 7 that the structures in the initial shear layer are more organized than those present in the approach boundary layer (this is consistent with the large increase in the peak shear stress magnitude through the expansion shown in Fig. 6). This result is in agreement with Petullo and Dolling,[28] who used a dual hot-wire probe to show that the large-scale structures in compressible free shear layers are generally more organized than those in turbulent boundary layers. Dawson and Samimy[9] and Arnette et al.[10] both found that rapid expansions also caused an increase in the organization of the large-scale structures for *attached* boundary layers. It appears that the strength of the rapid expansion (compare cases 1 and 2) may cause a slight increase in the organization of the shear stress, but the boundary layer separation process alone (not necessarily the expansion strength) appears to be a more dominant factor in the organization of the shear stress in the present case.

The orientation of the shear stress field was investigated further in the present study by computing the instantaneous shear angle ($\psi = \tan^{-1} v'/u'$) for each velocity realization and then sorting the entire ensemble of angles into histogram form. In this manner, velocity fluctuations that occur in the first and third quadrants will have $\psi>0$, while quadrants two and four will contain fluctuations with $\psi<0$. Note that $\psi=0$ corresponds to a velocity fluctuation along the u' axis (i.e., a purely streamwise fluctuation). The histograms generated for the data shown in Fig. 7 are presented in Fig. 8. As discussed above in relation to the quadrant decomposition, the approach boundary layer velocity fluctuations [Fig. 8(a)] occur over the entire range of possible shear angles, with no strongly dominant shear stress orientation. It is apparent from Fig. 8(a), however, that realizations in quadrants 2 and 4 ($\psi<0$) occur somewhat more frequently than in the other quadrants, which is consistent with the results of Willmarth and Lu[26] and Alving et al.[29] for turbulent boundary layers in subsonic flow. Downstream of boundary layer separation, the distribution of instantaneous shear angles takes quite a different character, as shown in Figs. 8(b) and 8(c) for cases 1

Phys. Fluids, Vol. 7, No. 1, January 1995
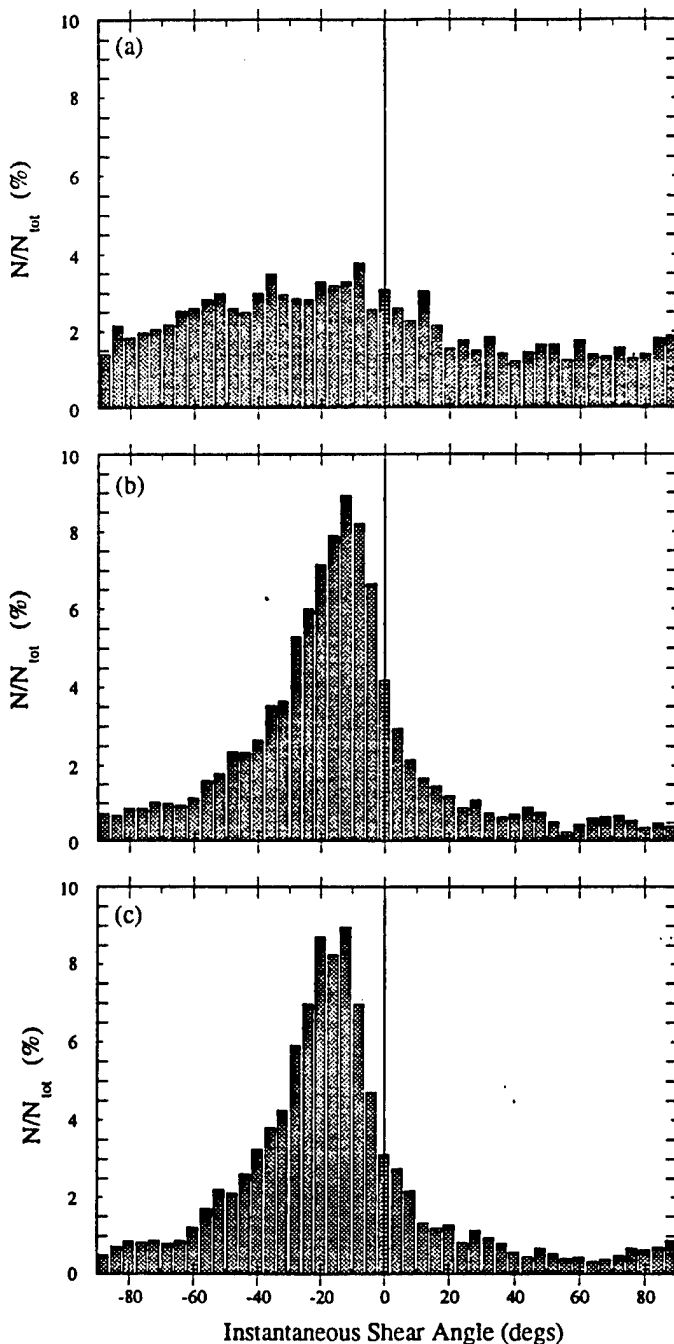
J. L. Herrin and J. C. Dutton   165

FIG. 8. Histograms of instantaneous shear angle: (a) approach boundary layer case 1; (b) downstream of separation case 1; (c) downstream of separation case 2 (same spatial locations as Fig. 7).

crease in the dominant shear angle magnitude with increasing expansion strength may be the result of an increase in the large-scale structure angle relative to the mean flow field. Although the present data are somewhat inconclusive on this point, Arnette et al.[10] provide some evidence to support this fact in rapidly expanded, attached, supersonic boundary layers.

The histograms of instantaneous shear angle shown in Fig. 8 are effective in identifying the dominant shear direction relative to the mean flow field, but yield no information as to the magnitude of the dominant velocity fluctuations. To circumvent this problem, the conditional quadrant detection technique of Willmarth and Lu[26] was applied to the data shown in Figs. 7 and 8. In this method, the instantaneous velocity fluctuations are conditionally sorted into one of five bins using the following algorithm: if $|u'v'|>H|\langle u'v'\rangle|$, then the individual realization is placed in its respective quadrant (e.g., when $u'>0$ and $v'<0$, $u'v'$ is placed in quadrant 4, which is denoted Q4 in the following discussion), but if $|u'v'|\leq H|\langle u'v'\rangle|$, the realization is placed into the fifth category, which is denoted the *hole*. After sorting the realizations, the five bins are individually averaged to show the quadrants in which large shear stress fluctuations exist. The hole size (H) is essentially a lower threshold for the sorting process and is altered parametrically. The conditional quadrant averages as a percentage of the total, ensemble-averaged shear stress ($\langle u'v'\rangle$) are shown as a function of the hole size (H) in Fig. 9 for the same data sets shown in Figs. 7 and 8. The quadrant average $\langle u'v'\rangle_n$ was computed by the following equation:

$$\langle u'v'\rangle_n = \frac{\Sigma(u'v')_n}{N_{tot}}, \qquad (1)$$

where $(u'v')_n$ is an individual realization in quadrant n and N_{tot} is the number of realizations in the entire data set (in this manner, the sum of the quadrant and hole averages is always equal to the total ensemble-averaged shear stress, $\langle u'v'\rangle$. In the boundary layer approaching separation [Fig. 9(a)], the dominant velocity fluctuations are shown to occur in Q2 ($u'<0$ and $v'>0$) and Q4 ($u'>0$ and $v'<0$), which, as discussed by Wallace et al.,[25] corresponds to fluid ejections and sweeps, respectively. At $H = 10$, the majority of the shear stress contribution comes from large fluctuations in Q2 (i.e., fluid ejections from the wall are large and contribute significantly to the total shear stress). These results are similar to those of Alving et al.[29] obtained in an incompressible turbulent boundary layer. Downstream of boundary layer separation [Figs. 9(b) and 9(c)], the dominance of the Q2 and Q4 fluctuations becomes very apparent, as the Q1 and Q3 contributions to $\langle u'v'\rangle$ have very small magnitudes for all values of the hole size (H). As discussed previously, the organization of the large-scale structures is enhanced in the shear layer after separation as compared to the approach boundary layer; hence, it is not surprising that the dominant fluctuations in the boundary layer (Q2 and Q4) become more pronounced in the shear layer. The effect of the strength of the rapid expansion on the shear stress quadrant contributions appears to be rather small, as shown by the similar distributions of Figs. 9(b) and 9(c).

and 2, respectively. For the weakly expanded case shown in Fig. 8(b), the shear stress is strongly oriented around an angle of approximately −12° from the mean flow direction, with a percentage of occurrences that is much larger than that in the approach boundary layer. This shows quantitatively the increase in organization of the turbulent structures in the separated shear layers. As the rapid expansion becomes stronger [Fig. 8(c)], the magnitude of the preferential shear stress angle becomes slightly larger (approximately −16°), although the general shape of the distribution is relatively unchanged from the weakly expanded case. The small in-
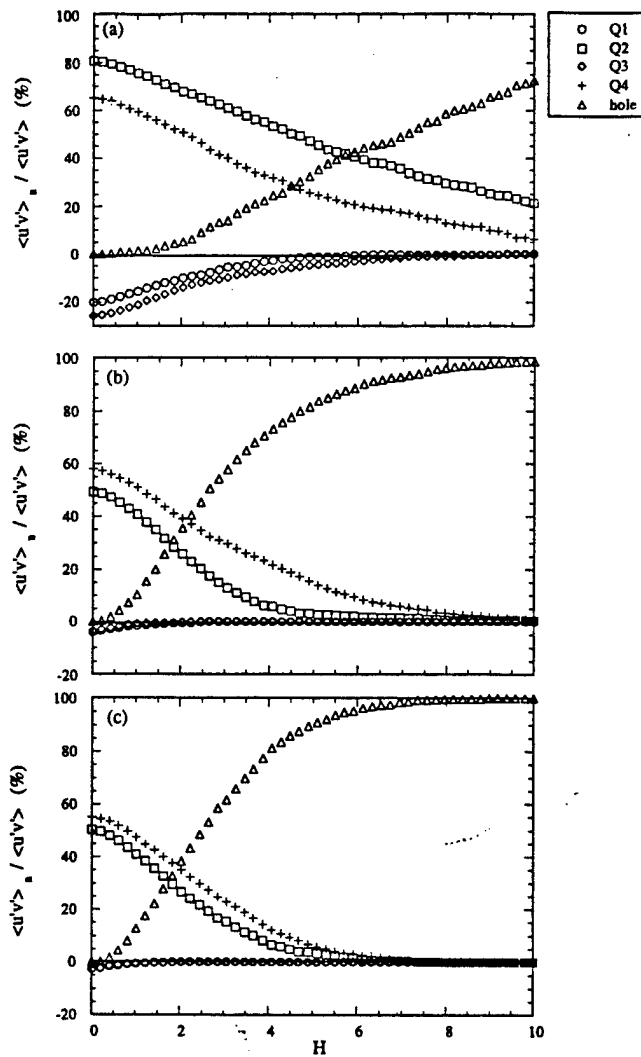
FIG. 9. Quadrant contributions to ensemble-averaged shear stress: (a) approach boundary layer case 1; (b) downstream of separation case 1; (c) downstream of separation case 2 (same spatial locations as Fig. 7).

B. Shear layer approach to self-similarity

In the previous section, the shear layer characteristics immediately downstream of separation were compared. The strength of the expansion was shown to have a significant effect on the turbulence structure at the inner edge of the shear layer. In general, large-scale turbulent motions become more organized than those present in the approach boundary layer, with a Reynolds stress distribution that is strongly aligned in a preferential direction ($\psi = -12°$ to $-16°$). In the current section, the effects of the rapid expansion are traced farther downstream into the region where the shear layer approaches similarity. As will be shown, many of the same features that were prominent in the shear layer immediately downstream of separation persist far downstream into the far field region.

1. Mean velocity .

As mentioned earlier, several authors have suggested that the shear layer initial conditions (i.e., conditions at boundary layer separation) can have a significant effect on
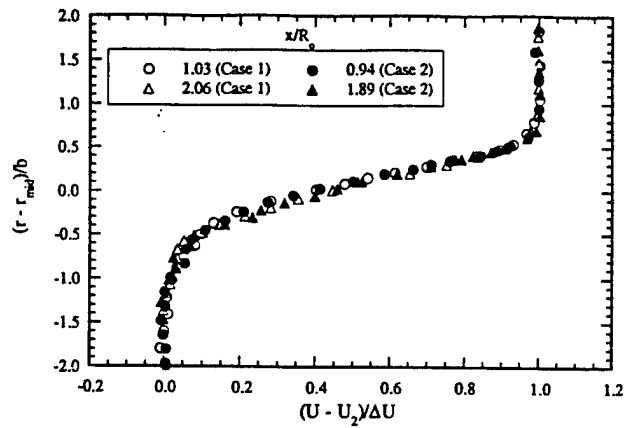

FIG. 10. Mean streamwise velocity profiles in similarity coordinates: open symbols, case 1; filled symbols, case 2.

the mean and turbulence properties in the fully developed state. Figure 10 is a comparison of the mean streamwise velocity profiles between case 1 and case 2, where the data are plotted in similarity coordinates typical of two-stream shear layers (b is the 10%–90% velocity thickness, r_{mid} is the physical center of the shear layer, U_2 is the mean velocity at the inner edge of the shear layer, and ΔU is the mean velocity difference). Note that both case 1 (open symbols) and case 2 (closed symbols) data are shown at two axial locations each, both of which are relatively far downstream of separation (in terms of the momentum thickness of the approach boundary layer, θ_1, mean velocity data are shown at $x/\theta_1 \approx 100$ and 200). The mean streamwise velocity profiles across the shear layer collapse reasonably well, suggesting that the dimensionless mean velocity field has become independent of streamwise distance from the separation point. In addition, the good comparison between case 1 and case 2 shown in Fig. 10 suggests that the relatively strong expansion of case 2, which distorted the *initial* shear layer mean velocity profile [Fig. 2(b)], has little effect on the mean velocity profile far downstream. This result is consistent with several previous investigations (e.g., Ref. 8), which found the mean velocity profiles to be fairly insensitive to any type of wind tunnel disturbance (i.e., recovery of the mean velocity field downstream of a disturbance is fairly rapid). All profiles shown exhibit a relatively sharp corner at the outer edge and a more rounded appearance at the inner edge, both of which are characteristic of fully developed compressible free shear layers.[16] Although mean velocity profiles are shown at only two axial stations for each case, several more data traverses were obtained, and, when plotted together, indicate that the mean velocity profiles collapse beyond $x/\theta_1 \approx 100$. In their studies of compressible shear layers generated by a constant pressure separation, Samimy et al.[15] and Petrie et al.[16] observed a reasonable collapse of their mean velocity profiles after $x/\theta_1 \approx 200$ and 250, respectively. The discrepancy between these results and the current data is most likely due to the choice of similarity variables, which, for the previous investigations,[15,16] neglected the recirculating flow at the inner edge of the shear layer ($U_2 \equiv 0$ using the nomenclature in Fig. 10).
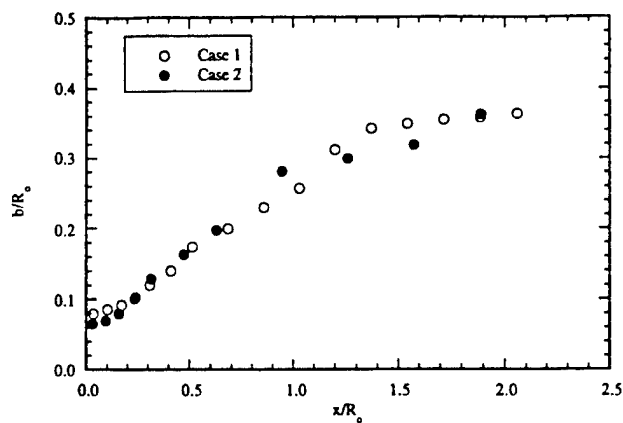
Phys. Fluids, Vol. 7, No. 1, January 1995

J. L. Herrin and J. C. Dutton   167

FIG. 11. Shear layer velocity thickness comparison.

FIG. 12. Streamwise Reynolds normal stress profiles in similarity coordinates for case 2.

To further compare the mean growth characteristics of the shear layers, the velocity thickness, b, is plotted against axial distance in Fig. 11. The shear layer velocity thickness distributions shown in Fig. 11 each seem to contain two distinct regions: a region of rapid linear growth almost immediately downstream of separation as the shear layer begins development, and a region of slower linear growth after the shear layer mean velocity field becomes independent of the streamwise location. The rapid initial growth is undoubtedly a result of the large mass entrainment at the inner edge of the shear layer immediately downstream of separation, and clearly shows the importance of the initial shear layer development region on the overall shear layer growth. The fact that a compressible shear layer grows linearly almost immediately after separation may be a cause for the relatively large discrepancies in the shear layer growth rates reported in the literature.[4] In the present experiments, the growth rate (db/dx) of the shear layer after the mean velocity profiles have collapsed ($x/R_0 > 1.3$ for case 1 and $x/R_0 > 0.9$ for case 2) was estimated to be 0.032 and 0.090 for case 1 and case 2, respectively. The large increase in growth rate for case 2 is a result of the increased strength of the turbulent eddies in the shear layer, as evidenced by increased peak Reynolds stresses for case 2 (to be discussed in detail below). The growth rate for case 2 compares favorably with the result of Samimy et al.[15] $(db/dx = 0.093)$, which was measured in a shear layer at nearly the same conditions as the present experiment.

2. Reynolds stresses

In addition to spatially independent mean velocity profiles, turbulence data must also collapse into a self-similar form in order for the shear layer to be labeled *fully developed*. Figure 12 shows the streamwise Reynolds normal stress profiles far downstream of the base corner for case 2. In this figure, the normal stress is nondimensionalized by the square of the velocity difference across the shear layer (ΔU), which changes only slightly with axial distance. Contrary to the mean velocity profiles of Fig. 10, the streamwise normal stress profiles do not collapse within the current measurement domain. The similar peak values shown for the last two
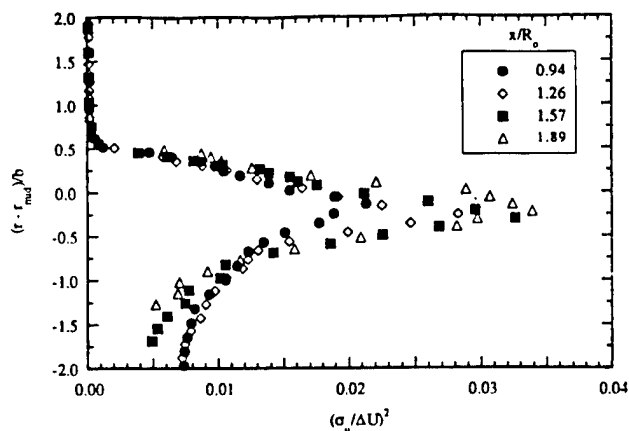
profiles ($x/R_0 = 1.57$ and 1.89) indicate that the shear layer is nearing self-similarity, although a longer development distance is needed for full development. Several authors (e.g., Refs. 2 and 3) have also found that turbulence properties develop more slowly than the shear layer mean velocity distribution. Profiles of the streamwise Reynolds normal stress for case 1 were very similar in shape to those shown in Fig. 12, but the peak values at the far downstream axial stations were reduced by approximately 10%. The transverse Reynolds normal stress $(\sigma_v/\Delta U)^2$ and the primary Reynolds shear stress $(\langle u'v' \rangle/\Delta U^2)$ profiles for each case exhibited even slower development than the streamwise normal stress, with no apparent self-similar distributions at the last measurement station. In addition, peak values at the last measurement station were again higher for case 2 (20% for the transverse normal stress and 11% for the primary shear stress) when compared to case 1. It is apparent from these data that information on the turbulence property development is essential when establishing the *fully developed* state of compressible shear layers. Also, the far field effect of increasing expansion strength at the shear layer origin is to increase the strength of the turbulent eddies, and, therefore, the overall turbulence levels in the shear layer; this, in turn, implies larger shear layer growth rates (see Fig. 11). Obviously, the elevated initial streamwise normal stress and shear stress levels along with larger initial turbulence production rates in case 2 combine to enhance the far field Reynolds stress magnitudes relative to case 1.

Immediately downstream of separation, the strength of the rapid expansion was shown to have a significant impact on the relative distribution of the Reynolds normal stresses (Fig. 5) at the inner edge of the shear layer; the peak normal stress anisotropy ratio (σ_u^2/σ_v^2) for case 2 was approximately a factor of 2 larger than that for case 1. To investigate the persistence of this disturbance in the far field, a comparison of the normal stress anisotropy profiles at the last measurement station of the present data is shown in Fig. 13. In addition to having reduced peak values from those immediately downstream of separation, both profiles appear similar in shape, although the peak magnitudes are slightly larger for the case 1 data. The decrease in the peak anisotropy ratio
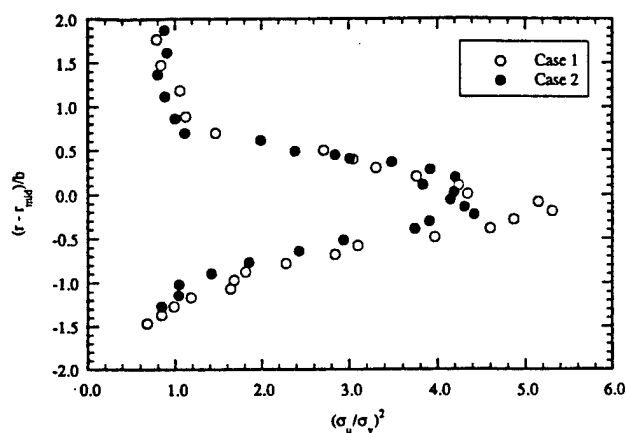
J. L. Herrin and J. C. Dutton

FIG. 13. Reynolds normal stress anisotropy comparison at $x/R_0 \approx 2$.

FIG. 14. Comparison of peak Reynolds normal stress distributions: (a) streamwise component; (b) transverse component.

from that immediately downstream of separation results from the continued redistribution of turbulent energy from the streamwise component to the transverse and tangential components via turbulent diffusion and pressure–strain mechanisms. The shear stress correlation coefficient, $\langle u'v'\rangle/(\sigma_u \sigma_v)$, was also similar between the two cases in the farfield, although immediately downstream of separation, the profiles for the stronger expansion case (case 2) are generally reduced from those in case 1. Hence, it appears that the *far field structure* of the shear layer turbulence field (i.e., distribution of turbulence energy between the Reynolds stress components) is relatively unaffected by the strength of the rapid expansion, although the absolute magnitudes of the individual Reynolds stress components increase with increasing expansion strength; results obtained from the quadrant decomposition technique applied to the far field data support this claim.

The rapid expansion was shown to strongly affect the streamwise normal stress immediately downstream of separation (Fig. 3), but to have little effect on the transverse component (Fig. 4). In Fig. 14, the peak streamwise and transverse normal stresses for each case are compared at various axial positions along the shear layer axis. The peak streamwise normal stress distributions for the two cases [Fig. 14(a)] are very similar in shape, with a peak immediately downstream of boundary layer separation followed by a relaxation to a local minimum, and then sustained growth to the end of the measurement domain. However, the magnitudes for case 2 are everywhere larger than those for case 1, especially immediately downstream of separation, where the effects of the rapid expansion are largest. This again supports the prior conclusion that the rapid expansion at the shear layer origin enhances the strength of the turbulent structures in the shear layer well downstream. The short relaxation region downstream of separation is similar to that observed by Gaviglio et al.[30] in their hot-wire study of supersonic base flows. This lag between the location of peak turbulence production (immediately downstream of separation) and the start of increasing streamwise normal stress levels, is similar to that found by Castro and Bradshaw[31] in a low-speed mixing layer, and appears to be a function of the expansion strength [Fig. 14(a)].
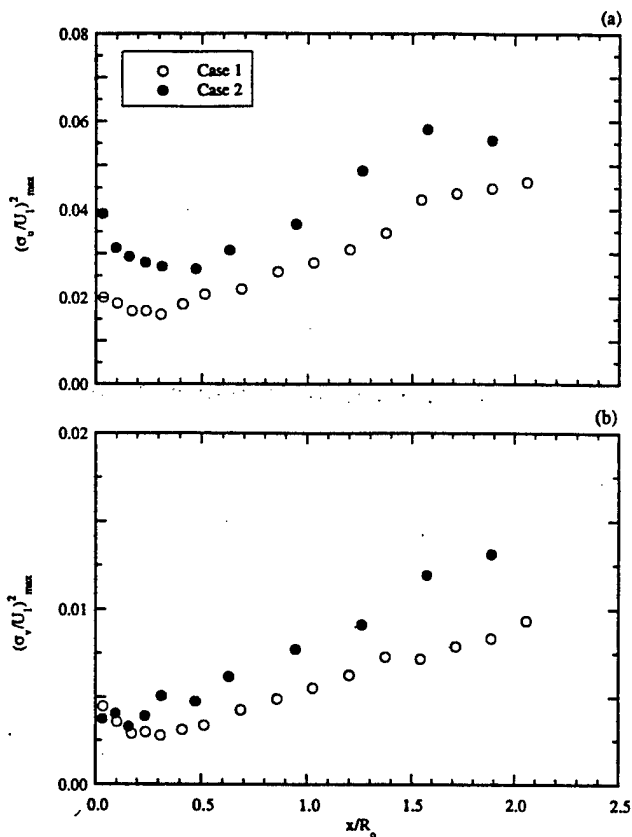
The peak transverse Reynolds normal stress distributions shown in Fig. 14(b) exhibit relatively small magnitudes shortly downstream of separation that increase with downstream distance over the majority of the measurement domain. As in the streamwise component, the transverse normal stress far downstream of the shear layer origin is greater for case 2 than for case 1. The redistribution of turbulent energy from the streamwise component to the transverse and tangential components via the pressure–strain and turbulent diffusion processes is primarily responsible for the increasing transverse normal stress shown in Fig. 14(b) (transverse normal stress production is small everywhere). Since the shear layer in case 2 has higher streamwise normal stress levels throughout its development than case 1, it is reasonable that the transverse normal stress far downstream should be larger for case 2. Notice that the difference between the two cases becomes greater with downstream distance due to the enhanced redistribution of turbulent energy into the transverse component for case 2.

IV. SUMMARY AND CONCLUSIONS

An experimental investigation of the effects of a rapid expansion on the development of compressible free shear layers has been presented. Two highly compressible shear layers ($M_c \approx 1.3$) originating from rapid expansions of different strengths have been compared, and from these data, the following conclusions can be drawn:

Phys. Fluids, Vol. 7, No. 1, January 1995

J. L. Herrin and J. C. Dutton   169

(1) The rapid expansion distorts the initial mean velocity profile of the shear layer in a manner similar to rapidly expanded, attached, supersonic boundary layers. Namely, a "kink" in the mean velocity profile or discontinuity in the mean velocity gradient is generated, which appears to mark the interface between two distinct regions in the initial shear layer: an inner region with significant turbulence activity and large mean strain rates, and an outer region where mean turbulence production has been destroyed and subsequent streamwise development is negligible. Transition from the distorted initial mean velocity profile to a typical error function-type shear layer profile occurs very rapidly as turbulent diffusion processes dominate.

(2) The turbulence field immediately downstream of separation is altered in magnitude and structure by the rapid expansion. Over the majority of the shear layer width, turbulence activity is reduced from the levels in the approach boundary layer due to bulk dilatation and streamline curvature effects; however, at the interface of the shear layer and the recirculating fluid at the inside edge, large streamwise normal stresses and shear stresses are present, which are magnified substantially by the rapid expansion. This may be due to an enhancement of the energy-containing, large-scale turbulent structures through the rapid expansion, which entrain low-speed fluid along the inside edge of the shear layer. The peak transverse Reynolds normal stress, on the other hand, is largely unaffected by the expansion due to the relatively long time scale associated with the turbulent energy redistribution processes.

(3) Analysis of the initial Reynolds stress field using the quadrant decomposition technique shows an increase in the shear stress organization when compared to the approach boundary layer, although the effect of the expansion strength on the degree of organization appears small over the range investigated here. At the peak shear stress location immediately downstream of separation, turbulent fluctuations from quadrants 2 and 4 contribute equally to the shear stress while fluctuations in quadrants 1 and 3 are negligible. These results are consistent with the engulfment process of low-speed fluid by large turbulent eddies at the inner edge of the shear layer.

(4) Far downstream of the rapid expansion ($x/\theta_1 > 100$), the mean velocity profiles collapse reasonably well into a common form that is apparently unaffected by the magnitude of the rapid expansion. The turbulence properties develop more slowly than the mean velocity and do not become independent of streamwise distance from separation within the present measurement domain.

(5) The strength of the rapid expansion at the shear layer origin is felt far downstream as an increase in the overall strength of the energy-containing turbulent eddies. At the last measurement station presented herein, the peak streamwise normal stress, transverse normal stress, and primary shear stress for the stronger expansion case were 10%, 20%, and 11% larger, respectively, than the peak values for the weakly expanded case. The large increase in the transverse normal stress is a result of the continued elevation of the streamwise normal stress, in conjunction with the redistribution mechanisms for turbulent energy exchange between the components. A similar argument holds for the primary shear stress,

which gains turbulent energy from the mean flow field primarily through transverse velocity fluctuations.

(6) Although the energy of the turbulent eddies is enhanced by the strength of a rapid expansion at its origin (as evidenced by increases in the magnitudes of the Reynolds normal and shear stresses), the relative distribution of the turbulence energy between the Reynolds stress components (i.e., turbulence structure) far downstream of the origin is relatively unaffected.

ACKNOWLEDGMENT

[1] D. Papamoschou and A. Roshko, "The compressible turbulent shear layer: An experimental study," J. Fluid Mech. 197, 453 (1988).

[2] M. Samimy and G. S. Elliott, "Effects of compressibility on the characteristics of free shear layers," AIAA J. 28, 439 (1990).

[3] S. G. Goebel and J. C. Dutton, "Experimental study of compressible turbulent mixing layers," AIAA J. 29, 538 (1991).

[4] J. R. Viegas and M. W. Rubesin, "A comparative study of several compressibility corrections to turbulence models applied to high-speed shear layers," AIAA Paper No. 91-1783, 1991.

[5] A. Bunyajitradulya and D. Papamoschou, "Acetone PLIF imaging of turbulent shear layer structure at high convective Mach number," AIAA Paper No. 94-0617, 1994.

[6] P. Bradshaw, "The effect of initial conditions on the development of a free shear layer," J. Fluid Mech. 26, 225 (1966).

[7] R. D. Mehta and R. V. Westphal, "Near-field turbulence properties of single and two-stream plane mixing layers," Exp. Fluids 4, 257 (1986).

[8] R. D. Mehta, "Effect of velocity ratio on plane mixing layer development: Influence of the splitter plate wake," Exp. Fluids 10, 194 (1991).

[9] J. A. Dawson and M. Samimy, "The effects of expansion on a supersonic boundary layer: Surface pressure measurements," AIAA Paper No. 94-0648, 1994.

[10] S. A. Arnette, M. Samimy, and G. S. Elliott, "The effect of expansion on the large scale structure of a compressible turbulent boundary layer," AIAA Paper No. 93-2991, 1993.

[11] J. P. Dussauge and J. Gaviglio, "The rapid expansion of a supersonic turbulent flow: Role of bulk dilatation." J. Fluid Mech. 174, 81 (1987).

[12] L. P. Hampton and R. A. White, "The effect of sudden expansions and compressions on turbulent boundary layer momentum thickness in supersonic flow," ASME Paper No. 86-WA/FE-11, 1986.

[13] D. R. Smith and A. J. Smits, "The rapid expansion of a turbulent boundary layer in a supersonic flow," J. Theor. Comput. Fluid Dyn. 2, 319 (1991).

[14] M. Samimy, H. L. Petrie, and A. L. Addy, "Reattachment and redevelopment of compressible turbulent free shear layers," Proceedings of the International Symposium on Laser Anemometry (ASME, New York, 1985), Vol. 33, pp. 159–166.

[15] M. Samimy, H. L. Petrie, and A. L. Addy, "A study of compressible turbulent reattaching free shear layers," AIAA J. 24, 261 (1986).

[16] H. L. Petrie, M. Samimy, and A. L. Addy, "Compressible separated flows," AIAA J. 24, 1971 (1986).

[17] A. J. Peace, "Turbulent flow predictions for afterbody/nozzle geometries including base effects," J. Prop. Power 7, 396 (1991).

[18] J. L. Herrin and J. C. Dutton, "Supersonic base flow experiments in the near wake of a cylindrical afterbody," AIAA J. 32, 77 (1994).

[19] J. L. Herrin and J. C. Dutton, "Effects of afterbody boattailing on the near wake of axisymmetric bodies in supersonic flow," AIAA Paper No. 94-0029, 1994.

[20] J. L. Herrin, "An experimental investigation of supersonic axisymmetric base flows including the effects of afterbody boattailing," Ph.D. thesis, University of Illinois at Urbana—Champaign, Urbana, IL, 1993.

[21] V. A. Amatucci, J. C. Dutton, D. W. Kuntz, and A. L. Addy, "Two-stream supersonic wake flowfield behind a thick base, part 1: General features," AIAA J. 30, 2039 (1992).

[22] J. L. Herrin and J. C. Dutton, "An investigation of LDV velocity bias

correction techniques for high-speed separated flows," Exp. Fluids **15**, 354 (1993).

[23] J. E. Bloomberg, "An investigation of particle dynamics effects related to LDV measurements in compressible flows," M.S. thesis, University of Illinois at Urbana—Champaign, Urbana, IL, 1989.

[24] M. Samimy and S. K. Lele, "Motion of particles with inertia in a compressible free shear layer," Phys. Fluids A **3**, 1915 (1991).

[25] J. M. Wallace, H. Eckelmann, and R. S. Brodkey, "The wall region in turbulent shear flow," J. Fluid Mech. **54**, 39 (1972).

[26] W. W. Willmarth and S. S. Lu, "Structure of the Reynolds stress near the wall," J. Fluid Mech. **55**, 65 (1972).

[27] S. S. Lu and W. W. Willmarth, "Measurements of the structure of the Reynolds stress in a turbulent boundary layer," J. Fluid Mech. **60**, 481 (1973).

[28] S. P. Petullo and D. S. Dolling, "Large-scale structure orientation in a compressible turbulent shear layer," AIAA Paper No. 93-0545, 1993.

[29] A. E. Alving, A. J. Smits, and J. H. Watmuff, "Turbulent boundary layer relaxation from convex curvature," J. Fluid Mech. **211**, 529 (1990).

[30] J. Gaviglio, J. P. Dussauge, J. F. Debieve, and A. Favre, "Behavior of a turbulent flow strongly out of equilibrium at supersonic speeds," Phys. Fluids **20**, 179 (1977).

[31] I. P. Castro and P. Bradshaw, "The turbulence structure of a highly curved mixing layer," J. Fluid Mech. **73**, 265 (1976).

Phys. Fluids, Vol. 7, No. 1, January 1995

J. L. Herrin and J. C. Dutton   171

APPENDIX A.5

STUDY OF SUBSONIC BASE CAVITY FLOWFIELD STRUCTURE USING PARTICLE IMAGE VELOCIMETRY

by

M. J. Molezzi and J. C. Dutton

Study of Subsonic Base Cavity Flowfield Structure Using Particle Image Velocimetry

Michael J. Molezzi* and J. Craig Dutton†

University of Illinois at Urbana–Champaign, Urbana, Illinois 61801

A new particle image velocimetry system has been used to study the near-wake structure of a two-dimensional base in subsonic flow to determine the fluid dynamic mechanisms of observed base drag reduction in the presence of a base cavity. Experiments were done over a range of freestream Mach numbers up to 0.8, including local flowfield velocities over 300 m/s. Effects of the base cavity on the von Kármán vortex street wake were found to be related to the expansion and diffusion of vortices near the cavity, although the effects are of small magnitude and no significant change in the vortex formation location or path was observed. The base cavity effects are also less significant at higher freestream velocities due to the formation of vortices further downstream from the base. The base cavity drag reduction was found to be mainly due to the displacement of the base surface to a location upstream of the low-pressure wake vortices, with only a slight modification in the vortex street itself.

Introduction

THE separated flow past a two-dimensional body at subsonic speed and large Reynolds number forms a wake structure made up of alternately shed vortices known as the von Kármán vortex street. This commonly occurring structure has been the subject of numerous studies beginning with von Kármán's first theoretical analysis of vortex streets.[1] A significant feature of this flowfield is the interaction of the low-pressure vortices in the near wake with the downstream surface or base of the body, inducing a net streamwise pressure force on the body known as base drag. The base drag is typically a significant component of total drag, even for slender bodies with a finite thickness base. For this reason, drag reduction methods based on the modification of the vortex street have received much attention.

One effective drag reduction method is the use of a base cavity, which is the subject of this study. It has been shown experimentally that the presence of a solid-walled cavity in the base of a slender two-dimensional body (see Fig. 1) increases the base pressure, resulting in base drag reduction of up to 30%.[2-5] Other effects of a base cavity that have been experimentally observed include an increase in vortex shedding frequency or Strouhal number as compared with a blunt base[4,5] and limited drag improvement for a cavity depth beyond approximately half the base height.

The mechanism of drag reduction due to base cavities is as yet unclear, although several theories have been proposed, all of which imply some modification of vortex formation location and reduction in vortex strength. The earliest published base cavity experiments were done by Nash et al.[2] They proposed that, although a vortex or eddy may not be completely trapped by the cavity, the cavity does have a stabilizing effect on standing eddies near the base, implying that the vortices form at least partially within the cavity where they are affected by the cavity walls. Pollock[3] performed experiments based on theoretical work by Ringleb[6] who suggested that a stable vortex may be trapped in a cavity, causing the wake to revert to a steady flow. Pollock used a special asymmetric cusp-shaped cavity that showed no advantage in drag reduction over a rectangular cavity,

in effect disproving Ringleb's theory. In a study of resonance effects on vortex shedding, Wood[7] showed that resonance of the base at the vortex shedding frequency causes vortex formation within the cavity, whereas formation normally occurs outside the cavity. He concluded that the drag reduction observed for base cavities must be due to some resonance or vibration in the flowfield, moving the vortices into the cavity where the solid walls restrict vortex growth and inhibit the strength of successive vortices.

A study of axisymmetric base cavities by Compton[8] suggested that recirculation within the cavity forms a coflowing stream at the cavity edge that interacts with the separated freestream, reducing the vorticity of the separated shear layer. In a subsequent study of axisymmetric base cavities, Morel[9] suggested that the coflowing stream could be an important effect in two-dimensional geometries as well. More recently, Kruiswyk and Dutton[4] used a combination of pressure measurements and flow visualization techniques to conclude that, although vortex motion does not extend into the cavity, oscillating airflow at the cavity boundary increases fluid mixing in the near wake, thereby reducing vortex strength. Their results concerning the change in base pressure and vortex shedding frequency due to a base cavity are shown in Table 1. The base cavity was rectangular with a streamwise depth equal to half the base height. A base cavity with a depth of one full base height was also used, but the results were similar to those of the half base height cavity. The results in Table 1 show an increase of 10–14% in the base pressure coefficient, which is nondimensionalized by reference conditions in the flow just before separation near the downstream edge of the base. The relative increase in the Strouhal number (vortex shedding frequency) is smaller, although still significant. Another evident feature is that both effects are largest at the lowest freestream Mach number. The experimental conditions used in the present study match those used by Kruiswyk and Dutton[4] to facilitate comparison of data.

Two notable computational simulations of two-dimensional base cavity flows have also been done. Rudy[10] obtained finite difference Navier-Stokes solutions using base configurations and freestream Mach numbers of 0.4 and 0.6 that matched those of Kruiswyk and Dutton.[4] However, Rudy's simulations were laminar, using freestream Reynolds numbers (based on base height) of 700 and 962 that are significantly lower than experimental values. Clements and Maull[5] used an inviscid discrete vortex method for simulations of their experimental results. Rudy's results more accurately predicted the experimentally measured base pressure increase due to a cavity, but both simulations showed vortex formation within the cavity and a decrease in shedding frequency due to the cavity, which disagrees with experimental results. Rudy concluded that the observed increase in base pressure with a cavity was mainly due to the physical displacement of the base surface away from the low-pressure vortices.

*Research Assistant, Department of Mechanical and Industrial Engineering; currently Staff Engineer, General Electric Corporate Research and Development, One River Rd., K1-ES121, Schenectady, NY 12309. Member AIAA.

†Professor, Department of Mechanical and Industrial Engineering. Associate Fellow AIAA.

Table 1   Base pressure and shedding frequency effects due to base cavity (taken from Kruiswyk and Dutton[4])

Freestream Mach no., M_∞	Freestream Reynolds no., Re_∞	Base pressure coefficient C_p increase,%	Strouhal no. St Increase, %
0.4	1.36×10^5	14.1	6.53
0.6	1.82×10^5	9.8	3.65
0.8	2.09×10^5	10.3	2.57

Fig. 1   Typical two-dimensional base cavity and subsonic vortex street wake.

The work presented here will take advantage of both the new results available from particle image velocimetry (PIV) and the extensive experimental and computational data available from Kruiswyk and Dutton[4] and Rudy,[10] respectively. The ability to directly compare results from several techniques for similar base geometries and flow conditions will allow a thorough analysis of the effects of a base cavity on the structure and properties of the flowfield, leading to a better understanding of the mechanisms of drag reduction.

Equipment

Test Section

Experiments for this study were performed in a previously fabricated transonic wind tunnel (Fig. 2) based on a design described by Little and Cubbage.[11] The tunnel has a 4 × 4 in. (101.6 × 101.6 mm) test section with solid sidewalls and slotted upper and lower inner walls to relieve the blockage effect of models in the subsonic to transonic speed range. Six-in.-diam round windows are mounted in both sidewalls to allow visualization of the downstream end and near wake of a base model. The tunnel is a blowdown type supplied with compressed dry air from a 140 m³ tank farm at 120 psia. The base model (Fig. 2) consists of an interchangeable afterbody mounted on a wedge-shaped forebody. Trip wires are mounted on the top and bottom surfaces near the upstream edge to assure a uniformly turbulent boundary layer at separation. When mounted in the test section, the upstream edge is located approximately 17 in. (432 mm) downstream of the wind tunnel entrance with approximately 0.75 in. (19 mm) of the downstream end of the model visible through the side windows. The afterbodies used are a blunt base and a rectangular base cavity with a depth of half the base height. The wind tunnel and base models are the same as those used by Kruiswyk and Dutton.[4]

Modifications have been made to the original wind tunnel for the flow seeding and optical access necessary for this study. Slot-shaped upper and lower windows have been fabricated and installed in the outer tunnel walls for access with a vertically propagating planar laser sheet. The sheet passes through the lower window and through one of the streamwise slots of the inner wall to enter the test section. The arrangement of the wall slots requires the position of the sheet to be 10 mm off the tunnel centerline in the spanwise direction, but surface flow visualization on the base model[4] and laser Doppler velocimetry (LDV) data in the near wake[12] indicate no significant variation of the flow within 10 mm of the centerline. Delivery of silicone oil droplet seeding for PIV is done by two TSI six-jet atomizers feeding a single 3/4-in. o.d. tube that enters the stagnation chamber. Flow from the stagnation chamber passes through a pair of screens (44 × 44 mesh screen with 57% open area) and enters an enclosure at the nozzle entrance to reduce turbulence. The atomized silicone oil is then injected through a manifold tube with a series of holes directed downstream and oriented in a transverse (vertical) plane aligned with the illuminating laser sheet. The flow then passes
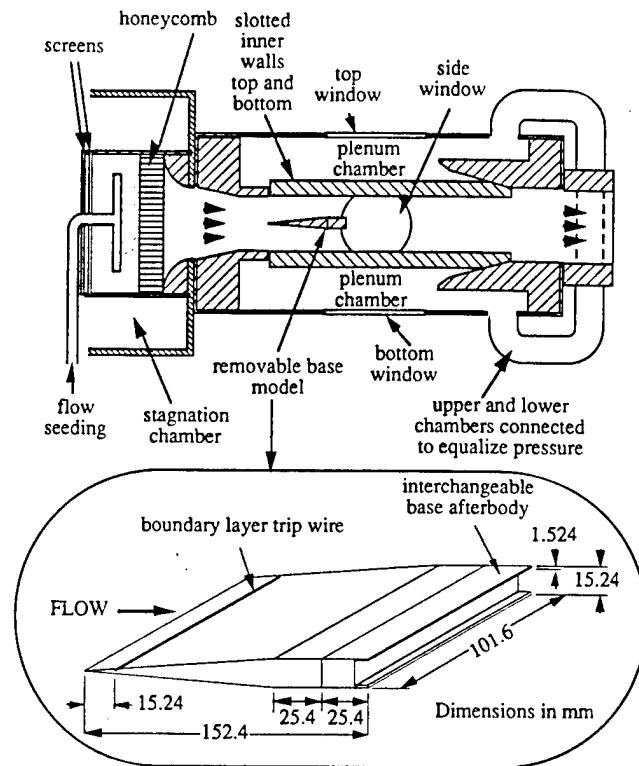
Fig. 2   Base flow test section and base model.

through a 2-in.-long section of honeycomb with a 3/16-in. cell diameter to further reduce turbulent fluctuations. The seed injection is done downstream of the screens due to experience with LDV indicating that silicone oil droplets tend to build up on screens, causing large drops to form and burst off, which bias velocity measurements. LDV data from the final tunnel configuration indicate tunnel-empty turbulence intensities of less than 1% at the freestream conditions used in this study.

PIV System

To meet the objectives set forth for this study, data were obtained with a nonintrusive velocity measurement technique called particle image velocimetry (PIV). PIV is performed by illuminating a seeded flowfield with a planar laser sheet that is pulsed at a known time interval, forming two or more sequential images of each seed particle within the light sheet (Fig. 3). The particle images are captured on film or another medium; then the local image separations and, therefore, velocities can be determined for the entire plane. Unlike pointwise techniques such as LDV, which provides statistical velocity data on a point-by-point basis, PIV can quantitatively identify instantaneous flow structures that may be random in nature but important to the overall behavior of the flow. PIV also reveals planar views of three-dimensional flow structures that are smeared by volume integration inherent in techniques such as schlieren photography. A detailed discussion of the design, development, and validation of the automated PIV system used in this study can be found in Refs. 12 and 13.

The current study used a beam thickness of 1.2 mm and width of 64 mm at the test section with a uniform interrogation region for each velocity measurement of 1 × 1 mm in the frame of reference of

Table 2 Experimental conditions

Freestream Mach no., M_∞	Reference Mach no., M_{ref}	Base configuration	Freestream Reynolds no., Re_∞	Notation
0.4	0.49	Blunt	1.36×10^5	M4b
0.4	0.49	Half-height cavity	1.36×10^5	M4c
0.6	0.74	Blunt	1.82×10^5	M6b
0.6	0.74	Half-height cavity	1.82×10^5	M6c
0.8	0.88	Blunt	2.09×10^5	M8b
0.8	0.88	Half-height cavity	2.09×10^5	M8c

Fig. 3 Principle of PIV.

PIV data on 0.5 mm grid $\rightarrow$ 275 m/s
(shown on 1 mm grid for clarity)

Fig. 4 M6b processed velocity vector plot.
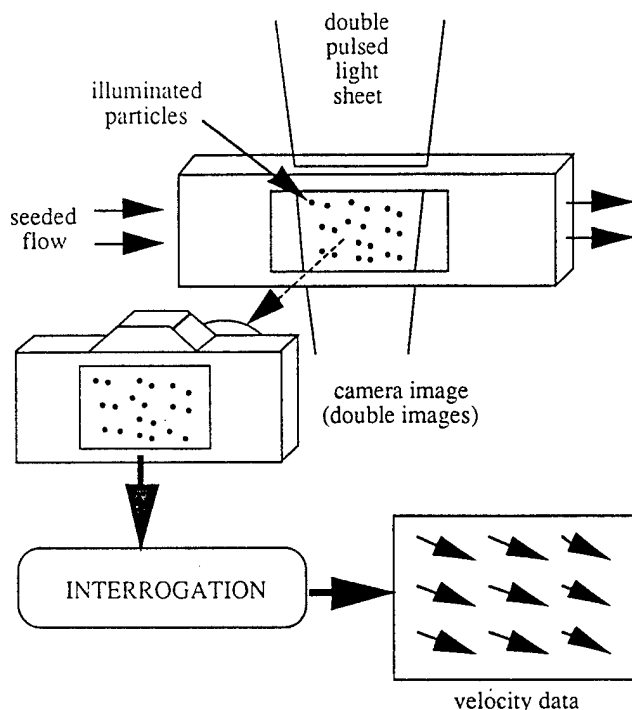
the test section. The probe volume is therefore 1×1 mm (spot size) by 1.2 mm (laser sheet thickness) or 1.2 mm.[3] Velocity vectors were determined on a grid with an increment of 0.5 mm in each direction (overlapping spots) to prevent biasing due to small-scale motions in the flowfield. The upstream edge of the vertically propagating beam passes just downstream of the aft edge of the base to avoid intense reflections from the base surfaces, thus preventing acquisition of PIV data within the base cavity.

Validation experiments have been performed with this PIV system using both simulations and high-speed flow experiments, indicating a maximum total error in raw PIV velocity measurements of less than 3%.[12] A large portion of this total is due to random error, which is reduced by processing operations performed on the raw data.[12,14]

Results and Discussion

Experimental Conditions

Experiments were initially performed with two base configurations at three freestream velocity conditions, resulting in six cases. Flow conditions for each case were determined by running the test section without the base model. The test section flow velocity was measured as a function of wind-tunnel stagnation pressure, allowing the appropriate stagnation pressure to be determined for each desired freestream velocity condition. This stagnation pressure was maintained for the corresponding experiments with the base model. A summary of the flow conditions and base configurations used in this study is shown in Table 2, including the freestream Reynolds number based on freestream velocity and base height, and shorthand notations for each case. As mentioned previously, these cases match those used by Kruiswyk and Dutton[4] and the Mach 0.4 and 0.6 freestream conditions used by Rudy[10] with similar base configurations.
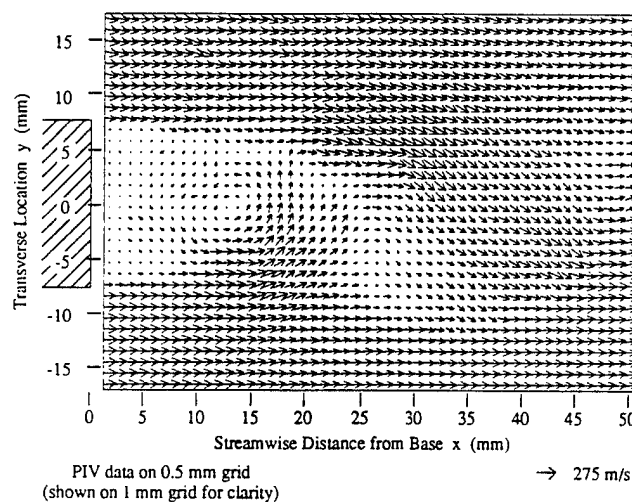
As expected from inviscid flow theory, the measured velocity just outside the boundary layer at the downstream edge of the base (reference Mach number in Table 2) is greater than the associated freestream velocity due to local compression of streamlines near the body. The mean measured reference Mach numbers for each case were found to match the reference Mach numbers quoted by Kruiswyk and Dutton[4] for the associated freestream conditions. The velocity data from individual flowfield realizations showed some variation from the desired reference velocities (maximum 9%) due to the lack of tunnel control valve resolution at the small stagnation pressures required and due to changes in the stagnation temperature of the supply air from run to run. The velocity data from each flowfield realization were therefore scaled to account for these variations.

Individual Flowfield Realizations

Fifteen flowfield realizations were obtained for each of the Mach 0.4 and Mach 0.6 cases listed. Realizations were also obtained for each of the Mach 0.8 cases, but difficulties with seeding density in the vortex street prevents the use of those cases in the quantitative analysis presented here.[12] Each individual realization consists of an array of 6831 (99×69) instantaneous velocity vectors with 0.5-mm spacing in the streamwise and transverse directions. By defining the coordinate system as positive x in the streamwise direction and positive y in the transverse direction with the origin at the center of the downstream base edge, each realization covers the wake from $x = 1$ to 50 mm and from $y = -17$ to 17 mm. This region extends 2.2 base heights in the transverse direction and 3.3 base heights downstream of the aft edge of the base.

The velocity vector plot from a single Mach 0.6 blunt base (M6b) realization is shown in Fig. 4. As noted in the figure, only every other vector in each direction is plotted for the sake of clarity. Processing of the velocity data includes automated elimination of invalid velocity vectors (2–8% of total) that are caused by photographic imperfections, lack of particle images, and other effects. Interpolation is used to replace invalid data, and then a low-pass spatial filter smooths the data to eliminate any high-frequency random error.[12,14]

Figure 4 reveals some of basic features of the flowfield, including the presence of distinct alternating vortices. The first counter

Table 3 Base flow shear layer length and separation

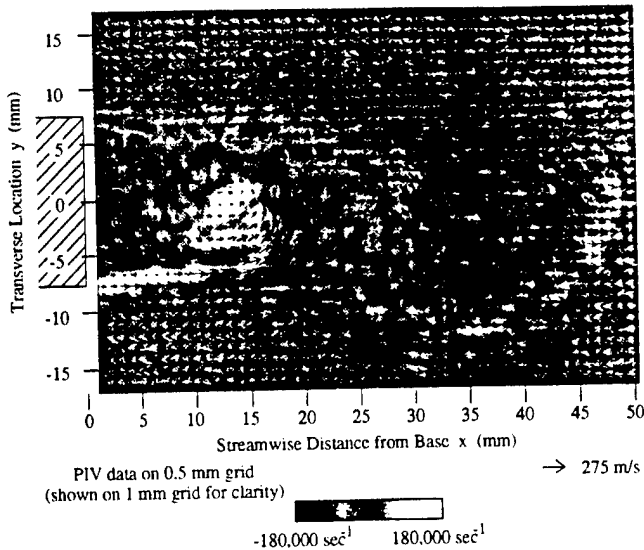| Experimental case	Average shear layer streamwise length, mm	Cavity % change	Shear layer endpoint transverse separation, mm	Cavity % change
M4b	6.9	——	13.0	——
M4c	6.8	−1.4	12.5	−3.8
M6b	8.0	——	13.5	——
M6c	7.4	−7.5	12.8	−5.2

Fig. 5 M6b color vorticity plot with velocity vector overlay.

clockwise vortex near the base is clearly seen, whereas the structure of the next two vortices is less distinct due to increasing convective velocity in the downstream direction. The separated region near the base is also evident, with low velocity magnitudes immediately downstream of the base edge and significant upstream fluid motion at the first fully formed vortex. There is also evidence of turbulence throughout the flowfield, with irregularities in the vortex motion, especially near the base edge.

To analyze vortex location and strength, the out-of-plane vorticity

$$\omega_z = \left(\frac{\partial v}{\partial x} - \frac{\partial u}{\partial y} \right) \qquad (1)$$

was computed for each flowfield realization. This was done by central differencing of the original velocity data. A color plot of vorticity with overlaid velocity vectors corresponding to Fig. 4 is shown in Fig. 5. These data present a new capability for quantitatively analyzing separated compressible flow structure that has to this point been impossible. One of the notable features in Fig. 5, which holds for all experimental conditions, is the significant fragmentation of the vortices as they shed from the separated shear layers at the aft edge of the base. This is indicative of the high level of boundary-layer turbulence before separation, confirmed by boundary-layer turbulence intensity measurements of up to 5% using LDV,[12] and its effect on the turbulent structure of the wake. Fast response pressure measurements made in the wake by Kruiswyk and Dutton[4] also showed a wide distribution of frequencies around the vortex shedding frequency, indicating the superposition of the vortex street on a random turbulent flowfield. Turbulence energy is therefore transferred in the wake from the large-scale vortices to smaller scales, causing the gradual breakdown of distinct vortices as they travel downstream.

Vorticity Statistics

As mentioned earlier, previous theories regarding the mechanism of base cavity drag reduction all hinge on some modification of vortex strength and/or position. For this reason, it is desirable to use the vorticity data now available to examine vortex path and strength, both with and without base cavities. Because of the turbulent nature

of the flowfield and the resulting vortex fragmentation discussed previously, it is rather difficult to select a particular location for each vortex in an instantaneous realization. Therefore, a statistical method was adopted to estimate vortex path and strength. Because of the alternate shedding of the wake vortices, successive vortices have peak vorticity values ω_z of alternating sign, causing the mean vorticity to go to zero where the opposing vortex paths overlap. Since only the vorticity magnitude is necessary for the determination of vortex strength and path, it was decided to derive the root mean square (rms) vorticity for each experimental case, which is defined at each flowfield location (x, y) by

$$\omega_{rms}(x, y) = \left[\frac{\sum_{i=1}^{N} [\omega_z(x, y)]_i^2}{N} \right]^{\frac{1}{2}} \qquad (2)$$

where the index i represents each individual realization for the experimental case of interest and N is the total number of realizations, or 15.

The results for the M4b, M4c, M6b, and M6c cases (see Table 2) are shown in Fig. 6. These plots show the region within approximately one base height of the aft edge to concentrate on the notable features. Although some data scatter is present due to the turbulence level and limited ensemble size, these plots do reveal useful information about cavity effects. One of the first noticeable features is the presence of the free shear layers at each separation point and their extension into the wake. At a point less than one-half base height downstream, they rapidly lose strength, indicating the mean location at which free vortices break off into the wake, or the vortex formation location. Lines have been included on the plots to identify the mean shear layer location, shape, and length. Each line was determined by a curvefit to the peak vorticity values in the shear layer, with the line terminating at the point where the vorticity drops below 67% of the maximum scale, or 67,000 s⁻¹ for the M4b and M4c cases, and 100,000 s⁻¹ for the M6b and M6c cases. This allows a relative comparison of the shear layer lengths between all four cases.

Table 3 shows the average shear layer length and the transverse separation distance of the shear layer endpoints for each case shown in Fig. 6. Although the average shear layer length is 0.6 mm shorter for the M6c case than the M6b case, the difference of 0.1 mm is not significant for the Mach 0.4 cases. The asymmetry in the shear layers propagating from the upper and lower base corners for a given case also prevents drawing any firm conclusion of a change in vortex formation location due to the cavity, although wake static pressure data were used by Kruiswyk and Dutton[4] to conclude that vortex formation occurs further downstream due to the cavity for a Mach 0.4 freestream velocity.

Figure 6 does, however, reveal that the angle of convergence of the shear layers toward the transverse centerline appears steeper for the base cavity cases than for the blunt base. There may also be a slight increase in shear layer curvature, although it is difficult to determine conclusively. Increased shear layer curvature would indicate a larger pressure gradient across the shear layer, which would, in turn, imply that the cavity causes lower mean static pressure in the region just inside the shear layer and just past the separation point. However, this must be only a local effect confined near the shear layer, since the cavity has been shown in previous research to increase the mean pressure over the base surface, which is upstream of the shear layers inside the cavity.

Convergence of the shear layers causes the transverse separation distance between the two shear layers to be reduced at their endpoints (see Table 3), explaining the increase in shedding frequency
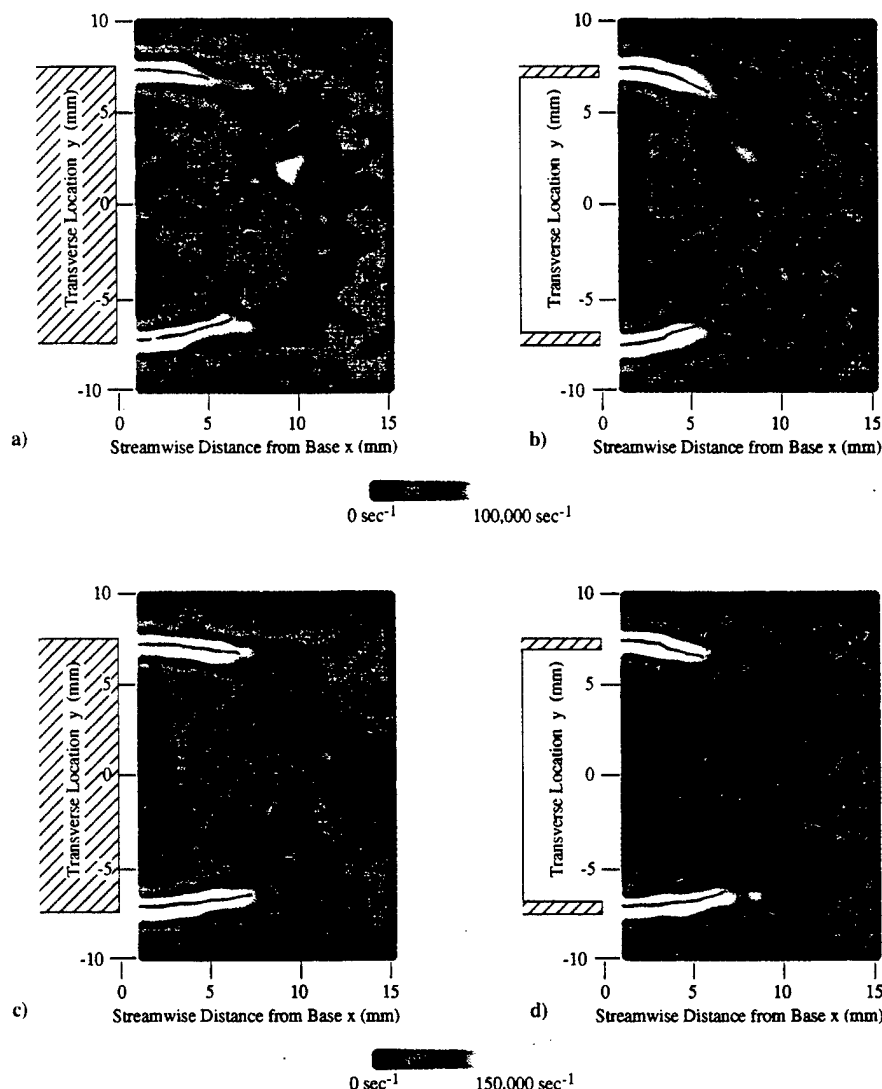
Fig. 6 Enlarged color rms vorticity plots indicating shear layers: a) M4b b) M4c, c) M6b, and d) M6c.

observed by Kruiswyk and Dutton[4] for the base cavity (see Table 1). As stated by Fage and Johansen,[15] the shedding frequency in a vortex street is inversely proportional to the separation distance of the shear layers in the wake. When the shear layer separation is reduced in the base cavity wake due to convergence, it follows that the shedding frequency increases.

In examining the vortex path just downstream of the shear layers. reduced vortex strength due to the base cavity can be seen in Fig. 6 for both freestream Mach numbers. In an effort to quantify this result, the spatially averaged rms vorticity was calculated for each case in Fig. 6 over a region extending between the two shear layer endpoints (in the transverse direction) and extending from the longest shear layer endpoint to 7.5 mm downstream of that endpoint (in the streamwise direction). This region was chosen to uniformly cover the initial vortex path for each case. The results are shown in Table 4. Although the data scatter in Fig. 6 makes small differences difficult to determine visually, the data in Table 4 show that the average rms vorticity level is indeed reduced by the cavity for both freestream Mach numbers, implying a small decrease in vortex strength.

Finally, any effect of the base cavity on mean vortex path is not clear from Fig. 6, although it is evident that turbulence causes the vortex path to be somewhat random, since the rms vorticity magnitude peaks are widely scattered in the wake for all cases.

The effects of increasing Mach number on the shear layers include a small increase in shear layer separation (see Table 3) that seems to be caused by a reduction in both the initial convergence angle and curvature of the shear layers, and can be attributed to increased streamwise momentum in the fluid stream outside the wake. The

Table 4 Base flow near-wake vortex strength

Experimental case	Spatially averaged rms vorticity, s^{-1}	Cavity % change
M4b	42.590	——
M4c	40.890	−4.0
M6b	66.120	——
M6c	62.490	−5.5

shear layers are also extended by approximately 1 mm for the Mach 0.6 freestream cases vs Mach 0.4, causing the vortex formation to occur further downstream of the base edge. However, any change in vortex path downstream of the shear layers due to the increase in freestream velocity is not evident from these data. Displacement of the vortex formation location further downstream of the base would serve to explain the reduced effectiveness of the cavity at higher Mach numbers as shown by Kruiswyk and Dutton[4] (see Table 1). As the vortices form further away from the base at higher Mach numbers, their effect on the pressure at the base surface is reduced, causing any modification of the vortex street due to the cavity to have less relative effect on the base pressure.

Instantaneous Wake Structure

Further information on base cavity wake effects can be obtained by comparing the instantaneous wake structure for the blunt base and base cavity at a similar point in the vortex shedding cycle. For
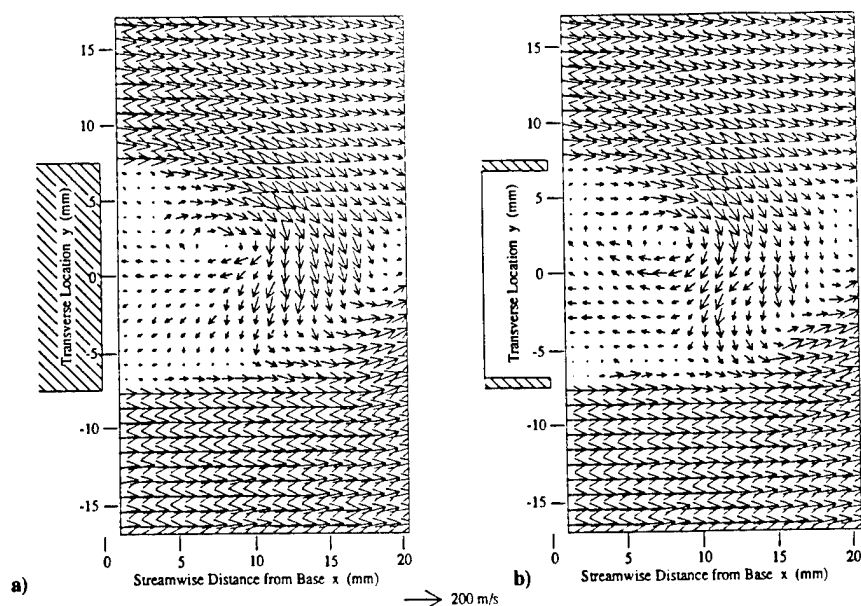
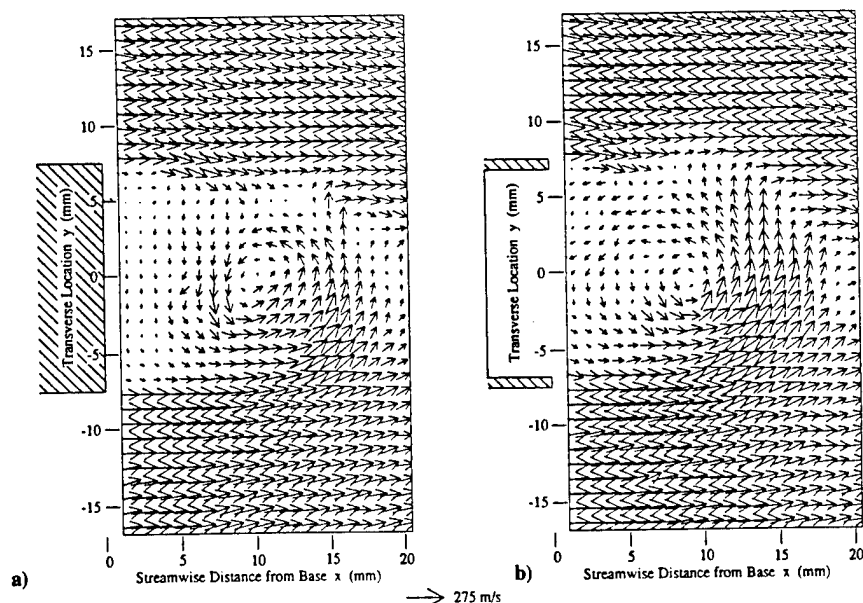Fig. 7   Instantaneous flow structure comparison—M_∞ = 0.4 velocity vectors: a) M4b and b) M4c.

Fig. 8   Instantaneous flow structure comparison—M_∞ = 0.6 velocity vectors: a) M6b and b) M6c.

each freestream velocity condition, realizations were selected from the two base configurations with closely matching vortex locations in the near wake. Velocity vector plots for the best match from the M4b and M4c cases are shown in Fig. 7, with plots from the M6b and M6c cases shown in Fig. 8. As in Figs. 4 and 5, these velocity vector plots show only every other vector in each direction for the sake of clarity. It is evident from Figs. 7 and 8 that for each pair of realizations the center stagnation point of the first vortex downstream of the base matches to within 1 mm in each direction.

Each of these realizations, along with others not shown here, indicates that the circulating region around a fully formed vortex entering the wake covers most of the base height, which is confirmed by the results of Kruiswyk and Dutton.[4] However, in both Figs. 7 and 8, a significant difference in vortex structure due to the cavity is evident. In the presence of the base cavity, the circulating region around the fully formed vortex is extended further in all directions, diffusing the vortex motion over a larger region. Although velocity data are available only to within 1 mm of the base boundary, the vortex seems to extend partially into the cavity boundary (see first column of vectors at $x = 1$ mm and $y = -7.5$ to 7.5 mm in Figs. 7b

and 8b), but the relatively small magnitude of this motion and the distance of the vortex center from the cavity preclude the vortex being significantly inhibited by the cavity walls. The extension of the vortices partially into the cavity is confirmed by tuft visualization experiments done by Kruiswyk and Dutton,[4] which showed that short strands of lightweight thread hung at the cavity boundary oscillated back and forth into the cavity in the streamwise direction, with small oscillations in the spanwise direction. However, surface flow visualization experiments performed to determine the interaction of the vortices with the inner walls of the cavity indicated very little fluid motion on the walls (i.e., very small cavity wall shear stress), even near the cavity boundary. The rms vorticity data obtained here also show no evidence of vortex formation near the cavity boundary (see Fig. 6), and so it is not likely that the vortices extend far enough into the cavity to be seriously inhibited by the cavity walls.

Another feature of the vortex expansion shown in Figs. 7 and 8 is that, with the base cavity, the vortices extend far enough across the wake to affect the opposing shear layer. For example, in Fig. 8b, the fully formed vortex shed from the lower separation point clearly interacts more strongly with the upper shear layer than is the case
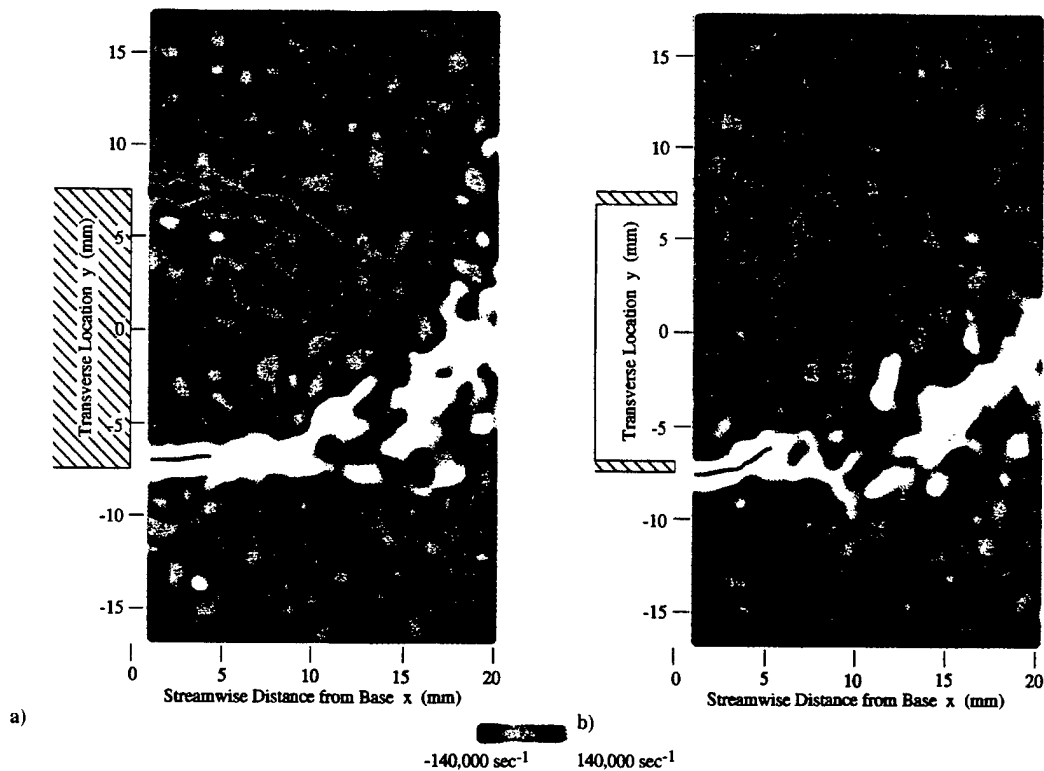
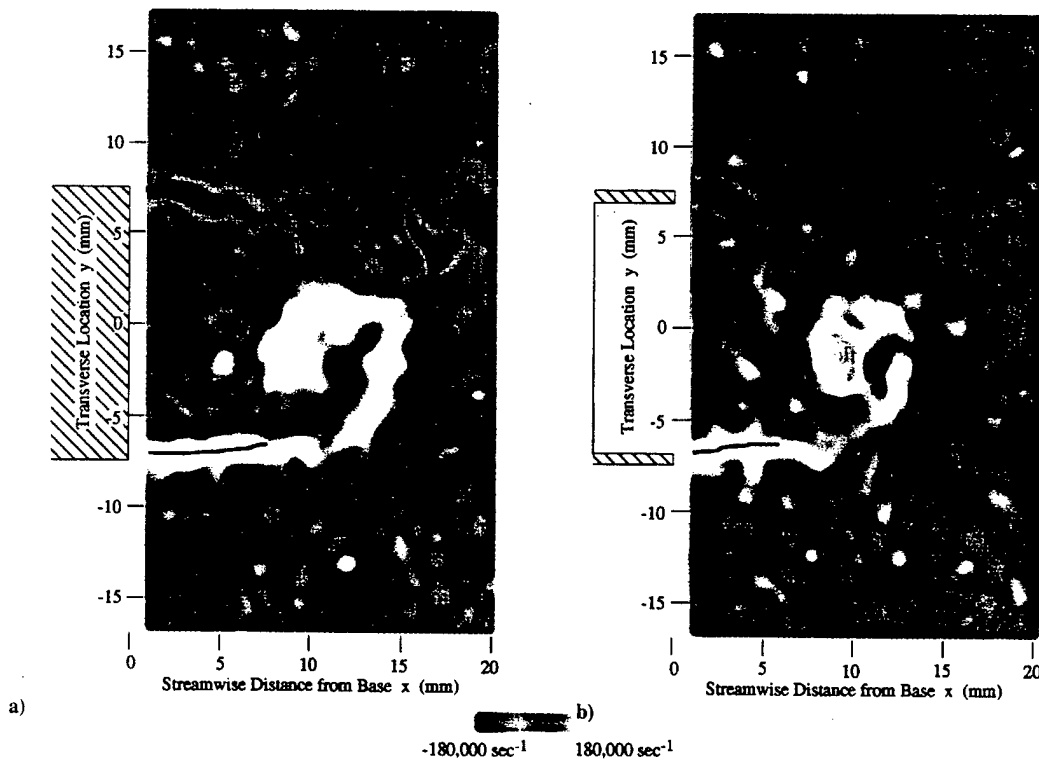**Fig. 9 Instantaneous flow structure comparison—M_∞ = 0.4 color vorticity plots: a) M4b and b) M4c.**

-140,000 sec⁻¹   140,000 sec⁻¹

Fig. 10 Instantaneous flow structure comparison—M_∞ = 0.6 color vorticity plots: a) M6b and b) M6c.

-180,000 sec⁻¹   180,000 sec⁻¹

for the blunt base in Fig. 8a. To examine this interaction, the instantaneous vorticity is plotted in Figs. 9 and 10 for each of the four realizations shown in Figs. 7 and 8. From these plots, the shear layer position can be determined and is indicated by a line in the same manner as in Fig. 6. The fluid motion near the shear layers due to vortex expansion across the wake is also shown with curved arrows. One effect from interaction of the expanded vortices with the opposing shear layers is a folding of the shear layer region toward the transverse centerline. For example, in Fig. 10b, the upper shear layer gains transverse momentum toward the centerline at locations

upstream of the vortex center. The subsequent increase in shear layer curvature and convergence angle in the area upstream of the vortex center is clearly evident from both base cavity plots (lower shear layer in Fig. 9b and upper shear layer in Fig. 10b). Evidence of the vortex interaction with remnants of the shear layer downstream of the vortex center is also apparent with the corresponding motion away from the transverse centerline.

Another effect of diffused vortex motion is that increased vorticity in the area just inside of the shear layers and downstream of the separation point can reduce the local pressure, thereby increasing the
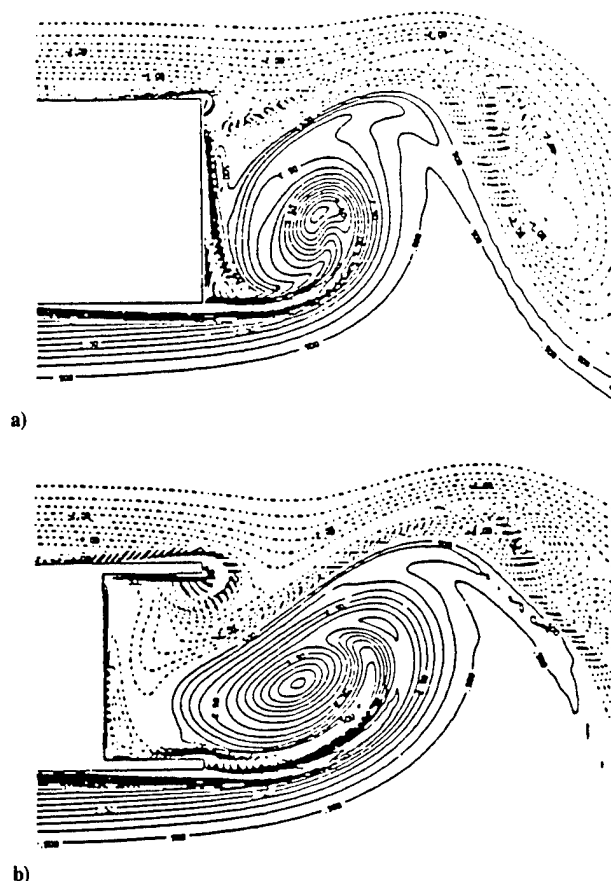
a)

b)

Fig. 11 Navier-Stokes numerical solution vorticity contours, taken from Rudy[10]: a) M6b and b) M6c.

curvature of the shear layer, an effect that was discussed previously. However, increases in vorticity magnitude near the shear layers that would be associated with reduced pressure are not readily apparent in Figs. 9b and 10b.

The instantaneous flow structure data can also be used for comparison to the numerical simulation of this flowfield done by Rudy.[10] This study used a time-accurate simulation of the Navier-Stokes equations to compute the laminar flow past base models similar to those used in the present experiments, with the only difference being in the transverse cavity height, which is equal to 90% of the total base height in the simulations and 80% of the base height in the present experiments. As previously mentioned, the simulations were done for freestream Mach numbers of 0.4 and 0.6 and at relatively low freestream Reynolds numbers (based on freestream velocity and base height) of 700 and 962 for Mach 0.4 and 0.6, respectively.

Instantaneous vorticity plots have been selected from the Mach 0.6 simulations (Fig. 11) that most closely match the stage of vortex development indicated by the experimental results shown in Fig. 10. In comparing the numerical and experimental results, it can be seen that there are some significant differences in the vortex structure. The lack of turbulence in the laminar flow simulations and the resultant discrepancy with the experimental flowfield (which includes small-scale turbulence and vortex fragmentation) are evident. The simulations also show that the vortices are elongated for both the blunt and cavity configurations, especially for the base cavity where the vortex stretches in the streamwise direction as it expands into the cavity, causing vortex motion far into the cavity. Additional data from Rudy[10] show distinct vortices forming near the cavity boundary at the transverse center of the wake. Although the PIV data do not extend into the cavity, the scale of the fluid motion at the boundary and the vortex formation location indicated by the experiments do not support these results. Rudy recognized the limitations of his computations and suggested future studies to include both higher Reynolds numbers and turbulence modeling to more accurately predict experimental results under typical Reynolds number conditions.

Conclusions and Summary

Analysis of the time-resolved flowfield structure in the turbulent separated wake of a base cavity has been made possible by implementation of a new particle image velocimetry (PIV) system. The data obtained have shed light on the effects of a two-dimensional base cavity and on the mechanism by which it reduces base drag.

The evidence presented indicates that the most prominent effects of a base cavity on the vortex street wake are the increased convergence of the separated shear layers from each base corner toward the transverse wake centerline, and the diffusion of vortex motion due to the expansion of individual vortices across the near wake and partially into the cavity. The diffusion of the vortices, in turn, reduces their strength by approximately 4–6%, although the vortices do not form further upstream and are not significantly inhibited by the cavity walls. This is seen at both freestream conditions examined here. It is also evident that the effects are less significant at higher freestream velocities due to the extension of the separated shear layers and the movement of the vortex formation location further downstream of the aft edge of the base, thereby reducing the effect of the cavity on the vortices. These specific effects provide the information necessary for determination of the drag reduction mechanisms of base cavities.

The apparent mechanism of the observed base cavity wake modifications depends on the replacement of the solid boundary of the blunt base with the compliant fluid boundary of the base cavity. This compliant boundary allows greater expansion of vortex motion and a resulting small increase in shear layer convergence toward the transverse centerline due to the interaction of each vortex on the upstream part of the opposite shear layer. However, vortex formation does not occur any closer to the aft edge of the base for the cavity case. These results refute the theories of Nash et al.,[2] Pollock,[3] Ringleb,[6] and Wood,[7] all of which assume that the vortices are somehow trapped or stabilized by interaction with the inner walls of the cavity. The suggestion by Compton[8] and Morel[9] that a coflowing stream sheds from the cavity wall is partially valid in that there is some momentary outflow from one edge of the cavity when vortex motion partially extends into the cavity, but the magnitude of the motion is very small and too short-lived to affect the vorticity level in the shear layer before vortex formation. This conclusion is confirmed by the surface flow experiments of Kruiswyk and Dutton[4] that indicate little or no fluid motion on the inner walls of the cavity. The proposal by Kruiswyk and Dutton[4] that periodic fluid mixing at the cavity boundary is responsible for a reduction in vortex strength is closest to being in agreement with the present results, since some mixing must occur as each vortex partly extends into the cavity, although the reduction in vortex strength is small.

Aside from the mechanisms of wake modification, one must consider the mechanism of the base pressure increase and subsequent drag reduction due to base cavities. It is true that the effects described earlier modify and slightly weaken the vortex street, which, in turn, should slightly increase the pressure in the vicinity of the vortices in the near wake. However, the wake structure changes are relatively small and the vortex formation location and path are not significantly modified. Without a significant change in the strength or location of the vortices in the near wake due to the base cavity, it seems that the most significant factor affecting the base pressure is the physical displacement of the base surface within the cavity to a position upstream of the wake, where it does not interact with the low-pressure vortices. This is the conclusion drawn by Rudy,[10] although his numerical simulations showed the vortices extending far into the cavity with corresponding effects on the wake structure.

In summary, the drag reduction mechanism of a base cavity in subsonic flow is the physical displacement of the base surface away from the vortex street wake, which is only slightly modified by the presence of the cavity.

References

[1]von Kármán, T., "Über den Mechanismus des Widerstandes, den ein bewegter Körper in einer Flüssigkeit erfährt," *Nachrichten von der Königlichen Gesellschaft der Wissenschaften zu Göttingen. Mathematisch-Physikalische Klasse*, 1911, pp. 509–517.

[2]Nash, J. F., Quincey, V. G., and Callinan, J., "Experiments on Two-Dimensional Base Flow at Subsonic and Transonic Speeds, British Aeronautical Research Council, ARC R&M 3427, 1963.

[3]Pollock, N., "Some Effects of Base Geometry on Two-Dimensional Base Drag at Subsonic and Transonic Speeds," Australian Aeronautical Research Lab., Aerodynamics Note 316, 1969.

[4]Kruiswyk, R. W., and Dutton, J. C., "Effects of a Base Cavity on Subsonic Near-Wake Flow," *AIAA Journal*, Vol. 28, No. 11, 1990, pp. 1885–1893.

[5]Clements, R. R., and Maull, D. J., "The Representation of Sheets of Vorticity by Discrete Vortices," *Progress in Aerospace Sciences*, Vol. 16, No. 2, 1975, pp. 129–146.

[6]Ringleb, F. O., "Separation Control by Trapped Vortices," *Boundary Layer and Flow Control*, edited by G. V. Lachmann, Pergamon Press, Oxford, England, UK, 1961, pp. 265–294.

[7]Wood, C. J., "The Effect of Lateral Vibrations on Vortex Shedding from Blunt-Based Aerofoils," *Journal of Sound and Vibration*, Vol. 14, No. 1, 1971, pp. 91–102.

[8]Compton, W. B., "Effect on Base Drag of Recessing the Bases of Conical Afterbodies at Subsonic and Transonic Speeds," NASA TN D-4821, 1968.

[9]Morel, T., "Effect of Base Cavities on the Aerodynamic Drag of an Axisymmetric Cylinder," *Aeronautical Quarterly*, Vol. 30, Pt. 2, 1979, pp. 400–412.

[10]Rudy, D. H., "A Numerical Study of Unsteady Two-Dimensional Subsonic Compressible Base Flow," Ph.D. Thesis, Dept. of Mechanical and Industrial Engineering, Univ. of Illinois at Urbana–Champaign, Urbana, IL, 1987.

[11]Little, B. H., Jr., and Cubbage, J. M., Jr., "The Development of an 8-inch by 8-inch Slotted Tunnel for Mach Numbers up to 1.28," NASA TN D-908, 1961.

[12]Molezzi, M. J., "Development and Application of Particle Image Velocimetry in High-Speed Separated Flow: Two-Dimensional Base Cavities," Ph.D. Thesis, Dept. of Mechanical and Industrial Engineering, Univ. of Illinois at Urbana–Champaign, Urbana, IL, 1993.

[13]Molezzi, M. J., and Dutton, J. C., "Application of Particle Image Velocimetry in High-Speed Separated Flows," *AIAA Journal*, Vol. 31, No. 3, 1993, pp. 438–446.

[14]Landreth, C. C., and Adrian, R. J., "Measurement and Refinement of Velocity Data Using High Image Density Analysis in Particle Image Velocimetry," *Proceedings of the Fourth International Symposium on Applications of Laser Anemometry to Fluid Mechanics* (Lisbon, Portugal), July 1988, pp. 485–497.

[15]Fage, A., and Johansen, F. C., "The Structure of Vortex Sheets," British Aeronautical Research Council, ARC R&M 1143, 1927.

APPENDIX A.6

BASE-BLEED EXPERIMENTS WITH A CYLINDRICAL AFTERBODY IN SUPERSONIC FLOW

by

T. Mathur and J. C. Dutton

Base-Bleed Experiments with a Cylindrical Afterbody in Supersonic Flow

Tarun Mathur* and J. Craig Dutton[†]

University of Illinois at Urbana–Champaign, Urbana, Illinois 61801

The effect of base bleed on the near-wake flowfield of a cylindrical afterbody in a Mach 2.5 flow with a unit Reynolds number of 45×10^6 m^{-1} has been investigated. This study is aimed at better understanding the complex fluid-dynamic interactions occurring in the near wake due to base bleed and is motivated by the lack of detailed velocity and turbulence data in this flowfield. The experimental techniques used include static pressure measurements along the afterbody and the base plane, schlieren and shadowgraph photography, and centerline traverses in the near wake using two-component laser Doppler velocimetry. Results indicate relatively uniform radial pressure profiles across the base plane. With increasing bleed flow rate, the average base pressure is found to increase initially, attain a peak value near an injection parameter of $I = 0.0148$, and then decrease with further increase in I. The optimum bleed condition near $I = 0.0148$ is also characterized by a weak corner expansion, a minimum value of the free-shear-layer angle, and the near-disappearance of the recirculation region (reverse velocity) along the centerline of the near wake.

Nomenclature

A_b	= base area, πR_0^2, m^2
C_f	= skin-friction coefficient
H	= compressible shape factor, δ^*/θ
I	= dimensionless injection parameter, $\dot{m}_{\text{bleed}}/\rho_1 U_1 A_b$
k	= turbulent kinetic energy, m^2/s^2
M	= Mach number
$\dot{m}_{\text{bleed}}$	= bleed mass flow rate, kg/s
P	= pressure, kPa
R_{jet}	= bleed jet radius, mm
R_0	= afterbody radius, mm
r	= radial coordinate, mm
T_0	= wind-tunnel stagnation temperature, K
U	= mean axial velocity, m/s
U_1	= freestream approach velocity, m/s
u_τ	= friction velocity, m/s
u'	= instantaneous axial velocity fluctuation, m/s
v_r'	= instantaneous radial velocity fluctuation, m/s
x	= axial (streamwise) position relative to the base plane, mm
y	= radial distance from sting surface, mm
δ	= boundary-layer thickness, mm
δ^*	= boundary-layer displacement thickness, mm
θ	= boundary-layer momentum thickness, mm
ν_w	= kinematic viscosity at the wall (sting surface) temperature, m^2/s
Π	= boundary-layer wake strength parameter
ρ	= density, kg/m^3
σ_U	= axial rms velocity fluctuation, m/s
σ_{V_r}	= radial rms velocity fluctuation, m/s
$(\ )$	= ensemble-averaged value

Subscripts

b	= base
0	= stagnation or afterbody
1	= freestream approach conditions

Introduction

FLOW separation at the base of aerodynamic vehicles such as missiles, rockets, and projectiles leads to the formation of a low-speed recirculation region near the base. The pressure in this region is generally significantly lower than the freestream pressure. Base drag, caused by this difference in pressures, can be up to two-thirds of the total drag on a body of revolution. Techniques such as boattailing, base burning, and base bleed have been used traditionally to reduce base drag; however, in the past, these techniques were applied in an empirical manner because of a lack of detailed data and understanding of the fluid-dynamic interactions occurring in the base region. With the advent of laser-based optical flow diagnostic techniques in the past decade, it is now possible to examine these flowfields in greater detail in a nonintrusive manner. Recently, a detailed investigation of supersonic axisymmetric base flows including the effects of afterbody boattailing was completed by Herrin and Dutton.[1,2] The research reported herein on base bleed is the logical extension of this recent investigation.

Figure 1 is a flowfield schematic of supersonic flow over a blunt, cylindrical body with base bleed. The supersonic freestream flow undergoes an expansion at the base corner as the turbulent approach boundary layer separates and forms a free shear layer. This shear layer eventually undergoes recompression, realignment, and redevelopment in the wake of the afterbody as it is constrained to turn along the axis of symmetry. The shear layer entrains fluid from the region behind the base and accelerates it. A recompression shock system returns this fluid to the base region, forming a recirculation region in the process. Injection of low-speed fluid into the base region displaces the forward stagnation point downstream of the base plane. The location of the forward stagnation point is determined by a balance between the momentum of the injected gas and that of the recirculating fluid. The magnitude of the bleed flow rate is quantified using a nondimensional injection parameter, I, defined as the bleed mass flow rate normalized by the product of the base area and the freestream mass flux. This definition of the injection parameter does not account for the approach boundary-layer thickness and the bleed flow momentum, both of which have been shown to affect the base pressure in a manner analogous to base bleed.

The effect of varying the bleed mass flow rate on the base pressure ratio, P_b/P_1, has been studied experimentally by several researchers.[3-7] The results of these experiments exhibit certain common trends and indicate three distinct operating regimes determined by the quantity of mass injected. The base pressure ratio increases fairly linearly with bleed rate at low values of I (regime 1). A peak in the base pressure ratio occurs at an intermediate value of I (near $I = 0.01$ for air), the value of which depends on several factors
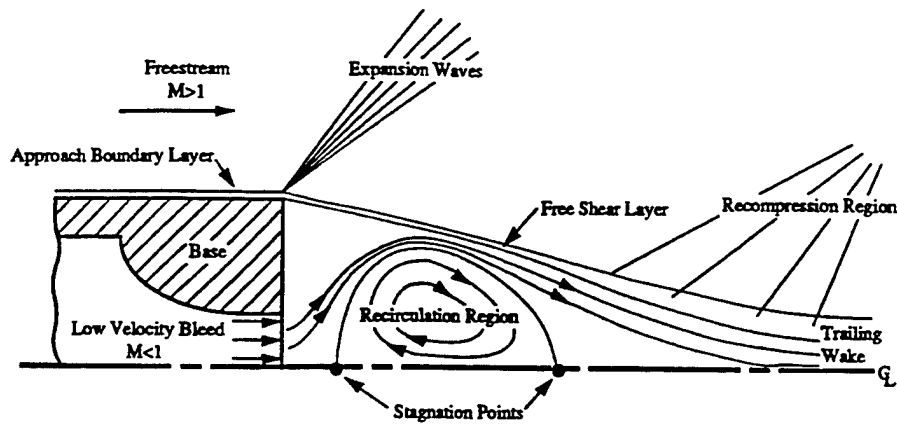
Fig. 1   Schematic of the near-wake flowfield with base bleed.

including the freestream Mach number, the size and geometry of the bleed orifice, and the flow rate, molecular weight, and temperature of the bleed gas. Increases in base pressure ratio (relative to the no-bleed case) from 10 to 90% have been reported for various combinations of the aforementioned parameters. As the bleed rate is increased past the optimum value, the base pressure ratio decreases (regime 2) until it reaches a relative minimum. A further increase in the bleed flow leads to the onset of power-on conditions (regime 3) when the bleed flow becomes supersonic, resulting in an increase in base pressure ratio.

From the combined results of the above experiments, base-bleed effectiveness is seen to increase with freestream Mach number, i.e., at higher Mach numbers, the peak base pressure occurs at lower I, and the percentage increase in base pressure is also higher. The effects of the bleed jet exit area on base pressure have also been investigated.[3,4,6-8] At very low bleed rates, the increase in base pressure with bleed is nearly independent of the area ratio; however, at higher bleed rates, the effectiveness of base bleed was shown to be improved by larger jet-to-base diameter ratios. Injection with porous bases is found to be the most effective.[7]

Experiments using air, hydrogen, helium, argon, and nitrogen have shown that base bleed is more effective when a bleed gas with lower molecular weight (relative to the freestream gas) is used.[8,9] The peak base pressure is higher, and occurs at a lower value of I with a lighter bleed gas. Significant increases in base pressure have also been observed using a heated bleed gas.[10] At low injection rates, the base pressure rise is nearly proportional to the enthalpy of the bleed gas. The peak base pressure is higher, and occurs at a lower value of I, than for the corresponding cold bleed case. Base burning with hydrogen results in even higher base pressures than with hot bleed.[9] Base bleed with fuel-rich solid combustion[11] has been shown to be even more effective. The advantage of combustion and burning over hot gas injection is suspected to be due to the different mechanisms and locations of enthalpy release in the wake. Investigation of the combined effects of boattailing and base bleed[12] showed that although the two effects were additive, there was a very weak dependence of optimum boattail angle on bleed rate, and of optimum bleed rate on boattail angle.

While the effectiveness of base bleed as a drag-reducing technique is well known, the details of the fluid-dynamic interactions caused by base bleed are not clearly understood. Most of the above experimental investigations were carried out prior to the development of reliable nonintrusive diagnostic methods, and their scope was primarily limited to determining the global influence of various base-bleed parameters on base pressure. Some results from earlier studies are also unreliable due to possible interference arising from model support effects[3,6] or nozzle flow nonuniformity. In addition, the results of some of the previous investigations of base bleed have been confounded by the added influences of boattailing, hot gas injection, and/or base burning. A clear understanding of the base-bleed phenomenon is hampered by a lack of detailed flowfield data.

Analytical models based on an empirical component-type approach[13] provide some insight into the physical processes that might be associated with base bleed. Although these models can only represent the base-bleed flowfield in a time-mean sense, and cannot account for its instantaneous turbulent nature, they have been fairly successful in predicting the qualitative effects of base bleed on base pressure.[14-17] Base-bleed computations[18-22] using the Reynolds-averaged Navier–Stokes equations have also been successful in predicting qualitative base pressure trends and in capturing flowfield structure details. Numerical techniques are currently limited by turbulence modeling issues, insufficient grid resolution, and lack of detailed experimental data for validation.[23]

Recent experimental efforts have provided insight into the complex interactions prevalent in the near-wake flowfields of blunt-based[1] and boattailed[2] afterbodies; however, no known detailed measurements of the base-bleed flowfield have been made to date. The objectives of the present research are to investigate the effects of base bleed on the near-wake flowfield of a cylindrical afterbody in supersonic flow, and to identify the dominant fluid-dynamic mechanisms inherent in this complex flow with the aid of laser-based optical diagnostic techniques. The measurements obtained provide a set of benchmark baseline data that will enhance the overall understanding of base flow phenomena and also serve to validate modeling and computational efforts in this field.

Experimental Facilities and Equipment

Figure 2 is a schematic of the supersonic, blowdown-type wind tunnel at the University of Illinois Gas Dynamics Laboratory designed solely for the study of axisymmetric base flows. High-pressure air from a tank farm enters the top of the stagnation chamber and passes through a screen–honeycomb–screen flow-conditioning module. The air is expanded to a design Mach number of 2.5 in the test section using a converging–diverging nozzle. The pressure and temperature in the stagnation chamber are 471 ± 3.5 kPa and 300 ± 2 K, respectively, for these experiments. Two square glass side windows provide optical access to the flowfield. The air in the test section exits through a conical diffuser and exhaust duct to the atmosphere. The afterbody is mounted at the end of a hollow sting, which is supported at two axial locations upstream of the nozzle to avoid support disturbances in the flowfield. A detailed description of the wind-tunnel design is provided in Ref. 24.

For the purposes of the base-bleed study, several additions were made to the existing wind tunnel. A stainless steel bleed line was designed and constructed with 50.8-mm-diam pipe sections to facilitate conditioning, measurement, and control of the bleed flow. Since the base pressure is significantly subatmospheric, ambient room air at 293 ± 2 K is an adequate source for the bleed air supply. The inlet consists of a screen followed by an elliptically rounded intake section to condition the incoming bleed flow. This is followed by about 1.3 m of pipe to ensure adequate flow development prior to the mass flowmeter. The electronic flowmeter consists of a temperature and a velocity probe and works on the hot-wire principle. The linearized output is directly proportional to the actual mass flow rate, and is unaffected by pressure and temperature fluctuations in
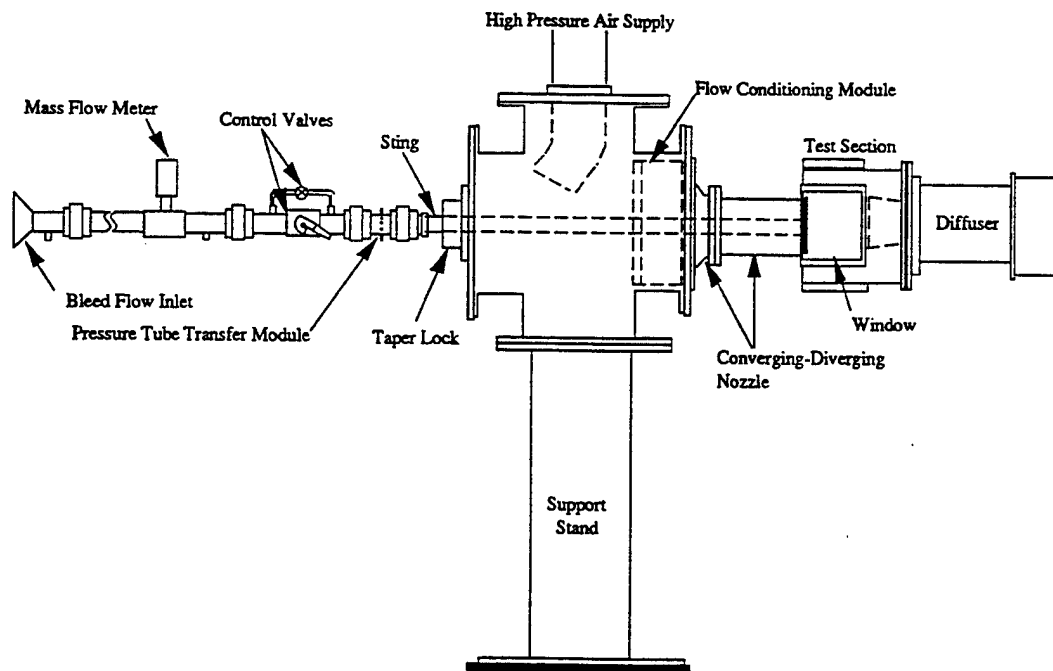
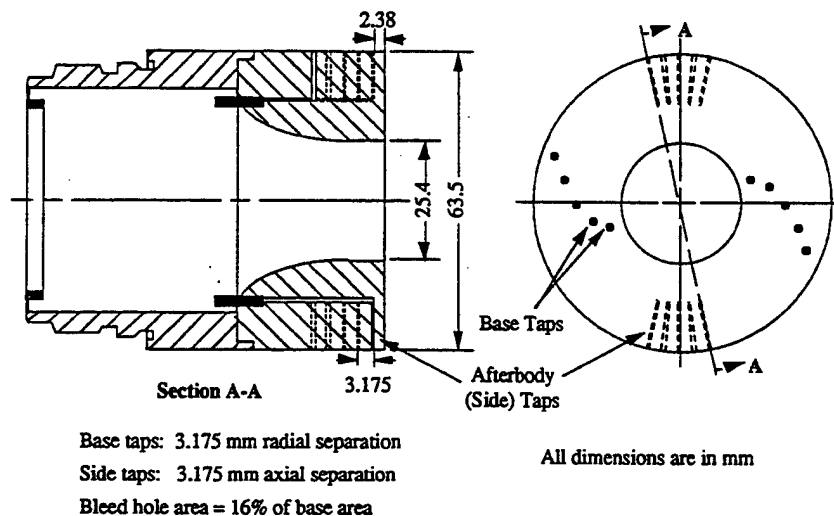Fig. 2   Axisymmetric wind-tunnel and base-bleed facility.

Base taps: 3.175 mm radial separation
Side taps: 3.175 mm axial separation
Bleed hole area = 16% of base area

All dimensions are in mm

Fig. 3   Location of static pressure taps on base-bleed afterbody.

the supply air. The flowmeter is followed by a butterball valve for coarse bleed flow control mounted in parallel with a needle valve for fine control.

A schematic of the afterbody used in the base-bleed studies is shown in Fig. 3. The 63.5-mm-diam cylindrical afterbody contains a 0.4 caliber bleed orifice, which is preceded by an elliptically contoured section based on ASME long-radius nozzle standards[25] to ensure a uniform velocity profile for the bleed flow exiting the base. Ten 0.635-mm-diam static pressure taps on the base plane are used to measure the radial distribution of the base pressure. Two sets of five taps each along the sting side surface, located diametrically opposite to each other, are used to measure the approach pressure distribution upstream of the base. The taps in each set are staggered along the periphery to prevent interference waves from the upstream taps affecting the measurements of the taps downstream. Static pressure measurements are obtained using a digital pressure transmitter controlled by a desktop computer via a serial interface. A removable retaining ring confines the pressure tubing near the inner wall of the afterbody in the region upstream of the bleed exit orifice to minimize disturbances in the bleed flow.

The two-component laser Doppler velocimetry (LDV) system used for this investigation uses the green (514.5 nm) and blue

(488 nm) lines of a 5-W argon-ion laser. The nominal blue and green fringe spacings are 10.3 and 11.3 μm, respectively. The measurement volume diameter is 120 μm. Upstream frequency shifting of 40 MHz is used to discriminate flow direction and reduce fringe biasing, and the beam pairs are oriented at ± 45 deg to the mean-flow direction to minimize fringe blindness. The receiving optics collect light scattered by particles crossing the measurement volume in 20-deg-off-axis forward scatter mode (effective length of measurement volume 730 μm). The scattered light intensity is converted to an analog voltage signal by photomultiplier tubes and fed to a digital burst correlator to extract frequency, and hence, velocity information. Three sets of stepper motors, encoders, and drives operate in a closed loop with a desktop computer to provide translation of the optical table in all three directions. A six-jet atomizer containing 50-cP silicone oil provides seed particles (nominal diameter 0.8 μm) to four seed tubes through a manifold and system of regulating valves. Three seed tubes for the freestream flow, arranged 120 deg apart circumferentially, are located just downstream of the flow-conditioning module. The seed tube for the bleed flow is located in the bleed line, just downstream of the butterball valve. A detailed description of the LDV system, including an error analysis, has been provided in Ref. 24. The worst-case rms error due

to particle lag just downstream of separation has been estimated at 6%. This error is 1.7% one base radius downstream of the base plane, and continues to diminish further downstream. The estimated worst-case uncertainty is 1.2% of U_1 in the mean velocity, and 2.3% of U_1 in the rms velocity fluctuation measurements.

Results and Discussion

Pressure Measurements

Static pressure distributions along the afterbody and on the base plane were obtained for ten bleed rates ranging from $I = 0$ to $I = 0.032$. The axial pressure distribution of the approach flow along the afterbody was independent of the bleed rate. The approach static pressure was also nearly constant in the streamwise direction at $P/P_0 = 0.061 \pm 0.001$, yielding an isentropic Mach number of 2.47. A slight rise in pressure approaching the base corner was consistent on both sets of diametrically opposed pressure taps, and was most probably due to weak waves originating at the wind-tunnel nozzle throat interacting with the boundary layer on the sting near the base plane.

The radial distribution of base pressure ratio is shown in Fig. 4 for all ten bleed flowrates. At any given bleed rate, the base pressure ratio profile is radially symmetric across the base annulus and fairly independent of radial location, except for a slight increase near the base corner in some cases. This slight increase in base pressure is probably due to the sharp change in flow direction during entrainment of the low-speed flow by the high-speed shear layer near the base corner. It is also evident that the base pressure ratio initially increases with bleed rate (solid-symbol cases), peaks at around $I = 0.0148$, and then decreases rapidly as the bleed rate is increased further (open-symbol cases). This behavior is more clearly seen when the average base pressure ratio, based on the area-weighted average of each profile, is plotted as a function of the injection parameter (Fig. 5). Data from the blunt base and the 5-deg boattailed afterbody results[1,2] are also presented in this plot. The peak average base pressure ratio of $P_b/P_1 = 0.669$ at $I = 0.0148$ is 18.5% higher
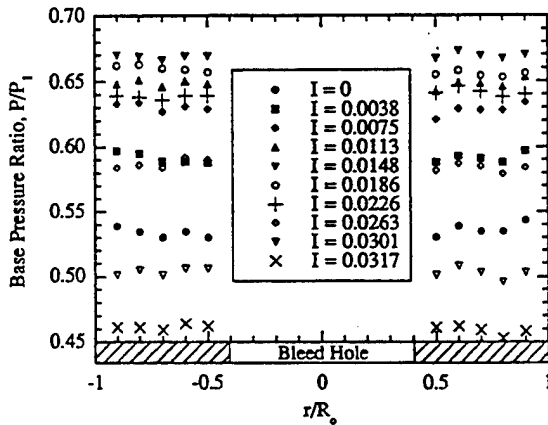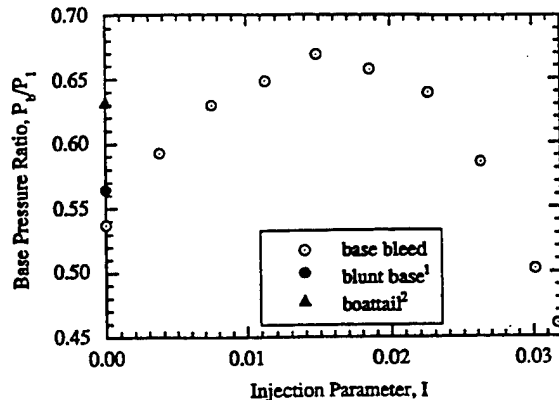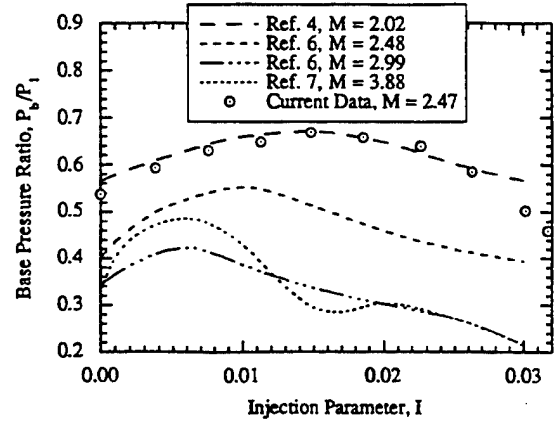

Fig. 6 Comparison of base-bleed results with other experiments (bleed orifice diameter ratio $d_j/d_b = 0.4$).

than the average base pressure ratio of the blunt-based cylinder and 5.7% higher than that of the boattailed afterbody. The difference in the average base pressure ratio between the blunt base[1] and the $I = 0$ no-bleed case is discussed later.

As seen in Fig. 6, the peak in the average base pressure ratio at $I = 0.0148$ is consistent with earlier experiments.[4,6,7] All of these data were obtained with bleed orifices of 0.4 caliber. There are, however, significant differences in the magnitudes of the base pressure curves. In spite of operating at nearly the same Mach number, the base pressure ratios of Ref. 6 are noticeably lower than those of the current study, possibly because of interference from the struts that were used to support their model. On the other hand, data[4] at Mach 2 are very similar to the current data. The difference in the bleed nozzle contours used in the two models could be responsible for the similarity of these data sets at different Mach numbers. The model used in the current study (and by Ref. 7) employs a contoured converging nozzle, whereas the orifice used in Ref. 4 was preceded by a 5-deg conical Mach 2.0 nozzle, similar to the one used in the study of Ref. 6. In addition, a thick boundary layer has a base-pressure-enhancing effect similar to that of base bleed. Differences in the approach boundary-layer thicknesses of the different experiments could therefore also contribute to the discrepancies discussed above. Although the second peak in base pressure in Ref. 7 is attributed to the converging nozzle preceding the bleed orifice, no secondary peak was observed in the current investigation. In view of the lower Mach number used in the present study, it is possible that the secondary peak could occur at a bleed rate higher than the range of the flowmeter.

Flow Visualization

Spark–schlieren photographs and shadowgraphs, obtained with a standard Z-type two-mirror configuration and a 1.4-μs micropulser light source, were used to confirm interference-free operation and to obtain qualitative information on the effect of base bleed on the near-wake flowfield. Schlieren photographs using a horizontal knife-edge at five different bleed rates are shown in Fig. 7. The absence of any strong interference waves emanating from the nozzle-exit/test-section junction confirms interference-free flow conditions in the test section at all of these bleed flow rates. At zero bleed, a strong recompression shock system is evident near the rear stagnation point. As expected, the shear-layer angle becomes flatter, the base corner expansion weakens, the wake widens, and the recompression shocks become weaker as the bleed flow rate is increased from zero to $I = 0.0033$. The recompression shock system seems to weaken considerably near $I = 0.0131$, when the bleed flow presumably provides most of the fluid required for shear-layer entrainment. As the bleed rate is increased further to $I = 0.0199$, the recompression shock system reappears slightly upstream of its earlier location. When the bleed exit velocity approaches sonic conditions at around $I = 0.0279$, the Mach disk emanating from the bleed orifice interacts with the oblique recompression shocks from the outer flow and forms a fairly complex shock system. This shock system also
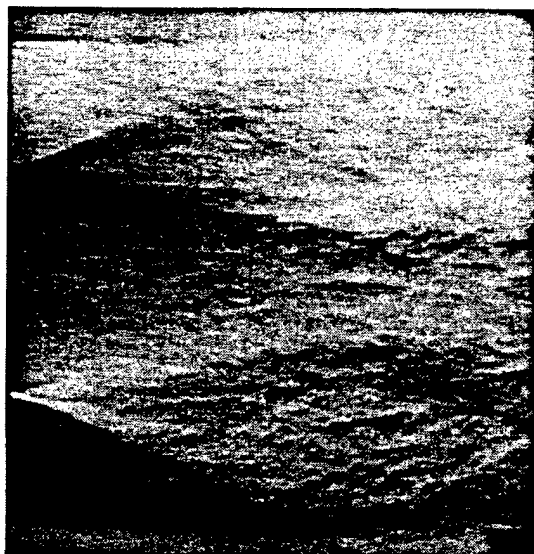

Fig. 4 Effect of base bleed on base pressure distribution.

Fig. 5 Effect of base bleed on area-averaged base pressure ratio.
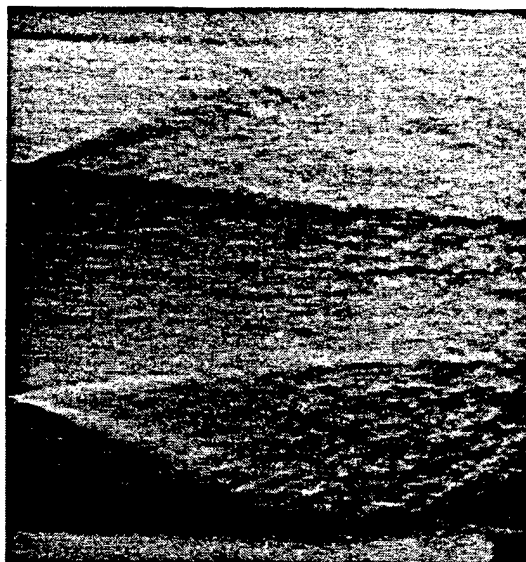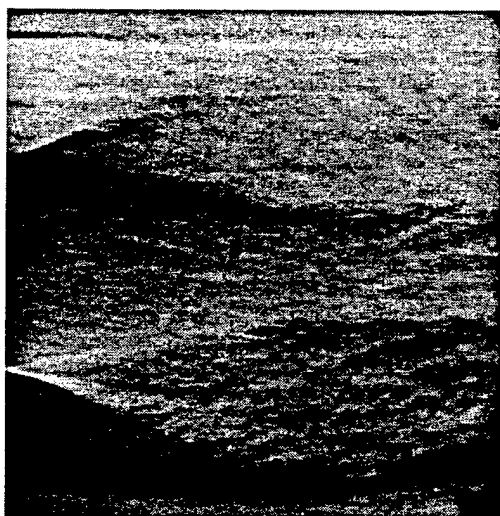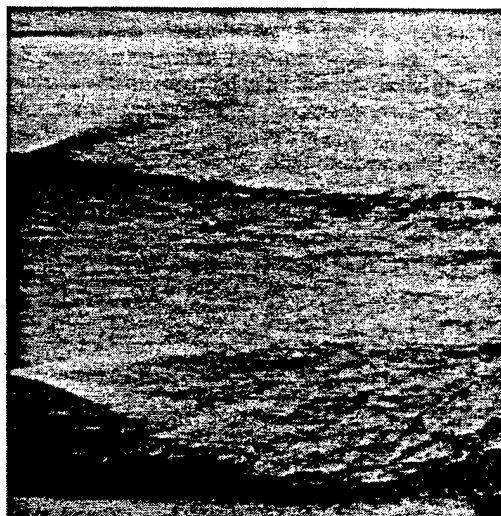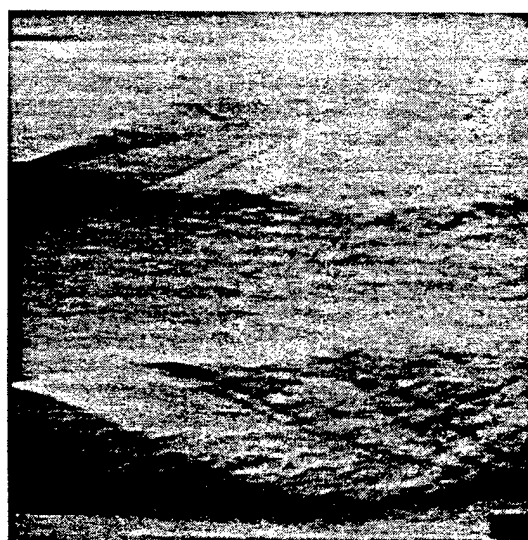
a) $I = 0$

b) $I = 0.0033$

c) $I = 0.0131$

d) $I = 0.0199$

e) $I = 0.0279$

Fig. 7   Schlieren photographs of the base flowfield at different bleed flow rates.

appears to be highly unsteady, as indicated by imaging the flowfield on a screen and by visual inspection of a series of photographs at this bleed rate. The horizontal knife-edge makes it difficult to discern the vertical Mach disk in the schlieren photographs; however, it is clearly visible in shadowgraphs taken at the high bleed rate. The axisymmetric nature of the flow also causes smearing of the flow features due to line-of-sight integration effects.

A parametric study of the mean axial velocity and turbulence quantities along the centerline has been performed using LDV. The approach flowfield and boundary layer and the flow conditions at the exit of the bleed jet have also been documented for the five bleed cases studied. Care was taken to match data rates at the freestream and bleed flow nozzle exits, in an effort to minimize particle concentration bias errors. Post-facto corrections for velocity bias were made using the interarrival time weighting method, which has been shown[26] to be the most reliable technique for high-speed separated flows.

The freestream approach flow was found to be uniform and independent of the bleed rate. The mean freestream approach velocity was found to be 574 m/s with 0.3% variation between the different bleed cases. The mean Mach number based on adiabatic expansion from the tunnel stagnation temperature to the freestream velocity was 2.45, in close agreement with the isentropic value of 2.47 based on pressure measurements. The unit Reynolds number was calculated to be 45×10^6 m^{-1} at the nozzle exit. Approach boundary-layer mean velocity profiles for all bleed cases were similar, as seen in Fig. 8. Curve fits[27] of these profiles were used to determine boundary-layer parameters such as integral thicknesses and skin-friction coefficient. These results (mean values and percentage variations over the five bleed cases) are presented in Table 1. The thicknesses and the friction velocity have been normalized by the afterbody radius and the freestream velocity, respectively. Rather large variations in the computed parameters (between the different bleed cases) are due to the sensitivity of the curve fit to accurate y-position determination (limited to ±0.1 mm due to hysteresis of the traverse table). The axial turbulence intensity and Reynolds shear stress distributions in the boundary layer collapse very well for the different bleed rates, as seen in Figs. 9 and 10. As expected, the magnitudes of these quantities are high in the boundary layer, dropping rapidly to low values in the freestream.

Radial traverses performed 1.5 mm downstream of the bleed exit plane show uniform velocity distributions in the bleed flow, as seen

Fig. 9 Streamwise turbulence intensity distributions in approach boundary layer.

Fig. 10 Reynolds shear stress distributions in approach boundary layer.
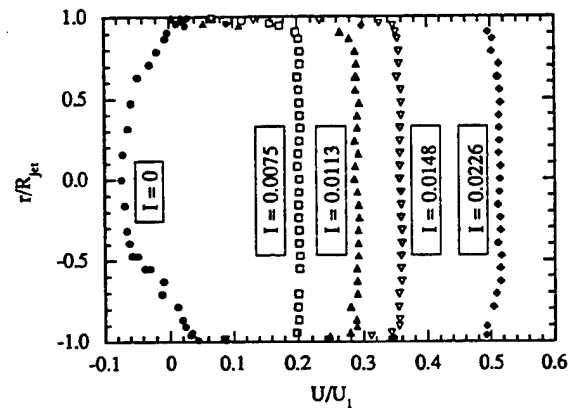
Fig. 11 Mean axial velocity distributions at bleed orifice exit (x/R_{jet} = 0.118; R_{jet}/R_0 = 0.4).

in Fig. 11. The effect of the compliant (open) boundary presented by the bleed hole can be seen for the bleed-off case. There is a mean inflow into the base along the centerline, and a mean outflow along the periphery of the bleed orifice. Bimodal velocity histograms were observed at all radial locations for the no-bleed case, indicating large-scale turbulence interaction between the recirculation region and the long passive cavity presented by the bleed hole and the hollow sting. The 5% difference in the average base pressure ratio between the blunt base[1] and the $I = 0$ case (Fig. 5) could be due to this compliant boundary effect.

The effect of base bleed on the mean axial velocity distribution along the centerline can be seen in Fig. 12. In all cases, the measured radial velocity component was less than 2% of U_1, and the Reynolds shear stresses were nearly zero, confirming that the LDV measurement volume was located at the centerline of the flowfield. For the no-bleed case, the peak reverse velocity (30% of U_1) and

Table 1 Approach boundary-layer properties

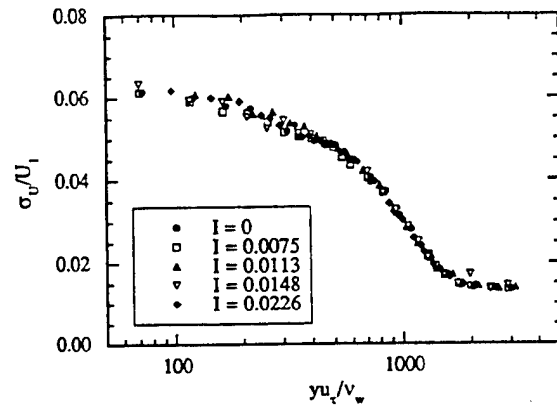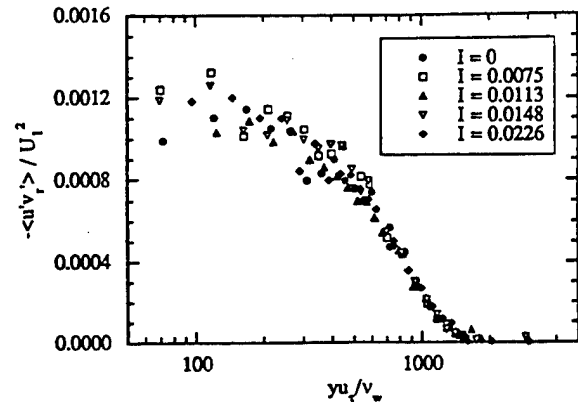|	
δ/R_0	0.102 ± 1.6%
δ^*/R_0	0.0241 ± 6.8%
θ/R_0	0.00682 ± 6.0%
H	3.53 ± 1.1%
Π	0.768 ± 17%
C_f	0.00170 ± 4.7%
u_τ/U_1	0.0414 ± 2.3%

Fig. 8 Approach boundary-layer mean velocity profiles (x/R_0 = −0.157).

Fig. 12 Mean axial velocities along the centerline.
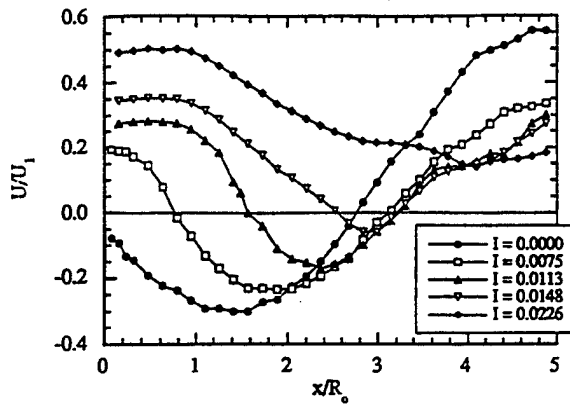
Fig. 14 Radial turbulence intensities along the centerline.

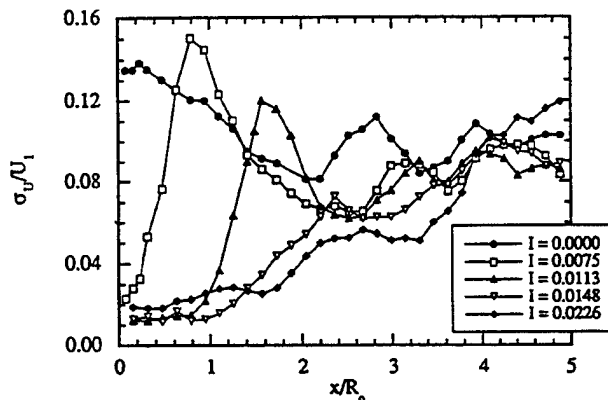Fig. 13 Axial turbulence intensities along the centerline.

Fig. 15 Turbulent kinetic energy distributions along the centerline.

the rear stagnation point occur 1.5 and 2.8 base radii downstream of the base, respectively. These results are nearly identical to measurements done with a blunt base.[1] At the base plane ($x = 0$), however, the extrapolated axial velocity is nonzero and negative, due to the compliant-boundary effect discussed above. As the bleed rate is increased, the bleed jet exit velocity increases, causing a downstream shift of the forward stagnation point where the bleed flow and reverse flow meet. This downstream shift of the forward stagnation point with increasing bleed rate has the effect of diminishing the size of the recirculation region, since the rear stagnation point location is nearly constant at $x/R_0 = 3.2$ (note that this position for the bleed-on cases is shifted relative to the bleed-off case). The peak reverse velocity location occurs progressively downstream, and its magnitude decreases with increasing bleed. At $I = 0.0148$, the optimum bleed rate from a base pressure viewpoint, the recirculation region along the centerline almost disappears. No reverse velocity is detected along the centerline for the $I = 0.0226$ case, indicating penetration of the bleed jet into the reattachment zone. The velocity profiles for the bleed-on cases become similar for $x/R_0 > 3$, the wake redevelopment region.

Figures 13 and 14 present the axial and radial turbulence intensity distributions along the centerline. For each bleed case (except $I = 0.0226$), two peaks are observed in the distribution of turbulence intensity. The first peak occurs at the forward stagnation point because of the change in flow direction from axial to radial when the bleed flow meets the reverse flow in the recirculation region. The magnitude of this peak is seen to decrease with increasing bleed rate, because of the smaller influence of the diminishing recirculation region. The second peak occurs at the rear stagnation point due to reattachment phenomena. The influence of the flow mechanisms occurring at both stagnation points is much stronger in the axial direction. Consequently, the peaks in the radial turbulence intensity distributions are not as pronounced as the axial intensity peaks. At the higher bleed rates, the bleed flow penetrates further into the wake, accounting for the low centerline turbulence intensities seen in Figs. 13 and 14 for these cases. Anisotropy of the turbulent normal
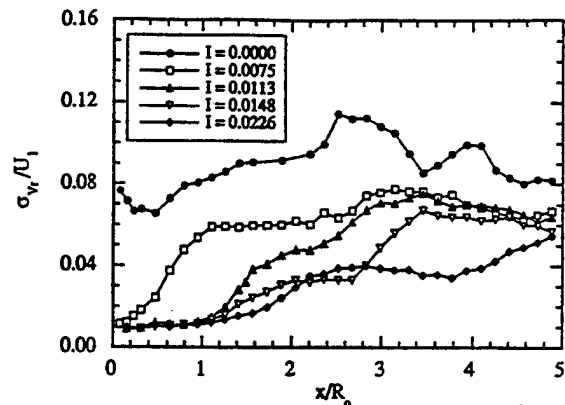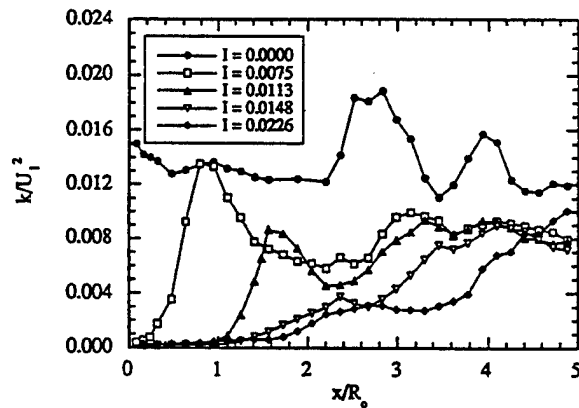
stress along the centerline is also evident from the differences in the axial and radial turbulence intensity profiles. Figure 15 shows the centerline distribution of turbulent kinetic energy, calculated using

$$k = 0.5\left(\sigma_U^2 + 2\sigma_{Vr}^2\right) \qquad (1)$$

The occurrence of the peak energy magnitudes at the stagnation points, and likewise the decreasing energy levels with increasing bleed rate, are similar to those discussed for the turbulence intensity distributions.

Conclusions

An experimental investigation has been conducted to study the effects of base bleed on the near-wake flowfield of a cylindrical afterbody in supersonic flow. Data have been obtained using static pressure measurements, schlieren and shadowgraph photography, and LDV traverses along the centerline. Results indicate nearly uniform radial pressure profiles across the base plane. With increasing bleed flow rate, the average base pressure is found to increase initially, attain a peak value, and then decrease with further increase in the injection parameter, I. The approach flowfield upstream of separation is unaffected by the bleed rate. An increase in the bleed rate is accompanied by the diminishing size and intensity of the recirculation region (due to the downstream displacement of the forward stagnation point) and a decrease in the peak axial and radial turbulence intensities at the forward stagnation point. Near the optimum bleed rate of $I = 0.0148$, the base pressure is maximized, and the flowfield is characterized by the widening of the wake, flattening of the shear-layer angle, and the near-disappearance of reverse velocity along the centerline.

Acknowledgment

References

[1] Herrin, J. L., and Dutton, J. C., "Supersonic Base Flow Experiments in the Near Wake of a Cylindrical Afterbody," *AIAA Journal*, Vol. 32, No. 1, 1994, pp. 77–83.

[2] Herrin, J. L., and Dutton, J. C., "Supersonic Near-Wake Afterbody Boat-tailing Effects on Axisymmetric Bodies," *Journal of Spacecraft and Rockets*, Vol. 31, No. 6, 1994, pp. 1021–1028.

[3] Corrright, E. M., and Schroeder, A. H., "Preliminary Investigation of Effectiveness of Base Bleed in Reducing Drag of Blunt-Base Bodies in Supersonic Stream," NACA RM E51A26, March 1951.

[4] Reid, J., and Hastings, R. C., "The Effect of a Central Jet on the Base Pressure of a Cylindrical Afterbody in a Supersonic Stream," Aeronautical Research Council (Great Britain), Reports and Memoranda No. 3224, Dec. 1959.

[5] Badrinarayanan, M. A., "An Experimental Investigation of Base Flows at Supersonic Speeds," *Journal of the Royal Aeronautical Society*, Vol. 65, 1961, pp. 475–482.

[6] Bowman, J. E., and Clayden, W. A., "Cylindrical Afterbodies in Supersonic Flow with Gas Ejection," *AIAA Journal*, Vol. 5, No. 6, 1967, pp. 1524, 1525.

[7] Valentine, D. T., and Przirembel, C. E. G., "Turbulent Axisymmetric Near-Wake at Mach Four with Base Injection," *AIAA Journal*, Vol. 8, No. 12, 1970, pp. 2279, 2280.

[8] Zakkay, V., and Sinha, R., "An Experimental Investigation of the Near Wake in an Axisymmetric Supersonic Flow with and without Base Injection," *Israel Journal of Technology*, Vol. 7, No. 1–2, 1969, pp. 43–53.

[9] Hubbartt, J. E., Strahle, W. C., and Neale, D. H., "Mach 3 Hydrogen External/Base Burning," *AIAA Journal*, Vol. 19, No. 6, 1981, pp. 745–749.

[10] Clayden, W. A., and Bowman, J. E., "Cylindrical Afterbodies at $M = 2$ with Hot Gas Ejection," *AIAA Journal*, Vol. 6, No. 12, 1968, pp. 2429–2431.

[11] Ding, Z., Chen, S., Liu, Y., Luo, R., and Li, J., "Wind Tunnel Study of Aerodynamic Characteristics of Base Combustion," *Journal of Propulsion and Power*, Vol. 8, No. 3, 1992, pp. 630–634.

[12] Bowman, J. E., and Clayden, W. A., "Boat-Tailed Afterbodies at $M = 2$ with Gas Ejection," *AIAA Journal*, Vol. 6, No. 10, 1968, pp. 2029, 2030.

[13] Korst, H. H., "A Theory for Base Pressures in Transonic and Supersonic Flows," *Journal of Applied Mechanics*, Vol. 23, No. 4, 1956, pp. 593–600.

[14] Korst, H. H., Page, R. H., and Childs, M. E., "A Theory for Base Pressures in Transonic and Supersonic Flow," Engineering Experiment Station, Mechanical Engineering Dept., Univ. of Illinois, ME TN 392-2, March 1955.

[15] Korst, H. H., Chow, W. L., and Zumwalt, G. W., "Research on Transonic and Supersonic Flow of a Real Fluid at Abrupt Increases in Cross Section (with Special Consideration of Base Drag Problems)," Engineering Experiment Station, Mechanical Engineering Dept., Univ. of Illinois, ME TR 392-5, Oct. 1964.

[16] Reijasse, P., Benay, R., Delery, J. M., and Lacau, R. G., "Missile and Projectile Base-Flow Prediction by Multi-Component Methods," AIAA TP 1988-90, Aug. 1988.

[17] Reijasse, P., Benay, R., Delery, J., and Lacau, R. G., "Prediction of Powered Missile or Projectile Base Flows by Multicomponent Methods," *La Recherche Aerospatiale*, Vol. 1989-4, 1989, pp. 15–32.

[18] Sahu, J., Nietubicz, C. J., and Steger, J. L., "Navier–Stokes Computations of Projectile Base Flow with and without Mass Injection," *AIAA Journal*, Vol. 23, No. 9, 1985, pp. 1348–1355.

[19] Sahu, J., "Supersonic Flow over Cylindrical Afterbodies with Base Bleed," AIAA Paper 86-0487, Jan. 1986.

[20] Danberg, J. E., and Nietubicz, C. J., "Predicted Flight Performance of Base Bleed Projectiles," AIAA Paper 90-2069, July 1990.

[21] Nietubicz, C. J., and Sahu, J., "Navier–Stokes Computations of Base Bleed Projectiles," *Base Bleed: First International Symposium on Special Topics in Chemical Propulsion*, edited by K. K. Kuo and J. N. Fleming, Hemisphere, New York, 1991, pp. 93–106.

[22] Nietubicz, C. J., and Gibeling, H. J., "Navier–Stokes Computations for a Reacting, M864 Base Bleed Projectile," AIAA Paper 93-0504, Jan. 1993.

[23] Dutton, J. C., Herrin, J. L., Molezzi, M. J., Mathur, T., and Smith, K. M., "Recent Progress on High-Speed Separated Base Flows," AIAA Paper 95-0472, Jan. 1995.

[24] Herrin, J. L., "An Experimental Investigation of Supersonic Axisymmetric Base Flow Including the Effects of Afterbody Boattailing," Ph.D. Thesis, Univ. of Illinois at Urbana–Champaign, Urbana, IL, July 1993.

[25] Bean, H. S. (ed.), *Fluid Meters—Their Theory and Application*, 6th ed., Report of the ASME Research Committee on Fluid Meters, American Society of Mechanical Engineers, 1971, pp. 216–220.

[26] Herrin, J. L., and Dutton, J. C., "An Investigation of LDV Velocity Bias Correction Techniques for High-Speed Separated Flows," *Experiments in Fluids*, Vol. 15, 1993, pp. 354–363.

[27] Sun, C. C., and Childs, M. E., "A Modified Wall Wake Velocity Profile for Turbulent Compressible Boundary Layers," *Journal of Aircraft*, Vol. 10, No. 6, 1973, pp. 381–383.

APPENDIX A.7

VELOCITY AND TURBULENCE MEASUREMENTS IN A SUPERSONIC BASE FLOW WITH MASS BLEED

by

T. Mathur and J. C. Dutton

Velocity and Turbulence Measurements in a Supersonic Base Flow with Mass Bleed

Tarun Mathur* and J. Craig Dutton†

University of Illinois at Urbana–Champaign, Urbana, Illinois 61801

Two-component laser Doppler velocimetry was used to obtain detailed mean velocity and turbulence measurements in the near wake of a cylindrical afterbody with base bleed in a Mach 2.5 flow. The bleed flow provides at least some of the fluid required for shear layer entrainment and shields the base annulus from the outer shear layer and the primary recirculation region, leading to an increase in base pressure. There is an overall reduction in turbulence levels throughout the base bleed flowfields relative to the near-wake flowfields of blunt-based and boattailed afterbodies. With increasing bleed, the formation of a strong bleed jet shear layer and secondary recirculation region near the base annulus offsets the benefits of base bleed, leading to a drop in the base pressure. The net benefits of base bleed are maximized at the optimum bleed condition, which corresponds to the highest base pressure, the disappearance of the primary recirculation region, and the lowest turbulence levels in the near-wake flowfield. Increased benefits from base bleed could be achieved by injecting the bleed fluid at the lowest possible velocity through the use of larger bleed orifices, porous bases, or bleed orifices located along the outer base annulus.

Nomenclature

A_b	= base area, πR_o^2
I	= injection parameter, $(\dot{m}_{\text{bleed}}/\rho_1 U_1 A_b)$
k	= turbulent kinetic energy, m^2/s^2
M	= Mach number
$\dot{m}_{\text{bleed}}$	= bleed mass flow rate, kg/s
P	= pressure, kPa
R_{jet}	= bleed jet radius, mm
R_o	= afterbody radius, mm
r	= radial coordinate, mm
S	= stagnation point (location of $U = 0$ along the axis of symmetry)
T_o	= wind-tunnel stagnation temperature, K
U	= mean axial velocity, m/s
U_1	= freestream approach velocity, m/s
u'	= instantaneous axial velocity fluctuation, m/s
V_r	= mean radial velocity, m/s
V_t	= mean tangential velocity, m/s
v_r'	= instantaneous radial velocity fluctuation, m/s
v_t'	= instantaneous tangential velocity fluctuation, m/s
x	= axial (streamwise) position relative to the base plane, mm
ρ	= density, kg/m^3
σ_U	= axial rms velocity fluctuation, m/s
σ_{V_r}	= radial rms velocity fluctuation, m/s
σ_{V_t}	= tangential rms velocity fluctuation, m/s
$\langle \rangle$	= ensemble-averaged value

Subscripts

b	= base
f	= forward
r	= radial component or rear
t	= tangential (swirl) component
0	= stagnation or afterbody
1	= freestream approach conditions

Introduction

AERODYNAMIC vehicles such as missiles, rockets, and projectiles suffer significant base drag as a result of flow separation at the base corner and the formation of a low-pressure, low-speed recirculation region near the base. Because of a lack of understanding of the fluid dynamic interactions occurring in the near-wake base region, drag-reducing techniques such as boattailing, base burning, and base bleed have traditionally been applied in an empirical manner to improve flight performance. The advent of laser-based optical flow diagnostic techniques in recent years has provided nonintrusive means to gain deeper insight into these complex flowfields. The first known study of base flows using these techniques was performed on cylindrical, boattailed, and flared afterbodies with supersonic central jets in a Mach 0.85 freestream.[1] A detailed investigation of supersonic axisymmetric base flows including the effects of afterbody boattailing was completed recently,[2,3] and a study of the effects of base bleed has been initiated by the present authors as a logical extension.[4]

Figure 1 is a schematic of a blunt cylindrical body with base bleed, aligned in a supersonic flow. The supersonic freestream flow expands at the base corner and the turbulent boundary layer separates and forms a free shear layer that eventually undergoes recompression, realignment, and redevelopment in the wake of the afterbody. The primary recirculation region (PRR) is formed as the fluid from the region adjacent to the base is entrained and accelerated by the outer shear layer and subsequently returned to the base region by a recompression shock system. With base bleed, low-speed fluid is introduced into the base region causing a downstream displacement of the PRR and the appearance of a forward stagnation point whose location depends on the relative strengths of the bleed jet and the recirculating fluid. The nondimensional injection parameter I,
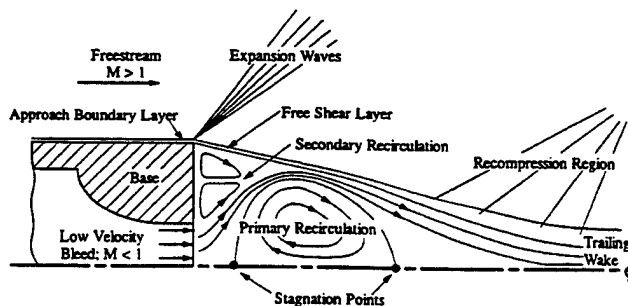

Fig. 1 Schematic of the near-wake flowfield with base bleed.

defined as the bleed mass flow rate normalized by the product of the freestream mass flux and base area, is used to quantify the base bleed in the current study and in most other experimental studies. Unlike the generalized injection coefficient,[5] the injection parameter I does not account for the approach boundary-layer thickness and the bleed flow momentum, both of which have been theorized to affect the base pressure in a manner analogous to base bleed.

Experiments performed by several researchers[6–10] to study the effect of bleed mass flow rate on the base pressure ratio (P_b/P_1) exhibit certain common characteristics and indicate three distinct operating regimes based on the quantity of bleed fluid injected. At low values of I (regime 1), the base pressure ratio increases fairly linearly with bleed rate. A peak in the base pressure ratio is observed at an intermediate value of I (near $I = 0.01$ for air). Increases in base pressure ratio (relative to the no-bleed case) from 10 to 90% have been reported for the optimum bleed condition, which depends on factors such as the freestream Mach number and the size and geometry of the bleed orifice. Past the optimum value (regime 2), the base pressure ratio decreases with increasing bleed rate until it reaches a relative minimum. Further increase in the bleed flow leads to an increase in base pressure ratio (regime 3) due to the onset of power-on flow conditions.

Over the past few decades, the effects on base pressure ratio of other bleed parameters such as the bleed jet exit area,[6,7,9–11] bleed gas molecular weight[11,12] (relative to the freestream gas), and bleed gas temperature[13] have also been investigated. Key results from these investigations have been summarized in Ref. 4. Most of the preceding experimental investigations were carried out before the development of reliable nonintrusive diagnostic methods, and their scope was primarily limited to determining the global influence of various bleed parameters on base pressure. Therefore, although the effectiveness of base bleed as a drag-reducing technique is well known, the details of the fluid dynamic interactions caused by base bleed are not clearly understood because of a lack of detailed flow-field data.

Analytical models based on an empirical component-type approach[14] have been fairly successful in predicting the qualitative effects of mass bleed on base pressure.[15,16] One of the drawbacks of these models is that they only represent the base bleed flow-field in a time-mean sense and cannot account for its instantaneous turbulent nature. Computations of the base bleed flowfield[17–22] using the Reynolds-averaged Navier–Stokes (RANS) equations have also had some degree of success in predicting both qualitative and quantitative base pressure trends and in capturing flowfield structure details. Of particular interest are the recent RANS predictions of Sahu and Heavey[22] for the same geometry and flow conditions presented here. Their computations of base pressure distributions agreed very well with the current experiments, although agreement between predictions and measurements for some mean velocity and especially turbulence quantities was not so favorable. In general, numerical predictions are currently limited by turbulence modeling issues, such as compressibility and streamline curvature effects, as well as insufficient grid resolution and lack of detailed experimental data for validation.[23]

As shown in Fig. 2, earlier experiments with base bleed by the current authors[4] have confirmed the base pressure ratio variation with bleed mass flow rate (as discussed earlier) in regimes 1 and 2, indicating a peak base pressure ratio at an injection parameter value of $I = 0.0148$. The peak area-averaged base pressure ratio at this
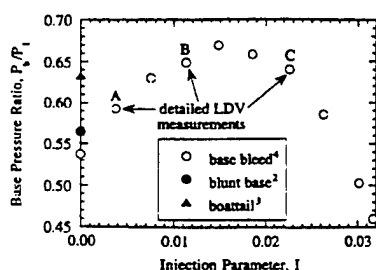
optimum bleed rate was 18.5% higher than the average base pressure ratio of a blunt-based afterbody.[2] Qualitative flowfield features such as flattening of the shear layer angle, widening of the wake, and weakening of the base corner expansion with increasing bleed rate in regime 1 were confirmed using schlieren and shadowgraph photography. Axial traverses along the near-wake centerline using two-component laser Doppler velocimetry (LDV) at several bleed rates show the PRR decreasing in size with increasing bleed rate and nearly disappearing at the optimum bleed rate. Peaks in the turbulent kinetic energy (and the individual axial and radial turbulence intensities) were observed at the forward and rear stagnation point locations along the centerline, with the magnitudes of the peaks decreasing with increasing bleed rate.

The primary objectives of the research presented here are to obtain detailed mean velocity and turbulence field data in the entire near-wake region of a cylindrical afterbody with base bleed in supersonic flow and to identify the dominant fluid dynamic mechanisms inherent in this complex flow. Since no known detailed measurements of the base bleed flowfield have been made prior to these, the measurements described here provide benchmark data that will enhance the overall understanding of base flow phenomena and will also serve to validate modeling and computational efforts in this field.

Experimental Facilities and Procedures

The experiments described were conducted in a supersonic, blowdown-type wind tunnel at the University of Illinois Gas Dynamics Laboratory designed solely for the study of axisymmetric base flows. As shown in Fig. 3, high-pressure air from a tank farm enters the top of the stagnation chamber, passes through a screen-honeycomb-screen flow conditioning module, and expands to supersonic conditions in the test section through an annular converging-diverging nozzle. The air then exits through a conical diffuser, silencing ducts, and a muffler to the atmosphere. Two square side windows provide optical access to the near-wake flowfield. The afterbody model is mounted at the end of a hollow sting, which is supported at two axial locations upstream of the nozzle entrance to avoid support disturbances in the flowfield. The mean Mach number approaching the afterbody is 2.47, the unit Reynolds number is 46 (10^6) m^{-1}, and the freestream turbulence intensity is less than 1%. A detailed description of the wind-tunnel design is provided in Ref. 24. The 63.5-mm-diam cylindrical afterbody contains a 25.4-mm-diam bleed orifice preceded by an elliptically contoured section to ensure a uniform velocity profile for the bleed flow exiting the base. A stainless steel bleed line constructed with 50.8-mm-diam pipe sections, a contoured inlet and screen, an electronic flowmeter, and valves facilitates conditioning, measurement, and control of the bleed flow. Since the base pressure is significantly subatmospheric, ambient air is an adequate source for the bleed air supply. Details of the base bleed afterbody and the bleed line design are provided in Ref. 4

The two-component LDV system used for the current experiments is identical to the setup used in earlier experiments.[4] The nominal fringe spacings are 10.4 and 11.2 μm for the blue and green beams, respectively. The measurement volume diameter and
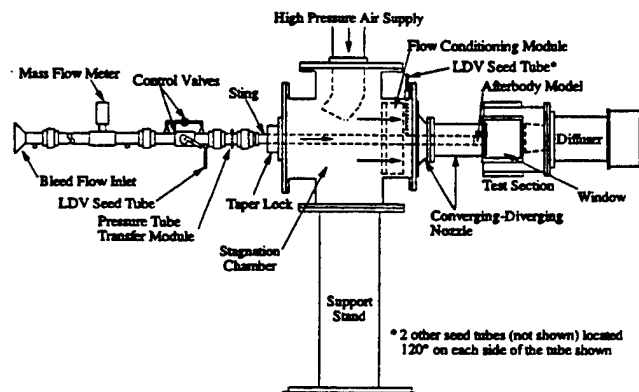

Fig. 2 Effect of base bleed on area-averaged base pressure ratio.

Fig. 3 Axisymmetric wind tunnel and base bleed facility.
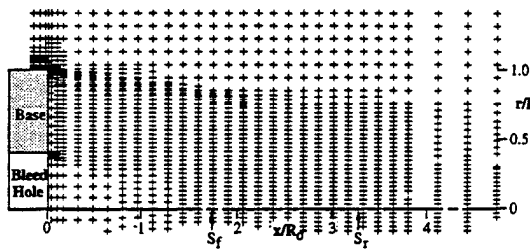
Fig. 4 LDV measurement locations, $I = 0.0113$ (case B).

Table 1 Experimental flow conditions and geometry

Tunnel stagnation pressure P_o, kPa	470 ± 4
Freestream static pressure P_1, kPa	28.7 ± 0.3
Approach Mach number based on pressure data	2.47 ± 0.01
Tunnel stagnation temperature T_o, K	300 ± 2
Approach velocity measured with LDV U_1, m/s	574 ± 3
Approach Mach number based on T_o and U_1	2.46 ± 0.03
Freestream unit Reynolds number, m^{-1}	$46 \pm 1(10^6)$
Bleed flow stagnation temperature $T_{0,bleed}$, K	293 ± 2
Base radius R_o, mm	31.75 ± 0.05
Bleed orifice radius R_{jet}, mm	12.70 ± 0.05

effective length are 120 and 730 μm, respectively. The beam pairs are oriented at ± 45 deg to the mean flow direction. Bragg cells provide 40-MHz upstream frequency shifting to discriminate flow direction and reduce fringe blindness. Light scattered by particles crossing the measurement volume is collected by receiving optics and photomultiplier tubes located in a 20-deg forward scatter direction and converted to an analog voltage. A digital burst correlator processes this voltage signal and provides frequency and, hence, velocity information. The freestream and bleed flows are seeded with silicone oil droplets (nominal mean diameter = 0.8 μm) provided by a six-jet atomizer. Three seed tubes for the freestream flow are located just downstream of the flow conditioning module and are arranged 120 deg apart circumferentially. The seed tube for the bleed flow is located just downstream of the control valves in the bleed line. Since the two flow streams are independently seeded, care was taken to match data rates at the freestream and the bleed jet nozzle exits in an effort to minimize errors because of particle concentration bias.

Because of the axisymmetric nature of the flowfield, radial traverses in two perpendicular planes (vertical and horizontal) passing through the axis of symmetry were used to measure the three mean velocity components (U, V_r, and V_t), the three Reynolds normal stresses (σ_U^2, $\sigma_{V_r}^2$, and $\sigma_{V_t}^2$), and two of the three Reynolds shear stresses ($\langle u'v_r' \rangle$ and $\langle u'v_t' \rangle$). Figure 4 shows a typical LDV measurement grid consisting of approximately 1200 spatial locations; each spatial location represents an ensemble of 4096 two-component instantaneous velocity realizations. The data obtained from the 8–18 spatial locations traversed radially during each blowdown (lasting 40–50 s) were processed to obtain velocity, turbulence intensity, and shear stress profiles. This information was used to adapt the measurement grid for subsequent tunnel runs. For each bleed case, the measurement grid was concentrated in regions of high-velocity gradients, such as the outer shear layer, the base corner, and the bleed jet shear layer. To provide a measure of repeatability between tunnel runs, LDV measurements during each blowdown were started at the spatial location at which the final measurements were made during the previous blowdown.

An error analysis of the LDV measurements[24] has estimated the worst-case uncertainties in the mean velocity and the rms velocity fluctuations to be 1.2 and 2.3% of U_1, respectively ($U_1 = 574$ m/s in the current experiments). Just downstream of separation, a worst case rms error of 6% because of particle lag was estimated. This error drops to 1.7% one afterbody radius downstream of the base plane and continues to decrease further downstream. Post facto velocity bias corrections were made for all of the LDV data using the interarrival time weighting technique. This method has been shown[25] to be the most reliable technique for high-speed separated flows such as those described here. Prior studies in similar flows have shown the effects of fringe bias to be negligible; hence the data presented here have not been corrected for fringe biasing.

Results

The experimental flow conditions and geometry are listed in Table 1. The uncertainties in the table are estimated using the small-sample method[26] with assumed 20:1 odds. These uncertainty values reflect the variations (two standard deviations) based on repeated measurements at various bleed rates for the primary variables such as pressure, temperature, and velocity. For the derived quantities, the error-propagation procedure of the small-sample method is used to estimate the uncertainty at the same 20:1 odds. Machining tolerances

are used as an indicator of uncertainty for the geometric dimensions. Earlier experiments[4] indicate uniform flow conditions at the wind tunnel nozzle exit and at the exit of the bleed jet at various bleed rates. The freestream approach flow conditions were found to be repeatable (to within the variations shown in Table 1) from one run to the next and were also independent of the bleed rate. For the detailed measurements described in this paper, three bleed flow rates with injection parameter values of $I = 0.0038$ (case A), 0.0113 (case B), and 0.0226 (case C) were selected to investigate the entire near-wake flowfield under low bleed, slightly suboptimal bleed, and slightly postoptimal bleed conditions, respectively (see Fig. 2). The optimum bleed rate was not chosen because the near disappearance of the PRR at this bleed rate (as indicated by prior measurements[4]) could make spatial resolution in that part of the flowfield difficult. The suboptimal bleed rates spanned by cases A and B represent the operating range of most practical base bleed projectiles.

Note that the injection parameter values used here are based on the direct output from the electronic mass flowmeter and do not account for the following: 1) the carrier air with the LDV seed particles in the bleed line, injected downstream of the flowmeter, adds an estimated $I = 0.0004$ to the measured primary bleed flow; and 2) no attempt was made to correct for the drift in the flowmeter calibration (estimated to be a maximum of 10%) as a result of gradual sensor degradation over the two-year span of the base bleed experiments. The effect of this drift was considered negligible because the mean flow and turbulence data from the centerline measurements[4] made nearly one year before the current experiments were found to be virtually identical to the current detailed measurements at $r = 0$ for the same injection parameter values. The following sections briefly describe the key results obtained from the near-wake LDV measurements.

Near-Wake Mean Velocity Measurements

Figure 5 shows the mean velocity vector fields in the near-wake region of the flowfield. The gray scale insets show mean flow streamlines computed using the incompressible axisymmetric stream function definition (i.e., by integrating the measured mean velocity field). The lack of density information in this compressible flow makes these streamlines somewhat qualitative in nature, although they provide a reasonably accurate representation of the base flow topology. In this figure and in all subsequent figures, the vertical scale has been expanded by 42% (relative to the horizontal scale) to display the flowfield features clearly. The data from the nonuniform measurement grids have been transformed to uniform grids with resolution equal to the minimum spacings of the corresponding experimental grids in each direction. The uniform grids are then filled by linear interpolation between the experimental values and are subsequently used to generate the vector and contour plots shown here.

The main features of the flowfield, the turning of the flow through the base corner expansion, the PRR (cases A and B), the bleed jet, and the secondary recirculation region (SRR) between the bleed jet and the outer shear layer (cases B and C), are clearly visible in Fig. 5. The mean freestream flow angles downstream of the base corner for each case are consistent with the Prandtl–Meyer turning angle based on the measured base pressure ratio and the approach freestream Mach number of 2.47.

With increasing bleed flow the size and strength of the PRR (bounded in the axial direction by the forward and rear stagnation points S_f and S_r, respectively) decrease (case A to B) until it finally disappears (case C) as the bleed flow penetrates the outer shear layer
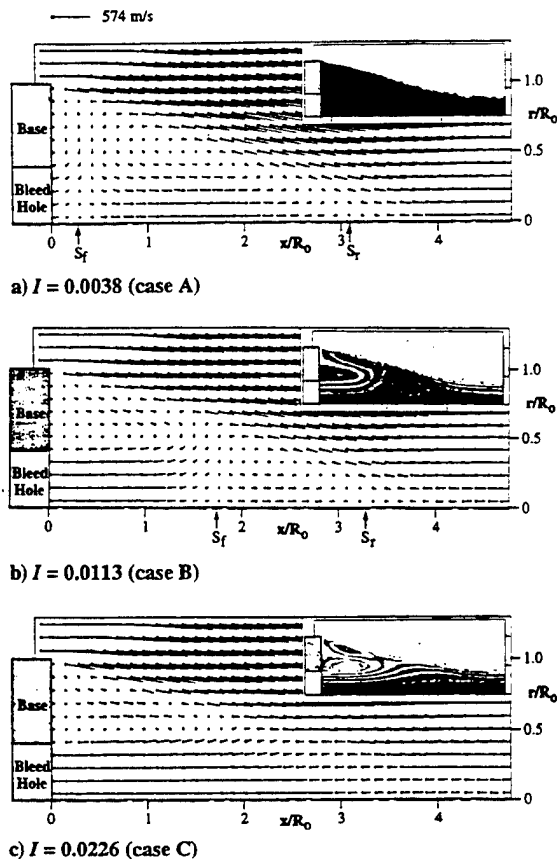
a) $I = 0.0038$ (case A)

b) $I = 0.0113$ (case B)

c) $I = 0.0226$ (case C)

Fig. 5 Mean velocity vector field (mean flow streamlines shown in insets).

a) $I = 0.0038$ (case A)

b) $I = 0.0113$ (case B)

c) $I = 0.0226$ (case C)

Fig. 6 Mean axial velocity field: U/U_1.

Fig. 7 Mean radial velocity field at $I = 0.0113$ (case B): V_r/U_1.

reattachment region. In addition, the forward stagnation point is displaced progressively downstream of the base plane, and the radial extent of the forward portion of the PRR decreases (case A to B). These observations confirm earlier predictions based on near-wake centerline measurements.[4] With increasing bleed, the SRR near the base annulus becomes more evident. Much of the reverse flow in the PRR is oriented parallel to the axis of symmetry (cases A and B). This is in contrast to the blunt base[2] and boattailed[3] afterbody cases where much of the recirculating flow is directed towards the point of separation (the base corner), similar to the SRR in the current cases. The downstream shift of the rear stagnation point locations (S_r at $x/R_o = 2.65, 3.08$, and 3.25 for the blunt base,[2] case A, and case B, respectively) is consistent with the increase in base pressure with base bleed.

The vector plots in Fig. 5 show that the bleed flow provides at least a portion of the fluid required for entrainment by the outer shear layer and shields the base annulus from the shear layer and the PRR, resulting in increased base pressures. However, the increased strength of the SRR near the base annulus and the increased entrainment by the inner bleed jet shear layer at higher bleed rates offset the aforementioned benefits. As shown in Fig. 2, at the low-bleed conditions corresponding to case A, the rate of pressure increase is very high. As the bleed rate is increased, the detrimental effects of the low-pressure SRR and entrainment by the inner shear layer become stronger, and the rate of pressure rise decreases. This trend continues until the optimum bleed condition is reached where the maximum net benefits of base bleed are achieved. As the bleed rate increases past the optimum value, the base pressure starts decreasing because of the overwhelming influence of the bleed jet shear layer and the SRR.

Mean axial velocity contours are shown in Fig. 6. The rapid growth of the outer shear layer is evident from the divergence of the contour lines with downstream distance from the base corner. Because of the presence of the bleed jet and the accompanying SRR, the mean axial velocity fields are quite different from the blunt base flowfield.[2] In cases B and C, the bleed jet velocity profiles remain uniform through a significant axial extent downstream of the base
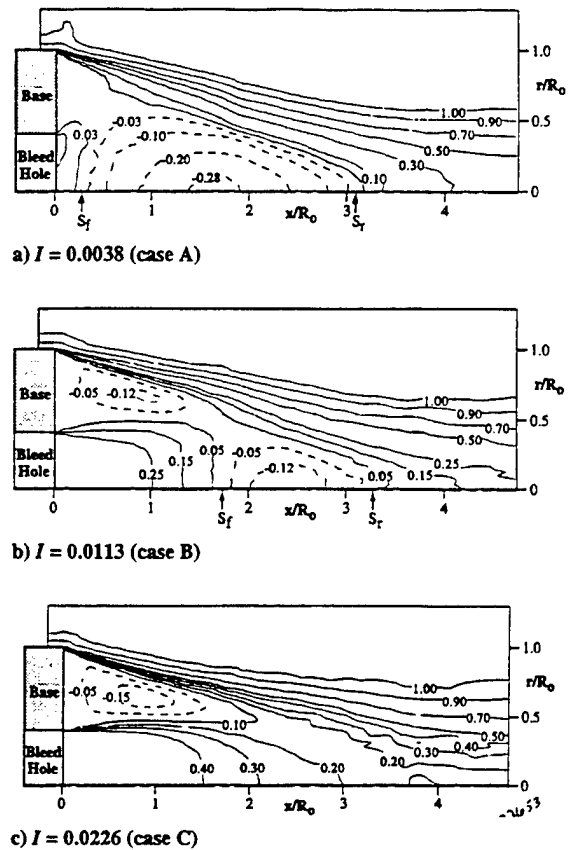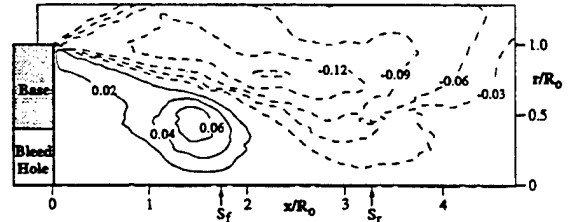
plane. The shear layer growth at the outer bleed jet boundary with increasing bleed rate is also apparent in Fig. 6.

Contours of the mean radial velocity component for case B are shown in Fig. 7. The small magnitudes relative to the mean axial approach velocity show the dominance of the axial component in the near-wake flowfield. The base corner expansion fan appears to be fairly well centered at the base corner. Peak magnitudes of radial velocity appear in the freestream downstream of the expansion where the mean flow is turned radially inward after separation. Positive values of radial velocity appear between the base plane and the forward stagnation point where entrainment into the outer shear layer causes a portion of the bleed flow to turn radially outward (see Fig. 5b). Radial velocity contours for cases A and C (not presented here for brevity) are similar to the ones shown for case B. In both cases A and C, the peak magnitudes of inward radial velocity are higher (and occur at locations upstream) relative to case B because of their lower base pressures and stronger base corner expansions. In case A, the peak positive radial velocities near the base are slightly larger in magnitude than in case B and are confined to the region $x/R_o \leq 1.5$ because of the strong PRR (see Fig. 5a). Since the bleed flow penetrates the shear layer recompression region in case C (see Fig. 5c), the peak positive radial velocities are lower than in case B and have a larger axial extent (approximately $x/R_o = 3$). The tangential component of mean velocity was also measured (for case B only) and, as expected, the magnitudes of this component were negligible because of the axisymmetric nature of the flow.

Table 2 Peak magnitudes of turbulence quantities

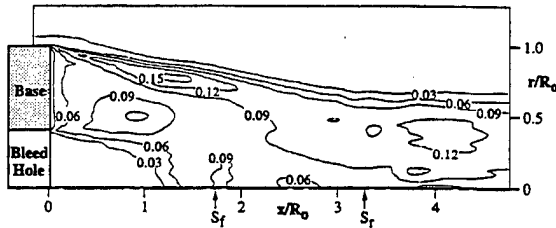|	Blunt base[2]	Boattail[3]	Base bleed, I		
			0.0038	0.0113	0.0226
σ_U/U_1	0.22	0.20	0.16	0.15	0.18
σ_{V_r}/U_1	0.16	0.13	0.12	0.11	0.13
σ_{V_t}/U_1	0.14	0.13	——	0.12	——
k/U_1^2	0.044	0.036	0.027[a]	0.025	0.030[a]
$\langle u'v'_r \rangle/U_1^2$	−0.019	−0.018	−0.012 and 0.0021	−0.011 and 0.0037	−0.013 and 0.012

[a]Estimated using $\sigma_{V_t} = \sigma_{V_r}$.

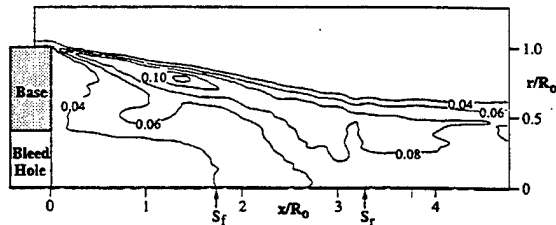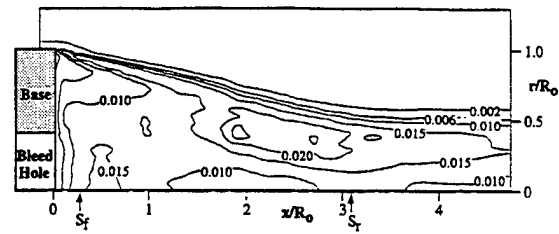Fig. 8 Axial turbulence intensity contours at $I = 0.0113$ (case B): σ_U/U_1.

Fig. 9 Radial turbulence intensity contours at $I = 0.0113$ (case B): σ_{V_r}/U_1.

Near-Wake Turbulence Measurements

The axial turbulence intensity distribution in the near-wake for case B is shown in Fig. 8. After the base corner expansion, the axial turbulence intensity in the outer shear layer increases to a global peak of approximately $\sigma_U/U_1 = 0.151$ at $x/R_o = 1.37$ downstream of the base corner. This global peak is smaller in magnitude and occurs at an upstream location relative to the maximum axial turbulence intensity in the blunt base flowfield[2] ($\sigma_U/U_1 = 0.220$ at $x/R_o = 2.20$), indicating a significant decrease in the outer shear layer's entrainment potential resulting from base bleed. It is also evident from Table 2 that the peak axial turbulence intensity at the slightly preoptimum case B is lower than in cases A and C. Beyond the peak location, the axial turbulence intensity magnitude decreases with downstream distance from the base. Local peaks in axial turbulence intensity occur in the SRR, the reattachment region, and near the forward stagnation point. The low axial turbulence intensity levels in the exiting bleed jet core are also evident from the figure. In case C (not shown), the local peak axial turbulence intensity level in the low-speed portion of the bleed jet shear layer is equal to the global peak value in the outer shear layer as a result of the increased mean jet shear at the high bleed rate.

Figure 9 shows the near-wake radial turbulence intensity levels for case B. Downstream of the base corner, the radial turbulence intensity increases to a peak of $\sigma_{V_r}/U_1 = 0.112$ at $x/R_o = 1.35$, the same location as for the peak axial turbulence intensity. The corresponding peak radial turbulence intensity magnitude in the blunt base study[2] was found to be $\sigma_{V_r}/U_1 = 0.156$ at $x/R_o = 2.20$. The local peaks in radial turbulence intensity near the forward and rear stagnation points are not particularly distinct because of the dominance of flow mechanisms in the axial direction at these points. Downstream of the peak levels in the shear layer, the radial turbulence intensity decays through the reattachment region and the developing wake. Once again, Table 2 shows that the peak radial

a) $I = 0.0038$ (case A, estimated TKE)
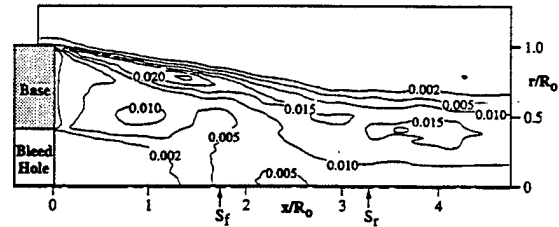
b) $I = 0.0113$ (case B)
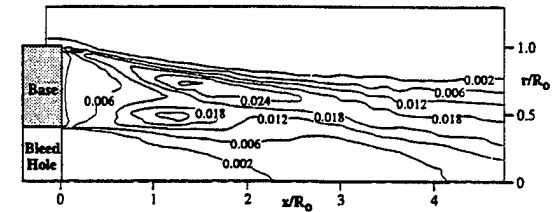
c) $I = 0.0226$ (case C, estimated TKE)

Fig. 10 TKE contours: k/U_1^2.

turbulence intensity at the slightly preoptimum case B is lower than in cases A and C. The tangential turbulence intensity was also measured for case B, and the distribution (not shown for brevity) was found to be similar in magnitude and distribution to the radial turbulence intensity field. The relative ordering of the turbulence intensities ($\sigma_U > \sigma_{V_r} \approx \sigma_{V_t}$) indicates the level of anisotropy of the normal stresses in the near-wake base bleed flowfield.

The turbulent kinetic energy (TKE) k for case B is determined from the measured Reynolds normal stresses using the relation

$$k = \tfrac{1}{2}\left(\sigma_U^2 + \sigma_{V_r}^2 + \sigma_{V_t}^2\right) \qquad (1)$$

The nondimensional turbulent kinetic energy (k/U_1^2) distributions shown in Fig. 10 for all three cases are quite similar to the corresponding axial turbulence intensity distributions that dominate the near-wake turbulence field. The low TKE levels in the bleed jet and in the redeveloping flow downstream of reattachment are also evident from the figure. Because of the similarity of the radial and tangential normal stress fields observed in case B and in the boattail study (and, to a lesser extent, in the blunt base case), the tangential turbulence intensity was not measured for cases A and C, and the TKE for these cases was estimated by substituting the measured radial normal stress value for the tangential term in Eq. (1). The estimated TKE field obtained by applying this procedure to case B was nearly identical to the measured values shown in Fig. 10b, indicating the validity of the substitution. From Table 2, it can be seen that the peak TKE levels in all of the bleed cases are lower than the blunt base and boattail values. The peak levels for case B are the lowest of all, indicating reduced entrainment capability for the outer shear layer at the near-optimum bleed condition. Figure 10c also shows that the increased velocity and mean shear of the bleed jet in the postoptimum case C leads to high TKE levels in the bleed jet shear layer, which in turn causes the base pressure to decrease.

The primary axial-radial Reynolds shear stress $\langle u'v'_r \rangle$ shown in Fig. 11 exhibits trends similar to those of the TKE with global peak magnitudes occurring near the corresponding peak TKE locations, followed by a decay to lower levels in the redeveloping wake. Once
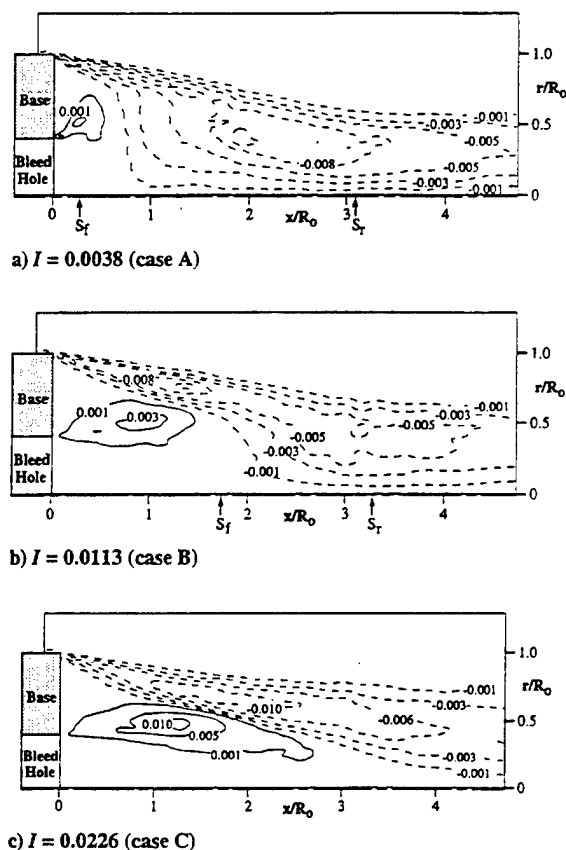
a) $I = 0.0038$ (case A)

b) $I = 0.0113$ (case B)

c) $I = 0.0226$ (case C)

Fig. 11 Reynolds shear stress (axial-radial) contours: $\langle u'v_r'\rangle/U_1^2$.

again, as shown in Table 2, the peak magnitudes for the bleed cases are lower than those found in the blunt base and boattail studies. The lowest peak magnitude in the outer shear layer is found in case B, indicating highly reduced entrainment by the outer shear layer for the near-optimum bleed condition. The positive $\langle u'v_r'\rangle$ values at the edge of the bleed jet indicate the presence of large turbulent structures in the shear layer formed by the bleed jet and their subsequent entrainment of fluid from the SRR. With increasing bleed, the increase in the magnitude of these positive $\langle u'v_r'\rangle$ values and their spatial extent is in accordance with the increased strength of the SRR and entrainment by the bleed jet shear layer and their detrimental base pressure-reducing effects. In all cases, the axial-radial shear stress vanishes (as it should) within 2 mm of the physical near-wake centerline and serves as an indicator of flowfield symmetry. The axial-tangential Reynolds shear stress $\langle u'v_t'\rangle$ was also measured for case B, and, as expected, the magnitudes were negligible compared with the primary shear stress for this case.

Based on the preceding findings, to achieve the maximum benefits of base bleed without the detrimental side effects of the strong bleed jet and SRR, the bleed mass should be injected into the near wake at very low velocities. This is consistent with earlier observations based on parametric global base pressure measurements which suggest the use of a larger bleed orifice relative to the base area [6,7,9-11] or a porous base.[10] The formation of the undesirable secondary recirculation region could also be avoided by locating the bleed orifice (holes or slots) along the outer annular periphery of the base. This configuration has been found to reduce base drag in the case of axisymmetric bodies in subsonic flow[27]; however, no known experiments with this configuration have been reported for the supersonic case.

Summary and Conclusions

Detailed mean velocity and turbulence measurements have been obtained in the near wake of a cylindrical afterbody with base bleed in a Mach 2.5 flow using two-component LDV. The three cases studied provide insight into the near-wake fluid dynamic interactions produced by low bleed, slightly preoptimal bleed, and slightly

postoptimal bleed conditions. The bleed flow displaces the primary recirculation region downstream of the base plane and reduces its size and strength by providing most of the fluid required for shear layer entrainment. The bleed fluid also shields the base annulus from the outer shear layer and the primary recirculation region, leading to an increase in base pressure. There is an overall reduction in turbulence levels throughout the base bleed flowfields relative to the near-wake flowfields of blunt-based and boattailed afterbodies. A secondary recirculation region is formed near the base annulus as a result of the interaction of the bleed jet and the outer shear layer. With increasing bleed, the increased strength of the secondary recirculation region and bleed jet shear layer offsets the benefits of base bleed, leading to a drop in the base pressure. The net benefits of base bleed are maximized at the optimum bleed condition, which corresponds to the highest base pressure, the disappearance of the primary recirculation region, and the lowest turbulence levels in the near-wake flowfield. The use of larger bleed orifices, porous bases, or bleed orifices located along the outer base annulus is suggested for maximizing the benefits from base bleed.

Acknowledgments

References

[1] Delery, J. M., "ONERA Research on Afterbody Viscid/Inviscid Interaction with Special Emphasis on Base Flows," Proceedings of the Symposium on Rocket/Plume Fluid Dynamic Interactions, Vol. 3, Univ. of Texas at Austin, TX, 1983, pp. 1-61.

[2] Herrin, J. L., and Dutton, J. C., "Supersonic Base Flow Experiments in the Near Wake of a Cylindrical Afterbody," AIAA Journal, Vol. 32, No. 1, 1994, pp. 77-83.

[3] Herrin, J. L., and Dutton, J. C., "Supersonic Near-Wake Afterbody Boattailing Effects on Axisymmetric Bodies," Journal of Spacecraft and Rockets, Vol. 31, No. 6, 1994, pp. 1021-1028.

[4] Mathur, T., and Dutton, J. C., "Base Bleed Experiments with a Cylindrical Afterbody in Supersonic Flow," Journal of Spacecraft and Rockets, Vol. 33, No. 1, 1996, pp. 30-37.

[5] Delery, J., and Lacau, R. G., "Prediction of Base Flows," AGARD Rept. R-754, 1987.

[6] Cortright, E. M., and Schroeder, A. H., "Preliminary Investigation of Effectiveness of Base Bleed in Reducing Drag of Blunt-Base Bodies in Supersonic Stream," NACA RM E51A26, March 1951.

[7] Reid, J., and Hastings, R. C., "The Effect of a Central Jet on the Base Pressure of a Cylindrical Afterbody in a Supersonic Stream," Aeronautical Research Council, Repts. and Memoranda 3224, Dec. 1959.

[8] Badrinarayanan, M. A., "An Experimental Investigation of Base Flows at Supersonic Speeds," Journal of the Royal Aeronautical Society, Vol. 65, July 1961, pp. 475-482.

[9] Bowman, J. E., and Clayden, W. A., "Cylindrical Afterbodies in Supersonic Flow with Gas Ejection," AIAA Journal, Vol. 5, No. 6, 1967, pp. 1524, 1525.

[10] Valentine, D. T., and Przirembel, C. E. G., "Turbulent Axisymmetric Near-Wake at Mach Four with Base Injection," AIAA Journal, Vol. 8, No. 12, 1970, pp. 2279, 2280.

[11] Zakkay, V., and Sinha, R., "An Experimental Investigation of the Near Wake in an Axisymmetric Supersonic Flow with and without Base Injection," Israel Journal of Technology, Vol. 7, No. 1-2, 1969, pp. 43-53.

[12] Hubbartt, J. E., Strahle, W. C., and Neale, D.H., "Mach 3 Hydrogen External/Base Burning," AIAA Journal, Vol. 19, No. 6, 1981, pp. 745-749.

[13] Clayden, W. A., and Bowman, J. E., "Cylindrical Afterbodies at $M = 2$ with Hot Gas Ejection," AIAA Journal, Vol. 6, No. 12, 1968, pp. 2429-2431.

[14] Korst, H. H., "A Theory for Base Pressures in Transonic and Supersonic Flows," Journal of Applied Mechanics, Vol. 23, No. 4, 1956, pp. 593-600.

[15] Korst, H. H., Chow, W. L., and Zumwalt, G. W., "Research on Transonic and Supersonic Flow of a Real Fluid at Abrupt Increases in Cross Section (With Special Consideration of Base Drag Problems)," Engineering Experiment Station, Mechanical Engineering Dept., ME TR 392-5, Univ. of Illinois, Urbana, IL, Oct. 1964.

[16] Reijasse, P., Benay, R., Delery, J., and Lacau, R. G., "Prediction of Powered Missile or Projectile Base Flows by Multicomponent Methods," La Recherche Aerospatiale, Vol. 1989-4, 1989, pp. 15-32.

[17] Sahu, J., Nietubicz, C. J., and Steger, J. L., "Navier-Stokes Computations of Projectile Base Flow with and without Mass Injection," AIAA Journal, Vol. 23, No. 9, 1985, pp. 1348-1355.

[18]Sahu, J., "Supersonic Flow over Cylindrical Afterbodies with Base Bleed," AIAA Paper 86-0487, Jan. 1986.

[19]Danberg, J. E., and Nietubicz, C. J., "Predicted Flight Performance of Base Bleed Projectiles," AIAA Paper 90-2069, July 1990.

[20]Nietubicz, C. J., and Sahu, J., "Navier–Stokes Computations of Base Bleed Projectiles," *Base Bleed: First International Symposium on Special Topics in Chemical Propulsion*, edited by K. K. Kuo and J. N. Fleming, Hemisphere, New York, 1991, pp. 93–106.

[21]Nietubicz, C. J., and Gibeling, H. J., "Navier–Stokes Computations for a Reacting, M864 Base Bleed Projectile," AIAA Paper 93-0504, Jan. 1993.

[22]Sahu, J., and Heavey, K. R., "Numerical Investigation of Supersonic Base Flow with Base Bleed," AIAA Paper 95-3459, Aug. 1995.

[23]Dutton, J. C., Herrin, J. L., Molezzi, M. J., Mathur, T., and Smith, K. M., "Recent Progress on High-Speed Separated Base Flows," AIAA Paper 93-0472, Jan. 1995.

[24]Herrin, J. L., "An Experimental Investigation of Supersonic Axisymmetric Base Flow Including the Effects of Afterbody Boattailing," Ph.D. Thesis, Dept. of Mechanical and Industrial Engineering, Univ. of Illinois at Urbana–Champaign, IL, July 1993.

[25]Herrin, J. L., and Dutton, J. C., "An Investigation of LDV Velocity Bias Correction Techniques for High-Speed Separated Flows," *Experiments in Fluids*, Vol. 15, No. 4/5, 1993, pp. 354–363.

[26]Kline, S. J., and McClintock, F. A., "Describing Uncertainties in Single-Sample Experiments," *Mechanical Engineering*, Vol. 75, No. 1, 1953, pp. 3–8.

[27]Freund, J. B., and Mungal, M. G., "Drag and Wake Modification of Axisymmetric Bluff Bodies Using Coanda Blowing," *Journal of Aircraft*, Vol. 31, No. 3, 1994, pp. 572–578.

APPENDIX A.8

THE TURBULENCE STRUCTURE OF A REATTACHING AXISYMMETRIC COMPRESSIBLE FREE SHEAR LAYER

by

J. L. Herrin and J. C. Dutton

The turbulence structure of a reattaching axisymmetric compressible free shear layer

J. L. Herrin
Diagnostics and Heat Transfer Program, GE Corporate Research and Development Center, Schenectady, New York 12301

J. C. Dutton
Department of Mechanical and Industrial Engineering, University of Illinois at Urbana-Champaign, Urbana, Illinois 61801

The reattachment of a supersonic, axisymmetric shear layer downstream of a blunt-based afterbody is studied. Of primary interest are the effects of the "extra" strain rates, such as bulk compression, concave streamline curvature, and lateral streamline convergence associated with shear layer reattachment on the structure of the turbulence field. Experimental turbulence data obtained throughout the reattachment region with a two-component laser Doppler velocimeter are presented. In general, the axisymmetric compliant boundary reattachment process is shown to be different in character compared to the planar solid wall case. Most notably, significant reductions in the Reynolds stresses occur through the reattachment region due to the dominating effect of lateral streamline convergence as the flow approaches the axis. Similar to the planar solid wall case, however, a reduction in the mean turbulent transport toward the axis in the reattachment region was found, which suggests a radial containment of the large-scale eddies near the axis of symmetry. The reattachment process was also seen to have profound effects on the large-scale structures in the shear layer, primarily through reduced structural organization as indicated by instantaneous shear angle histograms. © *1997 American Institute of Physics.* [S1070-6631(97)04011-7]

I. INTRODUCTION

The reattachment process of a compressible free shear layer impinging on a solid or compliant surface occurs in many practical fluid dynamic systems, including wing trailing edges, axial flow combustors, sting-supported wind tunnel models, and supersonic jets. In the solid boundary case, the reattachment point has importance because of the increased pressure loads and heat transfer rates that occur due to the interaction between the shear layer and the surface. In fact, the local thermal loads near reattachment in axial flow combustors can often dictate the design of the entire system. Understanding the compliant boundary reattachment problem is also important, especially in the case of conventional antiarmor projectiles which contain multiple bodies separated and aligned along a common axis.[1] In this case, each body except the first is immersed in the wake of the prior body and is generally located downstream of the previous body's wake reattachment point. Obviously, in this case understanding the flow physics in the reattachment zone is essential in defining the approach conditions for the following bodies.

The shear layer reattachment problem is also a critical part of the multicomponent modeling of missile and projectile afterbody flowfields.[2] Still a practical design tool, the success of multicomponent modeling intimately depends on the accurate prediction of the reattachment process downstream of the body. A typical flowfield downstream of a supersonic, axisymmetric projectile is sketched in Fig. 1 where the reattachment zone is that region contained within the dashed lines. Notice that the shear layer reattachment process contains many complicating fluid dynamic features such as an adverse pressure gradient, streamline curvature,

flow reversal, and fluid interactions across the axis of symmetry. In multicomponent analyses, the reattachment model dictates the amount of mass returned to the base due to the adverse pressure gradient and, therefore, directly affects the base pressure.

Although the general features of reattaching compressible shear layers have been documented in the planar solid wall case over the past three decades, relatively limited data are available in the compliant boundary case, especially detailed experimental data on the structure of the turbulence field near reattachment. It is now commonly known that compressibility plays a significant role in the development of high-speed free shear layers, but how it affects the reattachment process is still largely unknown. In addition, the fundamental differences in the reattachment process between solid and compliant boundaries and between planar and axisymmetric geometries have not been firmly established for either supersonic or subsonic flows.

The shear layer reattachment process also has fundamental interest. Eaton and Johnston[3] present a thorough review of previous work for the subsonic, solid wall case where a significant amount of experimental data exists. In general, the Reynolds stresses in the shear layer were found to decrease through the reattachment zone, although the physical mechanisms associated with this trend could not be firmly established. In contrast, data from the supersonic, planar, solid wall case indicate that the Reynolds stresses *increase* through reattachment with peak values occurring slightly downstream of the mean reattachment point.[4–6] Recent work[7] has indicated that the turbulent fluctuations in the reattachment region can directly affect the recompression shock system and, in general, large-scale dynamical motions
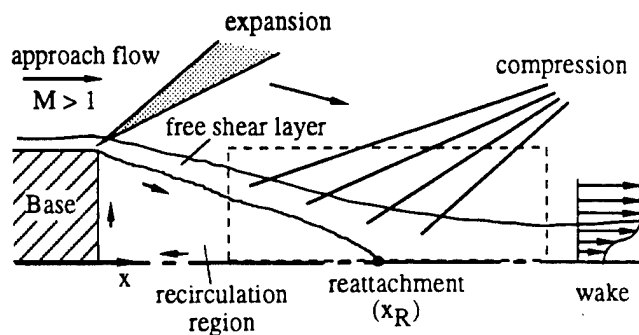
FIG. 1. Sketch of entire near-wake flowfield and region of interest.

FIG. 2. Shear layer mean axial velocity profiles upstream of reattachment in similarity coordinates.

of the shock system can result. Obviously, this finding is only applicable to supersonic shear layer reattachment where flow recompression occurs through a series of compression waves. Other differences between the subsonic and supersonic cases can be attributed, at least in part, to compressibility effects associated with the shear layer development and also the reattachment process. Consequently, it is apparent that the relatively large volume of subsonic, solid wall reattachment data can only provide qualitative insight into the supersonic, compliant boundary reattachment problem.

Although a limited amount of work has been done on the solid wall reattachment problem, the supersonic, compliant boundary case has received even less attention. Samimy and Addy[8] investigated the interaction of two compressible shear layers formed downstream of a two-dimensional, thick base with laser Doppler velocimetry (LDV). Although a relatively sparse data set was obtained in the reattachment region, the authors suggested that significant structural differences exist between the turbulence fields in supersonic and subsonic reattaching flows. Most notably, the transverse turbulence diffusion mechanisms in the reattachment zone were shown to differ significantly, as evidenced by large changes in the turbulent triple products $\langle u'u'v' \rangle$ and $\langle v'v'v' \rangle$. In a similar study, Amatucci et al.[9] recently confirmed several of these earlier findings while documenting the Reynolds stresses and turbulent triple products in the reattachment zone between a pair of planar shear layers. The Reynolds stresses peaked slightly downstream of reattachment with significant differences occurring between the two shear layers in the transverse normal stress and primary shear stress.

The primary objective of the present paper is to investigate the turbulence structure of an axisymmetric, supersonic shear layer undergoing compliant boundary reattachment as shown in Fig. 1. Detailed experimental turbulence data obtained with LDV will be presented, and the effect of the reattachment process on the Reynolds stress magnitudes and the structural characteristics of the turbulence field will be ascertained. In conjunction with other recent experimental data,[10] physical mechanisms associated with the observed changes in the turbulence properties through reattachment will be postulated.

II. EXPERIMENTAL APPARATUS AND PROCEDURE

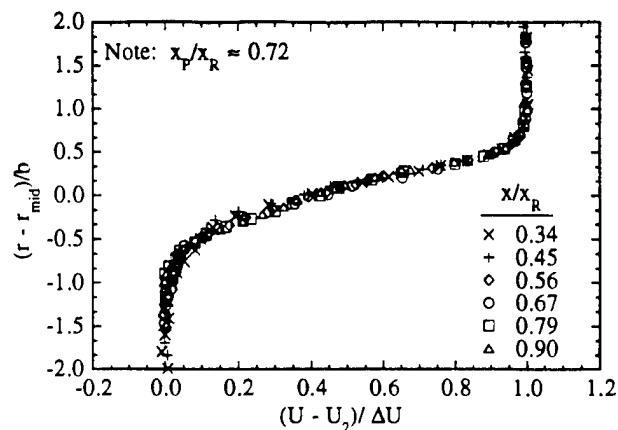The experiments for the current study were conducted in the axisymmetric base flow facility at the University of Illi-

nois Gas Dynamics Laboratory. This facility is a blowdown-type wind tunnel specifically designed for axisymmetric afterbody models and contains features to ensure axisymmetric flow by proper centering of the model. In addition, methods to eliminate interference waves from intersecting the near-wake flowfield downstream of the blunt-based body were utilized. A detailed description of the facility is given by Herrin.[11] The model used for the current study was a blunt-based, axisymmetric, boattailed afterbody with a base radius, R_b, of 28.97 mm. The Mach and unit Reynolds numbers of the freestream flow immediately upstream of the reattachment region were 2.72 and 43 (10^6) per meter, respectively. The general characteristics of the entire base flowfield have been presented elsewhere.[12] In this paper, emphasis is placed on the reattachment region from immediately upstream of the first recompression wave to the developing wake further downstream (outlined region in Fig. 1). The boundary layer at the bluntbody separation point was fully turbulent with a thickness $\delta/R_b = 0.15$, and the measured freestream turbulence levels throughout the flow were less than 1%; additional details concerning the approach freestream and boundary layer may be found in Ref. 11. The onset of the adverse pressure gradient associated with reattachment was estimated from the sidewall pressure data of Amatucci et al.[9] to occur near $x/x_R = 0.72$ where x is the axial distance downstream of the base plane and x_R is the reattachment length ($x_R = 89$ mm) obtained from the current mean velocity data set. Upstream of reattachment, the normalized mean velocity profile in the shear layer has become independent of axial position (i.e., self-similar in the mean sense). Figure 2 shows several mean velocity profiles obtained at different axial stations upstream of reattachment as plotted in similarity coordinates. In this figure, the nondimensionalizing factors are the 10%–90% shear layer velocity thickness (b) and the mean velocity difference across the shear layer (ΔU). Although the mean velocity profile has reached its fully developed state near reattachment, as shown in Fig. 2, the Reynolds stresses were found to be just approaching a self-similar condition.[12] At the onset of recompression, the shear layer velocity thickness (b) takes a value of approximately 11.3 mm. In addition, the convective Mach number of the

Phys. Fluids, Vol. 9, No. 11, November 1997

J. L. Herrin and J. C. Dutton   3503

shear layer ($M_c \equiv \Delta U/(2\bar{a})$ where $\bar{a}$ is the mean speed of sound) is approximately 1.3 at this location, which suggests that significant compressibility effects can be expected. Throughout the remainder of this paper, the mean velocity in the freestream approaching the recompression region ($U_{ref}=592.5$ m/s) will be used for nondimensionalization.

The primary diagnostic tool used in the experiments was a two-component LDV with frequency shifting that is capable of measuring the high turbulence intensity levels and reversed velocities in the reattachment region of the flow. A detailed discussion of the LDV system and its implementation in supersonic, separated flows has been given by Herrin.[11] The measurement volume diameter and length were approximately 120 and 700 μm, respectively, which provided adequate resolution to avoid significant spatial averaging effects in the data. The scattering media used in this investigation were silicone oil droplets with a mean diameter of approximately 0.8 μm.[13] A particle lag error analysis using the results of Samimy and Lele[14] predicts a worst-case root-mean-square slip velocity of less than 2% in the region of interest. An error analysis of the LDV data reduction procedure estimates a maximum uncertainty in the mean velocity of less than 1% of U_{ref} and in the rms velocity fluctuation of less than 2% of U_{ref}.

The LDV data were obtained along 20 radial traverses throughout the reattachment region in both the vertical and horizontal planes intersecting the axis of symmetry. This two-plane approach allowed direct measurement of three mean velocities (U, V, W), three kinematic Reynolds normal stresses ($\sigma_u^2, \sigma_v^2, \sigma_w^2$), and two kinematic Reynolds shear stresses ($\langle u'v' \rangle$, $\langle u'w' \rangle$) throughout the reattachment region. All data presented in the present paper are referenced to the wind tunnel coordinate system where the mean axial velocity (U) is aligned with the axis of symmetry. At each spatial location, approximately 4000 velocity samples were obtained to ensure minimal statistical uncertainty. The ensemble-averaged data were corrected for velocity bias using the interarrival time weighting method;[15] no correction for fringe bias was implemented. For all data presented herein, at least one profile upstream of reattachment (near $x/x_R = 0.56$) will be shown to document the shear layer properties prior to the onset of the recompression process.

III. RESULTS

The primary results of this investigation will now be presented. In the first section, the development of the kinematic Reynolds stresses through reattachment will be described and compared to previous compliant and solid boundary data. In two subsequent sections, the velocity triple products and primary turbulence structure parameters (e.g., shear stress correlation coefficient, R_{uv}) will be investigated. Finally, a quadrant decomposition analysis of the turbulence data will be presented that will provide additional insight into the effects of the reattachment process on the compressible turbulence field.

A. Reynolds stress development

As discussed earlier, the reattachment effects on the primary Reynolds stresses appear to be dependent on the flow
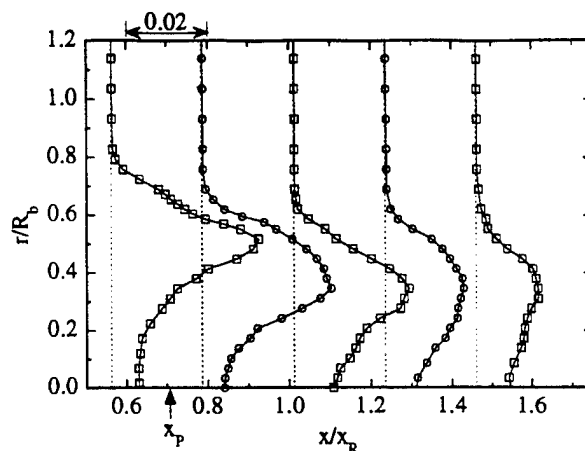

FIG. 3. Axial Reynolds normal stress profiles, $(\sigma_u/U_{ref})^2$.

speed regime (subsonic or supersonic) and the reattachment boundary condition (compliant or solid boundary). For the present supersonic, compliant boundary case, the development of the axial and radial Reynolds normal stresses through the reattachment region is shown in Figs. 3 and 4, respectively. The approximate location of the onset of the adverse pressure gradient is labeled on the abscissa as x_P, and the scale for the plotted variable is shown at the upper left of the figure. The strong peak in the axial normal stress shown upstream of reattachment is indicative of compressible free shear layers.[16] The location of the peak coincides roughly with the inflection point in the mean velocity profile which is approximately centered between the edges of the shear layer. As the shear layer enters the recompression region, the Reynolds stress profiles begin to broaden due to turbulence diffusion mechanisms and the increased turbulence activity along the centerline from the shear layer interaction. Near reattachment, the enterline axial and radial Reynolds stresses both reach local maxima which, along with the decreasing peak values away from the axis, appears as an overall broadening of the Reynolds stress profiles. Downstream of the reattachment point, the strong Reynolds stress peaks present in the shear layer prior to the adverse pressure
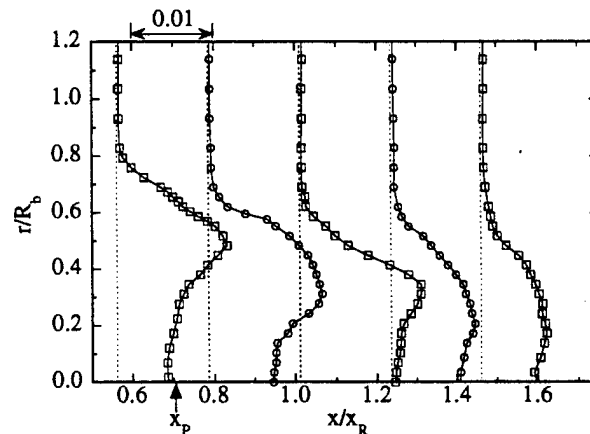

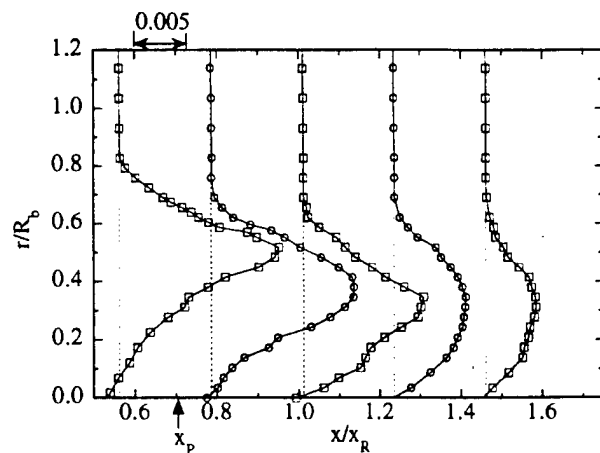FIG. 4. Radial Reynolds normal stress profiles, $(\sigma_v/U_{ref})^2$.

FIG. 5. Primary Reynolds shear stress profiles, $- \langle u'v' \rangle / U_{ref}^2$.

FIG. 6. Peak Reynolds stress distributions through reattachment.

gradient have all but disappeared in favor of a more radially uniform turbulence field of reduced magnitude. Of course, it is expected that the change in flow regime from a shear layer to wake will result in lower downstream turbulence levels since the wake does not contain the relatively large mean shear rates present in the approaching shear layer. In addition to the axial and radial Reynolds normal stresses, the tangential normal stress was also measured experimentally and found to closely follow the radial Reynolds stress trends shown in Fig. 4.

The development of the primary Reynolds shear stress ($\langle u'v' \rangle$) through the reattachment region is shown in Fig. 5 and is found to be somewhat more dramatic than the normal stresses. Upstream of reattachment, the shear stress profile is similar to that shown previously for the axial normal stress, except along the centerline where the shear stress vanishes by symmetry. The shear stress profile is seen to maintain its strong-peaked appearance up to the reattachment point. However, immediately downstream of reattachment, a significant change in the shear stress profile occurs; namely, the profile transitions to a more rounded appearance and the magnitude is greatly reduced from that near reattachment. At the last axial station shown, the wake shear stress distribution is far different, in magnitude and shape, than that in the shear layer approaching reattachment. In addition, the decrease in the peak shear stress magnitude prior to the reattachment point in the present case can be contrasted to both the supersonic, solid wall case and the supersonic, compliant boundary case measured in two-dimensional flows. More discussion as to this comparison and the possible physical mechanisms involved will be given below.

In addition to the Reynolds stress profiles shown in the previous figures, it is also instructive to plot the *peak* Reynolds stress magnitudes as a function of axial distance through the reattachment region, Fig. 6. By doing this, it becomes apparent that the reattachment process can be divided into three regions: a region upstream of the adverse pressure gradient ($x/x_R < 0.72$), a central region between the start of recompression and the reattachment point ($0.72 < x/x_R < 1.0$), and a postreattachment region ($x/x_R > 1.0$). As previously mentioned, the region upstream of the
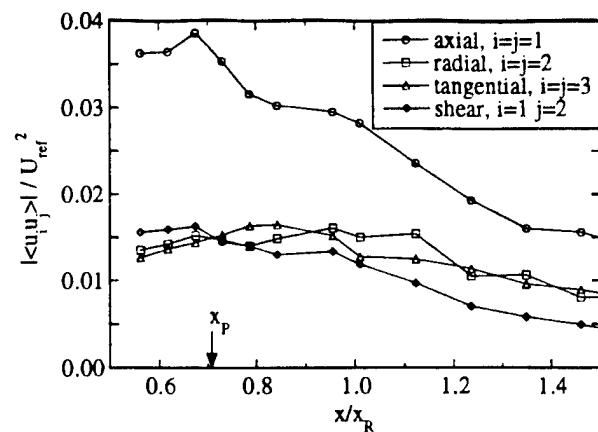
onset of the adverse pressure gradient ($x/x_R < 0.72$) is characterized by a compressible, axisymmetric shear layer developing at essentially constant pressure with strong Reynolds stress peaks that are slowly evolving with downstream distance.

At the onset of the adverse pressure gradient associated with reattachment, it is apparent that the peak Reynolds stresses are immediately affected (Fig. 6), although the magnitude of the effect varies considerably among the different components. The axial normal stress and primary shear stress are both attenuated in this region while the radial and tangential normal stresses actually *increase* modestly. To explain these different trends, one must consider the many competing fluid dynamic effects that occur in the reattachment region, including the bulk compression associated with adverse pressure gradients, destabilizing concave streamline curvature, lateral streamline convergence as the flow approaches the axis of symmetry, and the shear layer interaction occurring across the centerline. The effects of bulk compression, streamline curvature, and lateral convergence have been studied in detail for attached, subsonic, turbulent boundary layers[17-19] and are generally classified as "extra" rates of strain in addition to the strain rate of simple shear, $\partial U / \partial r$. Although the present flowfield is somewhat more complicated than the boundary layer flow for which the "extra" strain rate effects were determined, the fluid dynamic effects on the Reynolds stresses of the present flow are assumed known, at the very least, as to their direction. Consequently, bulk compression and concave streamline curvature should act to destabilize (increase) the Reynolds stresses in the reattaching shear layer while lateral streamline convergence should stabilize (decrease) the Reynolds stress magnitudes. To estimate the relative magnitudes of the "extra" strain rates, the previous analyses of Bradshaw[17] and Smits *et al.*[19] were used to quantify each strain rate in terms of local flowfield variables. Once calculated, these values are compared to the magnitude of the primary strain rate, $\partial U / \partial r$, and presented as a ratio, $e/(\partial U / \partial r)$. In the present case, the "extra" strain rates due to bulk compression, concave streamline curvature, and lateral streamline convergence relative to the primary strain rate take approximate values of 0.3, 0.06, and -0.1, respectively. These magnitudes signify

that the present "extra" strain rates can be classified as strong rates of strain according to the definition of Smits and Wood.[20] Unfortunately, the combined effect of these three "extra" strain rates acting together cannot be determined by a simple summation of their relative magnitudes, as a significant nonlinear coupling has been shown to exist.[20] The observed decreases in the axial normal stress and primary shear stress at the onset of reattachment in the present case, consequently, indicate the overwhelming influence of lateral streamline convergence when compared to the effects of bulk compression and concave streamline curvature. Since the turbulence field interacts with the mean flow primarily through the streamwise normal stress, the slight increase in the radial and tangential normal stresses in the initial reattachment region is most likely a result of the relatively long time scales associated with turbulence energy transfer among the components when compared to that between the mean flow and the axial normal stress. In fact, downstream of the reattachment point ($x/x_R > 1.0$) all of the Reynolds stress components experience decays to lower values in the developing wake.

By considering the "extra" strain rates described above, it is now possible to offer plausible explanations for the observed trends in the present data. At the start of the recompression region, the peak Reynolds stress regions of the shear layer are sufficiently far from the axis of symmetry that the cross-centerline shear layer interaction effects are most likely small (this is obvious from the Reynolds stress profiles shown in Figs. 3–5); therefore, the observed decrease in the axial normal stress and primary shear stress in this region are primarily a result of the stabilizing effect of lateral streamline convergence. As the shear layer approaches the axis of symmetry, the lateral streamline convergence effect *increases* approximately with the inverse of the radial coordinate,[19] and the shear layer interaction along the centerline begins to affect the Reynolds stress profiles resulting primarily in an increase in the centerline normal stresses. Since the peak turbulence region lies away from the centerline, the peak Reynolds stress magnitudes continue to decay through the reattachment point due to the streamline convergence effect. In two-dimensional compliant boundary reattachment, lateral convergence effects are not present so that the observed increase in the Reynolds stresses up to the reattachment point[8,9] can be explained by the overall destabilizing effects of streamline curvature and bulk compression. Immediately downstream of reattachment in the present case, the shear layer realignment process is gradually completed and the "extra" strain rates associated with bulk compression, streamline curvature, and lateral convergence vanish. Consequently, the Reynolds stresses decay to lower values as a result of the decreasing shear rates present in the wake flow relative to those in the upstream shear layer.

B. Velocity triple products

In addition to the Reynolds stresses, the velocity triple products provide information on the transport of turbulence energy throughout the reattachment region. It is well understood that the primary contribution to the triple products comes from large-scale turbulent structures which, in the
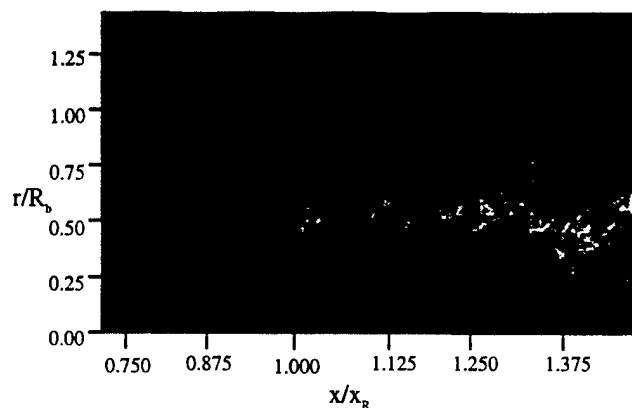

FIG. 7. Planar Mie scattering image of the reattachment region.

present flowfield, enter the reattachment region from the compressible shear layer. A typical planar Rayleigh/Mie scattering image (from condensed ethanol droplets in the supersonic freestream) of the reattachment region is presented in Fig. 7. Large-scale structures convecting from the shear layer into the reattachment region and developing wake are clearly seen. Figures 8 and 9 show the effect of the reattachment process on two triple products of interest, $\langle u'u'v' \rangle$ and $\langle u'v'v' \rangle$, respectively. In a planar mixing layer, the triple products are roughly antisymmetrical about the mixing layer centerline;[16,21] the same approximate behavior is shown upstream of the reattachment zone in Figs. 8 and 9. In general, negative values of $\langle u'u'v' \rangle$ (Fig. 8) imply that, on average, eddies with large streamwise velocity fluctuations move towards the centerline, away from the region of maximum Reynolds stress, and vice versa for positive values. As the shear layer approaches the reattachment point, the magnitude of the large negative $\langle u'u'v' \rangle$ peak at the inner edge is rapidly attenuated while the large positive peak at the outside edge of the shear layer broadens somewhat but maintains a relatively large magnitude. This trend suggests a containment of the large-scale eddies at the centerline due to the axisymmetric nature of the flow and is similar to that observed in subsonic, solid wall reattachment studies.[21] In other words, movement of the large-scale structures toward or
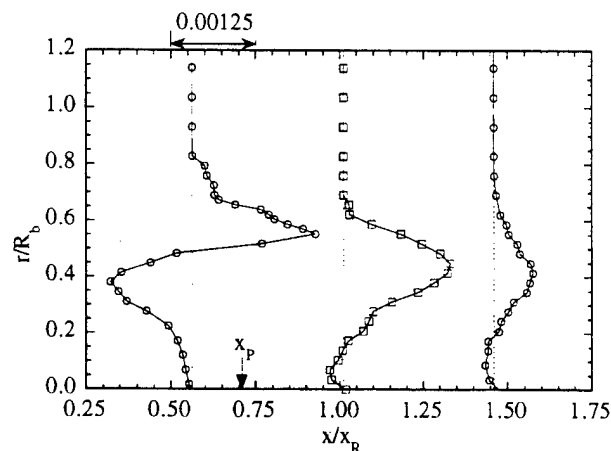

FIG. 8. Velocity triple product profiles, $\langle u'u'v' \rangle / U_{ref}^3$.
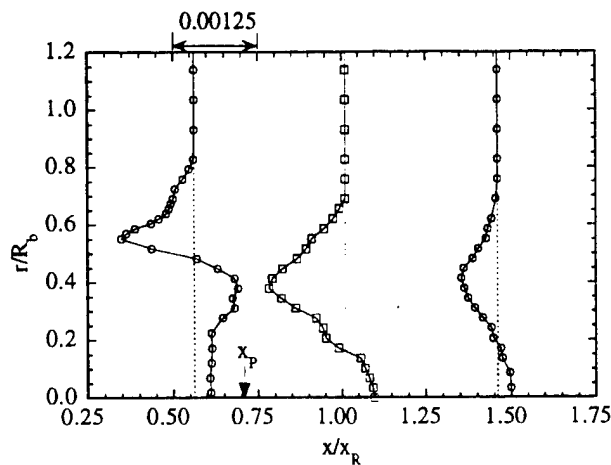
J. L. Herrin and J. C. Dutton

FIG. 9. Velocity triple product profiles, $\langle u'v'v'\rangle/U_{ref}^3$.

across the axis of symmetry is confined by the symmetry of the flow while movement of the structures away from the centerline is not so constrained. In two-dimensional, supersonic, compliant boundary studies,[8,22] the large negative peak near the inside edge of the shear layer persisted far downstream of the reattachment point. Consequently, it is apparent that the axisymmetric nature of the present flow has a significant impact on the nature of the turbulence field near the centerline where streamline convergence and transverse curvature effects are largest, but has a lesser effect for larger radial positions. Downstream of the reattachment point in Fig. 8, an overall decay in $\langle u'u'v'\rangle$ is shown as the wake develops.

The effect of the reattachment process on the streamwise transport of the radial normal stress, as indicated by $\langle u'v'v'\rangle$, is shown in Fig. 9. In contrast to the radial transport of turbulence energy shown in Fig. 8, the eddy containment near the axis of symmetry has a limited effect on the streamwise transport shown in Fig. 9. In fact, the initial antisymmetrical profile prior to recompression is approximately maintained to the reattachment point, although it is somewhat broadened due to turbulence diffusion and shifted toward the centerline as the shear layer undergoes realignment. Since flow symmetry about the axis is primarily a constraint on the mean radial velocity (i.e., $V = 0$ on the centerline), and not on the mean axial velocity, it is not surprising that the radial transport of turbulence energy is more strongly affected near the axis of symmetry. This suggests that the large-scale structures that enter the recompression region change orientation as they approach reattachment due to streamline curvature and centerline confinement effects and, subsequently, begin to lose coherence as the wake develops. This is not to suggest that large-scale structures are absent downstream of reattachment, but rather that the organization of the structures has diminished through the reattachment zone. Supporting evidence for this has been given by Smith and Dutton[10] who obtained planar Mie scattering images near the reattachment point in the planar supersonic base flowfield used previously in the study by Amatucci et al.[9] The images show quite clearly the presence of large-scale turbulent structures throughout the reattachment region

and in the downstream wake. However, statistical image processing analyses indicate a loss in coherence of the structures through reattachment similar to that postulated for the present flow. It is important to keep in mind that the turbulence field in the current axisymmetric flow is significantly attenuated by the reattachment process (Fig. 6) in contrast to the two-dimensional case, so it is reasonable to expect that the loss of eddy organization noted by Smith and Dutton[10] is magnified in the current case.

In addition to the data shown in Figs. 8 and 9, several other velocity triple products were calculated from the experimental data. These include $\langle u'u'u'\rangle$, $\langle v'v'v'\rangle$, $\langle u'u'w'\rangle$, $\langle u'w'w'\rangle$, and $\langle w'w'w'\rangle$. In this case, w' represents an instantaneous velocity fluctuation in the tangential (swirl) direction. As expected, the tangential transport of turbulence energy (as indicated by $\langle u'u'w'\rangle$ and $\langle w'w'w'\rangle$) was negligible compared to the axial and radial transport terms. In addition, the streamwise transport of the axial ($\langle u'u'u'\rangle$) and tangential ($\langle u'w'w'\rangle$) normal stresses closely follows the trends for the corresponding radial normal stress ($\langle u'v'v'\rangle$)shown in Fig. 9, although the radial and tangential component magnitudes are reduced by a factor of approximately three relative to the axial component. Finally, the radial transport of the radial normal stress ($\langle v'v'v'\rangle$) is similar to the corresponding axial normal stress transport ($\langle u'u'v'\rangle$) shown in Fig. 8 except that the magnitudes are reduced by about a factor of two.

C. Turbulence structure parameters

To this point, the turbulence field throughout the reattachment region has been discussed in terms of the overall changes in the Reynolds stress and triple product magnitudes. Since the flowfield undergoes a change in type through reattachment (from shear layer to wake), one would expect significant changes in these turbulence quantities. It is also instructive from a fundamental standpoint, and more important in some respects, to investigate the structural changes in the turbulence field brought on by the application of the "extra" strain rates in the reattachment zone. Many questions exist about the turbulence structure in highly compressible shear layers and the response to complicating features such as pressure gradient, streamline curvature, etc. For example, how is the overall turbulence energy distributed between the normal stresses? How quickly does the shear stress respond to these effects compared to the normal stresses? How are the Reynolds stress distributions different from incompressible flow?

Perhaps the most instructive parameter to investigate is the anisotropy of the Reynolds normal stresses. In the present case, a primary-to-secondary stress ratio, $(\sigma_u/\sigma_v)^2$, and a secondary-to-secondary stress ratio, $(\sigma_w/\sigma_v)^2$, are utilized to show the respective distributions of the Reynolds normal stress field. Figure 10 shows the development of these normal stress ratios determined at the peak shear stress location in the reattaching shear layer. Clearly, this figure reinforces the dominance of the axial normal stress indicated earlier in conjunction with Fig. 6. It is apparent that the initial stages of the reattachment process have a significant impact on the relative distribution of the normal stresses with
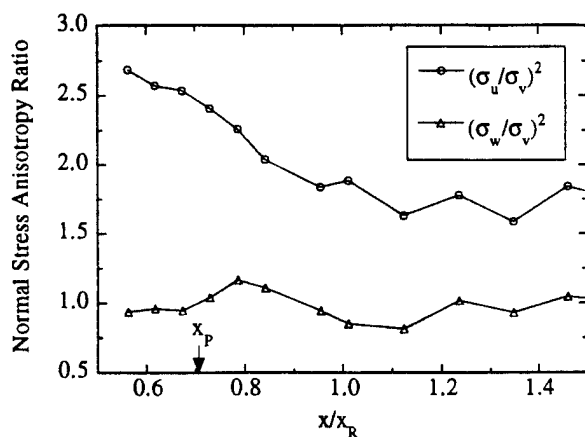
Phys. Fluids, Vol. 9, No. 11, November 1997

J. L. Herrin and J. C. Dutton   3507

FIG. 10. Normal stress anisotropy ratios at the peak shear stress locations.

FIG. 11. Turbulence structure parameters at the peak shear stress locations.

a rapid decay in $(\sigma_u/\sigma_v)^2$ occurring up to the reattachment point. Downstream of reattachment, the relative normal stress distributions appear to have reached an equilibrium state with only small variations as the wake develops. Throughout the reattachment region, the secondary-to-secondary stress ratio, $(\sigma_w/\sigma_v)^2$, maintains an approximately constant value of unity suggesting little difference in the turbulence energy redistribution mechanisms (e.g., pressure strain) in these components. In the two-dimensional case,[9] the primary-to-secondary normal stress ratio is relatively constant up to and even downstream of the reattachment point and takes a value $(\sigma_u/\sigma_v)^2 \approx 6$, which is significantly larger than the values shown in Fig. 10 for the present flow. This again illustrates the significant differences that exist in the turbulence field between two-dimensional and axisymmetric flows in the reattachment zone for the supersonic case.

For attached subsonic flows, it has been suggested by Bradshaw[23] and others that the primary turbulence structure parameters do not respond immediately to the application of "extra" strain rates. Similarly, the response of the turbulence structure parameters will not be instantaneous to the removal of the "extra" strain rates. Figure 10 suggests quite a different picture in the present flow. In fact, at the onset of the adverse pressure gradient, the primary-to-secondary normal stress ratio is already decaying to lower levels. At or slightly downstream of reattachment, the "extra" strain rates associated with streamline curvature, bulk compression, and streamline convergence are greatly diminished (i.e., realignment is almost complete), and the effect on the normal stress ratios shown in Fig. 10 is an asymptotic approach to lower values in the downstream wake. Of course, as the wake continues to develop, the anisotropy in the Reynolds normal stresses will eventually vanish as the turbulence energy redistribution mechanisms overwhelm the decreasing shear across the wake. The direct impact of the "extra" strain rates on the normal stress ratio, $(\sigma_u/\sigma_v)^2$, appears to be immediate, which may be an indication of an even stronger coupling between the strain rates and the turbulence field in compressible flows than those ascertained previously for incompressible flowfields.
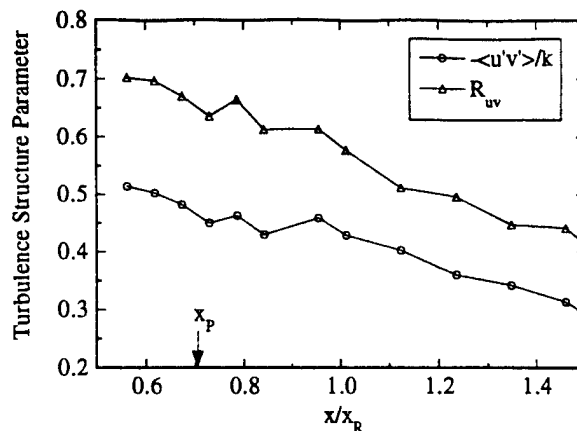
In addition to the distribution of the turbulence energy among the normal stresses, turbulence models oftentimes use a shear stress-to-normal stress ratio for Reynolds stress closure. Distributions of two popular ratios, $-\langle u'v'\rangle/k$ and R_{uv}, are shown in Fig. 11 where k is the turbulent kinetic energy defined by the following relation:

$$k = \frac{\sigma_u^2 + \sigma_v^2 + \sigma_w^2}{2} \tag{1}$$

and R_{uv} is the shear stress correlation coefficient defined by:

$$R_{uv} = \frac{-\langle u'v'\rangle}{\sigma_u\sigma_v}. \tag{2}$$

It is apparent from Fig. 11 that the reattachment process has a greater impact on the Reynolds shear stress than it does on the normal stresses as both ratios decay monotonically throughout the reattachment zone. Similar to the normal stress distributions of Fig. 10, the effects of the "extra" strain rates are felt immediately at the onset of recompression. In contrast, however, the shear stress-to-normal stress ratios shown in Fig. 11 continue to decrease beyond reattachment and do not appear to be approaching an equilibrium state at the last measurement station shown. The magnitude of the shear stress-to-turbulent kinetic energy ratio $-\langle u'v'\rangle/k$ is, in general, larger than but approaching the "typical" value of 0.3 first suggested by Harsha and Lee[24] and still commonly used in turbulent flow calculations. Similarly, the measured shear stress correlation coefficient R_{uv} is larger than but approaching the typical range of 0.4–0.5 for this parameter. The decay in R_{uv} is also an indication of the loss in organization of the large-scale turbulent structures through the reattachment region as discussed in the previous section.

D. Quadrant decomposition analysis

Additional insight into the structure of the turbulence field in the reattachment region can be gained by examining the instantaneous velocity fluctuations with the quadrant decomposition technique. The quadrant analysis method has been commonly used in boundary layer flows[25–27] to determine the frequency and strength of dynamic boundary layer

events such as eddy ejections and sweeps. Herrin and Dutton[28] have recently applied this technique to the initial stages of compressible shear layer development in the present flowfield and have found it to be useful in identifying the orientation and qualitative organization of the large-scale, energy-containing eddies. In this section, the quadrant decomposition analysis will be presented for the data in the reattachment region of the present flow.

In an attempt to better understand the organization (coherency) of the large-scale, energy-containing eddies, an instantaneous shear angle, Ψ, is defined:

$$\Psi = \tan^{-1}(v'/u'), \tag{3}$$

where u' and v' are instantaneous velocity fluctuations about the mean velocity. As this equation indicates, the shear angle is essentially the angle between the fluctuating velocity vector and the axial direction (assuming the swirl component of velocity is negligible). At each spatial location where LDV data were obtained, an ensemble of approximately 4000 shear angles $\{\Psi_i\}$ is determined. From this ensemble, discrete probability density functions (pdfs) can be generated which indicate the relative probability of Ψ_i falling within a range of angles, $\Psi_1 < \Psi_i \leq \Psi_1 + \Delta\Psi$, where $\Delta\Psi$ is the bin width of the pdf (taken as $4°$ in the present study). Figure 12 shows representative shear angle pdfs in the reattachment region of the present flow. Note that the shear angles in Fig. 12 are restricted to $-90° < \Psi_i < 90°$ to more clearly document pdfs with the necessarily limited size of each ensemble (i.e., much larger ensembles would be needed to obtain smooth pdfs over the entire $360°$ range). In the shear layer upstream of reattachment [Fig. 12(a)], a well-defined peak in the shear angle pdf is shown, which indicates a consistent orientation for the velocity fluctuations about the mean flow. This organization in the shear layer turbulence field is consistent with previous observations of large-scale turbulent structures in compressible shear layers, and is similar to that found in the present flowfield near the shear layer origin.[28] Note that the overwhelming majority of the velocity fluctuations yield negative shear angles which is indicative of dynamic events falling into quadrant 2 (Q2) or quadrant 4 (Q4). A Q2 event is generated by a slower moving ($u' < 0$) upward-oriented ($v' > 0$) fluid element relative to the local mean flow. Conversely, a faster moving ($u' > 0$) downward-oriented ($v' < 0$) fluid element generates a Q4 event. As Fig. 12 clearly shows, Q2 and Q4 events are the dominant physical processes in the shear layer throughout the reattachment region. It is also apparent from Fig. 12 that the organization of the turbulence field diminishes through reattachment. Although the shape of the pdf at the last measurement station [Fig. 12(c)] still resembles that upstream of recompression [Fig. 12(a)], the dominance of the peak at negative shear angles is no longer as strong. This behavior is consistent with the previous observation of significant reductions in the shear stress magnitude and correlation coefficient through the reattachment region as indicated in Figs. 6 and 11, respectively. Clearly, the large-scale structures present at the onset of recompression can negotiate the adverse pressure gradient associated with reattachment, but as a whole they lose strength and organization in the process.
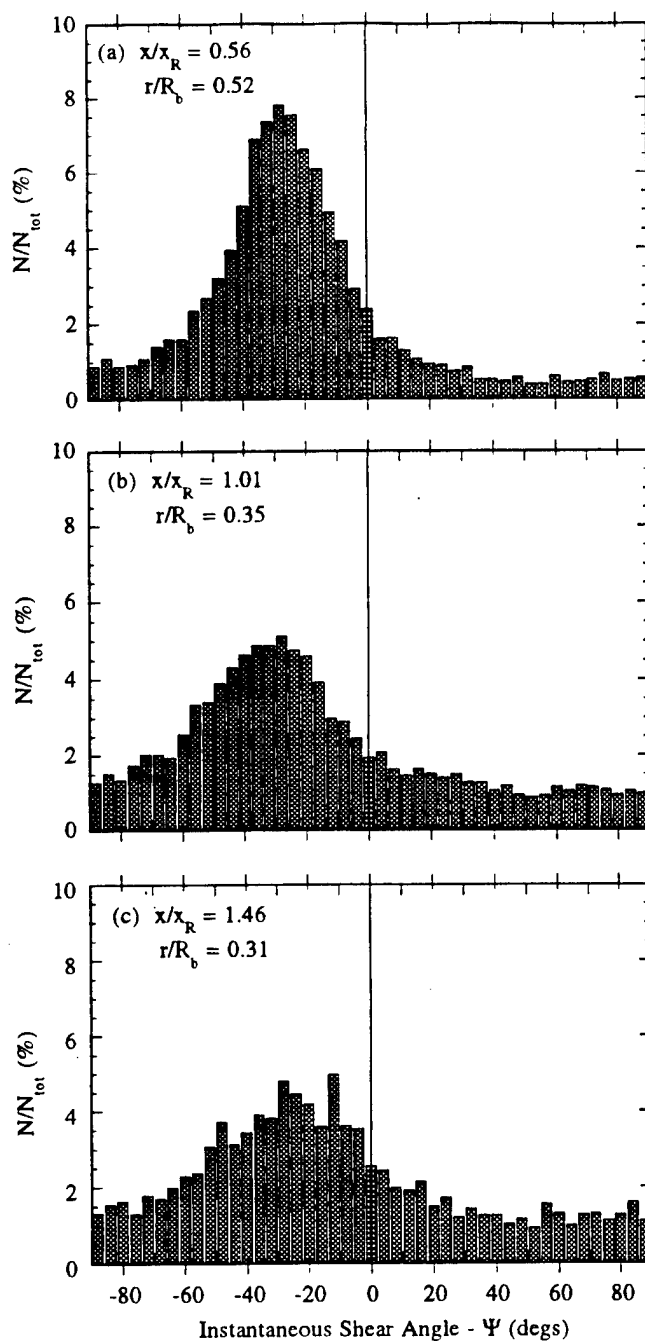
FIG. 12. Shear angle histograms near reattachment: (a) $x/x_R = 0.56$, (b) $x/x_R = 1.01$, (c) $x/x_R = 1.46$.

Due to space limitations, pdfs at only three spatial locations for the reattaching shear layer are shown in Fig. 12 (the radial locations correspond to those of peak shear stress for each axial location). Shear angle pdfs were also computed for several other locations in the shear layer along radial traverses at the same axial stations as the data in Fig. 12. By assuming that the overall degree of turbulence organization at any location is proportional to the peak value of the pdf, it is possible to make a two-dimensional comparison (axial and radial) of the overall effect of the reattachment process on the turbulence structure. Figure 13 presents such a comparison between the data upstream of reattachment (x/x_R

FIG. 13. Shear angle probability distributions upstream and downstream of reattachment.

$= 0.56$) and that obtained downstream of reattachment ($x/x_R = 1.46$). Radial profiles of the peak probability (in percent) of the pdf at each station are shown for each axial l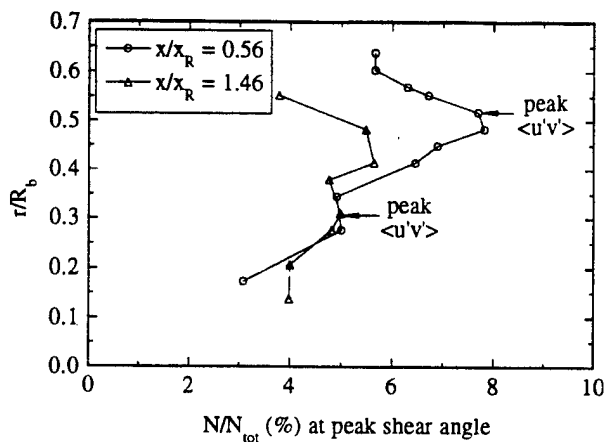ocation. In addition, the radial location of the local maximum total shear stress $\langle u'v' \rangle$ is also indicated for each profile. By comparing the two profiles in Fig. 13, it is apparent that the turbulence field upstream of reattachment is more organized over a large portion of the shear layer than that in the developing wake. Note that in the upstream shear layer, the probability profile in Fig. 13 forms a definite peak similar to that shown in Fig. 5 for the total shear stress profile and, as expected, is a maximum near the peak shear stress location. Not only is the probability profile downstream of the reattachment region of smaller magnitude than the peak levels in the upstream shear layer, but the peak probability also decreases in magnitude as the axis of symmetry is approached. Although somewhat inconclusive, due to limited data, it appears that the peak probabilities in the wake ($x/x_R = 1.46$) occur at radial distances beyond the peak shear stress location. The physical reasoning for this observation is not clear, but it suggests that the large-scale structures present in the wake flow, although weakened and less organized as a result of the reattachment process, are still present across a majority of the wake, particularly at larger radial positions, and play an important role in its subsequent development. Of course, as the mean shear rate ($\partial U/\partial r$) decays with downstream distance, one would expect the large-scale structures to continually weaken.

The shear angle analysis presented above considers only the angular orientation of the velocity fluctuations and, therefore, no information about the strength (magnitude) of the fluctuations at different stages in the reattachment process is provided. For this reason, a conditional quadrant sorting technique (sometimes referred to as a hole analysis) is utilized here to provide detailed information about the dynamic events that contribute most to the total shear stress magnitude. In this technique, the magnitude of the instantaneous product ($u'v'$) is compared to a preset threshold and subsequently sorted into a particular class of events. The sorting algorithm can be symbolically represented as follows:
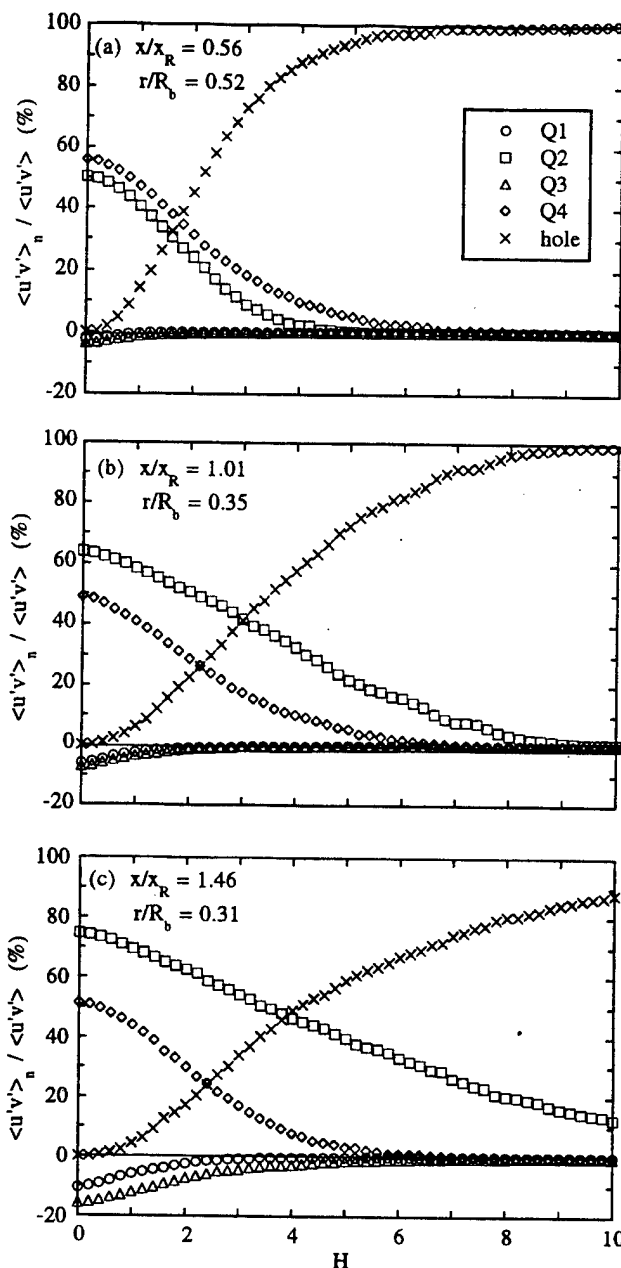
FIG. 14. Quadrant contributions to the total shear stress, $\langle u'v' \rangle$: (a) $x/x_R = 0.56$, (b) $x/x_R = 1.01$, (c) $x/x_R = 1.46$.

If $|u'v'| \leqslant H|\langle u'v' \rangle|$ then (hole)

$$\text{if } |u'v'| > H|\langle u'v' \rangle| \text{ then } Q1, Q2, Q3, \text{ or } Q4 \tag{4}$$

which indicates that ($u'v'$) realizations are placed in their respective quadrants if their magnitude exceeds the threshold; otherwise, they are placed in a fifth category called the hole which contains all of the "weak" velocity fluctuation products. The hole size is altered parametrically in the sorting process in order to determine which quadrant contains the strongest dynamic events in the flowfield.

Representative hole diagrams upstream ($x/x_R = 0.56$), at ($x/x_R = 1.01$), and after ($x/x_R = 1.46$) reattachment are shown in Fig. 14 for data at the local peak shear stress radial location. Note that the independent variable in these dia-

grams is the hole size (H) and the plotted variable is the percentage contribution of each quadrant and the hole region to the total shear stress. The quadrant values for $H = 0$ correspond to shear stress contributions in the absence of conditional sorting (i.e., vanishing hole region or conventional averaging). Upstream of reattachment [Fig. 14(a)], large and approximately equal contributions to the shear stress are indicated for Q2 and Q4 events with large instantaneous fluctuations of ($u'v'$) up to five times the ensemble-averaged value (i.e., shear stress contributions up to $H = 5$). Also, Q1 and Q3 events are shown to contribute very little to the total shear stress magnitude. The distributions shown in Fig. 14(a) are very similar to those presented previously[28] for the same shear layer near its origin (boundary layer separation point). At the shear layer reattachment point [Fig. 14(b)], however, the contribution from Q2 events exceeds that from Q4 events, and at the end of reattachment [Fig. 14(c)] a significant difference between the Q2 and Q4 contributions exists. By comparing all three plots in Fig. 14, it is apparent that the percentage contributions from Q4 events remain relatively constant throughout the reattachment process. It has been shown (Fig. 6) that the peak ensemble-averaged shear stress magnitude decreases sharply through reattachment [the conventionally averaged total shear stress $\langle u'v' \rangle$ for the data in Fig. 14(c) is at least three times smaller than that in Fig. 14(a)]. Therefore, Fig. 14 suggests that since the total contributions from Q4 events decrease at a rate nearly identical to that for the total shear stress, it is the attenuation of these events that plays a large role in the overall decrease of the Reynolds shear stress through reattachment. In contrast, the shear stress contribution from Q2 events increases *in percentage terms* through reattachment which implies a persistence of these events throughout the reattachment process. Notice that in the developing wake [Fig. 14(c)], large instantaneous Q2 fluctuations over ten times greater than the ensemble-averaged shear stress (i.e., $H > 10$) have been measured.

The obvious question that comes to mind after the preceding discussion is: what exactly are instantaneous Q2 and Q4 events in the shear layer and how are they related to the passage of large-scale turbulent structures? Considering the evolution of these structures, a Q4 event ($u' > 0, v' < 0$) is consistent with the influx (entrainment) of freestream fluid into the shear layer or wake as part of a clockwise eddy rollover process in the convective frame of reference. Conversely, a Q2 event ($u' < 0, v' > 0$) could correspond to the backside of a "typical" clockwise eddy that carries low-speed, turbulent fluid away from the centerline. It is understood that this description of Q2 and Q4 events is necessarily simplistic due to the complicating differences between incompressible planar mixing layers (where the dynamics of large-scale structures are better understood) and the current reattaching shear layer. However, by using these simplified descriptions, the decay in Q4 events relative to Q2 events through the reattachment region is consistent with a reduction in the entrainment of mass at the outside edge of the wake. In fact, the $\langle u'u'v' \rangle$ triple product profiles in Fig. 8 confirm the suspected loss in the

transport of turbulence energy toward the axis of symmetry in the wake region (axisymmetric containment effect), especially compared to that in the shear layer upstream of reattachment. In addition, the last axial station shown in Fig. 8 indicates that the overwhelming majority of the radial transport of turbulence energy in the wake is away from the axis, which is consistent with the quadrant decomposition analysis results discussed above.

IV. SUMMARY AND CONCLUSIONS

Experimental data on the turbulence structure of a reattaching supersonic axisymmetric shear layer have been presented. In contrast to the planar solid wall reattachment problem, the present work investigates reattachment onto the compliant boundary (i.e., no solid wall) at the axis of symmetry. Detailed mean velocity and turbulence measurements have been made throughout the reattachment region to document the overall effect of the many "extra" strain rates, including bulk compression, concave streamline curvature, and lateral streamline convergence. From these data, the following conclusions can be drawn:

(1) The Reynolds stress field throughout the reattachment zone is far different than that found in planar solid wall reattachment studies. In the present case, immediate reductions in the axial normal stress and primary shear stress are discernible at the onset of the adverse pressure gradient associated with reattachment. Downstream of the reattachment point, all Reynolds stresses decay as the mean shear rate decreases with downstream distance. These findings also indicate a significant difference between axisymmetric and two-dimensional reattachment flowfields most likely caused by the substantial effect of lateral streamline convergence near the axis of symmetry.

(2) The velocity triple products through the reattachment region indicate a containment of large-scale eddies along the centerline similar to that observed in subsonic, solid wall reattachment studies. This results in a relative decrease in the transport of turbulence energy toward the centerline downstream of reattachment. The reattachment effect on the streamwise transport of turbulence energy was minimal compared to that on the radial component.

(3) The axial-to-radial normal stress anisotropy ratio was strongly affected by the initial stages of the reattachment process, although shortly downstream of reattachment, relatively constant values were maintained. Throughout reattachment, the two secondary normal stresses (radial and tangential) maintained essentially equal magnitudes. Other turbulence structure parameters ($\langle u'v' \rangle / k$ and R_{uv}) showed significant reductions through reattachment which suggests a loss of organization of the large-scale, shear stress-producing structures.

(4) The results of a quadrant decomposition analysis of the turbulence data support the notion of decaying turbulent structures through the reattachment region. The overall organization of the velocity fluctuations is reduced in the wake relative to that in the shear layer approaching reattachment. In addition, a reduction in the strength of Q4 events ($u' > 0, v' < 0$) suggests reduced turbulence transport toward

the axis relative to that away from the axis in the developing wake, similar to that observed in the velocity triple product profiles.

ACKNOWLEDGMENTS

[1] V. Hohler and A. Stilp, "Penetration performance of segmented rods at different spacing-comparison with homogeneous rods at 2.5–3.5 km/s," *Proceedings of the 12th International Symposium on Ballistics* (American Defense Preparedness Association. San Antonio, Texas, 1990), Vol. III, pp. 178–187.

[2] H. H. Korst, "A theory for base pressures in transonic and supersonic flow," J. Appl. Mech. **78**, 593 (1956).

[3] J. K. Eaton and J. P. Johnston, "A review of research on subsonic turbulent flow reattachment," AIAA J. **19**, 1093 (1981).

[4] K. Hayakawa, A. J. Smits, and S. M. Bogdonoff, "Turbulence measurements in a compressible reattaching shear layer," AIAA J. **22**, 889 (1984).

[5] M. Samimy, H. L. Petrie, and A. L. Addy, "A study of compressible turbulent reattaching free shear layers," AIAA J. **24**, 261 (1986).

[6] B. Abu-Hijleh and M. Samimy, "An experimental study of a reattaching supersonic shear layer," AIAA Paper No. 89-1801 (1989).

[7] Z. H. Shen, D. R. Smith, and A. J. Smits, "Wall pressure fluctuations in the reattachment region of a supersonic free shear layer," Exp. Fluids **14**, 10 (1993).

[8] M. Samimy and A. L. Addy, "Interaction between two compressible, turbulent free shear layers," AIAA J. **24**, 1918 (1986).

[9] V. A. Amatucci, J. C. Dutton, D. W. Kuntz, and A. L. Addy, "Two stream, supersonic, wake flowfield behind a thick base, part 1: General features," AIAA J. **30**, 2039 (1992).

[10] K. M. Smith and J. C. Dutton, "Investigation of large-scale structures in supersonic planar base flows," AIAA J. **34**, 1146 (1996).

[11] J. L. Herrin, "An experimental investigation of supersonic axisymmetric base flows including the effects of afterbody boattailing," Ph.D. thesis, University of Illinois at Urbana-Champaign, Urbana, IL, 1993.

[12] J. L. Herrin and J. C. Dutton, "Supersonic near-wake afterbody boattailing effects on axisymmetric bodies," J. Spacecr. Rockets **31**, 1021 (1994).

[13] J. E. Bloomberg, "An investigation of particle dynamics effects related to LDV measurements in compressible flows," M.S. thesis, University of Illinois at Urbana-Champaign, Urbana, IL, 1989.

[14] M. Samimy and S. K. Lele, "Particle-laden compressible free shear layers," Phys. Fluids A **3**, 1915 (1991).

[15] J. L. Herrin and J. C. Dutton, "An investigation of LDV velocity bias correction techniques for high-speed separated flows." Exp. Fluids **15**, 354 (1993).

[16] S. G. Goebel, "An experimental investigation of compressible turbulent mixing layers," Ph.D. thesis, University of Illinois at Urbana-Champaign, Urbana, IL, 1990.

[17] P. Bradshaw, "The effect of mean compression or dilatation on the turbulence structure of supersonic boundary layers," J. Fluid Mech. **634**, 449 (1974).

[18] A. J. Smits, S. T. B. Young, and P. Bradshaw, "The effect of short regions of high surface curvature on turbulent boundary layers," J. Fluid Mech. **94**, 209 (1979).

[19] A. J. Smits, J. A. Eaton, and P. Bradshaw, "The response of a turbulent boundary layer to lateral divergence," J. Fluid Mech. **94**, 243 (1979).

[20] A. J. Smits and D. H. Wood, "The response of turbulent boundary layers to sudden perturbations," Annu. Rev. Fluid Mech. **17**, 321 (1985).

[21] C. Chandrsuda and P. Bradshaw, "Turbulence structure of a reattaching mixing layer," J. Fluid Mech. **110**, 171 (1981).

[22] V. A. Amatucci, "An experimental investigation of the two-stream, supersonic, near-wake flowfield behind a finite thickness base," Ph.D. thesis, University of Illinois at Urbana-Champaign, Urbana, IL, 1990.

[23] P. Bradshaw, "Effects of streamline curvature on turbulent flow," NATO AGARDograph No. 169, 1973.

[24] P. T. Harsha and S. C. Lee, "Correlation between turbulent shear stress and turbulent kinetic energy," AIAA J. **8**, 1508 (1970).

[25] J. M. Wallace, H. Eckelmann, and R. S. Brodkey, "The wall region in turbulent shear flow," J. Fluid Mech. **54**, 39 (1972).

[26] W. W. Willmarth and S. S. Lu, "Structure of the Reynolds stress near the wall," J. Fluid Mech. **55**, 65 (1972).

[27] S. S. Lu and W. W. Willmarth, "Measurements of the structure of the Reynolds stress in a turbulent boundary layer," J. Fluid Mech. **60**, 481 (1973).

[28] J. L. Herrin and J. C. Dutton, "Effect of a rapid expansion on the development of compressible free shear layers," Phys. Fluids **7**, 159 (1995).

APPENDIX A.9

TIME-SERIES ANALYSES OF WALL PRESSURE FLUCTUATIONS IN PLUME-INDUCED SEPARATED FLOWFIELDS

by

R. J. Shaw, J. C. Dutton, and A. L. Addy

TIME-SERIES ANALYSES OF WALL PRESSURE FLUCTUATION MEASUREMENTS MADE IN PLUME-INDUCED SEPARATED FLOWFIELDS

R.J. Shaw, Research Engineer
SY Technology, Inc.
Huntsville, Alabama 35806

J.C. Dutton, W. Grafton and Lillian B. Wilkins Professor
and
A.L. Addy, Professor Emeritus
Department of Mechanical and Industrial Engineering
University of Illinois at Urbana-Champaign
Urbana, Illinois 61801

ABSTRACT

The separation shock wave motion in a plume-induced, boundary layer separated flowfield was studied experimentally. The statistical properties of the shock wave motion were determined over the intermittent region using time-series analyses of wall static pressure fluctuation measurements. The standard deviation of the pressure fluctuations, nondimensionalized by the local mean pressure, reached a maximum of 0.22 near the middle of the intermittent region. The ratio of the maximum standard deviation of the pressure fluctuations over the intermittent region to the mean pressure difference across the intermittent region was calculated to be 0.43 for this flowfield. Both of these quantities demonstrate that the unsteady pressure loading caused by the shock wave motion has essentially the same magnitude in plume-induced separated flowfields as in flowfields produced by solid boundary protuberances.

INTRODUCTION

The phenomenon of plume-induced boundary layer separation (PIBLS) occurs on atmospheric flight vehicles when the boundary layer on the afterbody separates upstream of the base, rather than at the base, as a result of the exhaust plume expanding into and interacting with the external freestream. The unsteady separation shock wave motion, which is known to accompany the occurrence of plume-induced, turbulent boundary layer separation,[1] is a topic that has received little attention in the past and is the subject of the present investigation.

The only studies[2-4] of unsteady shock wave motion associated with plume-induced separation known to the authors were conducted with a wall-mounted, cone-cylinder-finned model in a variable Mach number (2.5 to 3.5) wind tunnel. A secondary jet of cold air, at an exit plane Mach number of 2.94 and an angle of 74° with respect to the freestream flow direction, exhausted from a conical nozzle near the aft-end of the model. The capability of pulsing the

1

plume was included in the wind tunnel model design to simulate combustion instabilities of liquid propellant engines. In summary, these studies[2-4] found a natural unsteadiness associated with the separation process in all of the PIBLS flowfields produced with the wind tunnel model (even in the absence of plume pulsing). Based upon measurements made from numerous schlieren movie frames, the unsteadiness associated with the separation process produced a length scale for the intermittent region that was on the order of a few boundary layer thicknesses. A sparsely distributed set of fast-response pressure transducer measurements was made across the intermittent region (i.e., the region of shock wave motion) and analyzed using standard time-series analysis techniques. A power spectral density estimate computed from one of the pressure-time histories suggested that the energy of the pressure fluctuations associated with the shock wave motion had a dominant characteristic frequency of approximately 100 Hz and was mostly contained below 1 kHz. The effect upon the separation shock wave motion of pulsing the plume flow at discrete frequencies over the range between 12.5 Hz and 1 kHz was minimal. Rather than the separation shock wave oscillating at the discrete pulsing frequency of the plume, the separation shock wave motions occurred over a wide frequency range regardless of the plume pulsing frequency.

In contrast to the unsteadiness found in shock wave/turbulent boundary layer interactions (SWBLIs) caused by a compliant aerodynamic boundary (PIBLS flowfields), unsteadiness in SWBLI flowfields produced by solid boundary protuberances has received a significant amount of attention over the past fifteen years.[5] Pressure fluctuation measurements have been made over the intermittent regions of SWBLI flowfields produced by compression ramps,[6-8] effectively semi-infinite circular cylinders,[9,10] sharp-edged fins at angles of attack,[11,12] and hemicylindrical blunt-edged fins at angles of attack.[13,14] The unsteady characteristics of the shock wave motion have been determined for these geometries by analyzing both individually and simultaneously acquired pressure-time histories with standard time-series analysis techniques and conditional analysis methods. Although quantitative differences in the unsteady characteristics of the separation shock wave motion exist for these four geometries, the

characteristics found in these interactions qualitatively show many similar features. The similarities include bimodal probability density function (PDF) estimates of the pressure fluctuation amplitudes over the intermittent region, streamwise distributions of the standard deviation of the pressure fluctuations that reach rather large (relative to the incoming boundary layer and the separated flowfield) maximum values near the middle of the intermittent region, and streamwise distributions of the skewness and kurtosis coefficients that reach rather large values near the upstream edge of the intermittent region. Also, in nominally two-dimensional or quasi-two-dimensional interactions, the power spectral density (PSD) estimates show that most of the energy contained in the pressure fluctuations caused by the shock wave motion is distributed over the frequency range between approximately 100 Hz and 1 kHz. The range of frequencies associated with the energy contained in the pressure fluctuations caused by the shock wave motion increases as the sweepback angle of the interaction increases for the compression ramp, circular cylinder, and blunt- and sharp-edged fin geometries.[15]

A two-part model that describes the physical mechanisms responsible for the unsteady separation shock wave motion in SWBLI flowfields has recently been hypothesized.[16] The model divides the separation shock wave motions into small-scale or "jittery" motions and large-scale or global motions. In the first part, the shock wave motions are caused by fluctuations (attributed to turbulence in the incoming boundary layer near the separation shock) in the ratio of static quantities across the shock foot. In the second part, the shock wave motions are caused by the expansions and contractions or "trembling motions" of the separated flow region. Thus, since the internal structure and dynamics of the separation bubble are unique to each type of geometry causing the SWBLI, it is not surprising that each geometry would have a set of unsteady shock wave characteristics with unique quantitative values.

As a result of these experimental studies,[6-15] the statistical characteristics of the separation shock wave motion in SWBLIs produced by solid boundary protuberances have been well documented. These studies have shown that the unsteady separation shock wave motion is responsible for some of the largest aerodynamic loads[17] and highest heat transfer rates[18] that

3

occur in high-speed flight. If the pressure fluctuations in PIBLS flows are similarly large, then the occurrence of PIBLS is indeed important because of the large aerodynamic loads and high heat transfer rates that would undoubtedly accompany the unsteady shock wave motion. However, no experimental measurements exist of these phenomena. Therefore, the objective of the current paper is to determine the unsteady characteristics of the separation shock wave motion in a PIBLS flowfield by analyzing surface pressure fluctuation measurements using standard time-series analysis techniques.

EXPERIMENTAL PROGRAM

Wind Tunnel Facility

The experiments were conducted in the Gas Dynamics Laboratory of the University of Illinois at Urbana-Champaign. A blowdown wind tunnel facility, which was specifically designed to produce plume-induced separated flowfields, was constructed for this investigation and is shown in Figure 1. Clean, dry, high-pressure air was supplied to the plenum chamber from a 146 m^3 capacity tank farm and two air compressors, while maintaining a constant stagnation pressure in the plenum chamber with an electro-pneumatic control valve installed in the air supply line. The plenum chamber fed two inlet pipes which, in turn, fed the two streams of the PIBLS wind tunnel test section.

A cross-sectional view along the centerline of the PIBLS wind tunnel test section is shown in the insert of Figure 1. The test section incorporates a two-dimensional planar geometry and produces two co-flowing, uniform, supersonic streams using fixed, converging-diverging, half-nozzles. A flowfield width of 50.8 mm was maintained in the test section from upstream of the nozzle blocks to downstream of the subsonic diffuser. A flow conditioning module, consisting of a honeycomb section and two screens, was installed upstream of each nozzle block. The Mach 1.5 lower stream (inner jet) impinged upon the Mach 2.5 upper stream (freestream) at a relative angle of 40° and across a 12.7 mm base height. Each test section inlet pipe contained a manually adjustable valve for independently regulating the stagnation pressure of each stream.

4

By adjusting the inner jet flow stagnation pressure, the boundary layer on the bottom wall of the freestream was induced to separate upstream of the base corner and thereby form a plume-induced separated flowfield in the test section. A glass window assembly mounted in each sidewall near the base region permitted optical access to the PIBLS flowfield, which was visualized using schlieren and shadowgraph techniques. The schlieren photo shown in Figure 2 clearly demonstrates that plume-induced, boundary layer separation occurs in the test section at a jet static pressure-to-freestream static pressure ratio (JSPR) of 2.35. When the schlieren (or shadowgraph) light source was operated in the continuous mode, the separation shock wave was clearly seen to undergo streamwise translations at all JSPRs of tunnel operation.

Flow Conditions

The stagnation pressure of each stream was measured with a stagnation pressure probe mounted upstream of each nozzle block, and the stagnation temperature was measured with an iron-constantan thermocouple mounted in the plenum chamber. The data reduction assumed adiabatic flow conditions. The stagnation temperature was 298 K ($\pm$1.5 K). In the freestream, the stagnation pressure was 503 kPa ($\pm$1.5 kPa) and the unit Reynolds number was 47.1 x 10^6 m^{-1} ($\pm$0.5 x 10^6 m^{-1}). The Mach number in this freestream was computed from static pressure measurements made using pressure taps mounted in the lower wall and was found to be 2.50 ($\pm$0.01) at a location 30 mm upstream of the base plane. Similarly, the Mach number of the inner jet was computed to be 1.51 ($\pm$ 0.01) at a location 12.7 mm upstream of the base plane.

One-component laser Doppler velocimeter (LDV) measurements were made along a vertical centerline traverse across the height of the freestream flow 30 mm upstream of the base plane. From these LDV measurements, the streamwise turbulence intensity was found to be 0.015 $\pm$ 10% across the uniform flow region of the freestream. From the mean velocity measurements made in the boundary layer adjacent to the lower wall of the freestream, a wall-wake velocity profile was curve fit to the experimental velocity data using the method of Sun and Childs.[19] The details of the procedure are given in Ref. 20. The incoming turbulent boundary layer

properties were determined from the Sun and Childs curve fit and are reported in Table 1. The boundary layer properties given in Table 1 generally compare favorably with other equilibrium turbulent boundary layer properties reported in the literature for similar Mach number and Reynolds number conditions.[20] While the wake strength parameter may be a bit high, Fernholz and Finley[21] suggest that a universal value of Π applicable to all equilibrium turbulent boundary layers may not exist for compressible flows due to upstream history effects.

Instrumentation

Instantaneous wall-pressure fluctuations were measured using two piezoresistive pressure transducers that were flush-mounted and spanwise-centered in the lower wall of the freestream. The upstream and downstream pressure transducers were located 19.1 mm and 16.5 mm upstream of the base plane, respectively. The pressure transducers were Kulite model XCS-062-15G transducers, which had an input pressure range of 103.4 kPa and a nominal full-scale output of 200 mV. Each transducer was configured to operate in the gage mode; i.e., the transducer produced an output voltage proportional to the pressure difference across the diaphragm. The back side of the diaphragm was referenced to the static pressure of the freestream. Each transducer diaphragm had an active diameter of 0.71 mm; the diaphragm natural frequencies were measured to be 168 and 198 kHz for the upstream and downstream transducers, respectively.[20] The transducers were statically calibrated since shock tube experiments[22] with similar transducers have shown that statically calibrated transducer responses are within a few percent of dynamically calibrated transducer responses. The calibration was performed in situ with a Sensotec model AG-300 digital pressure gage equipped with a 206.8 kPa pressure transducer accurate to within ± 103.4 Pa.

The analog output signal from each pressure transducer was amplified with a Measurements Group model 2311 signal conditioning amplifier and then low-pass filtered using an in-house built, active Butterworth filter circuit. The amplifier also supplied the 15 volt DC excitation source and the appropriate DC offset voltage to the transducer bridge. The amplifier had a

continuously variable output voltage gain, which ranged between 25 and 30 for all of the intermittent region measurements, and a -3 dB cutoff frequency of 125 kHz on the wide-band output filter setting (used in all the experiments described herein). The three-stage, six-pole, in-house built filter had a fixed voltage gain of 4.3, a -3 dB cutoff frequency of 50 kHz, and an attenuation of -36 dB/octave in the transition band. The output signal from the low-pass filter was digitized with a National Instruments model NB-A2000 analog-to-digital converter installed in an Apple Macintosh IIfx computer. Each channel of the A/D converter was equipped with track-and-hold circuitry, and had an input voltage range of ±5 volts and 12-bit resolution. Before every calibration, the voltage gain and DC offset voltage settings on each amplifier were adjusted to maximize the signal-to-noise ratio of the output signal. For the intermittent region measurements, this procedure was done at the largest JSPR used in each set of experiments. The rms signal-to-noise ratios for the pressure fluctuation measurements varied from 15 to 20 in the incoming boundary layer and from 55 to 300 over the intermittent region.

In addition to the two Kulite pressure transducers, 29 static pressure taps were installed in the lower wall adjacent to the freestream. The static pressure ports were 0.64 mm in diameter and were normal to the local surface along a single spanwise plane offset 4.78 mm from the centerline. Twenty-three static pressure ports were uniformly spaced every 1.6 mm beginning at 3.18 mm upstream of the base plane and extending to 38.1 mm upstream of the base plane. The remaining six static pressure ports were uniformly spaced every 6.35 mm starting at 42.9 mm upstream of the base plane. The mean pressure at each static pressure port was measured with a Pressure Systems model DPT-6400T digital pressure transmitter and stored on a Gateway 2000 486-33 computer. Each static pressure tap was connected to a 0-103.4 kPa pressure transducer mounted in the DPT-6400T using a piece of flexible vinyl tubing approximately 1.5 m long. Also, the stagnation pressure probe used to sense the stagnation pressure in each stream was connected, in the same manner, to a 0-689.5 kPa pressure transducer mounted in the DPT-6400T instrument. The pressure transducers in the DPT-6400T were calibrated with a Consolidated Electrodynamics Type 6-201-0001 dead-weight tester.

Data Acquisition

The two Kulite pressure transducers were rigidly mounted in the test section of the PIBLS wind tunnel. With the pressure transducer locations fixed, the JSPR was varied in order to move the intermittent region over the transducers. In these experiments, the JSPR was varied by unthrottling the stagnation pressure of the inner jet from 210 kPa to 269 kPa in increments of roughly 3.4 kPa.

Instantaneous wall-pressure fluctuation measurements were made throughout the intermittent region by sampling the two pressure transducers. At each JSPR, the individually sampled pressure transducer measurements were made by sampling the upstream transducer for 24 seconds at a rate of 166,667 samples/second and then sampling the downstream transducer for 24 seconds at the same rate. Mean static pressure measurements from the pressure taps in the lower wall of the freestream were also made in conjunction with the individually sampled pressure transducer measurements.

ANALYSIS TECHNIQUES

All statistical quantities presented herein were computed using the time-series analysis techniques recommended by Bendat and Piersol.[23] In addition, a conditional analysis method, the two-threshold method box-car conversion (TTMBCC) algorithm,[24] was employed to determine the intermittency (the percentage of time the shock wave was upstream of a given pressure transducer). Before discussing the results from either the remote (DPT-6400T) or in situ (Kulite) pressure measurements, several comments about the TTMBCC algorithm are appropriate.

The TTMBCC algorithm was developed by Dolling and colleagues[24-26] at the University of Texas at Austin. As the name suggests, the algorithm employs two threshold levels, $Th_1 = \bar{p}_{wo} + 3\sigma_{p_{wo}}$ and $Th_2 = \bar{p}_{wo} + 6\sigma_{p_{wo}}$, where $\bar{p}_{wo}$ is the mean pressure of the incoming boundary layer and $\sigma_{p_{wo}}$ is the rms of the pressure fluctuations in the incoming boundary layer.

By comparing each individual pressure realization in a pressure-time history to the two threshold levels, the instantaneous location of the separation shock wave can be determined as being either upstream or downstream of the pressure transducer. The precise time (to within the sampling period) when the shock wave crosses upstream of the pressure transducer, called the rise time, and downstream of the pressure transducer, called the fall time, can be determined for all shock wave passages in the pressure-time history. The intermittency is then calculated from

$$\gamma = \frac{\displaystyle\sum_{k=1}^{N_{sc}}(\text{Fall}_k - \text{Rise}_k)}{\text{Fall}_{N_{sc}} - \text{Rise}_1} \tag{1}$$

where Fall_k is the fall time associated with the k-th downstream shock wave crossing, Rise_k is the rise time associated with the k-th upstream shock wave crossing, and N_{sc} is the total number of fall times detected in the pressure-time history.

The intermittency calculations performed in the current study used, without any significant changes, the updated version of the TTMBCC algorithm.[26] A sensitivity analysis of the TTMBCC algorithm was performed with the PIBLS data[20] in order to evaluate the change in magnitude of the zero-crossing frequency (i.e., the average number of shock wave crossings per second) to different threshold level settings. After comparing the results from the sensitivity analysis performed on the PIBLS data to the results from the sensitivity analysis performed on Mach 5 circular cylinder interaction data,[25] it was concluded that the optimal settings for Th_1 and Th_2 given above were also reasonable choices for conditionally analyzing the data from the PIBLS flowfield experiments.[20]

We also note that by normalizing the rms of the pressure fluctuations in the incoming boundary layer with respect to the wall shear stress and freestream dynamic pressure, the values $\sigma_{p_{wo}}/\tau_w = 3.30$ and $\sigma_{p_{wo}}/q_\infty = 0.0044$ are obtained. These are consistent with previous studies of supersonic turbulent boundary layers.[20]

9

RESULTS

Results from the remote and in situ pressure transducer measurements will be presented and discussed in the following sections. Although the lower stream stagnation pressure, or the JSPR, was the actual independent variable in the experiments, some of the results will be presented as a function of intermittency rather than JSPR. A plot of intermittency versus JSPR over the intermittent region is shown in Figure 3 for both the upstream and downstream individually sampled transducer measurements. While the downstream transducer measurements spanned the intermittent region from $\gamma = 3.9\%$ to $\gamma = 96.2\%$ over a range of JSPR from 1.95 to 2.41, the upstream transducer measurements spanned the intermittent region from $\gamma = 3.8\%$ to $\gamma = 98.3\%$ over a range of JSPR from 2.05 to 2.49.

Mean Pressure Measurements

At each JSPR shown in Figure 3, four mean pressure data sets were acquired with the DPT-6400T transmitter under identical wind tunnel operating conditions. The four data sets were then averaged and the result is reported as the mean pressure distribution along the lower wall of the freestream. Figure 4 shows the mean static pressure distribution at five strategic JSPRs. Each distribution is plotted in terms of absolute pressure versus distance from the base plane, X. The X-axis is assumed to be positive in the downstream direction and X = 0 is at the base plane. Each of the mean static pressure distributions is labeled with the appropriate JSPR and the intermittency computed from the downstream pressure transducer measurements. Also, the mean pressures determined from the upstream and downstream in situ pressure transducer measurements (labeled as "Kulites" in the figure caption) are shown in Figure 4.

In addition to spanning the intermittent region, each of the streamwise mean static pressure distributions shown in Figure 4 also includes part of the incoming boundary layer and part of the separated flowfield downstream of the intermittent region. All of the distributions show that the mean pressure level of the incoming turbulent boundary layer is constant at approximately 29.6 kPa over the JSPR range from 1.95 to 2.41. The location where the mean static pressure first

10

rises above the mean pressure level of the incoming turbulent boundary layer, called the line of upstream influence, moves further upstream of the base plane as the JSPR increased from 1.95 to 2.41, as expected. The mean static pressure level in the separated flowfield was not constant over this JSPR range, nor was the mean static pressure distribution over the separated flowfield constant at any JSPR. Fully separated flow existed immediately downstream of the downstream pressure transducer location at a JSPR of 2.41; the mean pressure distribution for this case shows that a significant adverse pressure gradient existed in the separated flowfield. Based upon the other mean static pressure distributions shown in Figure 4, a significant adverse mean pressure gradient existed in the separated flowfield at other JSPR settings as well.

The mean pressure measured with the two in situ pressure transducers was observed to be slightly lower than the mean pressure measured with the static pressure taps over most of the intermittent region. This discrepancy is a well-known problem[27] in wind tunnel experiments involving unsteady pressure fields and exists because of pneumatic resonance effects that occur within the large length/diameter tubing connecting the remote pressure transducers to the static pressure taps. The mean pressures computed from the static taps were, at worst, no more than 10% larger than the mean pressures calculated from the in situ pressure transducers over the intermittent region. Since the mean pressure from the static pressure tap measurements was within approximately 1% of the mean pressure determined from the in situ pressure transducer measurements in both the low ($\gamma < 5\%$) and high ($\gamma > 95\%$) intermittency ranges, the mean pressure can be determined from the static pressure tap measurements near the line of upstream influence and near the separation line. This fact, when combined with the fast-response pressure transducer measurements and oil-streak visualization images, was used to estimate the length of the intermittent region.[20] With the intermittent region defined to exist between the $\gamma = 4\%$ and $\gamma = 96\%$ locations for any JSPR, the length of the intermittent region was estimated as 8.1-9.4 mm ($2.6\delta_0$-$3.0\delta_0$) and 17.3-17.5 mm ($5.4\delta_0$-$5.5\delta_0$) at JSPRs of 1.95 and 2.41, respectively. Thus, as the JSPR increased from 1.95 to 2.41, not only did the intermittent region become

11

longer, but the separated flow region also became longer and, in so doing, pushed the intermittent region further upstream.

PDFs of the Pressure Fluctuation Amplitudes

PDF estimates of the pressure fluctuation amplitudes were calculated at each JSPR for the upstream and downstream pressure transducer measurements. The trends in the PDF estimates over the intermittent region were similar for the upstream and downstream transducer data. Figure 5 shows PDF estimates of the pressure fluctuation amplitudes calculated from the downstream pressure transducer measurements in the incoming turbulent boundary layer, across the intermittent region at the same five JSPRs as Figure 4, and in the fully separated region at a JSPR of 2.52. Each of the PDF estimates is plotted in terms of $N_i/(N_t*W)$ versus pressure where N_i is the number of pressure realizations occurring with a value of $p_i \pm W/2$, N_t is the total number of pressure realizations in the pressure-time history, and W is the interval width of the PDF estimate centered at p_i (W = 172 Pa). Also shown in Figure 5 is the equivalent Gaussian PDF (with the same mean and standard deviation as the actual PDF) for each of the seven estimates.

The actual PDFs were essentially Gaussian distributions in the incoming boundary layer and in the fully separated region downstream of the intermittent region. The width of the PDF was much larger for the fully separated region at a JSPR of 2.52 than for the incoming boundary layer, indicating that the pressure fluctuation amplitudes were larger in the fully separated region than in the boundary layer.

The actual PDF was strongly skewed from its equivalent Gaussian distribution at each JSPR over the intermittent region. At low intermittency values ($\gamma < 25\%$), only a single visible peak was present in the actual PDF and the maximum probability associated with this peak occurred at approximately 29.6 kPa. The cause of the peak was clearly the pressure fluctuations present in the incoming turbulent boundary layer. Although not enough pressure fluctuations from the separated flowfield downstream of the shock wave were present to visibly skew the actual PDF

into a bimodal shape at these JSPRs, the equivalent Gaussian PDF was widened noticeably beyond the width of the actual PDF peak caused by the incoming turbulent boundary layer. This was because the pressure fluctuations that were present from the separated flowfield increased the standard deviation computed from the pressure-time history considerably above the incoming turbulent boundary layer value (at $\gamma = 3.9\%$, $\sigma_{p_w}/\sigma_{p_{wo}}$ was 2.4).

As the intermittency increased ($\gamma > 25\%$), the shock wave spent more time upstream of the pressure transducer and enough pressure fluctuations from the separated flowfield were present to visibly skew the actual PDF into a bimodal distribution. The second peak that formed in the actual PDF occurred at a higher pressure level than the peak caused by the incoming turbulent boundary layer and occurred at a pressure level that depended upon the JSPR. This trend of the second peak occurring at a higher pressure as the JSPR was increased is consistent with the results found from the streamwise mean pressure distribution measurements made with the static pressure taps along the lower wall of the freestream. Thus, the cause of the second peak in the actual PDF was clearly the pressure fluctuations present in the separated flowfield downstream of the instantaneous shock wave location. In SWBLI studies produced by solid protuberances,[7,8] PDF estimates of the pressure fluctuation amplitudes across the intermittent region were also found to be strongly skewed from equivalent Gaussian distributions and to exhibit the same bimodal nature as found in the current PIBLS experiments.

Higher-Order Moments

The first four moments (mean, variance, skewness, and kurtosis) were computed for each pressure-time history in the upstream and downstream pressure transducer data sets. For each moment, the data from both pressure transducers collapsed on each other over the entire intermittent region when plotted against intermittency.

The mean wall pressure, $\bar{p}_w$, is shown in Figure 6. The mean wall pressure continuously increased over the intermittent region from an incoming turbulent boundary layer pressure of 29.6 kPa at $\gamma = 0\%$ to an extrapolated pressure of 52.4 kPa at $\gamma = 100\%$. The mean pressure

13

increased in a nonlinear manner over the intermittent region because the pressure level increased in the separated flowfield and the region of separated flow extended further upstream as the JSPR increased.

The standard deviation of the pressure fluctuations (σ_{p_w}), nondimensionalized by the local mean pressure, is shown in Figure 7. From a second order polynomial equation that was least-squares curve fit to each experimental data set (shown as lines in Figure 7), $\sigma_{p_w}/\bar{p}_w$ reached a maximum value of 0.22 at $\gamma = 55\%$.

The occurrence of a local maximum in the rms pressure distribution over the intermittent region is a characteristic found in all separated SWBLI flowfields that contain unsteady shock wave motion. For unswept compression ramps at Mach 3, maximum values of $\sigma_{p_w}/\bar{p}_w$ were found to be 0.20 $(\delta_0 = 22$ mm) and 0.18 $(\delta_0 = 12$ mm) for a 24° ramp,[6] and 0.15 $(\delta_0 = 22$ mm) and 0.11 $(\delta_0 = 22$ mm) for a 20° and 16° ramp,[7] respectively. The maximum value of $\sigma_{p_w}/\bar{p}_w$ for a 28° unswept compression ramp interaction at Mach 5[9] was found to be 0.34. Dolling and Smith[10] reported maximum values of $\sigma_{p_w}/\bar{p}_w$ between 0.25 and 0.28 for circular cylinders at Mach 5, while Dolling and Bogdonoff[13] reported values ranging between 0.18 and 0.29 for hemicylindrical blunt fins at Mach 3. Thus, the maximum $\sigma_{p_w}/\bar{p}_w$ value of 0.22 for the PIBLS experiments at Mach 2.5 are within the range of values found in other SWBLI flowfields.

The strength of the unsteady shock wave motion, defined as $\sigma_{p_w,max}/\Delta P_{shock}$ (where ΔP_{shock} is the mean static pressure difference across the intermittent region, $\Delta P_{shock} = \bar{p}_{w,\gamma=96\%} - \bar{p}_{wo}$), for the PIBLS flowfield measurements was calculated to be 0.43. The strengths of the unsteady shock wave motion in compression ramp, circular cylinder, and blunt- and sharp-edged fin interactions[15] are plotted as $\sigma_{p_w,max}/\Delta P_{shock}$ versus sweepback angle in Figure 8 along with the results from the current PIBLS wind tunnel experiments. In Figure 8, all the results for the unswept cases[15] are offset to a sweepback angle of -1°, and the results from the PIBLS wind tunnel experiments are offset to a sweepback angle of +1° for clarity. The mean value of $\sigma_{p_w,max}/\Delta P_{shock}$ for all three solid protuberance geometries and all sweepback angles

14

was 0.46. Thus, the strength of the separation shock wave motion was essentially the same in the PIBLS flowfield as in the SWBLI flowfields produced by solid geometries.

Although not shown here due to length constraints (see Ref. 20), the skewness coefficient, α_3, and kurtosis coefficient, α_4, have also been computed for this PIBLS interaction. Both coefficients are noteworthy because of the large maximum values they attain near the line of upstream influence ($\alpha_3 = 5.9$ and $\alpha_4 = 62.8$ at $\gamma = 1.4\%$). A large maximum value of α_3 near the line of upstream influence is a characteristic that has been observed in many SWBLI experiments involving solid protuberances. The maximum value of α_3 near the line of upstream influence ranged between 8 and 10 for circular cylinder interactions[10] at Mach 5, between 7 and 8 for unswept compression ramp interactions[6,7] at Mach 3, and between 6 and 8 for hemicylindrical blunt fin interactions[13] at Mach 3. No maximum values for α_4 have been reported in the literature.

PSD Estimates of the Pressure Fluctuations

For a pressure-time history, $p(t)$, in which the time history is divided into n_d contiguous segments and each segment contains N data values ($p_{i,n}$; $n = 0,1,...,N-1$ and $i = 1,2,...,n_d$), the one-sided power spectral density function is estimated by

$$G_{pp}(f_k) = \frac{2}{n_d N \Delta t} \sum_{i=1}^{n_d} |P_i(f_k)|^2 \qquad k = 0,1,...,N/2 \qquad (2)$$

where Δt is the time between consecutive pressure realizations in $p(t)$ and the discrete fast Fourier transform (FFT) components for each segment are given by

$$P_i(f_k) = \Delta t \sum_{n=0}^{N-1} p_{i,n} \exp\left[\frac{-j2\pi kn}{N}\right] \qquad (3)$$

at the discrete frequencies $f_k = k/(N*\Delta t)$ $k = 0,1,...,N-1$.

For the purposes of computing the PSD estimates reported herein, each pressure-time history was divided into 488 contiguous segments ($n_d = 488$) having 8192 pressure realizations (N = 8192) in each segment. The frequency resolution of the PSD estimates (Δf) is given by

$\Delta f = 1/(N*\Delta t)$ to be 12.2 Hz, and the normalized random error of the PSD estimates (ε_r) is given by $\varepsilon_r = 1/\sqrt{n_d}$ to be 4.5%. PSD estimates of the pressure fluctuations computed from the downstream pressure transducer measurements are shown in Figure 9 for the incoming boundary layer upstream of the intermittent region, for the intermittent region at five strategic JSPRs, and for the separated flowfield downstream of the intermittent region at a JSPR of 2.55. The PSD estimates shown in Figure 9 are plotted as $G_{pp}(f)*f/\sigma_{p_w}^2$ versus f in a linear-log format. Each PSD estimate was normalized by the variance of the pressure-time history. Although this normalization was beneficial for comparison purposes, care must be taken when examining the magnitude of the normalized PSD estimates for the incoming boundary layer and the separated region because the variance of the pressure fluctuations (due to turbulence) in these two flow regimes may be underestimated due to frequency response limitations of the pressure transducers. Remember, however, that it is the pressure fluctuations caused by the much lower frequency separation shock wave motion (at intermediate intermittencies) that are of primary interest here.

The PSD estimate of the pressure fluctuations in the incoming boundary layer was dominated by frequency components below a few hundred Hz. Except for a disturbance centered at 387 Hz (which was found to be caused by the somewhat abrupt geometrical transition between the plenum chamber and the wind tunnel inlet pipes), these pressure fluctuations were not caused by physical disturbances in the boundary layer but were due to resonance effects associated with the reference port passageway of the pressure transducer. Although the pressure fluctuations caused by resonance in this passageway dominate the PSD estimate in the incoming boundary layer, these pressure fluctuations are small compared to the pressure fluctuations due to shock wave crossings that appear in the pressure-time histories across the intermittent region and, therefore, these pressure fluctuations have no effect on the PSD estimates across the intermittent region.

The PSD estimates computed for the pressure-time histories taken from the intermittent region showed that most of the energy in the pressure fluctuations was concentrated over the frequency range between about 100 Hz and a few thousand Hz. For pressure fluctuations above

10 kHz, the PSD estimates contained no significant energy until the highest intermittencies (e.g., $\gamma = 96.7\%$) were reached. The energy of the pressure fluctuations taken from the fully separated flowfield was distributed uniformly over a frequency range between a few hundred Hz and 50 kHz (the cutoff frequency of the analog filter). This change in the PSD distribution occurred because the PSD estimates taken from the intermittent region were dominated by the large pressure fluctuations caused by the separation shock wave translating over the pressure transducer, while the PSD estimate from the fully separated region contains high-frequency pressure fluctuations caused by turbulence in the shear layer and separated region. Thus, the PSD estimates from the intermittent region of the PIBLS flowfield show that the frequency of the shock wave motion was broadband with most of the energy occurring over a frequency range from approximately 100 Hz to a few thousand Hz, depending upon the exact location within the intermittent region.

The energy of the pressure fluctuations acquired from the intermittent region of unswept compression ramp interactions[7,8] was also distributed over the frequency range from a few hundred Hz to a few thousand Hz. Although the PSD estimates for the various ramp angles (16° to 28°) had the same basic broadband shape, the dominant center frequency of the spectral distribution was dependent upon the ramp angle. The center frequency decreased as the ramp angle increased. The center frequency was approximately 1,000 Hz for a 16° ramp angle, 500 to 1,800 Hz for a 20° ramp angle, and 200 to 500 Hz for 24° and 28° ramp angles. Thus, the spectral characteristics of the energy in the pressure fluctuations from the intermittent region of the PIBLS flowfield were very similar to the spectral characteristics of the unswept compression ramp interaction at the larger ramp angles of 24° and 28°.

CONCLUSIONS

The unsteady characteristics of the separation shock wave motion in a plume-induced separated flowfield were determined from pressure measurements made with in situ and remote pressure transducers over the jet static pressure ratio range from 1.95 to 2.55. Time-series

analysis techniques were applied to the pressure fluctuation measurements taken from upstream, across, and downstream of the intermittent region. The PDF estimates of the pressure fluctuation amplitudes computed from the intermittent region were highly skewed from the equivalent Gaussian distributions and typically were bimodal in character at intermittencies greater than approximately 25%. The maximum value of $\sigma_{p_w}/\overline{p}_w$ over the intermittent region was found to be 0.22 at $\gamma = 55\%$, and the strength of the unsteady shock wave motion (defined as $\sigma_{p_w,max}/\Delta P_{shock}$) for these experiments was calculated to be 0.43. Power spectral density estimates from the intermittent region show that the frequency of the shock wave motion was broadband with most of the energy occurring over a frequency range from approximately 100 Hz to a few thousand Hz.

In conclusion, many of the statistical properties computed for this plume-induced separated flowfield were qualitatively similar to the statistical properties computed for two-dimensional shock wave-boundary layer interaction flowfields produced by solid geometries. This is true even though the size of the separated region is much larger for this plume-induced separated flow than for solid boundary-induced separation and although the PIBLS separated region is enclosed by two fluid dynamically compliant shear layers rather than by a solid boundary and a single shear layer. Perhaps these observations will help shed some light on the source of the large-scale unsteadiness mechanisms in shock wave-boundary layer interactions. In any event, it is clear that the unsteady separation process that can accompany the occurrence of plume-induced, boundary layer separation in high-speed flight is important because of the large aerodynamic loads that occur over a broad frequency range.

ACKNOWLEDGMENTS

REFERENCES

[1] Jones, J.H., "Acoustic Environment Characteristics of the Space Shuttle," *Space Transportation System Technology Symposium*, NASA Lewis Research Center, Cleveland, Ohio, NASA TM X-52876, Volume 2-Dynamics and Aeroelasticity, 1970, pp. 285-300.

[2] Boggess, A.L., "An Investigation of the Unsteady Flow Associated with Plume Induced Flow Separation," University of Alabama, Bureau of Engineering Research, Report No. 149-02, Tuscaloosa, AL, 1972.

[3] Doughty, J.O., "Effects of Periodic Plume Pulsing on the Flow Field Generated by Plume Induced Flow Separation," University of Alabama, Bureau of Engineering Research, Report No. 164-02, Tuscaloosa, AL, 1973.

[4] Doughty, J.O., "A Study of a Plume Induced Separation Shock Wave, Including Effects of Periodic Plume Unsteadiness," University of Alabama, Bureau of Engineering Research, Report No. 207-02, Tuscaloosa, AL, 1976.

[5] Dolling, D.S., "Unsteadiness of Shock-Wave Induced Turbulent Boundary-Layer Separation - a Review," *Turbulent Shear-Layer/Shock-Wave Interactions*, edited by J. M. Délery, Springer-Verlag, Berlin, 1986, pp. 341-357.

[6] Dolling, D.S. and Murphy, M.T., "Unsteadiness of the Separation Shock Wave Structure in a Supersonic Compression Ramp Flowfield," *AIAA Journal*, Vol. 21, No. 12, 1983, pp. 1628-1634.

[7] Dolling, D.S. and Or, C.T., "Unsteadiness of the Shock Wave Structure in Attached and Separated Compression Ramp Flows," *Experiments in Fluids*, Vol. 3, 1985, pp. 24-32.

[8] Erengil, M.E. and Dolling, D.S., "Effects of Sweepback on Unsteady Separation in Mach 5 Compression Ramp Interactions," *AIAA Journal*, Vol. 31, No. 2, 1993, pp. 302-311.

[9] Gramann, R.A. and Dolling, D.S., "Detection of Turbulent Boundary-Layer Separation Using Fluctuating Wall Pressure Signals," *AIAA Journal*, Vol. 28, No. 6, 1990, pp. 1052-1056.

[10] Dolling, D.S. and Smith, D.R., "Separation Shock Dynamics in Mach 5 Turbulent Interactions Induced by Cylinders," *AIAA Journal*, Vol. 27, No. 12, 1989, pp. 1698-1706.

[11] Gibson, B.T. and Dolling, D.S., "Exploratory Study of Wall Pressure Fluctuations in a Mach 5, Sharp Fin-Induced Turbulent Interaction," *AIAA Journal*, Vol. 30, No. 9, 1992, pp. 2188-2195.

[12] Schmisseur, J.D. and Dolling, D.S., "Fluctuating Wall Pressures near Separation in Highly Swept Turbulent Interactions," *AIAA Journal*, Vol. 32, No. 6, 1994, pp. 1151-1157.

[13]Dolling, D.S. and Bogdonoff, S.M., "An Experimental Investigation of the Unsteady Behavior of Blunt Fin-Induced Shock Wave Turbulent Boundary Layer Interactions," AIAA Paper 81-1287, 1981.

[14]Brusniak, L. and Dolling, D.S., "Flowfield Dynamics in Blunt Fin-Induced Shock Wave Turbulent Boundary-Layer Interaction," AIAA Paper 93-3133, 1993.

[15]Gonsalez, J.C. and Dolling, D.S., "Correlation of Interaction Sweepback Effects on the Dynamics of Shock-Induced Turbulent Separation," AIAA Paper 93-0776, 1993.

[16]Erengil, M.E. and Dolling, D.S., "Physical Causes of Separation Shock Unsteadiness in Shock Wave / Turbulent Boundary-Layer Interactions," AIAA Paper 93-3134, 1993.

[17]Dolling, D.S., "Fluctuating Loads in Shock Wave/Turbulent Boundary Layer Interaction: Tutorial and Update," AIAA Paper 93-0284, 1993.

[18]Aso, S., Tan, A., and Hayashi, M., "The Structure of Aerodynamic Heating in Three-Dimensional Shock Wave/Turbulent Boundary Layer Interactions Induced by Sharp and Blunt Fins," AIAA Paper 89-1854, 1989.

[19]Sun, C.C. and Childs, M.E., "A Modified Wall Wake Velocity Profile for Turbulent Compressible Boundary Layers," *Journal of Aircraft,* Vol. 10, No. 6, 1973, pp. 381-383.

[20]Shaw, R.J., "An Experimental Investigation of Unsteady Separation Shock Wave Motion in a Plume-Induced, Separated Flowfield," Ph.D. dissertation, Dept. of Mechanical and Industrial Engineering, University of Illinois at Urbana-Champaign, Oct. 1995.

[21]Fernholz, H.H. and Finley, P.J., "A Critical Commentary on Mean Flow Data for Two-Dimensional Compressible Turbulent Boundary Layers," AGARDograph No. 253, 1980.

[22]Raman, K.R., "A Study of Surface Pressure Fluctuations in Hypersonic Turbulent Boundary Layers," NASA CR 2386, 1974.

[23]Bendat, J.S. and Piersol, A.G., *Random Data,* 2nd ed., John Wiley and Sons, New York, 1986.

[24]Brusniak, L., "Evaluation of Conditional Sampling Methods for Analysing Separation Shock Motion," AIAA Paper 88-0091, 1988.

[25]Dolling, D.S. and Brusniak, L., "Separation Shock Motion in Fin, Cylinder and Compression Ramp-Induced Turbulent Interactions," *AIAA Journal,* Vol. 27, No. 6, 1989, pp. 734-742.

[26]Erengil, M.E. and Dolling, D.S., "Unsteady Wave Structure near Separation in a Mach 5 Compression Ramp Interaction," *AIAA Journal,* Vol. 29, No. 5, 1991, pp. 728-735.

[27]Kazimierski, Z. and Trojnarski, J., "Time-Averaged Pressure of Fluctuating Gas Motion in Small-Diameter Tubes," *AIAA Journal,* Vol. 25, No. 4, 1987, pp. 567-572.

Table 1. Incoming turbulent boundary layer properties in the upper stream

Property	Value
boundary layer thickness, δ	3.1 mm
boundary layer displacement thickness, δ^*	0.91 mm
boundary layer momentum thickness, θ	0.25 mm
boundary layer shape factor, $H = \delta^*/\theta$	3.71
wake strength parameter, Π	1.58
skin friction coefficient, C_f	0.00131
friction velocity, u_τ	20.6 m/s

High Pressure Air Supply

Upper Stream
Gate Valve

Constant Area
Diffuser

Plenum
Chamber

Lower Stream
Globe Valve

Support
Stand

Cross-Sectional View of
the PIBLS Test Section

Figure 1.   Schematic of the PIBLS wind tunnel facility, including an enlarged cross-sectional view of the PIBLS test section.
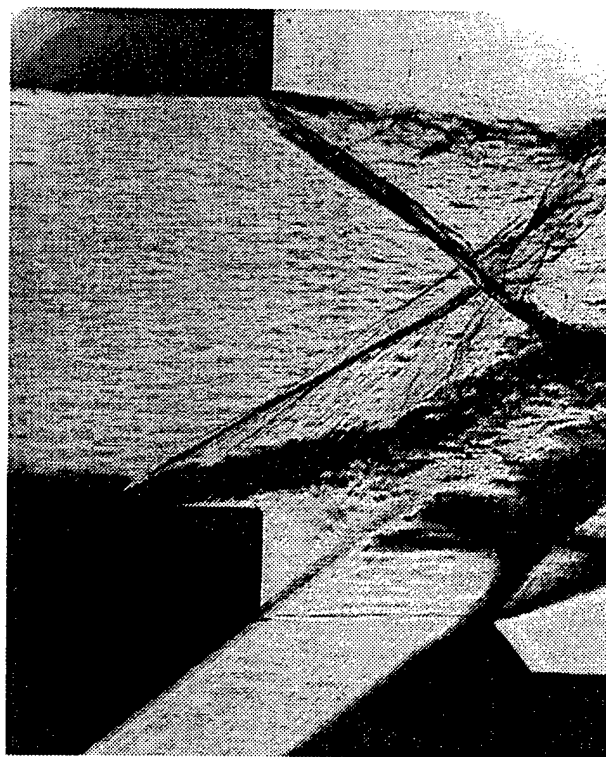
Figure 2.   Schlieren photograph (flashlamp pulse duration of 1.4 µs) of the near-wake region in the PIBLS wind tunnel at a JSPR of approximately 2.35.
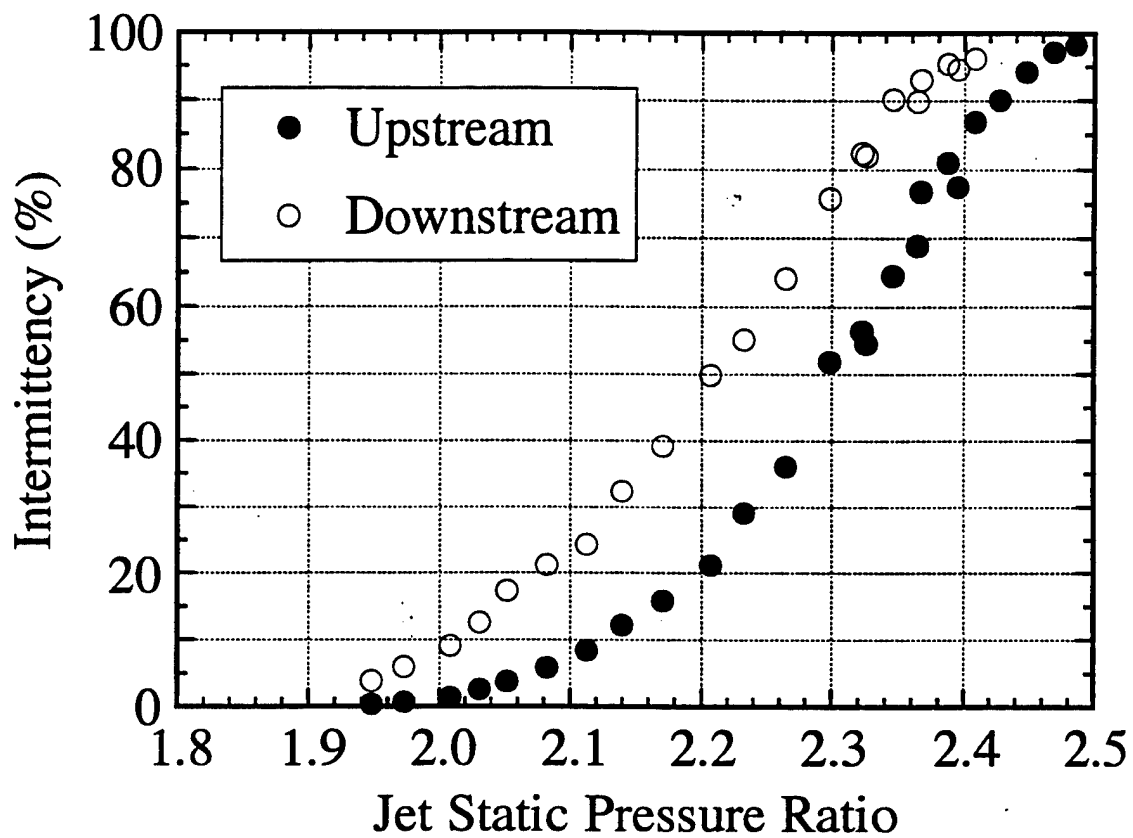
Figure 3.   Plot of intermittency versus the JSPR for the upstream and downstream pressure transducer measurements.
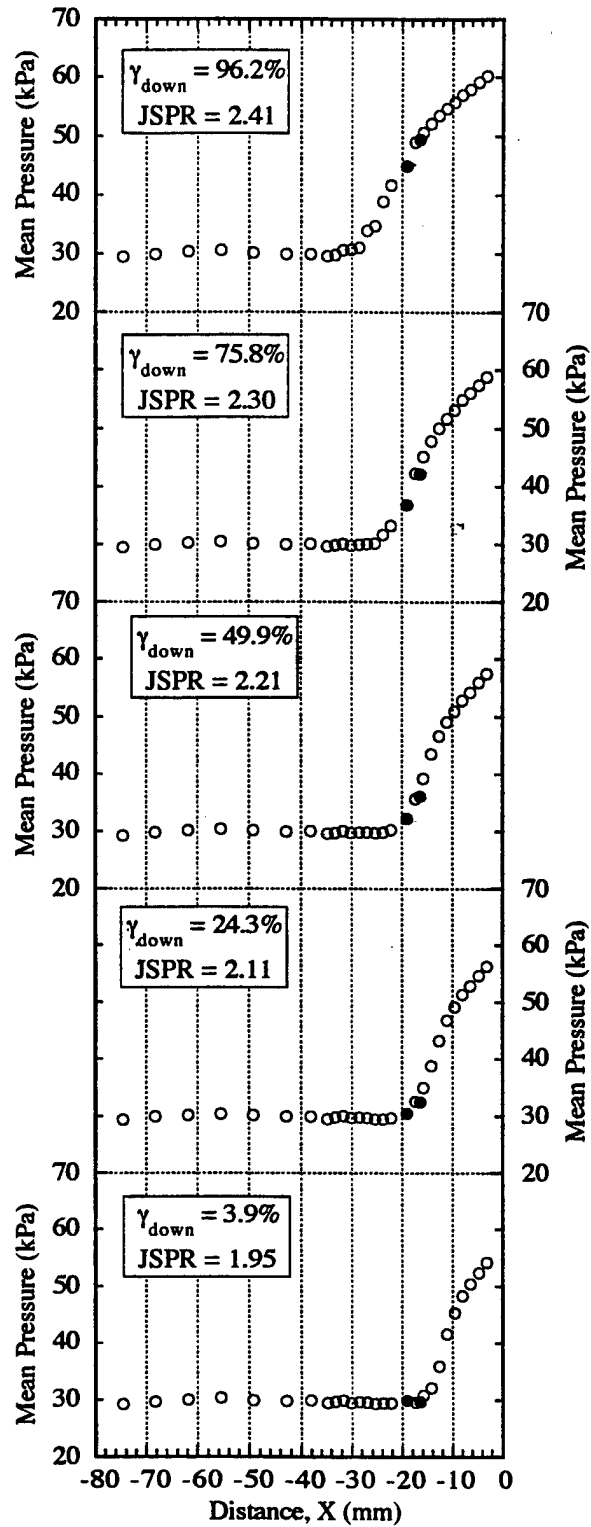
Figure 4.   Mean static pressure distributions on the lower wall of the freestream at five
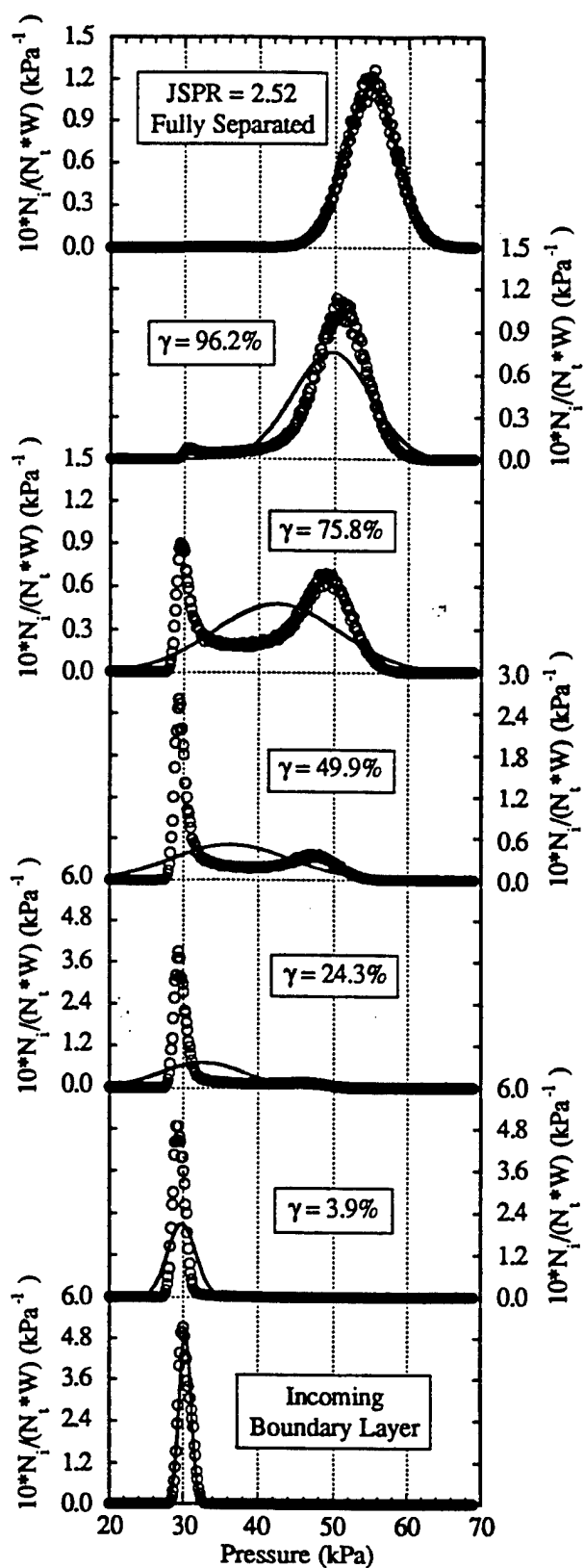JSPRs (● Kulites; ○ DPT-6400T).

Figure 5. PDF estimates of the pressure fluctuation amplitudes across the intermittent region (O - actual PDF; ———— - Gaussian PDF). JSPR values identical to those in Fig. 4 at the same γ.
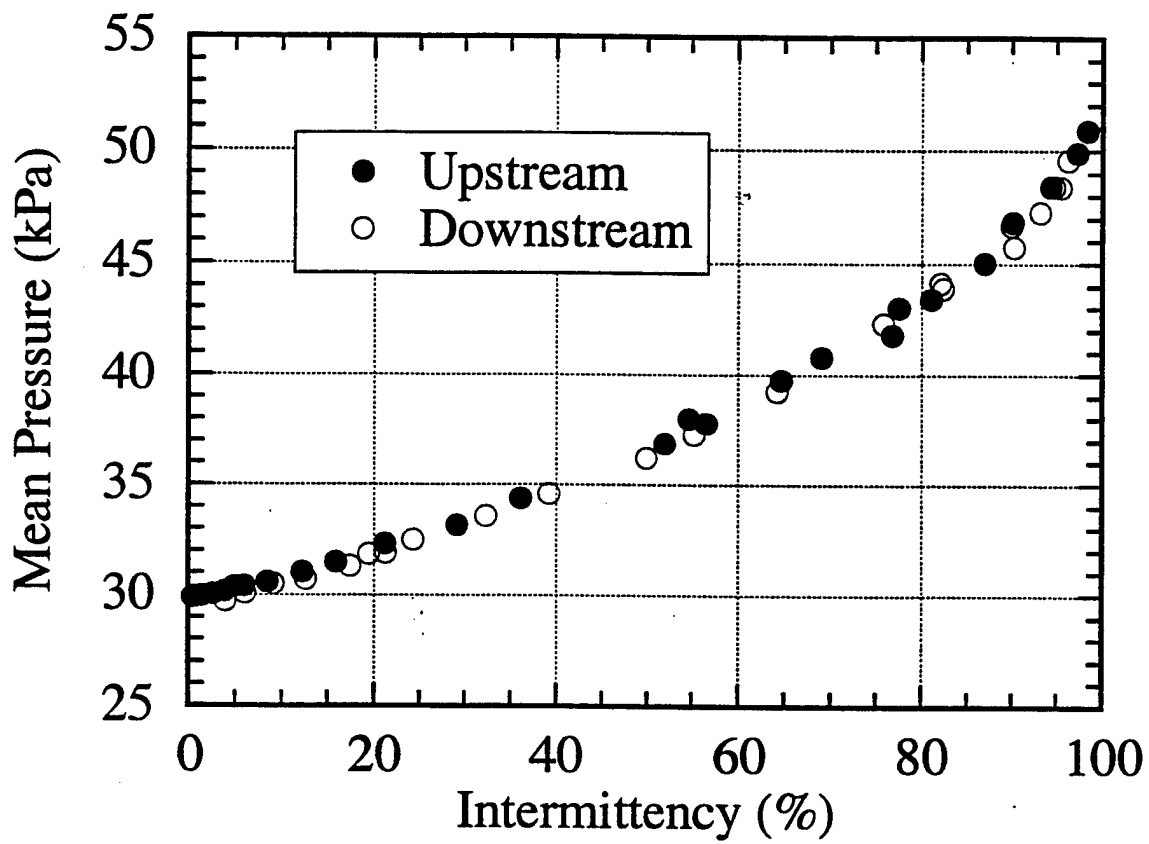
Figure 6.   Mean pressure versus intermittency across the intermittent region of the PIBLS wind tunnel.
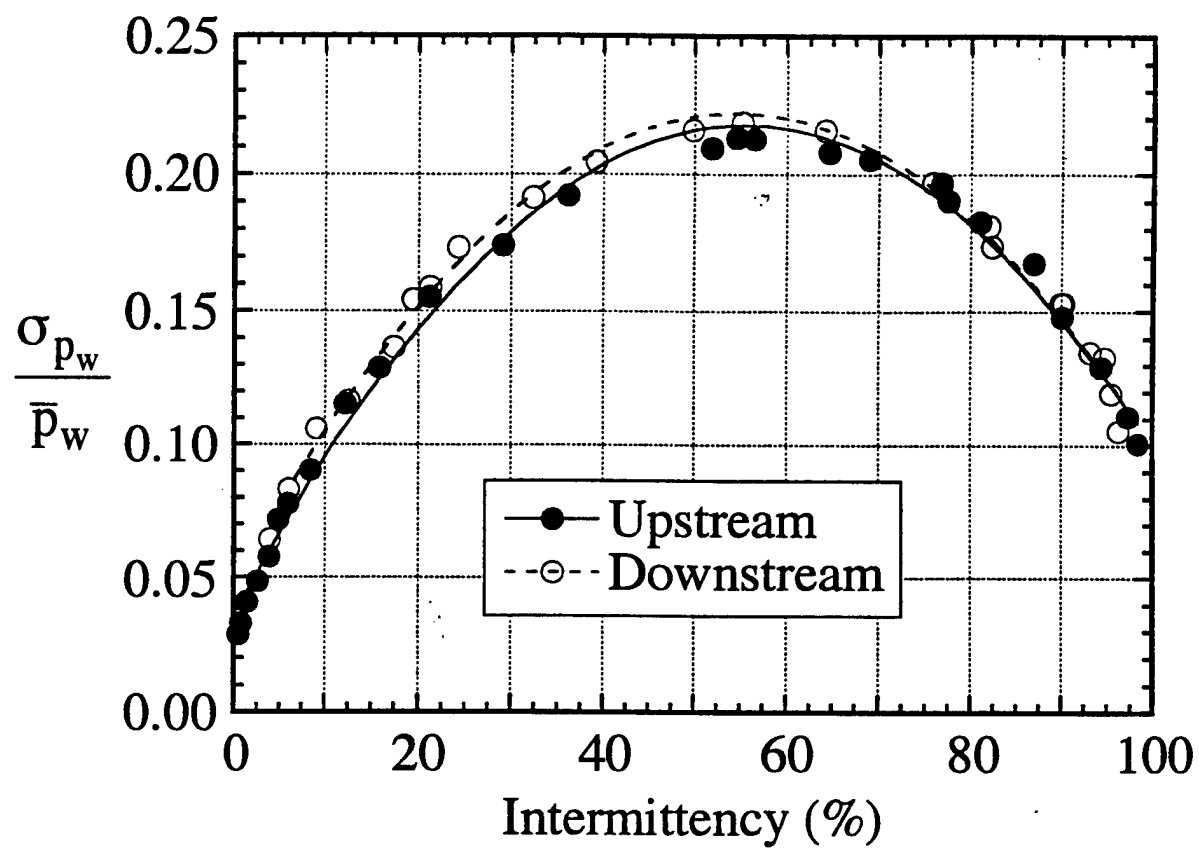
Figure 7. Nondimensionalized standard deviation of the pressure fluctuations versus intermittency across the intermittent region.
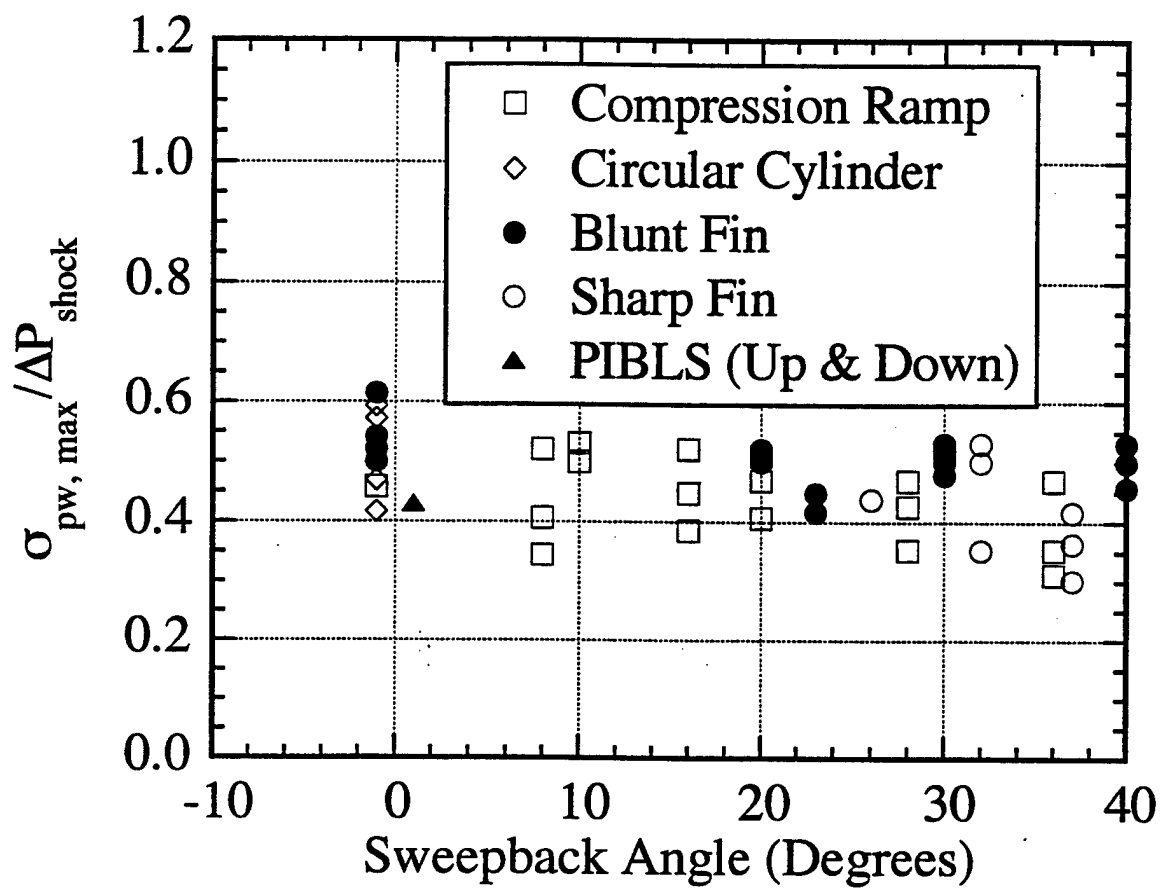
Figure 8.   Strength of the unsteady shock wave motion over the intermittent region for several SWBLI studies.
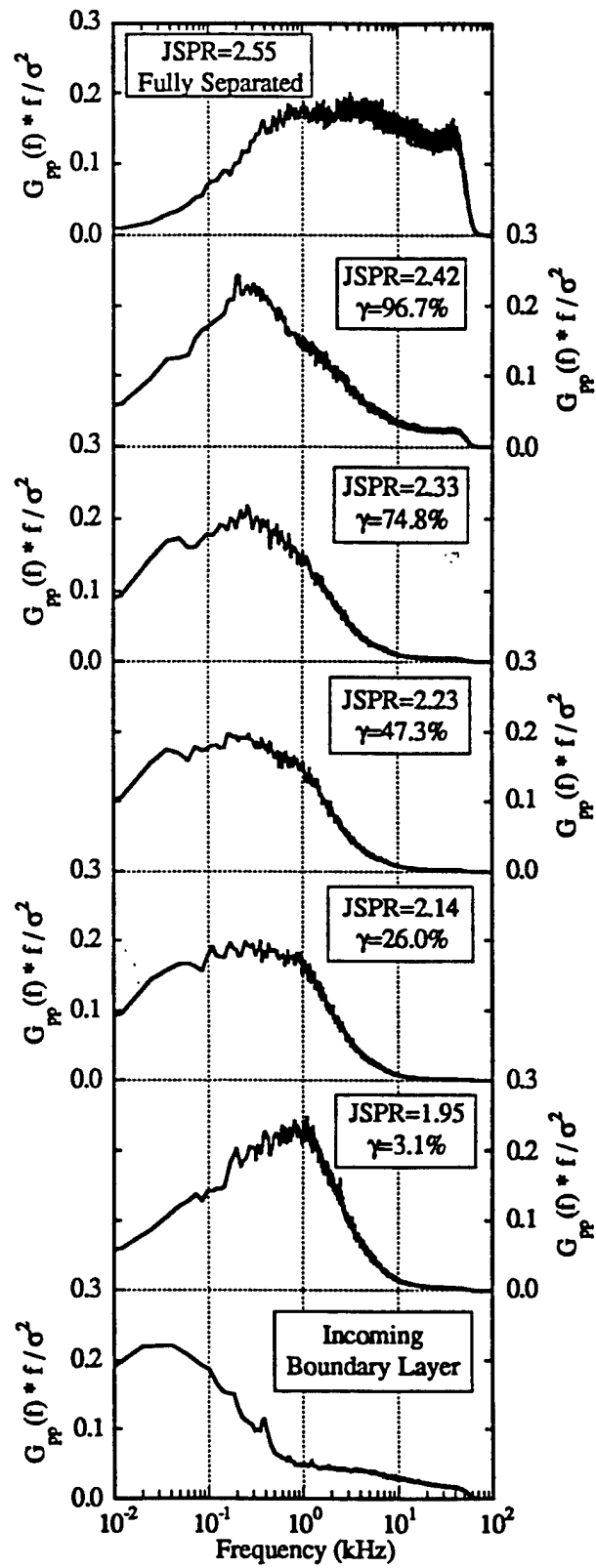
Figure 9. Normalized power spectral density estimates of the pressure fluctuations across the intermittent region.

APPENDIX A.10

A METHOD FOR SEPARATING SHOCK WAVE MOTION AND TURBULENCE IN LDV MEASUREMENTS

by

C. W. Palko and J. C. Dutton

A METHOD FOR SEPARATING SHOCK WAVE MOTION AND TURBULENCE IN LDV MEASUREMENTS

C. W. Palko, Ph.D.
Member of the Technical Staff
The Aerospace Corporation
P.O. Box 92957, MS M4/970
Los Angeles, CA 90009-2957

and

J. C. Dutton
W. Grafton and Lillian B. Wilkins Professor
Department of Mechanical and Industrial Engineering
University of Illinois at Urbana-Champaign
140 Mechanical Engineering Bldg., MC-244
1206 West Green Street
Urbana, Illinois 61801

NOMENCLATURE

M	Mach number, or estimate of the mean velocity
N	ensemble size
P	pressure
Re	Reynolds number
s	estimate of the root-mean-square velocity
TKE	turbulent kinetic energy
U	streamwise mean velocity
u	instantaneous streamwise velocity
U_∞	freestream velocity
v	instantaneous transverse velocity
x, X, y, Y	flowfield streamwise and transverse coordinates

Greek

δ_o	inflow boundary layer thickness
μ	actual mean velocity
σ	actual root-mean-square velocity

Symbol

$< >$	ensemble averaged

Superscript

'	fluctuation from the mean

Subscript

1, 2	high-speed and low-speed, respectively, or upper and lower streams, respectively

ABSTRACT

Two-component laser Doppler velocimetry (LDV) measurements were made in a planar, two-dimensional flow containing an unsteady oblique shock wave formed by the convergence of two supersonic streams past a thick plate. High-speed wall pressure measurements locate the shock wave and, consequently, allow separation of the effects of shock wave motion from the turbulence fluctuations in the LDV measurements of the shock-separated free shear layer. In the current flow isolating the large-scale changes in the position of the shock from the turbulence primarily reduces the experimental scatter rather than significantly changing the shapes or magnitudes of the turbulent stress profiles. Changes in the direction of shock motion do not significantly affect the mean velocity, but do affect the turbulent stresses.

1 INTRODUCTION

A supersonic plume-induced boundary layer separated (PIBLS) flowfield is caused by the interaction of the exhaust plume from an underexpanded jet with the boundary layer on the afterbody surface of a rocket or missile. As the flow around the vehicle encounters the blockage caused by the exhaust plume, an oblique shock is formed. This shock imposes an adverse pressure gradient on the afterbody boundary layer and, if strong enough, will cause separation. The separation process is unsteady with the shock wave oscillating in the streamwise direction. This unsteadiness complicates both prediction and measurement of PIBLS flowfields.

Although shock-induced shear layer formation in front of solid objects, such as in unswept compression corner flows, has been extensively investigated, (Adamson and Messiter 1980; Green 1970; Dolling 1993) only four studies of turbulence in such flows exist to our knowledge (Ardonceau 1984; Kuntz 1985; Smits and Muck 1987; Selig et al. 1989). However, no published investigations exist of turbulence in a shock-induced separation caused by a second fluid stream. Also, current computational models are unable to accurately predict unswept compression corner and PIBLS flowfields containing shock-induced separation, and detailed experimental data are needed to allow verification of improved numerical solutions, including improved turbulence models for these flows (Dussauge and Dupont 1995).

All four of the previously mentioned turbulence studies in compression corners noticed shock wave unsteadiness (i.e., streamwise translation), but did not use any conditional sampling technique to isolate its effects. Whether the increased turbulence levels measured by the four studies were due to actual turbulent velocity

2

fluctuations or by the shock wave unsteadiness is unclear. The measured turbulence levels may be inaccurate due to the motion of the shear layer across the measurement region. In a recent review, Dussauge and Dupont (1995) conclude that, to date, no measurements exist concerning the impact of shock motion on the downstream level of turbulence. Selig and Smits (1991) did, however, examine the effect of periodic blowing (inside the separated region) on the shock wave unsteadiness in a separated compression corner flow. Selig and Smits succeeded in changing the shock wave oscillation frequency, but did not observe any difference in the level of turbulence amplification due to the presence of blowing. These investigators concluded that the shock motion was not responsible for the turbulence amplification. Although Dussauge and Dupont (1995) cite Selig and Smits' (1991) study, they do not apparently consider it as conclusive evidence of the effect of shock motion on turbulence.

Several facts concerning shock wave unsteadiness in compression corners are now known. Erengil and Dolling (Erengil and Dolling 1990; Erengil and Dolling 1991) concluded from wall pressure measurements in compression corners that the high-frequency "jitter" of the shock wave position is caused by the convection of large-scale turbulent structures in the boundary layer through the interaction. The low-frequency (< 1 kHz), large-scale "sweeps" of the shock wave are most probably caused by pressure fluctuations inside the separation bubble. Erengil and Dolling also found that the separation bubble "expands and contracts like a balloon." This is believed to correspond to pressure fluctuations inside the separated region, and may cause the shock to rotate about its foot while translating in the streamwise direction. The separation shock is followed by a series of compression waves and is not simply a single shock as some previous researchers have suggested (Erengil and Dolling 1991; Dolling and Murphy 1983).

Conditional analysis has been successfully used with LDV in periodic flows for the past 15 years, but usually the flowfield has a single predictable frequency, such as in turbomachinery flows. For example, in an internal combustion engine the LDV measurements can be encoded with the instantaneous crank angle to allow conditional averages to be formed from measurements taken at a particular crank angle (i.e., cylinder position) (Rask 1981; Liou and Santavicca 1985; Witze et al. 1984). In the current study, however, the shock motion is a normally distributed random process with a broad range of frequency components.

The one previous study using a type of conditional analysis similar to that used here for a shock wave-boundary layer interaction was the study by Kussoy et al. (1988). In this study, Kussoy et al. used two-component LDV to investigate a Mach 2.85 flow past a flared cylinder. To increase the three-dimensionality of the flowfield,

3

the flare was swept with respect to the cylinder axis. The shock wave position was determined using high-speed

shadowgraph movies and six pressure transducers placed 5 mm apart along the cylinder centerline upstream of the

flare. These were differential pressure transducers using the undisturbed wall pressure upstream of the separation

shock wave as a reference pressure (as in the current study). Shock positions determined with the shadowgraph

visualizations and the pressure transducers were well correlated. This indicates that differential surface pressure

measurements can be used to accurately determine shock positions. Kussoy et al. used the following conditional

analysis algorithm to divide the shock positions into two states: "shock forward" and "shock back." The

shadowgraph movies were first used to determine which transducer was beneath the mean shock wave position. The

velocity realizations were then sorted according to the instantaneous pressure level at this transducer. Those with

pressures greater than one standard deviation above the mean pressure were considered the "shock forward" data set.

Those with pressures less than one-half standard deviation below the mean pressure were considered the "shock

back" data set (Brown et al. 1987).

The primary objective of this study is to demonstrate a technique to allow characterization of the

development of a shock-separated free shear layer while isolating the effects of shock unsteadiness from the

turbulent velocity fluctuations. To demonstrate this technique, conditionally analyzed LDV measurements have

been made along the spanwise center plane in a PIBLS flowfield to obtain the mean velocity components and

normal stresses in both the streamwise and transverse directions as well as the $<u'v'>$ primary Reynolds shear stress.

2   EQUIPMENT

2.1   Wind Tunnel

Figure 1 shows the blowdown-type supersonic wind tunnel used in this study. The tunnel supply air is

provided by a 146 m^3 tank farm which is at 892 kPa prior to each tunnel run. The tank farm is connected to

Ingersoll-Rand and Gardner-Denver air compressors which provide 0.68 kg/s at 892 kPa and 0.33 kg/s at 789 kPa of

dry air, respectively. This air supply system provides a tunnel run time of about 5 minutes at the operating point

used for this experiment. Shaw (1995) gives a detailed description of the tunnel design and testing.

For this study, absolute stagnation pressures of 506 kPa and 251 kPa are used for the upper and lower

streams (see Figure 2), respectively. These stagnation pressures are measured with pitot tubes located just upstream

of each converging-diverging nozzle. A globe valve in the lower inlet pipe is used to throttle the lower stream to

various stagnation pressures, which changes the static pressure ratio between the two streams and, therefore, the mean separation shock position. An iron-constantan thermocouple is used to measure the plenum chamber stagnation temperature during each tunnel run. Honeycombs and fine mesh screens are used in both streams to reduce turbulence in the incoming flow. (The lower stream's flow conditioning module is inside the tunnel and is not shown in Figure 1.)

2.2 Flowfield

Figure 2 shows a schematic of the planar, two-dimensional flowfield investigated in this study. The flowfield consists of an upper Mach 2.5 stream (unit Reynolds number, $Re=48.9 \times 10^6$ m^{-1}) and a lower Mach 1.5 stream ($Re=36.2 \times 10^6$ m^{-1}) converging at a $40°$ angle past a 12.7 mm high base plane. The static pressure ratio of the lower to the upper streams is $P_2/P_1=2.27$. The spanwise width of the flowfield and the height of the upper stream are both 50.8 mm. Surface oil flow visualization shows that the center 32 mm (63%) of the flowfield is free from sidewall effects and is, consequently, two-dimensional in this region. The upper stream is analogous to the supersonic freestream surrounding a rocket afterbody, while the lower stream is analogous to an underexpanded exhaust plume.

The primary subject of this study is the behavior of the boundary layer (δ_0 = 3 mm) and separated free shear layer of the upper stream. This boundary layer intercepts the separation shock, consequently separates, and forms a free shear layer, as shown in Figure 2. This shear layer then reattaches with the shear layer formed by the separation (at near zero pressure gradient) of the boundary layer of the lower stream. These two shear layers enclose a recirculating region behind the base, and their reattachment generates a recompression shock system and the resulting trailing wake. Figure 3 is a shadowgraph taken of the flowfield showing the separation shock, the incoming boundary layers of both streams bordering the base, the recirculation region behind the base plane, and the developing free shear layers, along with their reattachment and the accompanying system of recompression shocks. The shadowgraph shown in Figure 3 was produced using a 25 ns pulse from a Xenon model 437B Nanopulser at a jet static pressure ratio of $P_2/P_1=2.35$ between the two streams (Shaw 1995).

2.3   Pressure Data Acquisition System

The pressure data acquisition system consists of two Kulite model XCS-062-15G piezoresistive differential pressure transducers flush-mounted (in the spanwise center plane) along the bottom wall of the upper stream. Figure 2 shows the positions of the two pressure transducers located at 19.05 and 16.51 mm upstream of the base plane. Each transducer has a full scale of 103 kPa, an active element diameter of 1.6 mm, and uses the static pressure upstream of the separated region as a reference pressure. This reference pressure is measured through a port in the bottom wall of the upper stream located 65 mm upstream of the base plane (Shaw 1995).

The transducers are powered by two Measurements Group Inc. Model 2311 signal conditioning amplifiers that also provide an adjustable DC offset and gain to the output signals. The output from each amplifier is routed through a low pass, active Butterworth filter with a -3 dB cutoff frequency of 50 kHz. This cutoff frequency is less than any inherent frequency limitations in the rest of the pressure acquisition system.

2.4   Laser Doppler Velocimetry System

A schematic of the two-component LDV system, a TSI model 9100-7, used for the mean velocity and turbulence measurements, is shown in Figure 4. The system utilizes the 488 nm and 514.5 nm lines of a 5 watt Spectra-Physics argon-ion laser. A 40 MHz shift is added to one beam of each color to allow discrimination of negative velocities and to minimize fringe biasing. To further reduce fringe biasing and fringe blindness, the green and blue beam pairs are oriented at approximately $+45°$ and $-45°$, respectively, to the mean flow direction of the upper stream. The 13 mm beam spacing and 250 mm focal length transmitting lens result in a measurement volume diameter of 0.127 mm.

Separate TSI model 9306 six-jet atomizers are used to inject 50 centistoke, silicone oil from Dow Corning into each stream. The oil droplets are injected downstream of all flow-conditioning modules and upstream of the nozzle blocks through small stainless steel tubes. Bloomberg (1989) demonstrated that these six-jet atomizers produce a mean droplet diameter of 0.8 microns when using this fluid. The scattered light from the silicone oil droplets is collected in forward scatter with a 250 mm focal length lens at an off-axis collection angle of $10°$. This results in an effective measurement volume length of 1.5 mm. A TSI IFA 750 digital burst correlator operating in coincident mode determines the Doppler frequencies. Jenson (1991) gives a detailed discussion of the IFA 750 operation. A discussion of the accuracy of the LDV measurements is presented in Appendix A.

3 EXPERIMENTAL TECHNIQUE

In the current study, the shock motion spans a streamwise distance of $4.7\delta_0$ or 14 mm, contains frequencies as large as 10 kHz, and is captured by sampling each pressure transducer at 20 kHz. The Nyquist criterion was used to select the sampling frequency. Since the boundary layer separation point oscillates in the streamwise direction with the shock wave, the shear layer will also oscillate and cause biasing of unconditionally averaged velocity data. Consequently, a method is needed to minimize the bias in the velocity measurements of the developing shear layer due to the shock wave unsteadiness. This is provided by the following procedure.

3.1 Acquisition Timing

At the beginning of each tunnel run, a timing pulse initiates pressure measurements using the two transducers that are flush-mounted in the bottom wall of the upper stream (i.e., beneath the separation shock wave). The algorithm described below uses these wall pressure measurements to determine the shock position. This same timing pulse also produces a timing marker in the velocity data that provides a common time origin for both the pressure and velocity measurements. This allows the time histories of the pressure and velocity data to be merged. While the pressure is sampled at regular intervals, the velocity data are collected at random times (i.e., whenever an oil droplet produces a valid Doppler burst on both velocity channels). The IFA 750 Digital Burst Correlator, used to collect the velocity data, has a temporal resolution of ± 1 μsec. This is the limiting temporal resolution of the combined pressure/velocity data acquisition system.

3.2 TTMBCC Algorithm

The pressure time history for each of the two channels is analyzed using the two-threshold method boxcar conversion (TTMBCC) algorithm developed by Prof. D. S. Dolling and co-workers at the University of Texas-Austin (Dolling and Brusniak 1989). The TTMBCC algorithm isolates the pressure fluctuations due to the shock motion from those present in the incoming turbulent boundary layer and in the separated region behind the shock. This results in a boxcar time history (i.e., a binary representation of upstream and downstream shock positions) for each channel (see Figure 5). The TTMBCC algorithm has been used extensively in studies of shock motion in

7

unswept compression corner flows (Brusniak 1988; Dolling and Brusniak 1989; Erengil and Dolling 1990; Erengil and Dolling 1991).

Each channel's boxcar history is described by the time at which each rise or fall in pressure associated with a shock crossing occurs. The boxcar history is formed by first setting thresholds of 3σ and 6σ above the mean pressure in the incoming boundary layer (where σ is the standard deviation of the pressure fluctuations in the incoming boundary layer). Shaw (1995) describes in detail the criteria for picking the two thresholds used in this study. For a rise event to register (i.e., the shock moves upstream of the transducer), the pressure must initially be less than the lower threshold and must rise past the upper threshold. For a fall event to register (i.e., the shock moves downstream of the transducer), the pressure must initially be greater than the upper threshold and must fall past the lower threshold. The TTMBCC algorithm prevents the mistake of interpreting oscillations about the lower threshold prior to a rise event and oscillations about the upper threshold prior to a fall event as shock motions. The occurrence time of either a rise or fall event is defined as the time when the first pressure sample is taken after the upper threshold is crossed. Since only the upper threshold is used to determine the occurrence time of a shock motion, the position of the shock wave relative to the pressure transducer will be the same for both upstream and downstream shock crossings.

3.3   Conditional Analysis

A second algorithm is used to determine the position of the shock wave corresponding to each velocity realization. Figure 5 illustrates this process. The shock wave positions are defined using the numbers 1, 2, or 3, depending on whether the shock wave is upstream, between, or downstream of the two transducers, respectively. Additional categories are defined for various shock position transitions and error cases, which represent less than 1% of the acquired data. This small percentage of transitional cases indicates that the shock motion is accurately captured using this method.

Each velocity realization is matched to the corresponding point in the boxcar history of the pressure data, and the shock wave position for that realization is determined. Then the velocity measurement is saved with the corresponding shock wave position. Finally, for the constant shock position results, conditional averages are formed from the velocity realizations corresponding to shock wave position 2 (between the two transducers), thereby effectively "freezing" the shock position at this location. This conditional average retains only approximately 25%

8

of the velocity data and therefore necessitates collecting large data sets to obtain adequate statistical certainty from the ensemble averages.

The algorithm used for the current study has two advantages over that used by Kussoy et al. (1988). First, by using two transducers instead of only one, it is possible to form velocity data ensembles with the shock wave in a single position, region 2, instead of for only a range of positions, i.e., shock forward or shock back. Second, this technique uses only pressure measurements and consequently eliminates the subjective process of inspecting shadowgraph movies for the mean shock positions.

Since the transducers are placed at 19.0 and 16.5 mm upstream of the base plane, the mean shock foot position (i.e., the boundary layer separation point) for the region 2 data set is 17.75 mm upstream of the base plane. Increases in the jet-to-freestream static pressure ratio (JSPR) between the two streams shift the region of shock oscillation upstream, away from the base corner. As this shift occurs, the intermittency (i.e., the proportion of time spent by the shock upstream of a given transducer) increases for both transducers. However, the time spent by the shock between the two transducers (in region 2) at first increases, peaks at near 25%, and then decreases. The JSPR of 2.27 for this study was selected to maximize at approximately 25% (the difference in the two transducer intermittencies) the time spent by the shock in region 2 (between the transducers) and, thereby, to maximize the amount of data obtained from the conditional analysis.

4   RESULTS

This section presents data obtained using the technique described above. A complete mapping of the plume-induced separated flowfield has recently been completed and will be, along with a detailed discussion of the flowfield features and trends, the subject of a future paper (Palko and Dutton 1998). Therefore, this discussion will concentrate on the effects of changes in the shock position and in the direction of shock motion on the velocity statistics. This section presents conditionally and unconditionally averaged data at four streamwise stations. The four stations A, B, C, and D are located at x=-25, 0, +15, and +30 mm from the base plane, respectively (see Figure 2). These positions lie in the approach boundary layer upstream of the mean separation shock position, at the base plane, just before reattachment, and in the developing wake, respectively. Station A lies at the limit of optical access in the upstream direction.

9

All traverses are limited to 25 mm above the bottom wall (i.e., the bottom half of the upper stream); all flowfield features of interest are contained within this region. The laser beams become clipped at positions closer than 1 mm from the wall; therefore, each traverse begins at y=1 mm. Due to their inertia, LDV seed particles can produce curved pathlines behind an oblique shock wave instead of following the fluid streamlines that bend discontinuously at the shock front. This difference in the particle and fluid responses to shocks can introduce particle dynamics errors. The effects of particle dynamics in the current flowfield are negligibly small outside the region immediately downstream of the shock wave (1.4 mm normal to the shock or 2.8 mm in the streamwise direction[Palko, 1997 #83]. While stations B and C cross the separation shock wave, the shear layer at both of these locations lies below the region of significant particle lag. An additional advantage of the conditional analysis method employed here is the ability to locate the region of significant particle dynamics effects.

4.1   *Effects of Shock Position*

The primary motivation for the conditional averaging technique described earlier is to precisely locate the separation shock wave between the two flush-mounted pressure transducers at the instant in time at which a velocity measurement is made. This allows the effects of changes in shock position on the velocity field to be distinguished from the inherent turbulence in the velocity field. The effects of shock position on the flowfield may be discerned by comparing LDV data acquired when the shock is between the two transducers (in region 2) to LDV data acquired without accounting for shock position. Region 2 was chosen because it is the smallest region (only 2.5 mm in streamwise extent) in which the shock could be located.

To equalize the random error in the velocity measurements, which depends on the ensemble size (see Appendix A), both the unconditional (total data) and conditional (region 2) averages use an ensemble size of 4096 realizations. The systematic error or bias error in the LDV data is identical for the two sets. Any differences between the two sets are, therefore, due only to the shock motion or to random errors in the LDV data.

Figure 6 shows the dimensionless mean streamwise velocity (nondimensionalized by the freestream velocity, U_∞=590 m/s) for each station. Several features of Figure 6 should be noted. First, the "all data" and "region 2" profiles are very similar at all four stations. This shows that the mean velocity is unaffected by changes in the shock position. In addition, the inclination of the shear layer is apparent, since the noticeable trough in the velocity profiles (which is in the recirculation region) occurs at increasing heights above the base for each

10

successive station. The smoothness of the profiles also indicates that the random LDV errors are small. Finally, the slight variation (less than 2%) in the freestream mean velocity profile at station A may be due to a slight wake from the seed injection tube which is upstream of the converging-diverging nozzle that produces the supersonic freestream flow.

Figure 7 presents the dimensionless streamwise turbulent normal stress profiles for each station. In this study, the streamwise and transverse normal stresses are measured with respect to directions parallel and perpendicular, respectively, to the x axis shown in Figure 2, regardless of the local mean flow direction. As with the mean velocity data, the streamwise normal stress profiles for the unconditional and conditional data sets are nearly identical at stations B, C, and D. There are slight differences between the peak values of the "all data" and "region 2" profiles at these downstream stations, but these differences are not substantially larger than the measurement uncertainties at these locations. However, some significant differences are apparent near the wall at station A. In particular, the "region 2" profile appears to be much smoother than that of the "all data" profile. This difference between data sets seems to indicate that shock motion does increase the apparent normal stress inside the boundary layer. Although taken as far upstream as optical access allowed, Station A lies just within the region of oscillation of the separation shock wave. Consequently, the shock wave makes infrequent excursions upstream of station A. These excursions, however, occur during only a small fraction of the time during data collection. The result is increased random error in the resulting turbulence quantities in this region. This increased random error is at least partly due to particle dynamics effects at station A, which vary in strength due to the intermittent shock motion at station A.

The streamwise stress profiles obtained downstream of separation (B, C, D) show much less deviation between the "all data" and "region 2" data sets. This is expected since the effects of shock wave unsteadiness should be greatly diminished at these more downstream locations. Comparing station A with stations B and C shows that the shock-induced separation process greatly increases the streamwise normal stress. Comparing stations C and D shows the dramatic decrease in the peak streamwise normal stress through reattachment. As with the mean velocity profiles, the inclination of the shear layer above the wall is apparent since the dominant peak in the streamwise normal stress profiles occurs at increasing heights above the wall for each successive station.

The dimensionless transverse normal stress profiles for each station are presented in Figure 8. As in Figure 7 for the streamwise component, the "all data" and "region 2" data sets show close agreement at all stations

except within the boundary layer at station A. At station A, the transverse normal stress profile shows the same characteristics as that of the streamwise normal stress in that the "region 2" profile is notably smoother than the "all data" profile. Similar to Figure 7 for the streamwise normal stress, the dimensionless transverse normal stress is greatly increased by the shock-induced separation. The asymmetry of the main peak in the transverse normal stress at station C is due to the effects of the lower shear layer. Since this lower shear layer is inclined at 40° with respect to the x-axis, the turbulence in the lower shear layer has a large transverse component. The small secondary peaks in the transverse normal stress at stations B and C coincide with the location of the separation shock. This slight increase in turbulence is due to either small-scale shock unsteadiness that is below the resolution limit of the conditional averaging technique or to particle lag. As mentioned earlier, by using conditional analysis to locate the shock wave, the region of significant particle lag can be located with certainty.

Comparing Figures 7 and 8, it is apparent that the freestream turbulence is isotropic while the boundary layer and free shear layer turbulence is anisotropic. The peak normal stress anisotropy ratio, $<u'^2>/<v'^2>$, in the shear layer at stations B, C, and D is approximately 13, 9.5, and 5.6, respectively. The peak normal stress anisotropy in the approaching boundary layer at station A is difficult to estimate with certainty since the transverse normal stress may only be measured at positions above $y=1$ mm. However, over the outer portion of the boundary layer that has been probed, the anisotropy increases and levels off at approximately 3 as the wall is approached. This gives evidence of the much stronger amplification of the streamwise normal stress by the shock interaction than the amplification of the transverse normal stress. As the shear layer moves downstream from separation, there is a strong reorganization of the turbulence and a shift in the distribution of the turbulent kinetic energy from the streamwise to the transverse normal stress components. This occurs both during shear layer development and through reattachment.

The Reynolds shear stress profiles for each station are shown in Figure 9 where, following convention, the negative of the shear stress, $-<u'v'>/U_\infty^2$, is plotted. As in Figures 6-8, the profiles for the "all data" and "region 2" data sets agree closely at each station with the noticeable exception of the boundary layer at station A. At station A, the "region 2" profile is again much smoother than the "all data" profile. As expected, the Reynolds shear stress inside the boundary layer is negative. Also interesting is the near zero value of the Reynolds shear stress in the freestream at all four stations, as is expected. The outermost positive peak in the shear stress profiles at stations B

and C coincides with the location of the separation shock. Like the secondary peaks in the transverse normal stress, this is an artifact of either small-scale shock motion or particle lag.

Figure 10 shows the nondimensional turbulent kinetic energy profiles. Previous LDV measurements in related flows (Herrin and Dutton 1995) show that the spanwise turbulence intensities are approximately equal to the transverse turbulence intensities in compressible shear layers. Therefore, the turbulent kinetic energy in this study is approximated as

$$TKE = \frac{1}{2}\left(u'^2 + 2v'^2\right) \tag{1}$$

where the spanwise normal stress is approximated as equal to the transverse normal stress. This definition is slightly different than that used by some previous researchers such as Kuntz, (1985) where the spanwise normal stress is approximated as the arithmetic average of the streamwise and transverse normal stresses. This average definition has the effect of overestimating both the spanwise turbulence and, consequently, the turbulent kinetic energy.

The most obvious feature of the turbulent kinetic energy profiles in Figure 10 is their close similarity to the streamwise normal stress profiles (see Figure 7). The streamwise normal stress is much larger than the transverse normal stress over most of the flowfield and so dominates the turbulent kinetic energy. Like the streamwise and transverse normal stresses, the turbulent kinetic energy profiles show very little variation with changes in shock position, except in the approaching boundary layer.

It is not surprising that Kussoy et al.'s (1988) turbulent kinetic energy data showed a greater variation based on shock position than the data presented here. As described previously, Kussoy et al.'s algorithm formed data sets only for shock positions ahead of or behind a given transducer. This results in forward- and rearward-biased data sets, and a total data set of unknown bias. In the current study, which uses an algorithm utilizing two transducers, the data may be formed into a single data set of minimal bias (region 2 data). Based on the results of this study, it is apparent that a conditional analysis technique such as Kussoy's can overstate the effect of shock wave unsteadiness on the measured turbulence quantities.

4.2   *Effects of Shock Motion Direction*

The conditional averaging algorithm described earlier may be modified to isolate the effects of the *direction* of the shock motion rather than the effects of the shock *position* on the velocity field. As mentioned earlier, LDV data are acquired at random times (whenever a seed particle passes through the measurement volume),

13

while the pressure data (used to determine the shock position) are acquired at regular intervals. Therefore, each LDV point occurs within a time interval bounded by pressure samples. If the shock position at the beginning and the end of an interval containing an LDV data point are the same, the shock position is known for that LDV data point, and the corresponding shock region is assigned. However, if the shock position at the beginning and end of an interval containing an LDV data point are not the same, the shock wave must have transitioned between the two regions during the time interval in question. Inspection of typical data ensembles for this flow shows that these shock transitions occur in less than 1% of the sample intervals. The exact shock position is not known for LDV data points occurring during these transition intervals and so, instead, a classification number corresponding to the particular type of shock transition is assigned to each such LDV data point.

There are three such transition cases in each of the upstream and downstream directions. In the downstream direction, these correspond to transitions from upstream of both to between the two transducers (transition from region 1 to region 2), from between the two transducers to downstream of both (transition from region 2 to region 3), or from upstream of both to downstream of both transducers (transition from region 1 to region 3). Similar cases occur for the upstream direction.

For this study of the effects of the direction of shock motion, only transitions beginning or ending in region 2 (between the transducers) are considered. The transitions across both transducers are excluded due to their increased shock position uncertainty at *both* endpoints of the motion. Due to the low LDV data rates and the short tunnel run times possible, only 196,608 (i.e., 192k) velocity realizations could be acquired during each tunnel run. Despite acquiring data at only a single spatial location during a given tunnel run, the small number of transition cases (less than 1% of all acquired data) limited the directionally conditional ensemble size to 1100 velocity realizations for each direction. This is considerably smaller than the 4096 (i.e., 4k) realization ensembles used in all other data presented in this study, which substantially increases the random error in the resulting mean velocity and turbulent stresses (see Appendix A).

Because of the large number of velocity realizations required for statistically significant ensembles, direction conditional ensembles were obtained only within the shear layer at station B, the base plane (see Figure 2). This position was selected because of its proximity to the separation point and the presence of the recirculation zone. The traverse was limited to below y=8.5 mm, so as to lie beneath the region of particle lag lying downstream of the separation shock wave. To equalize the random error, which depends on the ensemble size, all of the conditional

14

(upstream, downstream, and region 2) averages for the data presented in this portion of the study use an ensemble size of 1100 realizations. The systematic error or bias error in the LDV data is identical for the three sets. Any differences between the three sets are, therefore, due only to changes in the direction of the shock motion or to random errors in the LDV data.

The profiles in Figure 11 for the streamwise mean velocity and turbulent stresses show the effects of changes in the direction of shock motion. As can be seen from Figure 11, no significant effect of the direction of shock motion can be distinguished from the direction-independent but position-conditioned (region 2) data for the mean streamwise velocity. As just discussed, the increased experimental scatter in these profiles is due to the reduced ensemble size compared to that in Figures 6-10. Interestingly, even with equal ensemble sizes, the downstream data set, rather than the region 2 data set, displays the most experimental scatter of the three conditional averages. This provides some evidence that the direction of the shock motion may have a more important effect on the velocity statistics than the position of the shock. The upstream and region 2 profiles in Figure 11 agree fairly closely for the mean streamwise velocity and transverse normal stress. However, for the streamwise normal stress the upstream data set exhibits less scatter than the region 2 profile. Also interesting is the agreement in the peak magnitude of the streamwise normal stress for the downstream and region 2 data sets. Comparing this peak value with that found in Figure 7 for the same location, but with a larger ensemble size (i.e., smaller random error), the values are found to agree. The peak streamwise normal stress for the upstream data profile, however, displays a smaller peak. This difference is well outside the 9% error bars at this location.

Examining the transverse normal stress and Reynolds shear stress profiles in Figure 11 reveals two other statistically significant trends. First, the transverse normal stress profile for the downstream data set deviates significantly from the upstream and region 2 profiles over the region 2 mm<y<5 mm. This deviation is also larger than the measurement uncertainties at these locations. Most noticeable in the downstream transverse normal stress profile is the presence of a distinct and large trough and peak in this region. The midpoint between these two features also coincides with the location of the peak streamwise normal stress (i.e., the center of the shear layer). The last noteworthy feature of Figure 11 is the greatly increased peak positive shear stress value displayed (note by convention that the negative of the shear stress has been plotted) by the downstream data profile. This peak value of approximately −0.0095 is almost twice the value of the approximately −0.005 peak exhibited by both the upstream and region 2 data profiles. Interestingly, comparing the region 2 shear stress profile in Figure 11 to those found in

Figure 9 at the same streamwise location reveals that the use of a larger ensemble size for the region 2 data does not change the peak value from that present in the upstream and region 2 profiles of Figure 11. The positive shear stress peak in Figure 9 does, however, occur closer to the wall than the positive shear stress peak of the downstream profile in Figure 11.

5   SUMMARY AND CONCLUSIONS

The technique described for separating shock motion from turbulence in LDV measurements has been successfully demonstrated. Data have been presented for streamwise locations upstream of mean separation, in the separated shear layer, and through the reattachment region. The shock motion has been shown to have a significant effect on the measured turbulence within the boundary layer upstream of the mean separation location, and a much smaller effect through the separated shear layer and reattachment regions. This study has shown that freezing the shock wave at a single position does not have a significant effect on measured mean velocities or turbulence quantities downstream of separation, as compared to the unconditionally analyzed data set.

This study indicates, however, that changes in the direction of shock wave motion do significantly alter the measured levels of downstream turbulence, although the mean velocity is still unaltered. Specifically, upstream shock motion decreases the apparent peak streamwise normal stress, but does not change the peak transverse normal stress or the Reynolds shear stress. Downstream shock motion increases the peak positive shear stress and shifts the location of this peak further from the wall. Motion in this direction also does not appreciably change the streamwise normal stress. Downstream motion decreases the transverse normal stress over a portion of the top of the shear layer, while increasing the transverse normal stress over a portion of the bottom of the shear layer. Taken together this indicates that there may be changes in the underlying turbulent structures inside the shear layer that correspond to changes in the direction of the shock motion. For example, the separation shock may rotate about its foot as it translates in the streamwise direction. This rotation would correspond to a varying shock strength and a varying adverse pressure gradient being imposed on the shear layer. This variation could alter the turbulent structures inside the shear layer, and therefore, alter the velocity statistics. Another possible mechanism would be a spanwise "wrinkling" of the shock front that is dependent on shock motion direction.

In general, upstream shock motion seems to decrease the turbulent kinetic energy (which is dominated by the streamwise normal stress), but does not alter the turbulence structure (i.e., the number and location of peaks in

16

the turbulence profiles are unchanged). Conversely, downstream shock motion does not significantly affect the overall turbulence energy level, but does affect the turbulence structure. Specifically, downstream shock motion affects the upper and lower portions of the shear layer differently (see the transverse normal stress profiles in Figure 11). Additional turbulence measurements in this flowfield, which are the subject of another paper (Palko and Dutton 1998), have also indicated two distinct layers in this shock-separated shear layer.

While future analysis of LDV data will attempt to elucidate the nature of the changes in turbulent structure due to changes in shock direction, ideally flow visualizations could be used to answer these questions. Recently, some flow visualization has begun in planar compression corner shock wave-boundary layer interactions (Chan et al. 1995; Beresh et al. 1997). This work has concentrated on uncovering a cause for the low-frequency shock wave unsteadiness. Specifically, no strong correlation was found between the low-frequency shock motion and changes in the thickness of the incoming boundary layer. Additional high resolution planar visualization studies are needed, however, to allow characterization of the dependence of turbulent structure on shock motion direction.

APPENDIX A

Experimental Uncertainty

A detailed error analysis has been performed [Palko, 1997 #83] for this experiment. The relative systematic or bias error in the mean velocity and normal stresses for both the streamwise and transverse velocity components was estimated to be no larger than 2% and is primarily due to uncertainty in the measurement of the LDV fringe spacing. Due to the careful choice of seeding levels, seed material, and beam angles, and from the use of both frequency shifting and interarrival time velocity debiasing (Herrin and Dutton 1993), the effects of fringe bias, velocity gradient bias, velocity bias, particle concentration bias, and particle lag were estimated to be negligibly small [Palko, 1997 #83]. As noted previously, particle lag is estimated to be significant only in the region immediately downstream of the shock wave, which is outside the region of interest.

The overall random or precision errors in both the mean and variance of the velocities are given by 95% confidence intervals (assuming a normal distribution of velocities). The limits of these confidence intervals depend both on the ensemble size and on the standard deviation of the velocity distribution, i.e., the rms velocity fluctuation (Bendat and Piersol 1986). Equations 2-5 below give the random error in the mean and variance estimates at 95% confidence, where M, μ, s, σ, and N are the estimate of the mean velocity, the actual mean velocity, the estimate of

the rms velocity, the actual rms velocity, and the ensemble size, respectively. Please note that these equations apply to both the streamwise and transverse velocities.

Specifically, for N=4096:

$$M - 0.031s \leq \mu < M + 0.031s \tag{2}$$

$$0.957s^2 \leq \sigma^2 < 1.046s^2 \tag{3}$$

and for N=1100:

$$M - 0.060s \leq \mu < M + 0.060s \tag{4}$$

$$0.920s^2 \leq \sigma^2 < 1.091s^2 \tag{5}$$

The random error in the estimate of the mean at any given point in the flow is directly proportional to the rms velocity at that point. However, the random error in the estimate of the variance of the velocity is independent of the mean velocity. For a fixed sample size, the random error in the velocity variance estimate is simply a fixed percentage of the velocity variance at each point.

The maximum measured streamwise rms velocity, or the square root of the streamwise normal stress, in the present study is $0.32U_\infty$ or 189 m/s and occurs just upstream of reattachment. This maximum rms velocity yields a random error in the streamwise mean velocity of 5.9 m/s or $0.01U_\infty$ for the data with ensemble sizes of 4096 points (i.e., Figures 6-10). The maximum measured transverse rms velocity, or the square root of the transverse normal stress, in the present study is $0.12U_\infty$ or 71 m/s and occurs just upstream of reattachment. This maximum rms velocity yields a random error in the streamwise mean velocity of 2.25 m/s or $0.0038U_\infty$ for data in Figures 6-10. The maximum random error in the two normal stresses is 4.6% for data in Figures 6-10.

Almost all of the data presented in this study use an ensemble size of 4096 points. However, for the shock transition conditional averages, the ensemble size was limited to 1100 points. For these transition conditional averages, the maximum rms velocities are $0.28U_\infty$ or 165 m/s and $0.11U_\infty$ or 65 m/s for the streamwise and transverse directions, respectively. The resulting maximum random errors in the mean velocity estimates are 9.9 m/s ($0.017U_\infty$) and 3.8 m/s ($0.0064U_\infty$) for the streamwise and transverse directions, respectively. The maximum random error in the two normal stresses for the shock transition data sets is 9.1%.

ACKNOWLEDGMENTS

REFERENCES

Adamson, T C, Jr.; Messiter, A F (1980) Analysis of Two-Dimensional Interactions Between Shock Waves and Boundary Layers. Annual Review of Fluid Mechanics 12: 103-138

Ardonceau, P L (1984) The Structure of Turbulence in a Supersonic Shock-Wave/Boundary-Layer Interaction. AIAA Journal 22: 1254-62

Bendat, J S; Piersol, A G (1986) Random Data. Wiley-Interscience, New York

Beresh, S J; Clemens, N T; Dolling, D S; Comninos, M (1997) Investigation of the Causes of Large-Scale Unsteadiness of Shock-Induced Separated Flow Using Planar Laser Imaging. AIAA Paper 97-0064

Bloomberg, J E (1989) An Investigation of Particle Dynamics Effects Related to LDV Measurements in Compressible Flows. M.S. Thesis, University of Illinois at Urbana-Champaign

Brown, J D; Brown, J L; Kussoy, M I; Holt, M; Horstman, C C (1987) Two-Component LDV Investigation of Three-Dimensional Shock/Turbulent Boundary Layer Interactions. AIAA Paper 87-0553

Brusniak, L (1988) Evaluation of Conditional Sampling Methods for Analysing Separation Shock Motion. AIAA Paper 88-0091

Chan, S C; Clemens, N T; Dolling, D S (1995) Flowfield Imaging of Unsteady, Separated Compression Ramp Interactions. AIAA Paper 95-2195

Dolling, D S (1993) Fluctuating Loads in Shock Wave/Turbulent Boundary Layer Interaction: Tutorial and Update. AIAA Paper 93-0284

Dolling, D S; Brusniak, L (1989) Separation Shock Motion in Fin, Cylinder, and Compression Ramp-Induced Turbulent Interactions. AIAA Journal 27: 734-742

Dolling, D S; Murphy, M T (1983) Unsteadiness of the Separation Shock Wave Structure in a Supersonic Compression Ramp Flowfield. AIAA Journal 21: 1628-1634

Dussauge, J P; Dupont, P (1995) Experimental Evidences of Compressibility Effects on Turbulence in High Speed Flows. In: Transitional and Turbulent Compressible Flows. (eds Kral, L D; Spina, E F; Arakawa, C). ASME FED-Vol. 224, pp 185-192, ASME

Erengil, M E; Dolling, D S (1990) Correlation of Separation Shock Motion in a Compression Ramp Interaction with Pressure Fluctuations in the Incoming Boundary Layer. AIAA Paper 90-1646

Erengil, M E; Dolling, D S (1991) Unsteady Wave Structure Near Separation in a Mach 5 Compression Ramp Interaction. AIAA Journal 29: 728-735

Green, J E (1970) Interactions Between Shock Waves and Turbulent Boundary Layers. Progress in Aerospace Sciences 11: 235-340

Herrin, J L; Dutton, J C (1993) An Investigation of LDV Velocity Bias Correction Techniques for High-Speed Separated Flows. Experiments in Fluids 15: 354-363

Herrin, J L; Dutton, J C (1995) The Turbulence Structure of a Reattaching Axisymmetric Supersonic Free Shear Layer. AIAA Paper 95-2250

Jenson, L (1991) Automatic Digital Signal Processing for LDV. In: Proceedings of the 4th International Conference on Laser Anemometry Advances and Applications. Vol. 2, pp 617-628, Cleveland, Ohio:

Kuntz, D W (1985) An Experimental Investigation of the Shock Wave-Turbulent Boundary Layer Interaction. Ph.D. Thesis, University of Illinois at Urbana-Champaign

Kussoy, M I; Brown, J D; Brown, J L; Lockman, W K; Horstman, C C (1988) Fluctuations and Massive Separation in Three-Dimensional Shock Wave/Boundary Layer Interactions. In: Transport Phenomena in Turbulent Flows: Theory, Experiment, and Numerical Simulation. (eds Hirata, M; Kasagi, N). pp 875-887, New York: Hemisphere

Liou, T-M; Santavicca, D A (1985) Cycle Resolved LDV Measurements in a Motored IC Engine. ASME Transactions: Journal of Fluids Engineering 107: 232-240

Palko, C W; Dutton, J C (1998) Velocity Measurements in a Shock-Separated Free Shear Layer. AIAA Paper Abstract accepted for presentation at the 36th AIAA Aerospace Sciences Meeting

Rask, R B (1981) Comparison of Window, Smoothed-Ensemble, and Cycle-by-Cycle Data Reduction Techniques for Laser Doppler Anemometer Measurements of In-Cylinder Velocity. In: Fluid Mechanics of Combustion Systems. (eds Morel, T; Lohmann, R P; Rackley, J M). pp 11-20, New York: ASME

Selig, M S; Andreopoulos, J; Muck, K C; Dussauge, J P; Smits, A J (1989) Turbulence Structure in a Shock Wave/Turbulent Boundary Layer Interaction. AIAA Journal 27: 862-869

Selig, M S; Smits, A J (1991) Effect of Periodic Blowing on Attached and Separated Supersonic Turbulent Boundary Layers. AIAA Journal 29: 1651-1658

Shaw, R J (1995) An Experimental Investigation of Unsteady Separation Shock Wave Motion in a Plume-Induced, Separated Flowfield. Ph.D. Thesis, University of Illinois at Urbana-Champaign

Smits, A J; Muck, K C (1987) Experimental Study of Three Shock Wave/Turbulent Boundary Layer Interactions. Journal of Fluid Mechanics 182: 291-314

Witze, P O; Martin, J K; Borgnakke, C (1984) Conditionally-Sampled Velocity and Turbulence Measurements in a Spark Ignition Engine. Combustion Science and Technology 36: 301-317
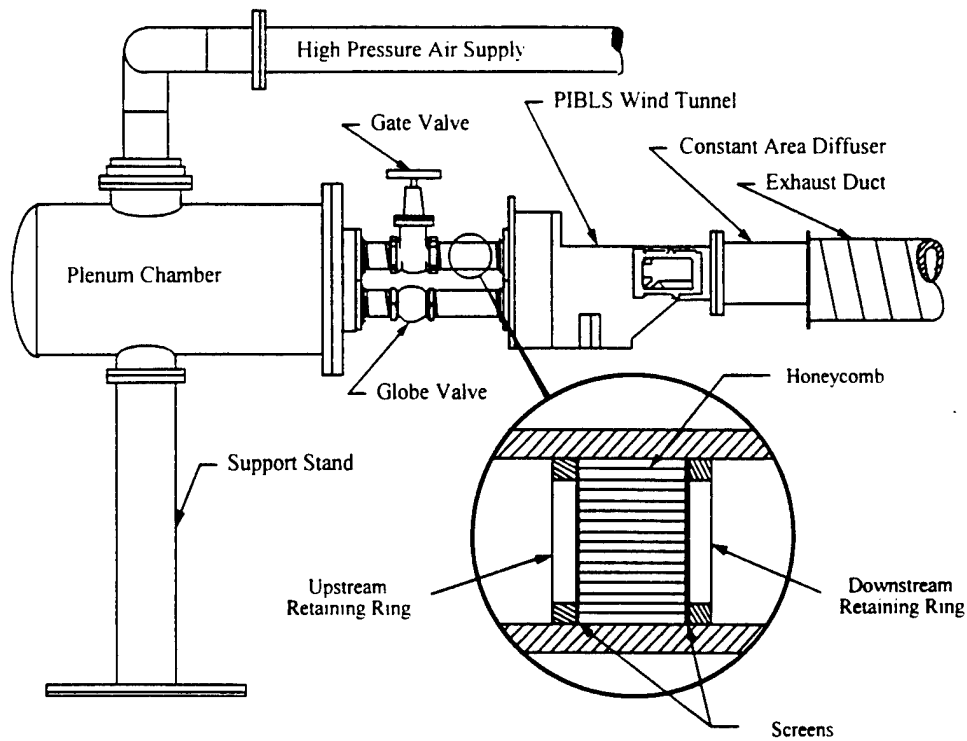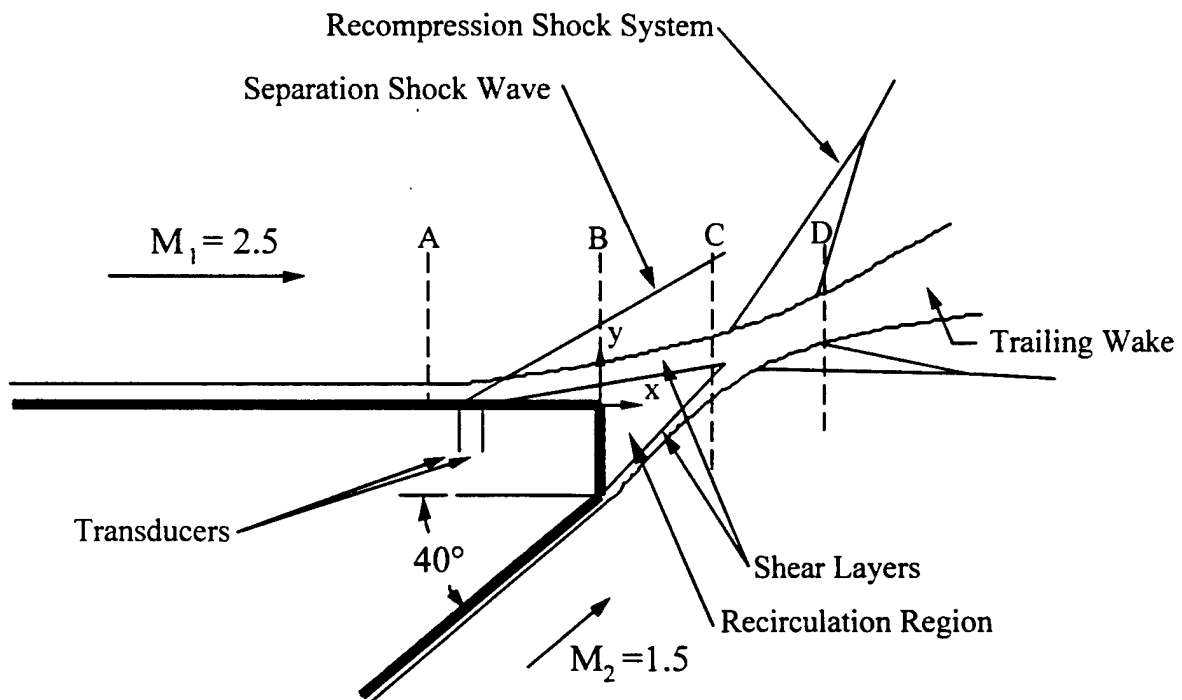
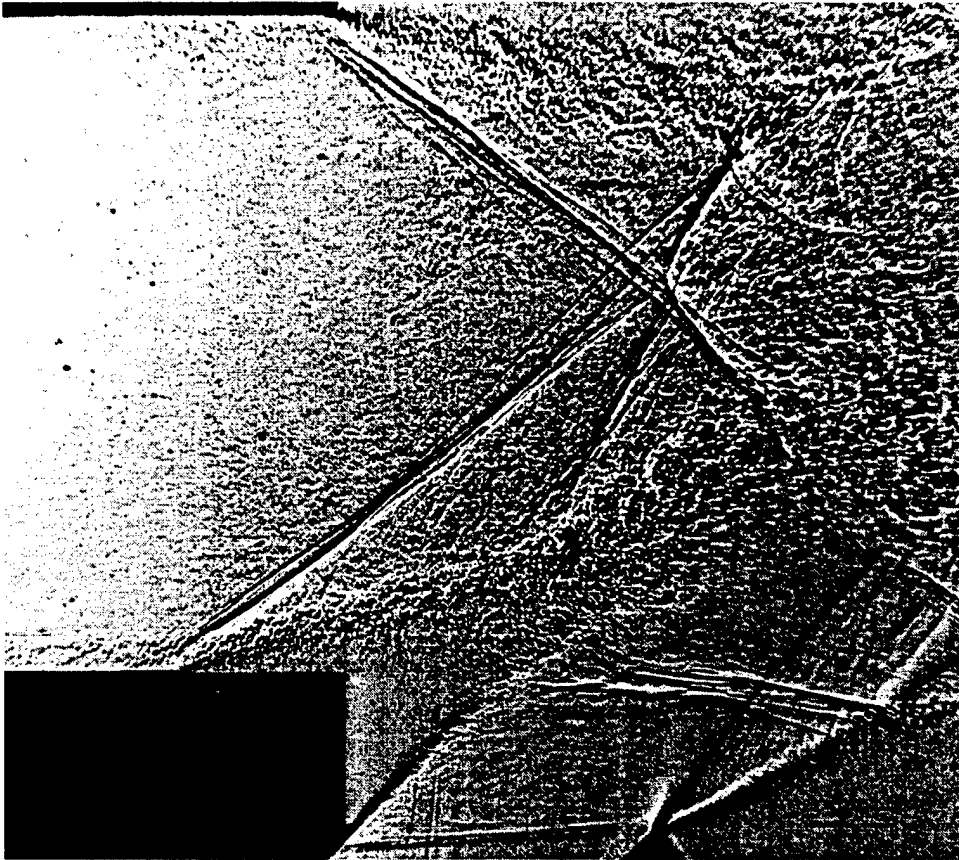**Figure 1 PIBLS tunnel schematic (Shaw 1995)**

Figure 2 Flowfield schematic

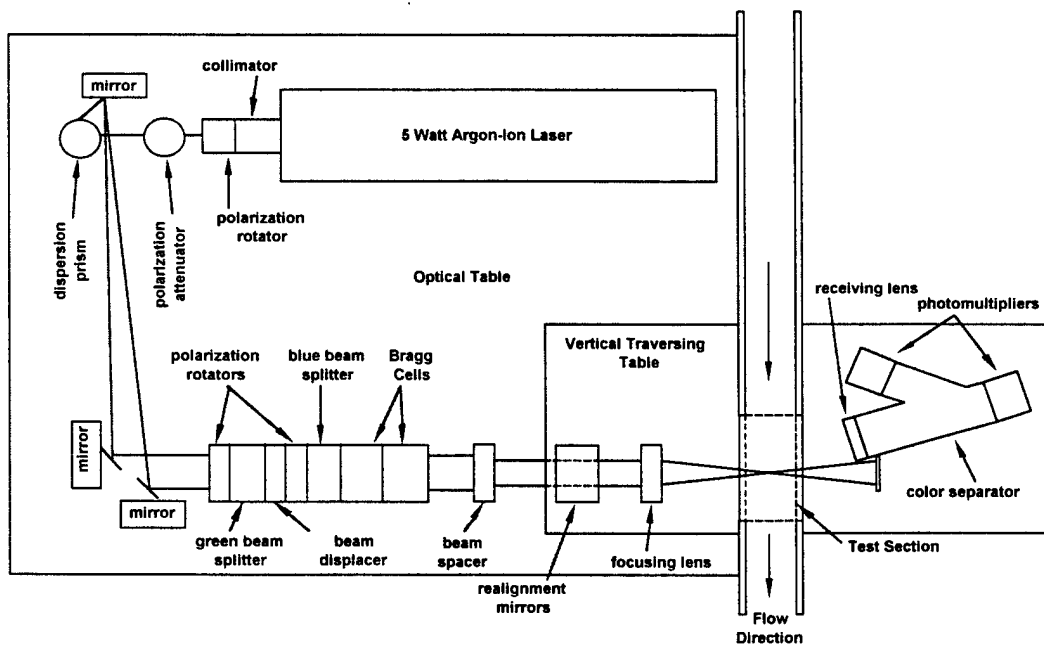**Figure 3 Flowfield shadowgraph** (Shaw 1995)

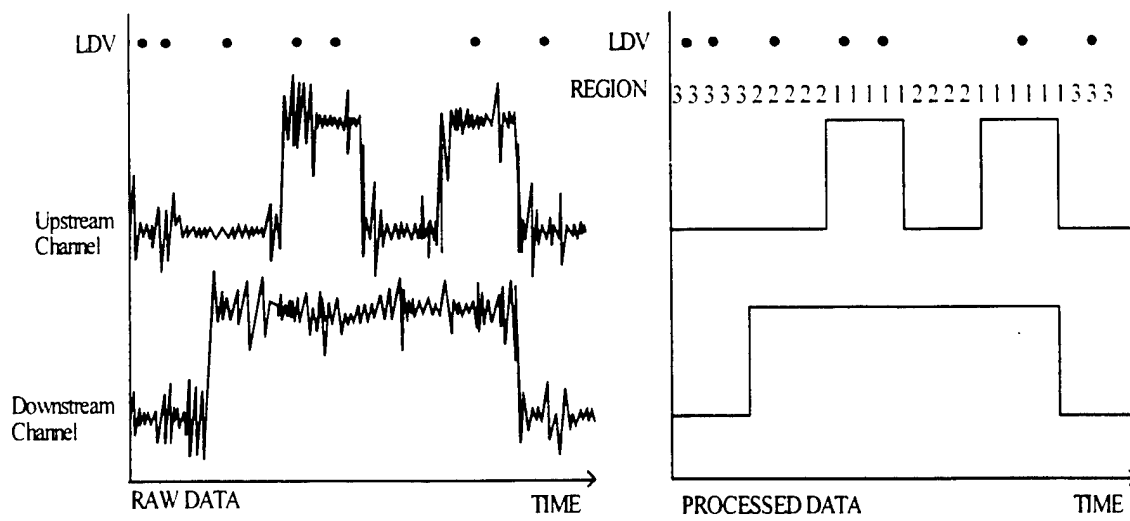**Figure 4 Laser Doppler velocimetry (LDV) system**

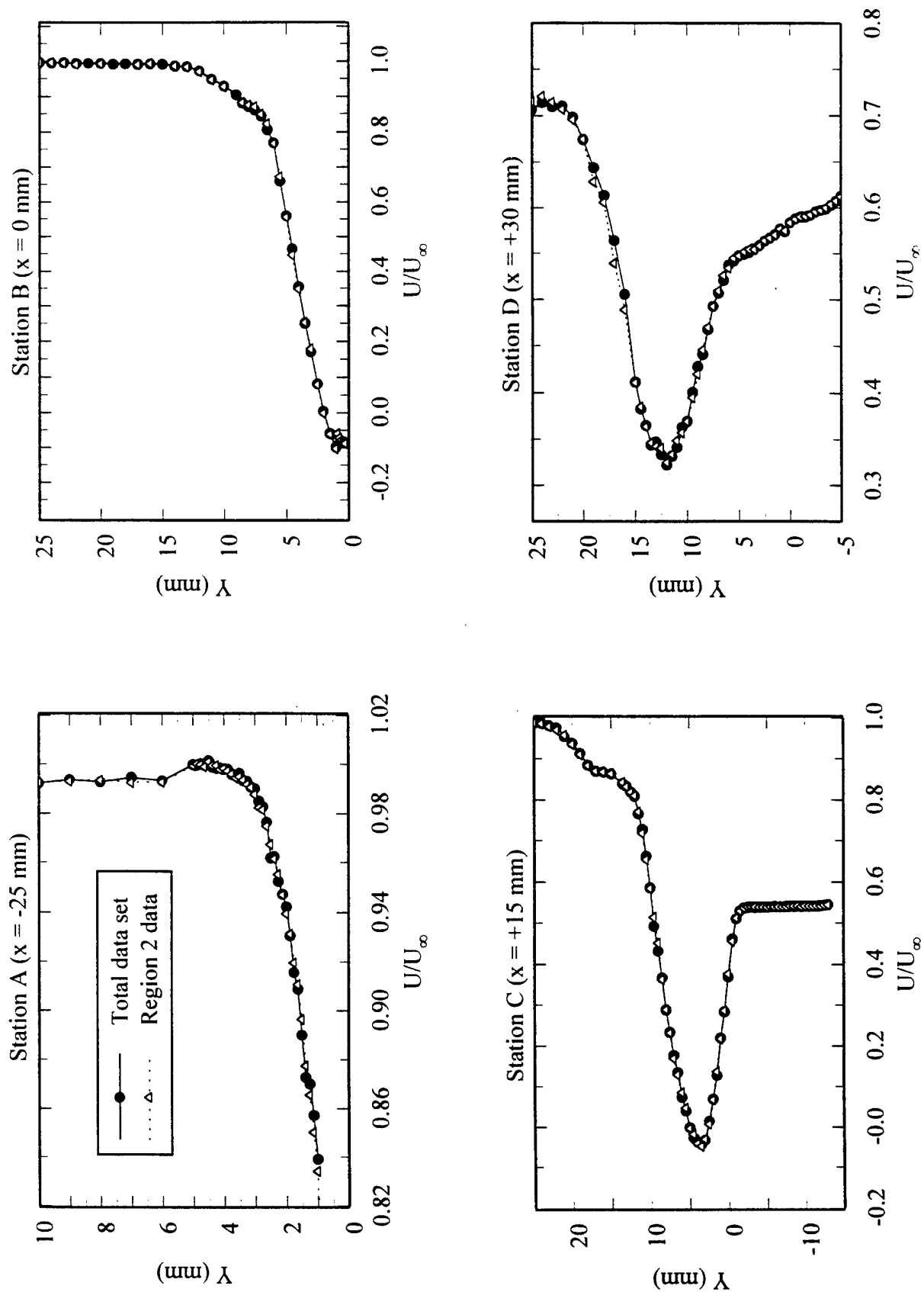**Figure 5 Conditional analysis algorithm**

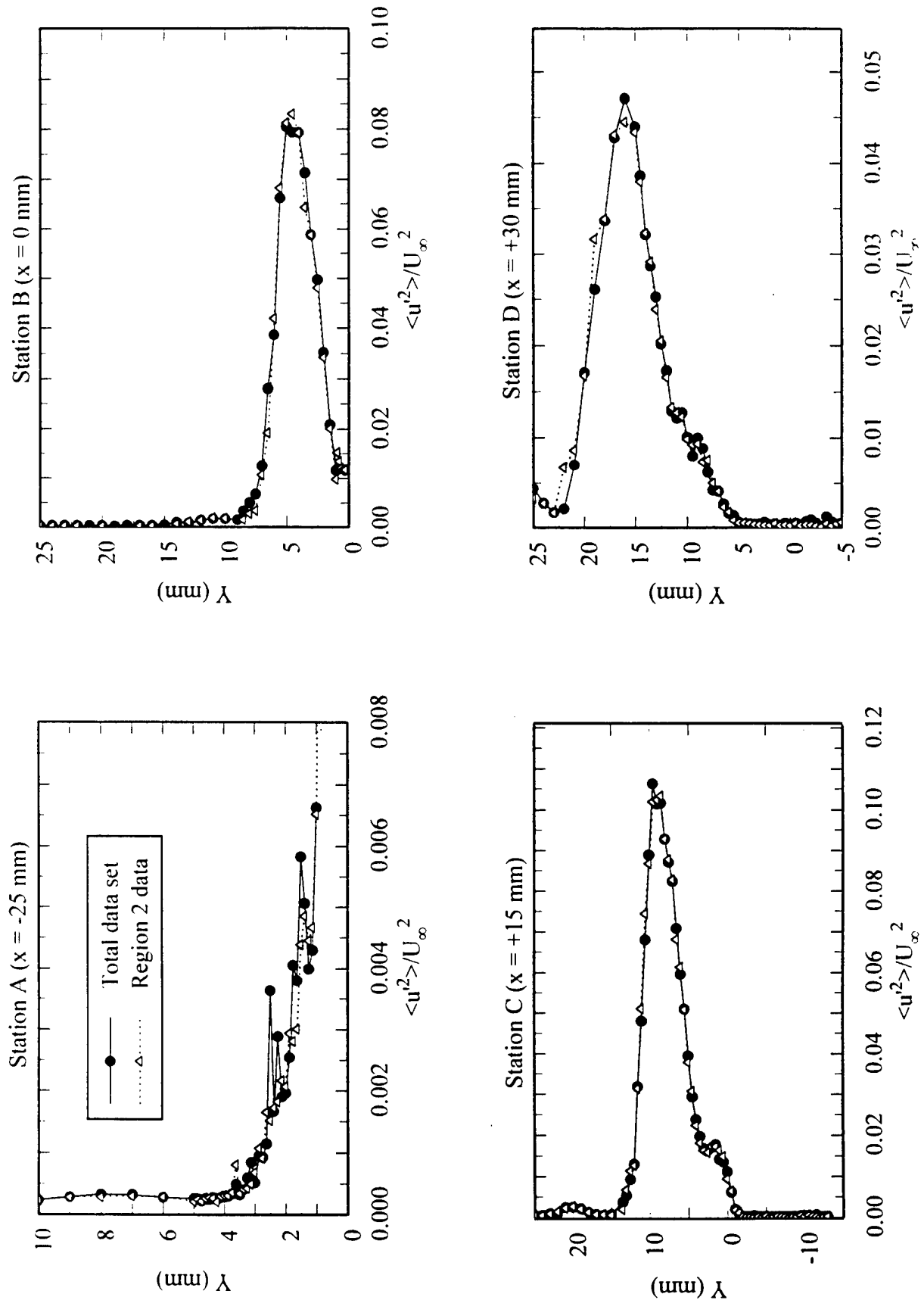Figure 6 Dimensionless mean streamwise velocity, U/U_∞

Figure 7 Dimensionless streamwise normal stress, $\langle u'^2 \rangle / U_\infty^2$
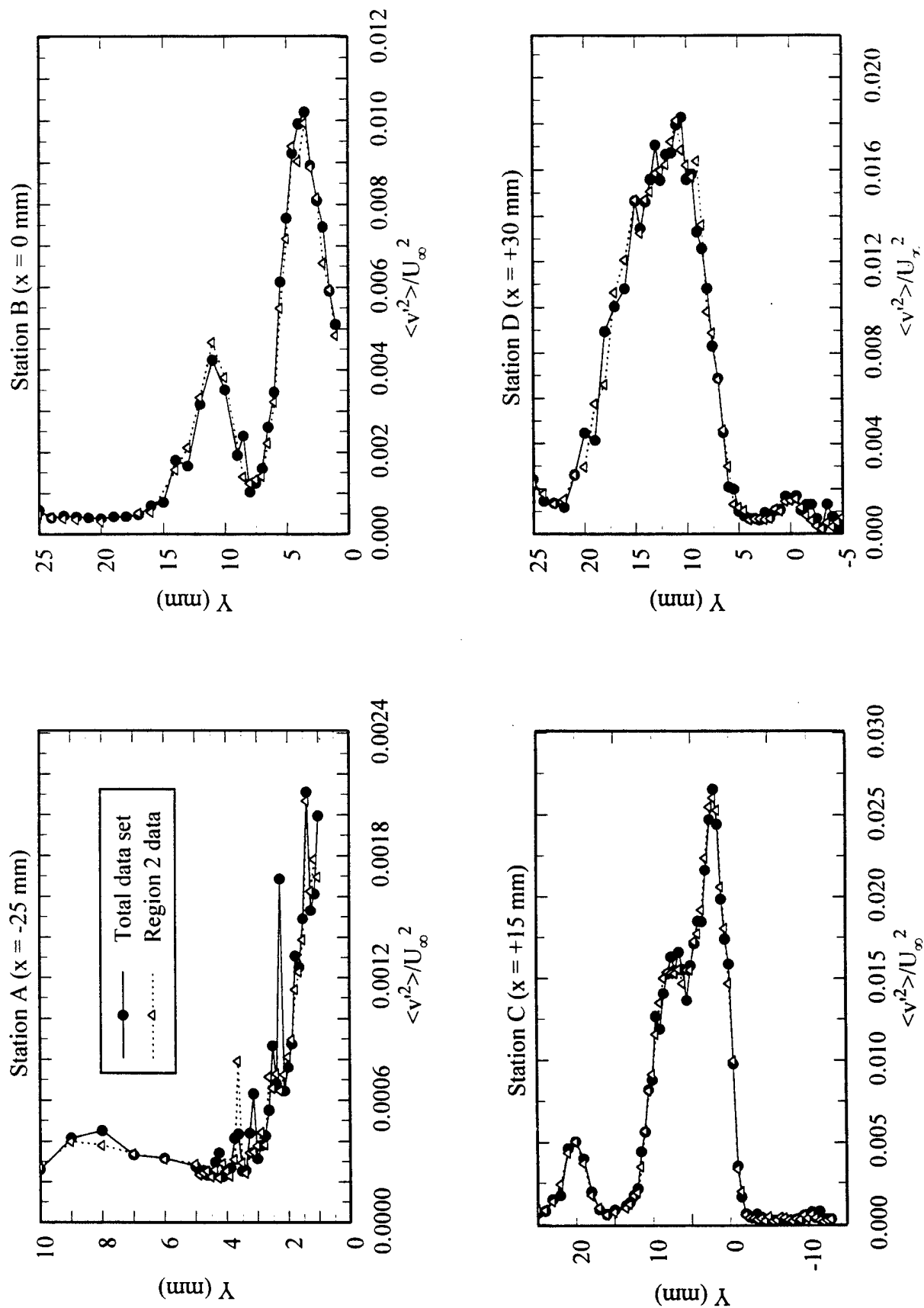
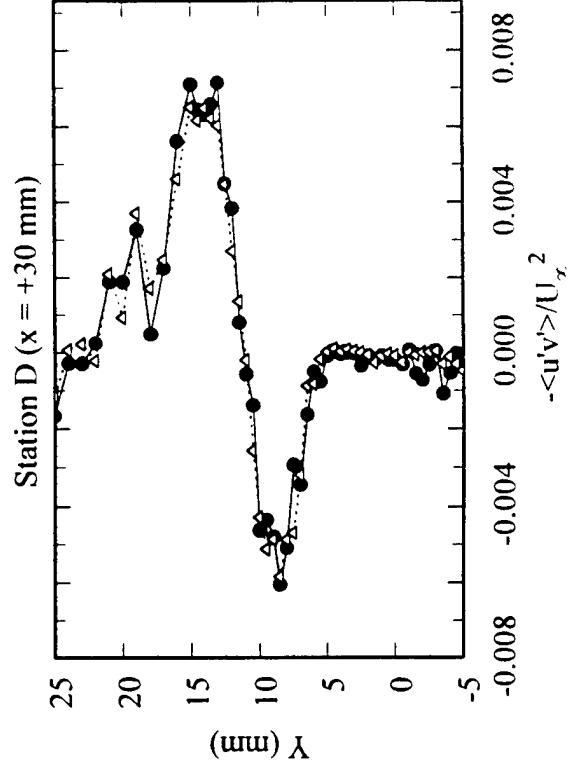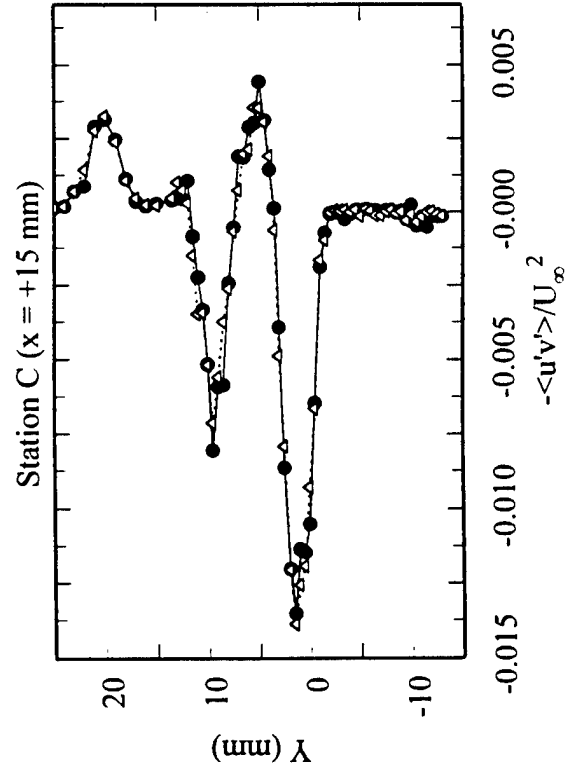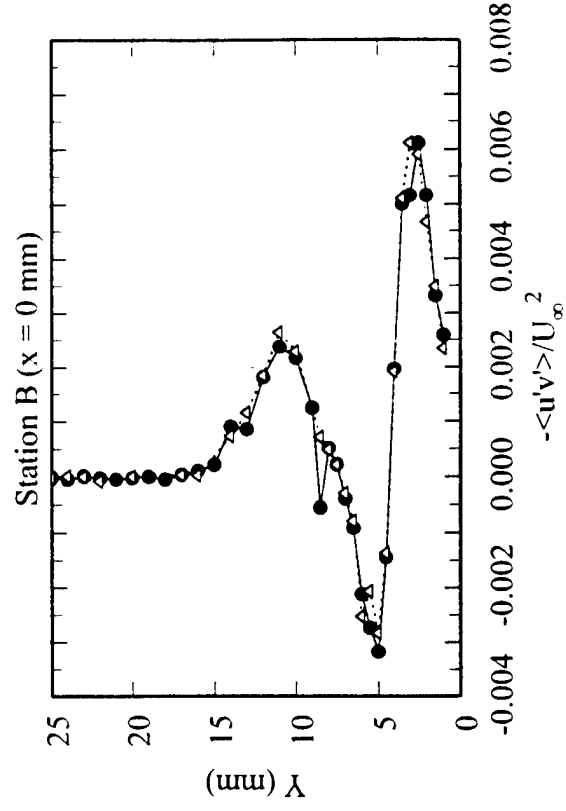Figure 8 Dimensionless transverse normal stress, $\langle v'^2 \rangle / U_\infty^2$
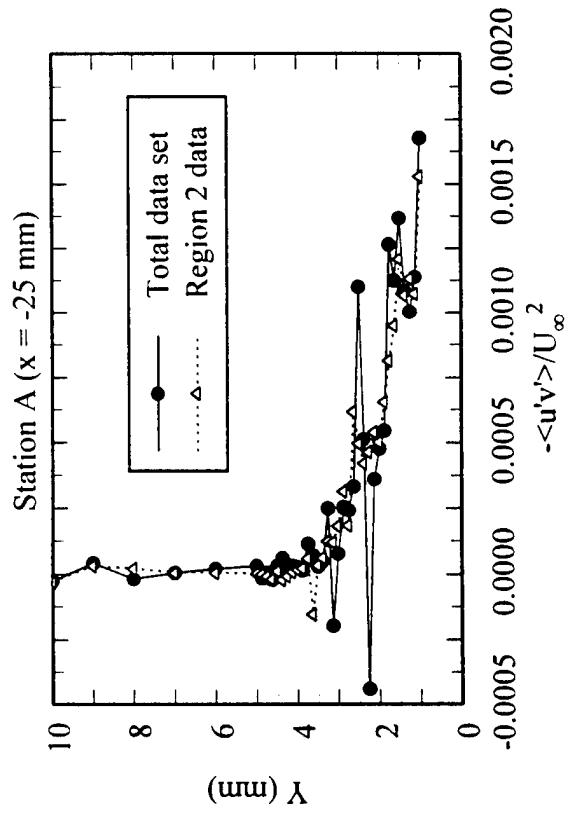
Figure 9 Dimensionless Reynolds shear stress, $-\langle u'v' \rangle / U_\infty^2$
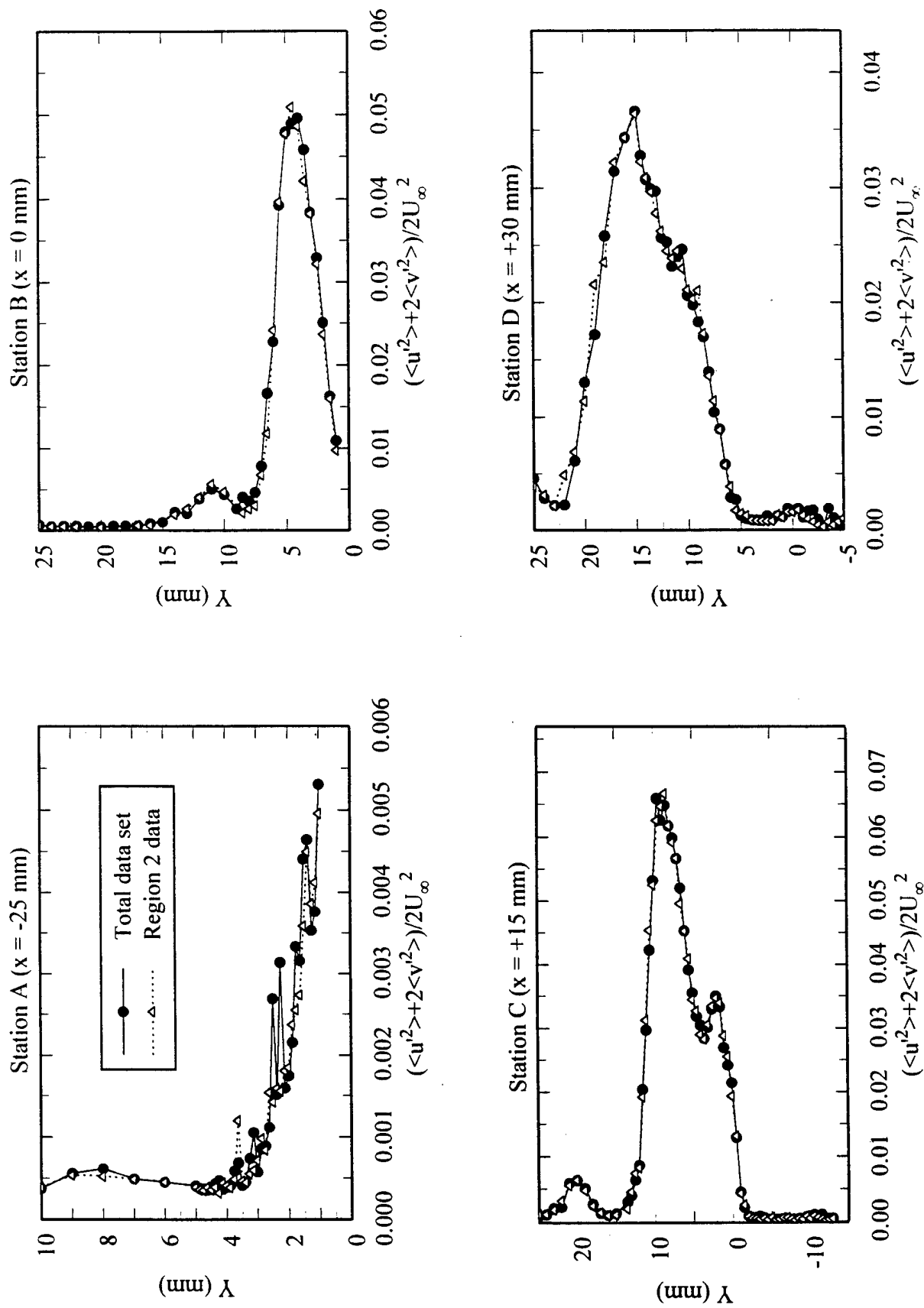
Figure 10 Dimensionless turbulent kinetic energy, $(\langle u'^2 \rangle + 2\langle v'^2 \rangle)/2U_\infty^2$
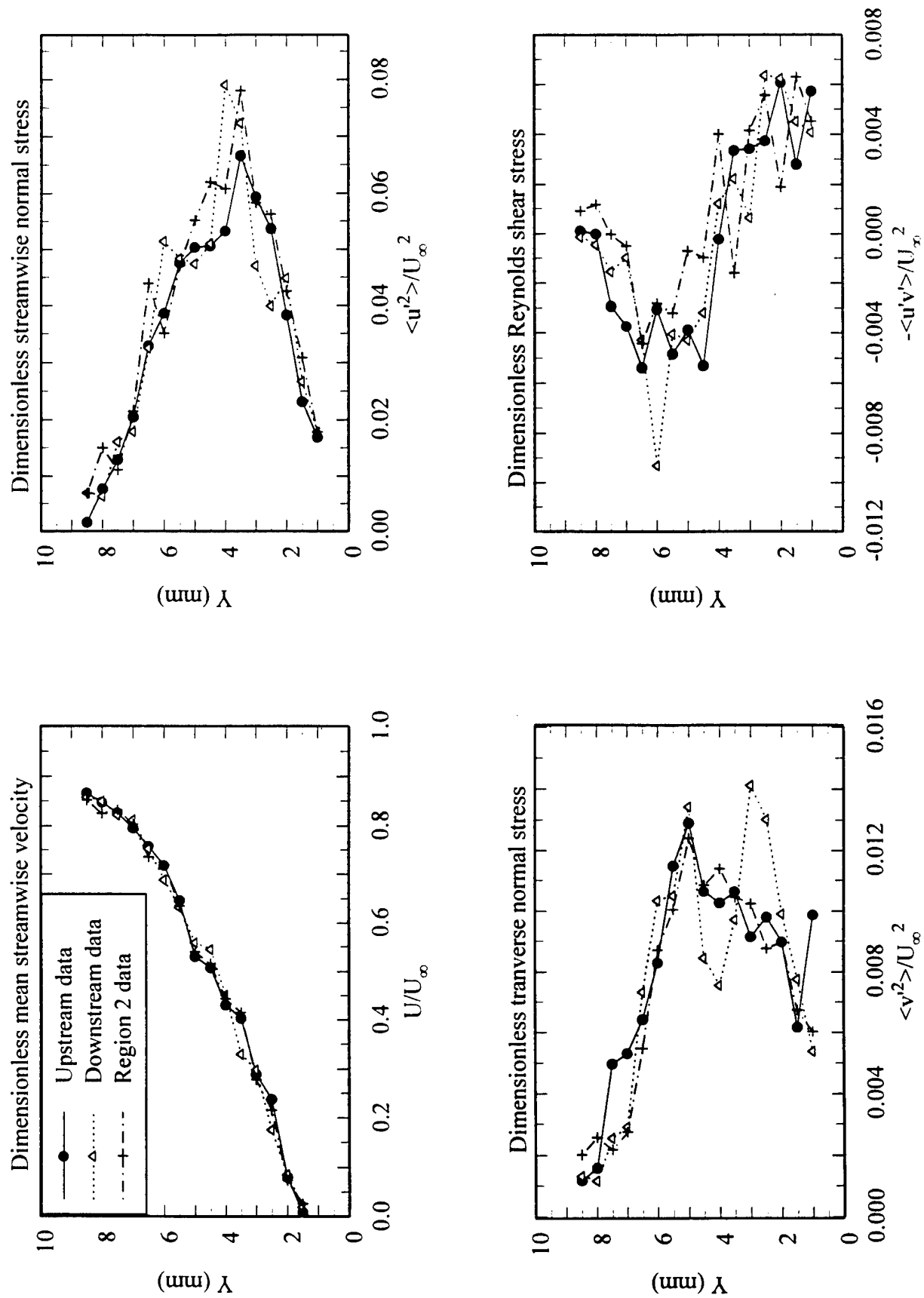
Figure 11 Shock direction results at station B (x = 0 mm)

APPENDIX A.11

VELOCITY MEASUREMENTS IN A SHOCK-SEPARATED FREE SHEAR LAYER

by

C. W. Palko and J. C. Dutton

VELOCITY MEASUREMENTS IN A SHOCK-SEPARATED FREE SHEAR LAYER

Carl Palko*
The Aerospace Corporation

Craig Dutton[†]
Univ. of Illinois at Urbana-Champaign

ABSTRACT

Two-component laser Doppler velocimetry (LDV) measurements were made in a planar, shock-separated free shear layer formed by the convergence of two supersonic streams past a thick plate. High-speed wall pressure measurements locate the unsteady shock wave formed by this interaction and, consequently, allow separation of the effects of shock motion from the turbulence fluctuations in the velocity measurements of the shear layer. Shock-induced separation dramatically increases the normal stresses and shear stress. The shock-separated shear layer displays a positive shear stress region between separation and reattachment. Reattachment produces a shift in turbulent kinetic energy from the streamwise component to the transverse component. The region of shock motion has a relatively constant width irrespective of distance from the wall.

---

* Ph.D., Member of the Technical Staff, Member AIAA, 118 Virginia St, #3, El Segundo, CA 90245. The research contained in this paper was completed prior to becoming a Member of the Technical Staff of the Aerospace Corporation.

† W. Grafton and Lillian B. Wilkins Professor, Associate Fellow AIAA, Rm 140 MEB, MC-244 UIUC, Urbana, IL 61801.

1

INTRODUCTION

While shock-induced boundary layer separation caused by a second fluid stream has been

investigated over the last 40 years, there are no known turbulence measurements in such

a flow. However, shock-induced shear layer formation in front of solid objects has been

investigated.[1-3] Among these geometries, unswept compression corner flows provide the

closest analogy to the current study.

To date only four studies of turbulence in unswept compression corners have been

performed: Ardonceau;[4] Kuntz;[5] Smits and Muck;[6] and Selig et al.[7] All of the studies, except

for that of Selig et al., considered a series of corner angles resulting in both unseparated and

separated flows. Unlike the other studies, Selig et al. investigated a flowfield with active forcing

(by mass addition). All of Kuntz's data and some of Ardonceau's were obtained using two-

component LDV. The remaining studies, including a portion of Ardonceau's, used constant

temperature hot-wire anemometry. The Mach numbers for the studies by Ardonceau, Kuntz,

Smits and Muck, and Selig et al. were 2.25, 2.94, 2.90, and 2.84, respectively. All of these

studies noted large increases in turbulence through the shock interaction and unsteady shock

motion. However, none of these studies used any conditional analysis to separate velocity

fluctuations due to the motion of the shock from those due to turbulence. Palko and Dutton[8]

have demonstrated a technique for separating the fluctuation contributions from these two

sources; this method is used in the measurements reported here.

Several mechanisms have been proposed to explain the turbulence amplification in shock

wave-boundary layer interactions. A nonlinear coupling of entropy, pressure, and vorticity

fluctuations involving the Rankine-Hugoniot jump conditions at the shock has been proposed by

Anyiwo and Bushnell.[9] Turbulence amplification as a direct result of shock wave

2

unsteadiness[10,11] is also widely cited. Finally, both bulk compression and concave streamline curvature present in shock wave-boundary layer interactions are known to be destabilizing and, therefore, turbulence enhancing.[12] All four of these mechanisms become more significant as the corner angle is increased, thereby increasing the shock strength and the range of shock motion. Another mechanism that is not often cited is the effect of separation itself.

The studies of Ardonceau, Kuntz, Selig et al. and Smits and Muck all involved relatively thick boundary layers (8, 8, 26, and 26 mm, respectively) and very small separated regions. The current study involves an approximately 3 mm thick turbulent incoming boundary layer and a large separated flow region. This separation bubble serves as a reservoir of low momentum fluid that may be entrained by turbulent structures within the free shear layer. Unfortunately, the lack of prior studies involving a large separated region makes the effects of separation caused by a second fluid stream rather than by a solid ramp face difficult to determine.

In contrast to the case of shock-separated free shear layers are expansion-separated shear layers. To help understand the flow physics of the shock-separated case, this paper will make comparisons with the work of Amatucci[13] and Herrin,[14] which represent comprehensive LDV investigations of the mean flow and turbulence in planar and axisymmetric expansion-separated shear layers, respectively. Herrin investigated a single $M = 2.5$ (before separation) shear layer while Amatucci studied both $M = 2.56$ and $M = 2.05$ shear layers. Like the current study, both Amatucci's and Herrin's flows involved relatively thin incoming boundary layers and a large separated flow region.

FLOW FACILITY

A schematic of the test section and flowfield features investigated in this study is shown in Figure 1. The upper Mach 2.5 stream (unit Reynolds number, $Re=48.9 \times 10^6 \, m^{-1}$) and the lower Mach 1.5 stream ($Re=36.2 \times 10^6 \, m^{-1}$) converge at a $40°$ angle past a 12.7 mm high base plane. The boundary layer of the upper stream intercepts the oblique separation shock, consequently separates, and forms a free shear layer, as shown in Figure 1. This shear layer then reattaches with the shear layer formed by the separation (at near zero pressure gradient) of the boundary layer of the lower stream, thereby enclosing a recirculating region behind the base. The reattachment of the shear layers generates a recompression shock system and the resulting trailing wake.

The upper and lower streams have absolute stagnation pressures of 506 kPa and 251 kPa, respectively, resulting in a static pressure ratio of the lower to the upper streams of $P_2/P_1=2.27$. Surface oil flow visualization shows that the center 32 mm (63%) of the flowfield is free from sidewall effects and is, consequently, two-dimensional in this region. The blowdown-type supersonic wind tunnel used to produce this flowfield is described briefly in Palko and Dutton[8] and comprehensively in Palko[15] and Shaw.[16]

EQUIPMENT

A two-component laser Doppler velocimetry (LDV) system, with a TSI IFA 750 digital burst correlator operating in coincident mode, was used for the mean velocity and turbulence measurements. A detailed discussion of the IFA 750 operation is given by Jenson.[17] One beam of each color is shifted by 40 MHz to minimize fringe biasing and to allow discrimination of

negative velocities. The blue and green beam pairs are also oriented at approximately $+45°$ and $-45°$, respectively, to the mean flow direction of the upper stream to minimize fringe blindness.

Separate TSI model 9306 six-jet atomizers introduce silicone oil droplets with a mean diameter of approximately 0.8 μm into each stream.[18] The oil droplets are injected downstream of all flow-conditioning modules and upstream of the nozzle blocks through small stainless steel tubes. The scattered light from the droplets is collected in forward scatter at an off-axis collection angle of $10°$ resulting in an effective measurement volume length of 1.5 mm. The 13 mm beam spacing and 250 mm focal length transmitting lens result in a measurement volume diameter of 0.127 mm (the spatial resolution in the two velocity measurement directions).

Due to their significant inertia, seed particles produce curved pathlines behind an oblique shock wave instead of following the fluid streamlines that bend discontinuously at the shock front. Using the Carlson-Hoglund[19] empirical drag law, significant particle lag effects in this study were estimated to be limited to a region extending 2.8 mm in the streamwise (x) direction downstream of the shock wave (i.e., 1.4 mm normal to the shock). This oblique shock wave represents by far the largest velocity gradient in the present flowfield. A detailed uncertainty analysis of the velocity measurements[15] predicts a maximum uncertainty outside the region of significant particle lag of ±3.1% for the mean velocity and ±4.6% for the turbulent stresses.

Since the boundary layer separation point oscillates in the streamwise direction with the shock wave, the shear layer will also oscillate and cause biasing of unconditionally averaged velocity data. Palko and Dutton[8] and Palko[15] describe in detail the conditional analysis technique used in the current study to minimize bias in the velocity measurements due to shock wave unsteadiness. This technique allows the shock position (upstream, between, or

5

downstream of the two transducers) to be determined for each velocity realization. By ensemble-averaging realizations that are obtained only when the shock is between the transducers, this procedure effectively "freezes" the shock in this position and minimizes the velocity fluctuations that would otherwise be recorded due to the shock motion. However, large data sets must be obtained to ensure adequate statistical certainty from the ensemble averages. Since the transducers are placed at 19.0 and 16.5 mm upstream of the base plane (Figure 1), the mean shock foot position (i.e., the boundary layer separation point) for the conditionally analyzed data set is 17.75±1.6 mm upstream of the base. Palko[15] describes in detail the entire pressure data acquisition system.

RESULTS

This paper presents data obtained at approximately 1500 spatial locations along the spanwise centerplane of the flowfield. The origin of the measurement grid is the upper base corner with the x-axis aligned parallel to the wall (Figure 1). The streamwise spacing of the measurement locations is a uniform 2.5 mm, but the transverse spacing varies from 0.125 mm in high-gradient regions to 1.0 mm in the almost uniform freestreams. Two-component velocity measurements are limited to $y > 1$ mm due to beam clipping at the wall below this point. The entire measurement grid has an *absolute* positional uncertainty (systematic error) in the streamwise and transverse directions of ±250 μm with respect to the base, but the *relative* positional uncertainty (random error) of each point with respect to each other within the measurement grid is only ±0.5 μm.

Previously, Palko and Dutton[8] presented selected profiles obtained with and without conditional analysis to illustrate the effects of shock motion on the turbulence. This paper

6

instead analyzes *global flowfield features* by presenting results (using 4096 instantaneous velocity realizations at each spatial location) obtained only when the shock was between the two transducers. The contour levels in the data plots do not represent regular intervals in the data, but instead were chosen to clearly illustrate the features of the flowfield. Furthermore, the mean velocities and Reynolds stresses have been non-dimensionalized using the freestream velocity in the upper stream, $U_\infty = 590$ m/s. Finally, all contour and line plots presented in this study are unsmoothed, and the data have been velocity debiased using the interarrival time weighting method shown by Herrin and Dutton[20] to be the most accurate debiasing method in this type of flow.

Mean Flow

Table 1 lists various properties of the incoming boundary layer of the upper stream. These properties were determined by applying a curve-fit for compressible, turbulent boundary layers[21] to the experimentally obtained boundary layer profile. The best curve-fit was found by varying the boundary layer thickness, δ, and the skin friction coefficient, C_f, until the mean square deviation between the curve-fit and the experimental data was minimized. The resulting profile equation was then numerically integrated to yield the boundary layer integral parameters listed in Table 1. The Reynolds number based on the various thicknesses may be estimated as $Re_\delta = 120,000$, $Re_{\delta^*} = 28,000$, and $Re_\theta = 7600$.

Figure 2 presents a contour plot of the normalized mean streamwise velocity component, U/U_∞. These results clearly indicate the approach boundary layer, the two shear layers, the recirculation region behind the base (denoted by negative values of U/U_∞), the separation shock, the upper system of recompression waves, and the trailing wake. The two shear layers reattach

at approximately 16.25 mm downstream of the base. (Due to the dominance of the streamwise velocity component, reattachment is defined here as the point of zero U/U_∞.) The reattachment point is noted by a small plus sign in Figure 2 and all subsequent contour plots. Also interesting is the sudden, almost discontinuous decrease in the streamwise mean velocity and subsequent thickening of the boundary layer at the shock foot location ($x = -17.75$ mm). The presence of this discontinuity at the expected location between the two transducers indicates that the shock position is being accurately "frozen" by the conditional analysis algorithm.

The combined mean velocity field (streamwise and transverse components) is presented as a vector plot in Figure 3. This figure clearly shows the uniform flow in each freestream approaching the base, the two shear layers, the separation shock, the reattachment point at $x = +16.25$ mm, and the wake development. The thickening of the upper boundary layer as the base plane is approached is also apparent in Figure 3. The inflection points in the velocity profiles immediately upstream of the base are expected since the flow is separated at these locations. To allow closer examination of the recirculation region, a vector plot of only the base region is presented in Figure 4. The two distinct recirculating eddies within the region of separated flow may be clearly seen in Figure 4 as well as the recirculating flow near the wall at the base plane below the upper shear layer. The reattachment of the two shear layers in the neighborhood of $x = +16$ mm is also more apparent in this expanded view.

An equivalent "ramp corner angle" may be defined for the current flow as the angle between the mean reattached wake direction (inviscid slip line) and the x-axis. This inviscid slip line is, of course, a compliant boundary rather than a rigid boundary such as the downstream ramp surface in a compression corner. By using a linear regression through the points of

minimum streamwise velocity at all measured streamwise locations downstream of reattachment, this equivalent corner angle is estimated to be 28°.

Figure 5 presents the mean Mach number distribution throughout the flowfield. The Mach number was obtained by measuring the stagnation temperature inside the plenum chamber of the wind tunnel and applying the assumption of adiabatic flow to extract the static temperature and speed of sound throughout the flowfield. Figure 5 clearly reveals the separation shock, the recompression wave systems and the large subsonic region downstream of the base. The dramatic change in compressibility across the upper shear layer is indicated by the highly compressible freestream on the outside ($M > 2.0$) and the large region of nearly incompressible flow near the base on the inside of this thin layer ($M < 0.3$).

To quantify the compressibility of the shock-separated shear layer one may use the mean velocity data to determine a convective Mach number, M_C.[22,23] The convective Mach number is the Mach number of each freestream relative to the large-scale turbulent structures in the free shear layer. For cases in which the freestream gases on each side of the shear layer are the same and stream 1 is the high-speed stream, the convective Mach number can be computed as:

$$M_C = \frac{U_1 - U_2}{a_1 + a_2} \tag{1}$$

For the upper shear layer in this study, the convective Mach number is approximately 1.4, which indicates very strong effects of compressibility. This value of M_C is also approximately equal to those of the planar and axisymmetric expansion-separated free shear layers in the studies of Amatucci[13] and Herrin,[14] respectively.

Reynolds Normal Stresses

The dimensionless streamwise normal stress distribution is displayed in Figure 6. Clearly, the turbulence in both freestreams is very small. The shock-induced separation process dramatically increases the streamwise normal stress, and the reattachment process and wake development dramatically decrease it in the upper shear layer. The shock interaction increases the streamwise normal stress by a factor of about 5.5 times the peak measured value in the incoming boundary layer of $0.02U_\infty^2$. The maximum streamwise normal stress value of $0.11U_\infty^2$ occurs immediately upstream of reattachment.

The increased streamwise turbulence levels in the current study match closely those cited by Ardonceau[4] in his separated, 18° compression corner flow, but exceed those cited in the other shock interaction studies. These differences could be attributable to possible difficulties in interpreting hot-wire measurements made in supersonic flows[6] and the lack of LDV data immediately downstream of the interaction in Kuntz's[5] study. The peak streamwise turbulence levels in the present study exceed those of both Herrin and Amatucci. This difference is due to the presence of the adverse pressure gradient, bulk compression, and concave streamline curvature at separation for the current shock-separated shear layer, as compared to the expansion-separated cases.

The transverse normal stress distribution is displayed in Figure 7. Separation of the upper shear layer dramatically increases the transverse normal stress by a factor of 5 over that in the incoming boundary layer. The lower shear layer displays large values of transverse normal stress, but this is primarily due to the inclination of the lower shear layer with respect to the x-

axis. Because of this, velocity fluctuations within the lower shear layer have a large transverse component.

While the transverse normal stress in the lower shear layer (and for the entire flowfield) peaks before reattachment (at $x = +12.5$ mm), the transverse normal stress in the upper shear layer increases throughout the recompression region and through reattachment. In general the developing wake exhibits decreasing turbulence levels, but large values ($> 0.018U_\infty^2$) of transverse normal stress persist for over 12.5 mm downstream of reattachment (to $x = +28.75$ mm). The far wake is characterized by decreasing transverse normal stress, but at the downstream limit of the measurement region ($x = +40$ mm), the values are still greater than $0.010U_\infty^2$ (which is equal to the value immediately after separation). This delayed decrease in the transverse normal stress may be indicative of a shift in turbulent energy with recompression and reattachment from the streamwise normal stress to the transverse and spanwise normal stresses. Herrin and Dutton[24] also note increasing normal stress isotropy through reattachment of an axisymmetric shear layer that is indicative of such a shift in turbulent energy. This delayed decrease may also be due to the large transverse normal stress in the lower shear layer that comes primarily from the inclination of the lower shear layer with respect to the x-axis.

The streamwise normal stress in the current study peaks immediately before reattachment. This feature is common to compressible free shear layers formed through both planar rapid expansions[13] and planar shock-induced separation,[15] but contrasts with the decreasing turbulence levels through recompression and reattachment in axisymmetric geometries.[24] This provides evidence of the stabilizing (i.e., turbulence-reducing) effect of lateral streamline convergence for the axisymmetric case, but not for the planar.

Turbulence Amplification

Turbulence amplification has been documented in many types of shock wave-boundary layer interactions. Smits and Muck[6] reported in their 8°, 16°, and 20° compression corner studies normal stress amplification factors of up to 14 times the incoming boundary layer values, with the larger corner angles (i.e., stronger shocks) exhibiting the larger turbulence amplification. Smits and Muck used the "Strong Reynolds Analogy" (SRA) to extract the kinematic turbulent stresses from the mass-weighted hot-wire measurements. However, the SRA assumes that pressure fluctuations are negligible, which is not true downstream of unsteady shock waves and therefore complicates the interpretation of hot-wire measurements in such flows. Kuntz[5] reported peak streamwise normal stress levels in the *reattached* boundary layer of between 2 and 10 times the levels in the approaching boundary layer, for his 8°, 12°, 16°, 20°, and 24° compression corners, respectively. Larger turbulence amplification factors may well have occurred in Kuntz's flow upstream of reattachment, but were not measured. By comparison, the streamwise normal stress in the present study peaks *upstream* of reattachment. In his 18° compression corner, Ardonceau[4] reports a peak streamwise normal stress value just below the center of his shear layer prior to reattachment of $0.114U_\infty^2$, an increase of a factor of 4.3 over the approaching boundary layer values. This agrees well with the peak value in the present study. The normal stress amplification ratios quoted for Kuntz and Ardonceau are estimated from turbulence intensity profiles and consequently have large uncertainties.

Ardonceau[4], Kuntz[5], and Smits and Muck[6] examined a range of compression corner angles. All these studies found increasing turbulence amplification with increasing corner angle and attributed it to increasing shock strength, bulk compression, and concave streamline

curvature. Both Ardonceau and Kuntz found no dramatic difference between separated (larger angles) and unseparated (smaller angles) corner flows, indicating that separation has little effect on turbulence amplification. Smits and Muck[6] concluded that for weak shocks turbulence amplification is primarily due to the effects of bulk compression, adverse pressure gradient, and concave streamline curvature. Smits and Muck assert that the turbulence amplification depends more on the overall pressure rise through the interaction than on the presence of a shock wave. They also proposed that shock wave oscillation becomes an important mechanism for stronger shocks.

Selig and Smits,[11] however, in a separated 24° compression corner study, concluded that shock unsteadiness is not an important mechanism, since the downstream turbulence showed no change when the shock wave was driven at a particular frequency. The shock wave was forced in this flow by periodic blowing into the separated region and, unlike the present study, no conditional analysis was used to isolate either shock position or shock motion direction from the turbulent fluctuations. In contrast, Palko and Dutton[8] found that shock motion direction does have a significant effect on downstream turbulence levels as well as on the organization of the turbulence.

Amatucci[13] and Herrin[14] also report turbulence increases smaller than the above-cited levels for their planar and axisymmetric base flows, respectively. Both researchers found that, despite the stabilizing influences of a favorable pressure gradient, bulk expansion, and convex streamline curvature, the turbulence at the inner (low-speed) edge of the free shear layer increases dramatically over its levels in the approaching boundary layer in response to the expansion at separation. In particular, Herrin found that the turbulence levels in the outer portion of his free shear layer formed through a rapid expansion were "frozen" at or below the upstream

13

levels, while the inner edge experienced streamwise normal stress increases of approximately 9 times the levels in the approaching boundary layer.

Ardonceau[4] and Kuntz[5] report increases of 9 and 20, respectively, over the peak transverse normal stress levels in their approaching boundary layers for their compression corner flows. Herrin[14] reports a peak transverse normal stress value of $0.024U_\infty^2$ for his rapidly expanded axisymmetric free shear layer. The data of Herrin reflect an increase of 3 over the transverse normal stress level in his approaching boundary layer. Amatucci's[13] data display amplifications of roughly 3 and 8 times the peak transverse normal stress levels in the approaching boundary layers for his upper (Mach 2.56) and lower (Mach 2.05) rapidly expanded planar shear layers, respectively. The peak transverse normal stress amplification factor in the present study lies within the range cited above.

Turbulent Kinetic Energy

The turbulent kinetic energy, TKE, distribution (where the spanwise normal stress is assumed equal to the transverse normal stress) is displayed in Figure 8. The turbulent kinetic energy contours resemble closely the streamwise normal stress contours, Figure 6. The streamwise normal stress is much larger than its transverse counterpart over most of the flowfield and so dominates the turbulent kinetic energy. Therefore, like the streamwise normal stress, the turbulent kinetic energy is much larger in the upper shear layer than in the lower shear layer and peaks near reattachment.

Unlike the present study, both Kuntz and Amatucci approximated the spanwise normal stress as the average of the streamwise and transverse normal stresses. This average definition may overstate the actual value of the TKE. Herrin,[14] however, was able to measure all three

velocity components and, therefore, determined the TKE without any approximations. The maximum TKE in the present study, $0.07U_\infty^2$, exceeds the maximum value of $0.042U_\infty^2$ Herrin found upstream of reattachment for his axisymmetric expansion-induced free shear layer. The reasons for the difference in the TKE values in the present study and those of Herrin are the additional mechanisms discussed earlier for turbulence production present in shock wave-boundary layer interactions that are not present in rapidly expanded compressible shear layers.

The maximum TKE value in the current study is also larger than the $0.05U_\infty^2$ maximum TKE value reported by Kuntz[5] after reattachment in his 24° compression corner (the largest ramp angle tested and largest TKE value reported). The larger equivalent corner angle (28°) in the present study than the actual corner angle of Kuntz's flow may also explain the larger TKE level of the present study. In addition a larger peak may have occurred near reattachment but upstream of the region of measurement in Kuntz's study. Amatucci[13], however, reports maximum TKE values occurring close to reattachment of approximately $0.06U_\infty^2$ and $0.07U_\infty^2$ for his upper (Mach 2.56 freestream) and lower (Mach 2.05 freestream) expansion-induced planar free shear layers, respectively. Both of these peak values are close to the peak value observed in the current study.

Residual Shock Motion

The transverse normal stress contour plot, Figure 7, indicates a narrow band of increased turbulence that lies well above the upper shear layer. By comparing the location of this band to the contour plot of mean streamwise velocity, Figure 2, this region is seen to correspond to the location of the separation shock wave. This increase in apparent transverse normal stress immediately downstream of the shock wave may be due to one of three factors: (1) small-scale

shock unsteadiness that is below the resolution limit of the conditional analysis technique (±1.6 mm); (2) particle lag downstream of the shock due to the finite sized LDV seed particles (2.8 mm extent in the streamwise direction); or (3) the slight polydisperse size distribution of seed particles.

Bloomberg[18] compared LDV data acquired using the same seeder and silicone oil used in this study with data acquired using monodisperse polystyrene latex particles behind an oblique shock wave slightly stronger than the separation shock in the current study. Bloomberg concluded that false turbulence due to the slight polydispersion of silicone oil droplet sizes was small compared to the overall turbulence levels in his flowfield. For this reason, the small increase in turbulence downstream of the separation shock wave in the current experiment is most probably not due to a polydisperse size distribution of seed particles.

Across an oblique shock wave, the tangential velocity component (relative to the shock front) is unaltered, but the normal velocity component is dramatically decreased. One may then expect that small-scale shock motion below the resolution limit of the conditional analysis technique would result in bimodal distributions in the velocity component normal to the shock at locations near the mean shock location (depending on whether the instantaneous shock location is ahead of or behind the measurement location). Figure 9 presents velocity histograms from the green LDV channel obtained at six different transverse (y) locations near the separation shock. The data in Figure 9 have been conditionally analyzed to contain only velocity realizations occurring when the shock foot was between the two pressure transducers, but have not been velocity debiased.

For these particular measurements the green LDV channel was aligned at 44° clockwise from the x-axis and the separation shock wave is inclined at a 32° angle counter-clockwise from

16

the x-axis. (Two slightly different alignments were used during the data collection for this study, but as noted in the equipment section both were approximately ±45° to the x-axis.) This particular alignment results in the green LDV channel being aligned at 76° to the separation shock (a perfect 90° alignment would simply further accentuate the observed bimodal nature of the velocity histograms). Figure 9 clearly shows that, at locations above (y = +18 mm) and below (y = +13 mm) the shock, a roughly unimodal velocity distribution occurs. As the mean shock location is approached from either above or below, however, the velocity distribution becomes increasingly bimodal with maximum bi-modality occurring at y = +15 mm.

One may estimate from the histograms shown in Figure 9 that significant bimodality exists over a transverse region of approximately 3 mm (y = +14 mm to y = +17 mm). This equates to a streamwise shock motion distance of 4.8 mm. Together, the resolution limit of the conditional analysis algorithm and particle lag are conservatively estimated to produce significant uncertainty over a streamwise region of roughly 6.0 mm. This length scale agrees with the length scales estimated from the velocity histograms in Figure 9 and from the relatively constant width band of increased apparent transverse normal stress near the shock location in Figure 7. Smits and Muck[6] also noted small peaks at the shock location in profiles of mass-weighted streamwise normal stress obtained with hot-wires in their compression corner flows without conditional analysis. Smits and Muck concluded that, like this study, the region of shock motion has an approximately constant length, independent of distance from the wall.

Reynolds Shear Stress

The dimensionless primary Reynolds shear stress distribution, $-<u'v'>/U_\infty^2$, is displayed in Figures 10 and 11. Since the primary Reynolds shear stress is negative in boundary layers, the

negative of the shear stress is often presented, i.e. $-\langle u'v' \rangle$. This study follows this convention in all shear stress plots. As can be seen from Figures 10 and 11, the shock-induced separation increases the magnitude of the primary shear stress. In their compression corner experiment, Smits and Muck[6] reported only negative values of $\langle u'v' \rangle$ and increases in the peak magnitude of the shear stress of up to 13 times the peak level in the approaching boundary layer. In the current experiment, a band of negative shear stress may be seen lying above the shear layer in Figure 10. By comparing Figure 10 with the contour plot of the streamwise mean velocity (Figure 2), this band of negative shear stress is again seen to coincide with the separation shock wave and is most likely due to particle dynamics and shock wave motion below the resolution limit of the conditional analysis technique.

The compression corner studies of Ardonceau,[4] Kuntz,[5] Smits and Muck,[6] and the expansion-induced separation studies of Amatucci[13] and Herrin[14] contain peak negative shear stress values of $-0.002U_\infty^2$, $-0.018U_\infty^2$, $-0.006U_\infty^2$, $-0.042U_\infty^2$, and $-0.012U_\infty^2$, respectively. The peak positive and negative shear stress values of $+0.007U_\infty^2$ and $-0.007U_\infty^2$, respectively, that are found inside the shock-induced shear layer of the present study exceed the peak values recorded in the separated compression corners of Ardonceau and Smits and Muck, but lie well below the value reported by Kuntz for his compression corner flows after reattachment. We believe that the scale of the shear stress plots in Ardonceau's article may be in error and that the true peak shear stress in this work may actually be an order of magnitude larger than the value cited above. The values of both Amatucci and Herrin in expansion-induced shear layers lie well above those of the present study, and indicate that the underlying turbulent structures in rapidly expanded compressible free shear layers differ from those in shock wave-boundary layer interactions.

18

Figure 11 clearly shows both the positive and negative shear stress peaks at the x = 0 and x = +12.5 mm locations (the two plotted profiles through the free shear layer). The top negative peak in <u'v'> in the x = 0 and x = +12.5 mm profiles is due to residual shock motion. The x = +12.5 mm profile shows a second large positive shear stress peak coinciding with the lower shear layer. This positive peak is expected, since the mean velocity profile has a negative slope inside the lower shear layer. Examining Figure 10, one sees that the region of positive shear stress within the shock-induced free shear layer only exists between separation and reattachment. Examining the x = +30 mm profile in Figure 11, one sees that single negative and positive peaks appear symmetrically across the wake. This is expected due to the deficit in the mean velocity profiles inside the wake, and matches the shear stress profiles found in other wake studies.

Can a Positive Shear Stress Exist?

The region of positive shear stress in the upper-half (high-speed side) of the shock-separated shear layer is not expected since the slope of the mean velocity profile there is positive. If a fluid element moves up or down between the high-speed and low-speed regions inside a shear layer with a positively sloped mean velocity profile, then the instantaneous shear stress, u'v', for the fluid element is expected to be negative. This argument, however, neglects the potential effects of coherent turbulent structures in the shear layer which physically allow a region of positive <u'v'> to exist.

The separated compression corner studies of Ardonceau[4] and Smits and Muck[6] include measurements of the free shear layer prior to reattachment, but did not indicate a positive shear stress region. This absence may be due to the difference in incoming boundary layer thickness relative to the size of the separated region or to the presence of a rigid downstream boundary

rather than a second fluid stream as in the present study. The absence of a positive shear stress region in the data of Ardonceau and Smits and Muck may also be due to the larger equivalent corner angle (28°) of the present flow than the corner angles in their two studies.

The disappearance of the positive shear stress region in the outer portion of the upper shear layer at reattachment may explain why Kuntz,[5] who made no measurements upstream of reattachment, did not measure a positive shear stress region in any of the compression corners he investigated. Similarly, the additional mechanisms for turbulence amplification and alteration present in shock wave-boundary layer interactions may explain why the expansion-induced free shear layer studies of Amatucci[13] and Herrin[14] include only a negative shear stress region.

A positive shear stress peak occurs at all but one of the 13 streamwise traverse locations in the shock-induced free shear layer of the current study. The locations of these positive peaks form a straight line along this free shear layer. Furthermore, these shear stress measurements (like the rest of the data presented in this study) are repeatable over a period of several months. Finally, other turbulence quantities, including higher order statistical moments such as the $<u'u'u'>$ triple product extracted from the same velocity ensembles used to calculate the shear stress, display the expected trends. This persistence and uniformity of these shear stress data, combined with the presence of expected trends in other quantities, provide evidence that the positive shear stress regions inside the upper shear layer are a true physical phenomenon and not an artifact of the measurement technique. However, if the instantaneous velocity data are rotated to coordinates parallel and perpendicular to the local shear layer direction rather than the tunnel coordinates (Figure 1) used in this paper, the positive shear stress values might disappear. This will be the subject of future work, but preliminary analysis indicates that this would cause the shear stress values to approach small positive values rather than significant negative values.

20

Counter-rotating vortex pairs oriented in the streamwise direction may exist inside the shock-separated free shear layer of the present study. These vortex pairs are similar to the Taylor-Görtler vortices that are known to form in boundary layers on walls with concave curvature. The shock-separated shear layer in the present study also displays a concave curvature, so an instability mode similar to the Taylor-Görtler mode may be expected. These vortex pairs are believed to produce powerful ejections of fluid (Quadrant I: $u' > 0$, $v' > 0$) that result in the observed region of positive shear stress. This vortex theory was first proposed by Palko[15] in conjunction with a further detailed analysis and discussion of the shock-separated shear layer turbulence structure that provides additional evidence of such vortex pairs. This analysis will be the subject of a future paper.

CONCLUSIONS

This study presents to our knowledge the first turbulence measurements obtained in a shock-separated shear layer and the first turbulence measurements in any two-dimensional, shock-separated free shear layer to account directly for shock wave unsteadiness.[25] Detailed experimental data are presented to allow verification of improved numerical solutions, including improved turbulence models for shock wave-boundary layer interactions. The results show that shock-induced separation dramatically increases the Reynolds normal stresses in the upper shear layer. The streamwise normal stress is much larger than the transverse normal stress and, consequently, dominates the turbulent kinetic energy through most of the flowfield (assuming that the transverse and spanwise normal stress magnitudes are similar, as has been found in previous related studies).

21

The subsequent reattachment of the two shear layers dramatically decreases the turbulence levels. The developing wake is dominated by a further reduction in all turbulent stresses. However, large values of the transverse normal stress are seen to persist well downstream of reattachment, possibly indicating a shift in turbulent energy from the streamwise component to the transverse (and presumably spanwise) components through recompression and reattachment. As in expansion-separated planar shear layers, the streamwise normal stress is seen to peak at reattachment rather than upstream of reattachment as in axisymmetric expansion-induced shear layers. This provides further evidence of the stabilizing effects of lateral streamline convergence on the turbulent flowfield for the axisymmetric case. Interestingly, regions of both positive and negative Reynolds shear stress exist inside the shock-separated shear layer. The positive shear stress region is formed at separation and disappears at reattachment, and may be explained by the presence of streamwise-oriented counter-rotating vortex pairs similar in nature to Taylor-Görtler vortices. Finally, velocity histograms obtained in the immediate neighborhood of the shock indicate that the range of unsteady shock motion has a relatively constant width irrespective of distance from the wall.

ACKNOWLEDGMENTS

REFERENCES

[1]Adamson, T.C., Jr. and A.F. Messiter, "Analysis of Two-Dimensional Interactions Between Shock Waves and Boundary Layers," *Annual Review of Fluid Mechanics*, Vol. 12, 1980, pp. 103-138.

[2]Green, J.E., "Interactions Between Shock Waves and Turbulent Boundary Layers," *Progress in Aerospace Sciences*, Vol. 11, 1970, pp. 235-340.

[3]Dolling, D.S., "Fluctuating Loads in Shock Wave/Turbulent Boundary Layer Interaction: Tutorial and Update," AIAA Paper 93-0284, 1993.

[4]Ardonceau, P.L., "The Structure of Turbulence in a Supersonic Shock-Wave/Boundary-Layer Interaction," *AIAA Journal*, Vol. 22, No. 9, 1984, pp. 1254-62.

[5]Kuntz, D.W., "An Experimental Investigation of the Shock Wave-Turbulent Boundary Layer Interaction," Ph.D. Thesis, University of Illinois at Urbana-Champaign, 1985.

[6]Smits, A.J. and K.C. Muck, "Experimental Study of Three Shock Wave/Turbulent Boundary Layer Interactions," *Journal of Fluid Mechanics*, Vol. 182, 1987, pp. 291-314.

[7]Selig, M.S., J. Andreopoulos, K.C. Muck, J.P. Dussauge, and A.J. Smits, "Turbulence Structure in a Shock Wave/Turbulent Boundary Layer Interaction," *AIAA Journal*, Vol. 27, No. 7, 1989, pp. 862-869.

[8]Palko, C.W. and J.C. Dutton, "A Method for Separating Shock Wave Motion and Turbulence in LDV Measurements," AIAA Paper 97-1919, 1997.

[9]Anyiwo, J.C. and D.M. Bushnell, "Turbulence Amplification in Shock Wave/Boundary Layer Interaction," *AIAA Journal*, Vol. 20, 1982, pp. 893-899.

[10]Hussaini, M.Y., F. Collier, and D.M. Bushnell, "Turbulence Alteration Due to Shock Motion," *IUTAM Symposium on Turbulent Shear Layer/Shock Wave Interaction*, Palaiseau, France, pp. 371-382, 1985.

[11]Selig, M.S. and A.J. Smits, "Effect of Periodic Blowing on Attached and Separated Supersonic Turbulent Boundary Layers," *AIAA Journal*, Vol. 29, No. 10, 1991, pp. 1651-1658.

[12]Bradshaw, P., "The Effect of Mean Compression or Dilatation on the Turbulent Structure of Supersonic Boundary Layers," *Journal of Fluid Mechanics*, Vol. 63, No. 3, 1974, pp. 449-464.

[13]Amatucci, V.A., "An Experimental Investigation of the Two-Stream, Supersonic, Near-Wake Flowfield Behind a Finite-Thickness Base," Ph.D. Thesis, University of Illinois at Urbana-Champaign, 1990.

[14]Herrin, J.L., "An Experimental Investigation of Supersonic Axisymmetric Base Flow Including the Effects of Afterbody Boattailing," Ph.D. Thesis, University of Illinois at Urbana-Champaign, 1993.

[15]Palko, C.W., "Conditionally Analyzed Mean Velocity and Turbulence Measurements in a Plume-Induced Boundary Layer Separated Flowfield," Ph.D. Thesis, University of Illinois at Urbana-Champaign, 1998.

[16]Shaw, R.J., "An Experimental Investigation of Unsteady Separation Shock Wave Motion in a Plume-Induced, Separated Flowfield," Ph.D. Thesis, University of Illinois at Urbana-Champaign, 1995.

[17]Jenson, L., "Automatic Digital Signal Processing for LDV," in *Proceedings of the 4th International Conference on Laser Anemometry Advances and Applications*, Cleveland, Ohio, 1991, pp. 617-628.

[18]Bloomberg, J.E., "An Investigation of Particle Dynamics Effects Related to LDV Measurements in Compressible Flows," M.S. Thesis, University of Illinois at Urbana-Champaign, 1989.

[19]Carlson, D.J. and R.F. Hoglund, "Particle Drag and Heat Transfer in Rocket Nozzles," *AIAA Journal*, Vol. 2, No. 11, 1964, pp. 1980-1984.

[20]Herrin, J.L. and J.C. Dutton, "An Investigation of LDV Velocity Bias Correction Techniques for High-Speed Separated Flows," *Experiments in Fluids*, Vol. 15, No. 4/5, 1993, pp. 354-363.

[21]Sun, C.C. and M.E. Childs, "A Modified Wall Wake Velocity Profile for Turbulent Compressible Boundary Layers," *Journal of Aircraft*, Vol. 10, No. 6, 1973, pp. 381-383.

[22]Bogdanoff, D.W., "Compressibility Effects in Turbulent Shear Layers," *AIAA Journal*, Vol. 21, No. 6, 1983, pp. 926-927.

[23]Papamoschou, D. and A. Roshko, "The Compressible Turbulent Shear Layer: An Experimental Study," *Journal of Fluid Mechanics*, Vol. 197, 1988, pp. 453-477.

[24]Herrin, J.L. and J.C. Dutton, "The Turbulence Structure of a Reattaching Axisymmetric Compressible Free Shear Layer," *Physics of Fluids*, Vol. 9, 1997, pp. 3502-3512.

[25]Dussauge, J.P. and P. Dupont, "Experimental Evidences of Compressibility Effects on Turbulence in High Speed Flows," in *Transitional and Turbulent Compressible Flows*, L.D. Kral, E.F. Spina, and C. Arakawa, eds., ASME FED-Vol. 224, 1995, pp. 185-192.

Table 1 Approach boundary layer properties

Boundary layer thickness, δ (mm)	3.2
Displacement thickness, δ^* (mm)	0.78
Momentum thickness, θ (mm)	0.21
Shape factor, $H = \delta^*/\theta$	3.7
Wake strength factor, Π	0.86
Skin friction coefficient, C_f	0.0016
Friction velocity, u_τ (m/s)	23.6

Figure 1 Flowfield schematic

Figure 2 Mean streamwise velocity field, U/U_∞

Figure 3 Mean velocity vector field

29

Figure 4 Base region mean velocity vector field

30

Figure 5 Mean Mach number field

Figure 6 Streamwise normal stress field, $<u'^2>/U_\infty^2$

31

Figure 7 Transverse normal stress field, $<v'^2>/U_\infty^2$

Figure 8 Turbulent kinetic energy (TKE) field, $(<u'^2>+2<v'^2>)/2U_\infty^2$

Figure 9 Green LDV channel velocity histograms near shock location (x=+7.5 mm)

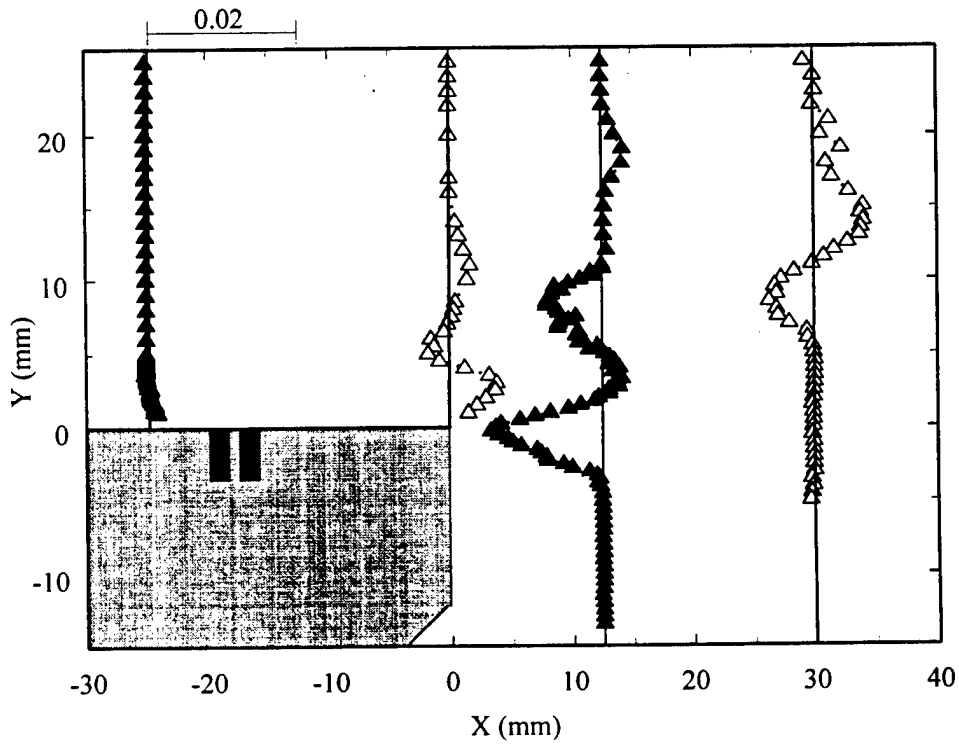**Figure 10 Reynolds shear stress field, $-<u'v'>/U_\infty^2$**

Figure 11 Reynolds shear stress profiles, $-<u'v'>/U_\infty^2$

APPENDIX A.12

CONDITIONAL ANALYSIS OF WALL PRESSURE FLUCTUATION MEASUREMENTS MADE IN PLUME-INDUCED SEPARATED FLOWFIELDS

by

R. J. Shaw, J. C. Dutton, and A. L. Addy

CONDITIONAL ANALYSIS OF WALL PRESSURE FLUCTUATION MEASUREMENTS MADE IN PLUME-INDUCED SEPARATED FLOWFIELDS

R.J. Shaw
Research Engineer
SY Technology, Inc.
Huntsville, Alabama 35806

J.C. Dutton
W. Grafton and Lillian B. Wilkins Professor
and
A.L. Addy
Professor Emeritus
Department of Mechanical and Industrial Engineering
University of Illinois at Urbana-Champaign
Urbana, Illinois 61801

ABSTRACT

The separation process in plume-induced, boundary layer separated flowfields was found to be unsteady. Two in-situ, fast-response pressure transducers were used to make individually and simultaneously sampled wall pressure fluctuation measurements over the intermittent region of separation shock wave motion. A conditional analysis technique was applied to the pressure-time histories, and statistical methods were then used to analyze the period, frequency, and velocity ensembles of the shock motion. The mean frequencies of this motion ranged between 1300 and 1500 Hz over the intermittent region, and the most probable shock wave frequencies occurred between 1 and 4 kHz over this region. The maximum zero-crossing frequency of the shock wave motion was approximately 500-600 Hz. The mean (approximately 3.5% of the freestream velocity) and most probable (approximately 6% of the freestream velocity) shock wave velocities in either direction were found to be essentially constant over the intermittent region. These results are compared to those for shock wave–boundary layer interactions caused by solid protruberances.

INTRODUCTION

Plume-induced boundary layer separation (PIBLS) is an important phenomenon that can adversely affect the aerodynamic and heat transfer characteristics of rockets and missiles. It occurs when the blockage caused by a highly underexpanded jet plume causes the afterbody boundary layer to separate upstream of the base corner. Our studies in a supersonic wind tunnel facility used to produce PIBLS have shown the separation process to be unsteady.[1,2] The separation shock wave was observed to translate randomly in the streamwise direction over a distance of several incoming boundary layer thicknesses. Wall static pressure fluctuation measurements were made in the intermittent region (i.e., the region of shock wave motion) using two flush-mounted, fast-response pressure transducers. Standard time-series analysis techniques

were applied to the pressure-time histories obtained from these pressure transducers and the resulting statistical properties were used to characterize the separation shock wave motion.[2] However, since each pressure-time history obtained from the intermittent region contains pressure fluctuations caused by the shock wave motion, as well as pressure fluctuations caused by turbulence in both the incoming boundary layer and the downstream separated region, it can be difficult to differentiate between effects caused by these two pressure fluctuation sources. In fact, the turbulence pressure fluctuations can entirely mask the effect of shock motion pressure fluctuations in some statistical properties. For example, the convection velocities of the shock wave motion could not be calculated from cross-correlation estimates because no convection times corresponding to the shock wave motions were found to exist in these estimates.[1] In order to isolate the pressure fluctuations caused by the shock motion from those caused by turbulence and then to analyze only those pressure fluctuations caused by the shock motion, a conditional analysis algorithm was applied to the pressure-time histories. The results obtained from conditionally analyzing the pressure fluctuation measurements made across the intermittent region of PIBLS flowfields are the subject of this paper.

The conditional analysis algorithm employed was the two-threshold method box-car conversion technique (TTMBCC) that has been developed by Dolling and colleagues.[3-6] The TTMBCC algorithm has been used to successfully calculate the unsteady characteristics of the separation shock wave motion in several shock wave–turbulent boundary layer interaction (SWBLI) flowfields produced by solid protuberances. Specifically, the zero-crossing frequency distributions across the intermittent region and the probability density function (PDF) estimates of the periods, frequencies, and velocities of the shock wave motions across the intermittent region have been calculated from pressure fluctuation measurements made in flowfields produced by compression ramps,[6,7] circular cylinders,[8] and hemicylindrical blunt fins.[9,10]

These studies have shown that the zero-crossing frequency, f_c, (i.e., the average number of times per second that the shock wave unidirectionally crosses a pressure transducer) along the line of symmetry upstream of the cylinders and fins appeared to be distributed parabolically over

2

the length of the intermittent region and reached a maximum value near an intermittency of 50%. For the circular cylinders,[8] $f_{c,max}$ ranged between 0.9 kHz and 1.6 kHz, depending upon the incoming boundary layer thickness and the cylinder diameter. The trends exhibited by $f_{c,max}$ for various cylinder diameters and boundary layer thicknesses were the same trends displayed by the dominant center frequency in the power spectral density (PSD) estimates. For the swept hemicylindrical blunt fin experiments,[9] $f_{c,max}$ ranged from 1.2 kHz to 2.2 kHz as the leading edge sweep angle increased from 0° to 45°. A PDF estimate of the shock wave periods at each location across the intermittent region showed that all the distributions of shock wave periods were strongly skewed toward shorter periods. The most probable period, which occurred somewhere over the 0.2-0.5 ms range, depending upon the intermittency, was always less than the mean period for each distribution. Similarly, PDF estimates of the shock wave frequencies have shown that, although frequencies as high as 10 kHz exist in the distributions, the most probable shock wave frequencies were in the 1-2 kHz range.[8]

From the ensembles of shock wave velocities calculated with the TTMBCC algorithm applied to swept hemicylindrical blunt fin, sharp fin, and swept compression ramp interactions, the mean and rms of the shock wave velocities, when nondimensionalized by the freestream velocity, were found to be independent of the geometry that produced the interaction and independent of the intermittent region length.[10] This result explained the inverse relationship between the length of the intermittent region and the zero-crossing frequency which was observed in several experiments. The average mean and rms of the shock wave velocities for these interactions were calculated to be $0.0304U_\infty$ and $0.0055U_\infty$, respectively, in the upstream direction and $0.0310U_\infty$ and $0.0056U_\infty$, respectively, in the downstream direction, where U_∞ is the freestream velocity approaching the fin or ramp.

The investigations mentioned above have shown that conditional analysis of pressure-time histories obtained from SWBLIs produced by solid protuberances has been beneficial primarily in determining the unsteady characteristics of the separation shock wave motions. By applying both standard time-series analysis and conditional analysis techniques to the pressure-

3

time histories obtained from SWBLIs, a more complete picture of the shock wave motion was obtained for solid boundary protuberances. By applying both analysis techniques in the present PIBLS flowfield study, a more complete picture of the shock wave motion is also obtained for separation caused by a compliant aerodynamic boundary. The time-series results for the PIBLS flow have previously been presented in Ref. 2; the conditional analysis measurements are presented and discussed below.

EXPERIMENTAL EQUIPMENT AND PROCEDURE

Wind Tunnel Facility

The experiments were conducted in a supersonic flow facility designed specifically to produce PIBLS flowfields. Figure 1 presents a schematic of the flow facility and a cross-sectional view of the test section. Plume-induced boundary layer separation of the upper $M = 2.5$ stream is caused by impinging it at a 40 deg angle, across a 12.7 mm base height, with the lower $M = 1.5$ stream. The test section is two-dimensional with a constant width of 50.8 mm. The height of the $M = 2.5$ stream is also 50.8 mm. Glass window assemblies are installed in each sidewall, allowing optical access to the entire PIBLS flow interaction.

Filtered, dry air was supplied to the test section via two screw compressors and air storage tanks. Flow conditioning screens and honeycomb sections were installed in the supply lines of both streams. In addition, the lower stream could be throttled using a manual valve. Varying the lower stream stagnation pressure in this way was used to adjust the jet static pressure ratio (JSPR = P_{lower}/P_{upper}) between the two streams and, therefore, the mean separation location of the boundary layer of the upper stream.

Figure 2 is a shadowgraph photo of the PIBLS flowfield taken at JSPR = 2.35. Plume-induced separation of the upper stream's boundary layer and the separation shock wave are clearly visible. When the shadowgraph light source was operated continuously, the separation shock was observed to experience unsteady streamwise motions at all JSPRs considered. Also

4

visible in Figure 2 are the separated shear layers from both streams, the enclosed recirculation region, the recompression waves near the shear layer reattachment point, and the trailing wake.

Instrumentation

Wall pressure fluctuations in the neighborhood of the separation location were measured with two Kulite piezoresistive pressure transducers flush-mounted in the upper wall of the center partition (Figure 1). The upstream and downstream transducers were located 19.1 mm and 16.5 mm upstream of the base, respectively, on the spanwise center plane of the test section. The transducer diaphragms had an active diameter of 0.71 mm and measured diaphragm natural frequencies of 168 and 198 kHz for the upstream and downstream transducers, respectively. The transducers were statically calibrated in situ using a Sensotec digital pressure gage that is accurate to within ±103 Pa. Amplification of the analog voltage signal from the transducers was carried out with a Measurements Group signal conditioning amplifier. Low-pass filtering of the amplified signals was performed with an active Butterworth filter circuit. The gain and DC offset of each channel were adjusted before each calibration to maximize the signal-to-noise ratio (SNR) of the output signal. The resulting SNRs for the fluctuating pressure measurements were in the range of 15 to 20 for the incoming boundary layer and from 55 to 300 for the intermittent region.

Data Acquisition

In these experiments the two Kulite pressure transducers were mounted at fixed positions on the center partition. As a result, the shock wave intermittent region was moved across the transducer locations by varying the JSPR. Specifically, the shock wave intermittency (fraction of time the shock is upstream of a transducer) was increased by increasing the lower jet stagnation pressure, and therefore the JSPR, from 210 kPa to 269 kPa in increments of approximately 3.4 kPa.

Both individually and simultaneously sampled pressure measurements were obtained at each JSPR. The individually sampled measurements were made at a rate of 166,667 samples/second for 24 seconds for each transducer. The simultaneously sampled transducer readings were obtained at 200,000 samples/second per channel for 20 seconds.

Further details concerning the flow facility, instrumentation, and data acquisition methods can be found in Refs. 1 and 2.

ANALYSIS TECHNIQUE

The updated version[6] of the two-threshold method box-car conversion (TTMBCC) algorithm, developed by Dolling and colleagues, was used in the analysis of the shock motion of the PIBLS flowfield. In this method each individual pressure measurement from a given transducer is compared to two threshold levels, Th_1 and Th_2, and the instantaneous shock location is then determined as either upstream or downstream of the transducer. The precise time at which the shock crosses upstream of the transducer, called the rise time, and downstream of the transducer, called the fall time, is determined for all shock passages in the time history of the pressure measurements. The resulting record of the shock rise and fall times is called the box-car function.

An analysis of the TTMBCC algorithm was performed with the PIBLS data in order to evaluate the sensitivity of the zero-crossing frequency f_c to different threshold settings. Two discrete settings of Th_1 were used in the sensitivity analysis: $Th_1 = \bar{p}_{wo}$ and $Th_1 = \bar{p}_{wo} + 3\sigma_{p_{wo}}$, where $\bar{p}_{wo}$ is the mean pressure and $\sigma_{p_{wo}}$ is the rms of the pressure fluctuations in the incoming boundary layer. For each of the two Th_1 settings, threshold level Th_2 was systematically varied according to $Th_2 = \bar{p}_{wo} + n\sigma_{p_{wo}}$, where n is an integer in the range $3 \leq n \leq 9$. For each of two pressure-time histories ($\gamma \approx 20\%$ and $\gamma \approx 50\%$), the TTMBCC algorithm was used to calculate f_c at each of the fourteen unique combinations of Th_1 and Th_2. The results are shown in Figure 3. Three main observations can be made about the sensitivity of f_c to the two threshold levels: (1) f_c decreased as threshold level Th_2 increased (larger n

6

values) at both intermittencies regardless of the setting for Th_1; (2) f_c was larger for $Th_1 = \bar{p}_{wo} + 3\sigma_{p_{wo}}$ than for $Th_1 = \bar{p}_{wo}$ at both intermittencies regardless of the setting for Th_2; and (3) f_c was more sensitive to the threshold level settings at $\gamma \approx 50\%$ than at $\gamma \approx 20\%$. The first two observations are obvious from Figure 3, but the last one required a separate, quantitative study,[1] whose results are not shown here for conciseness. Since the sensitivity analysis performed on the PIBLS data showed similar, albeit weaker, qualitative trends when compared to the sensitivity analysis performed on the Mach 5 circular cylinder interaction data,[5] it was concluded that threshold level settings of $Th_1 = \bar{p}_{wo} + 3\sigma_{p_{wo}}$ and $Th_2 = \bar{p}_{wo} + 6\sigma_{p_{wo}}$ were also reasonable choices for conditional analysis of the PIBLS data.

RESULTS

After specifying the flow conditions for the experiments, results from the pressure transducer measurements will be presented in two parts: individually sampled transducer measurements and simultaneously sampled transducer measurements. The individually sampled results were used to calculate period and frequency ensembles of the shock wave motion, and the simultaneously sampled data were used to calculate velocity ensembles of the shock motion.

Flow Conditions

The stagnation temperature of both streams was measured with an iron-constantan thermocouple mounted in the facility plenum chamber and was found to be 298 K ($\pm$1.5 K). The stagnation pressure of each stream was measured with a probe mounted upstream of each nozzle block. The stagnation pressure of the upper stream was 503 kPa ($\pm$1.5 kPa) and its unit Reynolds number was 47.1×10^6 m^{-1} ($\pm 0.5 \times 10^6$ m^{-1}). The Mach number of this freestream was determined from the stagnation pressure measurement and mean static pressure measurements made using taps located in the center partition and was found to 2.50 ($\pm$0.01). The Mach number of the lower jet was determined in a similar manner to be 1.51 ($\pm$0.01).

7

Velocity measurements were made in the upper stream along a vertical traverse 30 mm upstream of the base using a one-component laser Doppler velocimeter (LDV) setup. The freestream turbulence intensity was found to be less than 0.015 (±0.0015) across the uniform portion of the mean profile. A wall-wake velocity profile of the form suggested by Sun and Childs[11] was curve-fit to the mean velocity measurements made in the boundary layer, and from this fit the integral boundary layer parameters were determined (Table 1). These parameters agree well with those of other equilibrium turbulent boundary layers reported in the literature[12-16] for comparable Reynolds and Mach numbers.

Individually Sampled Pressure Transducer Measurements

Although the JSPR was the independent variable in the experiments, some results will be presented as a function of intermittency rather than JSPR. As mentioned earlier, intermittency, γ, is defined as the percentage of time the shock wave is upstream of a given pressure transducer and is calculated from

$$\gamma = \frac{\sum_{k=1}^{N} (Fall_k - Rise_k)}{Fall_N - Rise_1} \tag{1}$$

where $Fall_k$ is the fall time associated with the k-th downstream shock wave crossing, $Rise_k$ is the rise time associated with the k-th upstream shock crossing, and N is the total number of fall times detected in the pressure-time history. A plot of intermittency versus JSPR over the intermittent region is shown in Figure 4 for both the upstream and downstream transducers. For the downstream transducer measurements, the JSPR range from 1.95 to 2.41 spanned the intermittency range from $\gamma = 3.9\%$ to $\gamma = 96.2\%$. Similarly, the upstream transducer measurements spanned the intermittent region from $\gamma = 3.8\%$ to $\gamma = 98.3\%$ over a range of JSPR from 2.05 to 2.49.

8

Periods of the Shock Wave Motion

The period of the i-th shock wave event, T_i, in the box-car function can be calculated as the difference between two consecutive rise times $\left(T_i = \text{Rise}_{i+1} - \text{Rise}_i\right)$ or the difference between two consecutive fall times $\left(T_i = \text{Fall}_{i+1} - \text{Fall}_i\right)$. For both cases, statistical techniques can be applied to the ensemble of periods calculated from the box-car function to obtain the mean value, T_m, and the PDF of the ensemble. The distribution of mean periods over the intermittent region is shown in Figure 5 for the upstream and downstream pressure transducer measurements. At every discrete intermittency at which experimental measurements were acquired, the mean period calculated from the rise times was equal (to three significant figures) to the mean period calculated from the fall times. As shown in the figure, the mean periods computed from the upstream pressure transducer measurements also collapse on those determined from the downstream transducer measurements when the data are plotted versus intermittency. Although the mean period reached relatively large values at both low and high intermittencies, the value of the mean period decreased rapidly and was relatively constant as the midrange of intermittencies $(20\% < \gamma < 80\%)$ was approached from both the low and high ranges. The distribution of mean periods reached a minimum value at $\gamma \approx 60\%$ where the mean period was in the range of 1.74 to 1.78 ms.

The PDF estimates of the shock wave periods were also computed across the intermittent region using both rise times and fall times. At each location over the intermittent region, the PDF estimate of the shock wave periods computed using rise times was essentially identical in shape and magnitude to that computed using fall times. This was the case for the upstream pressure transducer measurements as well as for the downstream transducer measurements. Since the evolution (in terms of the shape and magnitude) of these PDF estimates over the intermittent region was similar for both transducers, only the PDF estimates of the shock wave periods computed using the rise times from the downstream transducer measurements are shown in Figure 6. The PDF estimates of the shock wave periods computed at five important locations over the intermittent region are shown in this figure. Each of the PDF estimates is plotted in

terms of $N_i/(N_{total} * W)$ versus the shock wave period, where N_i is the number of shock wave periods occurring with a value of T_i, N_{total} is the total number of shock wave period realizations in the box-car function, and W is the interval width of the PDF estimate centered at T_i ($W = 36$ μs). The mean period of each ensemble is also shown (with a solid black triangle) in each plot of Figure 6.

The behavior of the PDF estimates of the shock wave periods was similar over the entire intermittent region of the PIBLS flowfields. For each intermittency, the PDF quickly reached a maximum value at approximately 0.4 ms and then slowly decayed back to zero over the next 10 to 20 ms, depending upon the intermittency. Over the low (e.g., $\gamma = 3.9\%$) and high (e.g., $\gamma = 96.2\%$) intermittency ranges, a number of shock wave events had periods longer than 10 ms, as evidenced by the fact that the amplitude of the PDF was not zero at 10 ms. Over the midrange of the intermittent region $(20\% < \gamma < 80\%)$, nearly all of the individual shock wave periods were less than 10 ms. This trend explained the behavior of the mean period over the intermittent region. For the low and high intermittencies, the number of shock wave events with periods longer than 10 ms was sufficient to significantly increase the mean period to values well above (at least two or three times larger) those found over the midrange of the intermittent region.

Frequencies of the Shock Wave Motion

The frequency of the i-th shock wave event, f_i, in the box-car function is simply the inverse of the period of the i-th shock wave event, $f_i = 1/T_i$, and can be calculated from two consecutive rise times $(f_i = \{Rise_{i+1} - Rise_i\}^{-1})$ or from two consecutive fall times $(f_i = \{Fall_{i+1} - Fall_i\}^{-1})$. For both cases, statistical techniques can be applied to the ensemble of frequencies calculated from the box-car function to obtain the mean value, f_m, and the PDF of the ensemble. The distribution of mean frequencies over the intermittent region is shown in Figure 7 and was calculated using the rise times from the upstream and downstream transducer measurements. The mean frequency calculated from the rise times was slightly larger than that calculated from the fall times at every measurement location over the intermittent region and for

10

both the upstream and downstream transducer measurements. Thus, the mean frequency was more sensitive than the mean period to temporal differences between the rise times and the fall times. From Figure 7, it is seen that the mean frequencies calculated using the upstream transducer measurements collapse on those calculated from the downstream transducer measurements when the frequency data are plotted versus intermittency. The mean frequencies ranged between 1300 - 1400 Hz over the intermittent region from 20% to 50% and between 1400 - 1500 Hz over the intermittent region from 50% to 80%.

PDF estimates of the shock wave frequencies were made at each measurement location across the intermittent region using both rise times and fall times. At each location, the PDF computed using rise times was nearly identical in shape and magnitude to that computed using fall times. This was true for the upstream transducer measurements as well as for the downstream transducer measurements. Since the evolution of the PDF estimates of the shock wave frequencies over the intermittent region was similar for both transducers, only the PDFs of the shock wave frequencies computed using rise times from the downstream transducer measurements are shown in Figure 8.

The PDF estimates of the shock wave frequencies computed at the same five locations over the intermittent region as the shock wave period PDFs (shown earlier in Figure 6) are presented in Figure 8. Since the interval width of each PDF estimate, W_{f_i}, was variable over the frequency spectrum, each PDF estimate was reported as a simple histogram in order to eliminate the bias caused by W_{f_i} on the magnitude of the PDF estimate. Each PDF is plotted as N_i/N_{total} versus the shock wave frequency, where N_i is the number of shock wave frequency realizations occurring with a value of f_i and N_{total} is the total number of shock wave frequency realizations in the box-car function. The mean frequency of each ensemble is also shown (with a solid black triangle) in each plot of Figure 8. The behavior of the shock wave frequency PDFs was similar at all five locations over the intermittent region. The amplitude of the PDF increased substantially over the frequency range between 100 Hz and 1 kHz, reached a most probable value

11

between 1 kHz and 4 kHz, and then decreased back to zero again near 20 kHz. The mean frequency of each ensemble was less than the most probable frequency.

Since the frequencies in each PDF estimate were narrowly spaced over the low frequency range and widely spaced over the high frequency range, a probability distribution function estimate was calculated for each PDF in order to better interpret the evolution of the PDFs over the intermittent region. When the PDF is defined as a simple histogram, the probability distribution function is the running sum of the PDF over the frequency range. For each PDF estimate shown in Figure 8, a probability distribution function estimate was computed from $P_i = \sum_{j=1}^{i} N_j / N_{total}$, where P_i is the probability distribution function corresponding to f_i. The probability distribution function estimates of the shock wave frequencies are shown in Figure 9. The relative number of frequency realizations that occurred between 50 Hz and 1 kHz decreased while the relative number of frequency realizations that occurred between 1 kHz and 10 kHz increased as the $\gamma = 70\%$ location was approached from both the low and high intermittency ranges. Therefore, the individual frequency realizations in the ensembles occurred at higher frequencies as the $\gamma = 70\%$ location was approached. This trend explained why the mean frequency increased as the $\gamma = 70\%$ location was approached from the low and high intermittency ranges.

It is interesting to compare the PSD estimates of the pressure fluctuations computed from the pressure-time histories over the intermittent region[2] to the probability density function and probability distribution function estimates computed from the ensembles of shock wave frequencies. The PSD estimates showed that 50% to 60% of the energy in the pressure fluctuations occurred between approximately 50 Hz and 1 kHz. The probability distribution function estimates of the shock wave frequencies showed that 50% to 60% of the shock wave events occurred over this same frequency range. Thus, more than half of the shock wave events, which contained more than half of the energy in the power spectrum, occurred at frequencies in this range. The PSD estimates showed that the energy in the pressure fluctuations dropped off significantly at frequencies higher than 1 kHz. While only 15% to 30% of the energy in the PSD

12

estimates was contributed by pressure fluctuations in the frequency range between 1 kHz and 10 kHz, 40% to 50% of all the shock wave frequencies occurred in this range, including the most probable shock wave frequencies. Therefore, the most probable shock wave frequencies (in the 1 kHz to 4 kHz range) were not the most energetic frequencies (usually below 1 kHz).

The mean frequency over the intermittent region is not the only frequency that can be calculated for the shock wave motion. The zero-crossing frequency of the shock wave motion, computed as the inverse of the mean period, is also of interest. The distribution of the zero-crossing frequency over the intermittent region is shown in Figure 10 for both the upstream and downstream pressure transducer measurements. The zero-crossing frequency distribution for the downstream transducer measurements reached a maximum of 560 Hz at $\gamma \approx 60\%$. The zero-crossing frequency distribution for the upstream pressure transducer measurements displayed an unusual 50 Hz shift near $\gamma \approx 50\%$ which was caused by a leak in the sidewall seal during the latter phases of the experiments.[1] Had the rupture not occurred, the upstream pressure transducer measurements would have reached a maximum of about 520 Hz at $\gamma \approx 60\%$. Note that the maximum zero-crossing frequency computed from the downstream pressure transducer measurements was larger than that computed from the upstream pressure transducer measurements. The physical reason for this will become clear after discussing the shock wave velocity distributions in the next section.

Simultaneously Sampled Pressure Transducer Measurements

Since the cross-correlation estimates computed for each pair of pressure-time histories acquired across the intermittent region did not detect the convection times corresponding to the shock wave motion in the upstream and downstream directions,[1,2] the convection time associated with each pair of shock wave crossings was computed from the conditional analysis of each pair of pressure-time histories. The TTMBCC algorithm was used to convert each pair of pressure-time histories into a pair of box-car functions. An ensemble of convection times for the shock wave motion in the upstream direction and an ensemble of convection times for motion in the

13

downstream direction were formed at each JSPR by analyzing all the pairs of shock wave crossings in the two box-car functions.[1] Assuming the shock wave moves with uniform speed and direction between the two pressure transducers, the velocities of the shock wave motion in the upstream and downstream directions were computed from the convection times between the two transducers and the transducer spacing.

The PDF estimates of the shock wave velocities in the upstream and downstream directions computed at five discrete locations over the intermittent region are shown in Figures 11 and 12, respectively. Each of the PDFs is plotted as N_i/N_{total} versus U_{shock}/U_∞, where N_i is the number of shock wave velocity realizations at velocity U_{shock}; N_{total} is the total number of realizations (in either direction) in each pair of box-car functions; and U_∞ is the freestream velocity of the Mach 2.5 flow (565 m/s). While the behavior of the PDF estimates of the shock velocities in the upstream and downstream directions was similar over the intermittent region, the PDFs of the upstream shock velocity were less peaked and had a wider distribution than did those of the downstream shock velocity. As U_{shock}/U_∞ increased, the PDF estimates quickly reached a maximum value over the velocity range of $0.04U_\infty - 0.08U_\infty$ and then slowly decayed back to zero again by the time the shock wave velocity reached $0.30U_\infty$.

The most probable shock wave velocity in both the upstream and downstream directions was computed at 14 locations across the intermittent region and is shown in Figure 13. The most probable shock wave velocity in either direction was essentially constant over the intermittent region. The average value of the most probable shock wave velocities was $0.058U_\infty \pm 0.010U_\infty$ in the upstream direction and $0.060U_\infty \pm 0.009U_\infty$ in the downstream direction and, thus, was essentially the same in the two directions.

The mean shock wave velocity in both the upstream and downstream directions was also computed at 14 locations across the intermittent region and is shown in Figure 14. The mean shock wave velocity in either direction was fairly constant across the intermittent region. The average value of the mean shock wave velocity was $0.035U_\infty \pm 0.004U_\infty$ in the upstream direction and $0.034U_\infty \pm 0.006U_\infty$ in the downstream direction. Figure 14 shows that the mean

shock wave velocity in the upstream direction was consistently slightly greater than the mean shock wave velocity in the downstream direction over most of the intermittent region. After a close examination of the threshold levels used in the TTMBCC algorithm to compute the shock wave velocities, the small differences between the mean shock wave velocities in the two directions that developed over the intermittent region was believed *not* to be an artifact of the conditional analysis technique, but rather was most likely caused by the physics of the shock wave motion. The trend of the mean shock wave velocity in the upstream direction being increasingly greater than the mean shock wave velocity in the downstream direction as the JSPR (and intermittency) increased was consistent with the trend observed in the PDF estimates of the shock wave velocities in the upstream and downstream directions. As the JSPR increased from 1.95 to 2.41 ($\gamma = 3.9\%$ to $\gamma = 96.2\%$), more shock wave velocity realizations with a magnitude larger than the most probable value occurred in the upstream direction than in the downstream direction.

The conditional analysis of the two simultaneously sampled pressure transducer measurements revealed that the average mean shock wave velocity in either direction was approximately $0.034U_\infty - 0.035U_\infty$ and the mean shock wave velocity was independent of the intermittent region length. This explains why, for the same intermittency value, the zero-crossing frequency calculated from the pressure-time history acquired with the upstream pressure transducer was always less than the zero-crossing frequency calculated from the downstream transducer measurements. The length of the intermittent region increased from $2.6\delta_0 - 3.0\delta_0$ to $5.4\delta_0 - 5.5\delta_0$ (where δ_0 is the incoming boundary layer thickness) as the JSPR increased from 1.95 to 2.49.[1] For both pressure transducers to have the same intermittency value, the JSPR setting used for the upstream pressure transducer measurements was higher than that for the downstream transducer measurements. As a result, the intermittent region length associated with the upstream pressure transducer flowfield is longer than that for the downstream transducer measurement flowfield. Consequently, since the mean shock wave velocity is constant across

15

the intermittent region, the zero-crossing frequency must be less for the upstream pressure transducer measurements than for the downstream transducer measurements.

DISCUSSION AND CONCLUSIONS

While the zero-crossing frequency and the mean frequency of the shock wave motion in the current PIBLS flowfields were less than the frequencies found in other SWBLIs produced by solid protuberances,[6-10] the velocity characteristics of the shock wave motion were similar to the velocity characteristics of the shock wave motion in solid protruberance SWBLI flowfields. These similarities included the general shape of the PDF estimates of the shock wave velocities, which were highly skewed toward low-speed realizations relative to the freestream velocity, the most probable shock velocities of approximately $0.05U_\infty - 0.10U_\infty$, and average mean shock velocities of approximately $0.03U_\infty$. Although all these similarities are undoubtedly important, the latter similarity is especially noteworthy. Gonsalez and Dolling[10] found that the average mean shock wave velocities in either direction were approximately $0.030U_\infty - 0.031U_\infty$ and were independent of the intermittent region length for swept compression ramp interactions, hemicylindrical blunt fin interactions, and sharp fin interactions at angles of attack. The current PIBLS study found that the average mean shock wave velocity in either direction was approximately $0.034U_\infty - 0.035U_\infty$ and that it was independent of the intermittent region length. Thus, the average mean shock wave velocities from the plume-induced interactions were essentially the same as the average mean shock wave velocities from the interactions produced by the three solid geometries.

While there were many similarities between the velocity characteristics of the shock wave motion in the PIBLS flowfields and those in SWBLI flowfields produced by solid geometries, a difference found between the two types of interactions was that the upstream mean shock velocities were greater than the downstream mean shock velocities in the plume-induced interactions, whereas just the opposite situation was found in the solid geometry interactions.[6-10] A definitive explanation of this result must await further study.

16

ACKNOWLEDGMENTS

REFERENCES

[1]Shaw, R.J., "An Experimental Investigation of Unsteady Separation Shock Wave Motion in a Plume-Induced, Separated Flowfield," Ph.D. thesis, Dept. of Mechanical and Industrial Engineering, University of Illinois at Urbana-Champaign, 1995.

[2]Shaw, R.J., Dutton, J.C., and Addy, A.L., "Time-Series Analyses of Wall Pressure Fluctuation Measurements Made in Plume-Induced Separated Flowfields," accepted for publication in *AIAA Journal*.

[3]Dolling, D.S. and Narlo, J.C., "Driving Mechanism of Unsteady Separation Shock Motion in Hypersonic Interactive Flow," Chapter 7, AGARD CP-428, 1987.

[4]Brusniak, L., "Evaluation of Conditional Sampling Methods for Analysing Separation Shock Motion," AIAA Paper 88-0091, 1988.

[5]Dolling, D.S. and Brusniak, L., "Separation Shock Motion in Fin, Cylinder and Compression Ramp-Induced Turbulent Interactions," *AIAA Journal*, Vol. 27, No. 6, 1989, pp. 734-742.

[6]Erengil, M.E. and Dolling, D.S., "Unsteady Wave Structure near Separation in a Mach 5 Compression Ramp Interaction," *AIAA Journal*, Vol. 29, No. 5, 1991, pp. 728-735.

[7]Dolling, D.S., Boitnott, T., and Erengil, M.E., "Effects of Moderate Sweepback on the Separation Shock Wave Dynamics in a Mach 5 Compression Ramp Interaction," AIAA Paper 91-0254, 1991.

[8]Dolling, D.S. and Smith, D.R., "Separation Shock Dynamics in Mach 5 Turbulent Interactions Induced by Cylinders," *AIAA Journal*, Vol. 27, No. 12, 1989, pp. 1698-1706.

[9]Kleifges, K. and Dolling, D.S., "Control of Unsteady Shock-Induced Turbulent Boundary Layer Separation Upstream of Blunt Fins," AIAA Paper 93-3281, 1993.

[10]Gonsalez, J.C. and Dolling, D.S., "Correlation of Interaction Sweepback Effects on the Dynamics of Shock-Induced Turbulent Separation," AIAA Paper 93-0776, 1993.

[11]Sun, C.C. and Childs, M.E., "A Modified Wall Wake Velocity Profile for Turbulent Compressible Boundary Layers," *Journal of Aircraft*, Vol. 10, No. 6, 1973, pp. 381-383.

[12]Coles, D., "Measurements in a Flat Plate Boundary Layer at the Jet Propulsion Laboratory," Jet Propulsion Laboratory, California Institute of Technology, Report No. 20-71, 1953.

[13]Winter, K.G. and Gaudet, L., "Turbulent Boundary Layer Studies at High Reynolds Numbers at Mach Numbers Between 0.2 and 2.8," Aeronautical Research Council, R&M 3712, 1973.

[14]Shutts, W.H., Hartwig, W.H., and Weiler, J.E., "Final Report on Turbulent Boundary Layer and Skin Friction Measurements on a Smooth Thermally Insulated Flat Plate at Supersonic Speeds," University of Texas-Austin, Defense Research Laboratory, Report No. 364, 1955.

[15]Moore, D.R., "An Experimental Investigation of the Turbulent Boundary Layer Behind a Forward-Facing Step in Supersonic Flow," University of Texas-Austin, Defense Research Laboratory, Report No. 425, 1958.

[16]Mabey, D.G., Meier, H.U., and Sawyer, W.G., "Experimental and Theoretical Studies of the Boundary Layer on a Flat Plate at Mach Numbers from 2.5 to 4.5," Royal Aircraft Establishment, TR-74127, 1974.

Table 1.   Incoming turbulent boundary layer properties in the upper stream.

Property	Value
boundary layer thickness, δ	3.1 mm
boundary layer displacement thickness, δ^*	0.91 mm
boundary layer momentum thickness, θ	0.25 mm
boundary layer shape factor, $H = \delta^*/\theta$	3.71
wake strength parameter, Π	1.58
skin friction coefficient, C_f	0.00131
friction velocity, u_τ	20.6 m/s

High Pressure Air Supply

Upper Stream Gate Valve

Constant Area Diffuser

Plenum Chamber

Lower Stream Globe Valve

Support Stand

Cross-Sectional View of the PIBLS Test Section

Figure 1.   Schematic of the flow facility and PIBLS test section.
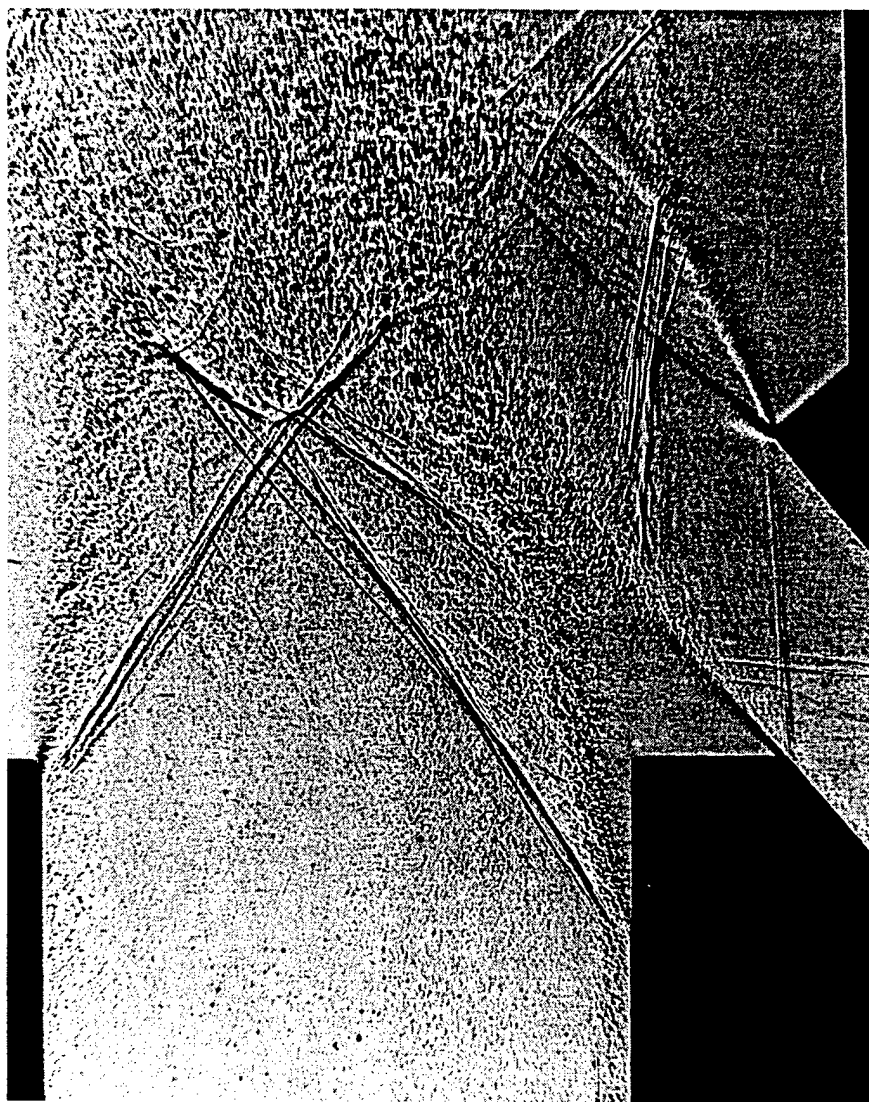
Figure 2.   Shadowgraph photo (flashlamp pulse duration of 25 ns) of the near-wake region in the PIBLS wind tunnel at a JSPR of approximately 2.35.
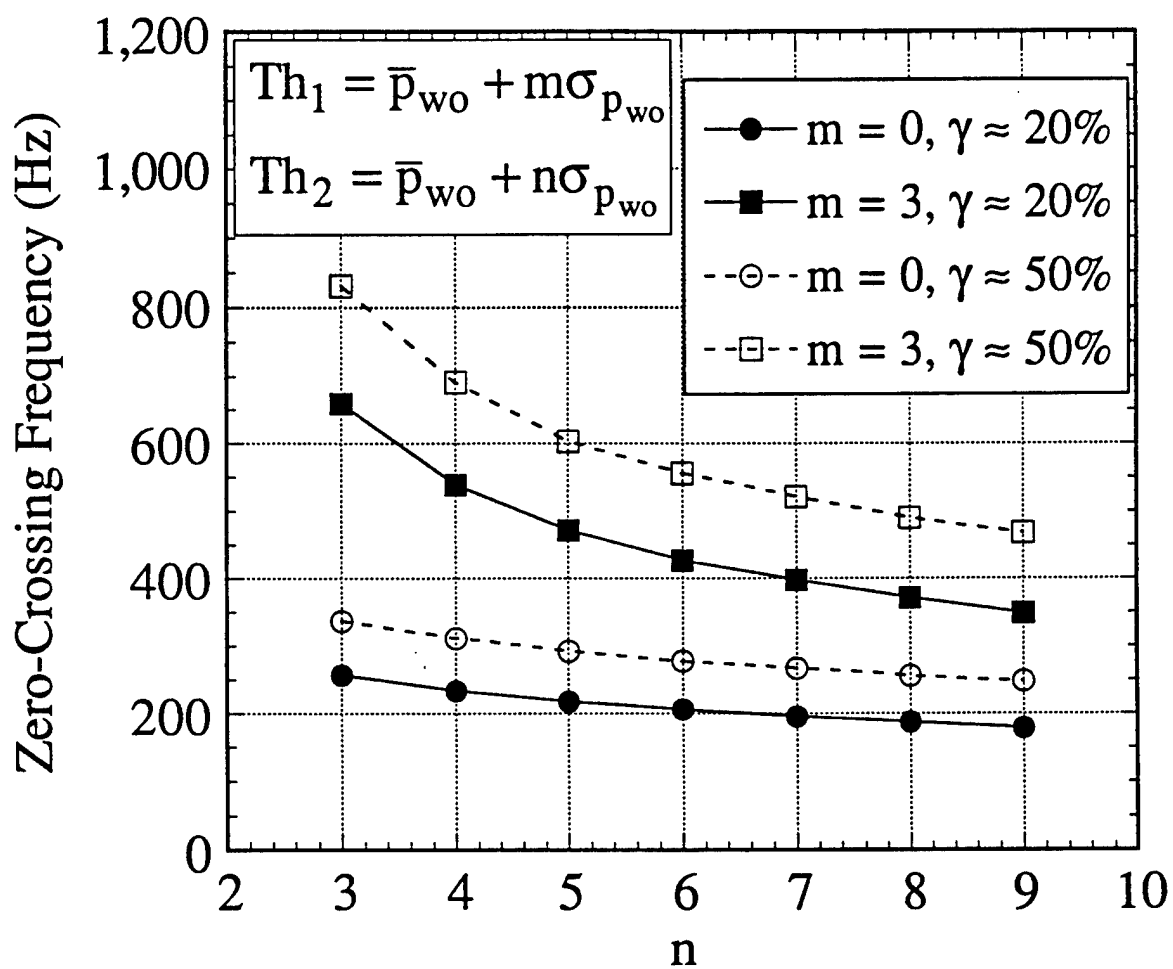
Figure 3.   Sensitivity of the zero-crossing frequency to the threshold levels in the TTMBCC algorithm for the PIBLS experiments.
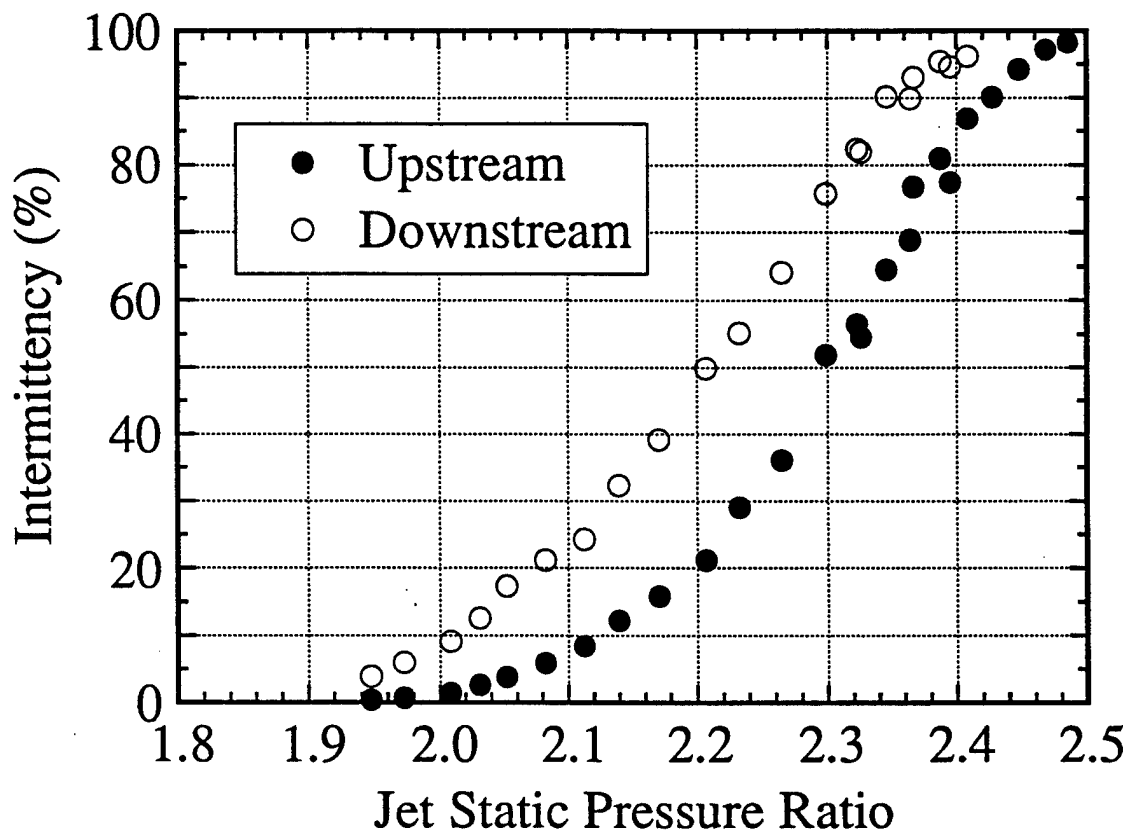
Figure 4.   Plot of intermittency versus JSPR for the upstream and downstream pressure
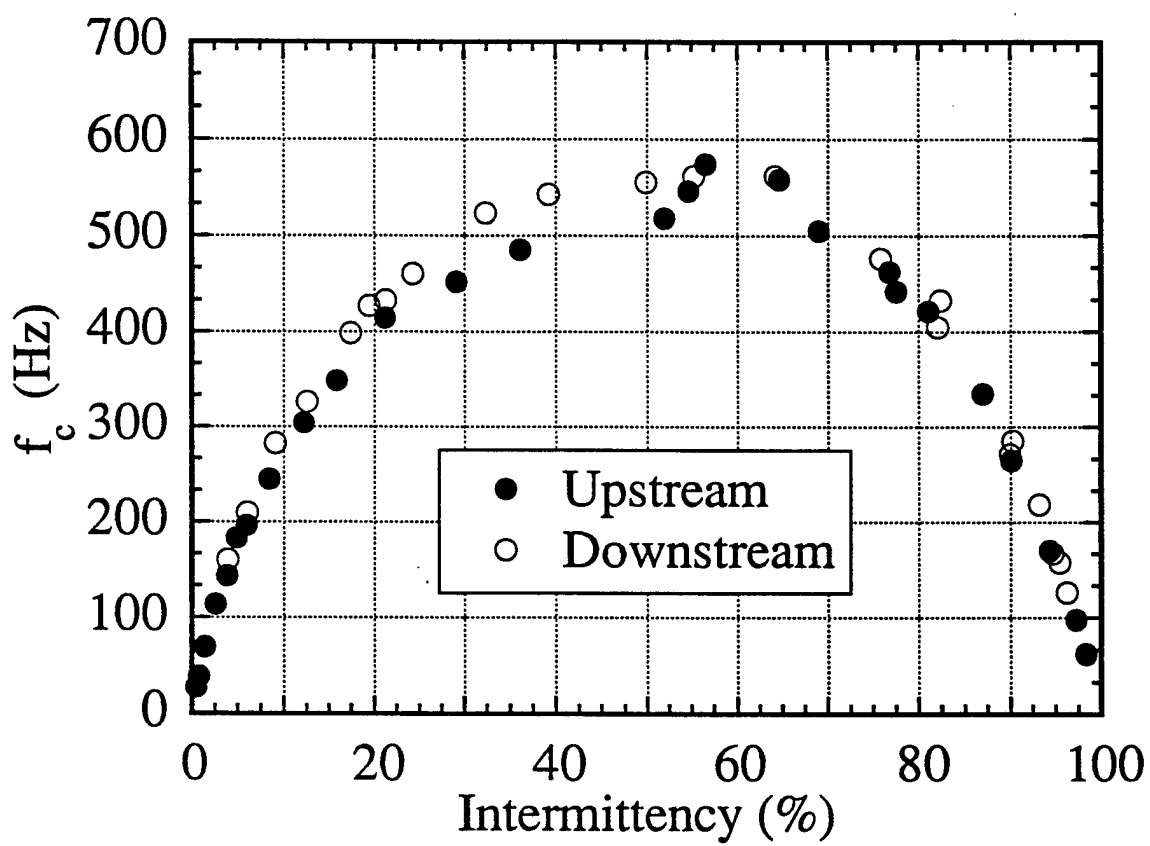transducer measurements.
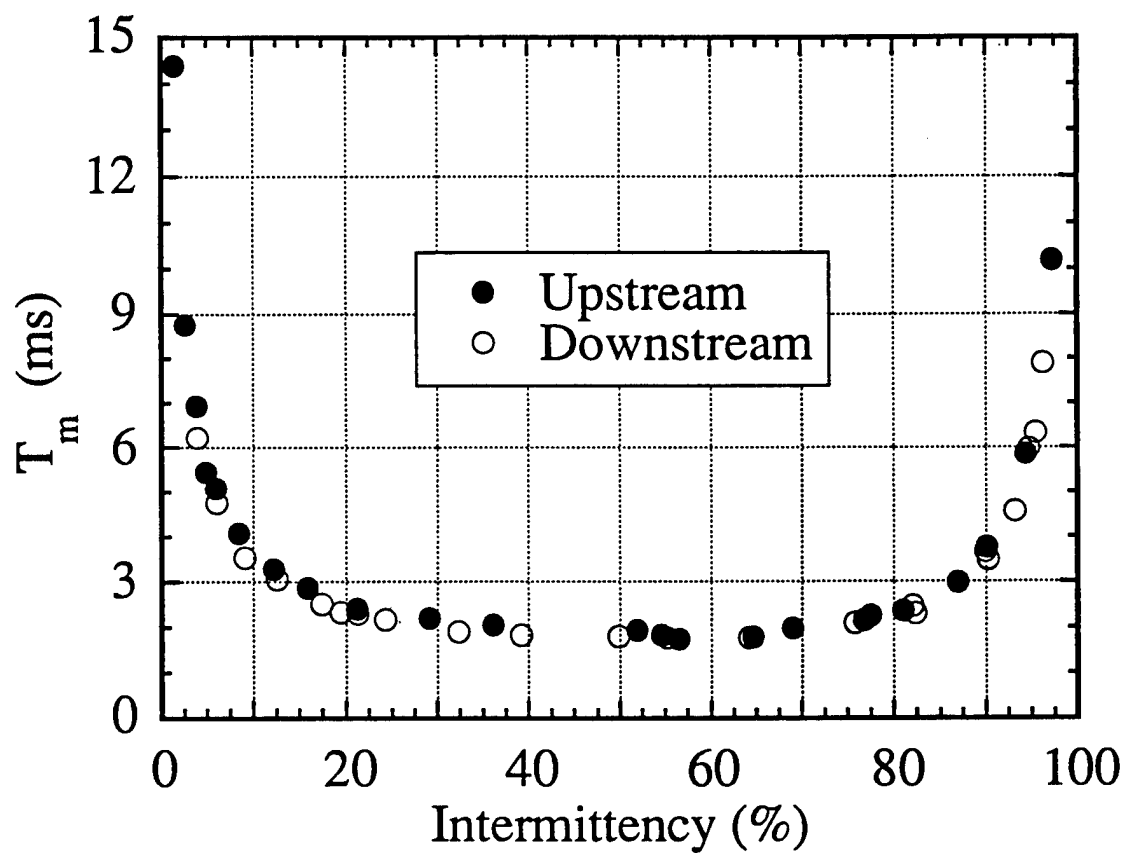
Figure 5.   Mean period of the shock wave motion versus intermittency across the intermittent region of PIBLS flowfields.
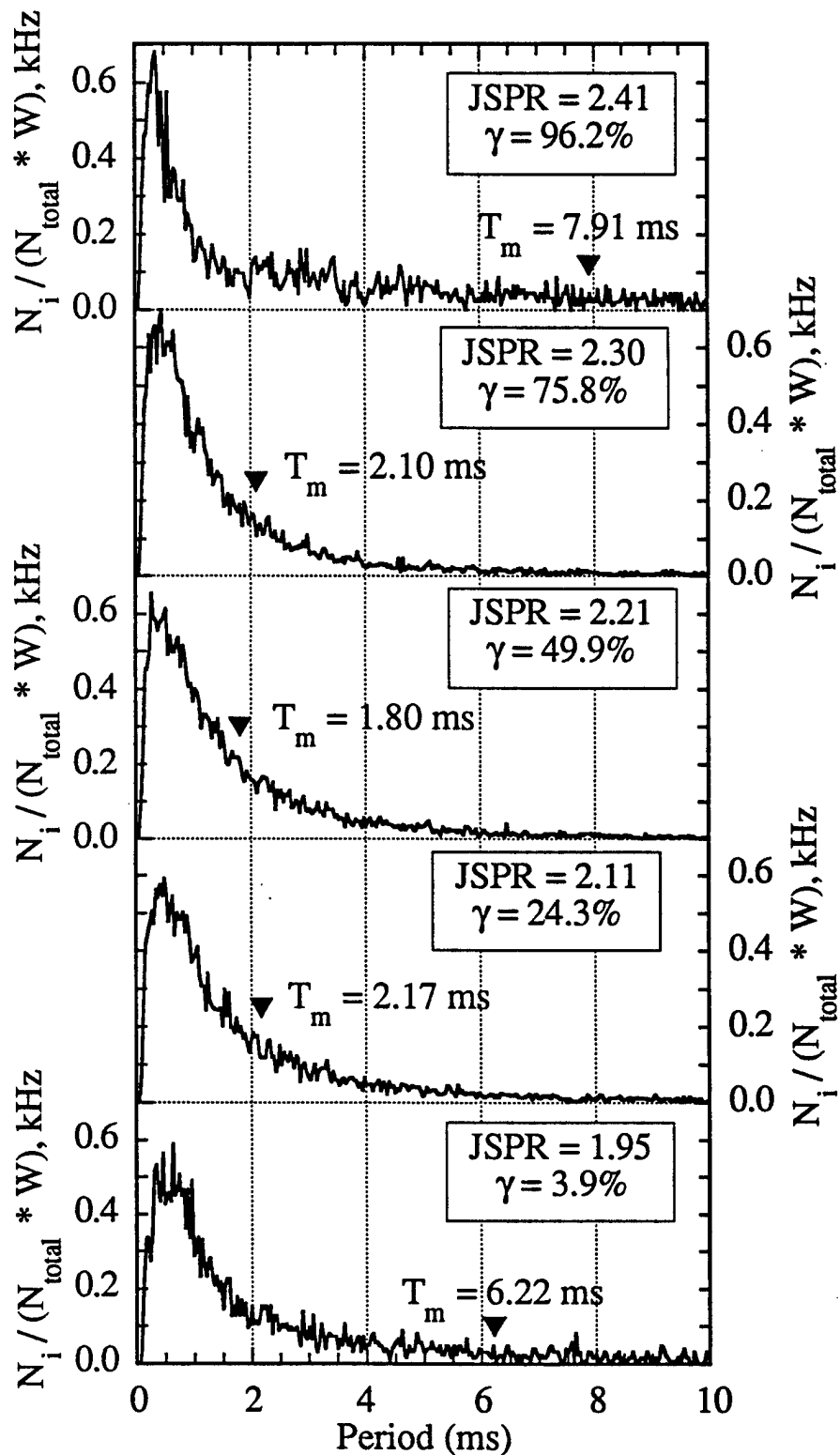
Figure 6.   PDF estimates of the shock wave periods at discrete locations across the intermittent region.
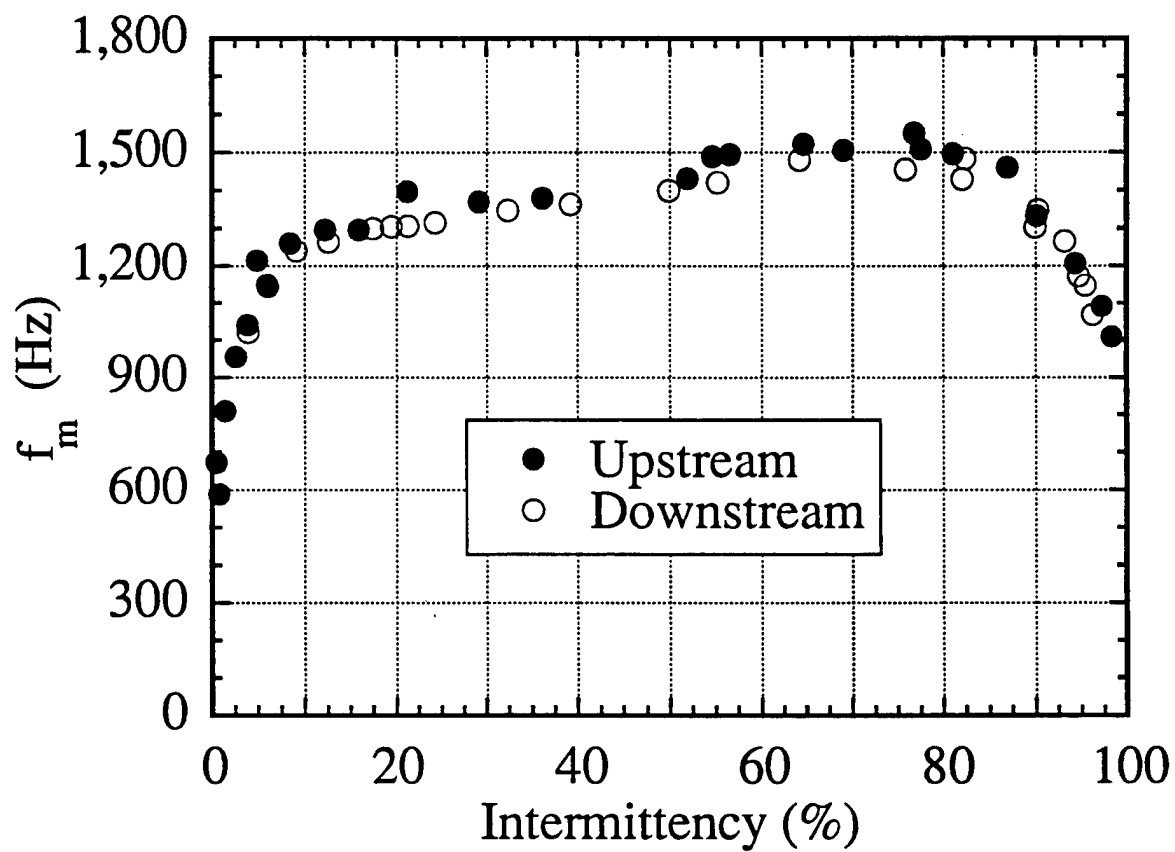
Figure 7.   Mean frequency of the shock wave motion versus intermittency across the intermittent region of PIBLS flowfields.
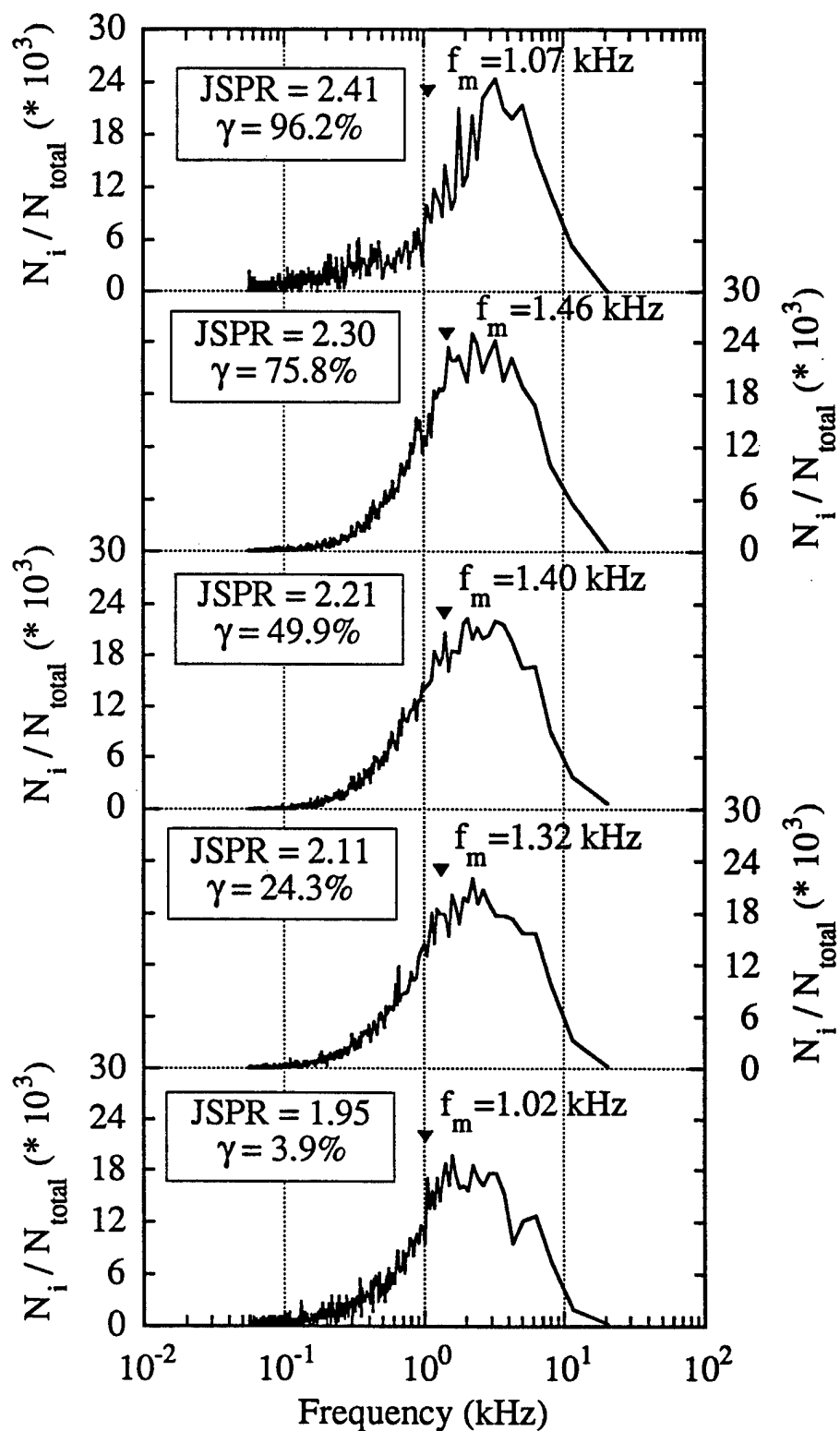
Figure 8. PDF estimates of the shock wave frequencies at discrete locations across the intermittent region.
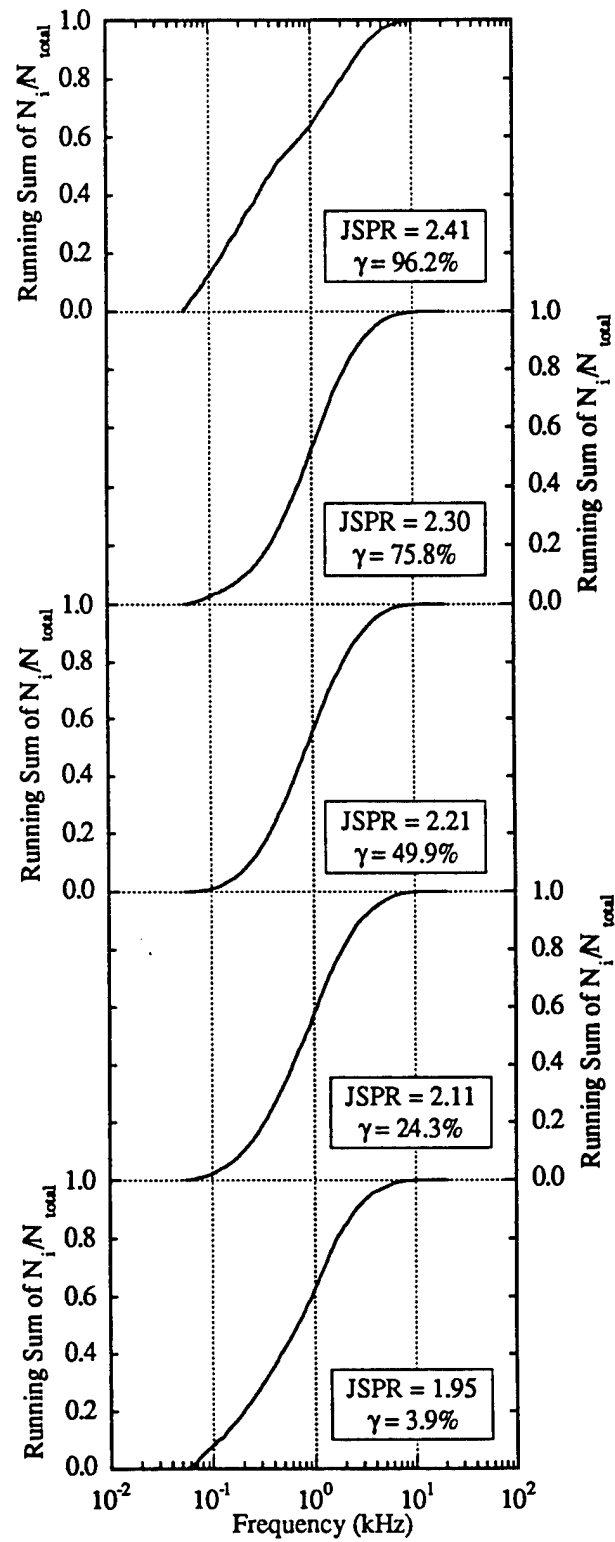
Figure 9.   Probability distribution function estimates of the shock wave frequencies at discrete locations across the intermittent region.

Figure 10.   Zero-crossing frequency of the shock wave motion versus intermittency across the intermittent region of PIBLS flowfields.
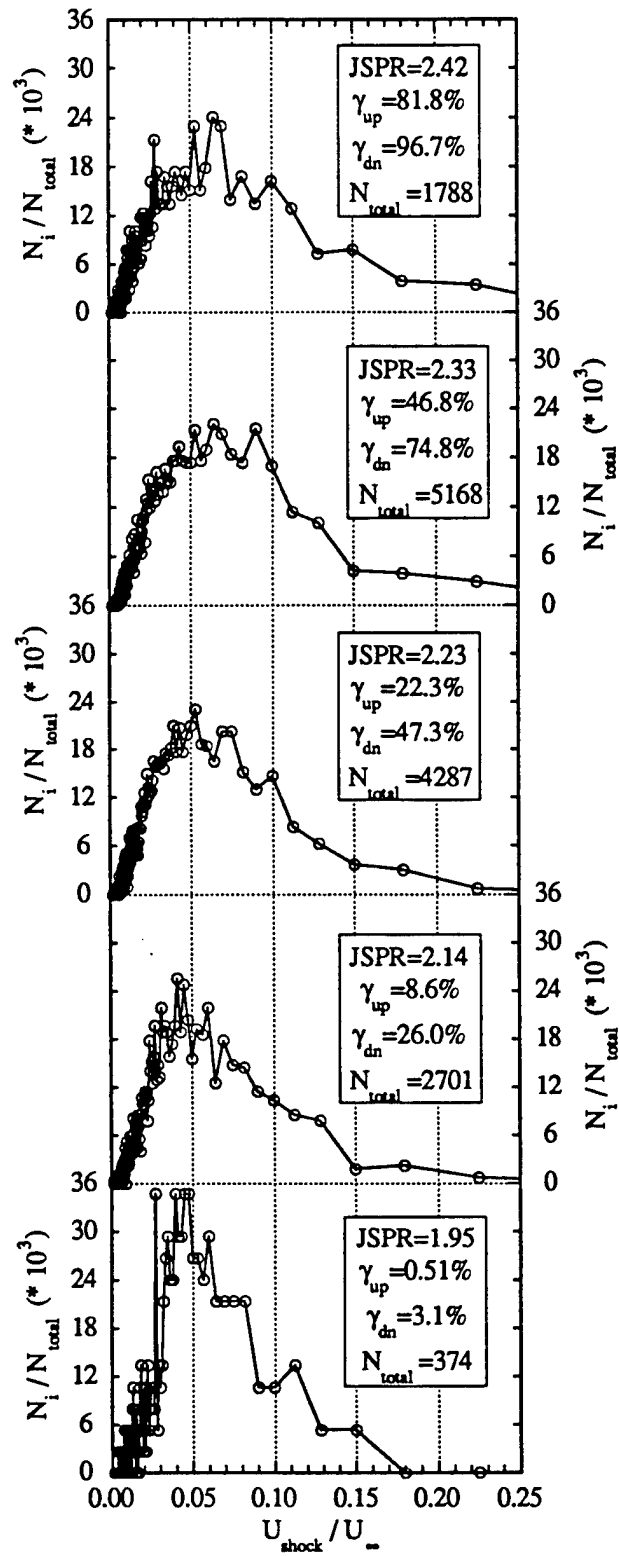
Figure 11.   PDFs of the shock wave velocity in the upstream direction across the intermittent region.
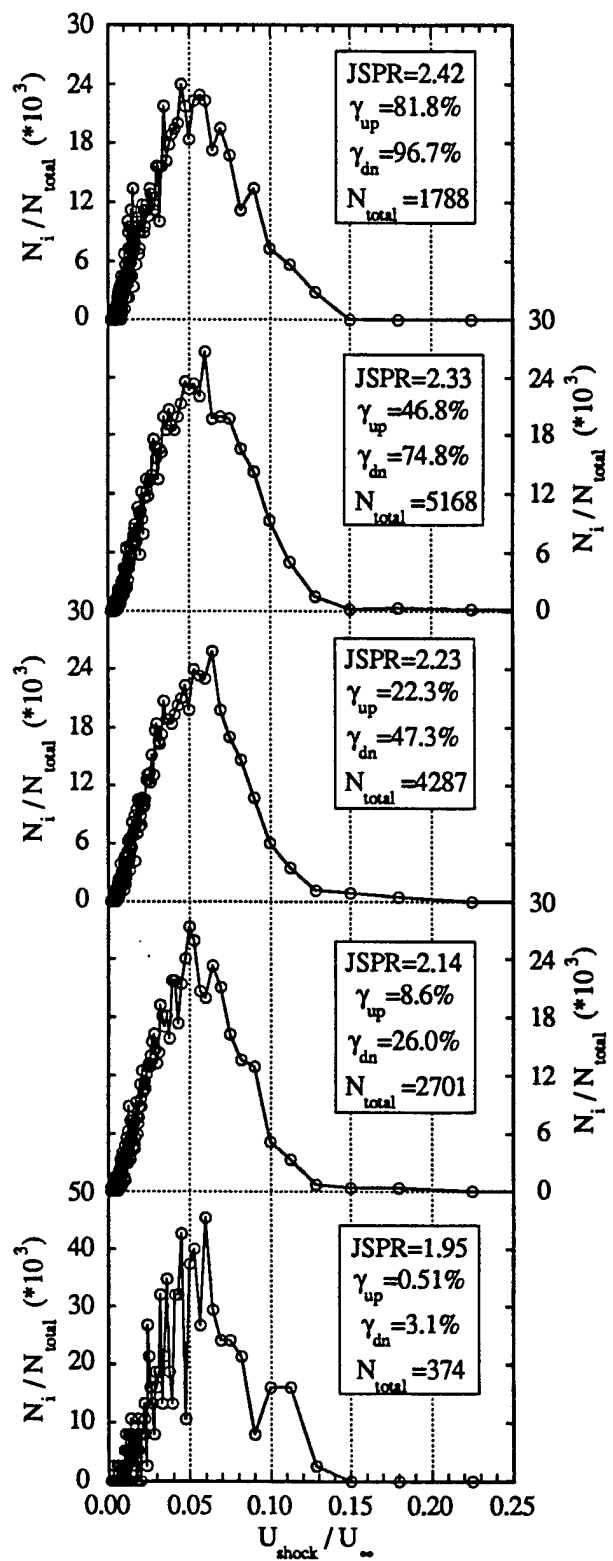
Figure 12.   PDFs of the shock wave velocity in the downstream direction across the intermittent region.
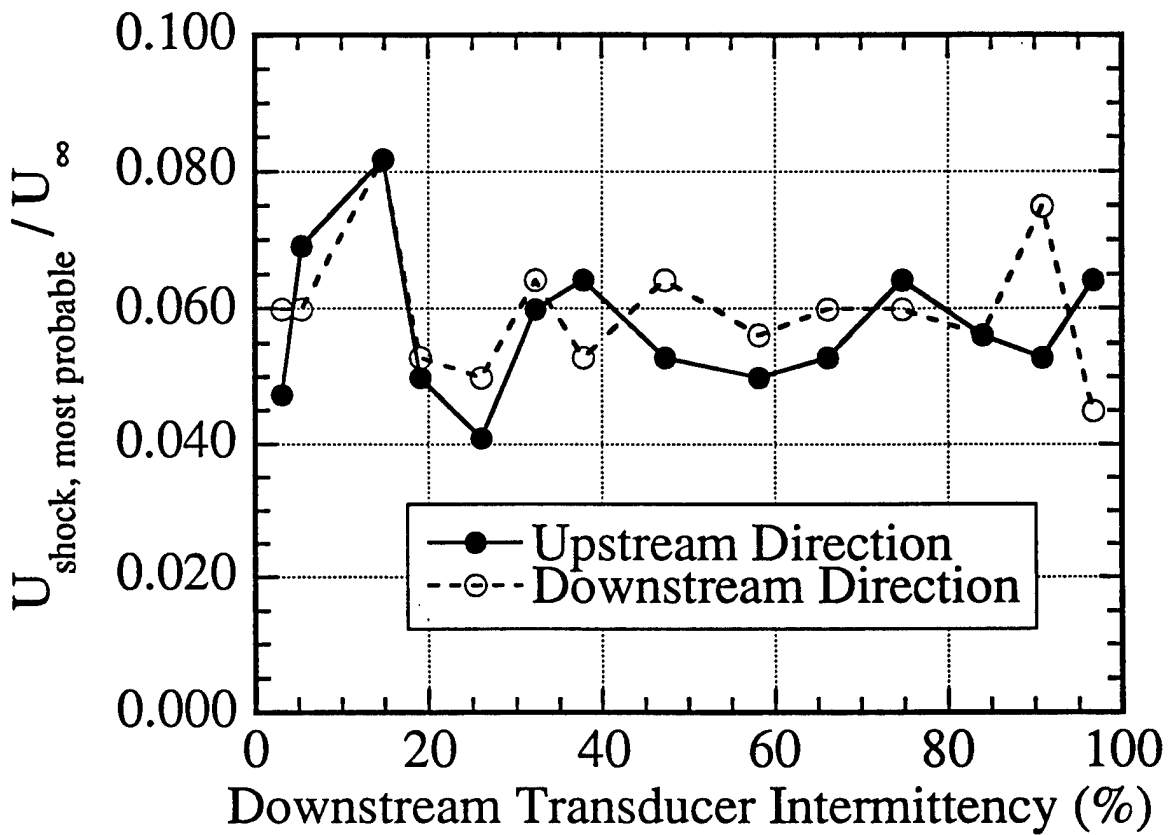
Figure 13.   Most probable shock wave velocity in the upstream and downstream directions across the intermittent region.
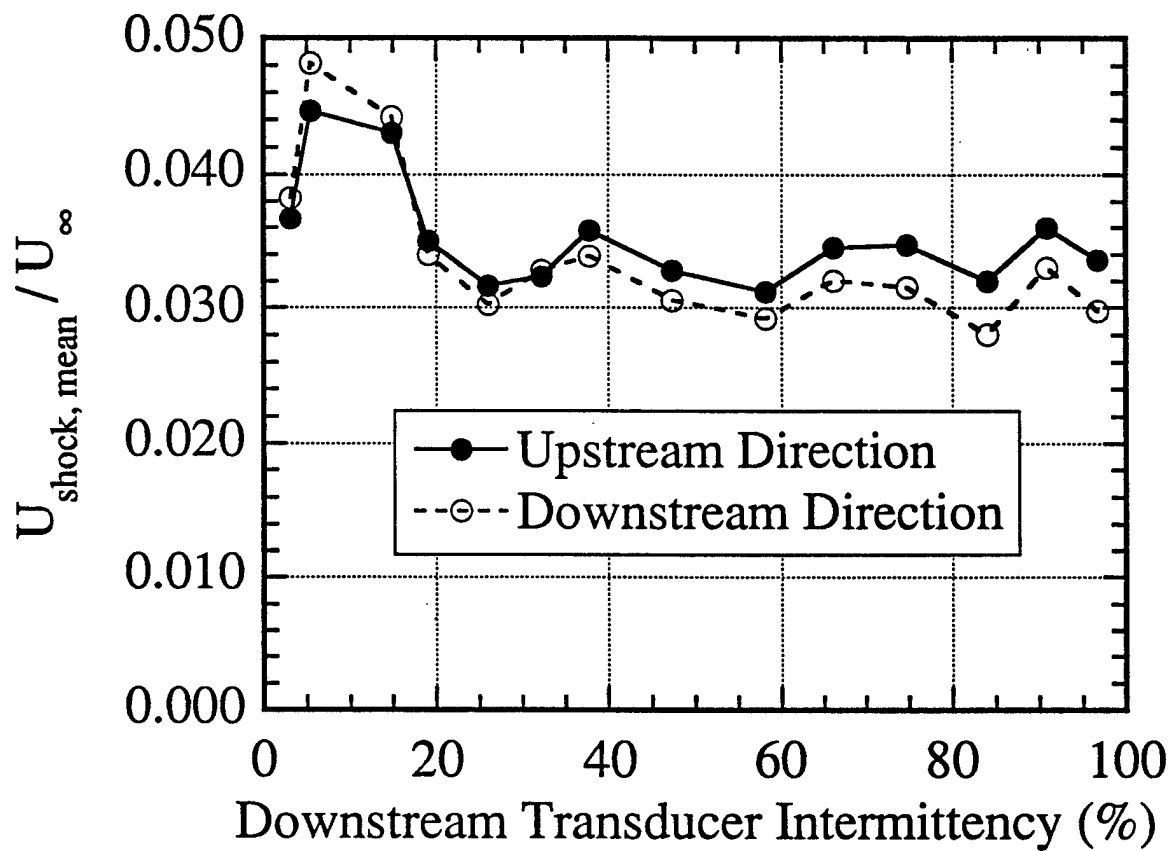
Figure 14.   Mean shock wave velocity in the upstream and downstream directions across the intermittent region.

APPENDIX A.13

SUPERSONIC BASE FLOW EXPERIMENTS IN THE NEAR-WAKE OF A CYLINDRICAL AFTERBODY

by

J. L. Herrin and J. C. Dutton

AIAA 93-2924

Supersonic Base Flow Experiments in the Near-Wake of a Cylindrical Afterbody

J.L. Herrin and J.C. Dutton
University of Illinois at Urbana-Champaign
Urbana, Illinois

AIAA 24th
Fluid Dynamics Conference
July 6-9, 1993 / Orlando, FL

SUPERSONIC BASE FLOW EXPERIMENTS IN THE NEAR-WAKE
OF A CYLINDRICAL AFTERBODY

J.L. Herrin[*] and J.C. Dutton[**]
University of Illinois at Urbana-Champaign
Urbana, Illinois

Abstract

The near-wake of a circular cylinder aligned with a uniform Mach 2.5 flow has been experimentally investigated in a wind tunnel designed solely for this purpose. Mean static pressure measurements were used to assess the radial dependence of the base pressure and the mean pressure field approaching separation. In addition, two-component laser Doppler velocimeter (LDV) measurements were obtained throughout the near-wake including the large separated region downstream of the base. The primary objective of the research was to gain a better understanding of the complex fluid dynamic processes found in supersonic base flowfields including separation, shear layer development, reattachment along the axis of symmetry, and subsequent development of the wake. Results indicate relatively large reverse velocities and uniform turbulence intensity levels in the separated region. The separated shear layer is characterized by high turbulence levels with a strong peak in the inner, subsonic region which eventually decays through reattachment as the wake develops. A global maximum in turbulent kinetic energy and Reynolds shear stress is found upstream of the reattachment point which is in contrast to data from the reattachment of a supersonic shear layer onto a solid wall.

Nomenclature

C_f = skin friction coefficient
C_p = dimensionless pressure coefficient
H = compressible shape factor, δ^* / θ
M = Mach number
k = turbulent kinetic energy
P = pressure
P_k = production of k
r = radial coordinate
R = base radius
S = location of reattachment point
t = tangential coordinate
u_τ = friction velocity
U = mean axial velocity
V_r = mean radial velocity
V_t = mean tangential velocity
x = axial coordinate
y = vertical distance, r-R
γ = ratio of specific heats

δ = boundary layer thickness
δ^* = displacement thickness
θ = momentum thickness
ν_w = kinematic viscosity at wall
Π = wake strength parameter
σ = root-mean-square value
$< >$ = ensemble-averaged value
$( )'$ = fluctuating value

Subscripts
1 = condition at nozzle exit
base = condition at base
u = axial component
v_r = radial component
v_t = tangential component

Introduction

The low pressures that act in the base region of bodies of revolution in supersonic flight can cause significant amounts of drag[1]. For this reason, practical methods such as boattailing, base bleed, and base burning have been developed in order to increase the base pressure on aerodynamic vehicles such as missiles, rockets, and projectiles. In order to further enhance vehicle performance, however, a more complete understanding of the complex fluid dynamic processes that occur in base flowfields is necessary. Past experimental efforts have provided an adequate description of the overall flowfield structure and some parametric trends, but very little detailed quantitative data exists, especially for supersonic flows. In fact, a comprehensive survey of the available experimental data on axisymmetric base flows was recently undertaken by GARTEUR Action Group AG09[2]. After an exhaustive search, the group concluded that no accurate, well-documented experimental data existed for the near-wake flowfield in supersonic, axisymmetric flow. Reliable turbulence information in the base region is especially scarce which presents a problem in validating numerical predictions of these flowfields (see Refs. 3-5). Clearly, the practical importance of increasing the understanding of axisymmetric base flowfields lies in the ability to someday control the near-wake flow interactions such that base drag can be reduced and vehicle stability and control can be enhanced.

A schematic diagram of the mean flowfield structure in the near-wake of a cylindrical afterbody aligned with a supersonic flow is shown in Fig. 1. The supersonic afterbody freestream flow undergoes a strong expansion centered at the base corner as the turbulent boundary layer separates geometrically from the body. A free shear layer is formed which separates

---

[*] Graduate Research Assistant, Department of Mechanical and Industrial Engineering, Student Member AIAA
[**] Professor, Department of Mechanical and Industrial Engineering, Associate Fellow AIAA

1

the outer inviscid flow from a relatively large recirculation region immediately downstream of the base. The intense turbulent mixing and energy exchange that characterize the free shear layer are important in determining the flowfield properties throughout the near-wake including the recirculation region. As the free shear layer approaches the axis of symmetry, a recompression process occurs which eventually realigns the flowfield with the axis. A rear stagnation point, where the mean velocity vanishes, is located on the centerline and separates the recirculation region from the wake which develops downstream.

The early theoretical model for turbulent base flows developed by Korst[6] prompted several experimental investigations which attempted to gather the empirical information necessary to complete the theory[7-10]. However, many experimental problems, including improper model mounting, probe interference effects, and lack of flowfield symmetry, hampered these efforts which resulted in data of questionable accuracy. These experimental difficulties stem primarily from the axisymmetric geometry of the body as well as the sensitivity of the separated region downstream of the base to wind tunnel interference effects[11]. Perhaps the most comprehensive previous study of supersonic power-off base flows was undertaken by Gaviglio et al.[12] using a hot-wire anemometer. The overall inviscid flow structure and downstream wake properties were determined; however, the recirculation region directly behind the base was not investigated due to possible probe interference effects which limits the utility of the data. Neale et al.[13] investigated the mean velocity field behind a circular cylinder with a pitot-static probe but, again, bypassed the separated region. Clearly, accurate experimental measurements in the recirculation region downstream of the base require non-intrusive diagnostic techniques. Laser Doppler velocimetry (LDV) is a non-intrusive velocity measurement tool well-suited for such flows. Delery[14] used LDV to successfully document the near-wake of a subsonic, axisymmetric base flowfield. Detailed mean velocity and turbulence data were gathered throughout the near-wake and provide a good data base for the subsonic case. Amatucci et al.[15] made similar LDV measurements in a supersonic, two-stream flowfield with a two-dimensional base that modeled the power-on case; however, the effects of the more practical axisymmetric configuration were not investigated. Heltsley et al.[16] used LDV to investigate the flowfield downstream of a transonic, axisymmetric, power-on base flow but encountered experimental problems throughout the measurements.

In the current study, experiments were conducted to document the entire near-wake flowfield structure behind a cylindrical afterbody immersed in a supersonic flow. Detailed LDV measurements were made in order to obtain a better understanding of the fluid dynamic processes throughout the near-wake including separation, shear layer growth and development, reattachment, and wake redevelopment.

To the authors' knowledge, these data also provide the first detailed investigation of the mean and turbulent velocity fields inside the recirculation region in a supersonic base flow. In addition, the data provided herein will aid both analytical and numerical modelers of supersonic, axisymmetric base flows.

Experimental Facility and Instrumentation
Wind Tunnel Facility

The experiments were conducted in a supersonic, blowdown-type wind tunnel designed solely for the study of axisymmetric base flows. Figure 2 is a schematic diagram of the axisymmetric wind tunnel facility which is located in the University of Illinois Gas Dynamics Laboratory. Dry, compressed air passes from the stagnation chamber through a flow conditioning module consisting of screens and honeycomb (used to dampen any large scale disturbances generated in the air supply process and to minimize freestream turbulence levels) and finally to the converging-diverging supply nozzle. The pressure and temperature in the stagnation chamber were consistently maintained at 515 ± 2.8 kPa and 294 ± 3 K, respectively. The nozzle takes an annular shape due to the central sting which supports the base model from upstream to prevent any interference with the near-wake flowfield. The cylindrical afterbody used in the present experiments is 63.5 mm in diameter and is attached by internal threads to the sting. Physical supports for the sting are located outside the rear of the stagnation chamber and inside the wind tunnel at the flow conditioning module. The sting supports are of sufficient rigidity such that sting vibration due to flowfield fluctuations was negligible. The nominal design Mach number and unit Reynolds number at the nozzle exit are 2.5 and 52 (10^6) per meter, respectively.

Proper centering of the afterbody/base within the nozzle is critical in obtaining axisymmetric flow in the near-wake. In these experiments, custom-designed wind tunnel adjusting blocks were used to adjust the relative position between the sting and nozzle until an axisymmetric flow was obtained. Oil-streak visualization performed on the base was used effectively to examine the sting/nozzle alignment and was found to be a very sensitive indicator of the symmetry of the near-wake flowfield. Micrometer measurements at the nozzle exit indicated a maximum afterbody misalignment of 0.13 mm from the physical nozzle centerline.

Experimental Methods

Conventional schlieren and shadowgraph photography were used to investigate the qualitative structure of the near-wake flowfield. The photographs were of only moderate quality due to the axisymmetric nature of the flow, but they were used successfully to confirm the flowfield structure shown in Figure 1 and to determine a proper operating condition that eliminated any wind tunnel interference effects.

2

Mean static pressure measurements were made at several locations on the base and afterbody surfaces using a Pressure Systems Inc. digital pressure transmitter (DPT 6400-T). Nineteen pressure taps (0.64 mm in diameter) were located symmetrically across the base at radial intervals of 3.18 mm. Along the afterbody, two sets of diametrically-opposed pressure taps (0.64 mm in diameter) were located starting 2.38 mm upstream of the base corner with each tap separated axially by 3.18 mm and a total of five taps in each set. In addition to the afterbody pressure taps, total pressure and temperature probes were mounted in the stagnation chamber.

The focus of this investigation involved the implementation of a two-component LDV system for measuring the near-wake velocity field. Artificial seed particles were generated by a TSI Inc. six-jet atomizer filled with 50 cp silicone oil. The droplets were injected into the flow upstream of the facility nozzle to avoid disturbing the flowfield with the injection process. In previous experiments with the same seeding apparatus, Bloomberg[17] deduced a mean droplet diameter of 0.8 μm and showed mean particle relaxation distances of approximately 2 mm downstream of an oblique shock wave generated by a 15 degree compression corner in a Mach 2.6 flow. The maximum velocity gradients in the present experiments (near boundary layer separation) are significantly weaker than for the oblique shock in Bloomberg's work; however, to ensure negligible particle lag in the current experiments, no data are presented within the first 5 mm downstream of the base corner separation point. In the separated shear layer, the Stokes number for this seeding configuration is estimated to be 0.15 which Samimy and Lele[18] have shown yields root-mean-square slip velocities (difference in velocity between the particle and the local fluid element) of approximately 1.5%.

The LDV measurement volume used in these experiments was 120 μm in diameter and had a fringe spacing of approximately 10.3 μm. A 20° off-axis, forward-scatter receiving optics configuration was used to reduce the effective measurement volume length to 0.70 mm. Bragg cells were used in each component to frequency shift one of the beams 40 MHz against the mean flow direction in order to discriminate reversed velocities. In addition, the two orthogonal fringe patterns were rotated to ±45 degrees relative to the wind tunnel axis to reduce fringe blindness. To measure accurately the Doppler frequencies in this demanding flow, a TSI IFA-750 autocorrelation processor was used. Data were gathered from the processor by a Gateway 2000 486-33 personal computer where further processing and analysis were performed. Positioning of the LDV measurement volume throughout the near-wake flowfield was accomplished using a three-axis, computer-controlled traversing table with a positioning resolution of 0.75 μm.

The LDV measurement locations were concentrated in the regions of high velocity gradients including the approach boundary layer, separated shear layer, developing wake, and also near the reattachment point. Radial traverses were completed at 21 axial stations throughout the near-wake with approximately 30 spatial locations per traverse. In addition, an axial traverse along the model centerline was performed to show the development of the centerline mean velocity and turbulence intensities. During each radial traverse, three or four locations below the axis of symmetry were measured to check the symmetry of the flow. In all cases, the measured wake centerline (defined as the location where $\langle u'v_r' \rangle = 0$) was within 2 mm of the geometric model centerline. Approximately 4000 instantaneous velocity realizations were gathered at each spatial location and probability density functions (pdfs) of each velocity component were calculated. The pdfs generally resembled a Gaussian profile except near the inner edge of the shear layer (near U = 0) where bimodal peaks in each pdf consistently occurred. The bimodal pdfs most likely indicate the presence of large-scale structures on the inner edge of the shear layer which play an important role in the entrainment of fluid from the recirculation region. The effects of velocity bias on the LDV data were accounted for by weighting each velocity realization with the interarrival time between realizations[19].

With the current two-component LDV arrangement, both the horizontal and vertical components of velocity were measured. In two-dimensional flows, this generally allows direct measurement of the streamwise and transverse velocities, but no measurement of the spanwise component. In the current axisymmetric flow, by using the same LDV configuration and making measurements independently in both the horizontal and vertical planes which pass through the axis of symmetry, all three mean and rms velocities have been measured. In addition, the axial-radial $\langle u'v_r' \rangle$ and axial-tangential $\langle u'v_t' \rangle$ Reynolds shear stresses have been directly measured. An error analysis including the uncertainties associated with velocity biasing, fringe biasing, velocity gradient biasing, finite ensemble size, processor resolution, optical misalignment, and fringe spacing determination has been completed. The estimated *worst-case* uncertainty in the mean velocity measurements is 1.2% of U_1 and, in the rms velocity fluctuations, 2.3% of U_1, where U_1 is the freestream velocity just prior to separation.

Results

Pressure Measurements

Static pressure measurements along the afterbody were used to assess the uniformity of the nozzle exit flow as well as any upstream influence of the separation process. As expected, the pressure field approaching the base corner was relatively uniform and takes a value consistent with an isentropically expanded Mach 2.44 flow. No upstream influence from the base corner separation was evident in the data.

Pressure measurements have also been made at nineteen locations on the base in order to assess the radial distribution of the mean static pressure. Figure

3

3 shows the dimensionless base pressure coefficient at each location, defined as:

$$C_{Pbase} = \frac{2\left\{\dfrac{P_{base}}{P_1} - 1\right\}}{\gamma M_1^2} \qquad (1)$$

where P is the static pressure, M the Mach number, and the subscript 1 denotes conditions at the nozzle exit. The pressure is shown to be relatively constant across the base (note the expanded vertical scale) with a slight increase toward larger radii where the maximum pressure measured was 3.9% higher than the pressure at the center of the base. Similar base pressure profiles were observed by Reid and Hastings[8] for a cylindrical afterbody in a Mach 2.0 flow with a maximum rise in pressure of approximately 3% across the base. An area-weighted average of the current data across the base was performed to determine an average base pressure coefficient of -0.102.

Flowfield Velocity Measurements

Approach Flow Measurements

The boundary layer approaching the base corner separation point was measured at three axial stations upstream of the base. Figure 4 is a plot of the boundary layer profile obtained 1 mm upstream of the base corner along with a curve fit by Sun and Childs[20] for compressible, turbulent boundary layers. The boundary layer properties derived from the curve fit are also shown in Figure 4. The values for the dimensionless properties (H, Π, and C_f) are typical of those found in equilibrium, compressible, turbulent boundary layers[21]. In order to determine the integral properties, the mean density profile through the boundary layer was determined using the ideal gas equation of state and the assumptions of negligible radial pressure gradient, adiabatic wall, and a recovery factor of 0.89 as suggested by Kays and Crawford[22]. The freestream Mach number across the nozzle exit was measured by LDV to be 2.46 ± 1% (the corresponding approach velocity was $U_1 = 567$ m/s). Also, measured freestream turbulence intensities in the approach flow were less than 1%.

Centerline Measurements

The LDV measurements along the model centerline were taken in 5 mm increments from the base to the end of the viewing window in the test section. A plot of the mean axial velocity along the model centerline is shown in Fig. 5. The origin of the cylindrical coordinate system has been arbitrarily set at the center of the base with all axial distances positive downstream. The axial location where the data crosses the U = 0 line clearly defines the rear stagnation point, S, since the other two measured velocity components are negligible along the centerline; this occurs at x/R = 2.65. The maximum reversed velocity occurs at x/R ≈ 1.5 and takes a value of approximately 27% of the approach freestream velocity. In a similar experiment using LDV in subsonic flow (Mach 0.85) behind a circular cylinder, Delery[14] found the rear stagnation

point located at 3.06 base radii downstream and a maximum reversed velocity of approximately 30% of the local freestream value and located at x/R = 1.8. It is interesting to note that for both the supersonic and subsonic cases, the maximum reversed velocity occurs at a location approximately 57% of the distance from the base to the reattachment point. Merz et al.[23] found that for all Mach numbers from 0.1-0.9, the maximum reversed velocity was 35-40% of the freestream velocity and occurred at a distance 60% of the length to reattachment. The degree of wake redevelopment in the present experiments is indicated in Fig. 5 by the maximum positive centerline velocity which takes the value of 57% of the approach velocity (M ≈ 1.05) at the furthest downstream station.

Near-Wake Mean Velocity Measurements

The mean velocity vector field in the near-wake is shown in Fig. 6. In this and subsequent figures, the vertical axis has been expanded by 42% compared to the horizontal axis in order to more clearly show the features of the flowfield (the axial-to-radial aspect ratio of the actual LDV measurement grid is 4.27:1). In order to place the experimental data on a uniform grid for the vectors shown in Fig. 6, a simple linear interpolation in both x and r between the unequally spaced data was completed. The velocity vectors show clearly the dominance of the axial velocity on the overall mean velocity field. The turning of the mean flow through the base corner expansion fan, the relatively low-speed recirculation region, and the realignment of the mean flow with the axis downstream of reattachment (S) are clearly shown.

A contour plot of the Mach number distribution throughout the near-wake is shown in Fig. 7. The steep velocity gradients through the initial portion of the shear layer are clearly evident in the figure. The spreading of the contour lines further downstream is indicative of the growth of the shear layer prior to reattachment and, also, the wake development downstream. Note that the flow along the axis reaccelerates to sonic velocity at approximately five base radii downstream which is similar to the measurements of Neale et al.[13] in a Mach 3 base flowfield where the sonic point was located at x/R = 5.1. The maximum Mach number of the reversed flow is 0.48 and is located on the centerline at approximately x/R = 1.5. The gradual recompression of the outer flow is indicated by the decreasing Mach number contours in the upper right of the figure.

The mean radial velocity contours are shown in Fig. 8. The small values relative to the mean axial approach velocity once again show the dominance of the axial velocity in the near-wake flowfield. The closely spaced contours emanating from the base corner mark the turning of the mean flow through the expansion fan. As the outer inviscid flow approaches the axis of symmetry, the radial velocity continues to increase in magnitude, due to the axisymmetric effect, to a peak value of 22% of the mean approach velocity

4

at a location approximately two base radii downstream. The location of flowfield realignment with the axis of symmetry appears to depend on whether the flow is supersonic or subsonic. The realignment process in the outer flow is shown in the upper right of Fig. 8 by the contour lines of decreasing magnitude and the relatively uniform flow region downstream of the last contour. However, closer to the axis of symmetry, a much slower realignment of the subsonic inner flow occurs, such that the mean radial velocity is appreciable out to $x/R = 4.5$. The mean tangential (swirl) velocity was also directly measured with the LDV system, and as expected, the magnitudes were negligible compared to the other two components.

Near-Wake Turbulence Measurements

The root-mean-square fluctuation velocities were directly measured in all three coordinate directions and will be presented in the form of turbulence intensities, σ/U_1. Figure 9 shows the axial turbulence intensity contours throughout the near-wake. The large increase in turbulent fluctuations from the outer freestream to the values in the shear layer and wake are apparent. A peak axial rms velocity fluctuation of 22% of the mean approach velocity occurs at a location 83% of the axial distance from the base to reattachment. Upstream of reattachment at any axial station, the radial location of the maximum axial turbulence intensity lies in the subsonic region of the shear layer. In contrast, Amatucci et al.[15] found peak levels of turbulence intensity near the sonic line in a two-dimensional, two-stream base flow. Throughout the recirculation region in the current study, the axial turbulence intensity is relatively constant except very close to the base where it is attenuated. Further downstream as the shear layer transforms into a wake, the overall level of turbulent fluctuations diminishes and a well-defined peak in the axial turbulence intensity profiles is no longer discernible.

Contours of constant radial turbulence intensity are shown in Fig. 10. The general trends follow closely those of the axial turbulence intensity, but the overall fluctuation levels are smaller. The peak radial velocity fluctuation is 15.6% of U_1 and occurs at roughly the same location as the peak axial fluctuation. The recirculation region contains a greater variation in radial turbulence intensity than axial turbulence intensity with a steady increase from the base to the reattachment point (not including the base effects at $x/R<0.5$). The turbulence relaxation beyond reattachment is fairly slow with a uniform radial turbulence intensity across the inner portion of the wake as it develops.

The tangential turbulence intensity represents fluctuations from the mean swirl velocity which, as mentioned above, is negligible for axisymmetric flows. Figure 11 is a plot showing the tangential turbulence intensity throughout the near-wake. The overall level of fluctuations in the tangential direction is reduced compared to the axial turbulence intensity and is generally smaller than the radial fluctuations. The peak value of the tangential velocity fluctuations is 13.5% of U_1 and occurs near the shear layer reattachment point at $x/R = 2.65$. The greatest variation in tangential turbulence intensity occurs at the outer edges of the shear layer and wake, and the radial profiles do not exhibit the sharp peaks evident in the axial and radial turbulence intensities.

The ratio of the turbulence intensity contributions from each component gives a relative indication of the anisotropy in the normal stress field. In the current flow, the axial turbulence intensity dominates with peak values approximately 30-50% higher than the peak radial fluctuations and 60-70% higher than the peak tangential fluctuations in the shear layer where anisotropy is largest. The relative ordering of the peak turbulence intensity magnitudes (axial-radial-tangential) found in the current base flow experiments can be contrasted with the recent data from Gruber and Dutton[24] for a two-dimensional, compressible, constant pressure mixing layer. In their study, the magnitude of the spanwise component of turbulence intensity exceeded the contribution from the transverse component by approximately 20% in the peak intensity region of the shear layer, probably due to the three-dimensional nature of the large scale structures in the planar, compressible mixing layer. In axisymmetric flow, the tendency of the structures to grow asymmetrically (in the tangential direction) is most likely dampened by the more stringent axisymmetric conditions imposed by the mean flowfield. In incompressible, constant pressure mixing layers, the spanwise component of turbulence intensity has been shown to be approximately equal to the transverse turbulence intensity[25].

An important turbulence quantity often used to describe the overall level of turbulent fluctuations is the turbulent kinetic energy defined as:

$$k = \frac{1}{2}(\sigma_u^2 + \sigma_{vr}^2 + \sigma_{vt}^2) \qquad (2)$$

In these experiments, all three mean square fluctuations (normal stresses) have been directly measured. Figure 12 is a plot of the turbulent kinetic energy as measured throughout the near-wake. Since the axial turbulence fluctuation levels dominate the flowfield, the contours of turbulent kinetic energy appear relatively similar to those of the axial turbulence intensity (Fig. 9). The turbulent kinetic energy grows rapidly after separation as the shear layer grows. Prior to reattachment, however, a maximum is reached and a subsequent decay to the relatively constant values in the wake occurs. Again, the sharp peaks in turbulent kinetic energy radial profiles occurring in the shear layer are nonexistent in the wake further downstream. In the recirculation region, the level of turbulent kinetic energy is reduced by the lack of turbulence production due to small mean velocity gradients. The maximum turbulent kinetic energy measured in the near-wake was 4.4% of U_1^2 and occurred at $x/R = 2.2$, or somewhat upstream of reattachment.

5

In the current experiments, both the axial-radial ($<u'v_r'>$) and axial-tangential ($<u'v_t'>$) Reynolds shear stresses have been measured directly. As expected, the axial-radial shear stress dominates the axial-tangential stress which is negligible throughout the near-wake. Figure 13 is a plot showing the axial-radial shear stress distribution downstream of the base. The shear stress peaks in the shear layer upstream of reattachment in approximately the same location as the peak in turbulent kinetic energy. Abu-Hijleh and Samimy[26] used LDV to investigate a supersonic shear layer reattaching onto a wall and found peak values of turbulent kinetic energy and Reynolds stress *downstream* of the reattachment location. The difference in the locations for the peak turbulence quantities between these experiments may possibly be attributed to the differences between solid wall and compliant surface reattachment.

The production of turbulent kinetic energy, defined as follows:

$$P_k = -<u_i'u_j'>\frac{\partial U_i}{\partial x_j} \qquad (3)$$

provides a measure of the amount of kinetic energy transferred from the mean flow to the turbulence field. Investigating the distribution of P_k throughout the near-wake provides insight into the structure of the turbulence field as well as establishing the role of turbulence production in different regions of the flow. In axisymmetric flow, only four of the nine production terms are non-zero which leaves the following expression for P_k:

$$P_k = -\sigma_u^2 \frac{\partial U}{\partial x} - <u'v_r'>(\frac{\partial U}{\partial r} + \frac{\partial V_r}{\partial x}) - \sigma_{vr}^2 \frac{\partial V_r}{\partial r} \qquad (4)$$

which is plotted in Fig. 14 (to avoid clutter, only a reference contour label is shown; all other contours are equally spaced with values increasing by 0.02). Strong turbulence production is seen to occur immediately downstream of the separation point on the inner edge of the shear layer. This is not surprising as the mean velocity gradients are very large in this region. As the shear layer develops, the mean velocity gradients decrease but the Reynolds stresses increase (Figs. 9-13) such that the total production remains significant up to the reattachment point. Downstream of reattachment, however, the Reynolds stresses and mean velocity gradients both decrease rapidly resulting in a diminished level of turbulence production.

Since the total production of turbulent kinetic energy is merely the sum of the production terms for each Reynolds normal stress, separating the total production expression into its individual components yields:

$$P_k = P_u + P_{vr} + P_{vt} \qquad (5)$$

where the individual production terms for each Reynolds normal stress are

$$P_u = -\sigma_u^2 \frac{\partial U}{\partial x} - <u'v_r'>\frac{\partial U}{\partial r} \qquad (6)$$

$$P_{vr} = -\sigma_{vr}^2 \frac{\partial V_r}{\partial r} - <u'v_r'>\frac{\partial V_r}{\partial x} \qquad (7)$$

$$P_{vt} = 0 \qquad (8)$$

From the current experiments, the relative magnitudes of each term indicate that $P_u \gg P_{vr} > P_{vt}$. Consequently, the majority of the energy exchange between the mean flow and the turbulence field occurs through the axial component of the Reynolds normal stress. The radial and tangential components, on the other hand, must receive their kinetic energy from other sources such as pressure-velocity interactions or momentum transport by turbulent velocity fluctuations. Therefore, the relative ordering of the Reynolds normal stresses ($\sigma_u^2 > \sigma_{vr}^2 > \sigma_{vt}^2$) is consistent with the amount of turbulence production that each component receives from the mean flow.

Summary and Conclusions

The turbulent near-wake of a circular cylinder aligned with a supersonic flow has been investigated using non-intrusive measurement techniques. The main objective of these experiments is to increase the understanding of the complex fluid dynamic phenomena that occur in supersonic base flowfields by the use of detailed quantitative data gathered throughout the near-wake. Specifically, afterbody and base pressure distributions, mean velocities, turbulence intensities, and Reynolds shear stresses have been obtained; these data have been tabularized on a floppy disk which is available from the authors. As a result of data analysis, the following conclusions concerning the near-wake flowfield can be made:

(1) The mean static pressure profile across the base is relatively uniform with an average base pressure coefficient of -0.102.

(2) The maximum reverse velocity along the wake centerline reached 27% of the mean approach velocity, or Mach 0.48, and occurs approximately 57% of the distance from the base to the reattachment point (located at $x/R = 2.65$). Along the centerline, the axial and radial turbulence intensities peak near the reattachment point and decay as the wake develops downstream.

(3) The recirculating flow is generally characterized by small mean velocity gradients and relatively uniform turbulence intensities.

(4) The separated shear layer is found to contain steep radial velocity gradients and sharp peaks in turbulence intensity in the subsonic region. Beyond reattachment, the sharp peaks decay toward nearly uniform turbulence intensities across the redeveloping wake.

(5) Peak values of turbulent kinetic energy and axial-radial shear stress are located in the subsonic region of the shear layer upstream of reattachment. This is in contrast to earlier results on compressible shear layer reattachment onto a solid surface which indicate peak levels at or downstream of the reattachment point. The production of turbulent kinetic energy peaks immediately downstream of separation along the inner edge of the shear layer.

6

References

[1] Rollstin, L., "Measurement of Inflight Base Pressure on an Artillery-Fired Projectile," AIAA Paper 87-2427, 1987.

[2] Delery, J., and Wagner, B., "Results of Garteur Action Group AG09 on Flow Past Missile Afterbodies," *Proceedings of the AGARD/FDP Symposium on Missile Aerodynamics*, Friedrichshafen, Germany, 1990.

[3] Peace, A.J., "Turbulent Flow Predictions for Afterbody/Nozzle Geometries Including Base Effects," *Journal of Propulsion and Power*, Vol. 7, No. 3, 1991, pp. 396-403.

[4] Sahu, J., "Supersonic Flow Over Cylindrical Afterbodies with Base Bleed," AIAA Paper 86-0487, 1986.

[5] Wilmoth, R.G., and Putnam, L.E., "Subsonic/Transonic Prediction Capabilities for Nozzle/Afterbody Configurations," AIAA Paper 84-0192, 1984.

[6] Korst, H.H., "A Theory for Base Pressures in Transonic and Supersonic Flow," *Journal of Applied Mechanics*, Vol. 23, No. 4, 1956, pp. 593-600.

[7] Zumwalt, G.W., "Analytical and Experimental Study of Axially-Symmetric Supersonic Base Pressure Problem," Ph.D. Thesis, Department of Mechanical Engineering, University of Illinois at Urbana-Champaign, 1959.

[8] Reid, J., and Hastings, R.C., "Experiments on the Axi-Symmetric Flow Over Afterbodies and Bases at M=2.0," Royal Aircraft Establishment, R.A.E. Report Aero. 2628, Farnborough, England, 1959.

[9] Badrinarayanan, M.A., "An Experimental Investigation of Base Flows at Supersonic Speeds," *Journal of the Royal Aeronautical Society*, Vol. 65, July 1961, pp. 475-482.

[10] Demetriades, A., "Mean-Flow Measurements in an Axisymmetric Compressible Wake," *AIAA Journal*, Vol. 6, No. 3, 1968, pp. 432-439.

[11] Hawkins, R., and Trevett, E., "Changes in the Flow at the Base of a Bluff Body Due to a Disturbance in its Wake," AGARD Report 539, 1966.

[12] Gaviglio, J., Dussauge, J.P., Debieve, J.F., and Favre, A., "Behavior of a Turbulent Flow Strongly Out of Equilibrium at Supersonic Speeds," *Physics of Fluids*, Vol. 20, No. 10, 1977, pp. 179-192.

[13] Neale, D.H., Hubbartt, J.E., Strahle, W.C., and Wilson, W.W., "Effects of External Compression on an Axisymmetric Turbulent Near Wake," *AIAA Journal*, Vol. 16, No. 9, 1978, pp. 940-947.

[14] Delery, J., "ONERA Research on Afterbody Viscid/Inviscid Interaction with Special Emphasis on Base Flows," *Proceedings of the Symposium on Rocket/Plume Fluid Dynamic Interactions*, University of Texas at Austin, 1983.

[15] Amatucci, V.A., Dutton, J.C., Kuntz, D.W., and Addy, A.L., "Two-Stream, Supersonic, Wake Flowfield Behind a Thick Base, Part I: General Features," *AIAA Journal*, Vol. 30, No. 8, 1992, pp. 2039-2046.

[16] Heltsley, F.L., Walker, B.J., and Nichols, R.H., "Transonic Nozzle-Afterbody Flow Field Measurements Using a Laser Doppler Velocimeter," AGARD CP-348, 1983.

[17] Bloomberg, J.E., "An Investigation of Particle Dynamics Effects Related to LDV Measurements in Compressible Flows," M.S. Thesis, Department of Mechanical and Industrial Engineering, University of Illinois at Urbana-Champaign, 1989.

[18] Samimy, M., and Lele, S.K., "Motion of Particles with Inertia in a Compressible Free Shear Layer," *Physics of Fluids - A*, Vol. 3, No. 8, 1991, pp. 1915-1923.

[19] Herrin, J.L., and Dutton, J.C., "An Investigation of LDV Velocity Bias Correction Techniques for High-Speed Separated Flows," *Experiments in Fluids*, to be published, 1993.

[20] Sun, C.C., and Childs, M.E., "A Modified Wall Wake Velocity Profile for Turbulent Compressible Boundary Layers," *Journal of Aircraft*, Vol. 10, No. 6, 1973, pp. 381-383.

[21] Fernholz, H.H., and Finley, P.J., "A Critical Commentary on Mean Flow Data for Two-Dimensional Compressible Turbulent Boundary Layers," AGARDograph No. 253, 1980.

[22] Kays, W.M., and Crawford, M.E., "The Turbulent Boundary Layer for a Gas with Variable Properties," *Convective Heat and Mass Transfer*, 2nd ed., McGraw-Hill, New York, 1980, pp. 305-309.

[23] Merz, R.A., Page, R.H., and Przirembel, C.E.G., "Subsonic Axisymmetric Near-Wake Studies," *AIAA Journal*, Vol. 16, No. 7, 1978, pp. 656-662.

[24] Gruber, M.R., Messersmith, N.L., and Dutton, J.C., "The Three-Dimensional Velocity Field in a Compressible Mixing Layer," *AIAA Journal*, to be published, 1993.

[25] Bell, J.H., and Mehta, R.D., "Interaction of a Streamwise Vortex with a Turbulent Mixing Layer," *Physics of Fluids*, Vol. 2, No. 11, 1990, pp. 2011-2023.

[26] Abu-Hijleh, B., and Samimy, M., "An Experimental Study of a Reattaching Supersonic Shear Layer," AIAA Paper 89-1801, 1989.
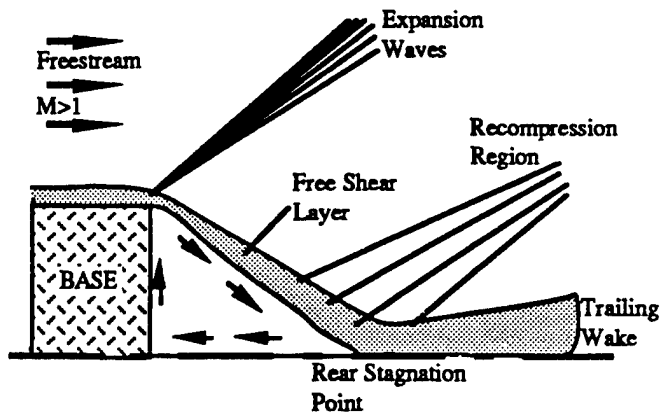
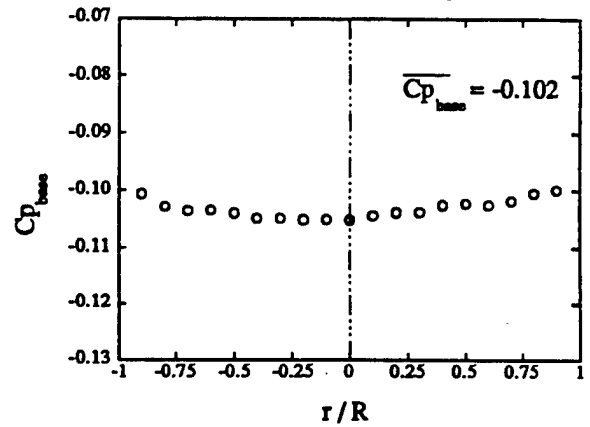7

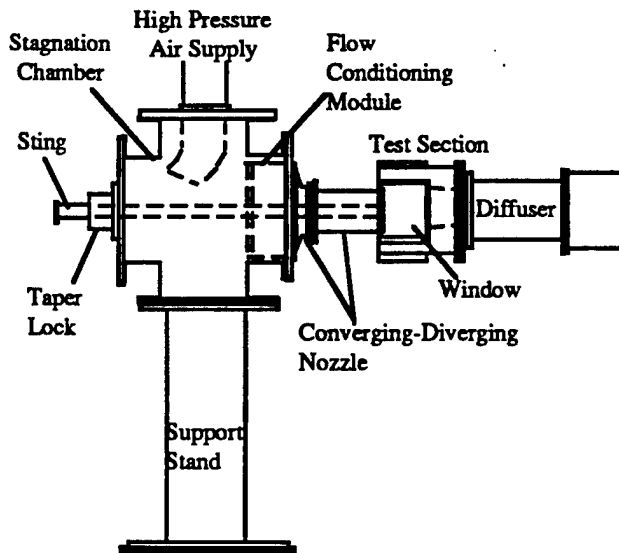Fig. 1   Supersonic, Axisymmetric Base Flow Schematic

Fig. 2   Schematic Diagram of Axisymmetric Wind Tunnel

$$\overline{Cp_{base}} = -0.102$$

Fig. 3   Base Pressure Profile

$\delta = 3.2$ mm
$\delta^* = 0.96$ mm
$\theta = 0.26$ mm
$H = 3.72$
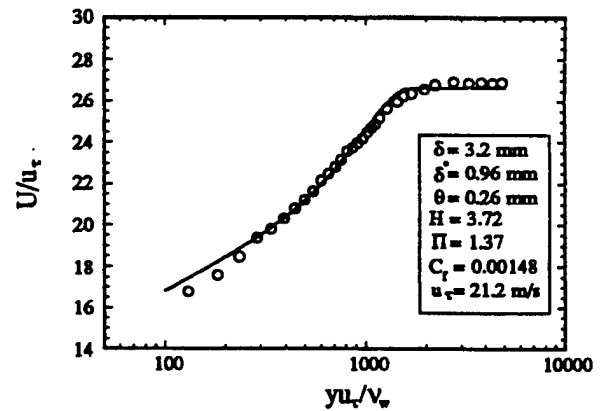$\Pi = 1.37$
$C_f = 0.00148$
$u_\tau = 21.2$ m/s

Fig. 4   Sun and Childs[20] Curve Fit of Afterbody Boundary Layer Upstream of Base Corner
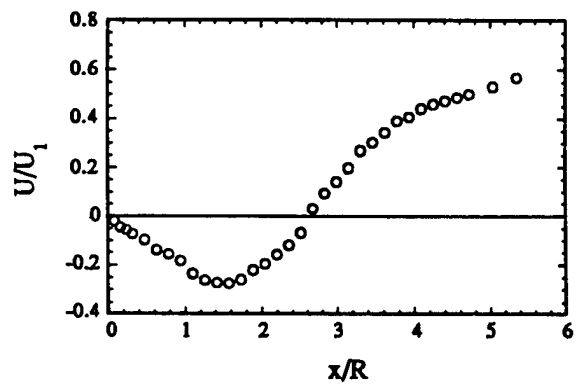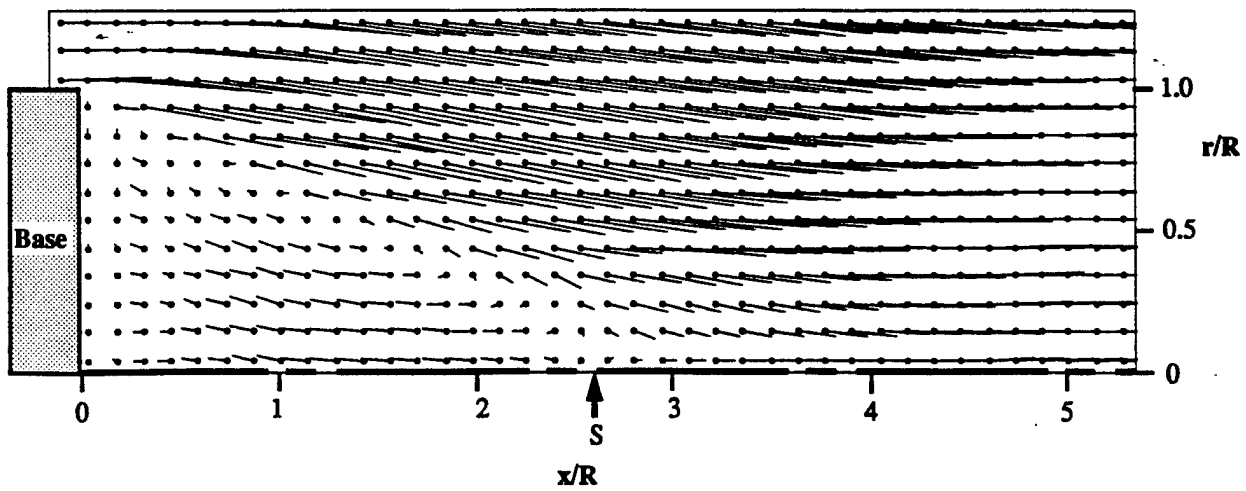

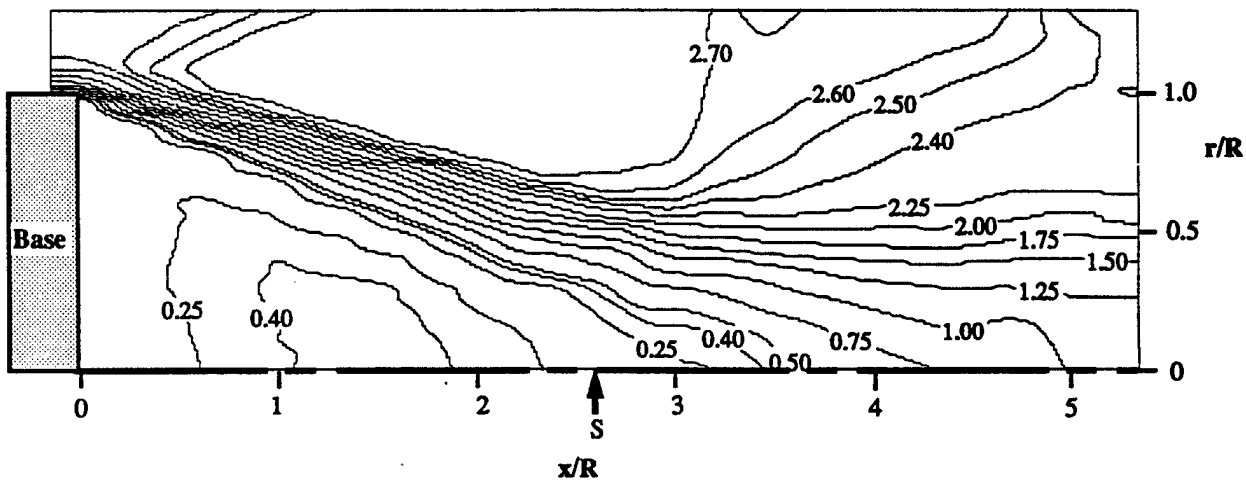Fig. 5   Mean Axial Velocity Along Model Centerline

Fig. 6   Mean Velocity Vector Field Throughout Near-Wake

Fig. 7   Mach Number Contours

Fig. 8   Mean Radial Velocity Contours - V_r / U_1
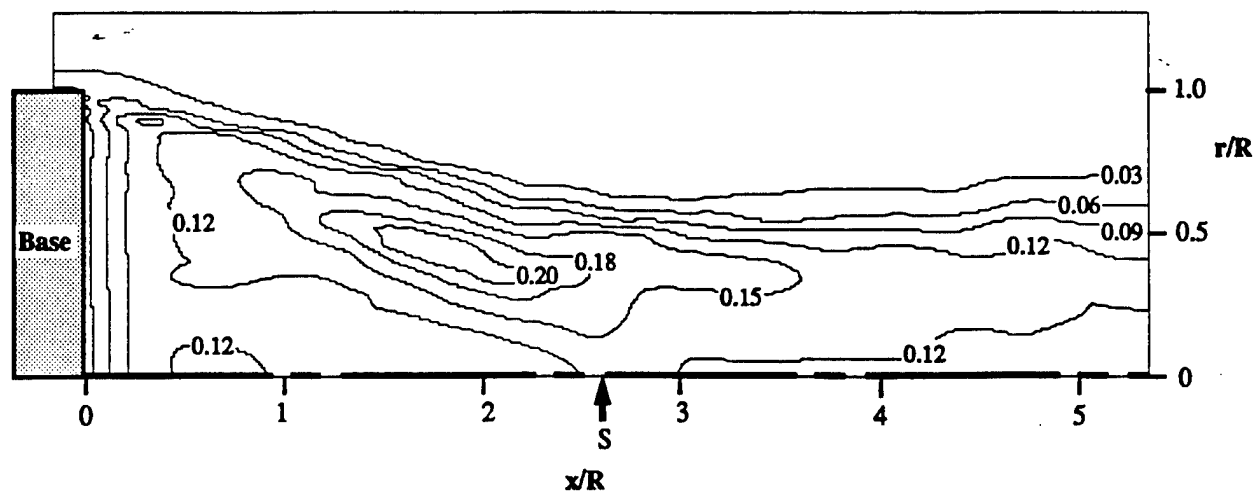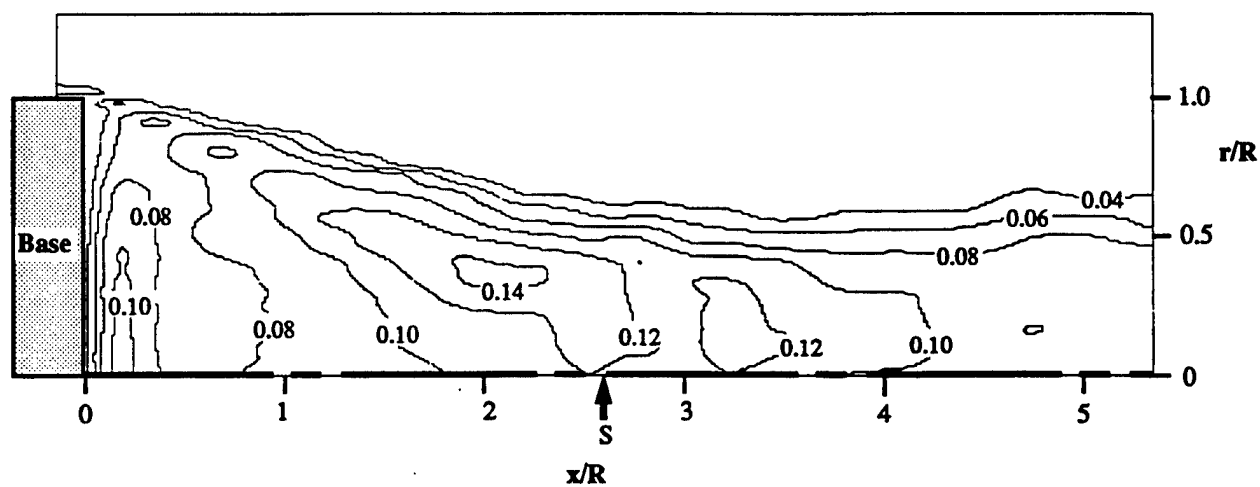
9

Fig. 9   Axial Turbulence Intensity Contours - σ_u / U_1

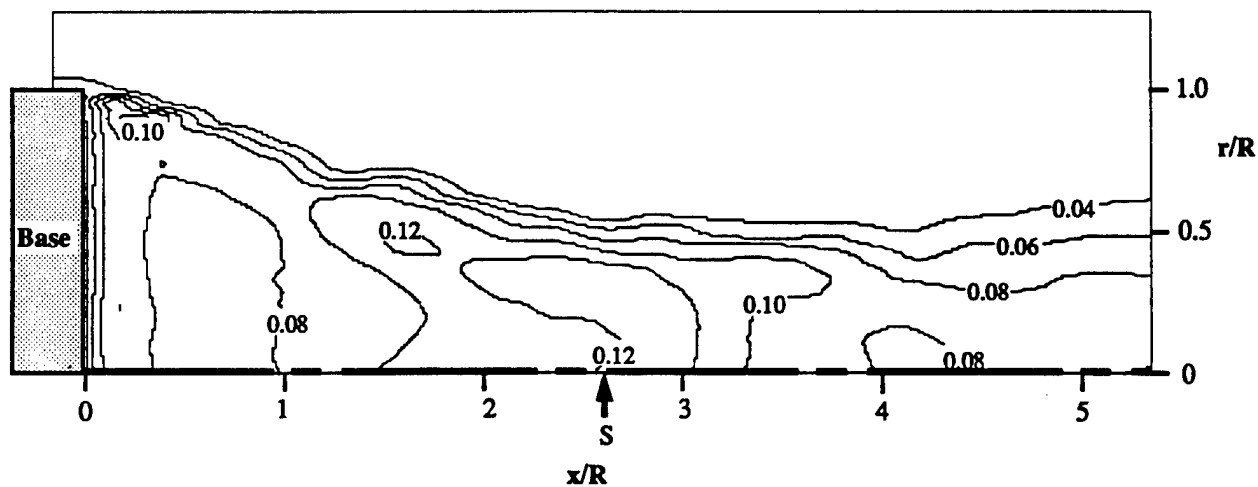Fig. 10   Radial Turbulence Intensity Contours - σ_{V_r} / U_1

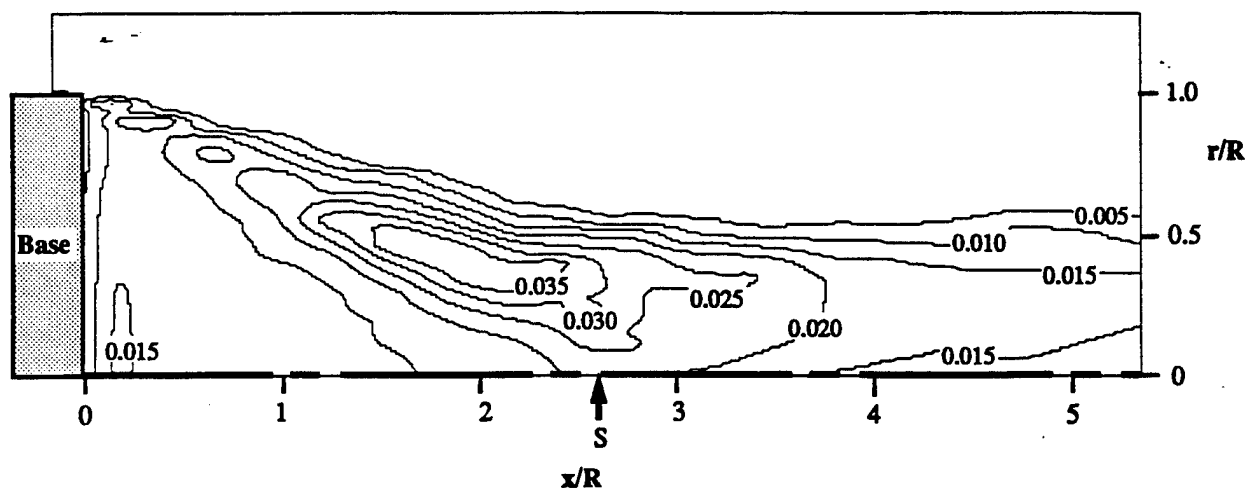Fig. 11   Tangential Turbulence Intensity Contours - σ_{V_t} / U_1

10

Fig. 12   Turbulent Kinetic Energy Contours - k / U_1^2
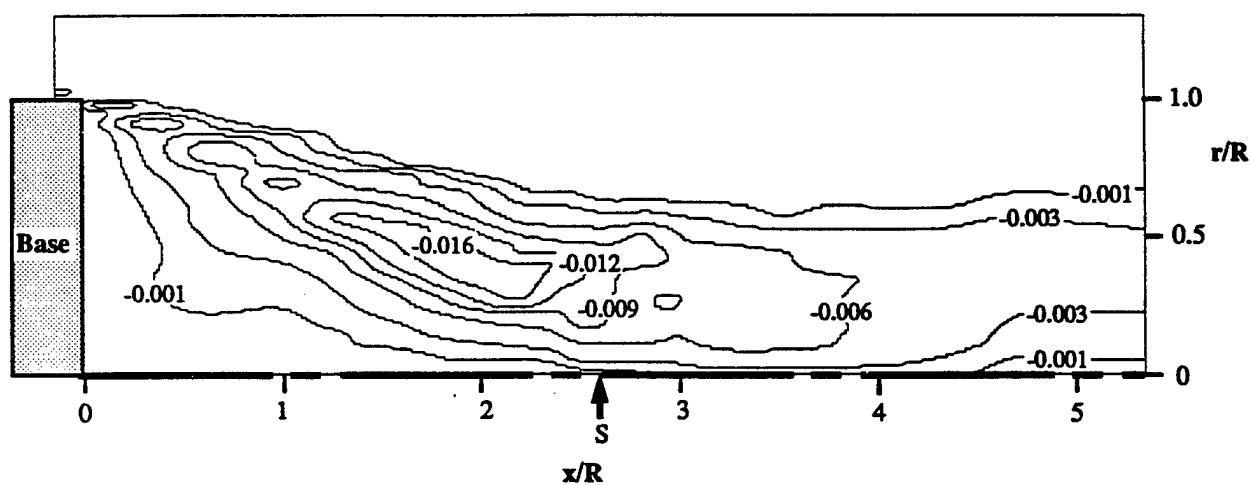

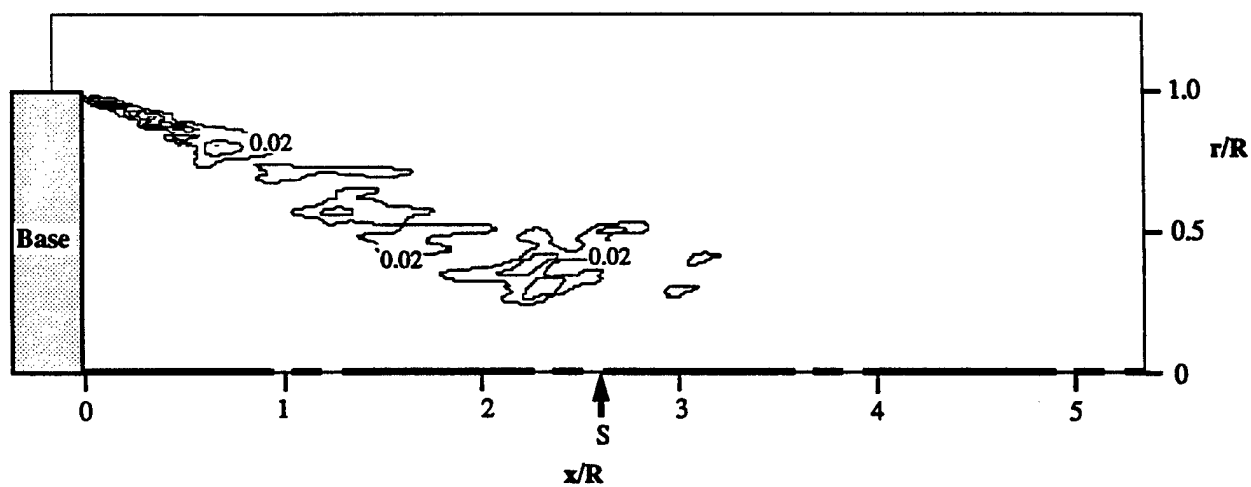Fig. 13   Reynolds Shear Stress Contours - $<u'v_r'> / U_1^2$

Fig. 14   Turbulence Production Contours - $P_k \cdot R / U_1^3$

11

APPENDIX A.14

STUDY OF THE NEAR-WAKE STRUCTURE OF A SUBSONIC BASE CAVITY FLOWFIELD USING PIV

AIAA Paper No. 93-3040

Presented at the *24th AIAA Fluid Dynamics Conference*

Orlando, Florida

July 1993

by

M. J. Molezzi and J. C. Dutton

AIAA 93-3040
Study of the Near-Wake Structure of a Subsonic Base Cavity Flowfield Using PIV

M. J. Molezzi and J. C. Dutton
Dept. of Mechanical & Industrial Engineering
University of Illinois at Urbana-Champaign
Urbana, IL

AIAA 24th
Fluid Dynamics Conference
July 6-9, 1993 / Orlando, FL

STUDY OF THE NEAR-WAKE STRUCTURE OF A
SUBSONIC BASE CAVITY FLOWFIELD USING PIV

M. J. Molezzi[*] and J. C. Dutton[**]
Department of Mechanical and Industrial Engineering
University of Illinois at Urbana-Champaign
Urbana, IL 61801

Abstract

A new particle image velocimetry (PIV) system has been used to study the near-wake structure of a two-dimensional base in subsonic flow in order to determine the fluid dynamic mechanisms of observed base drag reduction in the presence of a base cavity. Experiments were done over a range of freestream Mach numbers up to 0.8, including local flowfield velocities over 300 m/s. Effects of the base cavity on the von Kármán vortex street wake were found to be related to the expansion and diffusion of vortices near the cavity, although the effects are of small magnitude and no significant change in the vortex formation location or path was observed. The base cavity effects are also less significant at higher freestream velocities due to the formation of vortices further downstream from the base. The base cavity drag reduction was found to be mainly due to the displacement of the base surface to a location upstream of the low-pressure wake vortices, with only a slight modification in the vortex street itself.

Introduction

The separated flow past a two-dimensional body at subsonic speed and large Reynolds number forms a wake structure made up of alternately shed vortices known as the von Kármán vortex street. This commonly occurring structure has been the subject of numerous studies beginning with von Kármán's first theoretical analysis of vortex streets[1]. A significant feature of this flowfield is the interaction of the low pressure vortices in the near-wake with the downstream surface or base of the body, inducing a net streamwise pressure force on the body known as base drag. The base drag is typically a significant component of total drag, even for slender bodies with a finite thickness base. For this reason, drag reduction methods based on the modification of the vortex street have received much attention.

One effective drag reduction method is the use of a base cavity, which is the subject of this study. It has been shown experimentally that the presence of a solid-walled cavity in the base of a slender two-dimensional body (see Fig. 1) increases the base pressure, resulting in base drag reduction of up to 30%[2-5]. Other effects of a base cavity that have been experimentally observed include an increase in vortex shedding frequency or Strouhal number as compared to a blunt base[4,5] and limited base drag reduction for a cavity depth beyond approximately half the base height.

The mechanism of drag reduction due to base cavities is as yet unclear, although several theories have been proposed, all of which imply some modification of vortex formation location and reduction in vortex strength. The earliest published base cavity experiments were done by Nash et al.[2] They proposed that, although a vortex or eddy may not be completely trapped by the cavity, the cavity does have a stabilizing effect on standing eddies near the base, implying that the vortices form at least partially within the cavity where they are affected by the cavity walls. Pollock[3] performed experiments based on theoretical work by Ringleb[6] who suggested that a stable vortex may be trapped in a cavity, causing the wake to revert to a steady flow. Pollock used a special asymmetric cusp-shaped cavity which showed no advantage in drag reduction over a rectangular cavity, in effect disproving Ringleb's theory. In a study of resonance effects on vortex shedding, Wood[7] showed that resonance of the base at the vortex shedding frequency causes vortex formation within the cavity, while formation normally occurs outside the cavity. He concluded that the drag reduction observed for base cavities must be due to some resonance or vibration in the flowfield, moving the vortices into the cavity where the solid walls restrict vortex growth and inhibit the strength of successive vortices.

A study of axisymmetric base cavities by Compton[8] suggested that recirculation within the cavity forms a co-flowing stream at the cavity edge which interacts with the separated freestream, reducing the vorticity of the separated shear layer. In a subsequent

---

*   Currently employed at General Electric CR&D, P.O. Box 8, K1-ESB-121, Schenectady, NY 12301.
    Member AIAA.
** Professor. Associate Fellow AIAA.

1

study of axisymmetric base cavities, Morel[9] suggested that the co-flowing stream could be an important effect in two-dimensional geometries as well. More recently, Kruiswyk and Dutton[4] used a combination of pressure measurements and flow visualization techniques to conclude that, although vortex motion does not extend into the cavity, oscillating air flow at the cavity boundary increases fluid mixing in the near-wake, thereby reducing vortex strength. Their results concerning the change in base pressure and vortex shedding frequency due to a base cavity are shown in Table 1. The base cavity configuration was a rectangular cavity with a streamwise depth equal to half the base height. A base cavity with a depth of one full base height was also used, but the results were similar to the half base height cavity. The experimental conditions used in the present study match those used by Kruiswyk and Dutton[4] to facilitate comparison of data. The results in Table 1 show an increase of 10 to 14% in the base pressure coefficient which is non-dimensionalized by reference conditions in the flow just prior to separation near the downstream edge of the base. The relative increase in the Strouhal number (vortex shedding frequency) is less, although still significant. Another evident feature is that both effects are largest at the lowest freestream Mach number.

Two notable computational simulations of two-dimensional base cavity flows have also been done. Rudy[10] obtained laminar finite difference Navier-Stokes solutions using base configurations and freestream Mach numbers of 0.4 and 0.6 that matched those of Kruiswyk and Dutton[4], although Rudy's simulations used freestream Reynolds numbers (based on base height) of 700 and 962 (significantly lower than the experimental values). Clements and Maull[5] used an inviscid discrete vortex method for simulations of their experimental results. Rudy's results more accurately predicted the experimentally measured base pressure increase due to a cavity, but both simulations showed vortex formation within the cavity and a *decrease* in shedding frequency due to the cavity, which disagrees with experimental results. Rudy concluded that the observed increase in base pressure with a cavity was mainly due to the physical displacement of the base surface away from the low pressure vortices.

The work presented here will take advantage of both the new results available from PIV and the extensive experimental and computational data available from Kruiswyk and Dutton[4] and Rudy[10], respectively. The ability to directly compare results from several techniques for similar base geometries and flow conditions will allow a thorough analysis of the effects of a base cavity on the structure and properties of the

flowfield, leading to a better understanding of the mechanisms of drag reduction.

Equipment

Test Section

Experiments for this study were performed in a previously fabricated transonic wind tunnel (Fig. 2) based on a design described by Little and Cubbage[11]. The tunnel has a 4" x 4" (101.6 mm x 101.6 mm) test section with solid side walls and slotted upper and lower inner walls to relieve the blockage effect of models in the subsonic to transonic speed range. Six-inch diameter round windows are mounted in both sidewalls to allow visualization of the downstream end and near-wake of a base model. The tunnel is a blowdown type supplied with compressed dry air from a 140 m^3 tank farm at 120 psia. The base model (Fig. 3) consists of an interchangeable afterbody mounted on a wedge-shaped forebody. Trip wires are mounted on the top and bottom surfaces near the upstream edge to assure an equilibrium turbulent boundary layer at separation. When mounted in the test section, the upstream edge is located approximately 17" (432 mm) downstream of the wind tunnel entrance with approximately 0.75" (19 mm) of the downstream end of the model visible through the side windows. The afterbodies used are a blunt base and a rectangular base cavity with a depth of half the base height. The wind tunnel and base models are the same as those used by Kruiswyk and Dutton[4].

Modifications have been made to the original wind tunnel for the flow seeding and optical access necessary for this study. Slot-shaped upper and lower windows have been fabricated and installed in the outer tunnel walls for access with a vertically propagating planar laser sheet. The sheet passes through the lower window and through one of the streamwise slots of the inner wall to enter the test section. The arrangement of the wall slots requires the position of the sheet to be 10 mm off the tunnel centerline in the spanwise direction, but surface flow visualization on the base model[4] and laser Doppler velocimetry (LDV) data in the near-wake[12] indicate no significant variation of the flow from centerline conditions. Delivery of silicone oil seed for PIV is done by two TSI six-jet atomizers feeding a single 3/4" O.D. tube that enters the stagnation chamber. Flow from the stagnation chamber passes through a pair of screens (44 x 44 mesh screen with 57% open area) and enters an enclosure at the nozzle entrance to reduce turbulence. The silicone oil seed is then injected by a manifold tube with a series of holes directed downstream and oriented in a transverse (vertical) plane aligned with the illuminating laser sheet. The flow then passes through a 2" long section

of honeycomb with a 3/16" cell diameter to further reduce turbulent fluctuations. The seed injection is done downstream of the screens due to experience with LDV indicating that silicone oil droplets tend to build up on screens, causing large drops to form and burst off which bias velocity measurements. LDV data from the final tunnel configuration indicate tunnel-empty turbulence intensities of less than 1% at the freestream conditions used in this study.

PIV System

To meet the objectives set forth for this study, data were obtained with a non-intrusive velocity measurement technique called particle image velocimetry (PIV). PIV is performed by illuminating a seeded flowfield with a planar laser sheet that is pulsed at a known time interval, forming two or more sequential images of each seed particle within the light sheet (Fig. 4). The particle images are captured on film or another medium, then the local image separations and, therefore, velocities can be determined for the entire plane. Unlike pointwise techniques such as LDV, which provides statistical velocity data on a point-by-point basis, PIV can quantitatively identify instantaneous flow structures that may be random in nature but important to the overall behavior of the flow. PIV also reveals planar views of three-dimensional flow structures that are smeared by volume integration inherent in techniques such as schlieren photography. A detailed discussion of the design, development, and validation of the PIV system used in this study can be found in References 12 and 13; therefore, only a brief discussion is given below.

The acquisition system refers to the equipment used to obtain raw particle images from the test section flowfield (see Fig. 5). This system captures double images of each particle within the illuminated laser sheet by using two Continuum YG681C-10 Nd:YAG lasers equipped with frequency doubling crystals to provide a maximum output energy of 550 mJ/pulse at a wavelength of 532 nm (green light) with a pulsewidth of 4-6 ns. High-resolution black-and-white films are very sensitive to green wavelengths and the high visibility of the green light also simplifies alignment of the two beams which is a critical factor in obtaining double images of particles in the flow. Two separate lasers are required since a single laser cannot generate two distinct, equal energy pulses in the short time interval required for high-speed flows (typically less than 1 μs). The horizontally and vertically polarized beams of the two lasers are combined by a polarized beam splitter, then shaped by spherical and cylindrical lenses to form a planar beam profile. Beam thickness and width at the test section can be controlled by adjustment of the beam shaping optics. The current study used a beam thickness of 1.2 mm and width of 64 mm at the test section.

The photographic recording of particle images is done by a 35 mm camera mounted on the same optical table as the lasers and beam shaping optics. This allows maintenance of the relative position of all optical components for consistent alignment and focus. This table is also mounted on vibration-isolated supports to avoid the effects of laboratory vibrations. The camera has a flat field 100 mm macro lens with auto film wind and an electronic shutter for automated operation. Other features of the acquisition system include automated operation of the lasers, camera, and test section seeding by means of an Apple Macintosh II computer.

Derivation of velocity at each location in the flowfield is done through a digital analysis of the PIV photograph in a spot by spot fashion in an automated process performed by an interrogation system. The analysis technique used in the present PIV system is called the "autocorrelation method". Each velocity vector is determined from a small region of the flowfield photograph containing multiple particle image pairs, called an interrogation spot. Each spot is illuminated, magnified, and viewed by a video camera. The video image is then digitized into a two-dimensional array and passed to an array processor on a host computer. Two FFTs and other array operations are then performed to obtain the two-dimensional autocorrelation function of the original spot. The distance from the origin to a peak in the autocorrelation function corresponds to the separation distance of particle image pairs in the original spot, which in turn is proportional to the local particle velocity. The array processor uses a centroidal peak-finding routine to locate the three highest peaks in the autocorrelation array. Multiple peaks are found since the peak due to actual particle velocity is sometimes not the highest, but can be determined by later comparison of results with neighboring velocity data. The three peak locations are stored and the process is repeated for the next spot.

The size of the spot used for each individual velocity vector determines the spatial resolution, i.e., the in-plane dimensions of the effective probe volume. The data shown here were obtained using a uniform spot size of 1 mm x 1 mm in the frame of reference of the test section. The probe volume is therefore 1 mm by 1 mm (spot size) by 1.2 mm (laser sheet thickness) or 1.2 mm^3. Velocity vectors were found on a grid with an increment of 0.5 mm in each direction (overlapping spots) to prevent biasing due to small scale motions in the flowfield.

3

Validation experiments have been performed with this PIV system using both simulations and high-speed flow experiments, indicating a maximum total error in raw PIV velocity measurements of less than 3%[12]. Random error makes up a significant portion of the total, and is reduced by post-processing operations performed on the data as described in the following section.

Results and Discussion

Experimental Conditions

Experiments were initially performed with two base configurations at three freestream velocity conditions, resulting in six cases. Flow conditions for each case were determined by running the test section without the base model. The test section flow velocity was measured as a function of wind tunnel stagnation pressure, allowing the appropriate stagnation pressure to be determined for each desired freestream velocity condition. This stagnation pressure was maintained for the corresponding experiments with the base model. A summary of the flow conditions and base configurations used in this study is shown in Table 2, including the freestream Reynolds number based on freestream velocity and base height and shorthand notations for each case. As mentioned previously, these cases match those used by Kruiswyk and Dutton[4] and the Mach 0.4 and 0.6 freestream conditions used by Rudy[10] with similar base configurations.

As expected from inviscid flow theory, the measured velocity just outside the boundary layer at the downstream edge of the base (reference Mach number in Table 2) is greater than the associated freestream velocity due to local compression of streamlines near the body. The mean measured reference Mach numbers for each case were found to match the reference Mach numbers quoted by Kruiswyk and Dutton[4] for the associated freestream conditions. The velocity data from individual flowfield realizations showed some variation from the desired reference velocities (maximum 9%) due to the lack of tunnel control valve resolution at the small stagnation pressures required and due to changes in the stagnation temperature of the supply air from run to run. A simple scaling factor was therefore applied to the velocity data from each flowfield realization to account for these variations.

Fifteen flowfield realizations were obtained for each of the Mach 0.4 and Mach 0.6 cases listed. Realizations were also obtained for each of the Mach 0.8 cases, but difficulties with seeding density in the vortex street prevents the use of those cases in the quantitative analysis presented here[12]. Each individual realization consists of an array of 6831 (99 x 69) instantaneous velocity vectors with 0.5 mm spacing in both the streamwise and transverse directions. By defining the coordinate system as positive x in the streamwise direction and positive y in the transverse direction with the origin at the center of the downstream base edge, each realization covers the wake from x = 1 mm to 50 mm and from y = -17 mm to 17 mm. This region extends 3.3 base heights downstream of the aft edge of the base.

Individual Flowfield Realizations

An example raw velocity vector plot from a single Mach 0.6 blunt base (M6b) realization is shown in Fig. 6. As noted in the figure, only every other vector from the actual data set is plotted for the sake of clarity. The raw PIV data shown have a limited number of invalid vectors which have been removed. This is necessary in the application of PIV since photographic imperfections, lack of particle images at a particular location, and other random factors cause a small percentage of invalid measurements which must be corrected during processing. This is done automatically in software which scans the raw velocity field and uses an algorithm requiring satisfaction of both absolute velocity limits and velocity gradient limits in the flowfield for acceptance of data. The raw velocity realizations used in this study had anywhere from 92% to 98% valid data which is comparable to reported PIV data validation rates in the literature. The missing data are then filled in from neighboring data by a two-dimensional linear interpolation method[14]. Finally, the vector field is smoothed by convolution with a Gaussian kernel[14] to eliminate random noise caused by image imperfections, video noise, and other factors. The kernel convolution is the analog of a low-pass digital filter, only in two dimensions. The resulting smoothed velocity vector field corresponding to Fig. 6 is shown in Fig. 7. This step is crucial when spatial differentiation is to be performed on the vector field to derive quantities such as vorticity, since any high frequency random error will be accentuated by differentiation.

In order to analyze vortex location and strength, the out-of-plane vorticity

$$\omega_z = \left(\frac{\partial v}{\partial x} - \frac{\partial u}{\partial y} \right)$$

was computed for each flowfield realization. This was done by central differencing of the original velocity data. A color plot of vorticity with overlaid velocity vectors corresponding to Figs. 6 and 7 is shown in Fig. 8. These data present a new capability for quantitatively analyzing separated compressible flow structure which has to this point been impossible. One of the notable features in Fig. 8, which holds for all realizations at all experimental conditions, is the significant

4

fragmentation of the vortices as they shed from the separated shear layers at the aft edge of the base. This is indicative of the high level of boundary layer turbulence prior to separation and its effect on the turbulent structure of the wake. This is confirmed by boundary layer turbulence intensity measurements of up to 5% using LDV[12], and fast response pressure measurements made in the wake by Kruiswyk and Dutton[4] which showed a broad range of spectral density peaks along with the strongest peak at the vortex shedding frequency, indicating the superposition of the vortex street on a random turbulent flowfield. Turbulence energy is therefore transferred in the wake from the large scale vortices to smaller scales, causing the gradual breakdown of distinct vortices as they travel downstream.

Vorticity Statistics

As mentioned earlier, previous theories regarding the mechanism of base cavity drag reduction all hinge on some modification of vortex strength and/or position. For this reason, it is desirable to use the vorticity data now available to examine vortex path and strength, both with and without base cavities. Due to the turbulent nature of the flowfield and the resulting vortex fragmentation discussed previously, it is rather difficult to select a particular location for each vortex in an instantaneous realization. Therefore, a statistical method was adopted to estimate vortex path and strength. Due to the alternate shedding of the wake vortices, successive vortices have peak vorticity values, ω_z, of alternating sign, causing the mean vorticity to go to zero where the opposing vortex paths overlap. Since only the vorticity magnitude is necessary for the determination of vortex strength and path, it was decided to derive the root mean square (RMS) vorticity for each experimental case, which is defined at each flowfield location (x, y) by

$$\omega_{RMS}(x,y) = \left[\frac{\sum\limits_{i=1}^{N} \left[\omega_z(x,y)\right]_i^2}{N} \right]^{\frac{1}{2}}$$

where the index i represents each individual realization for the experimental case of interest and N is the total number of realizations, or 15.

The results for the M4b, M4c, M6b, and M6c cases are shown in Fig. 9. These plots show the region within approximately one base height of the aft edge to concentrate on the notable features. Although some data scatter is present due to the turbulence level and limited ensemble size, these plots do reveal useful

information about cavity effects. One of the first noticeable features is the presence of the free shear layers at each separation point and their extension into the wake. At a point less than half of a base height downstream, they rapidly lose strength, indicating the mean location at which free vortices break off into the wake, or the vortex formation location. Lines have been included on the plots to identify the mean shear layer location, shape, and length. Each line was determined by a curve fit to the peak vorticity values in the shear layer, with the line terminating at the point where the vorticity drops below 67% of the maximum scale, or 67,000 s^{-1} for the M4b and M4c cases, and 100,000 s^{-1} for the M6b and M6c cases. This allows a relative comparison of the shear layer lengths between all four cases.

Table 3 shows the average shear layer length and the transverse separation distance of the shear layer endpoints for each case shown in Fig. 9. Although the average shear layer length is 0.6 mm shorter for the M6c case than the M6b case, the difference of 0.1 mm is not significant for the Mach 0.4 cases. The asymmetry in the shear layers propagating from the upper and lower base corners for a given case also prevents drawing any firm conclusion of a change in vortex formation location due to the cavity, although wake static pressure data were used by Kruiswyk and Dutton[4] to conclude that vortex formation occurs further downstream due to the cavity for a Mach 0.4 freestream velocity.

Figure 9 does, however, reveal that the angle of convergence of the shear layers toward the transverse centerline appears steeper for the base cavity cases than for the blunt base. There may also be a slight increase in shear layer curvature, although it is difficult to determine conclusively. Increased shear layer curvature would indicate a larger pressure gradient across the shear layer, which would, in turn, imply that the cavity causes lower mean static pressure in the region just inside the shear layer and just past the separation point. However, this must be only a *local* effect confined near the shear layer, since the cavity has been shown in previous research to *increase* the mean pressure at the base surface, which is upstream of the shear layers inside the cavity.

Convergence of the shear layers causes the transverse separation distance between the two shear layers to be reduced at their endpoints (see Table 3), explaining the increase in shedding frequency observed by Kruiswyk and Dutton[4] for the base cavity (see Table 1). As stated by Fage and Johansen[15], the shedding frequency in a vortex street is inversely proportional to the separation distance of the shear layers in the wake. When the shear layer separation is reduced in the base

cavity wake due to convergence, it follows that the shedding frequency increases.

In examining the vortex path just downstream of the shear layers, reduced vortex strength due to the base cavity can be seen in Fig. 9 for both freestream Mach numbers. In an effort to quantify this result, the spatially averaged RMS vorticity was calculated for each case in Fig. 9 over a region extending between the two shear layer endpoints (in the transverse direction) and extending from the longest shear layer endpoint to 7.5 mm downstream of that endpoint (in the streamwise direction). This region was chosen to uniformly cover the initial vortex path for each case. The results are shown in Table 4. Although the data scatter in Fig. 9 makes small differences difficult to determine visually, the data in Table 4 show that the average RMS vorticity level is indeed reduced by the cavity for both freestream Mach numbers, implying a small decrease in vortex strength.

Finally, any effect of the base cavity on mean vortex path is not clear from Fig. 9, although it is evident that turbulence causes the vortex path to be somewhat random, since the RMS vorticity magnitude peaks are widely scattered in the wake for all cases.

The effects of increasing Mach number on the shear layers include a small increase in shear layer separation (see Table 3) which seems to be caused by a reduction in both the initial convergence angle and the curvature of the shear layers, and can be attributed to increased streamwise momentum in the fluid stream outside the wake. The shear layers are also extended by approximately 1 mm for the Mach 0.6 freestream cases versus Mach 0.4, causing the vortex formation to occur further downstream of the base edge. However, any change in vortex path downstream of the shear layers due to the increase in freestream velocity is not evident from these data. Displacement of the vortex formation location further downstream of the base would serve to explain the reduced effectiveness of the cavity at higher Mach number as shown by Kruiswyk and Dutton[4] (see Table 1). As the vortices form further away from the base at higher Mach number, their effect on the pressure at the base surface is reduced, causing any modification of the vortex street due to the cavity to have less relative effect on the base pressure.

Instantaneous Wake Structure

Further information on base cavity wake effects can be obtained by comparing the instantaneous wake structure for the blunt base and base cavity at a similar point in the vortex shedding cycle. For each freestream velocity condition, realizations were selected from the two base configurations with closely matching vortex locations in the near-wake. Velocity vector plots for

the best match from the M4b and M4c cases are shown in Fig. 10, with plots from the M6b and M6c cases shown in Fig. 11. As in Figs. 6-8, these velocity vector plots show only every other vector in each direction for the sake of clarity. It is evident from Figs. 10 and 11 that for each pair of realizations, the center stagnation point of the first vortex downstream of the base matches to within 1 mm in each direction.

Each of these realizations, along with others not shown here, indicates that the circulating region around a fully formed vortex entering the wake covers most of the base height, which is confirmed by the results of Kruiswyk and Dutton[4]. However, in both Figs. 10 and 11, a significant difference in the vortices due to the cavity is evident. In the presence of the base cavity, the circulating region around the fully formed vortex is more extended in all directions, diffusing the vortex motion over a larger region. Although velocity data are available only to within 1 mm of the base boundary, the vortex seems to extend partially into the cavity boundary (see first column of vectors at x = 1 mm and y = -7.5 mm to 7.5 mm in Figs. 10 (b) and 11 (b)), but the relatively small magnitude of this motion and the distance of the vortex center from the cavity precludes the vortex from being seriously inhibited by the cavity walls. The extension of the vortices partially into the cavity is confirmed by tuft visualization experiments done by Kruiswyk and Dutton[4], which showed that short strands of lightweight thread hung at the cavity boundary oscillated back and forth into the cavity in the streamwise direction, with small oscillations in the spanwise direction. However, surface flow visualization experiments performed to determine the interaction of the vortices with the inner walls of the cavity indicated very little fluid motion on the walls (i.e., very small cavity wall shear stress), even near the cavity boundary. The RMS vorticity data obtained here also show no evidence of vortex formation near the cavity boundary (see Fig. 9), so it is not likely that the vortices extend far enough into the cavity to be seriously inhibited by the cavity walls.

Another feature of the vortex expansion shown in Figs. 10 and 11 is that, with the base cavity, the vortices extend far enough across the wake to affect the opposing shear layer. For example, in Fig. 11 (b), the fully formed vortex shed from the lower separation point clearly interacts more strongly with the upper shear layer than is the case for the blunt base in Fig. 11 (a).

To examine this interaction, the instantaneous vorticity is plotted in Figs. 12 and 13 for each of the four realizations shown in Figs. 10 and 11. From these plots, the shear layer position can be determined, and is indicated by a line in the same manner as in Fig. 9.

The fluid motion near the shear layers due to vortex expansion across the wake is also shown with curved arrows. One effect from interaction of the diffused vortices with the opposing shear layers is a folding of the shear layer region toward the transverse centerline. For example, in Fig. 13 (b), the upper shear layer gains transverse momentum toward the centerline at locations upstream of the vortex center. The subsequent increase in shear layer curvature and convergence angle in the area upstream of the vortex center is clearly evident from both base cavity plots (lower shear layer in Fig. 12 (b) and upper shear layer in Fig. 13 (b)). Evidence of the vortex interaction with remnants of the shear layer *downstream* of the vortex center is also apparent with the corresponding motion *away* from the transverse centerline.

Another effect of diffused vortex motion is that increased vorticity in the area just inside of the shear layers and just downstream of the separation point can reduce the local pressure, thereby increasing the curvature of the shear layer, an effect which was discussed previously. However, increases in vorticity magnitude near the shear layers which would be associated with reduced pressure are not readily apparent in Figs. 12 (b) and 13 (b).

The instantaneous flow structure data can also be used for comparison to the numerical simulation of this flowfield done by Rudy[10]. This study used a time-accurate simulation of the Navier-Stokes equations to compute the laminar flow past base models similar to those used in the present experiments, with the only difference being in the transverse cavity height, which is equal to 90% of the total base height in the simulations and 80% of the base height in the present experiments. As previously mentioned, the simulations were done for freestream Mach numbers of 0.4 and 0.6 and at relatively low freestream Reynolds numbers (based on freestream velocity and base height) of 700 and 962 for Mach 0.4 and Mach 0.6, respectively.

Instantaneous vorticity plots have been selected from the Mach 0.6 simulations that most closely match the stage of vortex development indicated by the experimental results shown in Fig. 13. The simulations corresponding to the M6b and M6c experimental cases are shown in Figs. 14 (a) and (b). In comparing these plots to Figs. 13 (a) and (b), it can be seen that there are some significant differences in the vortex structure. The lack of turbulence in the simulations and the resultant discrepancy from the experimental wake structure (lack of small-scale turbulence and vortex fragmentation) are evident. The simulations also show that the vortices are elongated for both the blunt and cavity configurations, especially for the base cavity where the vortex stretches in the

streamwise direction as it expands into the cavity, causing vortex motion far into the cavity. Additional data from Rudy[10] also show distinct vortices forming near the cavity boundary at the transverse center of the wake. Although the PIV data do not extend into the cavity, the scale of the fluid motion at the boundary and the vortex formation location indicated by the experiments do not support these results. Rudy recognized the limitations of his computations and suggested future studies to include both higher Reynolds numbers and turbulence modeling to more accurately predict experimental results under typical Reynolds number conditions.

Conclusions and Summary

Analysis of the time-resolved flowfield structure in the turbulent separated wake of a base cavity has been made possible by implementation of a new particle image velocimetry (PIV) system. The data obtained have shed light on the effects of the base cavity and on the mechanism by which it reduces base drag.

The evidence presented indicates that the most prominent effects of a base cavity on the vortex street wake are the increased convergence of the separated shear layers from each base corner toward the transverse wake centerline and the diffusion of vortex motion due to the expansion of individual vortices partially into the cavity and across the near-wake. The diffusion of the vortices, in turn, reduces their strength by approximately 4% to 6%, although the vortices do not form further upstream due to the cavity and are not significantly inhibited by the cavity walls. These effects are seen at both freestream conditions examined here. It is also evident that the effects are less significant at higher freestream velocities due to the extension of the separated shear layers and the movement of the vortex formation location further downstream of the aft edge of the base, thereby reducing the effect of the cavity on the vortices. These specific wake structure effects provide the information necessary for determination of the drag reduction mechanisms of base cavities.

The apparent mechanism of the observed base cavity wake modifications depends on the replacement of the solid boundary of the blunt base with the compliant fluid boundary of the base cavity. This compliant boundary allows greater expansion of vortex motion and a resulting small increase in shear layer convergence toward the transverse centerline due to the interaction of each vortex on the upstream part of the opposite shear layer. However, the vortex formation location does not occur any closer to the aft edge of the base for the cavity case. These results refute the theories of Nash et al.[2], Pollock[3], Ringleb[6], and Wood[7], all of which assume that the vortices are

7

somehow trapped or stabilized by interaction with the inner walls of the cavity. The suggestion by Compton[8] and Morel[9] that a co-flowing stream sheds from the cavity wall is partially valid in that there is some momentary outflow from one edge of the cavity when vortex motion partially extends into the cavity, but the magnitude of the motion seems to be generally very small and too short-lived to affect the general vorticity level in the shear layer prior to vortex formation. This conclusion is confirmed by the surface flow experiments of Kruiswyk and Dutton[4] which indicate little or no fluid motion on the inner walls of the cavity. The proposal by Kruiswyk and Dutton[4] that periodic fluid mixing at the cavity boundary is responsible for a reduction in vortex strength is closest to being in agreement with the present results, since some mixing must occur as each vortex partly extends into the cavity, although the reduction in vortex strength is small.

Aside from the mechanisms of wake modification, one must consider the mechanism of the base pressure increase and subsequent drag reduction due to base cavities. It is true that the effects described above modify and slightly weaken the vortex street, which, in turn, should slightly increase the pressure in the vicinity of the vortices in the near-wake. However, the wake structure changes are relatively small and the vortex formation location and path are not significantly modified. Without a significant change in the strength or location of the vortices in the near-wake due to the base cavity, it seems that the most significant factor affecting the base pressure is the physical displacement of the base surface within the cavity to a position upstream of the wake, where it does not interact with the low pressure vortices. This is the conclusion drawn by Rudy[10], although his numerical simulations showed the vortices extending far into the cavity with corresponding effects on the wake structure.

In summary, the drag reduction mechanism of a base cavity in subsonic flow is the physical displacement of the base surface away from the vortex street wake, which is only slightly modified by the presence of the cavity.

Acknowledgments

References

1. von Kármán, T., "Über den Mechanismus des Widerstandes, den ein bewegter Körper in einer Flüssigkeit erfährt," *Nachrichten von der Königlichen Gesellschaft der Wissenschaften zu Göttingen. Mathematisch-Physikalische Klasse*, 1911, pp. 509-517.

2. Nash, J.F., Quincey, V.G., Callinan, J., "Experiments on Two-Dimensional Base Flow at Subsonic and Transonic Speeds," ARC R&M No. 3427, 1963.

3. Pollock, N., "Some Effects of Base Geometry on Two-Dimensional Base Drag at Subsonic and Transonic Speeds," Australian A.R.L., Aerodynamics Note 316, 1969.

4. Kruiswyk, R.W., Dutton, J.C., "Effects of a Base Cavity on Subsonic Near-Wake Flow," *AIAA Journal*, Vol. 28, No. 11, 1990, pp. 1885-1893.

5. Clements, R.R., Maull, D.J., "The Representation of Sheets of Vorticity by Discrete Vortices," *Progress in Aerospace Sciences*, Vol. 16, No. 2, 1975, pp. 129-146.

6. Ringleb, F.O., "Separation Control by Trapped Vortices," *Boundary Layer and Flow Control*, G. V. Lachmann, ed., Pergamon Press, 1961, pp. 265-294.

7. Wood, C.J., "The Effect of Lateral Vibrations on Vortex Shedding from Blunt-Based Aerofoils," *Journal of Sound and Vibration*, Vol. 14, No. 1, 1971, pp. 91-102.

8. Compton, W.B., "Effect on Base Drag of Recessing the Bases of Conical Afterbodies at Subsonic and Transonic Speeds," NASA Technical Note D-4821, 1968.

9. Morel, T., "Effect of Base Cavities on the Aerodynamic Drag of an Axisymmetric Cylinder," *Aeronautical Quarterly*, Vol. 30, Part 2, 1979, pp. 400-412.

10. Rudy, D.H., "A Numerical Study of Unsteady Two-Dimensional Subsonic Compressible Base Flow," Ph.D. Thesis, University of Illinois at Urbana-Champaign, 1987.

11. Little, B.H., Jr., Cubbage, J.M., Jr., "The Development of an 8-inch by 8-inch Slotted Tunnel for Mach Numbers up to 1.28," NASA Technical Note D-908, 1961.

12. Molezzi, M.J., "Development and Application of Particle Image Velocimetry in High-Speed Separated Flow: Two-Dimensional Base Cavities," Ph.D. Thesis, University of Illinois at Urbana-Champaign, 1993.

13. Molezzi, M.J., Dutton, J.C., "Application of Particle Image Velocimetry in High-Speed Separated Flows," *AIAA Journal*, Vol. 31, No. 3, 1993, pp. 438-446.

14. Landreth, C.C., Adrian, R.J., "Measurement and Refinement of Velocity Data Using High Image Density Analysis in Particle Image Velocimetry," *Proceedings, Fourth International Symposium on Applications of Laser Anemometry to Fluid Mechanics*, Lisbon, Portugal, July 1988, pp. 485-497.

15. Fage, A., Johansen, F.C., "The Structure of Vortex Sheets," ARC R&M No. 1143, 1927.

Table 1 Base pressure and shedding frequency effects due to base cavity (taken from Kruiswyk and Dutton[4])

Freestream Mach No. (M_∞)	Freestream Reynolds No. (Re_∞)	Base Pressure Coefficient (C_p) Increase, %	Strouhal No. (St) Increase, %
0.4	1.36×10^5	14.1	6.53
0.6	1.82×10^5	9.8	3.65
0.8	2.09×10^5	10.3	2.57

Table 2 Experimental conditions

Freestream Mach No. (M_∞)	Reference Mach No. (M_{ref})	Base Configuration	Freestream Reynolds No. (Re_∞)	Notation
0.4	0.49	blunt	1.36×10^5	M4b
0.4	0.49	half-height cavity	1.36×10^5	M4c
0.6	0.74	blunt	1.82×10^5	M6b
0.6	0.74	half-height cavity	1.82×10^5	M6c
0.8	0.88	blunt	2.09×10^5	M8b
0.8	0.88	half-height cavity	2.09×10^5	M8c

Table 3 Base flow shear layer length and separation

Experimental Case	Average Shear Layer Streamwise Length (mm)	Cavity % Change	Shear Layer Endpoint Transverse Separation (mm)	Cavity % Change
M4b	6.9	—	13.0	—
M4c	6.8	-1.4	12.5	-3.8
M6b	8.0	—	13.5	—
M6c	7.4	-7.5	12.8	-5.2

Table 4 Base flow near-wake vortex strength

Experimental Case	Spatially Averaged RMS Vorticity s^{-1}	Cavity % Change
M4b	42590	—
M4c	40890	-4.0
M6b	66120	—
M6c	62490	-5.5

9

Fig. 1   Typical two-dimensional base cavity
and subsonic vortex street wake

Fig. 2   Base flow test section
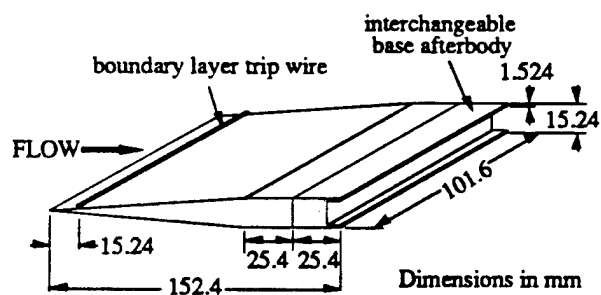
Fig. 3   Base cavity model
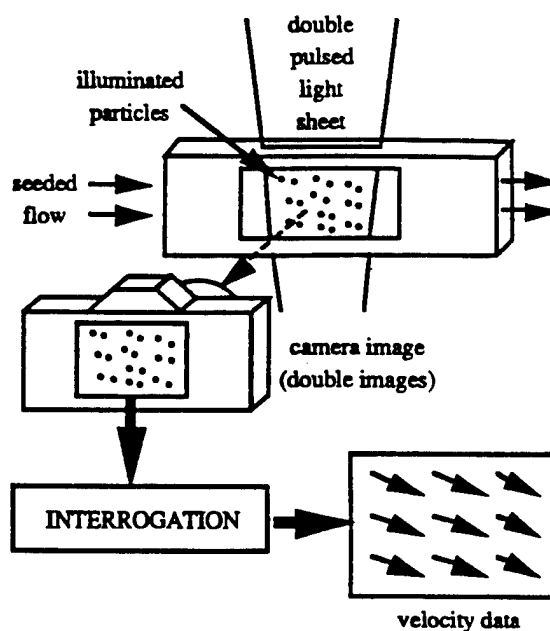
Fig. 4   Principle of PIV
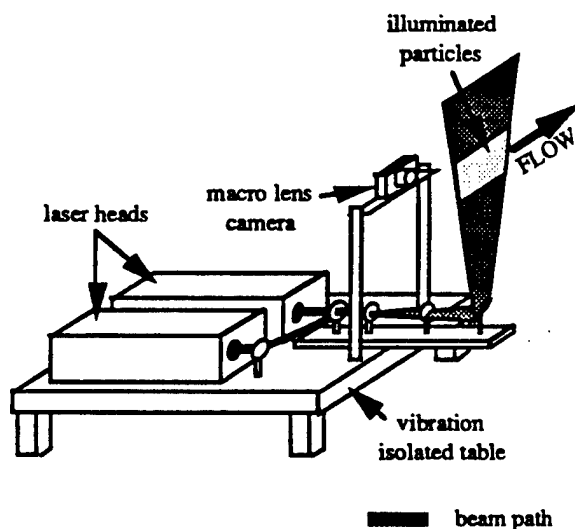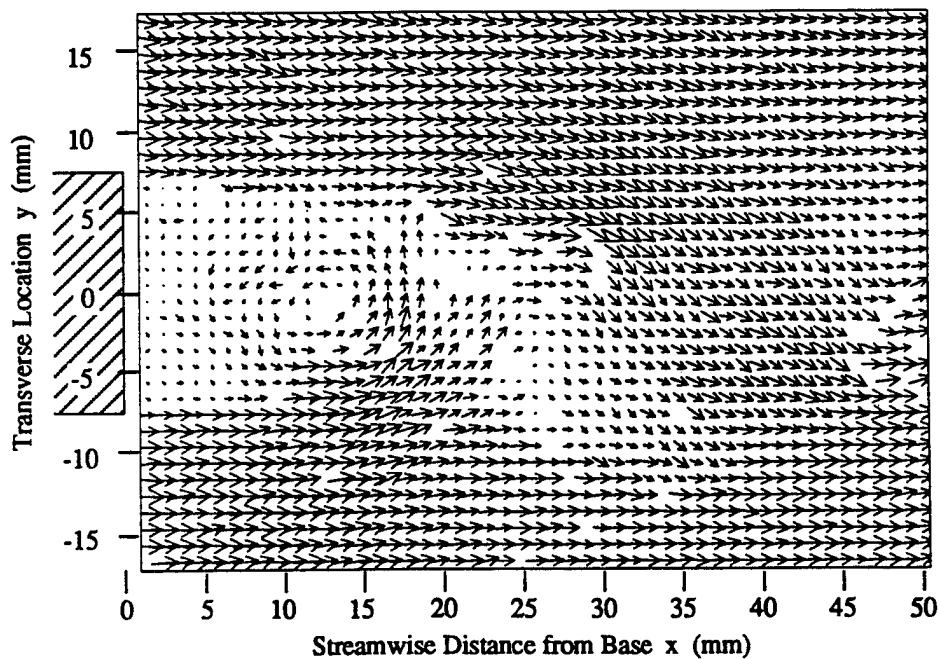

Fig. 5   PIV acquisition system

Actual data includes array of 99 x 69
vectors
(49 x 35 shown)

$\rightarrow$ 275 m/s

Fig. 6   M6b raw velocity vectors

Actual data includes array of 99 x 69
vectors
(49 x 35 shown)

$\rightarrow$ 275 m/s
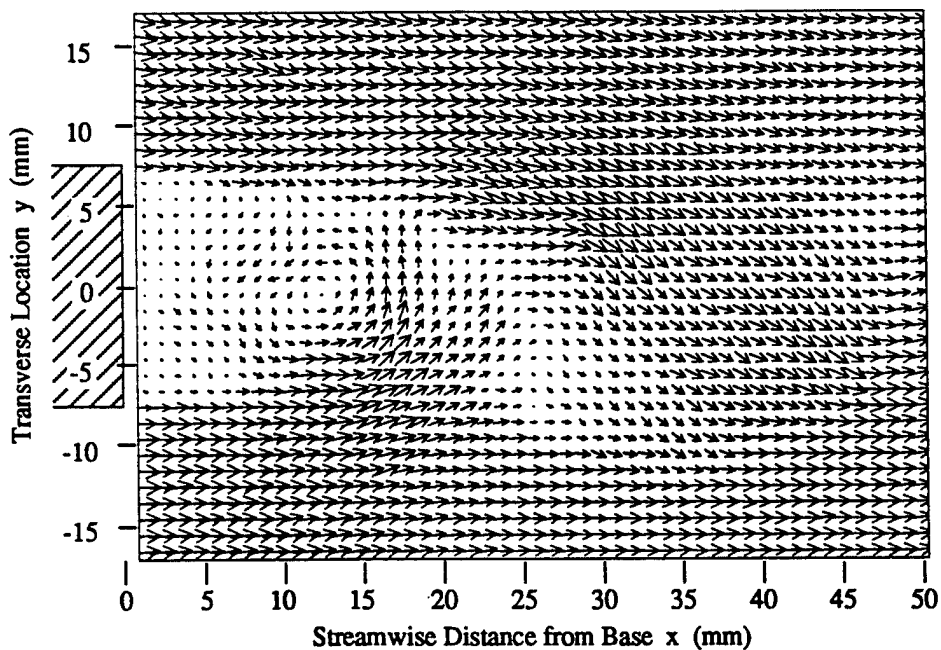
Fig. 7   M6b interpolated and smoothed velocity vectors
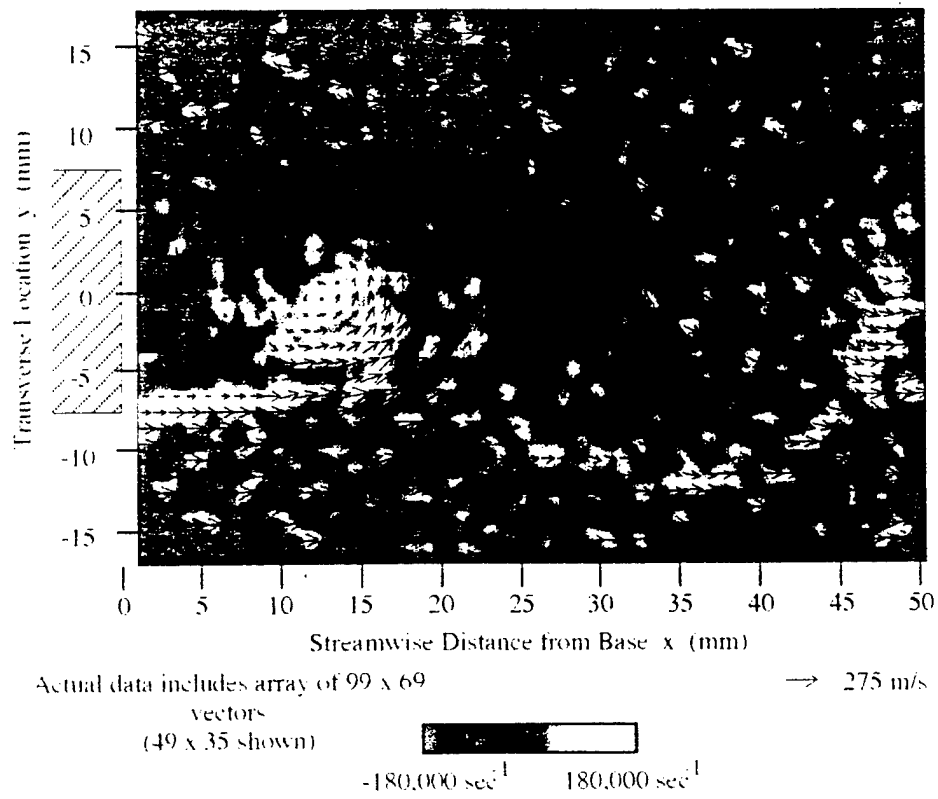
Fig. 8   M6b color vorticity plot with velocity vector overlay
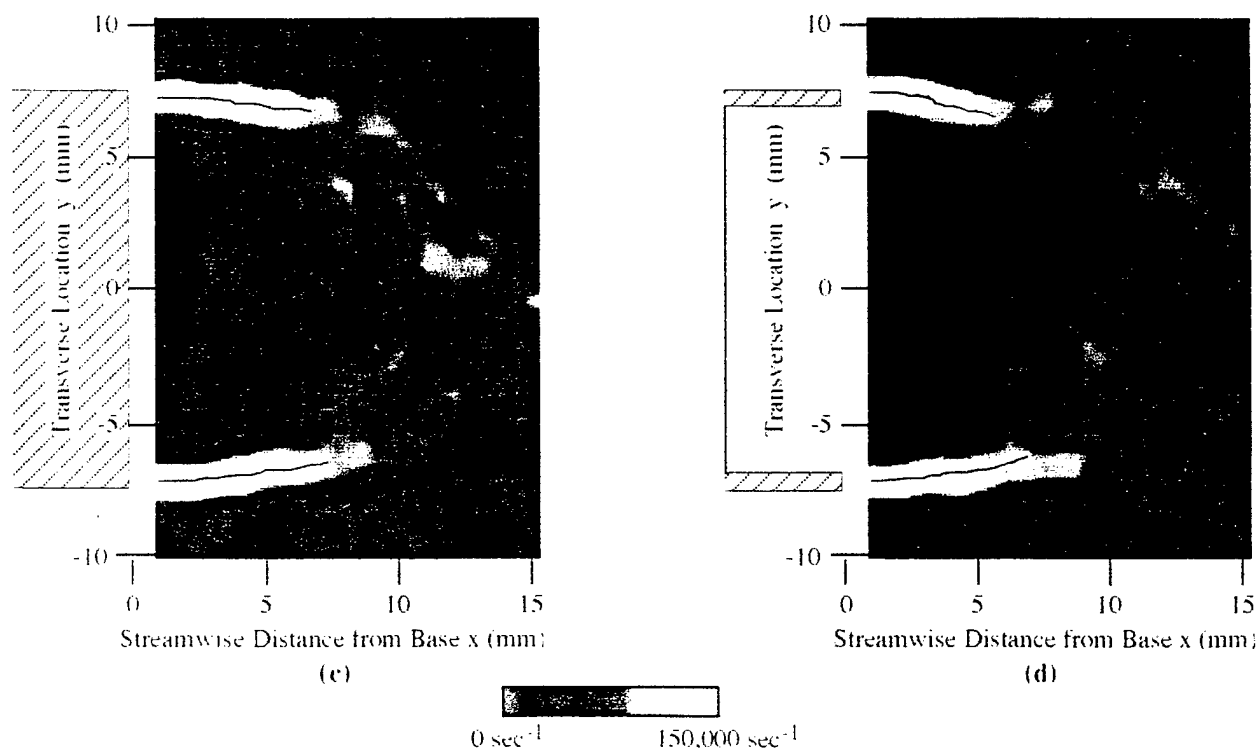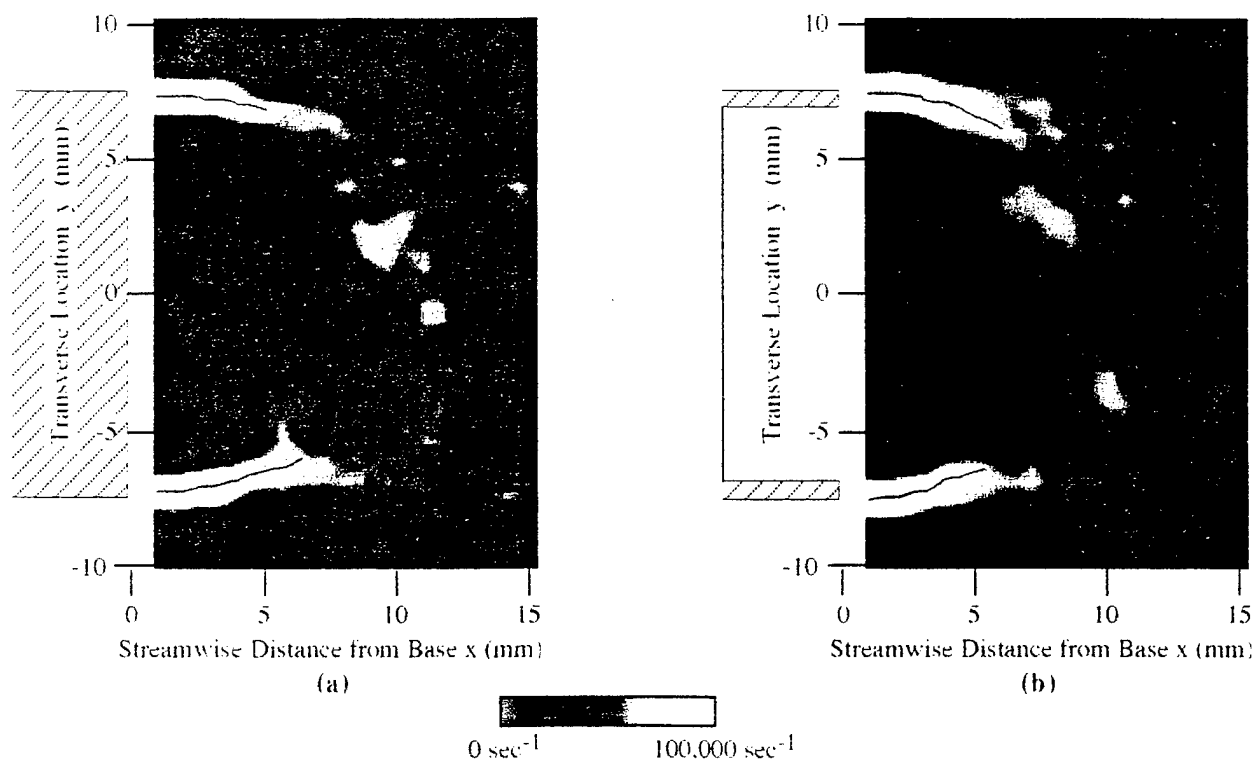
Fig. 9   Enlarged color RMS vorticity plots indicating shear layers
(a) M4b   (b) M4c   (c) M6b   (d) M6c
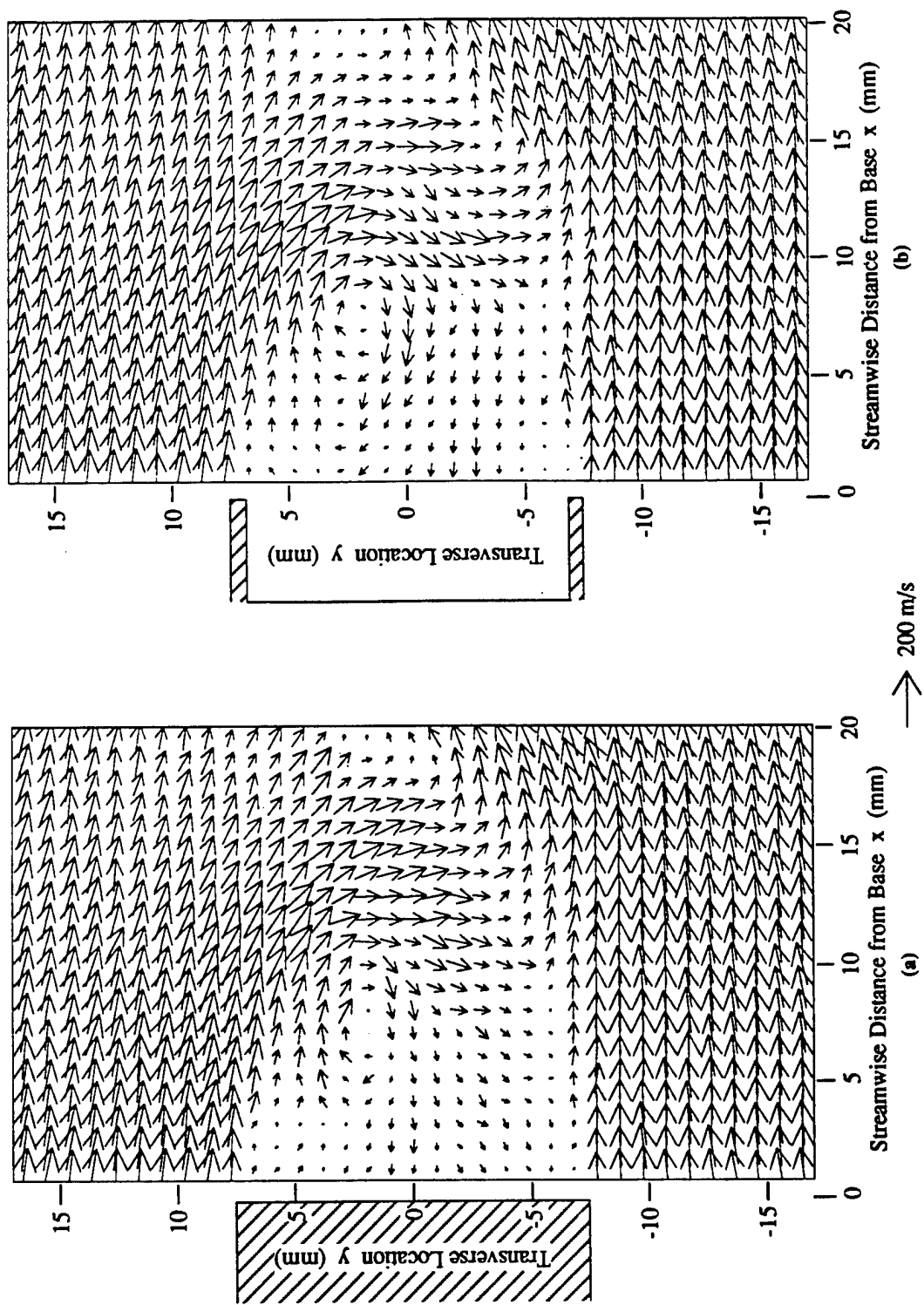
Fig. 10 Instantaneous flow structure comparison: $M_\infty = 0.4$ velocity vectors
(a) M4b (b) M4c

14
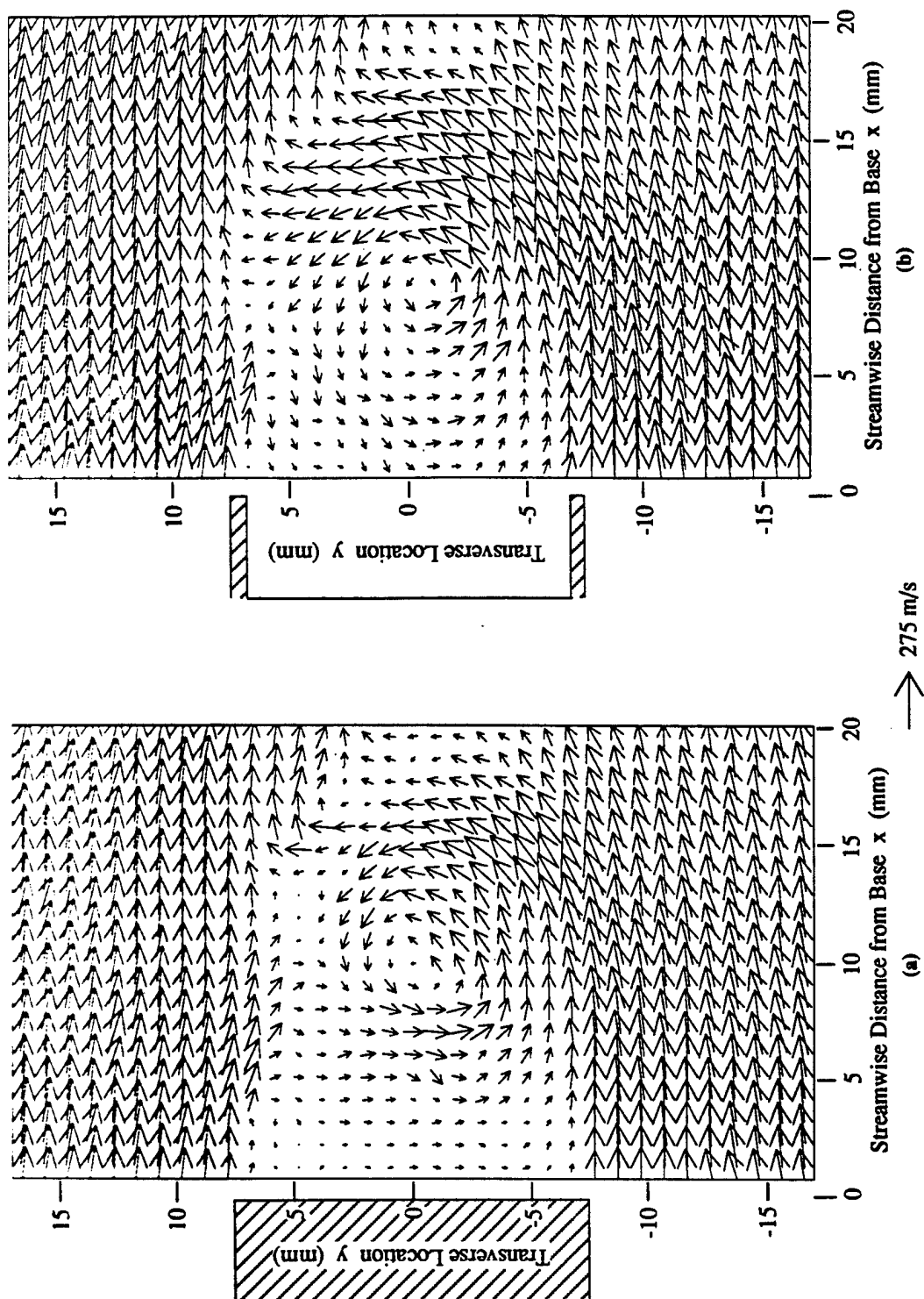
Figure 11 Instantaneous flow structure comparison: $M_\infty = 0.6$ velocity vectors
(a) M6b (b) M6c
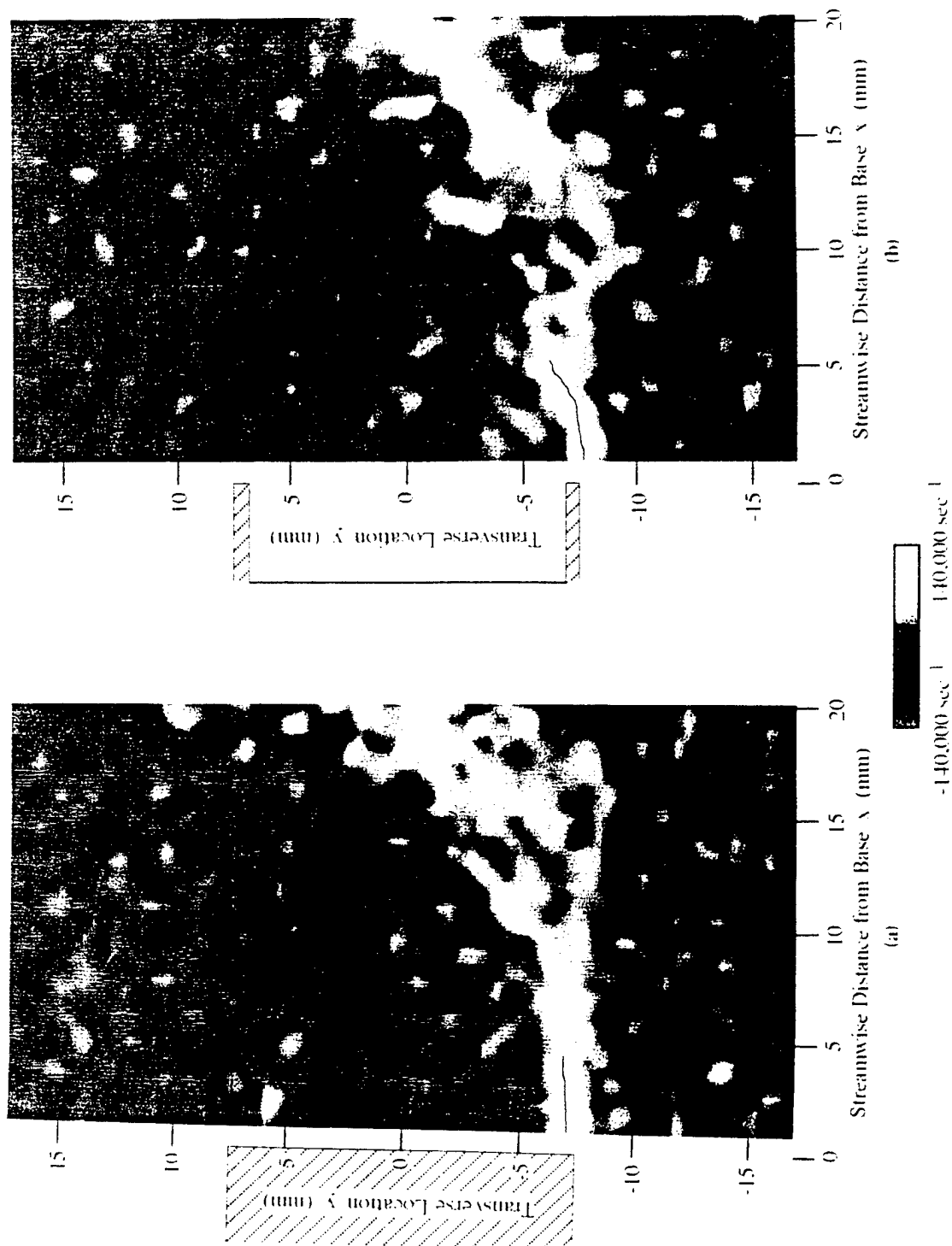
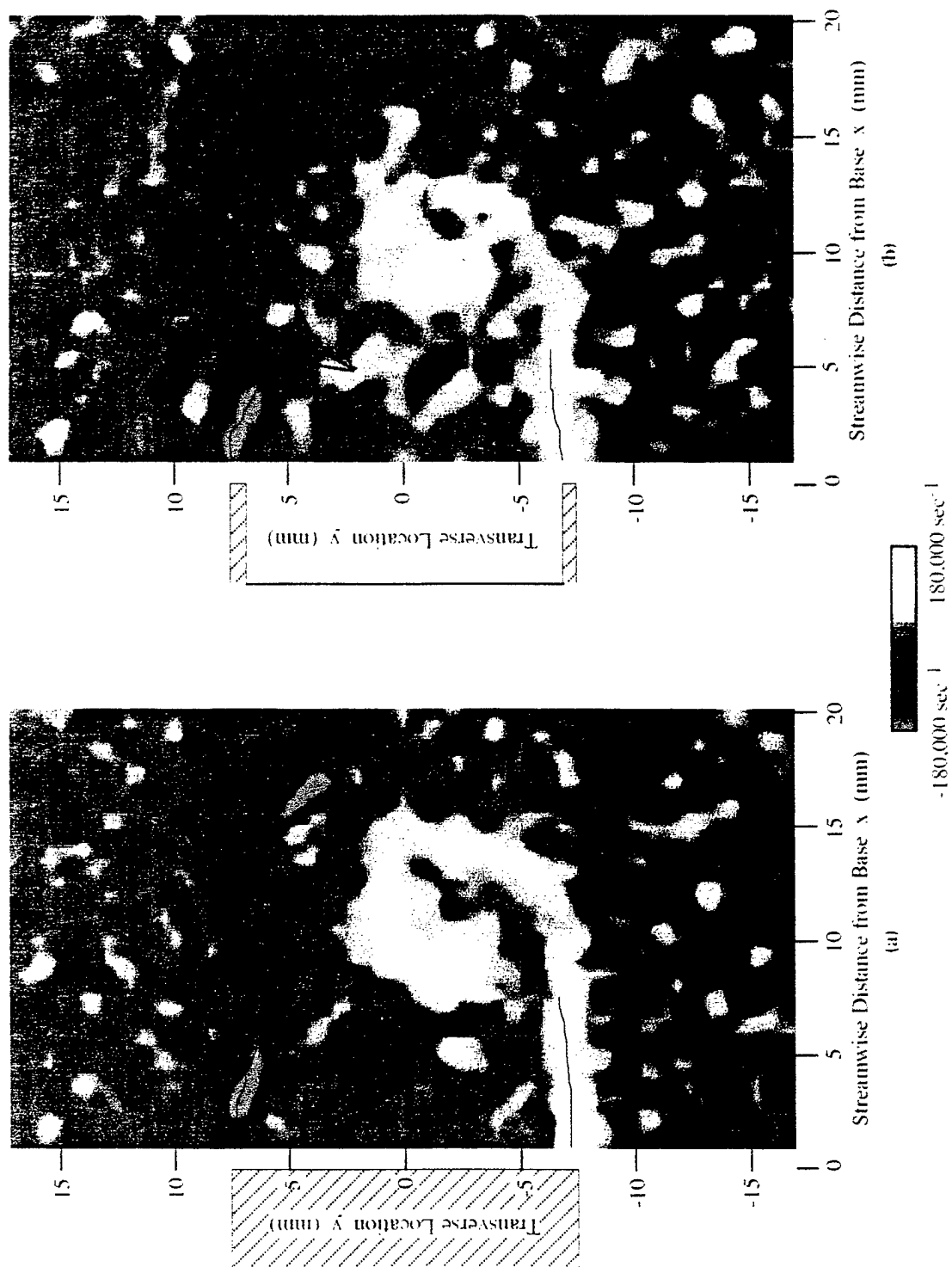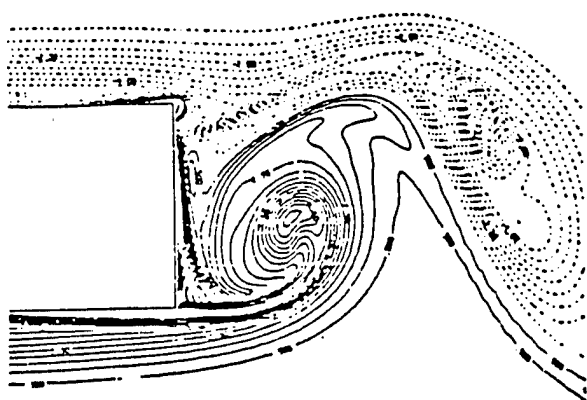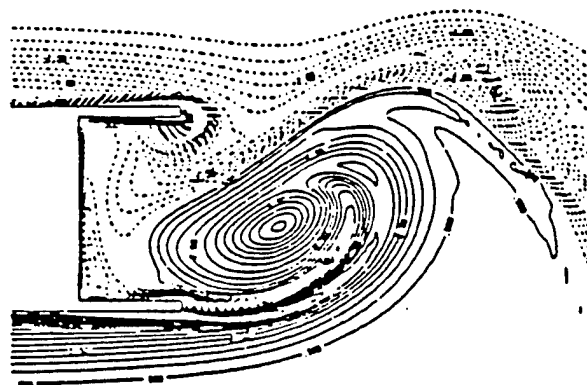Figure 12 Instantaneous flow structure comparison: M = 0.4 color vorticity plots
(a) M4b (b) M4c

Figure 13 Instantaneous flow structure comparison: $M_c = 0.6$ color vorticity plots (a) M6b (b) M6c

17

(a)   (b)

Fig. 14   Navier-Stokes numerical solution vorticity contours, taken from Rudy[10]
(a) M6b   (b) M6c

APPENDIX A.15

EFFECTS OF AFTERBODY BOATTAILING ON THE NEAR-WAKE OF AXISYMMETRIC BODIES IN SUPERSONIC FLOW

AIAA Paper No. 94-0029

Presented at the *32nd AIAA Aerospace Sciences Meeting*

Reno, Nevada

January 1994

by

J. L. Herrin and J. C. Dutton

AIAA 94-0029

Effects of Afterbody Boattailing on the Near-Wake of Axisymmetric Bodies in Supersonic Flow

J.L. Herrin and J.C. Dutton
University of Illinois at Urbana-Champaign
Urbana, Illinois

32nd Aerospace Sciences Meeting & Exhibit
January 10-13, 1994 / Reno, NV

EFFECTS OF AFTERBODY BOATTAILING ON THE NEAR-WAKE OF AXISYMMETRIC BODIES IN SUPERSONIC FLOW

J.L. Herrin[*] and J.C. Dutton[†]
University of Illinois at Urbana-Champaign
Urbana, Illinois

Abstract

An experimental investigation of the near-wake flowfield downstream of a conical boattailed afterbody in supersonic flow is presented. The afterbody investigated is typical of those for conventional boattailed missiles and projectiles in unpowered flight. Flow visualization, mean static pressure measurements, and three-component laser Doppler velocimeter data have been obtained throughout the near-wake of the body. The effects of afterbody boattailing on the physics of the near-wake flow are determined by comparing the present data with similar data obtained on a cylindrical afterbody. Results indicate that a net afterbody drag reduction of 21% is achieved with the current boattailed afterbody for an approach Mach number of 2.46. The shear layer growth rate, and therefore mass entrainment from the recirculation region behind the base, is shown to be significantly reduced by afterbody boattailing due to the reduction in turbulence levels throughout the near-wake as compared to the cylindrical afterbody.

Introduction

Modern missiles and projectiles can suffer significant amounts of drag during transonic and supersonic flight due to the low pressure acting on the rear of the body. Generally termed base drag, the pressure-area force acting on the base of a typical flight vehicle can make up a substantial portion of the total drag in many instances, especially for missiles or projectiles in unpowered flight where a high pressure propulsive jet is absent.[1] In fact, the base drag on the Space Shuttle Columbia has been shown to be approximately 50% of the total orbiter drag during reentry.[2] Throughout the last three decades, several methods to reduce base drag have been developed including afterbody boattailing, base bleed, base cavities, and base burning. The simplest of these to implement in practice is afterbody boattailing which generally involves only a slight modification to the afterbody surface angle with the payoff being a higher base pressure (reduced afterbody drag). Addy and White[3] have shown that conical boattails (constant afterbody surface angle, β, prior to separation) can reduce the net afterbody drag by up to 30% from that on a cylindrical afterbody ($\beta = 0°$) in unpowered, supersonic flight. Although the global benefits (i.e., drag reduction) of afterbody boattailing have been well established for different boattail angles, Mach numbers, and Reynolds numbers (e.g., Refs. 4-7), detailed studies of the fluid dynamic effects in the near-wake due to afterbody boattailing have not previously been conducted. An increased understanding of the flow physics in the base region is essential as new methods are developed to further reduce net afterbody drag on practical flight vehicles.

The near-wake flowfield of an axisymmetric, boattailed afterbody in a uniform supersonic flow is sketched in Figure 1. Several complicated fluid dynamic phenomena exist in the flowfield including the rapid expansion of the turbulent boundary layer at the body-boattail junction, geometric boundary layer separation at the base corner, growth of the compressible shear layer, and reattachment along the axis of symmetry. Obviously, the effects on the near-wake of adding a boattail to a cylindrical afterbody stem from the change in initial conditions at the base corner separation point which include a higher freestream Mach number, non-zero local flow angle, and non-zero pressure gradient due to the axisymmetric compression effect which occurs on the boattail as the flow approaches the axis of symmetry. In addition, the presence of the boattail alters the state of the turbulent boundary layer by the rapid expansion at the body-boattail junction and by the adverse pressure gradient on the boattail surface. As will be shown in this paper, the outer inviscid flow over the boattail can be adequately predicted by the axisymmetric method of characteristics; however, the boundary layer development along the boattail up to the separation point is much more difficult to predict. In addition, the mean and turbulent characteristics of the boundary layer at separation play an important role in determining the initial structure of the separated shear layer and, therefore, the turbulent mixing and mass entrainment rates in the near-wake.

---

[*]Graduate Research Assistant; Currently employed as a National Research Council Associate at the NASA Langley Research Center, Member AIAA.

[†]Professor, Department of Mechanical and Industrial Engineering, Associate Fellow AIAA.

1

Several authors have shown that rapid expansions (such as those at the body-boattail junction and base corner) can significantly distort the mean and turbulence characteristics of an attached turbulent boundary layer. Hampton and White[8] found a significant distortion in the mean velocity profiles downstream of a variety of centered expansions in supersonic flow. These authors noted the possibility that the distorted post-expansion boundary layer could have a significant effect on the separation characteristics, shear layer growth rates, and reattachment processes for boattailed afterbodies, the effect being greater for larger boattail angles. It has also been established that rapid expansions reduce the turbulence levels in compressible boundary layers.[9,10] Arnette et al.[11] used filtered Rayleigh scattering recently to show that the strong dilatation effect associated with the rapid expansion of a compressible boundary layer increases the scale of the turbulent structures present in the approach boundary layer. In addition, the small scale turbulence near the wall was shown to recover more quickly from the effects of the expansion than the relatively large scale motion in the outer region of the boundary layer. The effect of the strong expansion at the body-boattail junction on the afterbody boundary layer and, hence, on the initial conditions to the near-wake flowfield has generally been ignored in previous investigations of boattailed afterbody flowfields.

The primary objective of the present research is to investigate the fluid dynamic effects of afterbody boattailing on axisymmetric bodies in supersonic flow in an effort to shed new light on the mechanisms associated with the increase in base pressure (reduced afterbody drag) relative to the cylindrical afterbody case. To this end, schlieren/shadowgraph photography, static pressure measurements, and three-component laser Doppler velocimetry (LDV) data have been obtained throughout the near-wakes of both a cylindrical afterbody and a boattailed afterbody. The data obtained downstream of the cylindrical afterbody have been presented elsewhere[12]; in this paper, measurements with the boattailed afterbody are presented and comparisons to the cylindrical afterbody case are made to determine the fluid dynamic effects of adding a conical boattail to a cylindrical afterbody. In addition, a complete documentation of the mean velocity and turbulence fields throughout the near-wake of a boattailed afterbody will provide a valuable data base to which analytical and numerical modelers of base flows can compare solutions.

Experimental Facility and Instrumentation

The experiments described herein were conducted in the axisymmetric wind tunnel facility at the University of Illinois Gas Dynamics Laboratory. A detailed description of the axisymmetric wind tunnel and its use for the study of supersonic, axisymmetric afterbody flows has been given by Herrin and Dutton.[12] The mean Mach number approaching the afterbody is 2.46, the unit Reynolds number is 52 (10^6) per meter, and the measured freestream turbulence intensity is less than 1%. Physical support for the afterbody is provided by a cylindrical sting of radius $R_0 = 31.75$ mm which extends upstream through the nozzle in order to avoid any flow disturbances in the near-wake. The boattail chosen for the present study has a conical shape with an angle, β, relative to the horizontal of 5 degrees and an axial length, L_b, of 31.75 mm (0.5 caliber). Maise[13] has shown that the optimal boattail shape (i.e., shape yielding minimum afterbody drag) is essentially conical at moderate supersonic Mach numbers for typical boattail lengths. In addition, the boattail angle chosen is near the optimal angle given by Addy and White[3] for minimum total afterbody drag at Mach 2.5.

Conventional schlieren and shadowgraph photography were used to investigate the overall structure of the near-wake flowfield. These photographs were of only moderate quality due to the axisymmetric nature of the flow, but they were used successfully to confirm the mean flowfield sketched in Figure 1. Surface oil-streak visualization on the base surface was used to document the symmetry of the near-wake flowfield. By combining motor oil (10W-30) with a black pigment and then applying it to the base in small drops, the oil-streak pattern during a wind tunnel blowdown was found to be a very sensitive indicator of flow symmetry at the base.

Mean static pressure measurements were made on the afterbody and base surfaces with a Pressure Systems Inc. digital pressure transmitter (DPT 6400-T). Seventeen taps (0.64 mm in diameter) were located symmetrically across the base at radial intervals of 3.18 mm in order to assess the radial dependence of the time-averaged base pressure. In addition, 14 taps (0.64 mm in diameter) were located on the afterbody surface to document the mean static pressure field approaching and along the boattail. The afterbody taps were separated axially by 3.18 mm such that 4 taps were located upstream of the body-boattail junction and 10 taps were located axially along the boattail.

The primary experimental tool used in the current study was a two-component LDV system with frequency shifting, which was used to measure the

2

near-wake velocity field. The optical arrangement and system setup are identical to that used in the cylindrical afterbody case.[12] The measurement volume diameter and length are approximately 120 μm and 700 μm, respectively. Data were obtained in two perpendicular planes (horizontal and vertical) each intersecting the axis of symmetry. In the vertical plane, the two-component LDV system measures axial (u) and radial (v_r) velocities, while in the horizontal plane, the system measures axial and tangential (v_t) velocities. Hence, two independent planes of LDV data in the near-wake were obtained from which three mean velocities, three Reynolds normal stresses (σ_u^2, $\sigma_{v_r}^2$, and $\sigma_{v_t}^2$), and two of three Reynolds shear stresses ($<u'v_r'>$ and $<u'v_t'>$) were determined. The LDV measurement grid consisted of approximately 1300 spatial locations concentrated in regions of large velocity gradients (e.g., separated shear layer). An error analysis of the LDV data acquisition procedure was used to estimate a worst-case uncertainty in the mean velocity of 1.2% of U_1 and in the root-mean-square velocity fluctuation of 2.3% of U_1, where $U_1 = 567$ m/s is the mean freestream velocity approaching the afterbody.

Results
Pressure Measurements

The static pressure distribution along the boattailed afterbody is shown in Figure 2 along with a method of characteristics solution for irrotational, axisymmetric flow. The sharp decrease in pressure through the expansion at the body-boattail junction (located at $x/R_0 = -1.0$, where x is the axial distance from the base corner) is clearly evident. The experimental data are shown to relax gradually to the predicted pressure field downstream of the expansion such that near the base corner ($x/R_0 = 0.0$) the agreement between experiment and computation is quite good. The experimental pressure distribution shown in Figure 2 was numerically integrated along the boattail using a trapezoid rule technique to determine an area-averaged boattail drag coefficient (referenced to the projected boattail surface area in the axial direction) of $C_{D_{bt}} = 0.056$. For comparison, the integrated method of characteristics profile yields an average boattail drag coefficient of $C_{D_{bt}} = 0.061$, which is slightly higher than the experimental result because of the rapid drop in pressure predicted at the body-boattail junction.

The measured static pressure distribution across the base of the boattailed afterbody is shown in Figure 3 along with similar data obtained for the cylindrical afterbody.[12] In general, the two profiles are very similar with a slight increase in base pressure with increasing radius; however, the overall magnitudes of the pressure coefficient are substantially lower on the boattailed afterbody (reduced afterbody drag). The pressures at the outer edge of the base may be higher than at the center due to the severe streamline curvature which undoubtedly occurs near this region. As the low-speed fluid flowing radially outward at the base becomes entrained by the high-speed shear layer near the base corner, a change in flow direction in excess of 90 degrees results; for this reason, the static pressure imposed near the base corner should be increased when compared to the pressure at the center of the base.

The base pressure distributions shown in Figure 3 were numerically integrated using a trapezoid rule technique to obtain area-averaged base drag coefficients of $C_{D_{base}} = 0.086$ and $C_{D_{base}} = 0.102$ for the boattailed and cylindrical afterbodies, respectively. When examining the benefits of afterbody boattailing relative to a cylindrical afterbody, the net afterbody drag coefficients (boattail + base) must be compared. For the present boattailed afterbody, the net afterbody drag coefficient (referenced to the afterbody cross-sectional area upstream of the boattail, πR_0^2) was determined to be $C_{D_{net}} = 0.081$. For the cylindrical afterbody, the only contribution to the net afterbody form drag is from the base, $C_{D_{net}} = C_{D_{base}} = 0.102$. A comparison of the net afterbody drag coefficients for each afterbody shows a *21% reduction* in drag due to afterbody boattailing. This result compares well with the data of Rubin et al.[5] who measured a drag reduction of 25% in a study of a similar geometry and flow conditions. From the data presented above, it is obvious that afterbody boattailing is an effective method to reduce net afterbody drag on axisymmetric bodies in supersonic flight. The fluid dynamic effects associated with the drag reduction (increase in base pressure) have been investigated in the current study with detailed LDV measurements throughout the near-wake flowfield. These measurements are described below.

Velocity Measurements
Approach Flowfield

Mean velocity and turbulence data have been obtained upstream of the base corner along thirteen traverses normal to the afterbody surface. These data are used to fully document the approach conditions to the near-wake flowfield as well as to determine the effects of the centered expansion at the body-boattail junction on the characteristics of the turbulent boundary layer immediately upstream of separation. The mean streamwise velocity profiles at five axial locations upstream of the base corner are

plotted in conventional wall coordinates in Figure 4 (data from only five of the thirteen traverses are shown in the figure to avoid overcrowding). By comparing the data obtained upstream of the body-boattail junction (represented by the filled symbols in the figure) to those obtained at successive axial locations along the boattail, the expansion at the body-boattail junction is shown to reduce the outer wake of the original undisturbed boundary layer and to cause a gradual reduction in the slope of the log region. Relaxation of the mean velocity downstream of the body-boattail junction appears quite rapid initially, but the general shape of the profiles appears to be slowly evolving even at the last axial station prior to separation at the base corner ($x/R_o = -0.06$). These results are similar to those given by Dussauge and Gaviglio[9] who showed that the boundary layer downstream of a sudden expansion recovers quickly at first with significant changes in the mean profile occurring within the first 10 boundary layer thicknesses downstream of the expansion (this corresponds to the length of the boattail in the present case); a complete recovery of the mean velocity and turbulence profiles across the boundary layer generally requires a substantially longer distance.

The mean boundary layer velocity profile immediately upstream of the base corner ($x/R_o = -0.06$) is replotted in Figure 5 with a curve fit for compressible, turbulent boundary layers given by Sun and Childs.[14] The integral boundary layer properties as determined from the curve fit are important initial conditions to the near-wake flowfield and, therefore, are also included in the figure. The good agreement between the experimental data and the curve fit suggests that the boundary layer has nearly recovered (in the mean velocity sense) from the expansion at the body-boattail junction and is approximately in equilibrium prior to separation (note that this "new" equilibrium state is different than that existing upstream of the body-boattail junction). In the present case, the boundary layer thickness, δ, is approximately 15% of the base radius such that axisymmetric effects on the boundary layer due to lateral surface curvature are generally quite weak. The values shown in Figure 5 for the shape factor (H), wake strength parameter (Π), and skin friction coefficient (C_f) fall within the ranges established by previous investigators for equilibrium, compressible, turbulent boundary layers.[15] The freestream Mach number and unit Reynolds number immediately upstream of the base corner take values of 2.61 and 47 (10^6) per meter, respectively.

Although the mean velocity in the boundary layer recovers fairly quickly from the expansion at the body-boattail junction, previous experiments have shown that the turbulence properties generally recover much more slowly.[9,10] Figure 6 is a plot of the nondimensional streamwise root-mean-square (rms) velocity fluctuation (σ_u/u_τ) distribution at five axial stations along the afterbody (again, only a limited number of traverses are shown for clarity). A significant distortion in the streamwise rms velocity fluctuation profile occurs through the sudden expansion at the body-boattail junction with an overall reduction in the magnitude of the turbulence fluctuations (as characterized by σ_u). The collapse of the data obtained at the last two axial stations upstream of the base corner seems to indicate that a "new" equilibrium state of reduced turbulence levels has been reached prior to separation. Although not shown here for conciseness, the transverse rms velocity fluctuation (σ_{v_r}) profiles and the primary Reynolds shear stress ($<u'v_r>$) profiles also exhibited a significant decrease in magnitude through the expansion at the body-boattail junction.

As indicated above, the expansion at the body-boattail junction distorts both the mean velocity and turbulence quantities in the afterbody boundary layer such that the initial conditions for the near-wake flowfield are changed considerably from those in the cylindrical afterbody case. The implications of these changes in the approach boundary layer characteristics on the mean velocity, turbulence intensity, and Reynolds shear stress fields in the near-wake of the afterbody are discussed below.

Centerline Measurements

As part of the detailed documentation of the near-wake flowfield, an axial traverse on the centerline of the afterbody was completed. The LDV data were obtained in axial increments of $\Delta x/R_o = 0.157$ from the base downstream to the end of the test section window (approximately $x/R_o = 5.4$). The mean axial velocity distribution along the centerline is shown in Figure 7 along with similar data obtained downstream of the cylindrical afterbody.[12] The rear stagnation point (reattachment location) is defined as the location where the mean axial velocity along the centerline vanishes and is labeled in this and subsequent figures with the letter S (the subscripts "c" and "b" refer to the cylindrical and boattailed afterbodies, respectively). Note that the mean shear layer reattachment location moves downstream as the boattail is added to the cylindrical afterbody ($S_b/R_o = 2.81$ and $S_c/R_o = 2.65$). This is consistent with the higher base pressure on the boattailed afterbody which results in a shallower initial shear layer angle. The mean reattachment location for both afterbodies is in general agreement with the pitot probe measurements made by Neale et al.[16] who found

$S/R_0 = 2.9$ in a Mach 3 flow over a cylindrical afterbody. The peak reverse velocity in the separated region behind the base is approximately 29% of U_1 for the current boattailed afterbody which is only slightly larger than that measured for the cylindrical afterbody (27% of U_1). These results are very similar to those given by Delery[17] for a subsonic, power-off base flowfield which supports the notion of Merz et al.[18] that a similarity relationship may exist for the mean axial velocity along the centerline of axisymmetric bodies. In addition, the similarities in the mean axial velocity distributions at different approach Mach numbers suggest that compressibility effects are negligible in determining the mean structure of the recirculation region.

In addition to the mean axial velocity, the axial and radial rms velocity fluctuations were also determined along the centerline of each afterbody. In order to compare the overall turbulence fluctuation levels along the centerline, the turbulent kinetic energy (k) was calculated using the following relation:

$$k = \frac{1}{2}(\sigma_u^2 + \sigma_{v_r}^2 + \sigma_{v_t}^2) \qquad (1)$$

where the tangential Reynolds normal stress ($\sigma_{v_t}^2$) was set equal to the radial component ($\sigma_{v_r}^2$) along the centerline (this assumption is supported by data obtained throughout the near-wake where all three components of the Reynolds normal stress were directly measured). The turbulent kinetic energy distributions along the centerline of the cylindrical[12] and boattailed afterbodies are compared in Figure 8. Contrary to the mean axial velocity profiles shown in Figure 7, the effect of afterbody boattailing on the centerline turbulent kinetic energy is substantial. Although both centerline distributions peak near the reattachment point as the shear layer converges on the axis, the turbulent kinetic energy is significantly reduced in the boattailed afterbody case (peak value is reduced by approximately 22%). This suggests that the turbulence mechanisms in the near-wake, and particularly in the reattaching shear layer, are attenuated by afterbody boattailing. Of course, this result stems, in part, from the reduced turbulence levels in the separating boundary layer for the boattailed afterbody case. The effects of afterbody boattailing on the mean velocity and turbulence properties throughout the near-wake are discussed in more detail in the next two sections.

Near-Wake Mean Velocity Measurements

The mean velocity vector field throughout the near-wake of the current boattailed afterbody is shown in Figure 9. Note that in this and subsequent figures the vertical axis has been expanded by 42%

compared to the horizontal axis in order to more clearly show the important features of the flowfield. To enhance presentation of the mean velocity field, the uniformly spaced velocity vectors shown in Figure 9 have been generated by a linear interpolation in both x and r of the unequally spaced LDV data. The mean velocity vector field in Figure 9 shows qualitatively many of the features of the near-wake flowfield shown previously in Figure 1. The freestream flow is shown to undergo a series of deflections due to the expansions at the body-boattail junction and base corner, followed by the recompression shock wave system in the near-wake which realigns the flowfield with the axis of symmetry. The general shape of the recirculation region behind the base is also clearly shown in the figure. The location of the mean reattachment point is labeled along the horizontal axis (S_b) and provides a useful marker for the relative location of many important features of the near-wake flowfield.

A contour plot of the mean axial velocity field (U/U_1) in the near-wake is shown in Figure 10. The growth of the shear layer downstream of the base corner is shown in the figure by the diverging contour lines which initially are spaced very closely together indicating large mean axial velocity gradients in the shear layer immediately downstream of separation. It is interesting to note that the contours levels at the inner edge of the shear layer diverge rapidly from the base corner while those at the outer edge (contour levels 0.8-1.0) diverge slowly with downstream distance. This suggests that a two-layer description of the initial shear layer development (suggested by Hampton and White[8] for attached boundary layers downstream of a rapid expansion) may be appropriate where an inner layer of high turbulence levels and large mass entrainment rates grows rapidly within an outer layer of lower turbulence levels and relatively slow development. Eventually, as suggested in Figure 10, the inner layer overtakes the outer layer and consumes a majority of the overall shear layer width. Also shown in Figure 10, the recovery of the mean axial velocity profile downstream of reattachment is relatively rapid; however, at the far downstream extent of the present measurements, a velocity defect of approximately 42% still exists, which indicates that full recovery of the mean axial velocity in the wake does not occur within five base radii. Amatucci et al.[19] found that the wake in their two-dimensional base flow fully recovered (velocity defect vanished) at a downstream distance of 4.7 base heights (equivalent to 9.4 base radii in the present case). Although full wake recovery was not achieved in the present case, the mean flow at the last axial station surveyed was found to be entirely supersonic

5

such that disturbances generated further downstream by the wind tunnel geometry have no effect on the near-wake flowfield of interest.

In addition to the mean axial velocity, the mean radial velocity (V_r) was also determined from the three-component LDV data; contours of V_r/U_1 are shown throughout the near-wake in Figure 11. The location of the rapid expansions at the body-boattail junction and base corner are now more clearly shown by decreasing contour levels (more negative radial velocity); the expansions appear to be well centered at these locations. Beyond the base corner expansion fan, the mean radial velocity continues to increase in magnitude, due to the axisymmetric effect, to a peak value of $0.18U_1$ approximately two afterbody radii downstream. The gradual realignment of the freestream flow is shown to the right in Figure 11 by the increasing contour levels, and the realignment appears even slower in the inner region of the shear layer as evidenced by the persistence of a mean radial velocity "finger" at the lower right in the figure. This realignment pattern was also found in the cylindrical afterbody case[12] and is important in multi-component modeling of these flowfields as the recompression criterion provides the closure condition to the entire near-wake solution.[20] The mean radial velocity contours in Figure 11 also show the acceleration of the low speed fluid flowing radially outward (positive V_r) at the base as it becomes entrained into the shear layer near the base corner. Note the rapid change of flow direction (change in sign of the mean radial velocity) near the base corner which, as mentioned earlier, may be responsible for the rising base pressure with increasing radius from the base center. Lastly, the increasing contour levels at the upper right of Figure 11 mark the location of a compression wave generated by the reflection of the body-boattail junction expansion fan from a shear layer at the outer periphery of the test section; again, this region of the flow is entirely supersonic so that interference with the near-wake flowfield of interest does not occur.

By comparing the mean velocity field discussed above to that obtained downstream of a cylindrical afterbody[12], it is found that the overall structure of the mean flowfield in these cases is qualitatively similar. However, one important difference that exists due to afterbody boattailing is a reduction in the mean shear layer growth rate of approximately 20% from that in the cylindrical afterbody case. The growth rate of the shear layer is directly linked to the amount of mass entrainment from the recirculation region and, therefore, directly affects the base pressure. The reduction in shear layer growth for the boattailed afterbody is consistent

with the higher base pressure measured relative to a cylindrical afterbody (16% higher in the present case) and is an important factor in determining the overall effectiveness of afterbody boattailing in reducing base drag.

Near-Wake Turbulence Measurements

In the present experiments, five of the six components of the kinematic Reynolds stress tensor have been directly measured. In this section, the primary results of these turbulence measurements will be presented. Figure 12 is a contour plot of the axial turbulence intensity (σ_u/U_1) throughout the near-wake flowfield. The increase in the axial turbulence intensity from the relatively low levels in the freestream marks the outer edge of the shear layer in the figure. A peak value of approximately $\sigma_u/U_1 = 0.203$ occurs in the subsonic portion of the shear layer approximately two afterbody radii downstream of the base corner and represents a reduction from the peak level in the cylindrical afterbody case[12] of nearly 8%. In fact, throughout the shear layer and wake regions of the boattailed afterbody near-wake, the axial turbulence intensity is reduced from the cylindrical afterbody case. This is most likely a result of the reduced turbulence levels in the boundary layer upstream of the base corner. In addition, the reduced strength of the base corner expansion fan in the boattailed afterbody case results in less distortion of the mean velocity profiles and reduced turbulence production in the initial portions of the shear layer.[21] The axial turbulence intensity decays through the reattachment region in the present case which is in contrast to data obtained for a compressible shear layer reattaching onto a solid wall where it has been shown[22,23] that the axial turbulence intensity peaks downstream of the reattachment point. These differences in the locations for the peak axial turbulence intensity may be attributed to the difference in the boundary condition between the two cases. In the solid wall case, the velocity constraint at the wall ($v = 0$) holds in an *instantaneous* sense such that the mean velocity and rms velocity fluctuations both must vanish at the wall. However, in the compliant surface reattachment of the present case, the velocity constraint at the fictitious surface requires that the *mean* transverse velocity vanish but not the *instantaneous* transverse velocity, such that a non-zero transverse rms velocity fluctuation exists. The axial turbulence intensity also peaked upstream of the reattachment point for the cylindrical afterbody case.[12] Interestingly, peak turbulence intensities have also been shown to occur upstream of

6

reattachment for subsonic shear layers reattaching onto a solid wall.[24]

In addition to the axial turbulence intensity, the radial (σ_{v_r}/U_1) and tangential (σ_{v_t}/U_1) turbulence intensities were also determined from the LDV data; the radial turbulence intensity contours are shown in Figure 13. The qualitative trends are similar to the axial turbulence intensity with relatively large values in the shear layer that decay through the reattachment region into the downstream wake. A peak value of $\sigma_{v_r}/U_1 = 0.129$ occurs slightly upstream of reattachment and represents a 17% decrease from the peak value measured in the cylindrical afterbody case.[12] Note that the overall magnitudes of the radial turbulence intensity are reduced compared to the axial component with a typical anisotropy, σ_u/σ_{v_r}, of 1.6-2.0 in the shear layer. Throughout the recirculation region, the radial turbulence intensity remains fairly uniform at levels reduced from those in the shear layer. The tangential turbulence intensity distribution is similar to that shown in Figure 13 for the radial turbulence intensity with a peak value of 0.133 occurring near the reattachment point. The addition of the boattail caused little change in the peak tangential turbulence intensity (1.4% reduction) even though the other two turbulence intensity components were significantly reduced. Throughout the shear layer, a radial-to-tangential anisotropy ratio ($\sigma_{v_r}/\sigma_{v_t}$) of approximately unity is maintained; thus, the relative ordering of the Reynolds normal stresses in the present case is $\sigma_u > \sigma_{v_r} \sim \sigma_{v_t}$ which indicates the preferential orientation of the turbulence field with the axial direction.

Utilizing the three turbulence intensity distributions measured in the present study, the turbulent kinetic energy (see Equation 1) has been determined and is shown in Figure 14. As mentioned above, the axial turbulence intensity dominates the turbulence field, so the turbulent kinetic energy contours shown in Figure 14 appear similar to those of the axial turbulence intensity shown in Figure 12. The peak value of $k/U_1^2 = 0.0359$ occurs upstream of reattachment in the subsonic region of the shear layer. This global maximum in turbulent kinetic energy is significantly smaller than the value given by Amatucci et al.[19] who found a peak turbulent kinetic energy, k/U_1^2, of 0.07 near reattachment in their two-dimensional base flow study. The significant difference between these two values is most likely a result of the much weaker base corner expansion fan in the present case which results in less turbulence production immediately downstream of separation. In fact, Samimy et al.[25] measured a peak turbulent kinetic energy of approximately $k/U_1^2 = 0.042$ in the reattachment region of a supersonic shear layer which

had been separated at constant pressure from a backstep (i.e., no expansion at the separation point). The peak value in the present case also represents an 18% reduction from the peak turbulent kinetic energy measured in the cylindrical afterbody case.[12] The measured reduction in turbulence levels in the shear layer results in less mass entrainment from the recirculation region for the boattailed afterbody case which, as mentioned previously, is consistent with the reduction in measured shear layer growth rate (approximately 20%) and increased base pressure. In the recirculation region behind the base, the turbulent kinetic energy is fairly uniform at values significantly smaller than those in the shear layer.

In addition to the turbulence intensity components presented above, the axial-radial ($<u'v_r'>$) and axial-tangential ($<u'v_t'>$) Reynolds shear stresses have been directly measured. The measured axial-radial shear stress was larger than the measured axial-tangential shear stress by approximately an order of magnitude in the high turbulence regions of the shear layer. Contours of the dimensionless axial-radial shear stress ($<u'v_r'>/U_1^2$) are shown in Figure 15. As in the axial turbulence intensity contours shown previously, the peak dimensionless shear stress magnitude occurs upstream of reattachment and takes a value of 0.0175 which represents an 8% decrease from the peak value measured in the cylindrical afterbody case.[12] In addition, the peak shear stress measured in the current study is significantly smaller than that measured by Amatucci et al.[19] in their two-dimensional base flow study. Throughout the recirculation region, the shear stress magnitudes are small indicating the absence of any significant large scale turbulence in the separation bubble downstream of the base. The locus of peak shear stress magnitudes at each axial station in the near-wake consistently lies in the subsonic region of the shear layer which indicates the importance of large scale turbulent structures in the entrainment of fluid from the recirculation region.

In general, the effect of afterbody boattailing is to reduce the overall turbulence levels throughout the near-wake flowfield relative to a cylindrical afterbody. Table 1 presents a summary of the peak values of the primary turbulence quantities obtained for the current boattailed afterbody and those obtained previously for the cylindrical afterbody case.[12] The addition of the boattail is shown to significantly reduce both the axial and radial turbulence intensities with the strongest effect occurring in the radial component. In addition, the turbulent kinetic energy and Reynolds shear stress are reduced due to afterbody boattailing. From an analysis of the turbulence production in the near-

wake of both the cylindrical and boattailed afterbodies[21], the decrease in near-wake turbulence levels for the boattailed afterbody is found to be due, in part, to the reduced strength of the base corner expansion fan which directly affects the mean velocity gradient (and therefore turbulence production) in the initial portion of the shear layer. Of course, the reduced turbulence levels in the boattailed afterbody boundary layer also play a role in the overall reduction in turbulence levels in the near-wake of the boattailed afterbody. The practical significance of the reduced turbulence levels in the present case is the substantial reduction in mass entrainment from the recirculation region (shear layer growth rate reduced by approximately 20%) which directly implies a higher base pressure.

Summary and Conclusions

An experimental investigation of the near-wake flowfield behind a conical boattailed afterbody in supersonic flow has been presented. The primary objectives of this study are to investigate the fluid dynamic effects of afterbody boattailing and how they relate to the increase in base pressure on conventional unpowered missiles and projectiles in supersonic flight. The experimental procedure followed during the investigation was to obtain detailed non-intrusive experimental data on a simplified configuration (i.e., without afterbody control fins) both with and without a boattail. The data obtained include flow visualization photographs, mean static pressure measurements on the afterbody and base, and three-component LDV measurements throughout the near-wake. A second objective of this study was to provide experimental data of sufficient detail and quality that could be of use to numerical modelers of these flows. Toward this end, the entire set of data presented in this paper has been tabularized in an easily readable format and is available on disk from the authors. From the data presented herein, the following conclusions can be drawn:

(1) Afterbody boattailing is an effective means of decreasing the net afterbody drag on unpowered missiles and projectiles in supersonic flight. In the present case, the addition of a conical boattail ($\beta = 5$ degrees and $L_b/R_o = 1.0$) resulted in a net afterbody drag reduction of 21% as compared to a cylindrical afterbody ($\beta = 0$ degrees) at the same approach Mach number and Reynolds number.

(2) The rapid expansion at the body-boattail junction in supersonic flow can significantly alter the mean velocity and turbulence distributions in the afterbody boundary layer. In addition to a reduction of the outer wake component of the mean boundary

layer velocity profile, the rapid expansion causes a decrease in the turbulence intensity and Reynolds shear stress levels throughout the boundary layer which, if the boattail length is sufficiently short, can result in substantial changes in the boundary layer conditions at separation.

(3) The mean velocity field in the near-wake of unpowered axisymmetric bodies is qualitatively unaffected by afterbody boattailing. The most significant quantitative effect of boattailing is a reduction in the mean shear layer growth rate (approximately 20% in the present case) which is a result of reduced mass entrainment rates from the recirculation region behind the base. Obviously, this mechanism has direct influence on the base pressure and, therefore, is an important effect of afterbody boattailing in supersonic flow.

(4) Turbulence levels in the separated shear layer are significantly reduced (e.g., 18% reduction in the turbulent kinetic energy) by afterbody boattailing due to the diminished fluctuations in the boundary layer at separation and to the reduced strength of the expansion fan at the base corner which reduces turbulence production in the initial portion of the shear layer. In general, the axial Reynolds normal stress dominates the near-wake turbulence field with the radial and tangential normal stresses being approximately equal. Strong peaks in the axial Reynolds normal stress and Reynolds shear stress occur in the subsonic region of the shear layer at an axial location upstream of the reattachment point.

References

[1]Rollstin, L., "Measurement of Inflight Base Pressure on an Artillery-Fired Projectile," AIAA Paper 87-2427, 1987.

[2]Phillips, W.P., Compton, H.R., and Findlay, J.T., "Base Drag Determination for STS Flights 1-5," AIAA Paper 83-2719, 1983.

[3]Addy, A.L., and White, R.A., "Optimization of Drag Minimums Including Effects of Flow Separation," ASME Transactions: Journal of Engineering for Industry, Vol. 95, No. 1, 1973, pp. 360-364.

[4]Reid, J., and Hastings, R.C., "Experiments on the Axi-Symmetric Flow Over Afterbodies and Bases at M=2.0," R.A.E. Report Aero. 2628, Farnborough, England, 1959.

[5]Rubin, D.V., Brazzel, C.E., and Henderson, J.H., "The Effects of Jet Plume and Boattail Geometry on Base and Afterbody Pressures of a Body of Revolution at Mach Numbers of 2.0 to 3.5," RD-TR-70-5, U.S. Army Missile Command, Redstone Arsenal, Alabama, 1970.

[6]Agrell, J., and White, R.A., "An Experimental Investigation of Supersonic Axisymmetric Flow Over Boattails Containing a Centered Propulsive Jet," TN AU-913, The Aeronautical Research Institute of Sweden (FFA), 1974.

[7]Viswanath, P.R., and Narasimha, R., "Two-Dimensional Boat-Tailed Bases in Supersonic Flow," *The Aeronautical Quarterly*, Vol. 25, No. 3, 1974, pp. 210-224.

[8]Hampton, L.P., and White, R.A., "The Effect of Sudden Expansions and Compressions on Turbulent Boundary Layer Momentum Thickness in Supersonic Flow," ASME Paper 86-WA/FE-11, 1986.

[9]Dussauge, J.P., and Gaviglio, J., "The Rapid Expansion of a Supersonic Turbulent Flow: Role of Bulk Dilatation," *Journal of Fluid Mechanics*, Vol. 174, 1987, pp. 81-112.

[10]Smith, D.R., and Smits, A.J., "The Rapid Expansion of a Turbulent Boundary Layer in a Supersonic Flow," *Journal of Theoretical and Computational Fluid Dynamics*, Vol. 2, No. 5/6, 1991, pp. 319-328.

[11]Arnette, S.A., Samimy, M., and Elliott, G.S., "The Effect of Expansion on the Large Scale Structure of a Compressible Turbulent Boundary Layer," AIAA Paper 93-2991, 1993.

[12]Herrin, J.L., and Dutton, J.C., "Supersonic Base Flow Experiments in the Near-Wake of a Cylindrical Afterbody," *AIAA Journal*, to be published, 1993.

[13]Maise, G., "Wave Drag of Optimum and Other Boattails," *Journal of Aircraft*, Vol. 7, No. 5, 1970, pp. 477-478.

[14]Sun, C.C., and Childs, M.E., "A Modified Wall Wake Velocity Profile for Turbulent Compressible Boundary Layers," *Journal of Aircraft*, Vol. 10, No. 6, 1973, pp. 381-383.

[15]Fernholz, H.H., and Finley, P.J., "A Critical Commentary on Mean Flow Data for Two-Dimensional Compressible Turbulent Boundary Layers," AGARDograph No. 253, 1980.

[16]Neale, D.H., Hubbartt, J.E., Strahle, W.C., and Wilson, W.W., "Effects of External Compression on an Axisymmetric Turbulent Near Wake," *AIAA Journal*, Vol. 16, No. 9, 1978, pp. 940-947.

[17]Delery, J., "ONERA Research on Afterbody Viscid/Inviscid Interaction with Special Emphasis on Base Flows," Proceedings of the Symposium on Rocket/Plume Fluid Dynamic Interactions, University of Texas at Austin, 1983.

[18]Merz, R.A., Page, R.H., and Przirembel, C.E.G., "Subsonic Axisymmetric Near-Wake Studies," *AIAA Journal*, Vol. 16, No. 7, 1978, pp. 656-662.

[19]Amatucci, V.A., Dutton, J.C., Kuntz, D.W., and Addy, A.L., "Two-Stream, Supersonic, Wake Flowfield Behind a Thick Base, Part I: General Features," *AIAA Journal*, Vol. 30, No. 8, 1992, pp. 2039-2046.

[20]Korst, H.H., "Axisymmetric Wakes in Supersonic Unpowered Missile Flight," Proceedings of the Symposium on Rocket/Plume Fluid Dynamic Interactions, University of Texas at Austin, 1983.

[21]Herrin, J.L., "An Experimental Investigation of Supersonic Axisymmetric Base Flows Including the Effects of Afterbody Boattailing," Ph.D. Thesis, University of Illinois at Urbana-Champaign, 1993.

[22]Hayakawa, K., Smits, A.J., and Bogdonoff, S.M., "Turbulence Measurements in a Compressible Reattaching Shear Layer," *AIAA Journal*, Vol. 22, No. 7, 1984, pp. 889-895.

[23]Abu-Hijleh, B., and Samimy, M., "An Experimental Study of a Reattaching Supersonic Shear Layer," AIAA Paper 89-1801.

[24]Eaton, J.K., and Johnston, J.P., "A Review of Research on Subsonic Turbulent Flow Reattachment," *AIAA Journal*, Vol. 19, No. 9, 1981, pp. 1093-1100.

[25]Samimy, M., Petrie, H.L., and Addy, A.L., "A Study of Compressible Turbulent Reattaching Free Shear Layers," *AIAA Journal*, Vol. 24, No. 2, 1986, pp. 261-267.

Table 1 Comparison of Peak Value of Turbulence Quantities

	Cylindrical Afterbody	Boattailed Afterbody	Difference
σ_u/U_1	0.220	0.203	-7.7%
σ_{V_r}/U_1	0.156	0.129	-17.3%
σ_{V_t}/U_1	0.135	0.133	-1.4%
k/U_1^2	0.0440	0.0359	-18.4%
$-<u'v_r'>/U_1^2$	0.0190	0.0175	-7.9%

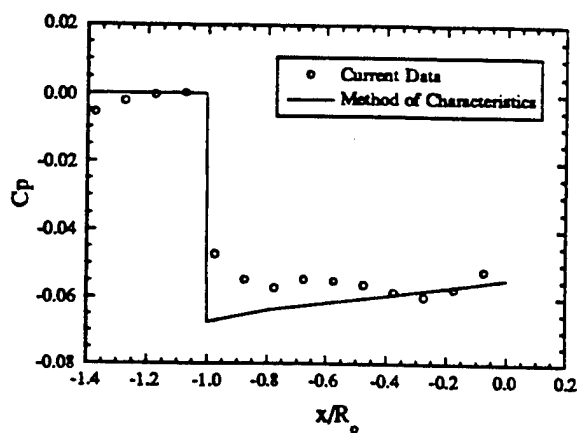Fig. 1   Schematic Diagram of Mean Flowfield Downstream of a Boattailed Afterbody
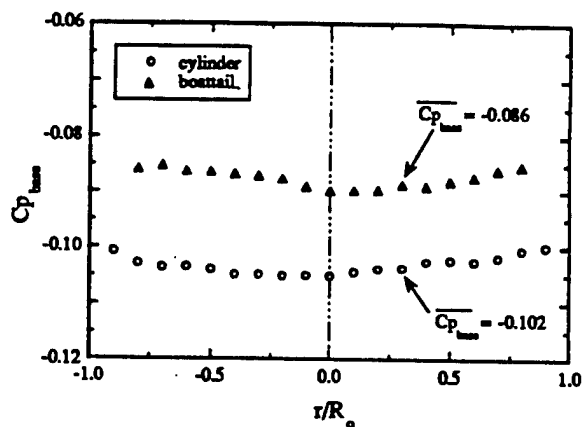

Fig. 2   Boattail Pressure Distribution

Fig. 3   Base Pressure Distributions for Boattailed and Cylindrical[12] Afterbodies
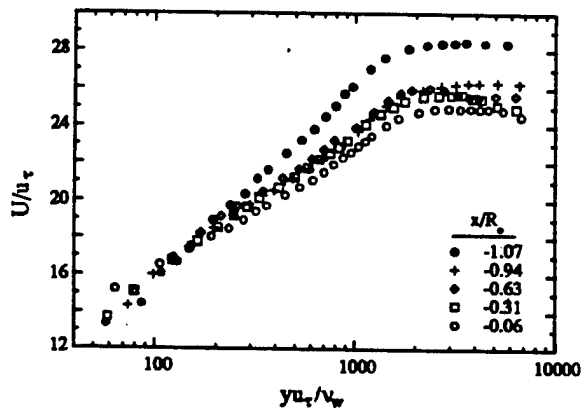
Fig. 4   Boundary Layer Profiles Perpendicular to Boattail Surface (Body-Boattail Junction Located at $x/R_o = -1.00$)
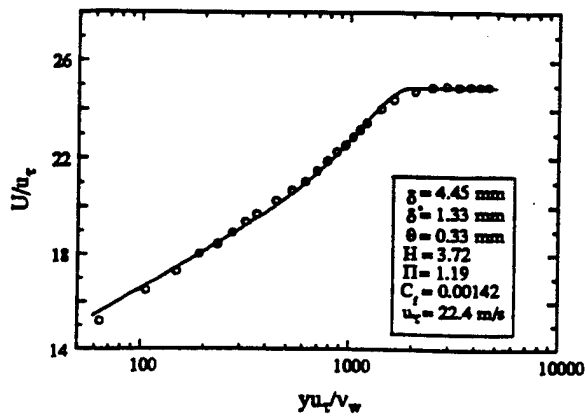
Fig. 5   Mean Boundary Layer Profile Immediately
Upstream of Base Corner ($x/R_o = -0.06$) Along
with Compressible Boundary Layer Curve Fit[14]
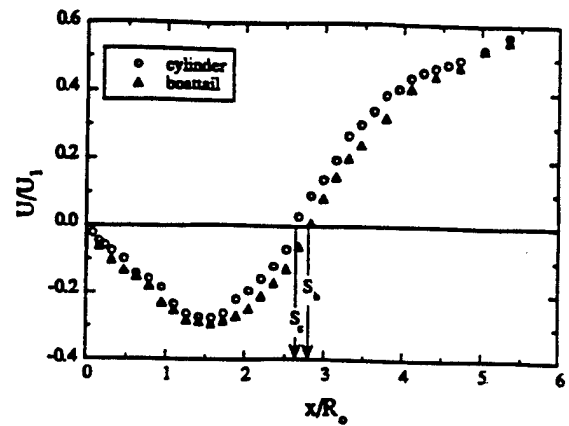
Fig. 7   Mean Axial Velocity Along Centerline:
Comparison Between Cylindrical[12] and
Boattailed Afterbodies
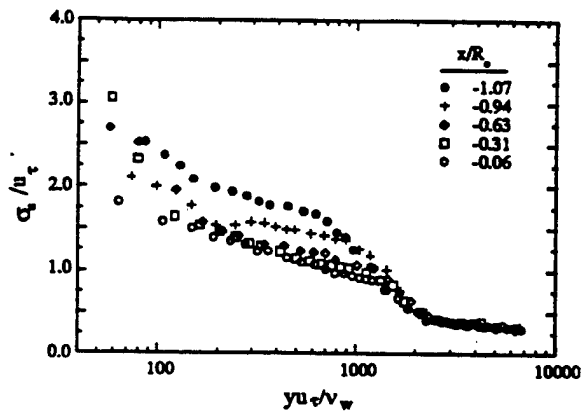
Fig. 6   Effect of Expansion at Body-Boattail Junction on
Streamwise RMS Velocity Fluctuation
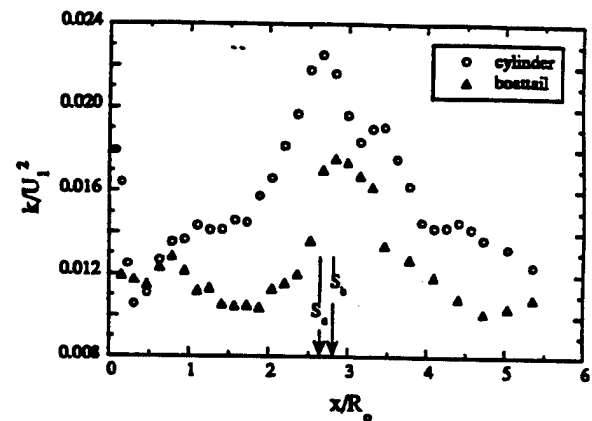
Fig. 8   Turbulent Kinetic Energy Distributions Along
Centerline: Comparison Between Cylindrical[12]
and Boattailed Afterbodies
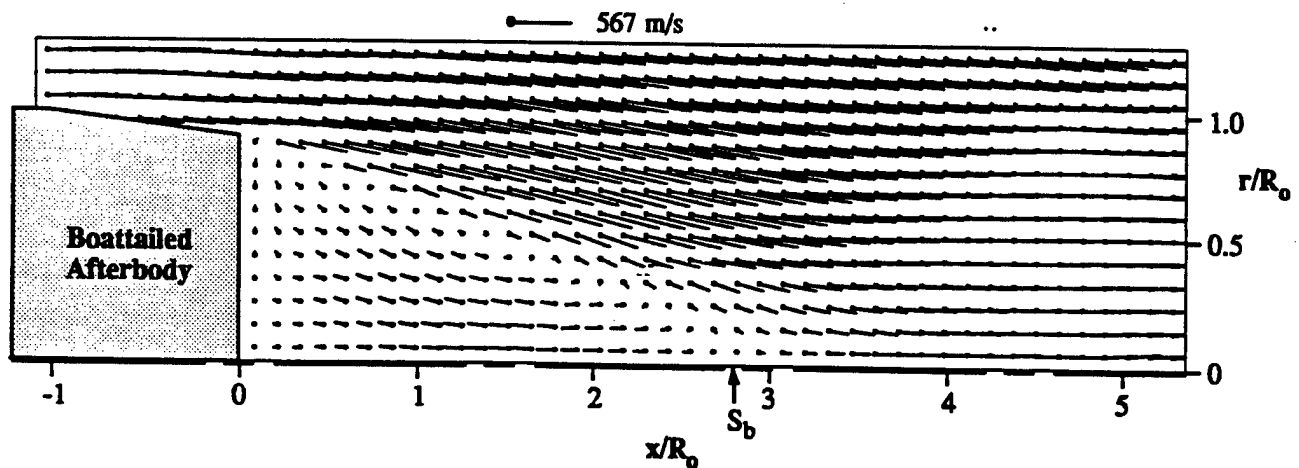
Fig. 9   Mean Velocity Vector Field

11
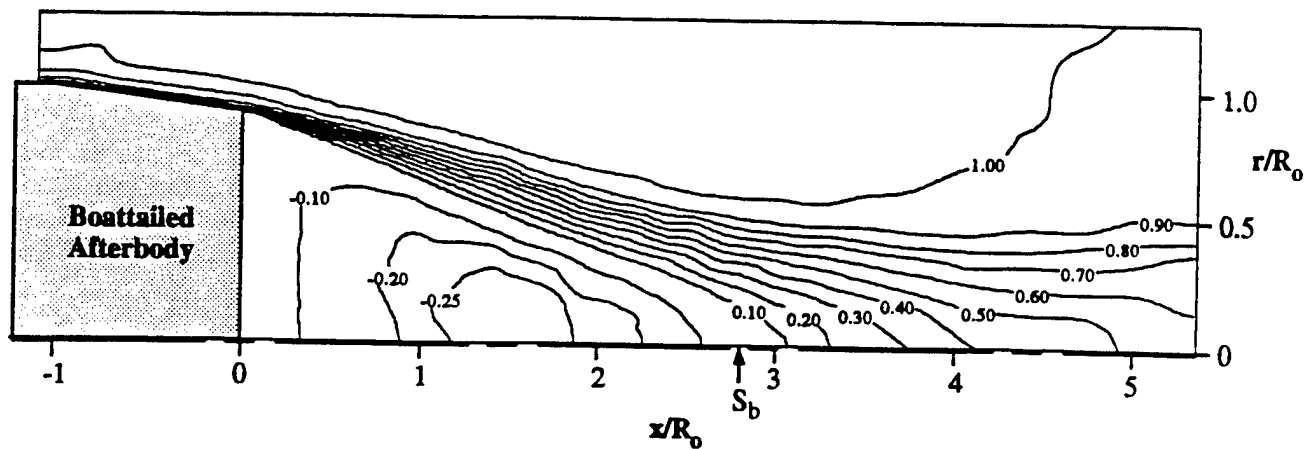
Fig. 10 Mean Axial Velocity Field - U/U_1
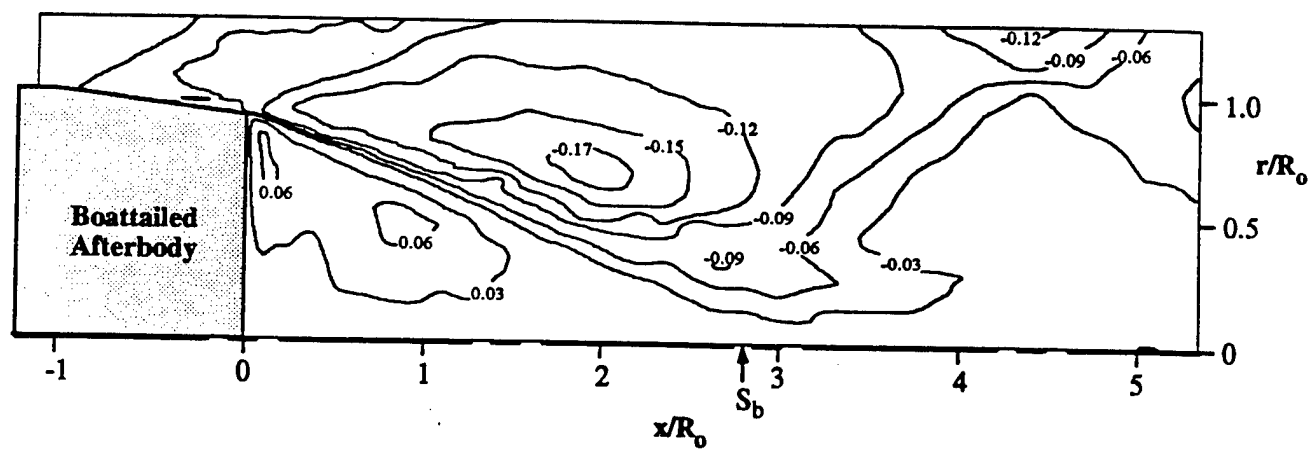
Fig. 11 Mean Radial Velocity Field - V_r/U_1

Fig. 12 Axial Turbulence Intensity Contours - σ_u/U_1

Fig. 13 Radial Turbulence Intensity Contours - σ_{V_r}/U_1
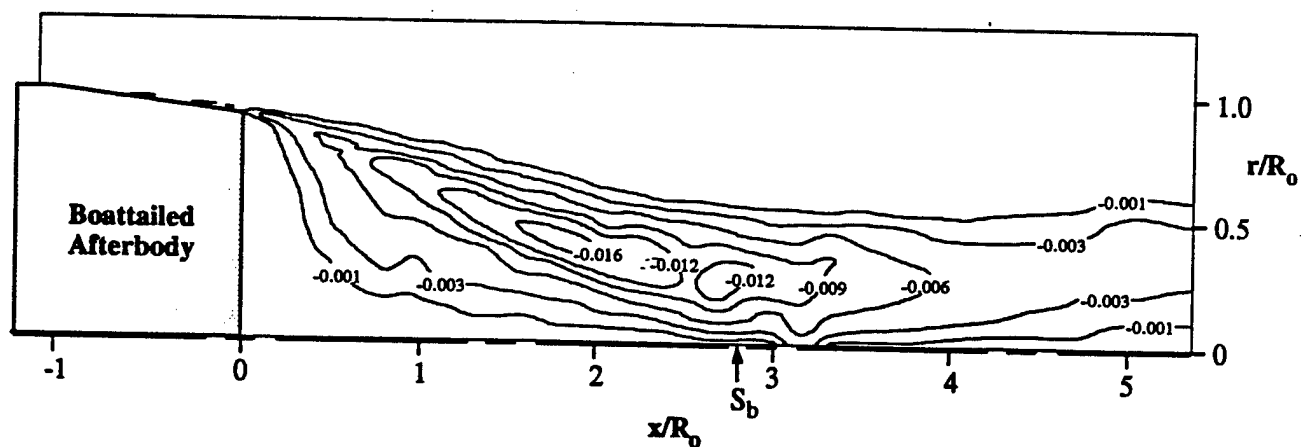

Fig. 14 Turbulent Kinetic Energy Contours - k/U_1^2

Fig. 15 Reynolds Shear Stress Contours - $<u'v_r'>/U_1^2$

APPENDIX A.16

EFFECT OF A RAPID EXPANSION ON THE DEVELOPMENT OF COMPRESSIBLE FREE SHEAR LAYERS

by

J. L. Herrin and J. C. Dutton

AIAA 94-2229

Effect of a Rapid Expansion on the Development of Compressible Free Shear Layers

J.L. Herrin
NASA Langley Research Center
Hampton, Virginia

and

J.C. Dutton
University of Illinois at Urbana-Champaign
Urbana, Illinois

25th AIAA Fluid Dynamics Conference
June 20-23, 1994 / Colorado Springs, CO

EFFECT OF A RAPID EXPANSION ON THE DEVELOPMENT OF COMPRESSIBLE FREE SHEAR LAYERS

J.L. Herrin[*]
NASA Langley Research Center
Hampton, Virginia 23681

and

J.C. Dutton[†]
University of Illinois at Urbana-Champaign
Urbana, Illinois 61801

ABSTRACT

Detailed mean velocity and turbulence data have been obtained with a laser Doppler velocimeter for two axisymmetric shear layers downstream of rapid expansions of different strengths. A comparison of the data in the near-field (immediately downstream of separation) and far-field (shear layer approaching self-similarity) is presented, and the fluid dynamic effects of the rapid expansion are ascertained for each regime. In general, the rapid expansion was found to distort the initial mean velocity and turbulence fields in the shear layer such that two distinct regions were evident: an outer region where the turbulent fluctuations are quenched by the expansion, and an inner region where turbulence levels are magnified by the expansion. For the streamwise Reynolds normal stress and primary Reynolds shear stress, the magnitude of the peak turbulence levels increased with increasing strength of the rapid expansion; the transverse normal stress field, however, was only mildly affected by the expansion. Further downstream after the shear layer mean velocity distributions become self-similar, elevated turbulence levels for the more strongly expanded case persist although the relative distribution of turbulence energy between the Reynolds stress components appears unaffected by the strength of the rapid expansion.

INTRODUCTION

The development of compressible free shear layers has received considerable attention in the scientific community over the past several years. Driven by the desire to design a practical supersonic combustion engine (i.e., scramjet), most research efforts have focused on documenting the growth rate and mixing of fully-developed, two-stream mixing layers for a variety of freestream conditions from the incompressible to compressible regimes. [1-3] The primary result of this research is that the shear layer growth rate, db/dx, and turbulence levels decrease significantly with increasing compressibility. Generally, the degree of compressibility is described in terms of either the convective Mach number (M_c) or the relative Mach number (M_r) of the mixing layer (for two streams with identical specific heat ratios, $M_r = 2M_c$). However, there appears to be growing skepticism as to the universality of these correlation parameters for all mixing layer scenarios. Viegas and Rubesin[4] show quite clearly the significant scatter in the measured shear layer growth rates obtained by different researchers at identical convective (or relative) Mach numbers. These authors suggest that the Mach numbers of each individual stream may impact the shear layer growth rate, even though the convective Mach number (calculated from the velocity difference across the shear layer) remains fixed. The recent data of Bunyatitradulya and Papamoschou[5] seem to support this claim. However, an additional problem, which is often overlooked when comparing shear layer data, is the effect of the initial conditions at the shear layer origin on the fully-developed shear layer characteristics. As pointed out by Bradshaw[6] and others for incompressible mixing layers, the initial conditions can have a dramatic effect on shear layer development and, in general, can affect the mean velocity and turbulence statistics of the shear layer in its fully-developed state. As a result, quantitative comparisons between experiments conducted at different sites (and, therefore, under different conditions) can be quite difficult.

Mehta and Westphal[7] discuss the significant sensitivity of the incompressible shear layer to small changes in its initial conditions (e.g., approach boundary layer state and thickness) and wind tunnel operating conditions (e.g., freestream turbulence levels) which, in practice, can be very difficult to control. In a later study of incompressible plane mixing layers with different velocity ratios, Mehta[8] showed conclusively that the interaction between the developing shear layer and the wake generated by the splitter plate strongly affected the distance required for the shear layer to achieve self-similarity with turbulence properties developing more slowly than the mean velocity. In fact, Mehta[8] showed

---

1

that, in most cases, the shear layer growth rate is approximately linear almost from the start of development which shows the importance of utilizing the spatial independence of the more slowly developing turbulence properties as a criterion for determining the achievement of self-similarity. Also, in many practical situations, the streamwise distance available for shear layer growth is insufficient for the shear layer to reach fully-developed conditions. In these cases, the shear layer development immediately downstream of boundary layer separation has increased importance.

Although little information is available in the initial development region of rapidly expanded compressible free shear layers (as discussed below), a considerable amount of research has been presented on the effects of rapid expansions on attached turbulent boundary layers. Dawson and Samimy[9] and Arnette et al.[10] used fast-response pressure measurements and filtered Rayleigh scattering, respectively, to show that rapid expansions quench the small-scale turbulence in supersonic, turbulent boundary layers while enhancing the turbulence energy in the large-scale structures present in the boundary layer (i.e., a reverse energy cascade from high to low wave numbers). Dussauge and Gaviglio[11] showed that the bulk dilatation associated with a rapid expansion causes a decrease in the Reynolds stresses, especially near the wall where small-scale turbulence dominates. Downstream of the rapid expansion, a new wall layer with increasing turbulence levels was found which grows with downstream distance within an outer layer of essentially frozen turbulence activity; eventually, the inner layer consumes the outer layer forming a "new" boundary layer with properties which may differ considerably from those upstream of the expansion. Hampton and White[12] also proposed a two-layer structure for the recovering boundary layer downstream of rapid expansions.

In addition to providing benchmark data on the effect of rapid expansions on turbulent boundary layers, Dussauge and Gaviglio[11] also used Rapid Distortion Approximations (RDAs) to the Reynolds stress transport equations to compute the evolution of the Reynolds stresses through the expansion. The RDAs neglect the effects of turbulence diffusion and dissipation through the expansion while retaining the turbulence production and pressure terms in the governing equations. Comparison to experimental data was generally good. Smith and Smits[13] also used RDA theory to compute the Reynolds stresses through a rapidly expanded turbulent boundary layer in supersonic flow. The expected decrease in the individual Reynolds stress components through the expansion was accurately calculated with the RDA. As will be discussed below, many of the same effects discussed for rapidly expanded attached boundary layers will also be important for boundary layers which separate through a rapid expansion.

The effects of a rapid expansion on the mean velocity and turbulence properties of a developing free shear layer were investigated by Samimy et al.[14,15] and Petrie et al.[16] using laser Doppler velocimetry (LDV). By comparing the development of a shear layer separated at constant pressure to that of a shear layer which was rapidly expanded at its origin (shear layer inclination angle, $\theta = 15.4$ degrees), the effects of the rapid expansion on the far-field mean velocity and Reynolds stress distributions were deduced. These authors found that the rapidly expanded shear layer had higher peak Reynolds stress values and a stronger normal stress anisotropy $(\sigma_u / \sigma_v)^2$ throughout the majority of the shear layer development. Unfortunately, detailed LDV data were not obtained immediately downstream of the expansion due to inadequate seeding in this region. Peace[17] points out the need for detailed Reynolds stress measurements immediately downstream of boundary layer separation in order to enhance the current computational capabilities for massively separated afterbody flowfields.

The objective of the present paper is to study the development of compressible free shear layers which are formed by separation of a turbulent boundary layer through a rapid expansion (see Fig. 1). The flow conditions in the present experiments are representative of those in the base region of a typical missile or projectile in unpowered supersonic flight. The focus of the investigation will be the shear layer properties immediately downstream of separation which play an important role in determining the mass entrainment rates and subsequent growth of the shear layer. It is the interaction of the shear layer with the recirculation region behind the base (Fig. 1) which directly affects the mean pressure acting on the base surface (i.e., base drag). Included in this study are extensive laser Doppler velocimetry (LDV) measurements made immediately upstream and downstream of the rapid expansion. In addition to the near-interaction region, the approach of the shear layer to self-similarity will be documented to determine the long-term effect of the rapid expansion on shear layer mean velocity and turbulence properties. The effect of the shear layer development on the entire near-wake flowfield of typical, unpowered projectiles has been presented earlier in two companion papers.[18,19]

EXPERIMENTAL FACILITY AND EXPERIMENTAL METHODS

The experiments described herein were conducted in the axisymmetric wind tunnel facility in the University of Illinois Gas Dynamics Laboratory. Specifically designed for the study of axisymmetric afterbody flows, the wind tunnel has several unique features which ensure uniform, axisymmetric flow in the test section; a detailed description of the wind tunnel facility and its operational characteristics can be found in Ref. 20. Two different axisymmetric afterbodies were used in the present investigation: a circular cylinder and a

conical boattailed afterbody (surface angle = 5 degrees). For the cylindrical afterbody, the approach boundary layer separated from the base corner through a rapid expansion with a mean turning angle (θ) of approximately 9 degrees. The rapid expansion at the corner of the boattailed afterbody was considerably weaker with a mean turning angle of approximately 2 degrees. Additional details concerning the approach boundary layer properties will be given below.

The primary diagnostic tool used in these investigations was a two-component LDV with frequency shifting; this system is capable of measuring the relatively high turbulence intensity levels and reversed velocity realizations present in the current separated flowfields. The measurement volume diameter and length were approximately 120 μm and 700 μm, respectively. The LDV data were obtained along radial traverses at several locations (approximately 15-20) along the shear layer axis. To eliminate any effects of the shear layer reattachment region for the present comparisons, only data obtained in the relatively constant pressure region of shear layer development will be presented. The onset of the adverse pressure gradient associated with reattachment is estimated from the data of Amatucci et al.[21] to occur near x = 65 mm for both afterbodies studied herein. The LDV data have been corrected for velocity bias using the interarrival time weighting method which has been shown[22] to be an effective technique in the present flowfields; no correction for fringe bias was necessary.[20] An error analysis of the LDV data reduction procedure was used to estimate a *worst-case* uncertainty in the mean velocity of 1.2% of U_1 and in the rms velocity fluctuation of 2.3% of U_1, where U_1 = 567 m/s is the mean freestream velocity approaching the cylindrical afterbody.

In the current study, silicone oil droplets produced with a conventional six-jet atomizer were used as the laser light scattering media. In a previous experiment with the same seeding apparatus, Bloomberg[23] tested the tracking ability of these particles by measuring their response downstream of an oblique shock wave generated by a 15 degree compression corner in a Mach 2.6 flow. He found mean relaxation distances of approximately 2 mm downstream of the shock and an estimated mean droplet diameter of 0.8 μm. Of course, the mean velocity gradient through the rapid expansion in the present experiments (maximum turning angle of 9 degrees) is considerably weaker than the shock wave in Bloomberg's experiment. The response of the droplets to turbulent fluctuations in the shear layer was also estimated with the results of Samimy and Lele.[24] Using the conditions immediately downstream of separation, the worst-case Stokes number in the present flowfields is approximately 0.6 which yields a *maximum* rms error due to particle lag of approximately 6%. As the shear layer grows, however, the local Stokes number will decrease such that at x = 31 mm downstream of separation, the rms

error due to particle lag is only 1.7%. Further downstream the particle lag error continues to diminish.

RESULTS

A comparison of the mean velocity and turbulence statistics downstream of the two afterbodies will now be presented. In both cases, the boundary layer approaching the separation point was fully turbulent as determined by measured turbulence intensity levels and by the good agreement of the mean velocity profile with a compressible turbulent boundary layer curve fit.[18,19] The pertinent properties of the approach boundary layer for each case are given in Table 1. Note that the afterbody flowfields to be compared have been labeled Case 1 and Case 2 for mean turning angles of θ = 2 degrees and θ = 9 degrees through the rapid expansion, respectively. This convention will be used for convenience throughout the remainder of the paper. The computed average relative Mach number of the developing shear layer is approximately 2.6 (M_c = 1.3) for each case. This relatively high value implies that compressibility undoubtedly has a significant impact on development of the current free shear layers.[1-3]

Initial Shear Layer Structure
Mean Velocity

In this section, the initial development of the shear layer immediately downstream of the separation point will be presented for both cases. Figure 2 shows the development of the nondimensional mean streamwise velocity, U/U_1, for each case where U_1 is the mean freestream velocity approaching the separation point (U_1 = 583 m/s for Case 1 and 567 m/s for Case 2). The magnitude of the plotted variable for each case is shown by the scale at the upper left of the figure. In addition, lines denoting the approximate inner ($U \approx 0.01\Delta U$) and outer ($U \approx 0.99\Delta U$) edges of the shear layer are shown in the figure. The axial (x) and radial (r) location of each data point has been nondimensionalized by the radius of the base at separation (R_o = 28.97 mm for Case 1 and 31.75 mm for Case 2), and the axial station for each data profile is shown by the dashed line to the left of that profile. It should be pointed out that the statistical data shown downstream of separation are relative to the mean shear layer coordinates (x,y as shown in Fig. 1) so that the streamwise velocity statistics are always along the axis of the shear layer.

The transition from the typical turbulent boundary layer mean velocity profile upstream of separation to an error function-type shear layer profile is shown to occur rather smoothly (and rapidly) for Case 1 (Fig. 2a). Immediately downstream of separation for Case 2, however, the mean streamwise velocity profile appears to develop a "kink" where the mean velocity gradient changes abruptly. The discontinuity in the profile slope is similar to that found in rapidly expanded boundary layers[11,12] and most likely represents the interface

3

between an overexpanded viscous sublayer and an outer boundary layer remnant which has reduced turbulence activity due to the rapid expansion. This contention will be shown to be a reasonable one as the turbulence data near separation is presented later in this section. By comparing the mean streamwise velocity profiles between the two cases, it is obvious that the stronger expansion does indeed cause a more pronounced slope discontinuity in the mean velocity profile immediately downstream of separation. The enhanced "kink" in the profile also leads to a larger peak mean velocity gradient as expansion strength increases such that, for only moderate changes in the shear stress, an increase in the primary turbulence production term, $<u'v'>\partial U/\partial y$, occurs. As will be shown, the increase in turbulence production immediately downstream of separation for Case 2 results in higher turbulence levels further downstream as the shear layer develops.

Reynolds Stresses

In addition to the mean velocity profiles near the separation point, the kinematic streamwise (σ_u^2/U_1^2) and transverse (σ_v^2/U_1^2) Reynolds normal stresses and the primary Reynolds shear stress ($<u'v'>/U_1^2$) have also been determined from the LDV data ensembles. Figure 3 shows a comparison of the dimensionless streamwise kinematic Reynolds stress profiles near the separation point for each case. Two rather obvious effects of the rapid expansion are shown in the figure: the decrease in the streamwise turbulent fluctuations over the middle portion of the shear layer as compared to the boundary layer and the large increase in the turbulence levels at the inner edge of the shear layer at the interface of the rapidly expanded boundary layer and the low-speed recirculating fluid immediately downstream of the base. In the more strongly expanded shear layer of Case 2 (Fig. 3b), both effects are amplified relative to Case 1. Recent evidence[11,13] suggests that the decrease in the Reynolds stresses in the outer part of the shear layer is a result of the bulk dilatation associated with the flow through the rapid expansion which becomes more severe as expansion strength increases. The increase in turbulence activity at the inner edge of the shear layer is most likely a result of significant mass entrainment from the low speed recirculation region by large-scale eddies, the effect of which is initially limited to a very narrow region of the shear layer. The location of the sharp peak in the profiles immediately downstream of separation coincides approximately with the location of the peak mean velocity gradient (see Fig. 2). Note also that the majority of the streamwise evolution downstream of separation occurs within the sharply peaked region of the profile with the remaining portion of the expanded boundary layer merely convecting downstream relatively unchanged from its initial profile (the turbulence field is essentially "frozen"). The data shown in Fig. 3 can be contrasted with the rapidly expanded boundary layer data presented by Dussauge and Gaviglio[11] and also to similar data obtained by Smith and Smits,[13] both of which show decreases in the longitudinal Reynolds normal stress across the entire boundary layer profile through the rapid expansion. Of course, it is important to recognize the different post-expansion boundary conditions in the present case (compliant boundary at the inner edge of the shear layer) relative to the rapid expansion of a turbulent boundary layer that remains attached to a solid wall. In fact, even the weakly expanded boundary layer shown in Fig. 3a produces a substantial increase in σ_u^2/U_1^2 relative to the approaching solid wall boundary layer.

The effect of the rapid expansion on the transverse Reynolds normal stress, σ_v^2/U_1^2, is shown in Fig. 4. Relative to the striking changes through the rapid expansion of the streamwise normal stress profiles shown in Fig. 3, the transverse normal stress is only moderately affected by the expansion. Although a peak does appear in the profiles immediately downstream of separation, the magnitude is relatively unchanged from the peak value upstream of separation for both Case 1 and Case 2. This suggests that the time scale associated with the rapid expansion is small enough such that significant turbulence reorganization (component redistribution from streamwise to transverse) does not occur for some distance downstream. Hence, the transverse normal stress, which depends intimately on the pressure-strain and turbulent diffusion reorganization mechanisms, is not immediately affected by the expansion. The bulk dilatation associated with the rapid expansion again causes a decrease in the transverse normal stress which can be seen in the middle of the shear layer when compared to similar regions in the approach boundary layer. By comparing the relative scales used to plot the turbulence data in Figs. 3 and 4, it is obvious that the streamwise Reynolds normal stress far exceeds the transverse component in the peak turbulence region of the shear layer immediately downstream of separation. This point is shown more clearly in Fig. 5 where the normal stress anisotropy (σ_u^2/σ_v^2) profiles near the separation point are shown. As for the peak streamwise normal stress, the peak normal stress anisotropy is approximately a factor of 2 larger for Case 2 than for the weakly expanded shear layer of Case 1, which is expected since the effect of the rapid expansion on the transverse normal stress component was found to be relatively weak. Disregarding the strong peak in the anisotropy profiles near the inner edge of the shear layer, it appears that the rapid expansion has little effect on the anisotropy profile across the remainder of the shear layer when compared to the approach boundary layer. In fact, this result is consistent with the calculations of Smith and Smits[13] who predicted little change in the normal stress anisotropy ratio of a rapidly expanded boundary layer using Rapid Distortion Approximations.

Profiles of the primary Reynolds shear stress, $-<u'v'>/U_1^2$, near the separation point are plotted in Fig. 6 for both cases. The effect of the rapid expansion is shown

to be similar to that shown in Fig. 3 for the streamwise normal stress, namely, a reduction in the stress level over the majority of the shear layer width (bulk dilatation effect) with a sharp peak at the inner edge where the separating boundary layer interfaces with the low-speed recirculating fluid behind the base. It is reasonable to expect large shear stress magnitudes at the inner edge of the shear layer as large-scale organized motions are the primary source of mass entrainment from the low-speed fluid behind the base. As mentioned above, the compliant boundary at the inner edge of the shear layer, which does not restrict the motion of these large-scale eddies, results in significant increases in the magnitudes of the Reynolds stresses when compared to rapidly expanded, supersonic boundary layers along a solid wall.[11,13] When compared to the streamwise normal stress profiles in Fig. 3, the shear stress appears to be more strongly affected by the expansion, as evidenced by the complete absence of any shear stress across the majority of the profile. The destruction of the shear stress in the outer part of the expanded boundary layer implies negligible turbulence production in this region which, as mentioned previously, results in a "frozen" turbulence field that changes very little with downstream distance. Of course, in the region of the strong shear stress peak, a totally different picture of the flow is found. The peak shear stress occurs approximately at the same location as the peak mean velocity gradient which, immediately downstream of separation, is quite large; hence, the primary production term, $<u'v'>\partial U/\partial y$, also reaches a strong peak at this point. Since the turbulence production is primarily centered within a very narrow region of the shear layer profile (i.e., near the peak shear stress location), the normal and shear stress profiles broaden rapidly with downstream distance as the turbulence energy is transferred from the streamwise component (primary extractor of turbulence energy from the mean flow) to the transverse and tangential components through pressure-strain and turbulent diffusion processes.

Quadrant Decomposition Analysis

In order to provide a more detailed description of the structure of the Reynolds stress field immediately downstream of separation, the individual LDV velocity realizations for both cases were analyzed using the quadrant decomposition technique.[25-27] The instantaneous velocity fluctuations (u',v') were determined for the entire ensemble of LDV data at a given spatial location and then plotted against each other as shown in Fig. 7. For all cases shown, the velocity fluctuations are nondimensionalized by the local streamwise root-mean-square velocity fluctuation, σ_u. In this manner, the decomposition provides a comparison of the typical turbulence structure upstream of separation (Fig. 7a, Case 1 shown although Case 2 results are similar) to that immediately downstream of separation for Case 1 (Fig. 7b) and Case 2 (Fig. 7c). The data ensembles shown in Fig. 7 correspond with the peak shear stress location in each case, with the actual (x,r) position of the data ensemble given at the upper right of each figure along with the ensemble-averaged shear stress value. Notice that, in general, the distribution of the turbulence energy (i.e., turbulence structure) changes drastically from the attached boundary layer to the separated shear layer. The quadrant decomposition in the boundary layer (Fig. 7a) displays a wide array of velocity fluctuations with no strong preferential orientation. This is in sharp contrast to the velocity fluctuations shown in Figs. 7b and 7c immediately downstream of separation for Case 1 and Case 2, respectively. In the separated shear layers, the velocity fluctuations tend to become more organized and aligned along a preferential stress direction. Since coherent, large-scale turbulent structures are the most significant contributor to the Reynolds shear stress, it follows from Fig. 7 that the structures in the initial shear layer are more organized than those present in the approach boundary layer. This result is in agreement with Petullo and Dolling[28] who used a dual hot-wire probe to show that the large-scale structures in compressible free shear layers are generally more organized than those in turbulent boundary layers. Dawson and Samimy[9] and Arnette et al.[10] both found that rapid expansions also caused an increase in the organization of the large-scale structures for *attached* boundary layers. In the present case, it appears that the strength of the rapid expansion (compare Cases 1 and 2) may cause a slight increase in the organization of the shear stress, but the boundary layer separation alone (not necessarily the expansion strength) appears to be a more dominant factor in the organization of the shear stress in the present case.

The orientation of the shear stress field was investigated further in the present study by computing the instantaneous shear angle ($\psi = \tan^{-1} v'/u'$) for each velocity realization and then sorting the entire ensemble of angles into histogram form. In this manner, velocity fluctuations which occur in the first and third quadrants will have $\psi > 0$, while quadrants two and four will contain fluctuations with $\psi < 0$. Note that $\psi = 0$ corresponds to a velocity fluctuation along the u' axis (i.e., a purely streamwise fluctuation). The histograms generated for the data shown in Fig. 7 are presented in Fig. 8. As discussed above in relation to the quadrant decomposition, the approach boundary layer velocity fluctuations (Fig. 8a) occur over the entire range of possible shear angles with no dominant shear stress orientation. It is apparent from Fig. 8a, however, that realizations in quadrants 2 and 4 ($\psi < 0$) occur somewhat more frequently that in the other quadrants, which is consistent with the results of Willmarth and Lu[26] and Alving et al.[29] for turbulent boundary layers in subsonic flow. Downstream of boundary layer separation, the distribution of instantaneous shear angles takes quite a different character as shown in Figs. 8b and 8c for Cases 1 and 2, respectively. For the weakly expanded case shown in Fig.

5

8b, the shear stress is strongly oriented around an angle of approximately -12 degrees from the mean flow direction with a percentage of occurrences which is much larger than that in the approach boundary layer. This shows quantitatively the increase in organization of the turbulent structures in the separated shear layers. As the rapid expansion becomes stronger (Fig. 8c), the magnitude of the preferential shear stress angle becomes slightly larger (approximately -16 degrees) although the general shape of the distribution is relatively unchanged from the weakly expanded case. The small increase in the dominant shear angle magnitude with increasing expansion strength may be the result of an increase in the large-scale structure angle relative to the mean flowfield. Although the present data is somewhat inconclusive on this point, Arnette et al.[10] provide some evidence to support this fact in rapidly expanded, attached, supersonic boundary layers.

The histograms of instantaneous shear angle shown in Fig. 8 are effective in identifying the dominant shear direction relative to the mean flowfield, but yield no information as to the magnitude of the dominant velocity fluctuations. To circumvent this problem, the conditional quadrant detection technique of Willmarth and Lu[26] was applied to the data shown in Figs. 7 and 8. In this method, the instantaneous velocity fluctuations are sorted into one of five bins using the following algorithm: if |u'v'| > H |<u'v'>| then the individual realization is placed in its respective quadrant (e.g., when u' > 0 and v' < 0, u'v' is placed in quadrant 4 which is denoted Q4 in the following discussion), but if |u'v'| ≤ H |<u'v'>| the realization is placed into the fifth category which is denoted the *hole*. After sorting the realizations, the five bins are individually averaged to show the quadrants in which large shear stress fluctuations exist. The hole size (H) is essentially a lower threshold for the sorting process and is altered parametrically. The conditional quadrant averages as a percentage of the total, ensemble-averaged shear stress (<u'v'>) are shown as a function of the hole size (H) in Fig. 9 for the same data sets shown in Figs. 7 and 8. The quadrant average $< u' v' >_n$ was computed by the following equation:

$$< u' v' >_n = \frac{\sum (u' v')_n}{N_{tot} < u' v' >} \quad (1)$$

where $(u' v')_n$ is an individual realization in quadrant n and N_{tot} is the number of realizations in the entire data set (in this manner, the sum of the quadrant and hole averages is always 100%). In the boundary layer approaching separation (Fig. 9a), the dominant velocity fluctuations are shown to occur in Q2 (u' < 0 and v' > 0) and Q4 (u' > 0 and v' < 0) which, as discussed by Wallace et al.,[25] correspond to fluid ejections and sweeps, respectively. At H = 10 the majority of the shear stress contribution comes from large fluctuations in Q2 (i.e., fluid ejections from the wall are large and contribute significantly to the total shear stress). These results are similar to those of Alving et al.[29] obtained in an incompressible turbulent boundary layer. Downstream of boundary layer separation (Figs. 9b and 9c), the dominance of the Q2 and Q4 fluctuations becomes very apparent as the Q1 and Q3 contributions to <u'v'> have very small magnitudes for all values of the hole size (H). As discussed previously, the organization of the large-scale structures is enhanced in the shear layer after separation as compared to the approach boundary layer; hence, it is not surprising that the dominant fluctuations in the boundary layer (Q2 and Q4) become more pronounced in the shear layer. The effect of the strength of the rapid expansion on the shear stress distribution appears to be rather small as shown by the similar distributions of Figs. 9b and 9c.

In Figs. 7-9 distributions of the Reynolds stresses at the peak stress locations in the boundary layer and separated shear layers have been presented. However, it is also instructive to investigate the shear stress quadrant distributions at locations other than the shear stress peak. Figure 10 shows conditional quadrant averages for two locations immediately downstream of separation for Case 2: one location on the high-velocity side of the shear stress peak (Fig. 10a) and one location on the low-velocity side of the peak (Fig. 10b). Note that the actual radial position of each data ensemble is shown at the upper left of each figure (as shown in Fig. 7c, the peak shear stress occurs at $r/R_o = 0.973$ for the axial station shown). Figure 10 shows quite clearly that significant changes occur in the Reynolds shear stress distribution near the peak shear location. Compared to the conditional quadrant averages shown in Fig. 9c for the peak shear stress location, the relative distributions between Q2 and Q4 change considerably, which is quite striking when considering the very small difference in absolute radial position between the data shown in Figs. 10a and 10b. On the high-velocity side of the peak, the velocity fluctuations in Q2 far outweigh those in Q4 while the opposite is true on the low-velocity side. At the peak shear stress location, the contributions from Q2 and Q4 are relatively equal (especially when compared to Fig. 10). These results are most likely an effect of the fluctuating interface that defines the inner edge of the shear layer (i.e., the intermittency at the inner edge). For spatial locations within the recirculation region but very near the mean location of the shear layer inner edge (Fig. 10b), significant Q4 events (u' > 0 and v' < 0) occur which can be associated with the passage of large-scale structures in the shear layer. In other words, large fluctuations to the mean flow occur from faster moving (u' > 0) fluid elements which are oriented at a steeper angle (v' < 0) relative to the mean flow (see Fig. 1). At locations where the majority of velocity realizations come from within the shear layer (Fig. 10a), large fluctuations occur in Q2 (u' < 0 and v' > 0) due to the engulfment of low-speed fluid from the recirculating region by the large eddies in the shear layer. As shown in Fig. 9c, peak ensemble-averaged shear stress values occur when the contributions

6

from Q2 and Q4 are approximately equal (i.e., an intermittency at the shear layer inner edge of approximately 0.5). This observed trend was consistent across several axial locations for Case 2 as well as for the weakly expanded shear layer of Case 1, so it is most likely a characteristic of separated shear layers, in general, and not necessarily an effect of the expansion strength itself.

Shear Layer Approach to Self-Similarity

In the previous section, the shear layer characteristics immediately downstream of separation were compared. The strength of the expansion was shown to have a significant effect on the streamwise normal stress and shear stress distributions. In addition, the shear layer appeared more organized than the approach boundary layer with a turbulence field that is strongly aligned in a preferential direction. In the current section, the effects of the rapid expansion are traced further downstream into the region where the shear layer approaches similarity. As will be shown, many of the same features that were prominent in the shear layer immediately downstream of separation persist far downstream into the self-similar region.

Mean Velocity

As mentioned earlier, several authors have suggested that the shear layer initial conditions (i.e., conditions at separation of the boundary layer) can have a significant effect on the mean and turbulence properties in the fully-developed state. Figure 11 is a comparison of the mean streamwise velocity profiles between Case 1 and Case 2 where the data are plotted in similarity coordinates typical of two-stream shear layers (b is the 10%-90% velocity thickness, r_{mid} is the physical center of the shear layer, U_2 is the mean velocity at the inner edge of the shear layer, and ΔU is the mean velocity difference). Note that both Case 1 (open symbols) and Case 2 (closed symbols) data are shown at two axial locations each, both of which are relatively far downstream of separation (in terms of the momentum thickness of the approach boundary layer, θ_1, mean velocity data are shown at $x/\theta_1 \approx 100$ and 200). The mean streamwise velocity profiles across the shear layer collapse reasonably well when plotted in similarity coordinates, suggesting that local self-similarity has been reached in the mean velocity. In addition, the good comparison between Case 1 and Case 2 shown in Fig. 11 suggests that the relatively strong expansion of Case 2, which distorted the *initial* shear layer mean velocity profile (Fig. 2b), has little effect on the mean velocity profile far downstream. All profiles shown exhibit a relatively sharp corner at the outer edge and a more rounded appearance at the inner edge, both of which are characteristic of fully-developed compressible free shear layers.[16] Although mean velocity profiles are shown at only two axial stations for each case, several more data traverses were obtained and, when plotted together, indicate that the mean velocity for both cases

becomes approximately self-similar at $x/\theta_1 \approx 100$. In their studies of compressible shear layers generated by a constant pressure separation, Samimy et al.[15] and Petrie et al.[16] observed mean velocity similarity after $x/\theta_1 \approx 200$ and 250, respectively. The discrepancy between these results and current data is most likely due to the choice of similarity variables which, for the previous investigations,[15-16] neglected the recirculating flow at the inner edge of the shear layer ($U_2 \equiv 0$ using the nomenclature in Fig. 11).

To further compare the mean growth characteristics of the shear layers, the velocity thickness, b, is plotted against axial distance in Fig. 12. Note that the shear layers in both cases shown in Fig. 12 grow approximately linearly beginning almost immediately downstream of separation where the approach to self-similarity is undoubtedly in its early stages. Mehta[8] reported similar behavior for subsonic mixing layers and concluded that linear shear layer growth (db/dx = constant) is a necessary but not sufficient condition for self-similarity. The shear layer velocity thickness distributions shown in Fig. 12 each seem to contain two distinct regions: a region of rapid linear growth almost immediately downstream of separation as the shear layer begins development, and a region of slower linear growth after the shear layer reaches mean velocity self-similarity. The fact that a compressible shear layer grows linearly almost immediately after separation may be a cause for the relatively large discrepancies in the shear layer growth rates reported in the literature.[4] In the present experiments, the growth rate (db/dx) of the shear layers after mean velocity self-similarity had been attained was estimated to be 0.032 and 0.090 for Case 1 and Case 2, respectively. The large difference in these two results will be discussed in detail below in conjunction with the shear layer turbulence characteristics for each case. The growth rate for Case 2 compares favorably with the result of Samimy et al.[15] (db/dx = 0.093) which was measured in a shear layer at nearly the same conditions as the present experiment.

Reynolds Stresses

In addition to spatially independent mean velocity profiles, turbulence data must also collapse into a self-similar form in order for the shear layer to be labeled *fully developed*. Figure 13 shows the streamwise Reynolds normal stress profiles far downstream of the base corner for Case 2. In this figure, the normal stress is nondimensionalized by the square of the velocity difference across the shear layer (ΔU) which changes only slightly with axial distance. Contrary to the mean velocity profiles of Fig. 11, the streamwise normal stress profiles do not reach a self-similar state within the current measurement domain. The last two profiles ($x/R_o = 1.57$ and 1.89), however, seem to collapse fairly well onto one another indicating that self-similarity could have been achieved given a slightly longer development distance.

Several authors (e.g., Refs. 2 and 3) have also found that turbulence properties develop more slowly than the shear layer mean velocity distribution. Profiles of the streamwise Reynolds normal stress for Case 1 were very similar in shape to those shown in Fig. 13, but the peak values at the far downstream axial stations were reduced by approximately 10%. The transverse Reynolds normal stress $(\sigma_v/\Delta U)^2$ and the primary Reynolds shear stress $(<u'v'>/\Delta U^2)$ profiles for each case exhibited even slower development than the streamwise normal stress with no apparent self-similar distributions at the last measurement station. In addition, peak values at the last measurement station were again higher for Case 2 (20% for the transverse normal stress and 11% for the primary shear stress) when compared to Case 1. It is apparent from these data that information on the turbulence property development is essential when establishing the *fully-developed* state of compressible shear layers. Also, the far-field effect of increasing expansion strength at the shear layer origin is to increase the overall turbulence levels in the shear layer which, in turn, implies larger shear layer growth rates (see Fig. 12). Obviously, the elevated initial streamwise normal stress and shear stress levels along with larger initial turbulence production rates in Case 2 combine to enhance the far-field Reynolds stress magnitudes relative to Case 1.

Immediately downstream of separation, the strength of the rapid expansion was shown to have a significant impact on the relative distribution of the Reynolds normal stresses (Fig. 5) in the shear layer; the peak normal stress anisotropy ratio (σ_u^2/σ_v^2) for Case 2 was approximately a factor of 2 larger than that for Case 1. To investigate the persistence of this disturbance in the far-field, a comparison of the normal stress anisotropy profiles at the last measurement station of the present data is shown in Fig. 14. In addition to having reduced peak values from those immediately downstream of separation, both profiles appear similar in shape although the peak magnitudes are slightly larger for the Case 1 data. The decrease in the peak anisotropy ratio from that immediately downstream of separation is largely a result of turbulent diffusion which transfers turbulent energy from the initially narrow Reynolds stress peak outward in the shear layer to regions of lower turbulence. The shear stress correlation coefficient, $<u'v'>/(\sigma_u\sigma_v)$, was also found to recover rather quickly from distorted profiles immediately downstream of separation. Hence, it appears that the effects of the rapid expansion persist far downstream in terms of the absolute magnitudes of the turbulence quantities, but become relatively unimportant in determining the far-field *structure* of the shear layer turbulence field (i.e., distribution of turbulence energy between the Reynolds stress components).

As discussed above, the quadrant decomposition technique is an effective method to present the distribution and organization of the Reynolds stress field. Figure 15 shows the hole diagram for Case 2 at the peak

shear stress location far downstream of the shear layer origin $(x/R_0 = 1.57)$. When compared to the similar diagram immediately downstream of separation (Fig. 9c), it is apparent that velocity fluctuations from Q2 and Q4 again dominate the shear stress field. However, it appears that the two positive shear stress quadrants (Q1 and Q3) play a more significant role in the shear layer turbulence field far downstream and, in fact, reach contribution levels (approximately -20%) that are very similar to those shown previously in the approach boundary layer (Fig. 9a). The hole diagram for Case 1 at $x/R_0 = 1.55$ was found to be very similar to that shown in Fig. 15 for Case 2. This observation supports the previous contention that the relative distribution of the Reynolds stresses in the far-field is relatively unaffected in the present case by the strength of the expansion at its origin.

The rapid expansion was shown to strongly affect the streamwise normal stress immediately downstream of separation (Fig. 3), but to have little effect on the transverse component (Fig. 4). In Fig. 16 the peak streamwise and transverse normal stress levels for each case are compared at various axial positions along the shear layer axis. The peak streamwise normal stress distributions for the two cases (Fig. 16a) are very similar in shape with a peak immediately downstream of boundary layer separation followed by a relaxation to a local minimum and then sustained growth to the end of the measurement domain. However, the magnitudes for Case 2 are everywhere larger than those for Case 1, especially immediately downstream of separation where the effects of the rapid expansion are largest. This again supports the prior conclusion that the rapid expansion affects the overall turbulence levels in the shear layer far downstream of the shear layer origin. The short relaxation region downstream of separation is similar to that observed by Gaviglio et al.[30] in their hot-wire study of supersonic base flows and is essentially a relaxation region downstream of the rapid expansion. The lag between the location of peak turbulence production (immediately downstream of separation) and the start of increasing streamwise normal stress levels appears to be a function of the expansion strength (Fig. 16a). The peak transverse Reynolds normal stress distributions shown in Fig. 16b exhibit relatively small magnitudes shortly downstream of separation that increase with downstream distance over the majority of the measurement domain. As in the streamwise component, the transverse normal stress far downstream of the shear layer origin is greater for Case 2 than for Case 1. In fact, the redistribution of turbulent energy from the streamwise component to the transverse and tangential components is the primary mechanism for increasing the transverse normal stress as shown in Fig. 16b (transverse normal stress production is small everywhere). Since the shear layer in Case 2 has higher streamwise normal stress levels throughout its development than Case 1, it is reasonable that the transverse normal stress far downstream should be larger

for Case 2. Notice that the difference between the two cases becomes greater with downstream distance which shows the continued effect of the elevated streamwise normal stress levels for Case 2.

SUMMARY AND CONCLUSIONS

An experimental investigation of the effects of a rapid expansion on the development of compressible free shear layers has been presented. Two shear layers with rapid expansions of different strengths have been compared, and from these data, the following conclusions can be drawn:

(1) The rapid expansion distorts the initial mean velocity profile of the shear layer in a manner similar to rapidly expanded, attached, supersonic boundary layers. Namely, a "kink" in the mean velocity profile or discontinuity in the mean velocity gradient is generated which appears to mark the interface between two distinct regions in the initial shear layer: an inner region with significant turbulence levels and rapid streamwise growth, and an outer region of "frozen" turbulence which convects downstream relatively unchanged. Transition from the distorted initial mean velocity profile to a typical error function-type shear layer profile occurs very rapidly.

(2) The turbulence field immediately downstream of separation is altered in magnitude and structure by the rapid expansion. Over the majority of the shear layer width, turbulence activity is reduced from the levels in the approach boundary layer most likely due to bulk dilatation effects; however, at the interface of the shear layer and the recirculating fluid at the inside edge, large streamwise normal stresses and shear stresses are present, which are magnified substantially by the rapid expansion. This may be due to an enhancement of the energy-containing, large-scale turbulent structures through the rapid expansion which entrain low-speed fluid along the inside edge of the shear layer. The peak transverse Reynolds normal stress, on the other hand, is largely unaffected by the expansion.

(3) Analysis of the initial Reynolds stress field using the quadrant decomposition technique shows an increase in the shear stress organization when compared to the approach boundary layer, although the effect of the expansion strength on the degree of organization appears small over the range investigated here. At the peak shear stress location immediately downstream of separation, turbulent fluctuations from quadrants 2 and 4 contribute equally to the shear stress while fluctuations in quadrants 1 and 3 are negligible.

(4) Far downstream of the rapid expansion $(x/\theta_1 > 100)$, the mean velocity profiles reach a common self-similar form that is apparently unaffected by the magnitude of the rapid expansion. The turbulence properties develop more slowly than the mean velocity and do not reach self-similarity within the present measurement domain.

(5) The strength of the rapid expansion at the shear layer origin is felt far downstream as an increase in the overall turbulence levels in the shear layer. At the last measurement station presented herein, the peak streamwise normal stress, transverse normal stress, and primary shear stress for the stronger expansion case were 10%, 20%, and 11% larger, respectively, than the peak values for the weakly expanded case. The large increase in the transverse normal stress is a result of the continued elevation of the streamwise normal stress in conjunction with the redistribution mechanisms for turbulent energy exchange between the components. A similar argument holds for the primary shear stress which gains turbulent energy from the mean flowfield primarily through transverse velocity fluctuations.

(6) Although the magnitudes of the Reynolds stresses in the shear layer are enhanced by the strength of a rapid expansion at its origin, the relative distribution of the turbulence energy between the Reynolds stress components (i.e., turbulence structure) far downstream of the origin is relatively unaffected.

ACKNOWLEDGMENT

REFERENCES

[1] Papamoschou, D., and Roshko, A., "The Compressible Turbulent Shear Layer: An Experimental Study," *Journal of Fluid Mechanics*, Vol. 197, 1988, pp. 453-477.

[2] Samimy, M., and Elliott, G.S., "Effects of Compressibility on the Characteristics of Free Shear Layers," *AIAA Journal*, Vol. 28, No. 3, 1990, pp. 439-445.

[3] Goebel, S.G., and Dutton, J.C., "Experimental Study of Compressible Turbulent Mixing Layers," *AIAA Journal*, Vol. 29, No. 4, 1991, pp. 538-546.

[4] Viegas, J.R., and Rubesin, M.W., "A Comparative Study of Several Compressibility Corrections to Turbulence Models Applied to High-Speed Shear Layers," AIAA Paper 91-1783, Honolulu, HI, June, 1991.

[5] Bunyatitradulya, A., and Papamoschou, D., "Acetone PLIF Imaging of Turbulent Shear Layer Structure at High Convective Mach Number," AIAA Paper 94-0617, Reno, NV, Jan. 1994.

[6] Bradshaw, P., "The Effect of Initial Conditions on the Development of a Free Shear Layer," *Journal of Fluid Mechanics*, Vol. 26, Part 2, 1966, pp. 225-236.

[7] Mehta, R.D., and Westphal, R.V., "Near-Field Turbulence Properties of Single and Two-Stream Plane Mixing Layers," *Experiments in Fluids*, Vol. 4, 1986, pp. 257-266.

[8] Mehta, R.D., "Effect of Velocity Ratio on Plane Mixing Layer Development: Influence of the Splitter

Plate Wake," *Experiments in Fluids*, Vol. 10, 1991, pp. 194-204.

[9]Dawson, J.A., and Samimy, M., "The Effects of Expansion on a Supersonic Boundary Layer: Surface Pressure Measurements," AIAA Paper 94-0648, Reno, NV, Jan. 1994.

[10]Arnette, S.A., Samimy, M., and Elliott, G.S., "The Effect of Expansion on the Large Scale Structure of a Compressible Turbulent Boundary Layer," AIAA Paper 93-2991, Orlando, FL, July 1993.

[11]Dussauge, J.P., and Gaviglio, J., "The Rapid Expansion of a Supersonic Turbulent Flow: Role of Bulk Dilatation," *Journal of Fluid Mechanics*, Vol. 174, 1987, pp. 81-112.

[12]Hampton, L.P., and White, R.A., "The Effect of Sudden Expansions and Compressions on Turbulent Boundary Layer Momentum Thickness in Supersonic Flow," ASME Paper 86-WA/FE-11, Anaheim, CA, Dec. 1986.

[13]Smith, D.R., and Smits, A.J., "The Rapid Expansion of a Turbulent Boundary Layer in a Supersonic Flow," *Journal of Theoretical and Computational Fluid Dynamics*, Vol. 2, No. 5/6, 1991, pp. 319-328.

[14]Samimy, M., Petrie, H.L., and Addy, A.L., "Reattachment and Redevelopment of Compressible Turbulent Free Shear Layers," *International Symposium on Laser Anemometry*, ASME, New York, FED Vol. 33, 1985, pp. 159-166.

[15]Samimy, M., Petrie, H.L., and Addy, A.L., "A Study of Compressible Turbulent Reattaching Free Shear Layers," *AIAA Journal*, Vol. 24, No. 2, 1986, pp. 261-267.

[16]Petrie, H.L., Samimy, M., and Addy, A.L., "Compressible Separated Flows," *AIAA Journal*, Vol. 24, No. 12, 1986, pp. 1971-1978.

[17]Peace, A.J., "Turbulent Flow Predictions for Afterbody/Nozzle Geometries Including Base Effects," *Journal of Propulsion and Power*, Vol. 7, No. 3, 1991, pp. 396-403.

[18]Herrin, J.L., and Dutton, J.C., "Supersonic Base Flow Experiments in the Near Wake of a Cylindrical Afterbody," *AIAA Journal*, Vol. 32, No. 1, 1994, pp. 77-83.

[19]Herrin, J.L., and Dutton, J.C., "Effects of Afterbody Boattailing on the Near Wake of Axisymmetric Bodies in Supersonic Flow," AIAA Paper 94-0029, Reno, NV, Jan. 1994.

[20]Herrin, J.L., "An Experimental Investigation of Supersonic Axisymmetric Base Flows Including the Effects of Afterbody Boattailing," Ph.D. Thesis, Dept. of Mechanical and Industrial Engineering, Univ. of Illinois at Urbana-Champaign, Urbana, IL, 1993.

[21]Amatucci, V.A., Dutton, J.C., Kuntz, D.W., and Addy, A.L., "Two-Stream Supersonic Wake Flowfield Behind a Thick Base, Part 1: General Features," *AIAA Journal*, Vol. 30, No. 8, 1992, pp. 2039-2046.

[22]Herrin, J.L., and Dutton, J.C., "An Investigation of LDV Velocity Bias Correction Techniques for High-Speed Separated Flows," *Experiments in Fluids*, Vol. 15, 1993, pp. 354-363.

[23]Bloomberg, J.E., "An Investigation of Particle Dynamics Effects Related to LDV Measurements in Compressible Flows," M.S. Thesis, Dept. of Mechanical and Industrial Engineering, Univ. of Illinois at Urbana-Champaign, Urbana, IL, 1989.

[24]Samimy, M., and Lele, S.K., "Motion of Particles with Inertia in a Compressible Free Shear Layer," *Physics of Fluids-A*, Vol. 3, No. 8, 1991, pp. 1915-1923.

[25]Wallace, J.M., Eckelmann, H., and Brodkey, R.S., "The Wall Region in Turbulent Shear Flow," *Journal of Fluid Mechanics*, Vol. 54, 1972, pp. 39-48.

[26]Willmarth, W.W., and Lu, S.S., "Structure of the Reynolds Stress Near the Wall," *Journal of Fluid Mechanics*, Vol. 55, 1972, pp. 65-92.

[27]Lu, S.S., and Willmarth, W.W., "Measurements of the Structure of the Reynolds Stress in a Turbulent Boundary Layer," *Journal of Fluid Mechanics*, Vol. 60, 1973, pp. 481-511.

[28]Petullo, S.P., and Dolling, D.S., "Large-Scale Structure Orientation in a Compressible Turbulent Shear Layer," AIAA Paper 93-0545, Reno, NV, Jan. 1993.

[29]Alving, A.E., Smits, A.J., and Watmuff, J.H., "Turbulent Boundary Layer Relaxation from Convex Curvature," *Journal of Fluid Mechanics*, Vol. 211, 1990, pp. 529-556.

[30]Gaviglio, J., Dussauge, J.P., Debieve, J.F., and Favre, A., "Behavior of a Turbulent Flow Strongly Out of Equilibrium at Supersonic Speeds," *Physics of Fluids*, Vol. 20, No. 10, Part II, 1977, pp. 179-192.

Table 1 Summary of Approach Boundary Layer and Freestream Properties

	Case 1	Case 2
M_1	2.61	2.46
M_2	2.71	2.85
Re_θ	15700	13700
δ (mm)	4.5	3.2
δ^* (mm)	1.33	0.98
θ (mm)	0.33	0.26
H	3.98	3.73
Π	1.19	1.37
C_f	0.00142	0.00148
u_τ (m/s)	22.4	21.2
θ (degs)	2	9

Figure 2 Mean Streamwise Velocity Profiles Near Separation, U/U_1: (a) Case 1, (b) Case 2

Figure 1 Sketch of the Mean Flowfield Near the Shear Layer Origin
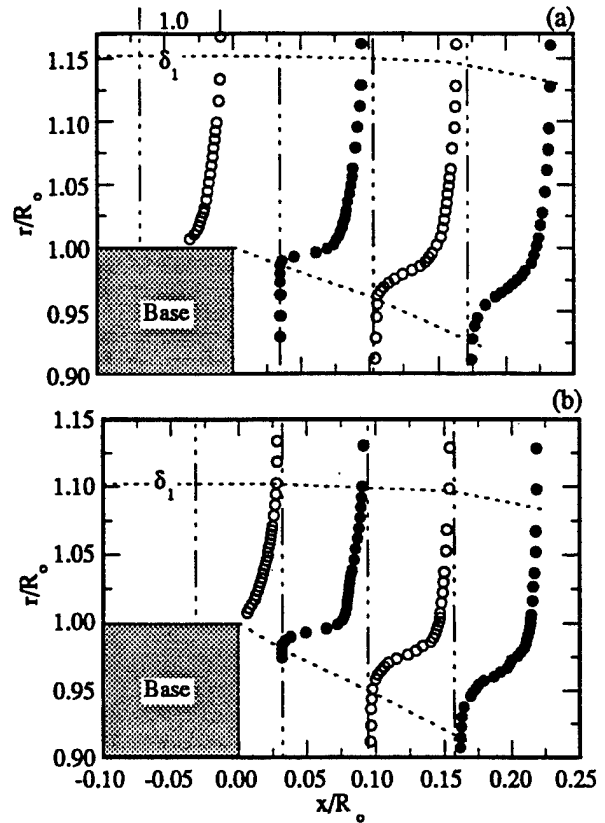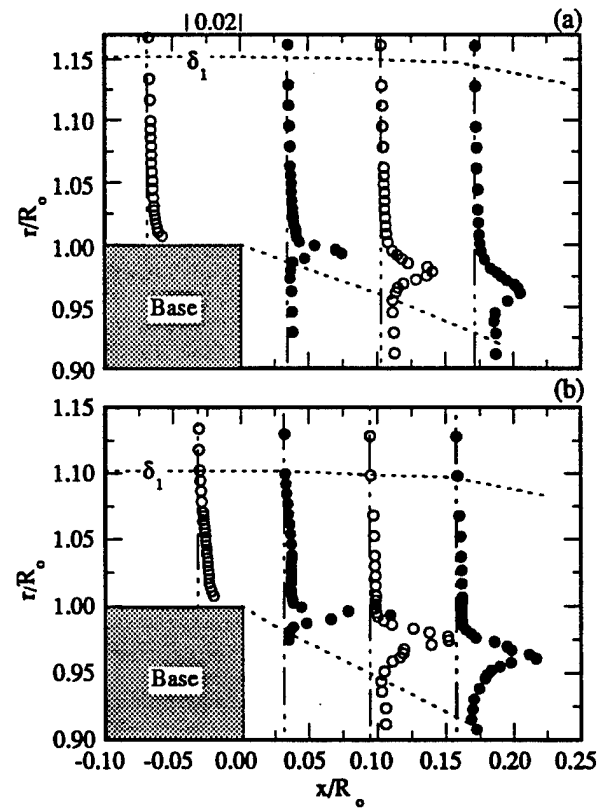
Figure 3 Streamwise Reynolds Normal Stress Profiles Near Separation, $(\sigma_u/U_1)^2$: (a) Case 1, (b) Case 2

11
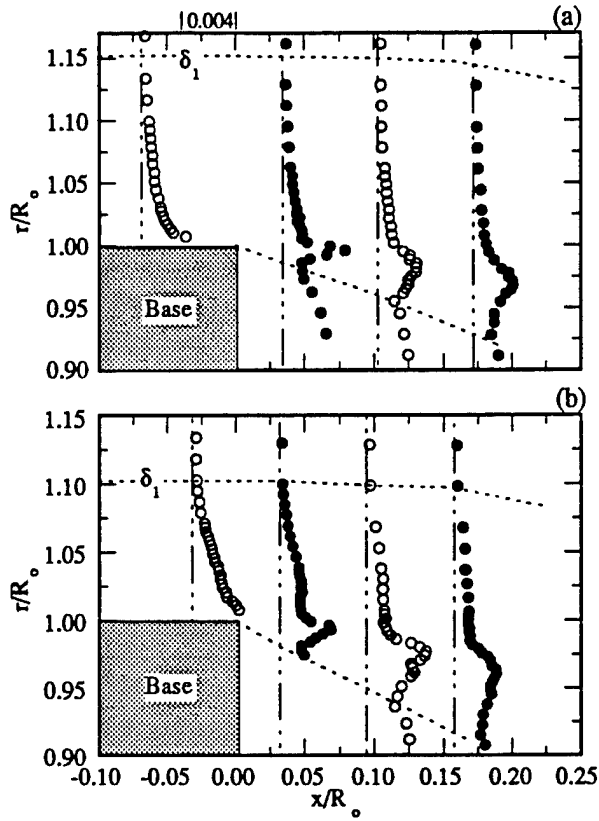
Figure 4 Transverse Reynolds Normal Stress Profiles
Near Separation, $(\sigma_v/U_1)^2$: (a) Case 1,
(b) Case 2
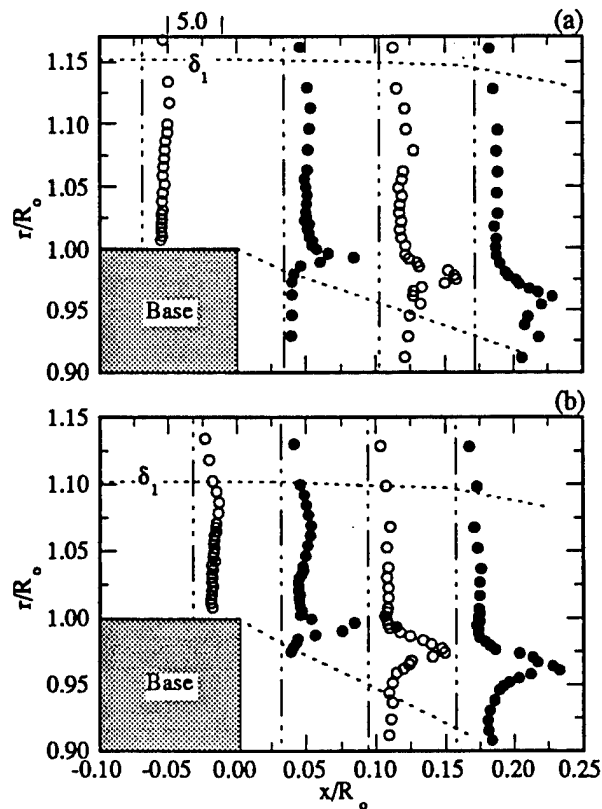
Figure 5 Normal Stress Anistropy Profiles Near
Separation, $(\sigma_u/\sigma_v)^2$: (a) Case 1, (b) Case 2
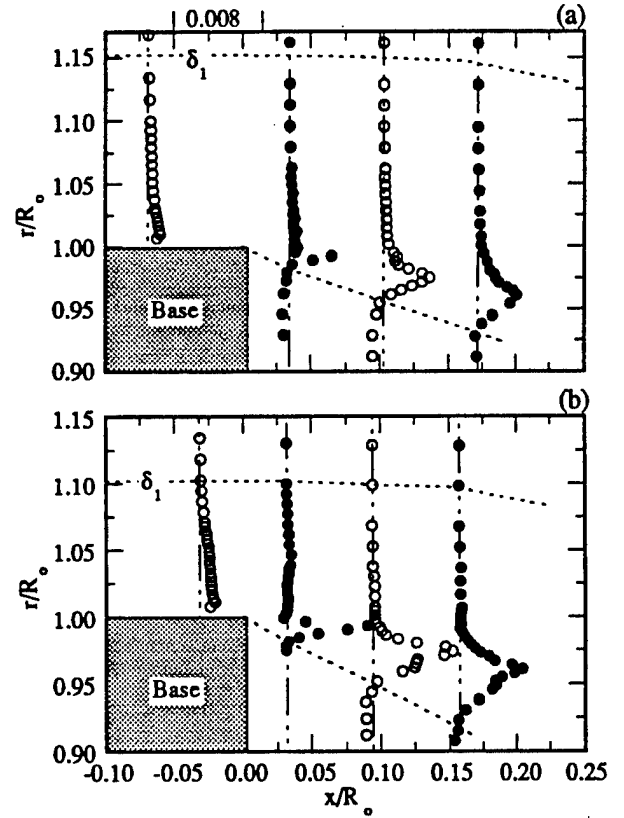
Figure 6 Primary Reynolds Shear Stress Profiles
Near Separation, $-\langle u'v' \rangle/U_1^2$: (a) Case 1,
(b) Case 2

12
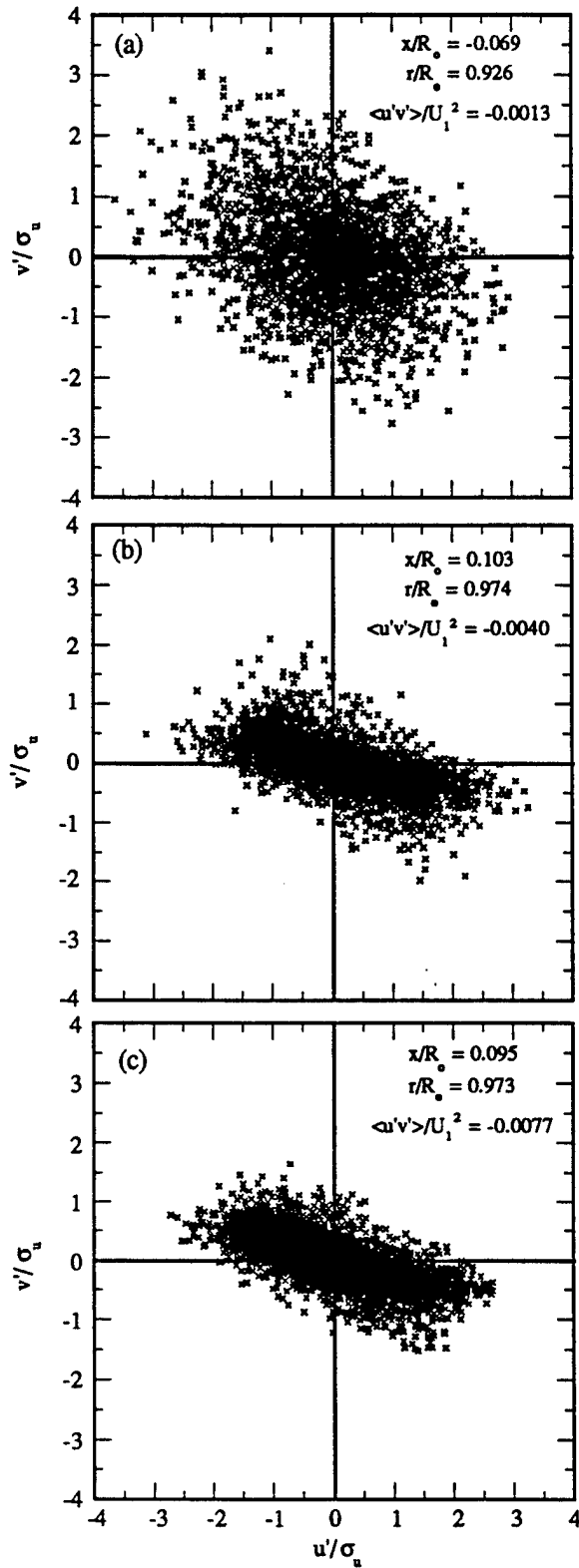
Figure 7 Shear Stress Quadrant Decomposition Near
Separation: (a) Approach Boundary Layer
Case 1, (b) Downstream of Separation Case
1, (c) Downstream of Separation Case 2
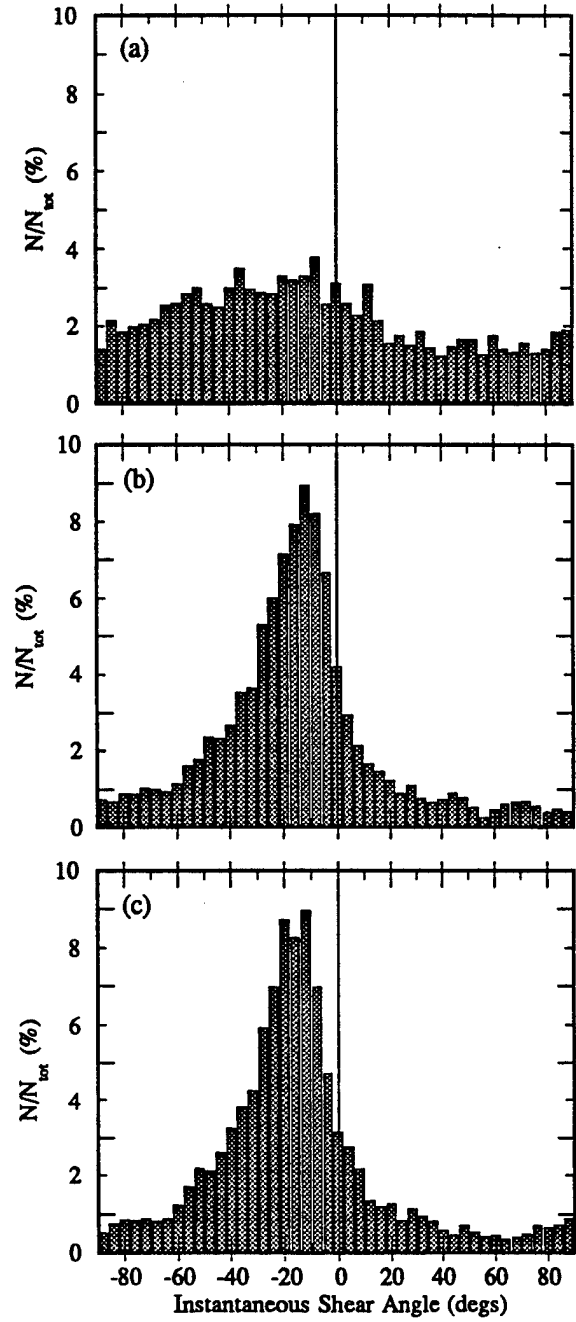
Figure 8 Histograms of Instantaneous Shear Angle:
(a) Approach Boundary Layer Case 1,
(b) Downstream of Separation Case 1,
(c) Downstream of Separation Case 2
(same spatial locations as Fig. 7)
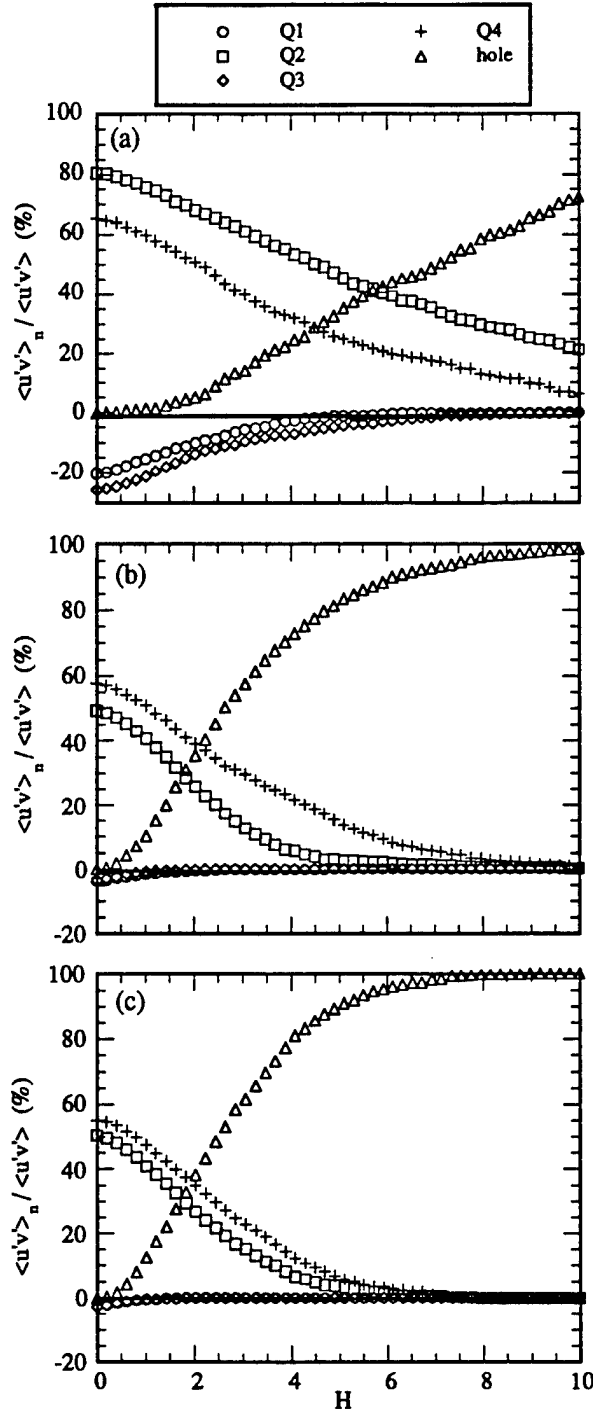
Figure 9 Quadrant Contributions to Ensemble-Averaged Shear Stress: (a) Approach Boundary Layer Case 1, (b) Downstream of Separation Case 1, (c) Downstream of Separation Case 2 (same locations as Fig. 7)
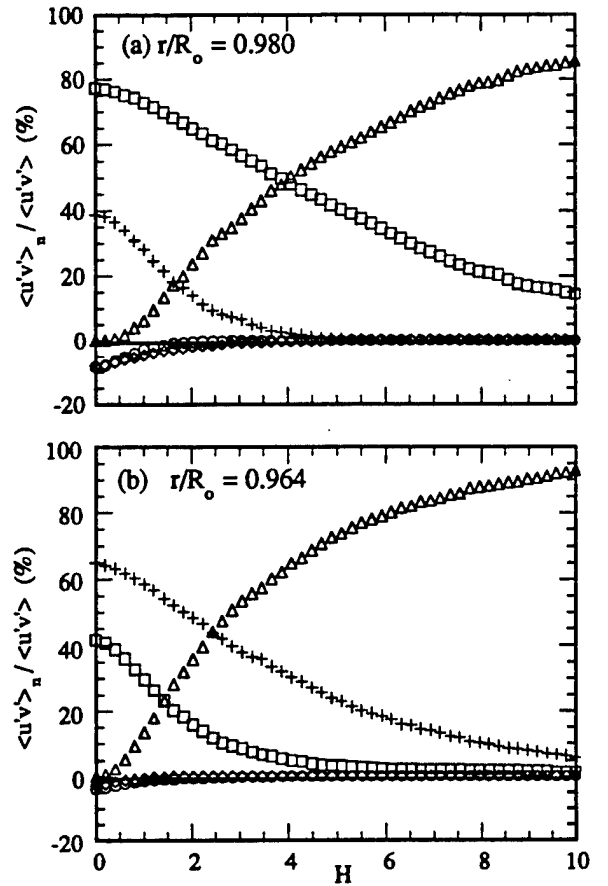
Figure 10 Quadrant Contributions to Ensemble-Averaged Shear Stress at $x/R_o = 0.095$ for Case 2: (a) High-Velocity Side of Peak $<u'v'>$ Location, (b) Low-Velocity Side of Peak $<u'v'>$ Location
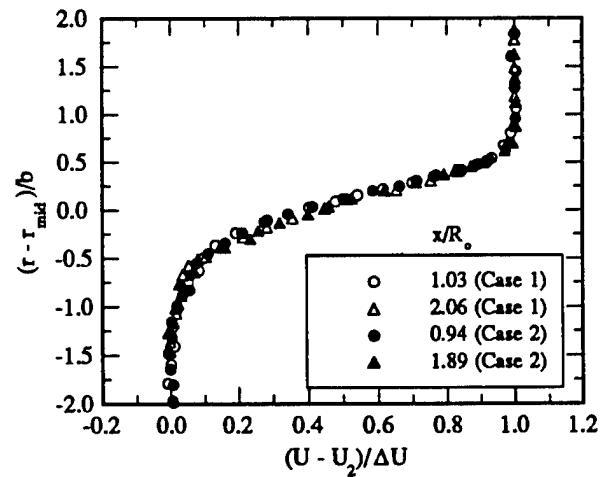
Figure 11 Mean Streamwise Velocity Profiles in Similarity Coordinates; Open Symbols - Case 1, Filled Symbols - Case 2
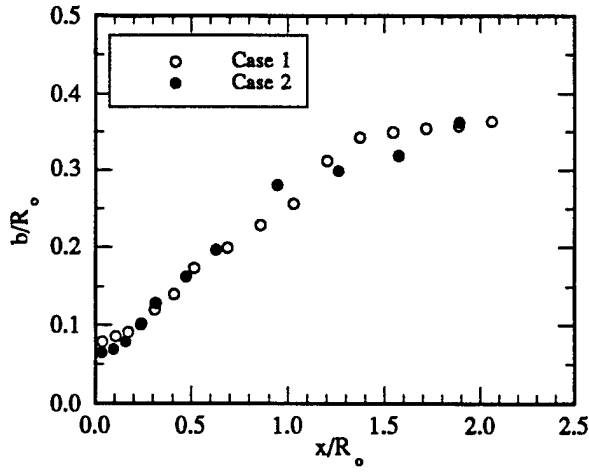
Figure 12 Shear Layer Velocity Thickness Comparison

Figure 15 Quadrant Contributions to Ensemble-Averaged Shear Stress at $x/R_o = 1.57$ and $r/R_o = 0.47$ for Case 2
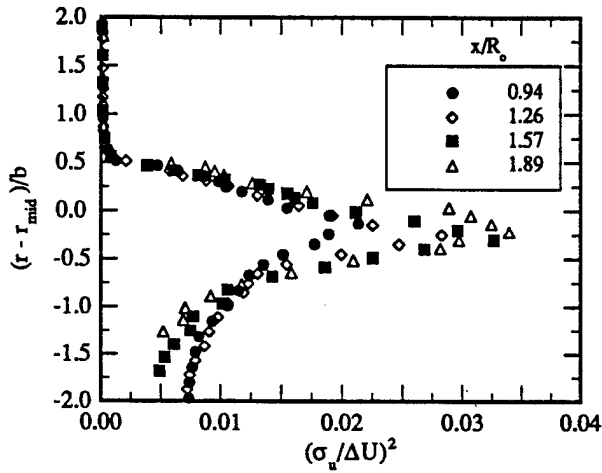
Figure 13 Streamwise Reynolds Normal Stress Profiles in Similarity Coordinates for Case 2
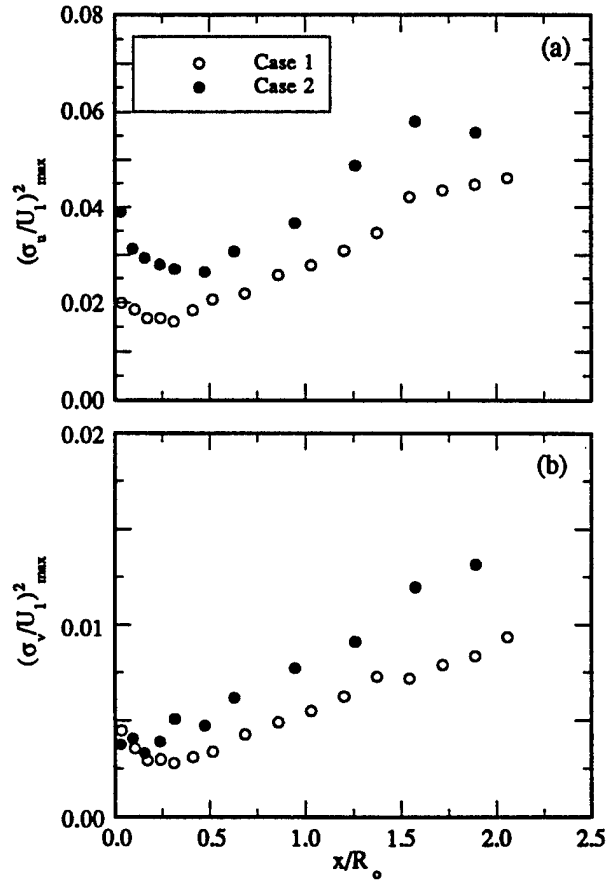
Figure 16 Comparison of Peak Reynolds Normal Stress Distributions: (a) Streamwise Component, (b) Transverse Component

Figure 14 Reynolds Normal Stress Anisotropy Comparison at $x/R_o \approx 2.0$

APPENDIX A.17

BASE BLEED EXPERIMENTS WITH A CYLINDRICAL AFTERBODY IN
SUPERSONIC FLOW

AIAA Paper No. 95-0062

Presented at the *33rd AIAA Aerospace Sciences Meeting*

Reno, Nevada

January 1995

by

T. Mathur and J. C. Dutton

AIAA 95-0062

Base Bleed Experiments with a Cylindrical Afterbody in Supersonic Flow

T. Mathur and J.C. Dutton
Department of Mechanical and Industrial Engineering
University of Illinois at Urbana-Champaign
Urbana, Illinois

33rd Aerospace Sciences Meeting and Exhibit
January 9-12, 1995 / Reno, NV

BASE BLEED EXPERIMENTS WITH A CYLINDRICAL AFTERBODY IN SUPERSONIC FLOW

T. Mathur[*] and J.C. Dutton[†]
Department of Mechanical and Industrial Engineering
University of Illinois at Urbana-Champaign
Urbana, Illinois

ABSTRACT

The effect of base bleed on the near-wake flowfield of a cylindrical afterbody aligned with a Mach 2.5 flow has been investigated. This study is aimed at better understanding the complex fluid dynamic interactions occurring in the near-wake due to base bleed and is motivated by the lack of detailed velocity and turbulence data in this flowfield The experimental techniques used include static pressure measurements along the afterbody and the base plane, schlieren and shadowgraph photography, and centerline traverses using two-component laser Doppler velocimetry (LDV). Results indicate relatively uniform radial pressure profiles across the base plane. With increasing bleed flowrate (quantified by the injection parameter, I), the average base pressure is found to increase initially, attain a peak value near $I = 0.0148$, and then decrease with further increase in I. The optimum bleed condition near $I = 0.0148$ is also characterized by a weak corner expansion, a minimum value of the free shear layer angle, and the near-disappearance of the recirculation region (reverse velocity) along the centerline of the near-wake.

INTRODUCTION

Flow separation at the base of aerodynamic vehicles such as missiles, rockets, and projectiles leads to the formation of a low-speed recirculation region near the base. The pressure in this region is generally significantly lower than the freestream pressure. Base drag, caused by this difference in pressures, can be up to two-thirds of the total drag on a body of revolution. Techniques such as boattailing, base burning, and base bleed have been used traditionally to reduce base drag; however, in the past, these techniques were applied in an empirical manner due to a lack of detailed data and understanding of the fluid dynamic interactions occurring in the base region. With the advent of laser-based optical flow diagnostic techniques in the past decade, it is now possible to examine these flowfields in greater detail in a non-intrusive manner. Recently, a detailed investigation of supersonic axisymmetric base flows including the effects of afterbody boattailing was completed by Herrin and Dutton[1,2]. The proposed research on base bleed is the logical extension of this recent investigation.

Figure 1 is a flowfield schematic of supersonic flow over a blunt, cylindrical body with base bleed. The supersonic freestream flow undergoes an expansion at the base corner as the turbulent approach boundary layer separates and forms a free shear layer. This shear layer eventually undergoes recompression, realignment, and redevelopment in the wake of the afterbody as it is constrained to turn along the axis of symmetry. The shear layer entrains fluid from the region behind the base and accelerates it. A recompression shock system returns this fluid to the base region, forming a recirculation region in the process. Injection of low-speed fluid into the base region displaces the forward stagnation point downstream of the base plane. The location of the forward stagnation point is determined by a balance between the momentum of the injected gas and that of the recirculating fluid. The magnitude of the bleed flow rate is quantified using a non-dimensional injection parameter, I, defined as the bleed mass flow rate normalized by the product of the base area and the freestream mass flux. This definition of the injection parameter does not account for the approach boundary layer thickness and the bleed flow momentum, both of which have been shown to affect the base pressure in a manner analogous to base bleed.

The effect of varying the bleed mass flowrate on the base pressure ratio has been studied experimentally by several researchers[3-7]. The results of these experiments exhibit certain common trends and indicate three distinct operating regimes determined by the quantity of mass injected. The base pressure ratio increases fairly linearly with bleed rate at low values of I (regime 1). A peak in the base pressure ratio occurs at an intermediate value of I (near $I = 0.01$ for air), the value of which depends on several factors including the freestream Mach number, the size and geometry of the bleed orifice, and the flowrate, molecular weight, and temperature of the bleed gas. Increases in base pressure ratio (relative to the no-bleed case) from 10 to 90% have been reported for various combinations of the aforementioned parameters. As the bleed rate is

---

[*]Graduate Research Assistant, Student Member AIAA.
[†]Professor, Associate Fellow AIAA.

1

increased past the optimum value, the base pressure ratio decreases (regime 2) until it reaches a relative minimum. A further increase in the bleed flow leads to the onset of power-on conditions (regime 3) when the bleed flow becomes supersonic, resulting in an increase in base pressure ratio.

From the combined results of the above experiments, base bleed effectiveness is seen to increase with freestream Mach number, i.e., at higher Mach numbers, the peak base pressure occurs at lower I, and the percentage increase in base pressure is also higher. The effects of the bleed jet exit area on base pressure have also been investigated[3,4,6-8]. At very low bleed-rates, the increase in base pressure with bleed is nearly independent of the area ratio; however, at higher bleed rates, the effectiveness of base bleed was shown to be improved by larger jet-to-base diameter ratios. Injection with porous bases is found to be the most effective.

Experiments using air, hydrogen, helium, argon, and nitrogen have shown that base bleed is more effective when a bleed gas with lower molecular weight (relative to the freestream gas) is used[8,9]. The peak base pressure is higher, and occurs at a lower value of I with a lighter bleed gas. Significant increases in base pressure have also been observed using a heated bleed gas[10]. At low injection rates, the base pressure rise is nearly proportional to the enthalpy of the bleed gas. The peak base pressure is higher, and occurs at a lower value of I, than the corresponding cold bleed case. Base burning with hydrogen results in even higher base pressures than the hot bleed case[9]. Base bleed with fuel-rich solid combustion[11] has been shown to be even more effective. The advantage of combustion and burning over hot gas injection is suspected to be due to the different mechanisms and locations of enthalpy release in the wake. Investigation of the combined effects of boattailing and base bleed[12] showed that although the two effects were additive, there was a very weak dependence of optimum boattail angle on bleed rate, and of optimum bleed rate on boattail angle.

While the effectiveness of base bleed as a drag reducing technique is well known, the details of the fluid dynamic interactions caused by base bleed are not clearly understood. Most of the above experimental investigations were carried out prior to the development of reliable non-intrusive diagnostic methods, and their scope was primarily limited to determining the global influence of various base bleed parameters on base pressure. Some results from earlier studies are also unreliable due to possible interference arising from model support effects[3,6] or nozzle flow nonuniformity effects. In addition, the results of some of the previous investigations of base bleed have been confounded by

the added influences of boattailing, hot gas injection, and/or base burning/combustion. A clear understanding of the base bleed phenomenon is hampered by a lack of detailed flowfield data.

Analytical models based on an empirical component-type approach[13] provide some insight into the physical processes that might be associated with base bleed. Although these models can only represent the base bleed flowfield in a time-mean sense, and can not account for its instantaneous turbulent nature, they have been fairly successful in predicting the qualitative effects of base bleed on base pressure[14-17]. Base bleed computations using the Reynolds-averaged Navier-Stokes equations carried out at the Army Research Laboratory[18-22] have also been successful in predicting qualitative base pressure trends and in capturing flowfield structure details. Numerical techniques are currently limited by turbulence modeling issues, insufficient grid resolution, and lack of detailed experimental data for validation.

Recent experimental efforts have provided insight into the complex interactions prevalent in the near-wake flowfields of blunt-based[1] and boattailed[2] afterbodies; however, no known detailed measurements of the base bleed flowfield have been made to date. The objectives of the present research are to investigate the effects of base bleed on the near-wake flowfield of a cylindrical afterbody in supersonic flow, and to identify the dominant fluid dynamic mechanisms inherent in this complex flow with the aid of laser-based optical diagnostic techniques. The measurements obtained provide a set of benchmark baseline data that will enhance the overall understanding of base flow phenomena and also serve to validate modeling and computational efforts in this field.

EXPERIMENTAL FACILITIES AND EQUIPMENT

Figure 2 is a schematic of the supersonic, blow-down type wind tunnel at the University of Illinois Gas Dynamics Laboratory designed solely for the study of axisymmetric base flows. High pressure air from a tank farm enters the top of the stagnation chamber, and passes through a screen-honeycomb-screen flow conditioning module. The air is expanded to a design Mach number of 2.5 in the test section using a converging-diverging nozzle. The pressure and temperature in the stagnation chamber are 471 ± 3.5 kPa and 300 ± 2 K, respectively. Two square glass side windows provide optical access to the flowfield. The air in the test section exits through a conical diffuser and exhaust duct to the atmosphere. The afterbody is mounted at the end of a hollow sting, which is

supported at two axial locations upstream of the nozzle to avoid support disturbances in the flowfield. A detailed description of the wind tunnel design is provided by Herrin[23].

For the purposes of the base bleed study, several additions were made to the existing wind tunnel. A stainless steel bleed line was designed and constructed with 2" diameter pipe sections to facilitate conditioning, measurement, and control of the bleed flow. Since the base pressure is significantly sub-atmospheric, ambient room air at 293 ± 2 K is an adequate source for the bleed air supply. The inlet consists of a screen followed by an elliptically rounded intake section to condition the incoming bleed flow. This is followed by about 4 feet of pipe to ensure adequate flow development prior to the mass flow meter. The Sierra 760 electronic flow meter consists of a temperature and a velocity probe and works on the hot-wire principle. The linearized output is directly proportional to the actual mass flow rate, and is unaffected by pressure and temperature fluctuations in the supply air. The flowmeter is followed by a butterball valve for coarse bleed flow control mounted in parallel with a needle valve for fine control.

A schematic of the afterbody used in the base bleed studies is shown in Figure 3. The 63.5 mm diameter cylindrical afterbody contains a 0.4 caliber bleed orifice which is preceded by an elliptically contoured section based on ASME long-radius nozzle standards[24] to ensure a uniform velocity profile for the bleed flow exiting the base. Ten 0.025" diameter static pressure taps on the base plane are used to measure the radial distribution of the base pressure. Two sets of five taps each along the sting side surface, located diametrically opposite to each other, are used to measure the approach pressure distribution upstream of the base. The taps in each set are staggered along the periphery to prevent interference waves from the upstream taps affecting the measurements of the taps downstream. Static pressure measurements are obtained using a Pressure Systems Inc. DPT 6400-T Digital Pressure Transmitter controlled by a desktop computer via serial interface. A removable retaining ring confines the pressure tubing near the inner wall of the afterbody in the region upstream of the bleed exit orifice to minimize disturbances in the bleed flow.

The two-component LDV system used for this investigation uses the green (514.5 nm) and blue (488 nm) lines of a 5-Watt Argon-ion laser. The nominal blue and green fringe spacings are 10.3 and 11.3 μm, respectively. The measurement volume diameter is 120 μm. Upstream frequency shifting of 40 MHz is used to discriminate flow direction and reduce fringe biasing,

and the beam pairs are oriented at $\pm 45°$ to the mean flow direction to minimize fringe blindness. The receiving optics collect light scattered by particles crossing the measurement volume in 20° off-axis forward scatter mode (effective length of measuring volume = 730 μm). The scattered light intensity is converted to an analog voltage signal by photomultiplier tubes and fed to an IFA-750 Digital Burst Correlator to extract frequency, and hence, velocity information. Three sets of stepper motors, encoders, and drives operate in a closed loop with a desktop computer to provide translation of the optical table in all three directions. A TSI six-jet atomizer containing 50 cp silicone oil provides seed particles (nominal diameter = 0.8 μm) to four seed tubes through a manifold and system of regulating valves. Three seed tubes for the freestream flow, arranged 120° apart circumferentially, are located just downstream of the flow conditioning module. The seed tube for the bleed flow is located in the bleed line, just downstream of the butterball valve. A detailed description of the LDV system, including an error analysis, has been provided by Herrin[23]. The worst case rms error due to particle lag just downstream of separation has been estimated at 6%. This error is 1.7% one base radius downstream of the base plane, and continues to diminish further downstream. The estimated worst case uncertainty is 1.2% of U_1 (the freestream velocity just prior to separation) in the mean velocity, and 2.3% of U_1 in the rms velocity fluctuation measurements.

RESULTS AND DISCUSSION
Pressure Measurements

Static pressure distributions along the afterbody and on the base plane were obtained for ten bleed rates ranging from $I = 0$ to $I = 0.032$. The axial pressure distribution of the approach flow along the afterbody is independent of the bleed rate. The approach static pressure is also relatively constant in the streamwise direction at $P/P_0 = 0.061 \pm 0.001$, yielding an isentropic Mach number of 2.47. A slight rise in pressure approaching the base corner is consistent on both sets of diametrically opposed pressure taps, and is most probably due to a minor nonuniformity in the nozzle flow.

The radial distribution of base pressure ratio is shown in Figure 4 for all ten bleed flow rates. At any given bleed rate, the base pressure ratio profile is radially symmetric across the base annulus, and fairly independent of radial location, except for a slight increase near the base corner in some cases. The slight increase in base pressure is probably due to streamline curvature effects caused by the sharp change in flow direction during entrainment of the low-speed flow by

3

the high-speed shear layer near the base corner. It is also evident that the base pressure ratio initially increases with bleed rate (solid symbol cases), peaks at around I = 0.0148, and then decreases rapidly as the bleed rate is increased further (open symbol cases). This behavior is more clearly seen when the average base pressure ratio, based on the area-weighted average of each profile, is plotted as a function of the injection parameter, Figure 5. Data from the blunt base and the five degree boattailed afterbody results of Herrin and Dutton[1,2] are also presented in this plot. The peak average base pressure ratio of $P_b/P_\infty = 0.669$ at I = 0.0148 is 18.5% higher than the average base pressure ratio of the blunt based cylinder and 5.7% higher than that of the boattailed afterbody. The difference in the average base pressure ratio between the blunt base[1] and the I = 0 no-bleed case is discussed later.

As seen in Figure 6, the average base pressure ratio peak at I = 0.0148 is consistent with earlier experiments[4,6,7]. All of these data were obtained with bleed orifices of 0.4 caliber. There are, however, significant differences in the magnitudes of the base pressure curves. In spite of operating at nearly the same Mach number, the base pressure ratios of Bowman and Clayden[6] are noticeably lower than those of the current study. This could be partly due to interference from the struts that were used to support their model. On the other hand, the data of Reid and Hastings[4] at Mach 2 are very similar to the current data. The difference in the bleed exit contours used in the two models could be responsible for the similarity of these data sets at different Mach numbers. The model used in the current study (and by Valentine and Przirembel[7]) employs a contoured converging nozzle while Reid and Hastings' orifice was preceded by a 5° conical Mach 2.0 nozzle, similar to the one used by Bowman and Clayden. In addition, a thick boundary layer has a base pressure enhancing effect similar to that of base bleed. Differences in the approach boundary layer thicknesses of the different experiments could therefore also contribute to the discrepancies discussed above. Although Valentine and Przirembel attribute the second peak in their base pressure to the converging nozzle preceding their bleed orifice, no secondary peak was observed in the current investigation. Due to the lower Mach number used in the present study, it is possible that the secondary peak could occur at a bleed rate higher than the range of the flowmeter.

Flow Visualization

Spark-schlieren photographs and shadowgraphs, obtained with a standard Z-type two mirror configuration and a 1.4 μs micropulser light source, were used to confirm interference-free operation and to obtain qualitative information on the effect of base bleed on the near-wake flowfield. Schlieren photographs using a horizontal knife-edge at five different bleed rates are shown in Figure 7. The absence of any strong interference waves emanating from the nozzle exit/test section junction confirms interference-free flow conditions in the test section at all of these bleed flow rates. At zero bleed, the wake is closed and a strong recompression shock system is evident. As expected, the shear layer angle becomes flatter, the base corner expansion weakens, the wake widens, and the recompression shocks become weaker as the bleed flow rate is increased from zero to I = 0.0033. The recompression shock system seems to weaken considerably near I = 0.0131, when the bleed flow presumably provides most of the fluid required for shear layer entrainment. As the bleed rate is increased further to I = 0.0199, the recompression shock system reappears slightly upstream of its earlier location. When the bleed exit velocity approaches sonic conditions at around I = 0.0279, the Mach disk emanating from the bleed orifice interacts with the oblique recompression shocks from the outer flow and forms a fairly complex shock system. This shock system also appears to be highly unsteady, as indicated by imaging the flowfield on a screen and by visual inspection of a series of photographs at this bleed rate. The horizontal knife-edge makes it difficult to discern the vertical Mach disk in the schlieren photographs; however, it is clearly visible in shadowgraphs taken at the high bleed rate. The axisymmetric nature of the flow also causes smearing of the flow features due to line-of-sight integration effects.

LDV Measurements

A parametric study of the mean axial velocity and turbulence quantities along the centerline has been performed using LDV. The approach flowfield and boundary layer, and the flow conditions at the exit of the bleed jet have also been documented for the five bleed cases studied. Care was taken to match data rates at the freestream and bleed flow nozzle exits, in an effort to minimize particle concentration bias errors. Post-facto corrections for velocity bias were made using the interarrival time weighting method, which has been shown[25] to be the most reliable technique for high-speed separated flows.

The freestream approach flow was found to be uniform and independent of the bleed rate. The mean freestream approach velocity (U_1) was found to be 574 m/s with 0.3% variation between the different bleed

4

cases. The mean Mach number based on adiabatic expansion from the tunnel stagnation temperature (T_o) to the freestream velocity was 2.45, in close agreement with the isentropic value of 2.47 based on pressure measurements. The unit Reynolds number was calculated to be 45 (10^6) m^{-1} at the nozzle exit. Approach boundary layer mean velocity profiles for all bleed cases were similar, as seen in Figure 8. Curve fits[26] of these profiles were used to determine boundary layer parameters such as integral thicknesses and skin friction coefficient. These results (mean values and percentage variations over the five bleed cases) are presented in Table 1 below. The thicknesses and the friction velocity have been normalized by the afterbody radius, R_o, and the freestream velocity, U_1, respectively. Rather large variations in the computed parameters (between the different bleed cases) are due to the sensitivity of the curve fit to accurate y-position determination (limited to ±0.1 mm due to hysteresis of the traverse table). The axial turbulence intensity and Reynolds shear stress distributions in the boundary layer collapse very well for the different bleed rates, as seen in Figures 9 and 10. As expected, the magnitudes of these quantities are high in the boundary layer, dropping rapidly to low values in the freestream.

Table 1. Approach Boundary Layer Properties

Boundary Layer Thickness, δ/R_o	0.102 ± 1.6%
Displacement Thickness, δ^*/R_o	0.0241 ± 6.8%
Momentum Thickness, θ/R_o	0.00682 ± 6.0%
Shape Factor, $H = \delta^*/\theta$	3.53 ± 1.1%
Wake Strength Parameter, Π	0.768 ± 17%
Skin Friction Coefficient	0.00170 ± 4.7%
Friction Velocity, u_τ/U_1	0.0414 ± 2.3%

Radial traverses performed 1.5 mm downstream of the bleed exit plane show uniform velocity distributions in the bleed flow, as seen in Figure 11. The effect of the compliant boundary presented by the bleed hole can be seen for the bleed-off case. There is a mean inflow into the base along the centerline, and a mean outflow along the periphery of the bleed orifice. Bimodal velocity histograms were observed at all radial locations for the no-bleed case, indicating large scale turbulence interaction between the recirculation region and the long passive cavity presented by the bleed hole and the hollow sting. The 5% difference in the average base pressure ratio between

the blunt base[1] and the I = 0 case (Figure 5) could be due to this compliant boundary effect.

The effect of base bleed on the mean axial velocity distribution along the centerline can be seen in Figure 12. In all cases, the measured radial velocity component was less than 2% of U_1, and the Reynolds shear stresses were nearly zero, confirming that the LDV measurement volume was located at the centerline of the flowfield. For the no-bleed case, the peak reverse velocity (30% of the freestream value) and the rear stagnation point occur 1.5 and 2.8 base radii downstream of the base, respectively. These results are nearly identical to measurements done with a blunt base[1]. At the base plane (x = 0), however, the extrapolated axial velocity is non-zero and negative, due to the compliant boundary effect discussed above. As the bleed rate is increased, the bleed jet exit velocity increases, causing a downstream shift of the forward stagnation point where the bleed flow and reverse flow meet. This has the effect of diminishing the size of the recirculation region since the rear stagnation point location is relatively constant at $x/R_o = 3.2$ (note that this position for the bleed-on cases is shifted relative to the bleed-off case). The peak reverse velocity location occurs progressively downstream, and its magnitude decreases with increasing bleed. At I = 0.0148, the optimum bleed rate from a base pressure viewpoint, the recirculation region along the centerline almost disappears. No reverse velocity is detected along the centerline for the I = 0.0226 case, indicating penetration of the bleed jet into the reattachment zone. The velocity profiles for the bleed-on cases become similar for $x/R_o > 3$, the wake redevelopment region.

Figures 13 and 14 present the axial and radial turbulence intensity distributions along the centerline. For each bleed case (except I = 0.0226), two peaks are observed in the distribution of turbulence intensity. The first peak occurs at the forward stagnation point location due to the change in flow direction from axial to radial when the bleed flow meets the reverse flow in the recirculation region. The magnitude of this peak is seen to decrease with increasing bleed rate due to the smaller influence of the diminishing recirculation region. The second peak occurs at the rear stagnation location due to reattachment phenomena. The influence of the flow mechanisms occurring at both stagnation point locations is much stronger in the axial direction. Consequently, the peaks in the radial turbulence intensity distributions are not as pronounced as the axial intensity peaks. At the higher bleed rates, the bleed flow penetrates further into the wake, accounting for the low overall turbulence intensity levels seen in Figures 13 and 14 for these cases. Anisotropy of the

turbulent normal stress along the centerline is also evident from the differences in the axial and radial turbulence intensity profiles. Figure 15 shows the centerline distribution of turbulent kinetic energy, calculated using

$$k = 0.5(\sigma_U^2 + 2\sigma_{V_r}^2)/U_1^2 \qquad (1)$$

The occurrence of the peak energy magnitudes at the stagnation point locations, and the decreasing energy levels with increasing bleed rate are similar to those discussed for the turbulence intensity distributions.

SUMMARY AND CONCLUSIONS

An experimental investigation has been conducted to study the effects of base bleed on the near-wake flowfield of a cylindrical afterbody in supersonic flow. Data have been obtained using static pressure measurements, schlieren and shadowgraph photography, and LDV traverses along the centerline. Results indicate relatively uniform radial pressure profiles across the base plane. With increasing bleed flowrate, the average base pressure is found to increase initially, attain a peak value, and then decrease with further increase in I. The approach flowfield upstream of separation is unaffected by the bleed rate. An increase in the bleed rate is accompanied by the diminishing size and intensity of the recirculation region (due to the downstream displacement of the forward stagnation point), and a decrease in the peak axial and radial turbulence intensities at the forward stagnation point. Near the optimum bleed rate of I = 0.0148, the base pressure is maximized, and the flowfield is characterized by the widening of the wake, flattening of the shear layer angle, and the near disappearance of reverse velocity along the centerline.

ACKNOWLEDGMENT

REFERENCES

[1]Herrin, J.L. and Dutton, J.C., "Supersonic Base Flow Experiments in the Near Wake of a Cylindrical Afterbody," *AIAA Journal*, Vol. 32, No. 1, pp. 77-83, 1994.

[2]Herrin, J.L. and Dutton, J.C., "Effects of Afterbody Boattailing on the Near-Wake of Axisymmetric Bodies in Supersonic Flow," AIAA Paper 94-0029, 1994.

[3]Cortright, E.M. and Schroeder, A.H., "Preliminary Investigation of Effectiveness of Base Bleed in Reducing Drag of Blunt-Base Bodies in Supersonic Stream," NACA RM E51A26, 1951.

[4]Reid, J. and Hastings, R.C., "The Effect of a Central Jet on the Base Pressure of a Cylindrical Afterbody in a Supersonic Stream," Aeronautical Research Council (Great Britain), Reports and Memoranda No. 3224, 1959.

[5]Badrinarayanan, M.A., "An Experimental Investigation of Base Flows at Supersonic Speeds," *Journal of the Royal Aeronautical Society*, Vol. 65, pp. 475-482, 1961.

[6]Bowman, J.E. and Clayden, W.A., "Cylindrical Afterbodies in Supersonic Flow with Gas Ejection," *AIAA Journal*, Vol. 5, No. 6, pp. 1524-1525, 1967.

[7]Valentine, D.T. and Przirembel, C.E.G., "Turbulent Axisymmetric Near-Wake at Mach Four with Base Injection," *AIAA Journal*, Vol. 8, No. 12, pp. 2279-2280, 1970.

[8]Zakkay, V. and Sinha, R., "An Experimental Investigation of the Near Wake in an Axisymmetric Supersonic Flow with and without Base Injection," *Israel Journal of Technology*, Vol. 7, No. 1-2, pp. 43-53, 1969.

[9]Hubbartt, J.E., Strahle, W.C., and Neale, D.H., "Mach 3 Hydrogen External/Base Burning," *AIAA Journal*, Vol. 19, No. 6, pp. 745-749, 1981.

[10]Clayden, W.A. and Bowman, J.E., "Cylindrical Afterbodies at M = 2 with Hot Gas Ejection," *AIAA Journal*, Vol. 6, No. 12, pp. 2429-2431, 1968.

[11]Ding, Z., Chen, S., Liu, Y., Luo, R., and Li, J., "Wind Tunnel Study of Aerodynamic Characteristics of Base Combustion," *Journal of Propulsion and Power*, Vol. 8, No. 3, pp. 630-634, 1992.

[12]Bowman, J.E. and Clayden, W.A., "Boat-Tailed Afterbodies at M = 2 with Gas Ejection," *AIAA Journal*, Vol. 6, No. 10, pp. 2029-2030, 1968.

[13]Korst, H.H., "A Theory for Base Pressures in Transonic and Supersonic Flows," *Journal of Applied Mechanics*, Vol. 23, No. 4, pp. 593-600, 1956.

[14]Korst, H.H., Page, R.H., and Childs, M.E., "A Theory for Base Pressures in Transonic and Supersonic Flow," Engineering Experiment Station, Mechanical Engineering Department, University of Illinois, ME Technical Note 392-2, 1955.

[15]Korst, H.H., Chow, W.L., and Zumwalt, G.W., "Research on Transonic and Supersonic Flow of a Real Fluid at Abrupt Increases in Cross Section (With Special Consideration of Base Drag Problems)," Engineering Experiment Station, Mechanical Engineering Department, University of Illinois, ME Technical Report 392-5, 1964.

[16]Reijasse, P., Benay, R., Delery, J.M., and Lacau, R.G., "Missile and Projectile Base-Flow Prediction by Multi-Component Methods," *AIAA*

Atmospheric Flight Mechanics Conference, T.P. No. 1988-90, Minneapolis, 1988.

[17]Reijasse, P., Benay, R., Delery, J., and Lacau, R.G., "Prediction of Powered Missile or Projectile Base Flows by Multicomponent Methods," *La Recherche Aerospatiale*, Vol. 1989-4, pp. 15-32, 1989.

[18]Sahu, J., Nietubicz, C.J., and Steger, J.L., "Navier-Stokes Computations of Projectile Base Flow with and without Mass Injection," *AIAA Journal*, Vol. 23, No. 9, pp. 1348-1355, 1985.

[19]Sahu, J., "Supersonic Flow Over Cylindrical Afterbodies with Base Bleed," AIAA Paper 86-0487, 1986.

[20]Danberg, J.E. and Nietubicz, C.J., "Predicted Flight Performance of Base Bleed Projectiles," AIAA Paper 90-2069, 1990.

[21]Nietubicz, C.J. and Sahu, J., "Navier-Stokes Computations of Base Bleed Projectiles," in *Base Bleed: First International Symposium on Special Topics in Chemical Propulsion*, ed. K.K. Kuo and J.N. Fleming, Hemisphere Publishing Corp., pp. 93-106, 1991.

[22]Nietubicz, C.J. and Gibeling, H.J., "Navier-Stokes Computations for a Reacting, M864 Base Bleed Projectile," AIAA Paper 93-0504, 1993.

[23]Herrin, J.L., "An Experimental Investigation of Supersonic Axisymmetric Base Flow Including the Effects of Afterbody Boattailing," Ph.D. Thesis, University of Illinois at Urbana-Champaign, 1993.

[24]Bean, H.S., ed., *Fluid Meters - Their Theory and Application*, 6th ed., Report of the ASME Research Committee on Fluid Meters, 1971.

[25]Herrin, J.L. and Dutton, J.C., "An Investigation of LDV Velocity Bias Correction Techniques for High-Speed Separated Flows," *Experiments in Fluids*, Vol. 15, pp. 354-363, 1993.

[26]Sun, C.C. and Childs, M.E., "A Modified Wall Wake Velocity Profile for Turbulent Compressible Boundary Layers," *Journal of Aircraft*, Vol. 10, No. 6, pp. 381-383, 1973.
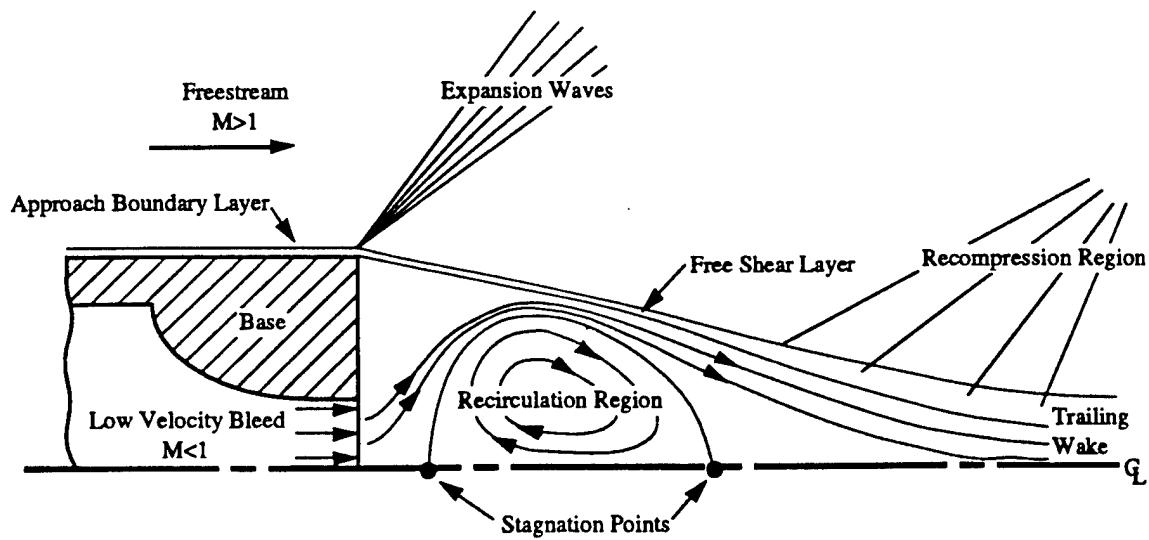
Figure 1. Schematic of the Near-Wake Flowfield with Base Bleed
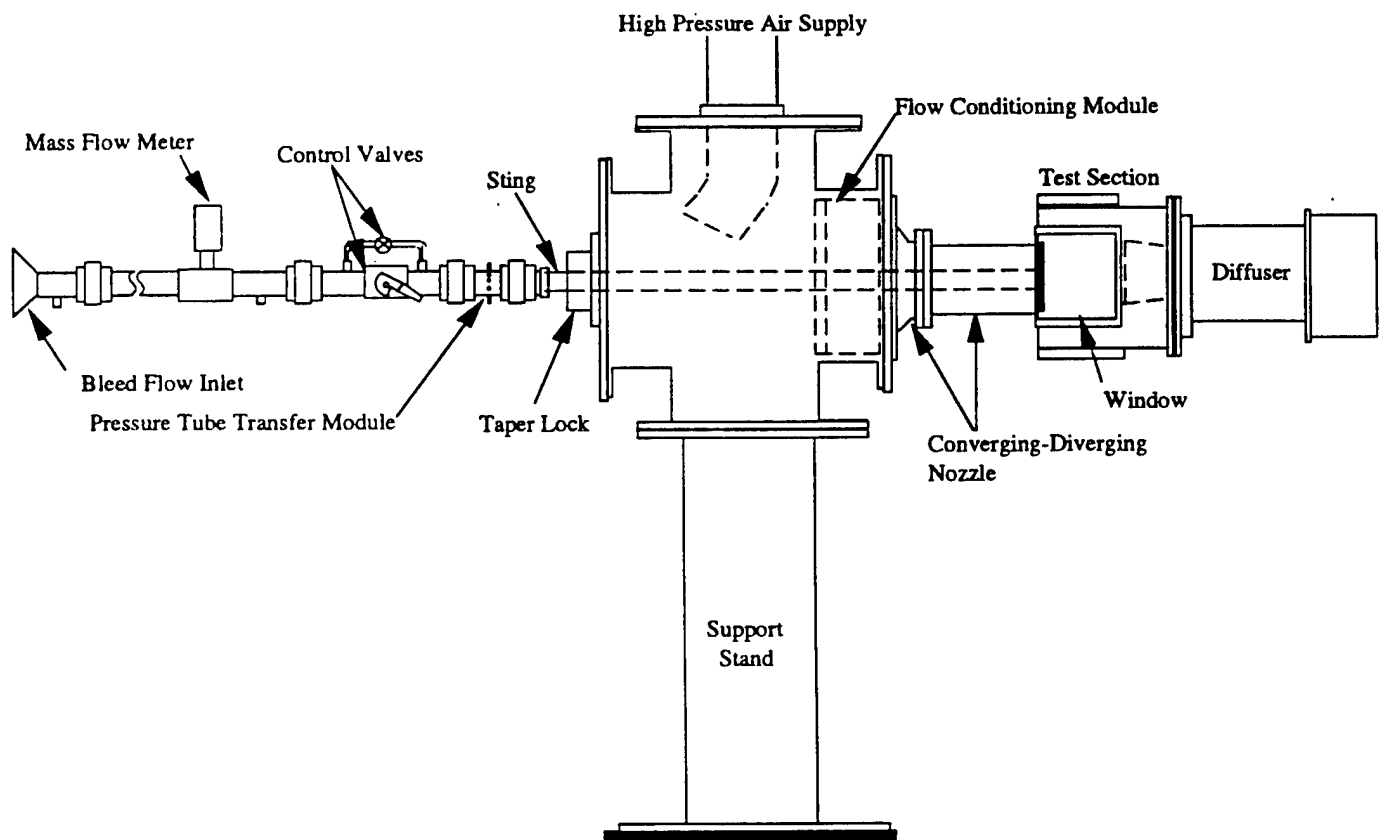
Figure 2. Axisymmetric Wind Tunnel and Base Bleed Facility

Base Taps -> 1/8" Radial Separation
Side Taps -> 1/8" Axial Separation
Bleed Hole Area = 16% of Base Area
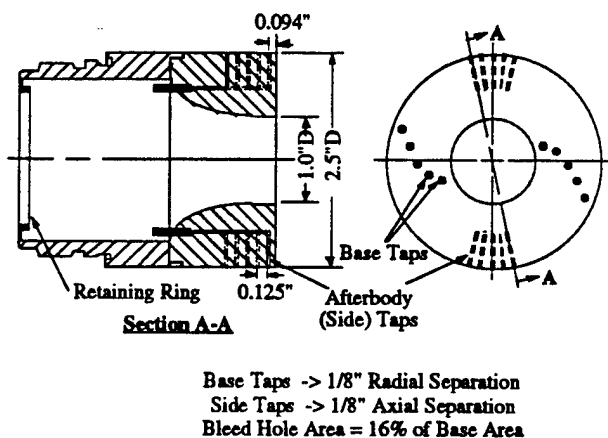
Figure 3. Location of Static Pressure Taps on Base Bleed
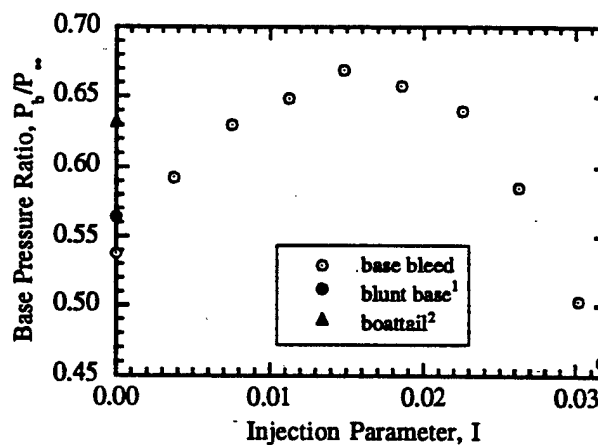Afterbody
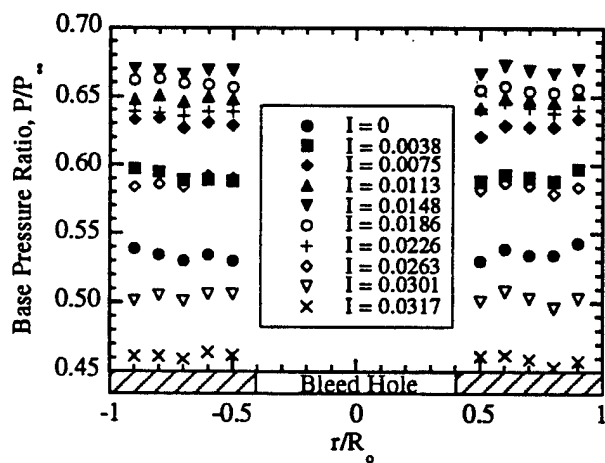

Figure 5. Effect of Base Bleed on Area-Averaged
Base Pressure Ratio

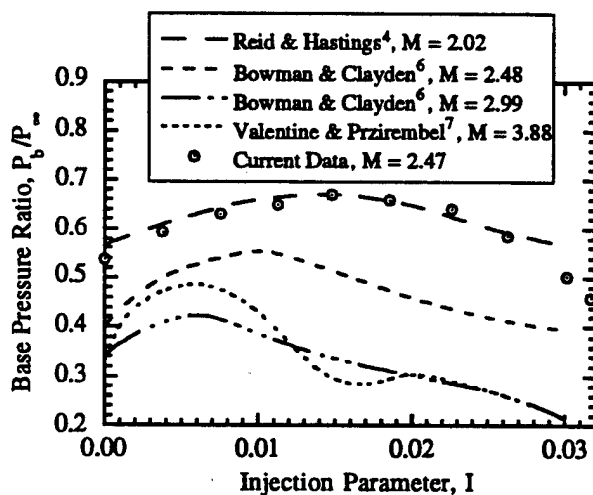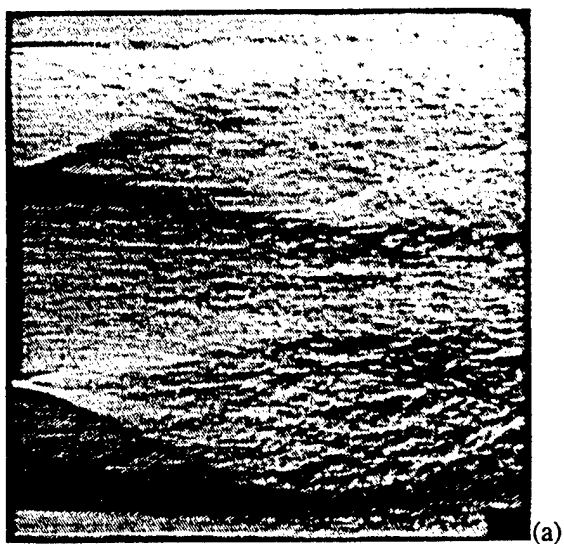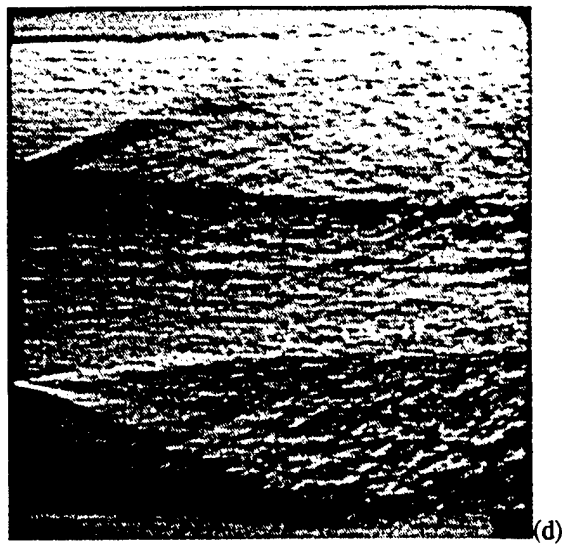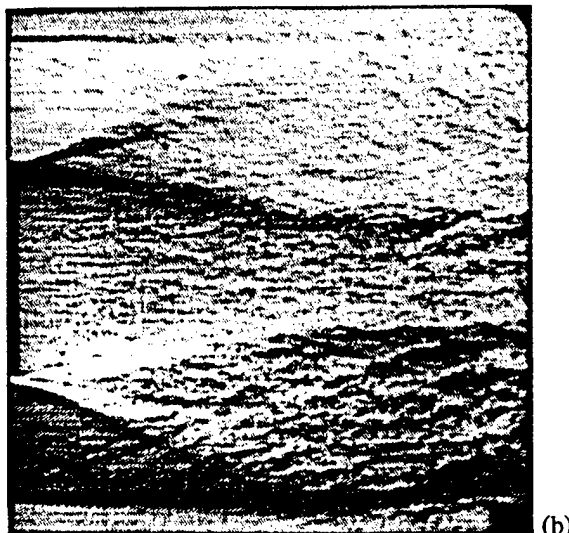Figure 4. Effect of Base Bleed on Base Pressure
Distribution

Figure 6. Comparison of Base Bleed Results with Other
Experiments (bleed orifice diameter ratio, $d_j/d_b = 0.4$)

9
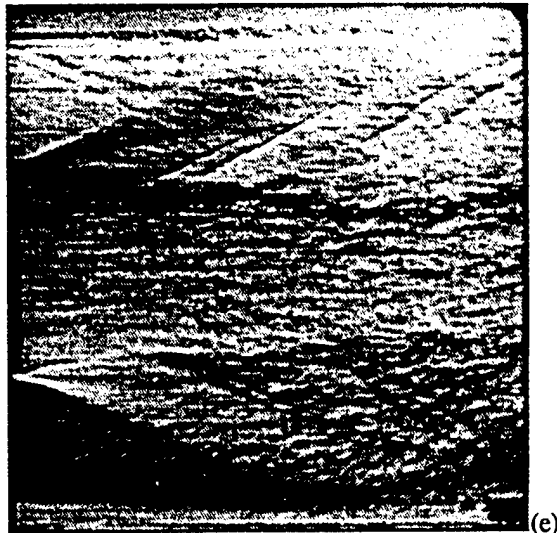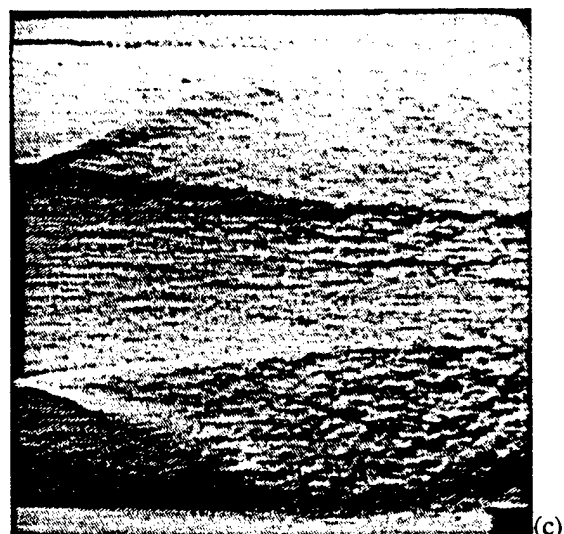
Figure 7. Schlieren Photographs of the Base Flowfield at Different Bleed Flow Rates: (a) I = 0; (b) I = 0.0033; (c) I = 0.0131; (d) I = 0.0199; (e) I = 0.0279
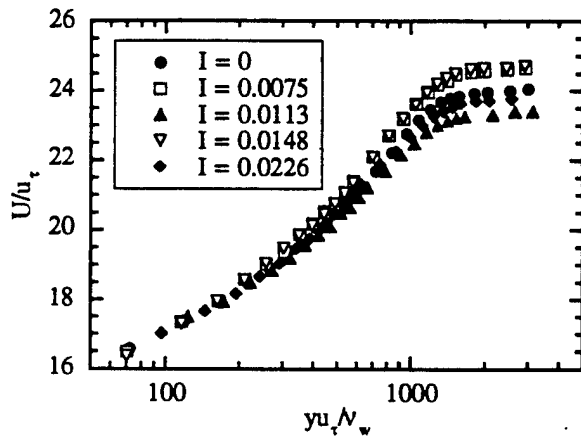
Figure 8. Approach Boundary Layer Mean Velocity
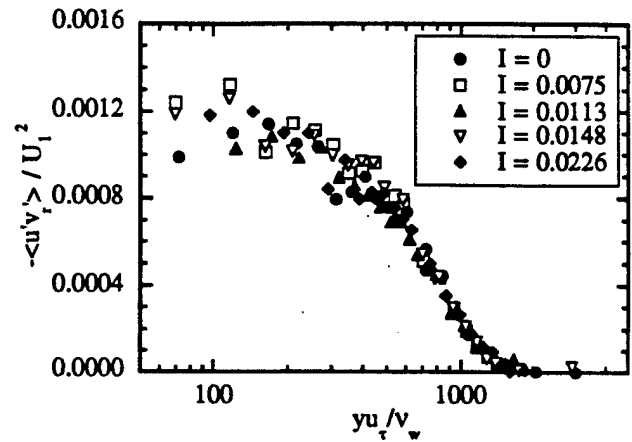Profiles (x/R$_o$ = -0.157)

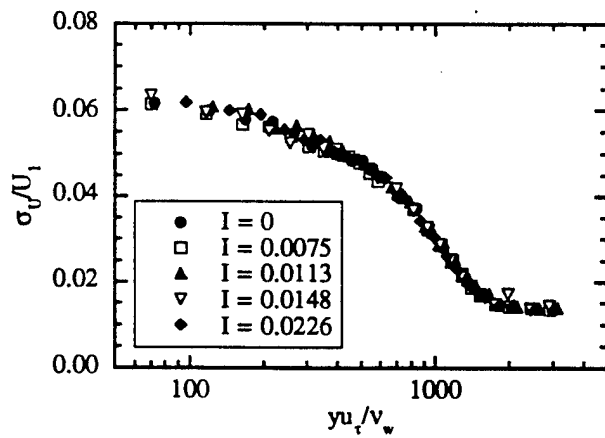Figure 10. Reynolds Shear Stress Distributions in
Approach Boundary Layer

Figure 9. Streamwise Turbulence Intensity Distributions
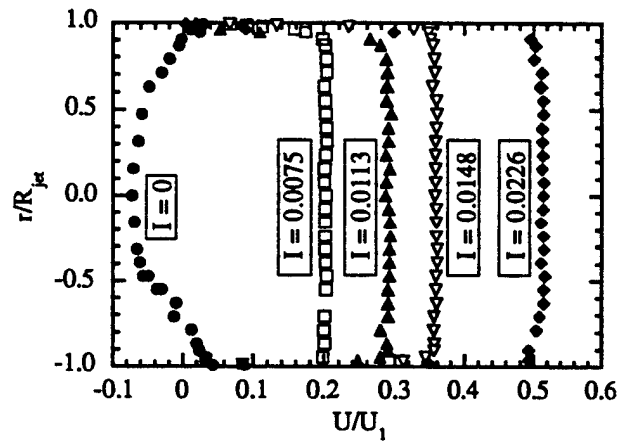in Approach Boundary Layer

Figure 11. Mean Axial Velocity Distributions at
Bleed Orifice Exit
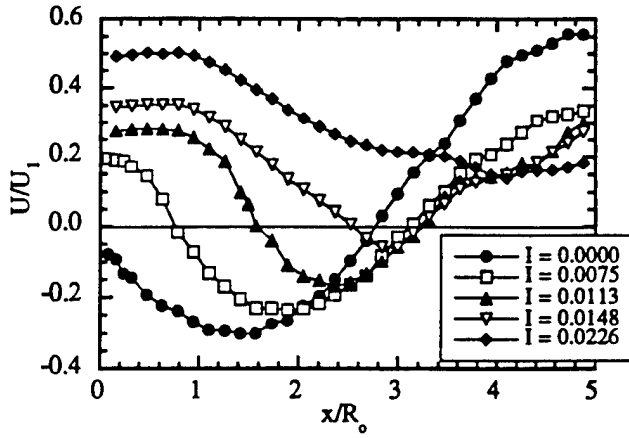(x/R$_{jet}$ = 0.118; R$_{jet}$/R$_o$ = 0.4)

11

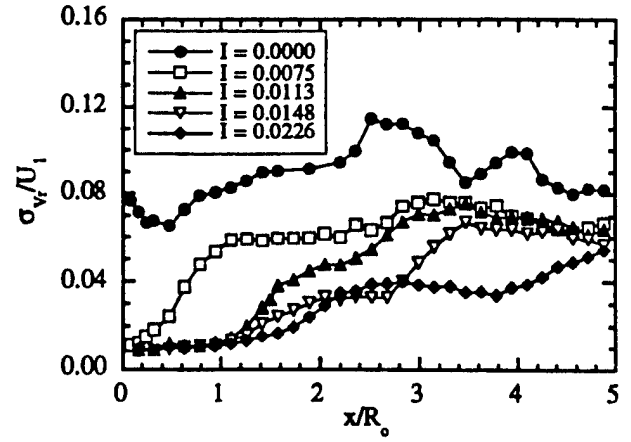Figure 12. Mean Axial Velocities Along the Centerline

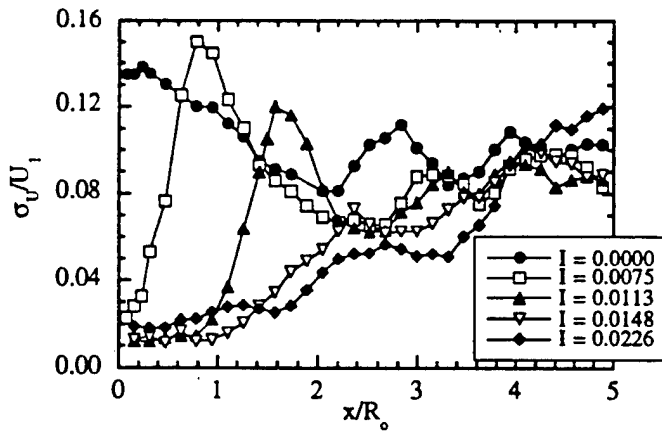Figure 14. Radial Turbulence Intensities Along the Centerline

Figure 13. Axial Turbulence Intensities Along the Centerline
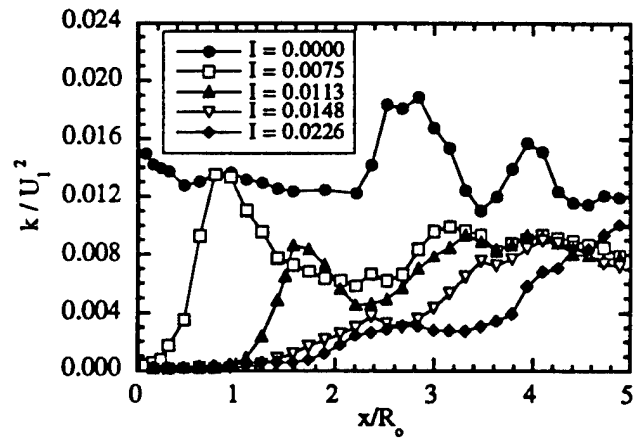

Figure 15. Turbulent Kinetic Energy Distributions Along the Centerline

12

APPENDIX A.18

RECENT PROGRESS ON HIGH-SPEED SEPARATED BASE FLOWS

by

J. C. Dutton, J. L. Herrin, M. J. Molezzi, T. Mathur, and K. M. Smith

AIAA 95-0472

Recent Progress on High-Speed Separated Base Flows

J.C. Dutton, J.L. Herrin, M.J. Molezzi, T. Mathur, and K.M. Smith

Department of Mechanical and Industrial Engineering
University of Illinois at Urbana-Champaign
Urbana, Illinois 61801

33rd Aerospace Sciences Meeting and Exhibit
January 9-12, 1995 / Reno, NV

RECENT PROGRESS ON HIGH-SPEED SEPARATED BASE FLOWS

J.C. Dutton[*], J.L. Herrin[†], M.J. Molezzi[‡], T. Mathur[§], and K.M. Smith[§]
Department of Mechanical and Industrial Engineering
University of Illinois at Urbana-Champaign
Urbana, Illinois 61801

ABSTRACT

Recent work in the area of high-speed separated flows is reviewed with particular emphasis on problems related to missile and projectile afterbody and base flows. A brief summary is first given of the current state-of-the-art in base flow numerical predictions and previous experimental studies. This is followed by discussions of our recent experimental work in this area. The particular experiments described are: detailed mean velocity and turbulence measurements for a cylindrical afterbody in Mach 2.5 flow, a similar study for a five degree boattailed afterbody that explains the associated drag reduction effects, initial pressure and velocity measurements quantifying the effects of base bleed in supersonic base flow, a particle image velocimetry study that has delineated the mechanisms of base drag reduction for a planar bluff body with a base cavity in subsonic flow, and Mie scattering visualizations of large-scale turbulent structures in the shear layers and trailing wake of a two-dimensional, supersonic base flow.

INTRODUCTION

Motivation and Problem Description

The study of separated flows is an important basic fluid dynamics research area since the occurrence and behavior of separated flow regions are generally poorly understood and difficult to predict. In addition, the investigation of high-speed separated flows is of relevance in a number of important application areas such as projectile and missile afterbody and base flows. This area is the primary motivation for the work described herein. Understanding of the fluid dynamic mechanisms that occur in high-speed base flows is critically important to the performance of projectile and missile systems from a number of standpoints. In particular, these near-wake flowfield interactions determine the base drag which is a major component of

the total drag, especially at transonic and supersonic flight conditions (Rollstin, 1987), and is the most difficult component to predict (Sahu, 1994). The fluid dynamic, chemical composition, and thermodynamic conditions in the separated flow region of a powered missile also determine the occurrence of base burning (Strahle et al., 1982) which, on the one hand, can dramatically reduce base drag, but on the other, can result in loss of vehicle stability and unwanted afterbody and base heating. In addition, the near-wake flow structure is of critical importance in establishing the power-on missile plume signature (Dash et al., 1980) through the pressure, temperature, and chemical species variations resulting from the near-field shock and expansion wave flow structure.

Figure 1 presents a schematic diagram of the mean flow in the base region of a projectile or unpowered missile with a conical boattail in the supersonic flight regime. In this case the supersonic freestream flow and its associated boundary layer are first expanded at the body/boattail juncture and then approach the base corner where they separate geometrically through a centered expansion to form a free shear layer with an enclosed recirculating region. The shear layer is recompressed through an oblique shock system as it is constrained to turn along the axis of symmetry (for the zero angle-of-attack case sketched) near the rear stagnation point with redevelopment of the trailing wake occurring downstream. There are a number of phenomena present in this flow that make its prediction difficult. One complicating factor is that the shear layer for supersonic flight conditions exists under highly compressible conditions, i.e. at a high convective Mach number. Recent work for constant pressure two-stream mixing layers (Goebel and Dutton, 1991; Clemens and Mungal, 1992) has shown the turbulence structure to be substantially altered under compressible conditions as compared to the incompressible case. In addition, only the initial part of the base region shear layer is at approximately constant pressure before encountering an adverse pressure gradient near the reattachment point. Further, the centered expansions that occur at the body/boattail juncture and at the base corner influence the initial turbulence structure of the shear layer and, hence, its downstream development. Other complicating factors include streamline curvature that occurs near shear layer

---

[*]Professor, Associate Fellow AIAA.
[†]Currently NRC Associate at NASA Langley Research Center, Member AIAA.
[‡]Currently Staff Engineer at General Electric CR&D, Schenectady, NY, Member AIAA.
[§]Graduate Research Assistant, Student Member AIAA.

reattachment and existence of the enclosed recirculating region which imposes a highly energetic and nonuniform reverse velocity at the inner edge of the shear layer.

In the following sections we present brief reviews of previous numerical and experimental research in the area of high-speed separated base flows, concentrating on recent work for the supersonic flight regime. This material will provide context for the results presented later in the paper.

Numerical Predictions

Historically, the first predictive techniques developed for base flows were the Chapman-Korst component method (Chapman, 1950; Korst, 1956) and the viscid-inviscid integral interaction technique first presented by Crocco and Lees (1952). Several good reviews of these early base flow modeling methods have been presented, most recently by Delery and Lacau (1987). The component and integral interaction techniques are still useful today for preliminary design and parametric studies (Reijasse et al., 1989). However, solution of the full, Reynolds-averaged Navier-Stokes equations using currently available numerical methods offers the ability to more realistically predict the details of the base flowfield structure, i.e. to remove many of the assumptions inherent in the component and integral techniques. In addition, the extension from simple two-dimensional and axisymmetric geometries to more complex three-dimensional geometries, including non-circular body shapes, afterbodies having fins and/or base cavities, and effects of angle-of-attack, can only be analyzed accurately using numerical techniques. In order to avoid the difficulties inherent in turbulence modeling for the Reynolds-averaged Navier-Stokes (RANS) approach, the large eddy simulation (LES) or direct numerical simulation (DNS) techniques will eventually be applied to high-speed base flows. However, because of the complexity of these compressible separated flows, with their large Reynolds numbers, the associated wide range of turbulent scales, and resulting large computational requirements, efforts along these lines have only recently begun (Tourbier and Fasel, 1994). Also, these LES/DNS studies are currently directed at understanding the stability characteristics and large-scale turbulent structure of the near-wake, rather than at an engineering prediction of the flow. As a result, the RANS approach with appropriate turbulence modeling is the method of choice in the near future for analysis and design of practical missile and projectile systems.

Numerical simulations of this type have been conducted for high-speed separated base flows since the late 1970s. In 1985 Putnam and Bissinger published the results of an assessment conducted by AGARD Working Group 08 concerning the state-of-the-art for predicting the flow over nozzle afterbodies. They concluded that, as of mid-1984, Navier-Stokes methods were accurate for predicting afterbody pressure distributions only up to the point of separation. They also strongly recommended that the assessment criteria for numerical predictions should be based on agreement with surface pressure distributions and flowfield characteristics and not simply on the overall afterbody drag. At about the same time, Petrie and Walker (1985) tested the true predictive capability of Navier-Stokes codes by soliciting numerical solutions from a number of groups for a power-on base flow geometry for which detailed experimental data had already been obtained. The experimental data were not provided to the contributing parties prior to the computations. While the simulations were able to qualitatively capture some of the most basic features of the flow, several fundamental parameters such as the base pressure magnitude and radial variation, recirculation region size, and Mach disk location and size were not accurately predicted, with large variations in the predictions of these quantities among the various simulations. Petrie and Walker also pointed out inconsistencies among the predictions for the various turbulence models used, as well as the occurrence of grid-dependent solutions.

Since the time that this comparison was performed, several groups have obtained numerical results in better agreement with the experimental data reported by Petrie and Walker. Factors affecting the accurate Navier-Stokes simulation of these flows were identified as solution-adapted grid alignment in the high-gradient shear layer regions and improved turbulence modeling, including the effects of compressibility and streamline curvature (Benay et al., 1987; Childs and Caruso, 1987, 1989; Caruso and Childs, 1988; Peace, 1991). Childs and Caruso (1987) also suggested that comparison of simply the base pressure between computation and experiment, without any complementary flowfield data, can lead to false conclusions regarding the accuracy of the numerical solutions, due to cancellation of errors caused by inaccurate turbulence modeling and insufficient grid resolution. With the availability of improved computational hardware in recent years, the problem of inadequate grid resolution has been successfully addressed, at least for the two-dimensional planar or axisymmetric base flow geometries. For example, Childs and Caruso (1989) and Tucker and Shyy (1993) both obtained grid-independent solutions for supersonic freestream flow over axisymmetric afterbodies.

Unsurprisingly, then, the difficult problem of turbulence modeling is the most critical outstanding issue in the accurate RANS prediction of these complex separated flows. Several recent studies have been directed at this issue and have used for comparison purposes our experimental measurements (described below) for Mach 2.5 flow over a cylindrical afterbody. Sahu (1994) employed two algebraic turbulence models (Baldwin-Lomax and Chow) and Chien's low Reynolds number k-ε model to compute this case. Tucker and Shyy (1993) reported results using several variations of two-equation k-ε type turbulence models, including the original Jones-Launder formulation and extensions to allow improved response to the mean strain rate as well as corrections to account for compressibility. Chuang and Chieng (1994) recently published a study in which three higher-order models were investigated: Chien's two-equation k-ε model, a two-layer algebraic stress model, and Shima's Reynolds stress model. All of these studies showed improved agreement with the experimental measurements for the more sophisticated turbulence models used in each case. In some instances, predictions in relatively good agreement with the measured base pressure distribution and some aspects of the near-wake mean velocity field were obtained. For example, both Sahu's k-ε computation and Chuang and Chieng's Reynolds stress prediction of the base pressure agreed reasonably well with experiment. However, other characteristics of the mean velocity and turbulence fields were poorly predicted. Indeed, both Tucker and Shyy (1993) and Chuang and Chieng (1994) found that all of the turbulence models employed failed to correctly predict the shear layer spreading rate, which is a fundamental characteristic of the near-wake flow. Interestingly, all three of these studies utilized a "standard" k-ε model and obtained substantially different predictions of the base pressure distribution. This suggests that these RANS base flow computations are also dependent on other factors in the numerical implementation, possibly including grid resolution, accuracy of the numerical solver, and treatment of boundary conditions.

Experimental Studies

A large number of experimental investigations of high-speed separated base flows have been conducted since the early 1950s. A variety of flow geometries and conditions have been considered, with early work in this area primarily concentrated on surface pressure measurements and flow visualization studies in order to quantify the base drag or to provide empirical information needed for component or integral modeling of the near-wake region (e.g., Fuller and Reid, 1956;

Reid and Hastings, 1959a; Lilienthal et al., 1970). Model support interference was an issue in many of these early studies. Also, as described above, acquisition of accurate mean and turbulent *flowfield* measurements is widely recognized to be of crucial importance for improving understanding of the physics of these complex high-speed separated flows and for providing validation data for development of improved Navier-Stokes computational models of these flows.

The initial flowfield data reported for high-speed base flows were mean velocity measurements obtained with pitot probes. However, the reliability of these data must be questioned due to the disturbances that the probes introduced into the flow. In addition, pitot probes are incapable of providing *turbulence* information which is critically important for better understanding the fluid dynamic mechanisms in the near-wake region and for providing a sensitive test of a numerical technique's predictive capabilities. Perhaps the most comprehensive previous probe-based study of a supersonic base flow problem was undertaken by Gaviglio et al. (1977) with a hot-wire anemometer. The authors, however, avoided the recirculation region immediately behind the base due to probe interference effects. Measurements were obtained in the approach flow, shear layers, and developing wake and provide a relatively detailed description of the mean velocity and turbulence characteristics in these regions.

Laser Doppler velocimetry (LDV) is a non-intrusive experimental technique that is well suited for the study of high-speed separated base flows due to its ability to measure the reversed velocities and high turbulence intensities characteristic of these flowfields. However, few non-intrusive flowfield measurements have been obtained previously for high-speed base flows. An exception is the two-component LDV measurements reported by Petrie and Walker (1985) for an axisymmetric afterbody in transonic flow with a supersonic central jet. The authors noted several problems with the LDV measurements, particularly particle lag effects in the high acceleration regions of the flow. We are also aware that Berner (1993) has recently made LDV measurements for cylindrical and boattailed afterbodies in Mach 2 flow, although these measurements have not been extensively presented in the literature to date.

As evidence of the lack of high quality experimental data for high-speed base flows, the recent comprehensive survey by Delery and Wagner (1990) was able to identify only six previous experiments that made flowfield measurements (using multi-component LDV) of sufficient accuracy and spatial resolution to be useful for comparison to modern Navier-Stokes computations, and all of these are in the subsonic flight

regime. Thus, as of 1990, there were no known well documented flowfield measurements available in the open literature for the important transonic and supersonic flight cases for any base geometry. As will be discussed in the following sections, our current and future work is directed, in part, at obtaining just such accurate, spatially well-resolved, statistical velocity information. In addition, we are developing and applying *planar* techniques, both for qualitative visualization and quantitative measurements, in these high-speed separated flows. The purpose of these planar measurements is to better understand the time-resolved *structure* of turbulent base flows as a complement to the time-averaged, pointwise velocity data. We are unaware of any other previous studies of the instantaneous turbulence structure in high-speed base flows.

STATISTICAL STUDIES OF SUPERSONIC, AXISYMMETRIC BASE FLOWS

In order to document in detail the flow mechanisms occurring in the near-wake regions of supersonic base flows, we have obtained pressure measurements, flow visualizations, and extensive velocity measurements for several cases of interest. The experiments described here include three axisymmetric geometries: a cylindrical afterbody, a boattailed afterbody, and a cylindrical afterbody with base bleed. Results from these studies are described below.

Cylindrical Afterbody

The simplest axisymmetric base geometry that retains all of the primary features of a typical missile or projectile flowfield is the blunt base, circular cylinder afterbody without a propulsive jet or control fins. The mean flowfield near this type of afterbody is similar to that sketched in Fig. 1, but without the boattail. In general, the boundary layer approaching the base corner is fully turbulent and relatively thin compared to the afterbody radius. As the flow separates from the base corner, a low pressure recirculation region behind the base is formed which is the source of base drag. Of special note in Fig. 1 are the solid wall boundary conditions along the afterbody surface, both near the base corner and along the base surface. Nearly all base drag reduction schemes attempt to manipulate these boundary conditions such that the pressure in the large separated region downstream of the base is increased. Hence, a thorough understanding of the flow physics in the base region of a solid-walled, cylindrical afterbody is necessary so that the effects of added complicating features (e.g., base bleed) can be ascertained and the benefits of current base drag reduction methods can be understood.

Recently, experiments to investigate the flowfield near a cylindrical afterbody in a uniform Mach 2.5 flow have been completed (Herrin and Dutton, 1994a). The experiments were carried out using the Axisymmetric Base Flow Facility in the Gas Dynamics Laboratory. This facility, including the hardware required for base bleed experiments, is sketched in Fig. 2. The facility has been specifically designed to avoid the model support interference effects that have plagued earlier studies. In particular, the cylindrical sting which supports the base models is carefully centered in the annular converging-diverging nozzle and is supported at only two locations upstream of the nozzle throat. Details of the wind tunnel design and operational features have been presented elsewhere (Herrin, 1993). Conventional flow visualization, static pressure measurements, and laser Doppler velocimetry (LDV) data have been obtained on and near the afterbody surface. The non-intrusive nature of the current instrumentation systems is essential in base flow studies as probe interference effects in the sensitive near-wake region have been shown to be potentially significant (Hawkins and Trevett, 1966).

The pressure distribution along the base surface of the cylindrical afterbody is shown in Fig. 3. As may be expected, the profile shows an essentially constant pressure acting over the entire base surface with only a slight increase in pressure near the outer edge of the base. Integrating the pressure profile shown in Fig. 3 yields an average base pressure coefficient of $\overline{C_{p_{base}}}$ = -0.102 and, consequently, a net base drag coefficient of $C_{D_{net}}$ = 0.102. These values will be used as a datum to show the global benefits of various drag reduction methods later in this paper. Although obtaining the base pressure distribution was a relatively simple task in practice, it has been very useful as a validation criterion for computational base flow predictions (Tucker and Shyy, 1993; Sahu, 1994; Chuang and Chieng, 1994).

As indicated in Fig. 1 and discussed earlier, the mean flowfield downstream of a cylindrical afterbody in supersonic flow contains many fluid dynamic features (or "components") that interact to form the base flow "solution." A compressible shear layer, formed by the geometric separation of the afterbody boundary layer, separates the outer inviscid flow from the recirculation region behind the base. Mass, momentum, and energy are exchanged through the shear layer as it drives the recirculation region downstream of the body. Any change in the physical characteristics of the shear layer will also affect the flow in the base region and, therefore, the base pressure. The development of the shear layer downstream of the cylindrical afterbody can be seen in the mean axial velocity contours shown in

4

Fig. 4. The majority of the shear layer growth occurs at the inner edge (shown by diverging contour lines) as large eddies entrain low speed fluid from the recirculation region. Approximately two base radii downstream, the shear layer enters the recompression and realignment region and eventually reattaches along the centerline of the wake at x/R = 2.65. This reattachment point (or rear stagnation point) separates the downstream wake flow from the fluid that is returned to the base by the adverse pressure gradient associated with shear layer realignment. The recirculating fluid accelerates from the rear stagnation point toward the base to a peak reverse mean velocity of 27% of the velocity approaching the afterbody. When compared to previous base flow measurements (Delery, 1983; Merz et al., 1978), it appears that a similarity relationship may exist for the centerline velocity distribution downstream of axisymmetric bodies. In fact, some characteristics of the near-wake mean flowfield change little over a wide range of Mach numbers.

One of the primary benefits of utilizing LDV in the current flow environment is the capability of extracting turbulence data without introducing a probe into the flow. By utilizing two separate orthogonal measurement planes, each containing the axis of symmetry, five of the six kinematic Reynolds stress components were measured directly. These include the three normal stresses (σ_u^2, σ_v^2, σ_w^2) and two of the three shear stresses (<u'v'> and <u'w'>). In general, the majority of the turbulence energy in the near-wake is concentrated in the compressible shear layer from the base corner to the reattachment point. An investigation of the primary production term for the turbulent kinetic energy, <u'v'>$\partial U/\partial r$, reveals that turbulence production is a maximum near the inside edge of the shear layer immediately downstream of the base corner and decays rapidly as the shear layer develops. The transfer of energy from the mean flow to the turbulence field via classical production mechanisms occurs primarily through the axial component of the Reynolds normal stress. The radial and tangential components acquire energy via more passive redistribution mechanisms such as pressure-velocity interactions and turbulent diffusion. Consequently, it is not surprising that the relative ordering of the Reynolds normal stresses in the near-wake flowfield was found to be $\sigma_u^2 > \sigma_v^2 - \sigma_w^2$.

Figure 5 shows the turbulent kinetic energy contours throughout the near-wake of the cylindrical afterbody. The turbulent kinetic energy distribution is similar to its dominant component, the axial normal stress, σ_u^2. As the figure indicates, the turbulent kinetic energy increases as the shear layer develops up to approximately two base radii downstream of the base

where a local maximum occurs. As the shear layer undergoes recompression and realignment, the turbulence activity is reduced and continues to diminish into the downstream wake. Note also that the magnitude of the turbulent kinetic energy in the shear layer is significantly larger than in the approach boundary layer indicating that rapid mixing and entrainment undoubtedly occur along the shear layer boundaries.

As previously discussed, the energy exchange through the highly turbulent compressible shear layer plays an important role in the dynamics of the near-wake flowfield. In our recent study (Herrin and Dutton, 1994c) of the effects of the rapid expansion at the base corner on the shear layer characteristics, we found that the inlet conditions to the base corner separation process, as well as the strength of the expansion, are extremely important in defining the shear layer characteristics throughout the near-wake. As an example, Fig. 6 shows the development of the axial and radial Reynolds normal stress profiles near the base corner. The effect of the separation process through the rapid expansion is to magnify the axial normal stress along the inner edge of the shear layer while attenuating the energy in the outer portions of the profile (Fig. 6a). The bulk dilatation occurring through the expansion is the primary turbulence attenuation mechanism (Dussauge and Gaviglio, 1987) and dominates the majority of the expanding boundary layer. Near the inner edge, however, the active entrainment of fluid from the base region by large-scale turbulent structures causes a significant increase in the axial normal stress from the levels in the approach boundary layer. Interestingly, the radial normal stress profiles (Fig. 6b) do not exhibit significant increases through the separation region (note the difference in scales between Figs. 6a and 6b). This is most likely a result of the longer time scale associated with turbulent energy transport to the two secondary normal stress components (radial and tangential). The primary Reynolds shear stress (<u'v'>) profiles near separation are similar to those shown in Fig. 6a for the axial normal stress.

To further enhance understanding of the separation process, a conditional quadrant decomposition analysis (Willmarth and Lu, 1972) was completed on the Reynolds stress data near the base corner. To examine the organization of the turbulence field, the individual turbulent fluctuations (u',v') were plotted against each other in an attempt to find a dominant instantaneous shear angle. Figure 7 presents a comparison of two (u',v') scatter plots, one obtained immediately upstream of separation (Fig. 7a) and the other immediately downstream of separation (Fig. 7b).

5

These data clearly show a significant increase in the turbulence organization from the afterbody boundary layer to the separated shear layer due, most likely, to enhancement of the large-scale structure in the flowfield. This is consistent with the large increase in the streamwise Reynolds normal stress near the inner edge of the shear layer shown in Fig. 6a. Since the turbulent structures are the primary source of entrainment from the recirculation region, their behavior is critically important to the overall flow physics in the base region. It is also apparent that by controlling these structures, one can also directly affect the base flowfield and, therefore, the base pressure. However, to date, shear flow control techniques have not been utilized in modern base drag reduction methods.

It is clear from the preceding discussion that the inner edge of the separated shear layer is a region containing large-scale, organized, turbulent motions that entrain mass from the low-speed fluid behind the base. The energy exchange which occurs during the entrainment process directly affects the streamwise normal stress and, in a secondary manner, the transverse and tangential normal stresses. The relative contributions from each component along the shear layer axis are important in understanding the evolving state of the shear layer. Figure 8 shows the peak Reynolds normal stresses along the shear layer axis up to the onset of the recompression region. As for the entire near-wake flowfield, the streamwise normal stress dominates the shear layer turbulence field throughout its development, the contributions from the transverse and tangential components being significantly smaller and relatively similar. From a quadrant analysis of the Reynolds stress data in the developing shear layer, it appears that the turbulence organization shown immediately downstream of separation in Fig. 7b, persists further downstream and, consequently, the overall turbulence activity increases with downstream distance to a global peak upstream of the onset of recompression, Fig. 5.

Boattailed Afterbody

One of the most common drag reduction techniques in use on current missiles and projectiles is afterbody boattailing. By properly altering the afterbody surface to a shallow angle relative to the cylindrical body, the net afterbody drag on the vehicle can be reduced. The primary parameters describing a boattailed afterbody are the mean angle, length, and shape of the boattail. In practice, axisymmetric boattails are generally conical with an angle relative to the approach flow of 3-7 degrees and a boattail length of 0.5-1.5 caliber. In the experimental study presented in this section (Herrin and Dutton, 1994b), a conically boattailed, axisymmetric afterbody with an angle of 5 degrees and 0.5 caliber length was investigated. The objective of the study was to determine the near-wake fluid dynamic effects of afterbody boattailing in comparison to those downstream of the unboattailed, cylindrical afterbody just discussed. As in the cylindrical afterbody case, the primary diagnostic tools were static pressure measurements and two-component laser Doppler velocimetry. The approach flowfield to the boattailed afterbody was essentially identical to that for the cylindrical afterbody with a mean approach Mach number of 2.46.

To quantify the net drag reduction from afterbody boattailing in the present case, static pressure data along the boattail and on the base were obtained. Figure 9 shows the pressure distribution on the boattail surface relative to a predicted solution from the inviscid method of characteristics for axisymmetric flow. Notice that the overall pressure level on the boattail is higher than the base pressure for the cylindrical afterbody (Fig. 3); hence, the annular ring formed by the projection of the boattail surface in the axial direction experiences a drag reduction when compared to the same annular ring on the base of the cylindrical afterbody. In comparison to the method of characteristics solution (Fig. 9), the measured afterbody pressure profile is somewhat rounded near the boattail origin, due to boundary layer effects, but relaxes to the predicted solution near the end of the boattail. It is important to note that, in this case, boundary layer effects cause higher boattail pressures near the body-boattail junction compared to the MOC predictions, which contribute to the net drag reduction.

One important fluid dynamic feature on boattailed afterbodies in supersonic flow is the rapid expansion at the body-boattail junction (Fig. 1). Not only does the freestream flow accelerate through the expansion, but the afterbody boundary layer is disturbed as it enters the boattail region. In general, the recovery of turbulent boundary layers from rapid expansions occurs rapidly for mean flow quantities and more slowly for the turbulence field. As an example, streamwise rms velocity fluctuation profiles are shown in Fig. 10 at five different axial stations, one upstream (solid symbols) and four downstream (open symbols) of the body-boattail junction. It is apparent that σ_u decreases through the expansion, especially over the inner portions of the boundary layer where the streamwise pressure gradient is most severe. This reduction in turbulence activity directly affects the overall turbulence levels and entrainment in the initial portion of the shear layer and, therefore, the base pressure. The transverse rms velocity fluctuation (σ_v) and the primary shear stress ($<u'v'>$) were also reduced through the expansion.

In addition to the turbulence attenuation through the expansion at the body-boattail junction, the mean freestream flow is accelerated and the mean flow angle is altered to that of the boattail surface. These effects of the boattail change the inlet conditions for the near-wake base flow as compared to those for the cylindrical afterbody case. Of course, the effect of afterbody boattailing on the pressure in the base region is the critical element in determining whether a net gain or loss in afterbody drag occurs. In the present case, the average base pressure coefficient on the base of the boattailed afterbody, $\overline{Cp_{base}} = -0.086$, was 16% higher than that on the cylindrical afterbody, Fig. 3. When the projected pressure-area force on the boattail in the axial direction is considered, a net afterbody drag reduction of 21%, $C_{Dnet} = 0.081$, is found compared to the cylindrical case. It is quite amazing that this significant drag reduction was generated by only a slight modification to the original cylindrical afterbody geometry.

Although the global benefits of afterbody boattailing have been well established, it is the flow physics in the base region of the boattailed afterbody that are the primary focus of the current study. When comparing the structure of the mean velocity fields throughout the near-wake of the cylindrical and boattailed afterbodies, it becomes obvious that, in general, there are subtle but significant differences. For example, the mean axial velocity distribution along the wake centerline (Fig. 11) shows only slight increases in the mean shear layer reattachment location and the maximum reverse velocity magnitude in the boattailed afterbody case, suggesting relatively small changes in the overall mean flow near-wake structure. However, the mean shear layer growth rate in the cylindrical afterbody case was found to be nearly three times that downstream of the boattailed afterbody. The flow mechanisms involved in the growth rate reduction become clearer when we consider the turbulence structure in the near-wake and, more specifically, in the developing shear layer.

As in the cylindrical afterbody case, the conditional quadrant decomposition technique was applied to the turbulence data obtained in the boattailed afterbody shear layer. From this analysis, it is apparent that a turbulence organization similar to that in the cylindrical afterbody case (Fig. 7b) exists. Although the structure of the turbulence fields may be similar between the two afterbodies, the absolute magnitudes of the turbulence quantities differ considerably. Namely, the shear layer turbulence properties for the boattailed afterbody are generally reduced from those downstream of the cylindrical afterbody. This reduction in near-wake turbulence activity by afterbody boattailing is shown by

comparing the near-wake turbulent kinetic energy contours for the boattailed afterbody (Fig. 12) with those previously presented for the cylindrical afterbody (Fig. 5). Direct comparison of the turbulent kinetic energy distributions along the near-wake centerline for the two afterbodies is also shown in Fig. 13. Although the global peak in each case occurs in nearly the same location relative to the base, the peak magnitude is reduced by 18% by afterbody boattailing. Turbulence reductions were found in all components of the Reynolds stress with axial, radial, and tangential rms velocity fluctuations reduced by 8%, 17%, and 1%, respectively. In addition, the peak primary shear stress, $<u'v'>$, was reduced by 8% by afterbody boattailing. The primary ramification of the reduced turbulence activity in the boattailed afterbody shear layer is reduced mass entrainment from the recirculation region behind the base and, therefore, an increased base pressure when compared to the cylindrical afterbody case. The reduced shear layer growth rate for the boattailed afterbody supports this contention.

Summarizing, the reduction in net afterbody drag by afterbody boattailing results from several factors. The increased pressure on the boattail surface relative to the cylindrical afterbody base pressure reduces drag on the outer periphery of the projected base surface. More importantly, though, the base pressure on the boattailed afterbody is increased through changes in the near-wake mean velocity and turbulence fields. One important result of the present study is the overall reduction in measured turbulence activity and, hence, growth rate of the boattailed afterbody shear layer relative to an unboattailed cylindrical afterbody.

Base Bleed

<u>Background</u>

Base bleed is a drag reducing technique which involves injection of low-speed fluid into the base region to increase the base pressure. The magnitude of the bleed flow rate is quantified using a non-dimensional injection parameter, I, defined as the bleed mass flow rate normalized by the product of the base area and the freestream mass flux.

The effect of varying the bleed mass flowrate on the base pressure ratio has been studied experimentally by several researchers (Cortright and Schroeder, 1951; Reid and Hastings, 1959b; Badrinarayanan, 1961; Bowman and Clayden, 1967; Valentine and Przirembel, 1970). The results of these experiments exhibit certain common trends and indicate three distinct operating regimes determined by the quantity of mass injected. The base pressure ratio increases fairly linearly with bleed rate at low values of

I (regime 1). A peak in the base pressure ratio occurs at an intermediate value of I (near I = 0.01 for air), the value of which depends on several factors including the freestream Mach number, the size and geometry of the bleed orifice, and the molecular weight and temperature of the bleed gas. Increases in base pressure ratio (relative to the no-bleed case) from 10 to 90% have been reported for various combinations of the aforementioned parameters. As the bleed rate is increased past the optimum value, the base pressure ratio decreases (regime 2) until it reaches a relative minimum. A further increase in bleed flow leads to the onset of power-on conditions (regime 3) when the bleed flow becomes supersonic, resulting in an increase in base pressure ratio.

From the combined results of the above experiments, base bleed effectiveness is seen to increase with freestream Mach number, i.e., at higher Mach numbers, the peak base pressure occurs at lower I, and the percentage increase in base pressure is also higher. Investigations by Reid and Hastings (1959b), Bowman and Clayden (1967), and Valentine and Przirembel (1970) indicate that at very low bleed rates, the increase in base pressure with bleed is nearly independent of the bleed jet area; however, at higher bleed rates, the effectiveness of base bleed was shown to be improved by larger jet-to-base diameter ratios. Injection with porous bases was found to be the most effective.

Analytical models based on the component-type approach of Korst (1956) provide some insight into the physical processes that are associated with base bleed. Although these models can only represent the base bleed flowfield in a time-mean sense and can not account for its instantaneous turbulent nature, they have been fairly successful in predicting the qualitative effects of bleed on base pressure (Korst et al., 1964; Reijasse et al., 1989). Base bleed computations using the Reynolds-averaged Navier-Stokes equations carried out at the Army Research Laboratory (Sahu et al., 1985; Sahu, 1986; Nietubicz and Sahu, 1991) have also been successful in predicting qualitative base pressure trends and in capturing flowfield structure details. As discussed in the introduction, however, RANS predictions are currently limited by turbulence modeling issues and lack of detailed experimental data for validation.

While the effectiveness of base bleed as a drag reducing technique is well known, the details of the fluid dynamic interactions caused by base bleed are not clearly understood. Most of the previous experimental investigations were carried out prior to the development of reliable non-intrusive diagnostic methods, and their scope was primarily limited to determining the global influence of various base bleed parameters on base pressure. Some results from earlier studies are also unreliable due to possible interference arising from model support effects. Since no known detailed measurements of the base bleed flowfield are known to exist, a research effort aimed at investigating the effects of base bleed on the near-wake flowfield of a cylindrical afterbody in supersonic flow has been initiated as a logical extension to the blunt base and boattail studies described in the previous sections. Initial results from this effort are described below.

Experimental Results

For the base bleed study, the Axisymmetric Base Flow Facility shown in Fig. 2 was used. The 63.5 mm diameter cylindrical afterbody contains a 0.4 caliber bleed orifice which is preceded by an elliptically contoured section based on ASME long-radius nozzle standards (Bean, 1971) to ensure a uniform velocity profile for the bleed flow exiting the base. The bleed line also contains components for throttling, metering, and conditioning the bleed flow. Details of the wind tunnel and the base bleed facility are provided by Herrin (1993) and Mathur and Dutton (1995), respectively.

Spark-schlieren photographs (not shown here for brevity) were taken at five different bleed rates using a horizontal knife-edge and were used to obtain qualitative information on the effect of base bleed on the near-wake flowfield. At zero bleed, the wake is closed and a strong recompression shock system is evident. As expected, the shear layer angle becomes flatter, the base corner expansion weakens, the wake widens, and the recompression shocks become weaker as the bleed flow rate is increased. At very high bleed rates, when the bleed exit velocity becomes sonic, the Mach disk emanating from the bleed orifice interacts with the outer flow, forming a fairly complex shock system. This shock system appears to be highly unsteady, as indicated by imaging the flowfield on a screen and by visual inspection of a series of photographs at this bleed rate. Further details are provided by Mathur and Dutton (1995).

Static pressure distributions along the afterbody and on the base plane were obtained for ten bleed rates ranging from I = 0 to I = 0.032. The radial distribution of base pressure coefficient is shown in Fig. 14 for all ten bleed flow rates. At any given bleed rate, the base pressure distribution is radially symmetric across the base annulus, and fairly independent of radial location. The slight increase in base pressure near the base corner in some cases is probably due to streamline curvature effects caused by the sharp change in flow direction during entrainment of the low-speed flow from the recirculation region by the high-speed shear layer

8

near the base corner. It is also evident that the base pressure initially increases with bleed rate (solid symbol cases), peaks at around I = 0.0148, and then decreases rapidly as the bleed rate is increased further (open symbol cases). This behavior is more clearly seen when the average base pressure coefficient, based on the area-weighted average of each profile, is plotted as a function of the injection parameter, Fig. 15. Data from the blunt base and the five degree boattailed afterbody results discussed previously are also presented. The peak average base pressure coefficient is $\overline{C}_{Pbase}$ = -0.078 at I = 0.0148. Neglecting the thrust of the bleed flow, this results in a net base drag coefficient of C_{Dnet} = 0.078 which is a reduction of approximately 24% compared to the blunt base case and 4% compared to the boattailed afterbody. The difference in the average base pressure coefficient between the blunt base and the I = 0 no-bleed case is probably due to the compliant boundary presented by the bleed orifice and the hollow sting cavity upstream. The average base pressure ratio peak at I = 0.0148 is consistent with earlier experiments (Reid and Hastings, 1959b; Bowman and Clayden, 1967; Valentine and Przirembel, 1970), all of which were performed with bleed orifices of 0.4 caliber.

A parametric study of the mean axial velocity and turbulence quantities along the near-wake centerline has been performed using LDV. The effect of base bleed on the mean axial velocity distribution along the centerline can be seen in Fig. 16. For the no-bleed case, the peak reverse velocity (30% of the freestream value) and the rear stagnation point occur 1.5 and 2.8 base radii downstream of the base, respectively. These results are nearly identical to measurements done with the blunt base. At the base plane (x = 0), however, the extrapolated axial velocity is non-zero and negative, due to the compliant boundary presented by the bleed orifice. As the bleed rate is increased, the bleed jet exit velocity increases, causing a downstream shift of the forward stagnation point where the bleed flow and reverse flow meet. This has the effect of diminishing the size of the centerline recirculation region since the rear stagnation point location is relatively constant at x/R_O = 3.2 (note that this position for the bleed-on cases is shifted relative to the bleed-off case). The peak reverse velocity location occurs progressively downstream, and its magnitude decreases, with increasing bleed. At I = 0.0148, the optimum bleed rate from a base pressure viewpoint, the recirculation region along the centerline almost disappears. No reverse velocity is detected along the centerline for the I = 0.0226 case, indicating penetration of the bleed jet into the wake.

Figures 17 and 18 present the axial and radial turbulence intensity distributions along the centerline. For each bleed case (except I = 0.0226), two peaks are observed in the distribution of turbulence intensity. The first peak occurs at the forward stagnation point location due to the change in flow direction from axial to radial when the bleed flow meets the reverse flow in the recirculation region. The magnitude of this peak is seen to decrease with increasing bleed rate due to the smaller influence of the diminishing recirculation region. The second peak occurs at the rear stagnation location due to reattachment phenomena. The influence of the flow mechanisms occurring at both stagnation point locations is much stronger in the axial direction. Consequently, the peaks in the radial turbulence intensity distributions are not as pronounced as the axial intensity peaks. At the higher bleed rates, the bleed flow penetrates further into the near-wake, accounting for the low overall turbulence intensity levels seen in Figs. 17 and 18 for these cases. Anisotropy of the turbulent normal stresses along the centerline is also evident from the differences in the axial and radial turbulence intensity profiles. Figure 19 shows the centerline distribution of turbulent kinetic energy. Comparing these results to those in Fig. 13 for the cylindrical and boattailed afterbodies, the substantially reduced centerline turbulence levels for the bleed-on cases are evident.

PLANAR VISUALIZATIONS AND MEASUREMENTS OF TWO-DIMENSIONAL BASE FLOWS

It has been shown in the preceding sections that pointwise statistical measurements provide clues on the nature of both small- and large-scale turbulent structures which control the dynamics of mixing and energy exchange occurring within high-speed separated flowfields, especially in the shear layer, reattachment, and wake development regions. Direct examination of these structures, in conjunction with statistical data, offers the possibility of improving understanding of the effects of the turbulent structures on these flows. In turn, this information may be used to better control and model high-speed separated flows over a wide range of conditions.

Such direct examination of turbulent structures in compressible separated flows requires non-intrusive multi-point time-resolved measurements. Planar optical techniques which provide this capability have been applied, with consideration of the special requirements for high-speed separated flows, in the following studies of two-dimensional base flows.

9

PIV Measurements of Subsonic Base Cavity Flows

Although the mean velocity field in the wake of a two-dimensional body at large Reynolds number and subsonic velocity is similar in appearance to supersonic base flows (shear layers, recirculation region, and rear stagnation point as shown in Fig. 1), the instantaneous wake structure is actually made up of alternately shed vortices known as the von Kármán vortex street. This commonly occurring structure has been the subject of numerous studies beginning with von Kármán's first theoretical analysis of vortex streets in 1911. A salient feature of this flowfield is the interaction of the low pressure vortices in the near-wake with the base surface, inducing base drag, which is typically a significant component of the total drag. For this reason, drag reduction methods based on modification of the vortex street have received much attention.

One effective drag reduction technique is the use of a base cavity. It has been shown experimentally that the presence of a solid-walled cavity in the base region of a slender two-dimensional body (see Fig. 20) increases the base pressure, resulting in base drag reductions of up to 30% (Nash et al., 1963; Pollock, 1969; Clements and Maull, 1975; Kruiswyk and Dutton, 1990). Other effects of a base cavity that have been experimentally observed include an increase in Strouhal number (dimensionless vortex shedding frequency) as compared to a blunt base (Clements and Maull, 1975; Kruiswyk and Dutton, 1990) and limited drag reduction for a cavity depth beyond approximately half the base height.

Although these effects of base cavities are well documented, the *mechanism* of base cavity drag reduction was unclear based on these and other previous studies. Several theories were proposed based on modeling and measurement of the wake structure, all of which implied some modification of vortex formation location and reduction in vortex strength.

Particle image velocimetry (PIV) was applied in a recent study of two-dimensional base cavities to resolve the mechanism of base cavity drag reduction (Molezzi and Dutton, 1993a; Molezzi and Dutton 1995). PIV is an optical-based technique used to measure flow velocities over an entire planar region simultaneously. The PIV system developed for this work is described in detail by Molezzi and Dutton (1993b). PIV has the ability to identify turbulent flow structures which can be random in nature but important to the overall behavior of the flow. PIV also reveals planar views of three-dimensional flow structures which are smeared by line-of-sight integration inherent in techniques such as schlieren or shadowgraph photography.

Experiments were performed in a blowdown-type transonic wind tunnel (Fig. 21) with a design based on that of Little and Cubbage (1961). The tunnel has a 101.6 mm square test section with solid sidewalls and slotted upper and lower inner walls to relieve the blockage effect of models in the subsonic to transonic speed range. Six-inch diameter round windows are mounted in both sidewalls to allow visualization of the downstream end and near-wake of a base model. Slot-shaped upper and lower windows are also mounted in the outer tunnel walls for PIV optical access. The base model is made up of an interchangeable afterbody mounted on a wedge-shaped forebody. The afterbodies used are a blunt base and a rectangular base cavity with a depth of half the base height. The experimental facilities and flow conditions were selected to match those used by Kruiswyk and Dutton (1990) to facilitate comparison of results.

Data were obtained for quantitative analysis with the blunt base and base cavity models at both of the freestream conditions shown in Table 1, resulting in four experimental cases. PIV data were also obtained for both base models at a Mach 0.8 freestream condition, but inconsistent seeding density in some regions of the wake limited those results to a qualitative confirmation of the existence of a turbulent vortex street wake similar to that observed in the Mach 0.4 and 0.6 cases.

Table 1 Experimental Flow Conditions

Freestream Mach No. (M_∞)	Freestream Reynolds No. (Re_∞)
0.4	1.36×10^5
0.6	1.82×10^5

Fifteen flowfield realizations were obtained for each of the Mach 0.4 and Mach 0.6 cases listed. Each individual realization consists of an array of 6831 (99 x 69) instantaneous velocity vectors with 0.5 mm spacing in the streamwise and transverse directions for resolution of small-scale motions within the flowfield. Out-of-plane vorticity was also calculated for each realization to directly analyze vortex location and strength, which had previously been impossible in high-speed separated flows.

A gray scale plot of vorticity with overlaid velocity vectors from a single Mach 0.6 realization is shown in Fig. 22. One of the notable features, which holds for all realizations, is the significant fragmentation of the vortices as they shed from the

10

separated shear layers at the aft edge of the base. This is indicative of the high level of boundary layer turbulence prior to separation, confirmed by LDV measurements showing an increase of turbulence intensity from 1% in the freestream to 5% in the boundary layer as the afterbody surface is approached just prior to separation (Molezzi, 1993). Propagation of small-scale turbulent structures throughout the flowfield is also evident. This result is confirmed by fast response pressure measurements made in the wake by Kruiswyk and Dutton (1990) which showed a distributed spectrum around the vortex shedding frequency, indicating the superposition of the vortex street on a random turbulent flowfield. A classical turbulence energy cascade from the large-scale vortices to the smaller scales takes place downstream of the base, causing the gradual breakdown of distinct vortices into the small-scale structures.

In order to analyze the path and strength of vortices in the near-wake, the root mean square (RMS) vorticity was calculated from the 15 realizations for each case to reveal the magnitude and location of vorticity peaks in the wake. The RMS vorticity for each case is presented in Fig. 23. These plots show the region within approximately one base height of the aft edge to concentrate on notable features. One of the features revealed in these plots is the presence of the free shear layers propagating from each separation point. At a point less than one-half base height downstream, they end abruptly, indicating the mean location at which free vortices break off into the wake, i.e. the vortex formation location. Lines fit to the peak vorticity values along the shear layers are shown to aid in identifying the mean shear layer location, shape, and length. Each shear layer line ends at the point where the vorticity drops below 67% of the maximum for each flow condition, allowing a relative comparison of the shear layer lengths between all four cases.

Table 2 shows the average shear layer length for each experimental case. Although wake static pressure data were used by Kruiswyk and Dutton (1990) to conclude that vortex formation occurs slightly further downstream due to the cavity for the Mach 0.4 freestream condition, the data here show small absolute reductions in average shear layer length between the blunt and cavity cases for each freestream condition. However, since the differences are small and considering the asymmetry in length of the upper and lower shear layers, no evidence of significant change in vortex formation location due to the cavity can be claimed based on these data.

Figure 23 does, however, reveal that the angle of convergence of the shear layers toward each other is notably steeper for the base cavity cases than for the blunt base cases. Convergence causes the transverse

separation distance between the shear layers to be reduced at their endpoints (shown in Table 3), explaining the increase in shedding frequency observed by Kruiswyk and Dutton (1990) for the base cavity, given that the shedding frequency in a vortex street is inversely proportional to the distance between the shear layers (Fage and Johansen, 1927).

Table 2 Base Flow Shear Layer Length

Experimental Case	Average Shear Layer Streamwise Length (mm)	% Change from Blunt
M_∞=0.4 blunt	6.9	—
M_∞=0.4 cavity	6.8	-1.4
M_∞=0.6 blunt	8.0	—
M_∞=0.6 cavity	7.4	-7.5

Table 3 Base Flow Shear Layer Separation

Experimental Case	Shear Layer Endpoint Separation (mm)	% Change from Blunt
M_∞=0.4 blunt	13.0	—
M_∞=0.4 cavity	12.5	-3.8
M_∞=0.6 blunt	13.5	—
M_∞=0.6 cavity	12.8	-5.2

Table 4 Base Flow Near-Wake Vortex Strength

Experimental Case	Spatial Average RMS Vorticity (s^{-1})	% Change from Blunt
M_∞=0.4 blunt	42590	—
M_∞=0.4 cavity	40890	-4.0
M_∞=0.6 blunt	66120	—
M_∞=0.6 cavity	62490	-5.5

In an effort to quantify the strength of the vortices just after formation, the spatially averaged RMS vorticity was calculated for each experimental case over a uniform region just past the shear layer endpoints. The results are shown in Table 4. Although the data scatter in Fig. 23 makes small differences difficult to determine visually, Table 4 shows that the average RMS vorticity level is indeed reduced somewhat by the cavity for both freestream Mach numbers, implying a small decrease in vortex strength. Also, the effect of the base cavity on mean vortex path is not clear from Fig. 23, although it is evident that the vortex path is somewhat random due to near-wake turbulence.

The effects of increasing Mach number on the shear layers include a small increase in shear layer separation (see Table 3) which seems to be caused by a reduction in both the initial convergence angle and curvature of the shear layers, and can be attributed to increased streamwise momentum in the fluid stream outside the wake. The shear layers are also extended by approximately 1 mm for the Mach 0.6 freestream cases versus Mach 0.4 (Table 2), causing vortex formation to occur further downstream of the base edge. This serves to explain the reduced effectiveness of the cavity at higher Mach number as shown by Kruiswyk and Dutton (1990) since, as the vortices form further away from the base at higher Mach number, their effect on the pressure at the base surface is reduced.

Further information on base cavity wake effects can be obtained by comparing the instantaneous wake structure for the blunt base and base cavity at a similar point in the vortex shedding cycle. For each freestream condition, pairs of blunt base and base cavity realizations were selected with closely matching vortex locations in the near-wake for comparison. Figure 24 shows one such realization pair at the Mach 0.6 freestream condition. These realizations, along with others not shown here, indicate that the circulating region around a fully formed vortex entering the wake covers most of the base height. However, it is evident that the base cavity allows the circulating region around the first fully formed vortex to extend further in all directions, diffusing the vortex motion over a larger region. Although velocity data are available only to within 1 mm of the base boundary, the vortex seems to extend partially into the cavity boundary (see first column of vectors at x = 1 mm), but the relatively small magnitude of this motion and the distance of the vortex center from the cavity preclude the vortex from being significantly inhibited by the cavity walls. This is confirmed by surface flow visualization experiments performed by Kruiswyk and Dutton (1990) which indicated very little fluid motion on the inner cavity walls, even near the cavity edge. Figure 24(d) also shows very low vorticity near the cavity boundary, indicating little, if any, effect of the cavity walls on vortex formation.

Another feature of the vortex expansion shown in Fig. 24 is that, with the base cavity, the vortices extend far enough across the wake to affect the opposing shear layer. For example, in Fig. 24(b), the fully formed vortex shed from the lower separation point clearly interacts more strongly with the upper shear layer than is the case for the blunt base in Fig. 24(a). This is especially evident from the vorticity plots in Figs. 24(c) and (d). Shear layers are indicated by solid lines in the same manner as in Fig. 23. The fluid

motion near the shear layers due to vortex expansion across the wake is also shown in Fig. 24(d) with a curved arrow. The most significant effect of the interaction of the expanded vortex with the opposing shear layer is a folding of the shear layer region. In Fig. 24(d), the upper shear layer is folded toward the centerline at locations upstream of the vortex center due to downward fluid momentum in this region. Interaction of the expanded vortex with remnants of the upper shear layer downstream of the vortex center is also apparent with the shear layer folding away from the transverse centerline.

The evidence presented indicates that the most prominent effects of a base cavity on the vortex street wake are the expansion of individual vortices across the near-wake and partially into the cavity and the resulting increased convergence of the separated shear layers from each base corner toward the transverse wake centerline. The diffusion of vortex motion, in turn, reduces vortex strength by approximately 4% to 6%, although the vortices do not form significantly further upstream and are not inhibited by the cavity walls. This is seen at both freestream conditions examined here. It is also evident that the effects are less significant at higher freestream velocities due to the extension of the separated shear layers and the movement of the vortex formation location further downstream, away from the base.

Aside from these wake modifications, the mechanism of base pressure increase due to base cavities must be considered. The effects described above modify and slightly weaken the vortex street, which, in turn, should slightly increase the pressure in the vicinity of the vortices in the near-wake. However, these changes are relatively small and the vortex formation location and path are not significantly modified. Therefore, since neither the strength nor location of the vortices is significantly altered with the base cavity, the most significant factor affecting the base pressure appears to be the upstream displacement of the base surface to a location where it does not interact strongly with the low pressure vortices.

The lack of sensitivity of wake structure to base cavity modifications may have several implications in base flow research and design, including areas such as the prediction of wake signatures and performance of modified base cavity geometries.

Mie Scattering Visualizations of Large-Scale Structures in Supersonic Base Flow

Background

This section describes an ongoing experimental investigation of the complex interaction region

generated by the separation of two supersonic streams past a finite-thickness base. This type of flowfield is frequently encountered in practical applications such as powered missiles in supersonic flight, the trailing edge of a blunt supersonic airfoil, chemical lasers, supersonic exhaust nozzles, and supersonic combustors. Previous research has shown the near-wake region to be dominated by strong velocity gradients, pronounced turbulence levels, and expansion-compression processes covering the full range of gas dynamic regimes (Petrie et al., 1986; Samimy and Addy, 1986; Samimy et al., 1986; Amatucci, 1990).

Although the concept of large-scale (or coherent) structures within incompressible shear layers is well established (Cantwell, 1981; Coles, 1985; Hussain, 1986), only recently have analytical, computational, and experimental studies shown the presence of these structures in supersonic shear layers (Papamoschou and Roshko, 1988; Elliott and Samimy, 1990; Clemens and Mungal, 1992; Messersmith, 1992). At low compressibility, two-dimensional roller-type large-scale structures with distinct braid and core regions are discernible. As the compressibility of the mixing layer increases, plan views show degeneration of the spanwise organization of the structure, first by skewing of the structure, followed by a nearly complete breakdown in two-dimensional organization. At the highest levels of compressibility, the structures appear to have few similarities to the well-defined Brown-Roshko rollers typical of incompressible mixing layers (Brown and Roshko, 1974); instead, they seem to exhibit a more random and less coherent organization.

Recognizing the importance of coherent motions in supersonic free shear layers and that these shear layers are such a dominant feature of supersonic base flows, an understanding of the large-scale structures and their behavior in the near-wake region is clearly important. The primary objective of this research effort is to obtain a more complete understanding of the detailed fluid dynamic processes, specifically the behavior and evolution of large-scale turbulent structures, inherent to supersonic planar base flowfields. The present study is believed to be the first to employ planar imaging techniques for the near-wake interaction of two dissimilar supersonic streams separated by a finite-thickness splitter plate. The qualitative images and quantitative measurements will help clarify the influence of the large-scale structures on the shear layers and recirculation region, as well as their contribution to wake development.

Experimental Facilities and Diagnostics

This research is being conducted in a supersonic, blowdown-type wind tunnel designed specifically for the study of planar base flows. Figure 25 is a schematic diagram of the wind tunnel facility. The converging-diverging nozzles that produce the two supersonic streams were designed by Amatucci (1990) using a method of characteristics analysis for the desired Mach number and nozzle exit height. These nozzle blocks were modified by inserting slot windows flush-mounted along the floor and ceiling of the test section to provide optical access for a laser sheet. The two-dimensional test section (100 mm X 50 mm cross-section) produces a Mach 2.5 upper stream and a Mach 2.0 lower stream (with intentional boundary layer thickness mismatches) both of which undergo geometric separation past a thick splitter plate (25 mm in height). The resulting expansion and mixing processes before recompression, reattachment, and development of the wake flow provide the opportunity to characterize the evolution of the coherent motions in the shear layers throughout initial formation, zero pressure gradient mixing, and subsequent adverse pressure gradient conditions.

The present study employs planar Mie scattering from condensed ethanol droplets as the primary visualization diagnostic. This non-intrusive visualization technique provides instantaneous structural information without the detrimental volumetric-averaging inherent to line-of-sight techniques such as schlieren or shadowgraph photography. This is especially important in the present study because the convective Mach number (Bogdanoff, 1983), M_c, of these shear layers is large enough that the large-scale structures are expected to be highly three-dimensional in character. In the present study, liquid ethanol in minute quantities, typically 0.35 percent mass fraction, is introduced far upstream of the test section where it completely evaporates into the carrier air. Due to the rapid cooling as the air expands to supersonic conditions, sudden condensation occurs, forming a fine "fog" of ethanol droplets which can be visualized with a laser sheet. It is important to remember that Mie scattering visualizes particles in the flow, not the actual flow itself. Based on a conservative estimate of the ethanol droplet size and the experimental conditions (described later), a representative Stokes number for the present investigation is 0.06, which is nearly an order-of-magnitude less than Samimy and Lele's (1991) criterion of 0.5 for reliable Mie scattering images.

Figure 26 illustrates the image acquisition hardware and physical arrangement. The output from a high-power pulsed Nd:YAG laser is frequency doubled to 532 nm, shaped by a series of spherical and cylindrical lenses into a planar sheet, and used to illuminate the scattering medium. The planar beam sheet is approximately 300 microns thick and 75 mm

wide. The laser has a temporal pulse width of 4-6 nanoseconds which is sufficiently short to freeze the particle motion. A high-resolution scientific-grade charged-coupled-device (CCD) camera with array dimensions of 512 pixels x 512 pixels x 14-bit resolution is used to collect the scattered signals through standard photographic lenses.

Results and Discussion

By applying the isentropic procedure of Bogdanoff (1983), the convective Mach number for the shear layers has been computed to be $M_c = 1.38$, well into the supersonic regime where three-dimensional structures are anticipated. For purposes of computing the convective Mach number, the boundary condition on the low-speed side of the shear layers, i.e. the recirculation zone, was determined from LDV survey data. Prior research has shown that certain locations within the recirculation region can possess reverse velocities as high as 20 percent of the freestream velocity (Amatucci, 1990).

Figure 27 illustrates the location and orientation of each field-of-view for the images to be presented. All views are drawn *to scale*. Views B and C are inclined relative to the tunnel floor so as to be aligned with the mean flow direction of the shear layer. Note that Views A and E overlap by one-quarter base-height. All images are presented with the flow from left to right. View B is centered in the zero-pressure gradient region of the upper free shear layer, while View C is centered in the adverse pressure gradient, i.e. recompression, region prior to reattachment. These two views will be useful for determining the effect of pressure gradient on structural characteristics and evolution.

Figure 28 presents a global image of the near-wake interaction using View A. A base model (drawn to scale) has been included as an orientation aid. At both the upper and lower separation corners, the signal level is initially low due to the effects of boundary layer heating. The recovery temperatures near the splitter plate correspond to a relatively high ethanol saturation pressure, thus inhibiting condensation. Upon negotiating the expansion corners, the shear layers experience a rapid cooling leading to the formation of condensate. Although the flow is globally seeded, no condensate was observed in the recirculation zone. This is attributed to the relatively low velocities in this region and the correspondingly high temperature. The base region provides evidence that re-evaporation of the ethanol is occurring in this flowfield; therefore, special consideration of the thermodynamic conditions throughout the flowfield must be maintained when interpreting the images.

Inspecting the results in Fig. 28, the Mach 2.0 boundary layer (lower) undergoes a much stronger expansion than the Mach 2.5 boundary layer; consequently, the initial portion of the bottom shear layer has a more uniform and consistent signal than the upper separated shear layer. The signal dropout in the upper layer may also be attributed to the boundary layer thickness mismatch at separation; the Mach 2.5 boundary layer is approximately 2.3 times thicker than the Mach 2.0 layer. The rapid distortion at the corners may also be responsible for the disparity in large-scale activity between the two shear layers. The upper layer is immediately characterized with stringy, filament-like structures projecting into the recirculation region; see Fig. 29, View B. The structures' highly-strained appearance is consistent with the observations of Messersmith (1992) and Clemens and Mungal (1992) for their high compressibility cases. These structures are not seen in the lower shear layer until later streamwise stations. Note that Mach and/or weak shock waves are emanating from within the shear layer, apparently due to the presence (interference) of the large-scale structures within the supersonic outer flow.

Although the structures generally appear small relative to the base height, they are large in the sense that they possess a spatial extent of the order of the local shear layer thickness. It is believed that the vigorous expansion of the Mach 2.0 boundary layer may act as a filter, damping out the instabilities that lead to vortex formation (Narasimha and Viswanath, 1975; Dussauge and Gaviglio, 1987; Herrin and Dutton, 1994c). It is important to note that for base flows, the intrusion of these large-scale structures into the recirculation region introduces an additional mechanism for entrainment and mixing. Entrainment in the shear layers just aft of the body ultimately determines the amount of recompression that can be supported by the flow and, hence, the base pressure (Crocco and Lees, 1952).

The large-scale structures remain fairly consistent in size and shape during recompression (Fig. 30, View C), but appear to bloom immediately after reattachment (approximately 1.4 base-heights downstream of the base), where large sweeping motions into the wake are evident. Figure 31, View D shows the complex flow structure at reattachment consisting of large-scale organized motions, shock structures, and entrainment/mixing processes. It is clear that nascent structures formed immediately following separation do survive the recompression and reattachment processes intact. From these large views, it is difficult to characterize what effects, if any, the transition from a zero pressure gradient region to an adverse pressure gradient region has on the structures. This topic will be

14

the focus of future efforts. The absence of condensed ethanol downstream of the reattachment point in Fig. 31 also clearly indicates that base fluid is being pumped into the wake.

An image of the downstream wake development is presented in Fig. 32, View E. Dominant organized motions are clearly evident, usually with small-scale structures residing on the large-scale structures. The diversity of the structures is evident in their size, shape, and orientation. For example, in the lower shear layer of Fig. 32, the structures appear to be fairly disorganized, while in the upper shear layer, the structures appear to be periodically spaced with an inclination of approximately 50 degrees to the slip plane. The eddies also appear to be quite elliptical in shape, which is characteristic of structures contained within highly compressible shear layers (Messersmith, 1992).

In both the upstream and downstream shear layer views, B and C (Figs. 29 and 30), weak shocks originating in the shear layer are observed. Prior to recompression, these shocks were confirmed to be Mach waves through angular measurements. Approaching reattachment, however, the shocks grow in strength becoming rather intense, ultimately coalescing into the main recompression shocks. Closer examination reveals that the individual shocks usually originate at the same relative location on their respective large-scale eddy. Figure 33, View F is a magnified view of Fig. 32 at a position immediately after reattachment. Several shocks are evident, which coalesce to form the bounding wake recompression shock. A shock of non-uniform strength can clearly be seen originating at the left-most structure's pinnacle normal to the eddy and then rapidly becoming oblique to the flow. These observations are indicative of the eddy shocklets discussed by Dimotakis (1991). These eddy shocklets have been predicted for highly compressible flows based on two-dimensional considerations, but thought not to exist due to three-dimensional relief effects. Closer examination of the eddy shock generation mechanisms is warranted.

The overall goal of this study is to document the spatial evolution of organized motions within the near-wake interaction region of supersonic planar base flows, and what effects these structures have on mixing, entrainment, and flowfield dynamics. The diverse fluid dynamic regions inherent to this class of flows provide the opportunity to investigate the structural characteristics of the large-scale eddies over a broad range of conditions. Future efforts will concentrate on obtaining statistical characterization of the eddies' size, shape, and orientation, as well as convection velocity via double-pulsed Mie scattering techniques.

SUMMARY AND CONCLUSIONS

High-speed base flows contain a number of fluid dynamic mechanisms that make their accurate prediction difficult. While recent RANS computations have shown improved agreement with measured base pressure distributions, many aspects of the near-wake mean velocity and turbulence fields are poorly predicted. Improved turbulence modeling appears to be the critical issue that must be addressed in this regard.

For supersonic base flows the shear layers are clearly key components of the near-wake flow, as they govern the mass, momentum, and energy exchange between the inviscid freestream and the recirculating flow. The measurements presented here demonstrate that these shear layers are highly compressible so that the large-scale turbulence structure is three-dimensional in nature. The shear layer turbulence field is also quite anisotropic with the streamwise normal stress dominant in comparison to the other components. The base corner separation process, both in terms of the inlet conditions to separation and the strength of the expansion, has been shown to be critical to the development of the near-wake flow. In fact, a majority of the shear layer growth and turbulence production occurs at the inner edge of the shear layer near separation where several components of the Reynolds stress tensor are also substantially amplified. Turbulence organization in the shear layer immediately after separation is also increased compared to the upstream boundary layer, which is consistent with the observation of large turbulent structures immediately after separation. Boattailing reduces the boundary layer turbulence at separation, resulting in reduced turbulence throughout the near-wake and, therefore, reduced shear layer entrainment and increased base pressure. Not only are large-scale turbulent structures visualized immediately after separation, but they appear to be even more dominant in the latter portions of the shear layer and especially at reattachment and into the developing wake. The introduction of base bleed has also been shown to increase base pressure by altering the near-wake mean velocity and turbulence fields. The optimum base pressure occurs at a bleed flowrate such that the centerline recirculation region nearly vanishes.

For subsonic base flows the near-wake mean velocity field is similar to that for the supersonic case, but the instantaneous wake structure is that of a vortex street. Therefore, this vortex structure must be manipulated in order to increase base pressure. The PIV study summarized here has shown that a base cavity causes expansion of vortices across the near-wake, with an accompanying small reduction in strength, but with little change in the vortex formation location. Thus,

15

the base pressure is increased primarily because the cavity allows the base surface to be displaced upstream to a location away from the low pressure vortices.

ACKNOWLEDGMENTS

REFERENCES

Amatucci, V.A. (1990), "An Experimental Investigation of the Two-Stream, Supersonic, Near-Wake Flowfield Behind a Finite-Thickness Base," Ph.D. Thesis, University of Illinois at Urbana-Champaign.

Badrinarayanan, M.A. (1961), "An Experimental Investigation of Base Flows at Supersonic Speeds," Journal of the Royal Aeronautical Society, Vol. 65, pp. 475-482.

Bean, H.S. (1971), ed., Fluid Meters - Their Theory and Application, 6th ed., Report of the ASME Research Committee on Fluid Meters.

Benay, R., Coet, M.C., and Delery, J. (1987), "Validation of Turbulence Models Applied to Transonic Shock-Wave/Boundary-Layer Interaction," La Recherche Aerospatiale, No. 1987-3, pp. 1-16.

Berner, C. (1993), "Supersonic Base Flow Investigation Over Axisymmetric Afterbodies," Proceedings of the Fifth International Conference on Laser Anemometry Advances and Applications, Koningshof, Veldhoven, Netherlands.

Bogdanoff, D.W. (1983), "Compressibility Effects in Turbulent Shear Layers," AIAA Journal, Vol. 21, No. 6, pp. 926-927.

Bowman, J.E. and Clayden, W.A. (1967), "Cylindrical Afterbodies in Supersonic Flow with Gas Ejection," AIAA Journal, Vol. 5, No. 6, pp. 1524-1525.

Brown, G.L. and Roshko, A. (1974), "On Density Effects and Large Structure in Turbulent Mixing Layers," Journal of Fluid Mechanics, Vol. 64, Part 4, pp. 775-816.

Cantwell, B.J. (1981), "Organized Motion in Turbulent Flow," Annual Review of Fluid Mechanics, Vol. 13, pp. 457-515.

Caruso, S.C. and Childs, R.E. (1988), "Aspects of Grid Topology for Reynolds-Averaged Navier-Stokes Base Flow Computations," AIAA Paper 88-0523.

Chapman, D.R. (1950), "An Analysis of Base Pressure at Supersonic Velocities and Comparison with Experiment," NACA TN 2137.

Childs, R.E. and Caruso, S.C. (1987), "On the Accuracy of Turbulent Base Flow Predictions," AIAA Paper 87-1439.

Childs, R.E. and Caruso, S.C. (1989), "Assessment of Modeling and Discretization Accuracy for High Speed Afterbody Flows," AIAA Paper 89-0531.

Chuang, C.C. and Chieng, C.C. (1994), "Supersonic Base Flow Computations by Higher Order Turbulence Models," Proceedings of the 1994 International Symposium on Turbulence, Heat and Mass Transfer, Lisbon, Portugal.

Clemens, N.T. and Mungal, M.G. (1992), "Two- and Three-Dimensional Effects in the Supersonic Mixing Layer," AIAA Journal, Vol. 30, No. 4, pp. 973-981.

Clements, R.R. and Maull, D.J. (1975), "The Representation of Sheets of Vorticity by Discrete Vortices," Progress in Aerospace Sciences, Vol. 16, No. 2, pp. 129-146.

Coles, D. (1985), "Dryden Lecture: The Uses of Coherent Structure," AIAA Paper 85-0506.

Cortright, E.M. and Schroeder, A.H. (1951), "Preliminary Investigation of Effectiveness of Base Bleed in Reducing Drag of Blunt-Base Bodies in Supersonic Stream," NACA RM E51A26.

Crocco, L. and Lees, L. (1952), "A Mixing Theory for the Interaction Between Dissipative Flows and Nearly Isentropic Streams," Journal of the Aeronautical Sciences, Vol. 19, No. 10, pp. 649-676.

Dash, S.M., Pearce, B.E., Pergament, H.S., and Fishburne, E.S. (1980), "Prediction of Rocket Plume Flowfields for Infrared Signature Studies," Journal of Spacecraft and Rockets, Vol. 17, No. 3, pp. 190-199.

Delery, J. (1983), "ONERA Research on Afterbody Viscid/Inviscid Interaction with Special Emphasis on Base Flows," Proceedings of the Symposium on Rocket/Plume Fluid Dynamic Interactions, Vol. III-Flow Fields, Univ. of Texas at Austin, Austin, TX.

Delery, J. and Lacau, R.G. (1987), "Prediction of Base Flows," AGARD Report 754.

Delery, J. and Wagner, B. (1990), "Results of GARTEUR Action Group AG09 on Flow Past Missile Afterbodies," AGARD/FDP Symposium on Missile Aerodynamics, Friedrichshafen, Germany.

Dimotakis, P.E. (1991), "On the Convection Velocity of Turbulent Structures in Supersonic Shear Layers," AIAA Paper 91-1724.

Dussauge, J.P., and Gaviglio, J. (1987), "The Rapid Expansion of a Supersonic Turbulent Flow: Role of Bulk Dilatation," Journal of Fluid Mechanics, Vol. 174, pp. 81-112.

Elliott, G.S. and Samimy, M. (1990), "Compressibility Effects in Free Shear Layers," Physics of Fluids A, Vol. 2, No. 7, pp. 1231-1240.

Fage, A. and Johansen, F.C. (1927), "The Structure of Vortex Sheets," ARC R&M No. 1143.

Fuller, L. and Reid, J. (1956), "Experiments on Two-Dimensional Base Flow at M=2.4," Royal Aircraft Establishment Report No. Aero 2569.

Gaviglio, J., Dussauge, J.P., Debieve, J.F, and Favre, A. (1977), "Behavior of a Turbulent Flow Strongly Out of Equilibrium at Supersonic Speeds," The Physics of Fluids, Vol. 20, No. 10, Part II, pp. 179-192.

Goebel, S.G. and Dutton, J.C. (1991), "Experimental Study of Compressible Turbulent Mixing Layers," AIAA Journal, Vol. 29, No. 4, pp. 538-546.

Hawkins, R., and Trevett, E. (1966), "Changes in the Flow at the Base of a Bluff Body Due to a Disturbance in its Wake," AGARD Report 539.

Herrin, J.L. (1993), "An Experimental Investigation of Supersonic Axisymmetric Base Flow Including the Effects of Afterbody Boattailing," Ph.D. Thesis, University of Illinois at Urbana-Champaign.

Herrin, J.L. and Dutton, J.C. (1994a), "Supersonic Base Flow Experiments in the Near Wake of a Cylindrical Afterbody," AIAA Journal, Vol. 32, No. 1, pp. 77-83.

Herrin, J.L. and Dutton, J.C. (1994b), "Effects of Afterbody Boattailing on the Near-Wake of Axisymmetric Bodies in Supersonic Flow," AIAA Paper 94-0029.

Herrin, J.L., and Dutton, J.C. (1994c), "Effect of a Rapid Expansion on the Development of Compressible Free Shear Layers," AIAA Paper 94-2229.

Hussain, A.K.M.F. (1986), "Coherent Structures and Turbulence," Journal of Fluid Mechanics, Vol. 173, pp. 303-356.

Korst, H.H. (1956), "A Theory for Base Pressures in Transonic and Supersonic Flow," Journal of Applied Mechanics, Vol. 23, No. 4, pp. 593-600.

Korst, H.H., Chow, W.L., and Zumwalt, G.W. (1964), "Research on Transonic and Supersonic Flow of a Real Fluid at Abrupt Increases in Cross Section (With Special Consideration of Base Drag Problems)," Engineering Experiment Station, Mechanical Engineering Department, University of Illinois, ME Technical Report 392-5.

Kruiswyk, R.W. and Dutton, J.C. (1990), "Effects of a Base Cavity on Subsonic Near-Wake Flow," AIAA Journal, Vol. 28, No. 11, pp. 1885-1893.

Lilienthal, P.F., Brink, D.F., and Addy, A.L. (1970), "Experimental Program for the Study of Supersonic and Transonic Axisymmetric Base-Pressure Problems," Final Report for Contract No. DA-01-021-AMC-13902(Z), Department of Mechanical and Industrial Engineering, University of Illinois at Urbana-Champaign.

Little, B.H., Jr. and Cubbage, J.M., Jr. (1961), "The Development of an 8-inch by 8-inch Slotted Tunnel for Mach Numbers up to 1.28," NASA Technical Note D-908.

Mathur, T. and Dutton, J.C. (1995), "Base Bleed Experiments with a Cylindrical Afterbody in Supersonic Flow," AIAA Paper 95-0062.

Merz, R.A., Page, R.H., and Przirembel, C.E.G. (1978), "Subsonic Axisymmetric Near-Wake Studies," AIAA Journal, Vol. 16, No. 7, pp. 656-662.

Messersmith, N.L. (1992), "An Experimental Investigation of Organized Structure and Mixing in Compressible Turbulent Free Shear Layers," Ph.D. Thesis, University of Illinois at Urbana-Champaign.

Molezzi, M.J. (1993), "Development and Application of Particle Image Velocimetry in High-Speed Separated Flow: Two-Dimensional Base Cavities," Ph.D. Thesis, University of Illinois at Urbana-Champaign.

Molezzi, M.J. and Dutton, J.C. (1993a), "Study of the Near-Wake Structure of a Subsonic Base Cavity Flowfield Using PIV," AIAA Paper 93-3040.

Molezzi, M.J. and Dutton, J.C. (1993b), "Application of Particle Image Velocimetry in High-Speed Separated Flows," AIAA Journal, Vol. 31, No. 3, pp. 438-446.

Molezzi, M.J. and Dutton, J.C. (1995), "Study of Subsonic Base Cavity Flowfield Structure Using PIV," AIAA Journal, to be published, Vol. 33, No. 1.

Narasimha, R. and Viswanath, P.R. (1975), "Reverse Transition at an Expansion Corner in Supersonic Flow," AIAA Journal, Vol. 13, No. 5, pp. 693-695.

Nash, J.F., Quincey, V.G., and Callinan, J. (1963), "Experiments on Two-Dimensional Base Flow at Subsonic and Transonic Speeds," ARC R&M No. 3427.

Nietubicz, C.J. and Sahu, J. (1991), "Navier-Stokes Computations of Base Bleed Projectiles," in Base Bleed: First International Symposium on Special Topics in Chemical Propulsion, ed. K.K. Kuo and J.N. Fleming, Hemisphere Publishing Corp., pp. 93-106.

Papamoschou, D. and Roshko, A. (1988), "The Compressible Turbulent Shear Layer: An Experimental Study," Journal of Fluid Mechanics, Vol. 197, pp. 453-477.

Peace, A.J. (1991), "Turbulent Flow Predictions for Afterbody/Nozzle Geometries Including Base Effects," Journal of Propulsion and Power, Vol. 7, No. 3, pp. 396-403.

Petrie, H.L., Samimy, M., and Addy, A.L. (1986), "Compressible Separated Flows," AIAA Journal, Vol. 24, No. 12, pp. 1971-1978.

Petrie, H.L. and Walker, B.J. (1985), "Comparison of Experiment and Computation for a Missile Base Region Flowfield with a Centered Propulsive Jet," AIAA Paper 85-1618.

Pollock, N. (1969), "Some Effects of Base Geometry on Two-Dimensional Base Drag at Subsonic and Transonic Speeds," Australian A.R.L., Aerodynamics Note 316.

Putnam, L.E. and Bissinger, N.C. (1985), "Results of AGARD Assessment of Prediction Capabilities for Nozzle Afterbody Flows," AIAA Paper 85-1464.

Reid, J. and Hastings, R.C. (1959a), "Experiments on the Axi-Symmetric Flow Over Afterbodies and Bases at M=2.0," Royal Aircraft Establishment Report No. Aero 2628.

Reid, J. and Hastings, R.C. (1959b), "The Effect of a Central Jet on the Base Pressure of a Cylindrical Afterbody in a Supersonic Stream," Aeronautical Research Council (Great Britain), Reports and Memoranda No. 3224.

Reijasse, P., Benay, R., Delery, J., and Lacau, R.G. (1989), "Prediction of Powered Missile or Projectile Base Flows by Multicomponent Methods," La Recherche Aerospatiale, No. 1989-4, pp. 15-32.

Rollstin, L. (1987), "Measurement of Inflight Base Pressure on an Artillery-Fired Projectile," AIAA Paper 87-2427.

Sahu, J. (1986), "Supersonic Flow Over Cylindrical Afterbodies with Base Bleed," AIAA Paper 86-0487.

Sahu, J. (1994), "Numerical Computations of Supersonic Base Flow with Special Emphasis on Turbulence Modeling," Technical Report ARL-TR-438, Army Research Laboratory, Aberdeen Proving Ground, Maryland.

Sahu, J., Nietubicz, C.J., and Steger, J.L. (1985), "Navier-Stokes Computations of Projectile Base Flow with and without Mass Injection," AIAA Journal, Vol. 23, No. 9, pp. 1348-1355.

Samimy, M. and Addy, A.L. (1986), "Interaction between Two Compressible, Turbulent Free Shear Layers," AIAA Journal, Vol. 24, No. 12, pp. 1918-1923.

Samimy. M. and Lele, S.K. (1991), "Motion of Particles with Inertia in a Compressible Free Shear Layer," Physics of Fluids A, Vol. 3, No. 8, pp. 1915-1923.

Samimy, M., Petrie, H.L., and Addy, A.L. (1986), "A Study of Compressible Turbulent Reattaching Free Shear Layers," AIAA Journal, Vol. 24, No. 2, pp. 261-267.

Strahle, W.C., Hubbartt, J.E., and Walterick, R. (1982), "Base Burning Performance at Mach 3," AIAA Journal, Vol. 20, No. 7, pp. 986-991.

Tourbier, D. and Fasel, H. (1994), "Numerical Investigation of Transitional Axisymmetric Wakes at Supersonic Speeds," AIAA Paper 94-2286.

Tucker, P.K. and Shyy, W. (1993), "A Numerical Analysis of Supersonic Flow Over an Axisymmetric Afterbody," AIAA Paper 93-2347.

Valentine, D.T. and Przirembel, C.E.G. (1970), "Turbulent Axisymmetric Near-Wake at Mach Four with Base Injection," AIAA Journal, Vol. 8, No. 12, pp. 2279-2280.

von Kármán, T. (1911), "Über den Mechanismus des Widerstandes, den ein bewegter Körper in einer Flüssigkeit erfährt," Nachrichten von der Königlichen Gesellschaft der Wissenschaften zu Göttingen, Mathematisch-Physikalische Klasse, pp. 509-517.

Willmarth, W.W. and Lu, S.S. (1972), "Structure of the Reynolds Stress Near the Wall," Journal of Fluid Mechanics, Vol. 55, pp. 65-92.
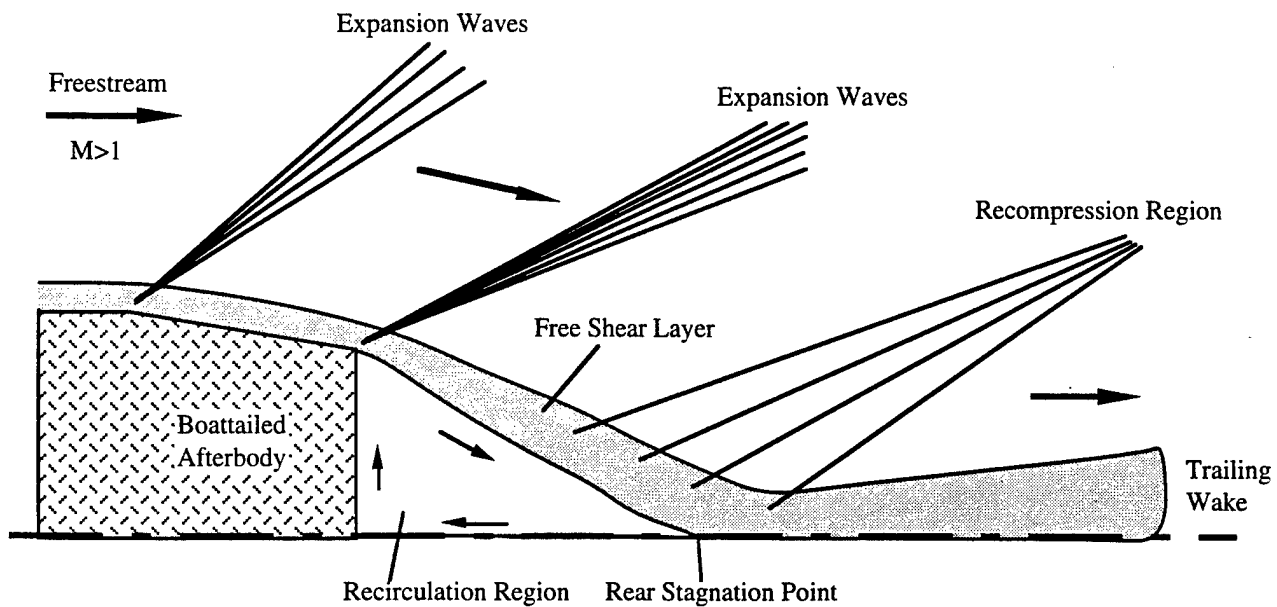
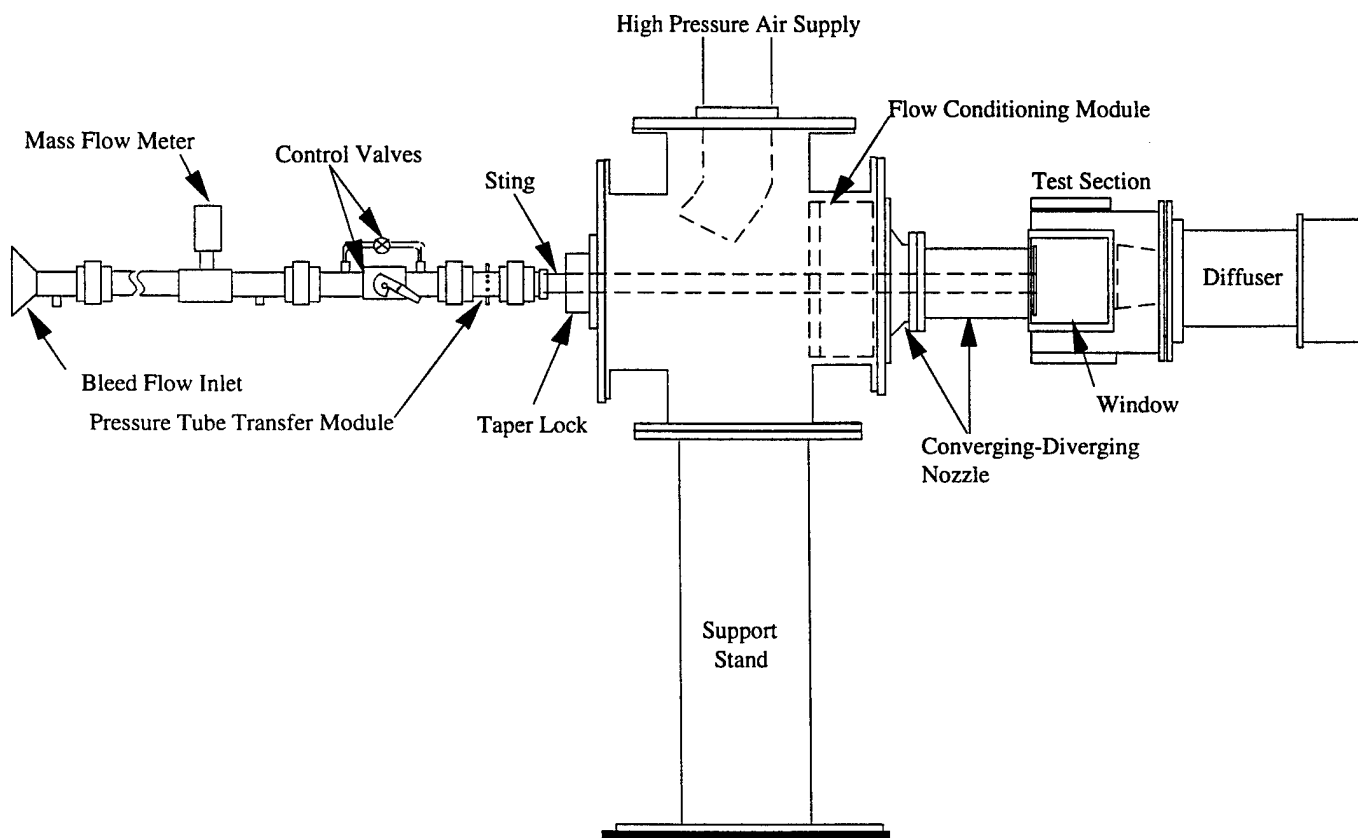Fig. 1 Supersonic, Axisymmetric Base Flow Schematic
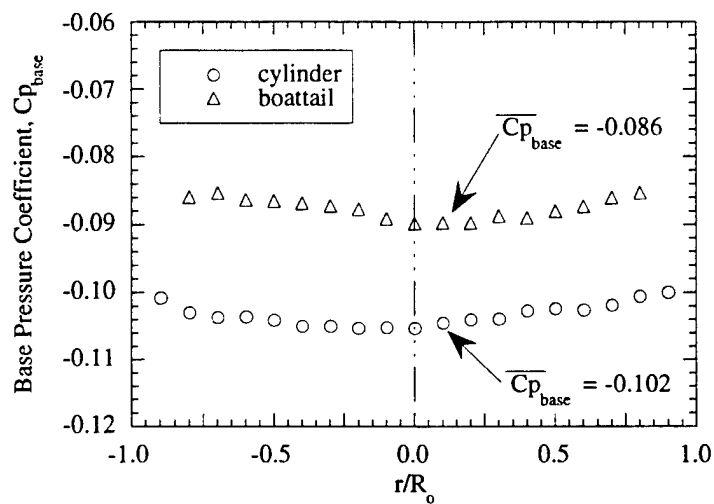

Fig. 2 Sketch of Axisymmetric Base Flow Facility

19

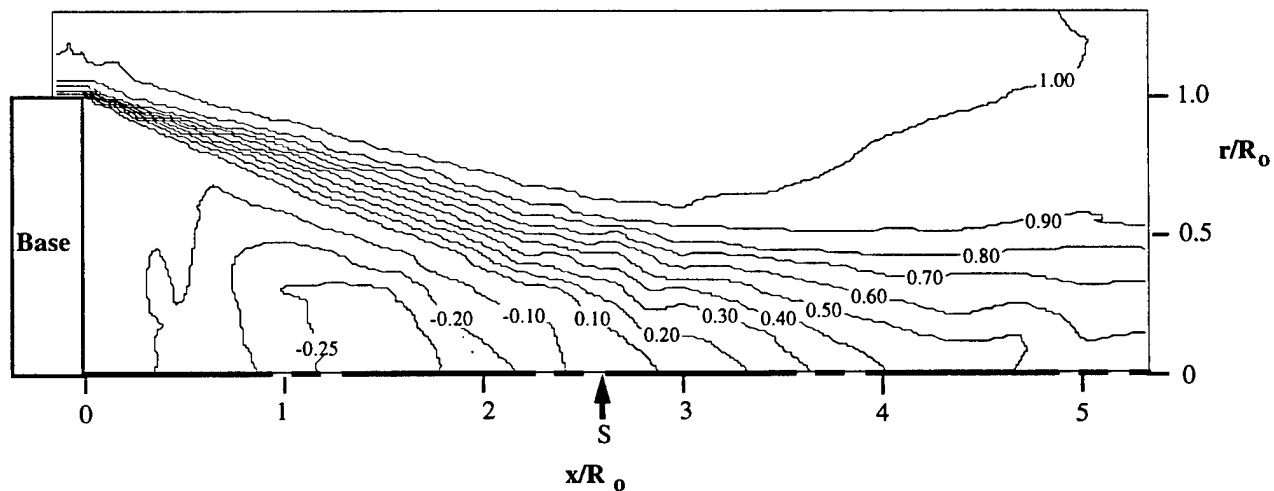Fig. 3 Base Pressure Profiles on Cylindrical and Boattailed Afterbodies

Fig. 4 Mean Axial Velocity Field Downstream of the Cylindrical Afterbody - U/U_1
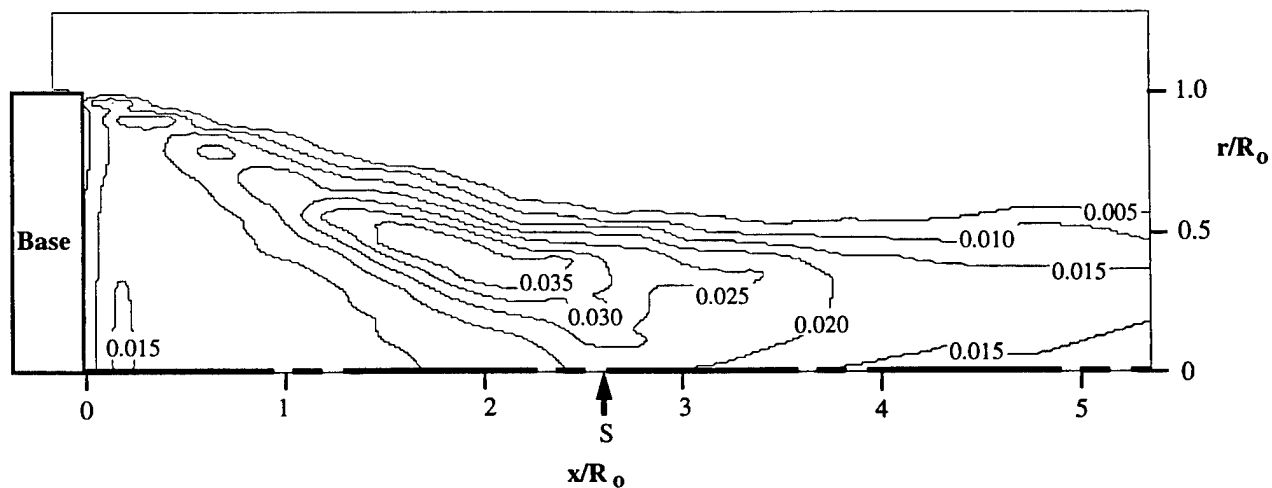

Fig. 5 Turbulent Kinetic Energy Contours Downstream of the Cylindrical Afterbody - k/U_1^2
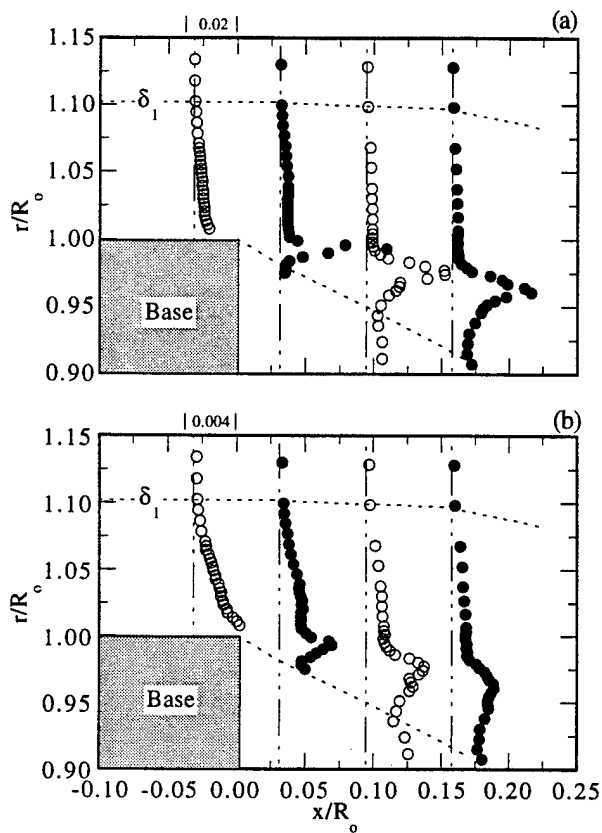
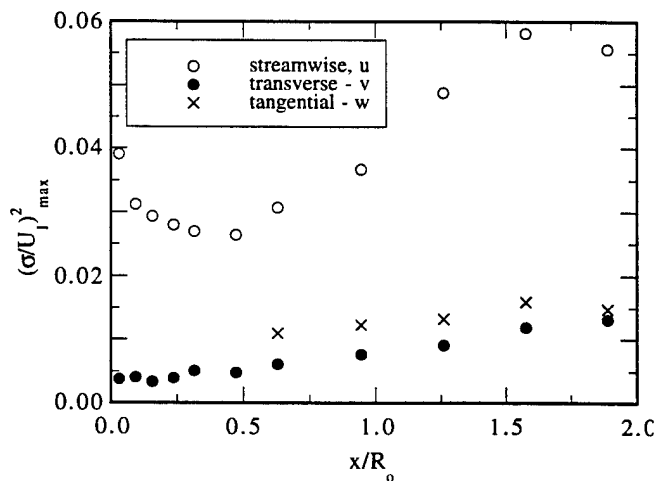Fig. 6 Reynolds Normal Stress Profiles Near the Base Corner: (a) Streamwise - $(\sigma_u/U_1)^2$, (b) Transverse - $(\sigma_v/U_1)^2$

Fig. 7 Shear Stress Quadrant Decomposition Near the Base Corner: (a) Approach Boundary Layer, (b) Immediately Downstream of Separation

Fig. 8 Peak Reynolds Normal Stress Distributions in Shear Layer
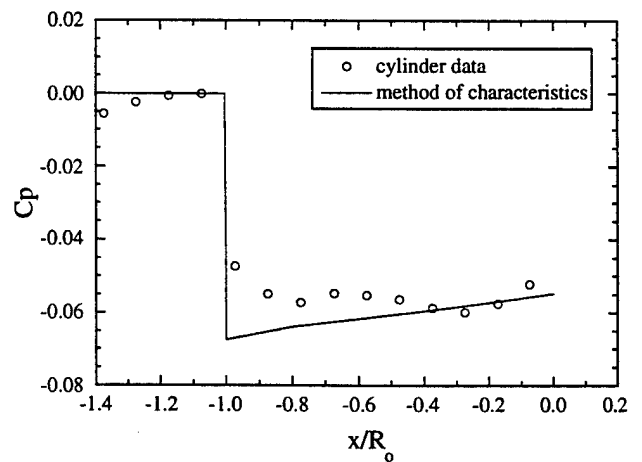
Fig. 9 Boattail Pressure Distribution

21
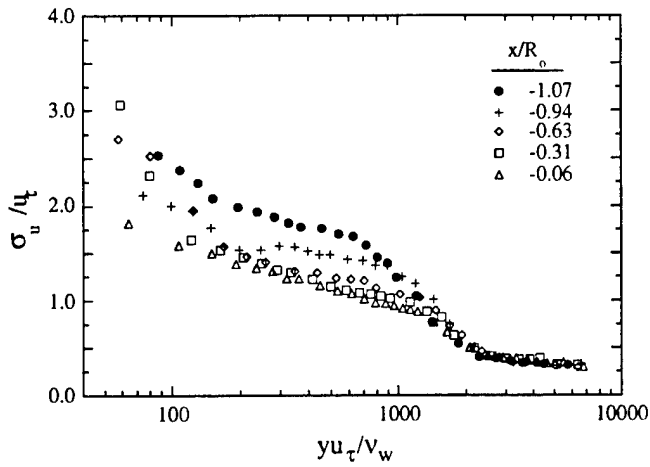
Fig. 10 Streamwise RMS Velocity Fluctuation Profiles Along the Boattail
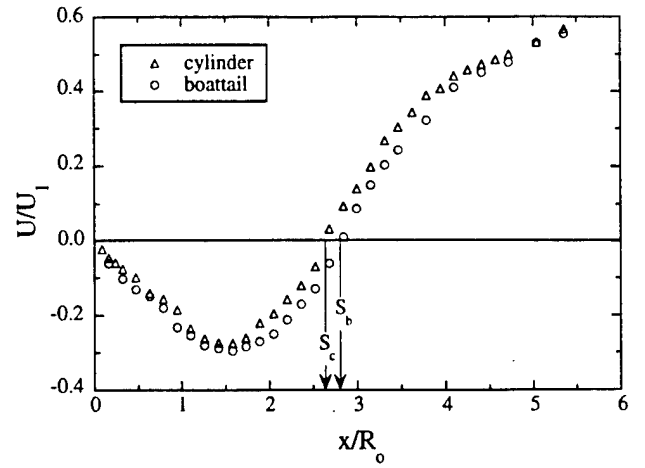
Fig. 11 Mean Axial Velocity Along Centerline: Comparison Between Cylindrical and Boattailed Afterbodies
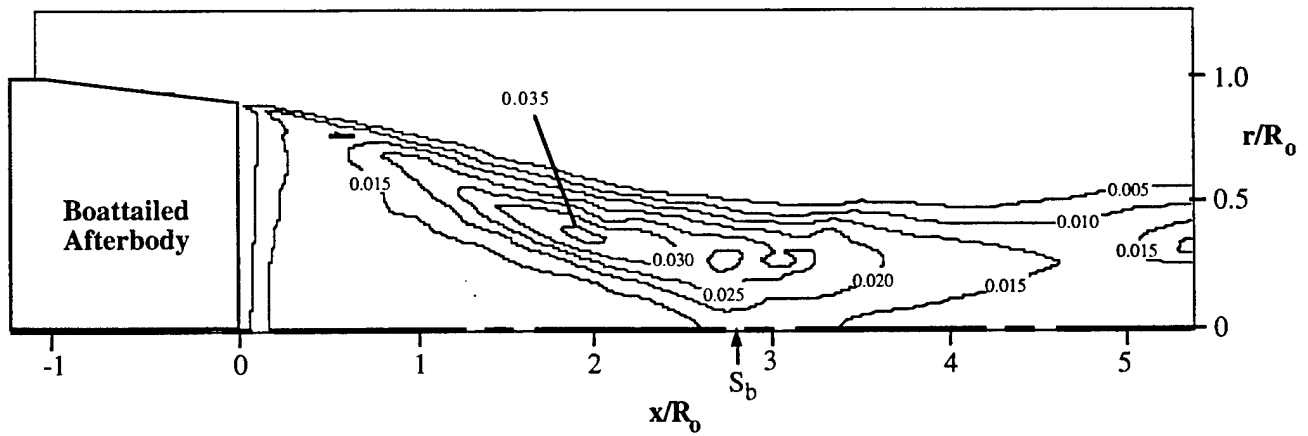
Fig. 12 Turbulent Kinetic Energy Contours, k/U_1^2, for Boattailed Afterbody
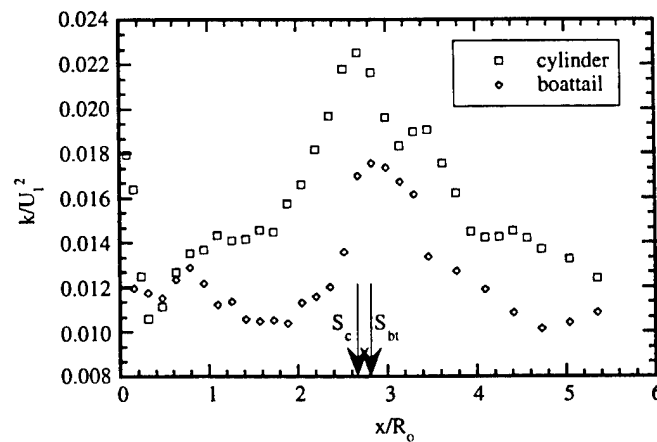
Fig. 13 Turbulent Kinetic Energy Distributions Along the Near-Wake Centerline of Each Afterbody

22
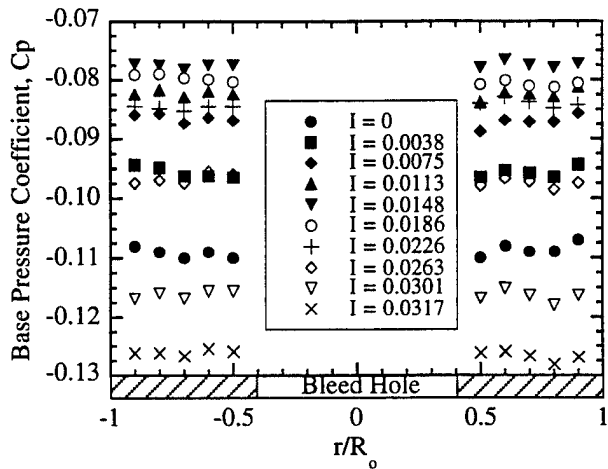
Fig. 14 Effect of Base Bleed on Base Pressure Distribution

Fig. 17 Axial Turbulence Intensities Along the Centerline
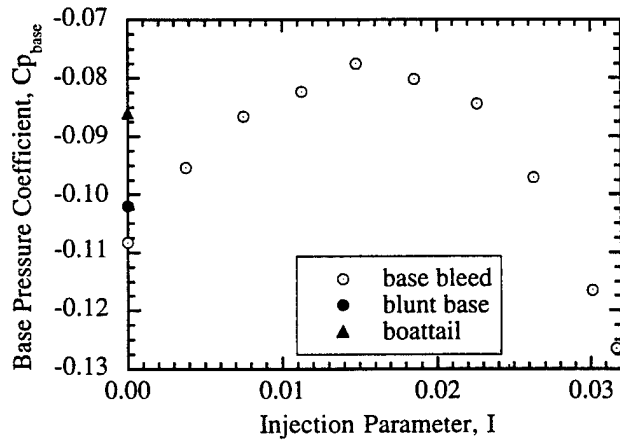
Fig. 15 Effect of Base Bleed on Area-Averaged Base Pressure Coefficient
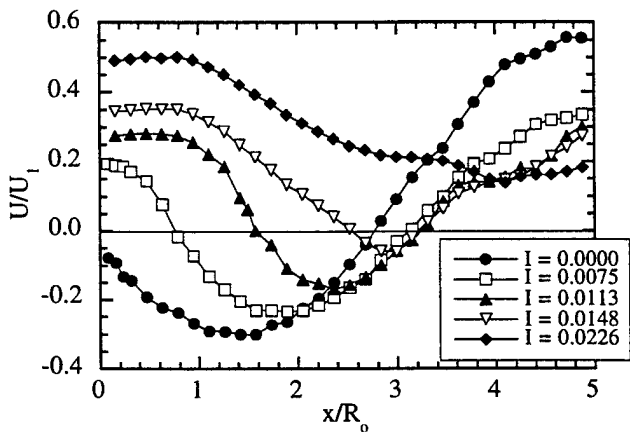
Fig. 18 Radial Turbulence Intensities Along the Centerline
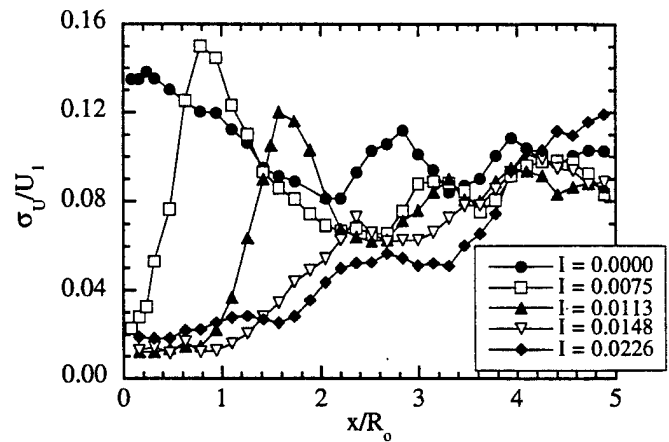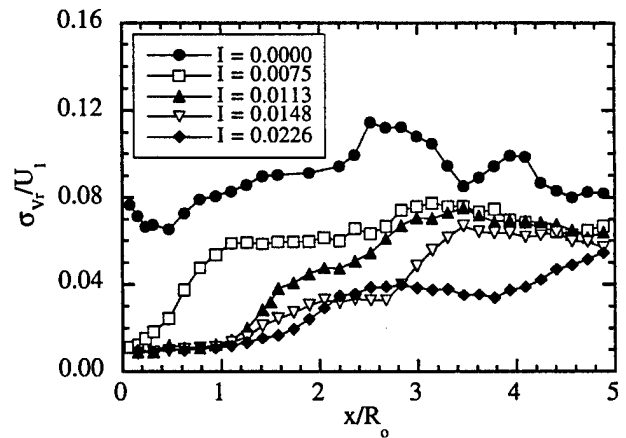
Fig. 16 Mean Axial Velocities Along the Centerline
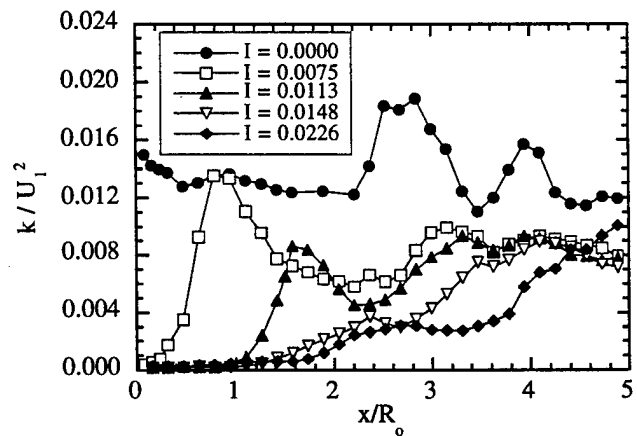
Fig. 19 Turbulent Kinetic Energy Distributions Along the Centerline

Fig. 20 Two-Dimensional Base Cavity and Subsonic Vortex Street Wake
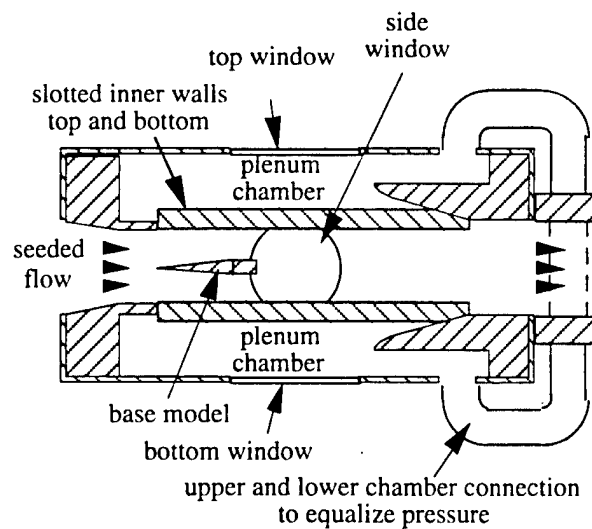
Fig. 21 Two-Dimensional Transonic Base Flow Facility

PIV data on 0.5 mm grid
(shown on 1 mm grid for clarity)

$\rightarrow$ 275 m/s

-180,000 sec^{-1} 180,000 sec^{-1}
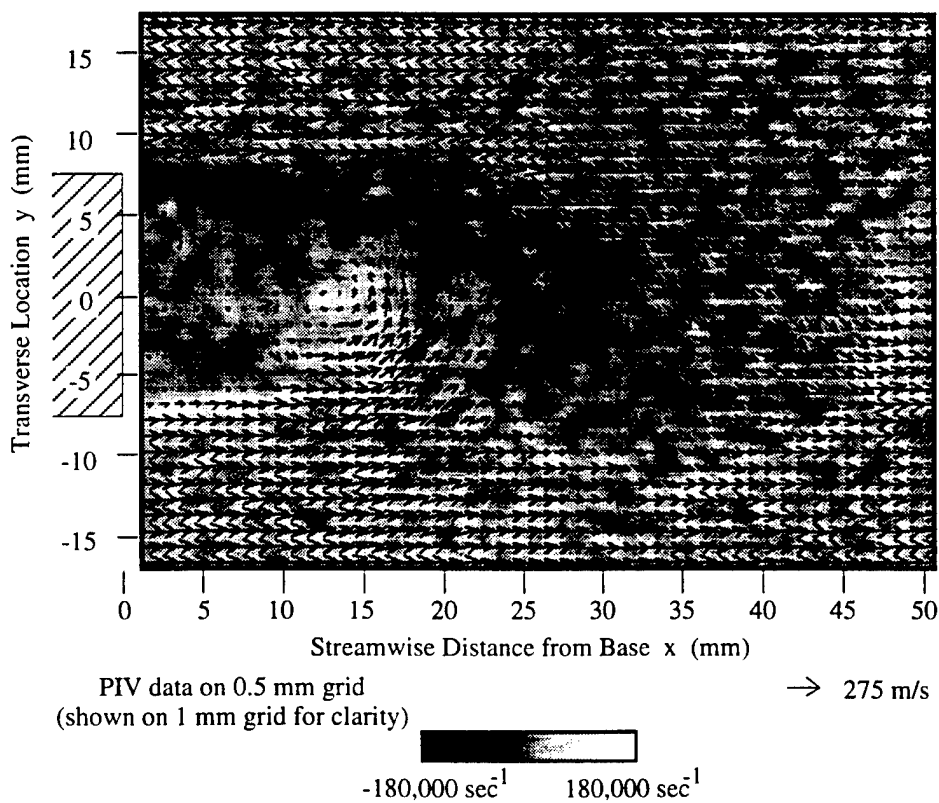
Fig. 22 M_∞=0.6 Blunt Base Vorticity Plot with Velocity Vector Overlay

24
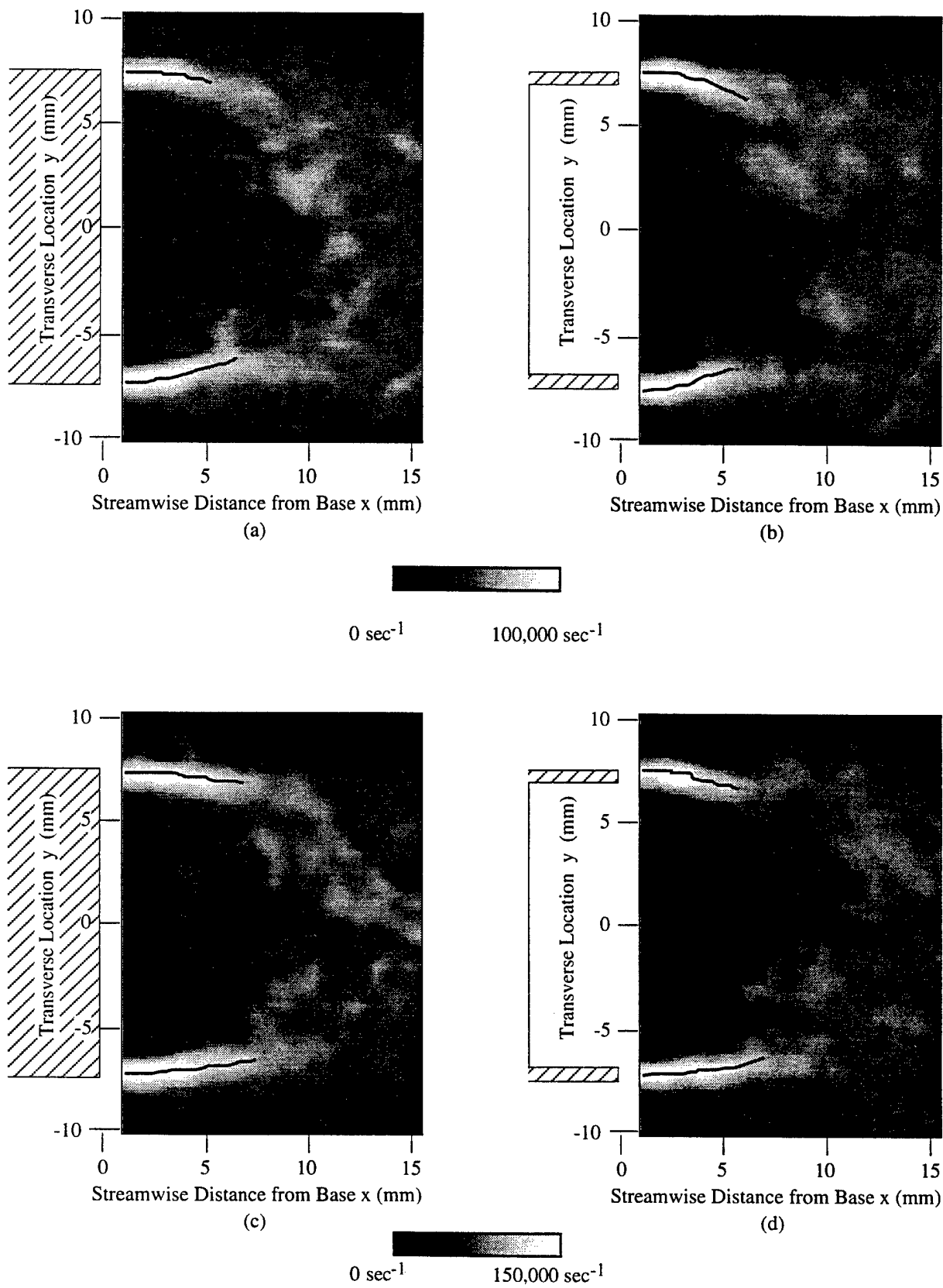
Fig. 23 RMS Vorticity Plots Indicating Shear Layers: (a) M_∞=0.4 Blunt Base; (b) M_∞=0.4 Base Cavity; (c) M_∞=0.6 Blunt Base; (d) M_∞=0.6 Base Cavity
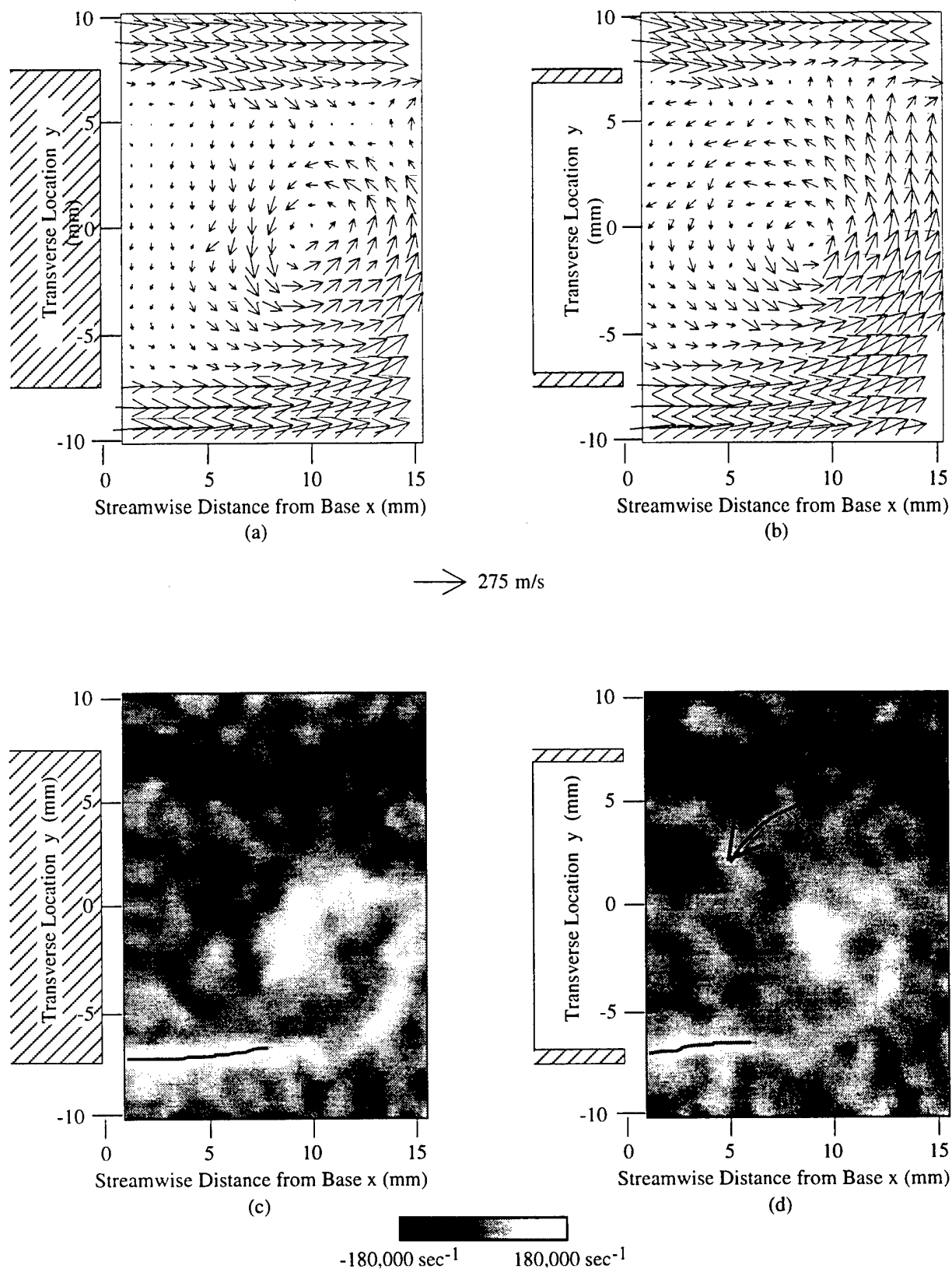
Fig. 24 Instantaneous Flow Structure Comparison: (a) M_∞=0.6 Blunt Base Velocity Vectors;
(b) M_∞=0.6 Base Cavity Velocity Vectors; (c) M_∞=0.6 Blunt Base Vorticity; (d) M_∞=0.6 Base Cavity Vorticity
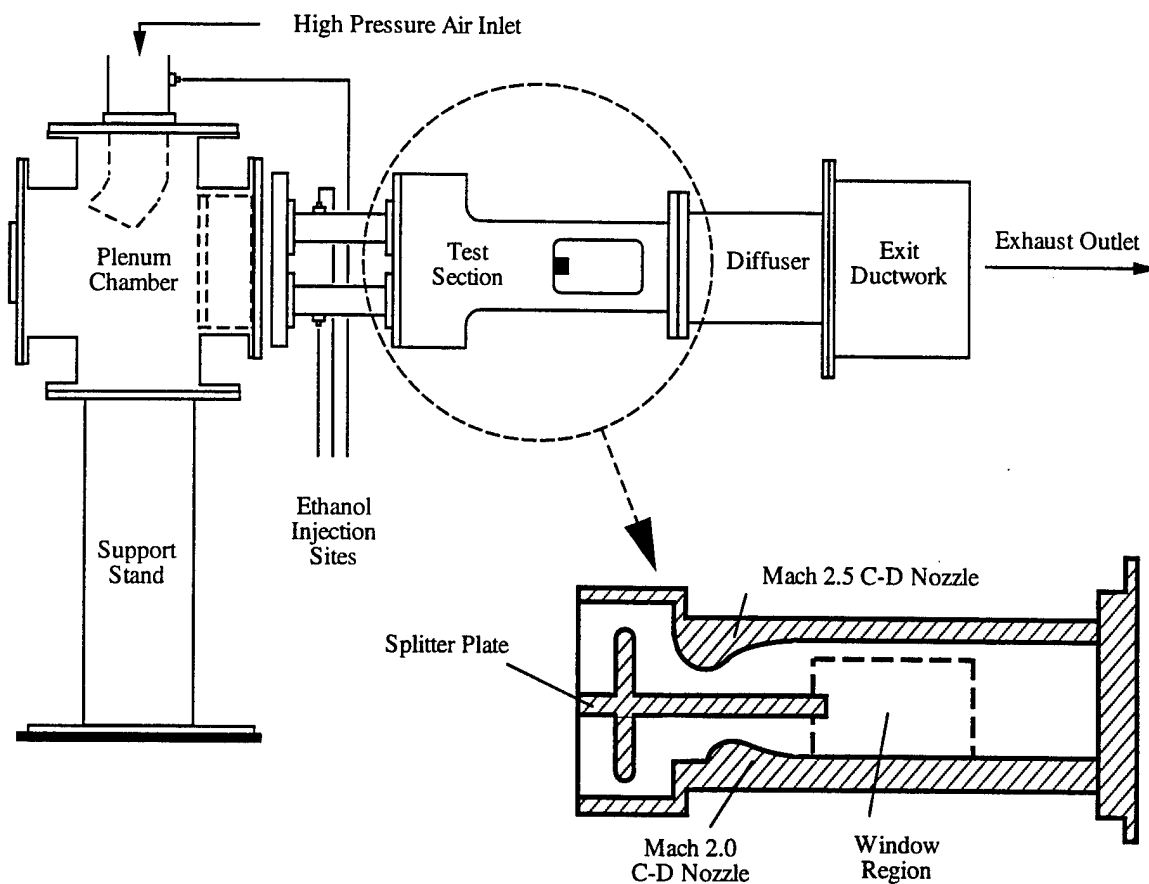
26

High Pressure Air Inlet

Plenum Chamber

Test Section

Diffuser

Exit Ductwork

Exhaust Outlet

Support Stand

Ethanol Injection Sites

Mach 2.5 C-D Nozzle

Splitter Plate

Mach 2.0 C-D Nozzle

Window Region

Fig. 25 Physical Arrangement and Test Section Internals of Planar Base Flow Wind Tunnel

Translation / Rotation Stages

CCD Camera

Beam Sheet

Camera Platform

Test Section

Laser Heads

Beam Shaping Optics

Vibration-Isolated Table
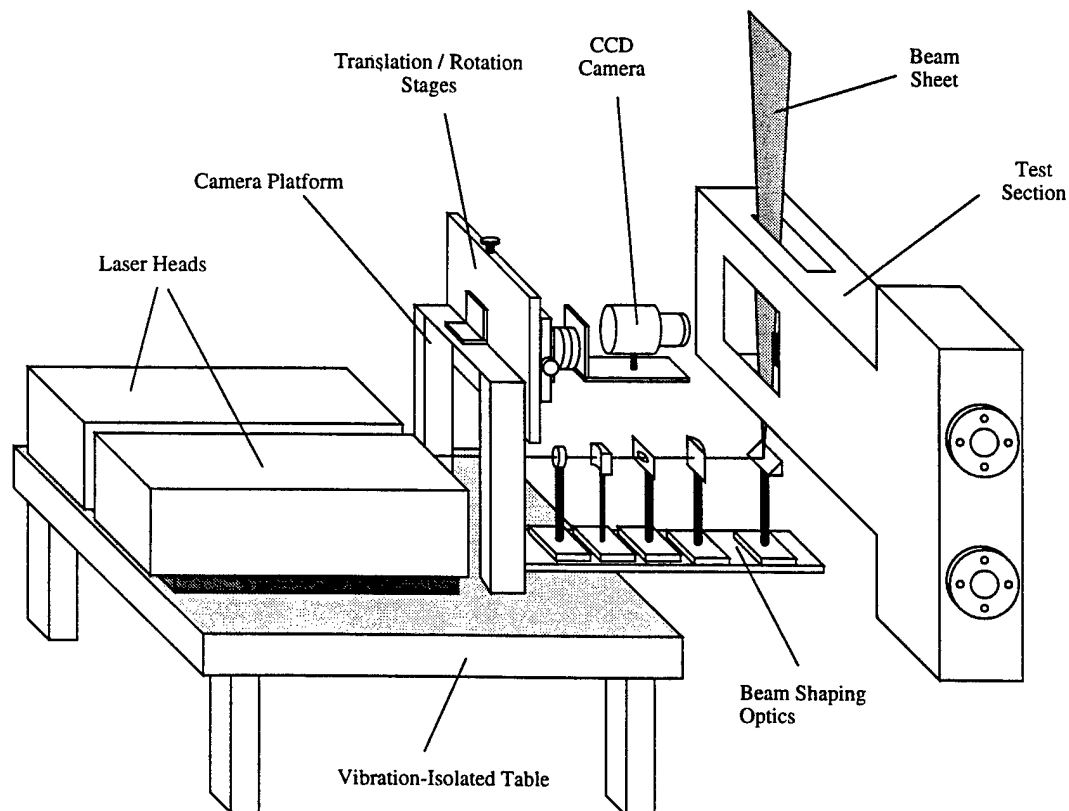
Fig. 26 Mie Scattering Image Acquisition System

27
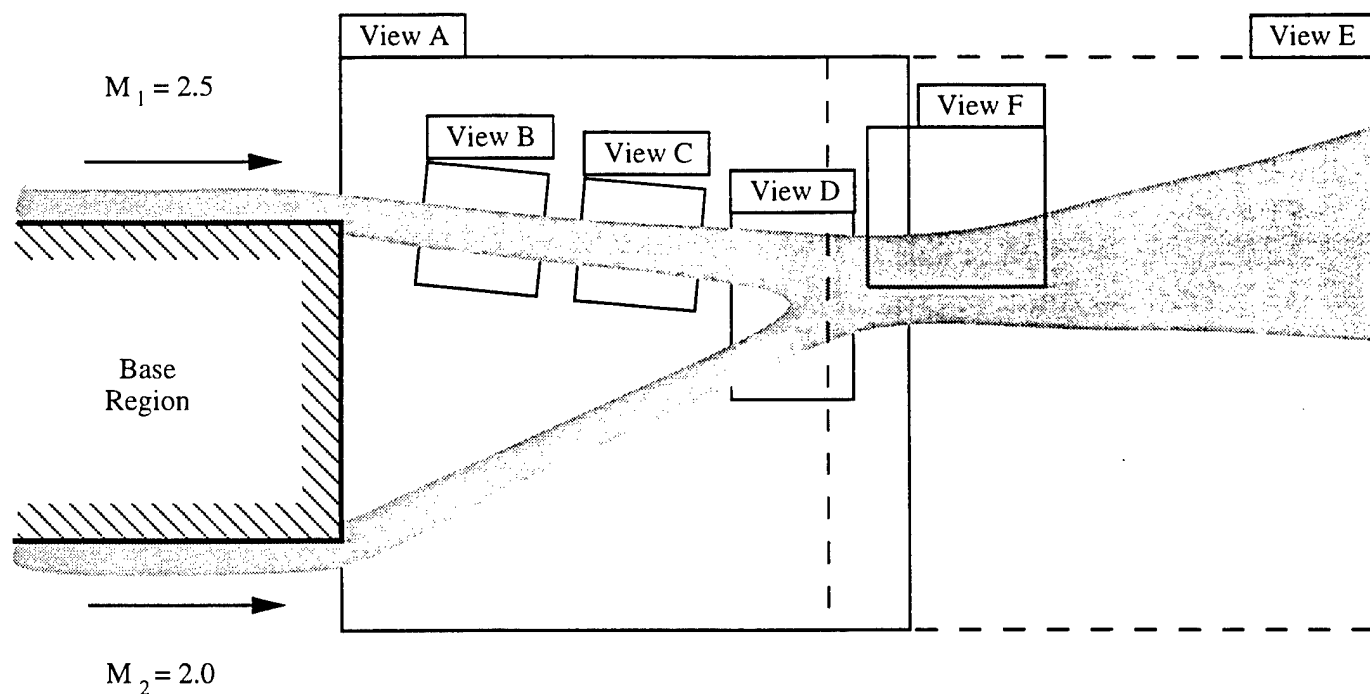
Fig. 27 Description of Fields-of-View Used in this Study
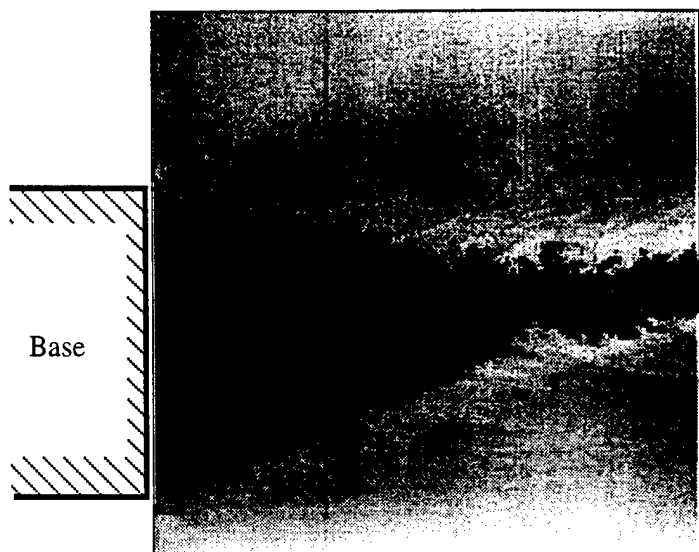

Fig. 28 Mie Scattering Image of Near-Wake Region (View A)
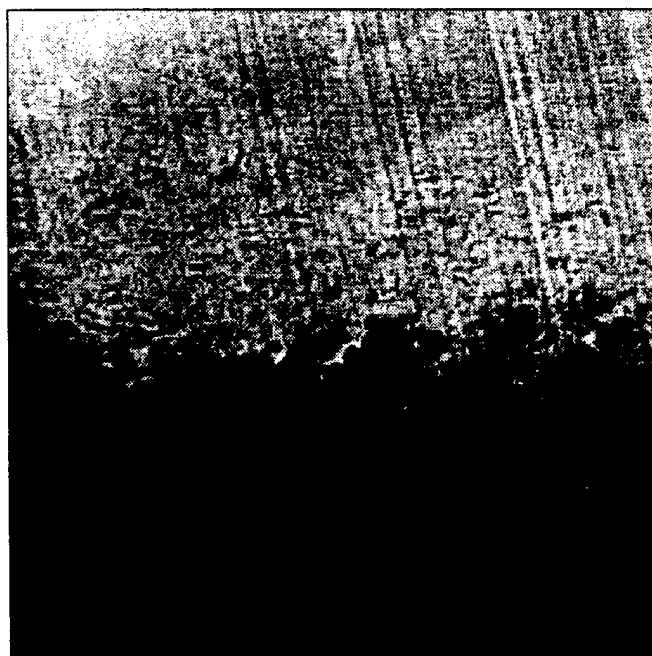

Fig. 29 Mie Scattering Image of Upper Shear Layer Immediately
After Separation (View B)

Fig. 30 Mie Scattering Image of Upper Shear Layer During
Recompression Prior to Reattachment (View C)
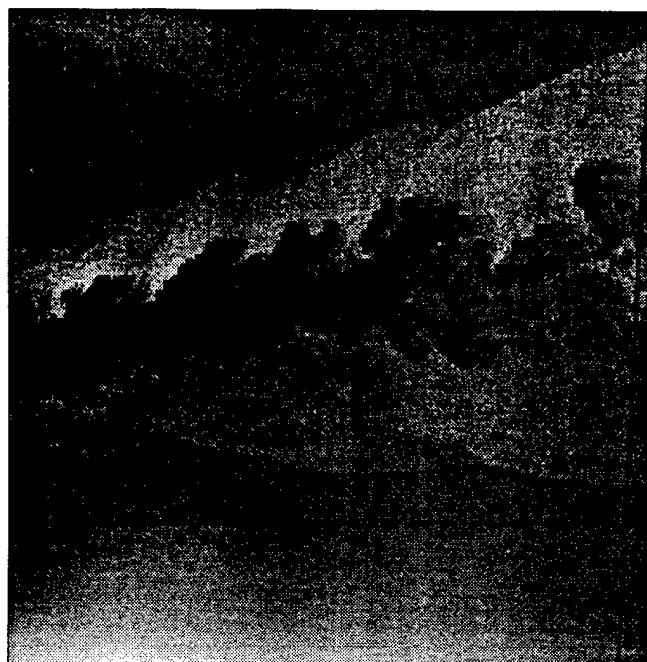

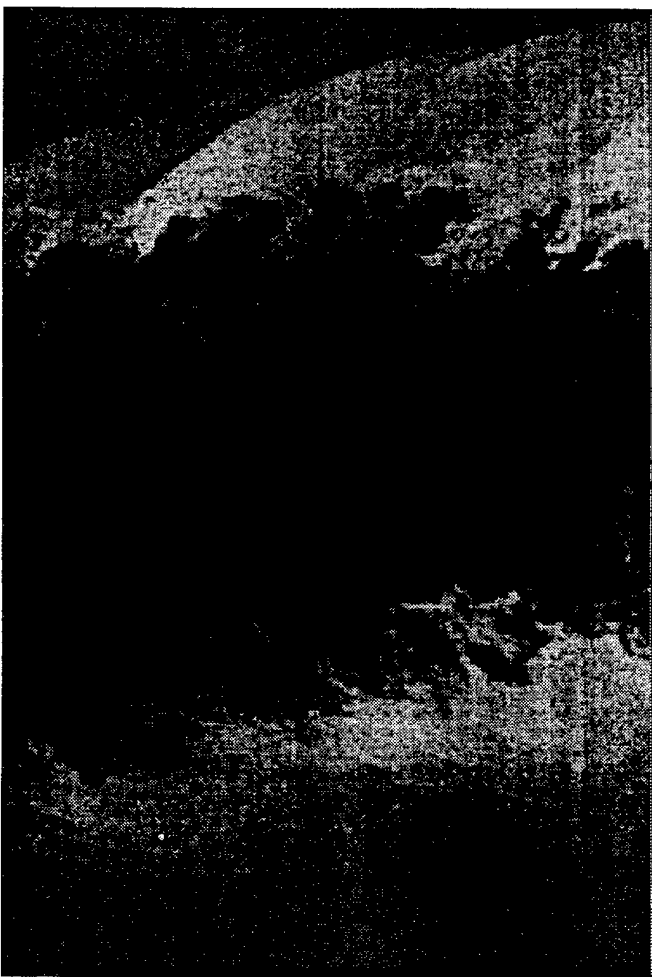Fig. 32 Mie Scattering Image of Wake Region (View E)

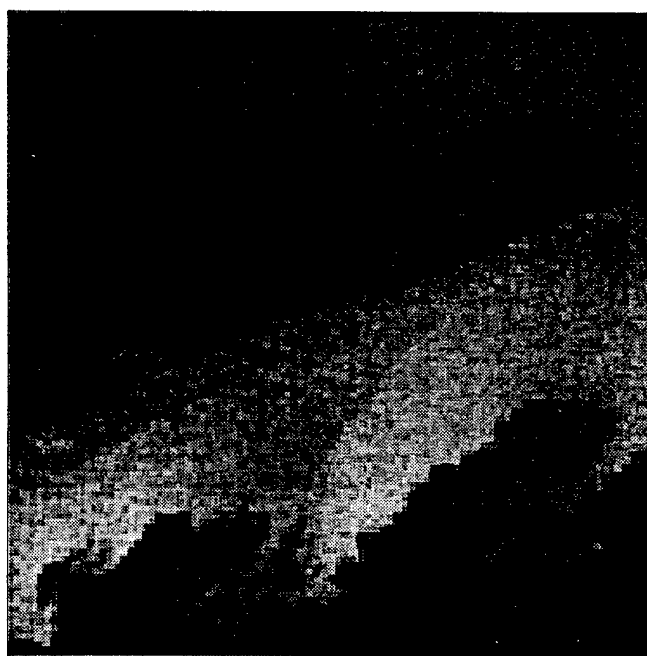Fig. 31 Mie Scattering Image of Shear Layers at Reattachment
(View D)

Fig. 33 Magnified Region of Fig. 32 Depicting Upper Shear
Layer Immediately After Reattachment (View F)

APPENDIX A.19

THE TURBULENCE STRUCTURE OF A REATTACHING AXISYMMETRIC
SUPERSONIC FREE SHEAR LAYER

by

J. L. Herrin and J. C. Dutton

AIAA 95-2250

The Turbulence Structure of a Reattaching Axisymmetric Supersonic Free Shear Layer

J.L. Herrin
NASA Langley Research Center
Hampton, Virginia

and

J.C. Dutton
University of Illinois at Urbana-Champaign
Urbana, Illinois

26th AIAA Fluid Dynamics Conference
June 19-22, 1995/San Diego, CA

THE TURBULENCE STRUCTURE OF A REATTACHING AXISYMMETRIC SUPERSONIC FREE SHEAR LAYER

J.L. Herrin[*]
NASA Langley Research Center
Hampton, VA 23681

J.C. Dutton[†]
University of Illinois at Urbana-Champaign
Urbana, IL 61801

ABSTRACT

The reattachment of a supersonic, axisymmetric shear layer downstream of a blunt based afterbody is studied. Of primary interest are the effects of the "extra" strain rates, such as bulk compression, concave streamline curvature, and lateral streamline convergence associated with shear layer reattachment, on the structure of the turbulence field. Experimental turbulence data obtained throughout the reattachment region with a two-component laser Doppler velocimeter are presented. In general, the compliant boundary reattachment process is shown to be different in character compared to the solid wall case. Most notably, significant reductions in the Reynolds stresses occur through the reattachment region due to the dominating effect of lateral streamline convergence as the flow approaches the axis. Similar to the solid wall case, however, a reduction in the mean turbulent transport toward the axis in the reattachment region was found, which suggests a radial containment of the large scale eddies near the axis of symmetry. The reattachment process was also seen to have profound effects on the large scale structures in the shear layer primarily through reduced structural organization as indicated by the instantaneous velocity fluctuations.

INTRODUCTION

The reattachment process of a compressible free shear layer impinging on a solid or compliant surface occurs in many practical fluid dynamic systems including wing trailing edges, axial flow combustors, sting-supported wind tunnel models, and supersonic jets. In the solid boundary case, the reattachment point has importance because of the increased pressure loads and heat transfer rates that occur due to the interaction between the shear layer and the surface. In fact, the local thermal loads near reattachment in axial flow combustors can often dictate the design of the entire system. Understanding the compliant boundary reattachment problem is also important, especially in the case of conventional anti-armor projectiles which contain multiple bodies separated and aligned along a common axis (Hohler and Stilp, 1990). In this case, each body except the first is immersed in the wake of the prior body and is generally located downstream of the previous body's wake reattachment point. Obviously, in this case understanding the flow physics in the reattachment zone is essential in defining the approach conditions to the following bodies.

The shear layer reattachment problem is also a critical part of the multi-component modeling of missile and projectile afterbody flowfields (Korst, 1956). Still a practical design tool, the success of multi-component modeling intimately depends on the accurate prediction of the reattachment process downstream of the body. A typical flowfield downstream of a supersonic, axisymmetric projectile is sketched in Fig. 1 where the reattachment zone is that region contained within the dashed lines. Notice that the shear layer reattachment process contains many complicating fluid dynamic features such as an adverse pressure gradient, streamline curvature, flow reversal, and fluid interactions across the axis of symmetry. In multi-component analyses, the reattachment model dictates the amount of mass returned to the base due to the adverse pressure gradient and, therefore, directly affects the base pressure. Most models use the dividing streamline concept which locates the streamline within the shear layer that eventually intersects the rear stagnation point (reattachment point) on the axis of symmetry.

Although the general features of reattaching compressible shear layers have been documented in the solid wall case over the past three decades, relatively limited data are available in the compliant boundary case, especially detailed experimental data on the structure of the turbulence field near reattachment. It is now commonly known that compressibility plays a significant role in the development of high-speed free shear layers, but how it affects the reattachment process is still largely unknown. In addition, the fundamental differences in the reattachment process between solid and compliant boundaries have not been firmly established in either supersonic or subsonic flows.

The shear layer reattachment problem also has fundamental interest. Eaton and Johnston (1981) present a thorough review of previous work in the subsonic, solid wall case where a significant amount of experimental data exists. In general, the Reynolds stresses in the shear layer were found to decrease through the reattachment zone although the physical mechanisms associated with this trend could not be firmly established. In contrast, data from the supersonic, solid wall case indicate that the Reynolds stresses *increase* through reattachment with peak

---

[*]National Research Council Associate, Flow Modeling and Control Branch, Member AIAA.

[†]Professor, Department of Mechanical and Industrial Engineering, Associate Fellow AIAA.

1

values occurring slightly downstream of the mean reattachment point (Hayakawa et al., 1984; Samimy et al., 1986; Abu-Hijleh and Samimy, 1989). Recent work (Shen et al., 1993) has indicated that the turbulent fluctuations in the reattachment region can directly affect the recompression shock system and, in general, large scale dynamical motions of the shock system can result. Obviously, this finding is only applicable to supersonic shear layer reattachment where flow recompression occurs through a series of compression waves. Other differences between the subsonic and supersonic cases can be attributed, at least in part, to compressibility effects associated with the shear layer development and also the reattachment process. Consequently, it is apparent that the relatively large volume of subsonic, solid wall reattachment data can only provide qualitative insight into the supersonic, compliant boundary reattachment problem.

Although a limited amount of work has been done on the solid wall reattachment problem, the supersonic, compliant boundary case has received even less attention. Samimy and Addy (1986) investigated the interaction of two compressible shear layers formed downstream of a two-dimensional, thick base with laser Doppler velocimetry (LDV). Although a relatively sparse data set was obtained in the reattachment region, the authors suggested that significant structural differences exist between the turbulence fields in supersonic and subsonic reattaching flows. Most notably, the transverse turbulence diffusion mechanisms in the reattachment zone were shown to differ significantly as evidenced by large changes in the turbulent triple products $<u'u'v'>$ and $<v'v'v'>$. In a similar study, Amatucci et al. (1992) recently confirmed several of these earlier findings while documenting the Reynolds stresses and turbulent triple products in the reattachment zone between a pair of planar shear layers. The Reynolds stresses peaked slightly downstream of reattachment with significant differences occurring between the two shear layers in the transverse normal stress and primary shear stress.

The primary objective of the present paper is to investigate the turbulence structure of an axisymmetric, supersonic shear layer undergoing compliant boundary reattachment as shown in Fig. 1. Detailed experimental turbulence data obtained with LDV will be presented, and the effect of the reattachment process on the Reynolds stress magnitudes and the structural characteristics of the turbulence field will be ascertained. In conjunction with other recent experimental data (Smith and Dutton, 1995), physical mechanisms associated with the observed changes in the turbulence properties through reattachment will be postulated. An additional objective of the present paper is to compare the results obtained in the current compliant boundary case with those obtained previously in solid wall reattachment studies. Comparing and contrasting the data from the compliant and solid boundary cases will provide new insight to analytical modelers of afterbody flowfields who often utilize data obtained with the backstep geometry (solid wall case) in their modeling of the compliant boundary reattachment process.

EXPERIMENTAL APPARATUS AND PROCEDURE

The experiments for the current study were conducted in the axisymmetric base flow facility at the University of Illinois Gas Dynamics Laboratory. This facility is a blowdown-type wind tunnel specifically designed for axisymmetric afterbody models and contains features to ensure axisymmetric flow by proper centering of the model. In addition, methods to eliminate interference waves from intersecting the near-wake flowfield downstream of the blunt based body were utilized. A detailed description of the facility is given by Herrin (1993). The model used for the current study was a blunt based, axisymmetric, boattailed afterbody with a base radius, R_b, of 28.97 mm. The Mach and unit Reynolds numbers of the freestream flow near the onset of the reattachment region were 2.72 and 43 (10^6) per meter, respectively. The general characteristics of the entire base flowfield have been presented elsewhere (Herrin and Dutton, 1994); in this paper, emphasis is placed on the reattachment region from immediately upstream of the first recompression wave to the developing wake further downstream (outlined region in Fig. 1). The onset of the adverse pressure gradient associated with reattachment was estimated from the sidewall pressure data of Amatucci et al. (1992) to occur near $x/x_R = 0.72$ where x is the axial distance downstream of the base plane and x_R is the reattachment length ($x_R = 89$ mm). At this location, the mean velocity profile in the shear layer is independent of axial position (i.e., self-similar in the mean sense), although the Reynolds stresses are still in the late stages of development (Herrin and Dutton, 1994). In addition, the shear layer 10%-90% velocity thickness (b) at the onset of recompression is approximately 11.3 mm. Throughout this paper, the mean velocity in the freestream approaching the recompression region ($U_{ref} = 592.5$ m/s) will be used for non-dimensionalization. Significant compressibility effects are expected, as the convective Mach number of the shear layer takes a value of approximately 1.3.

The primary diagnostic tool used in the experiments was a two-component LDV with frequency shifting that is capable of measuring the high turbulence intensity levels and reversed velocities in the reattachment region of the flow. A detailed discussion of the LDV system and its implementation in supersonic, separated flows has been given by Herrin (1993). The measurement volume diameter and length were approximately 120 μm and 700 μm, respectively, which provided adequate resolution to avoid significant spatial averaging effects in the data. The scattering media used in this investigation were silicone oil droplets with a mean diameter of approximately 0.8 μm (Bloomberg, 1989). A particle lag error analysis using the results of Samimy and Lele

2

(1991) predicts a worst-case root-mean-square slip velocity of less than 2% in the region of interest. An error analysis of the LDV data reduction procedure estimates a maximum uncertainty in the mean velocity of less than 1% of U_{ref} and in the RMS velocity fluctuation of less than 2% of U_{ref}.

The LDV data were obtained along twenty radial traverses throughout the reattachment region in both the vertical and horizontal planes intersecting the axis of symmetry. This two-plane approach allowed direct measurement of three mean velocities (U, V, W), three kinematic Reynolds normal stresses (σ_u^2, σ_v^2, σ_w^2), and two kinematic Reynolds shear stresses (<u'v'>, <u'w'>) throughout the reattachment region. All data presented in the present paper are referenced to the wind tunnel coordinate system where the mean axial velocity (U) is aligned with the axis of symmetry. At each spatial location, approximately 4000 velocity samples were obtained to ensure minimal statistical uncertainty. The ensemble-averaged data were corrected for velocity bias using the interarrival time weighting method (Herrin and Dutton, 1993); no correction for fringe blindness was implemented. For all data presented herein, at least one profile upstream of reattachment (near $x/x_R = 0.56$) will be shown to document the shear layer properties prior to the onset of the recompression process.

RESULTS

The primary results of this investigation will now be presented. In the first section, the development of the kinematic Reynolds stresses through reattachment will be described and compared to previous compliant and solid boundary data. In two following sections, the velocity triple products and primary turbulence structure parameters (e.g., shear stress correlation coefficient, R_{uv}) will be investigated. Finally, a quadrant decomposition analysis of the turbulence data will be presented that will provide additional insight into the effects of the reattachment process on the compressible turbulence field.

Reynolds Stress Development

As discussed earlier, the reattachment effects on the primary Reynolds stresses appear to be dependent on the flow speed regime (subsonic or supersonic) and the centerline boundary condition (compliant or solid boundary). In the subsonic, solid wall case, Chandrsuda and Bradshaw (1981) show marked decreases in the longitudinal normal stress and shear stress through the reattachment region with the transverse normal stress maintaining a relatively constant value throughout the initial stages of reattachment. In contrast, the supersonic, solid wall data of Hayakawa et al. (1984) and Samimy et al. (1986) both show peak Reynolds stresses occurring downstream of the reattachment point. The relatively sparse data available in the supersonic, compliant boundary case suggest that the Reynolds stresses peak at the reattachment point (Samimy and Addy, 1986; Amatucci et al., 1992).

The development of the axial and radial Reynolds normal stresses through the reattachment region of the present work is shown in Figs. 2 and 3, respectively. The approximate location of the onset of the adverse pressure gradient is labeled on the abscissa as xp, and the scale for the plotted variable is shown at the upper left of the figure. The strong peak in the axial normal stress shown upstream of reattachment is indicative of compressible free shear layers. The location of the peak coincides roughly with the inflection point in the mean velocity profile which is approximately centered between the edges of the shear layer. As the shear layer enters the recompression region, the Reynolds stress profiles begin to broaden due to turbulence diffusion mechanisms and the increased turbulence activity along the centerline from the shear layer interaction. Near reattachment, the centerline axial and radial Reynolds stresses both reach local maxima which, along with the decreasing peak values away from the axis, appears as an overall broadening of the Reynolds stress profiles. Downstream of the reattachment point, the strong Reynolds stress peaks present in the shear layer prior to the adverse pressure gradient have all but disappeared in favor of a more radially uniform turbulence field of reduced magnitude. Of course, it is expected that the change in flow regime from shear layer to wake will result in lower downstream turbulence levels since the wake does not contain the relatively large mean shear rates present in the approaching shear layer. In addition to the axial and radial Reynolds normal stresses, the tangential normal stress was also measured experimentally and found to closely follow the radial Reynolds stress trends discussed above.

The development of the primary Reynolds shear stress (<u'v'>) through the reattachment region is shown in Fig. 4 and is found to be somewhat more dramatic than the normal stresses. Upstream of reattachment, the shear stress profile is similar to that shown previously for the axial normal stress, except along the centerline where the shear stress vanishes by symmetry. The shear stress profile is seen to maintain its strong-peaked appearance up to the reattachment point. However, immediately downstream of reattachment, a significant change in the shear stress profile occurs; namely, the profile transitions to a more rounded appearance and the magnitude is greatly reduced from that near reattachment. At the last axial station shown, the wake shear stress distribution is far different, in magnitude and shape, than that in the shear layer approaching reattachment. In addition, the decrease in the peak shear stress magnitude prior to the reattachment point in the present case can be contrasted to both the supersonic, solid wall case and the supersonic, compliant boundary case measured in two-dimensional flows. More discussion as to this comparison and the possible physical mechanisms involved will be given below.

3

In addition to the Reynolds stress profiles shown in the previous figures, it is also instructive to plot the *peak* Reynolds stress magnitudes as a function of axial distance through the reattachment region, Fig. 5. By doing this, it becomes apparent that the reattachment process can be divided into three regions: a region upstream of the adverse pressure gradient ($x/x_R < 0.72$), a central region between the start of recompression and the reattachment point ($0.72 < x/x_R < 1.0$), and a post-reattachment region ($x/x_R > 1.0$). As previously mentioned, the region upstream of the onset of the adverse pressure gradient ($x < x_P$) is characterized by a compressible, axisymmetric shear layer developing at essentially constant pressure with strong Reynolds stress peaks that are slowly evolving with downstream distance.

At the onset of the adverse pressure gradient associated with reattachment, it is apparent that the peak Reynolds stresses are affected, although the magnitude of the effect varies considerably among the different Reynolds stress components. The axial normal stress and primary shear stress are both attenuated in this region while the radial and tangential normal stresses actually *increase* modestly. To explain these different trends, one must consider the many competing fluid dynamic effects that occur in the reattachment region, including the bulk compression associated with adverse pressure gradients, destabilizing concave streamline curvature, lateral streamline convergence as the flow approaches the axis of symmetry, and the shear layer interaction occurring across the centerline. The effects of bulk compression, streamline curvature, and lateral convergence have been studied in detail for attached, subsonic, turbulent boundary layers (Bradshaw, 1974; Smits et al., 1979a, 1979b) and are generally classified as "extra" rates of strain in addition to the strain rate of simple shear, $\partial U/\partial r$. Although the present flowfield is somewhat more complicated than the boundary layer flow for which the "extra" strain rate effects were determined, the fluid dynamic effects on the Reynolds stresses of the present flow are known, at the very least, as to their direction. Consequently, bulk compression and concave streamline curvature should act to destabilize (increase) the Reynolds stresses in the reattaching shear layer while lateral streamline convergence should stabilize (decrease) the Reynolds stress magnitudes. Unfortunately, the combined effect of these three extra strain rates cannot be determined by a simple summation of their relative magnitudes (Smits and Wood, 1985). The observed decreases in the axial normal stress and primary shear stress at the onset of reattachment, consequently, indicate the overwhelming influence of the lateral streamline convergence when compared to the effects of bulk compression and concave streamline curvature. Since the turbulence field interacts with the mean flow primarily through the streamwise normal stress, the slight increase in the radial and tangential normal stresses in the initial reattachment region is a result of the relatively long time scales associated with

turbulence energy transfer among the components when compared to that between the mean flow and the axial normal stress. In fact, downstream of the reattachment point ($x/x_R > 1.0$) all of the Reynolds stress components experience decays to lower values in the developing wake.

By considering the "extra" strain rates described above, it is now possible to offer plausible explanations for the observed trends in the present data. At the start of the recompression region, the peak Reynolds stress regions of the shear layer are sufficiently far from the axis of symmetry that the shear layer interaction effects are most likely small (this is obvious from the Reynolds stress profiles shown in Figs. 2-4); therefore, the observed decrease in the axial normal stress and primary shear stress in this region are primarily a result of the stabilizing effects of lateral streamline convergence. As the shear layer approaches the axis of symmetry, the lateral streamline convergence effect increases approximately with the inverse of the radial coordinate (Smits et al., 1979b), and the shear layer interaction along the centerline begins to affect the Reynolds stress profiles resulting primarily in an increase in the centerline normal stresses. Since the peak turbulence region lies away from the centerline, the peak Reynolds stress magnitudes continue to decay through the reattachment point due to the streamline convergence effect. In two-dimensional compliant boundary reattachment, lateral convergence effects are negligible so that the observed increase in the Reynolds stresses up to the reattachment point (Samimy and Addy, 1986; Amatucci et al., 1992) can be explained by the overall destabilizing effects of streamline curvature and bulk compression. Immediately downstream of reattachment in the present case, the shear layer realignment process is gradually completed and the "extra" strain rates associated with bulk compression, streamline curvature, and lateral convergence vanish. Consequently, the Reynolds stresses decay to lower values that are indicative of the decreasing shear rates present in wake flows relative to those in compressible shear layers.

Velocity Triple Products

In addition to the Reynolds stresses, the velocity triple products provide information on the transport of turbulence energy throughout the reattachment region. It is well understood that the primary contribution to the triple products comes from large scale turbulent structures which, in the present flowfield, enter the reattachment region from the compressible shear layer. Figures 6 and 7 show the effect of the reattachment process on two triple products of interest, $<u'u'v'>$ and $<u'v'v'>$, respectively. In a planar mixing layer, the triple products are roughly antisymmetrical about the mixing layer centerline (Chandrsuda and Bradshaw, 1981; Goebel, 1990), and the same approximate behavior is shown upstream of the reattachment zone in Figs. 6 and 7. In general, negative values of $<u'u'v'>$ (Fig. 6) imply that, on average, eddies with large streamwise velocity fluctuations move towards

4

the centerline, away from the region of maximum Reynolds stress, and vice versa for positive values. As the shear layer approaches the reattachment point, the magnitude of the large negative <u'u'v'> peak at the inner edge is rapidly attenuated while the large positive peak at the outside edge of the shear layer broadens somewhat but maintains a relatively large magnitude. This trend suggests a containment of the large scale eddies at the centerline due to the axisymmetric nature of the flow and is similar to that observed in subsonic, solid wall reattachment studies (e.g., Chandrsuda and Bradshaw, 1981). In other words, movement of the large scale structures toward or across the axis of symmetry is confined near the axis of symmetry. In previous two-dimensional, supersonic, compliant boundary studies (Samimy and Addy, 1986; Amatucci, 1990), the large negative peak near the inside edge of the shear layer persisted far downstream of the reattachment point. Consequently, it is apparent that the axisymmetric nature of the present flow has a significant impact on the nature of the turbulence field near the centerline where streamline convergence and transverse curvature effects are largest. Downstream of the reattachment point in Fig. 6, an overall decay in <u'u'v'> is shown as the wake develops.

The effect of the reattachment process on the streamwise transport of the radial normal stress, as indicated by <u'v'v'>, is shown in Fig. 7. In contrast to the radial transport of turbulence energy shown in Fig. 6, the eddy containment near the axis of symmetry has a limited effect on the streamwise transport shown in Fig. 7. In fact, the initial antisymmetrical profile prior to recompression is approximately maintained to the reattachment point, although it is somewhat broadened due to turbulence diffusion and shifted toward the centerline as the shear layer undergoes realignment. Since flow symmetry about the axis is primarily a constraint on the mean radial velocity (i.e., $V = 0$ on the centerline), and not on the mean axial velocity, it is not surprising that the radial transport of turbulence energy is more strongly affected near the axis of symmetry. This suggests that the large scale structures that enter the recompression region change orientation as they approach reattachment due to streamline curvature and centerline confinement effects and, subsequently, begin to lose coherency as the wake develops. This is not to suggest that large scale structures are absent downstream of reattachment, but rather that the organization of the structures has diminished through the reattachment zone. Evidence of this has been given by Smith and Dutton (1995) who obtained planar Mie scattering images near the reattachment point in the two-dimensional supersonic base flowfield used previously in the study by Amatucci et al. (1992). The images show quite clearly the presence of large scale turbulent structures throughout the reattachment region and in the downstream wake. However, statistical image processing analyses indicate a loss in coherence of the structures through reattachment similar to that postulated for the present

flow. It is important to keep in mind that the turbulence field in the current axisymmetric flow is significantly attenuated by the reattachment process in contrast to the two-dimensional case, so it is reasonable to expect that the loss of eddy organization noted by Smith and Dutton (1995) is magnified in the current case.

In addition to the data shown in Figs. 6 and 7, several other velocity triple products were calculated from the experimental data. These include <u'u'u'>, <v'v'v'>, <u'u'w'>, <u'w'w'>, and <w'w'w'>. In this case, w' represents an instantaneous velocity fluctuation in the tangential (swirl) direction. As expected, the tangential transport of turbulence energy (as indicated by <u'u'w'> and <w'w'w'>) was negligible compared to the axial and radial transport terms. In addition, the streamwise transport of the axial (<u'u'u'>) and tangential (<u'w'w'>) normal stresses follows closely the trends for the corresponding radial normal stress (<u'v'v'>) shown in Fig. 7, although the radial and tangential component magnitudes are reduced by a factor of approximately three relative to the axial component. Finally, the radial transport of the radial normal stress (<v'v'v'>) is similar to the corresponding axial normal stress transport (<u'u'v'>) shown in Fig. 6 except that the magnitudes are reduced by about a factor of two.

Turbulence Structure Parameters

To this point, the turbulence field throughout the reattachment region has been discussed in terms of the overall changes in the Reynolds stress and triple product magnitudes. Since the flowfield undergoes a change in type through reattachment (from shear layer to wake), one would expect significant changes in these turbulence quantities. It is also instructive from a fundamental standpoint, and more important in some respects, to investigate the *structural* changes in the turbulence field brought on by the application of the "extra" strain rates in the reattachment zone. Many questions exist about the turbulence structure in highly compressible shear layers and the response to complicating features such as pressure gradient, streamline curvature, etc. For example, how is the overall turbulence energy distributed between the normal stresses? How quickly does the shear stress respond to these effects compared to the normal stresses? How are the Reynolds stress distributions different from incompressible flow?

Perhaps the most instructive parameter to investigate is the anisotropy of the Reynolds normal stresses. In the present case, a primary-to-secondary stress ratio, $(\sigma_u/\sigma_v)^2$, and a secondary-to-secondary stress ratio, $(\sigma_w/\sigma_v)^2$, are utilized to show the respective distributions of the Reynolds normal stress field. Figure 8 shows the development of these normal stress ratios determined at the peak shear stress location in the reattaching shear layer. Clearly, this figure reinforces the dominance of the axial normal stress indicated earlier in conjunction with Fig. 5. It is apparent that the initial stages of the

5

reattachment process have a significant impact on the relative distribution of the normal stresses with a rapid decay in $(\sigma_u/\sigma_v)^2$ occurring up to the reattachment point. Downstream of reattachment, the relative normal stress distributions appear to have reached an equilibrium state with only small variations as the wake develops. Throughout the reattachment region, the secondary-to-secondary stress ratio, $(\sigma_w/\sigma_v)^2$, maintains an approximately constant value of unity suggesting little difference in the turbulence energy redistribution mechanisms (e.g., pressure-strain) in these components. In the two-dimensional case (Amatucci et al., 1992), the primary-to-secondary normal stress ratio is relatively constant up to and even downstream of the reattachment point and takes a value $(\sigma_u/\sigma_v)^2 \approx 6$, which is significantly larger than the values shown in Fig. 8 for the present flow. This again illustrates the significant differences that exist in the turbulence field between two-dimensional and axisymmetric flows in the reattachment zone.

For attached subsonic flows, it has been suggested by Bradshaw (1973) and others that the primary turbulence structure parameters do not respond immediately to the application of "extra" strain rates. Similarly, the response of the turbulence structure parameters will not be instantaneous to the removal of the "extra" strain rates. Figure 8 suggests quite a different picture in the present flow. In fact, at the onset of the adverse pressure gradient, the primary-to-secondary normal stress ratio is already decaying to lower levels. At or slightly downstream of reattachment, the "extra" strain rates associated with streamline curvature, bulk compression, and streamline convergence are greatly diminished (i.e., realignment is almost complete) and the effect on the normal stress ratios shown in Fig. 8 is an asymptotic approach to constant values in the downstream wake. Consequently, the direct impact of the "extra" strain rates on the normal stress ratio, $(\sigma_u/\sigma_v)^2$, is immediate, which may be an indication of an even stronger coupling between the strain rates and the turbulence field in compressible flows than those ascertained previously for incompressible flowfields.

In addition to the distribution of the turbulence energy among the normal stresses, turbulence models oftentimes use a ratio of shear stress to normal stress for Reynolds stress closure. Distributions of two popular ratios, $-<u'v'>/k$ and R_{uv}, are shown in Fig. 9 where k is the turbulent kinetic energy defined by the following relation:

$$k = \frac{\sigma_u^2 + \sigma_v^2 + \sigma_w^2}{2} \qquad (1)$$

and R_{uv} is the shear stress correlation coefficient defined by:

$$R_{uv} = \frac{-<u'v'>}{\sigma_u \sigma_v} \qquad (2)$$

It is apparent from Fig. 9 that the reattachment process has a greater impact on the Reynolds shear stress than it does on the normal stresses as both ratios decay monotonically throughout the reattachment zone. Similar to the normal stress distributions of Fig. 8, the effects of the "extra" strain rates are felt immediately at the onset of recompression. In contrast, however, the shear stress-to-normal stress ratios shown in Fig. 9 continue to decrease beyond reattachment and do not appear to be approaching an equilibrium state at the last measurement station shown. The magnitude of the shear stress-to-turbulent kinetic energy ratio $-<u'v'>/k$ is, in general, larger than but approaching the "typical" value of 0.3 first suggested by Harsha and Lee (1970) and still commonly used in turbulent flow calculations. Similarly, the shear stress correlation coefficient R_{uv} is larger than, but approaching the typical range of 0.4-0.5 for this parameter. The decay in R_{uv} is another indication of the loss in organization of the large scale turbulence structures through the reattachment region. Planar Mie scattering photographs in the reattachment region of the present flow, similar to those obtained by Smith and Dutton (1995) in the two-dimensional case, would be valuable in determining the role of large scale structures in the axisymmetric reattachment process.

Quadrant Decomposition Analysis

Additional insight into the structure of the turbulence field in the reattachment region can be gained by examining the instantaneous velocity fluctuations with the quadrant decomposition technique. The quadrant analysis method has been commonly used in boundary layer flows (Wallace et al., 1972; Willmarth and Lu, 1972; Lu and Willmarth, 1973) to determine the frequency and strength of dynamic boundary layer events such as eddy ejections and sweeps. Herrin and Dutton (1995) have recently applied this technique to the initial stages of compressible shear layer development in the present flowfield and have found it to be useful in identifying the orientation and qualitative organization of the large scale, energy-containing eddies. In the current section, a brief overview of the quadrant decomposition analysis technique will be presented, followed by the results of its application to the turbulence data in the present reattachment region.

The quadrant analysis technique utilizes ensembles of instantaneous velocity data and first computes the velocity fluctuations (u',v'), which are simply the arithmetic differences between the instantaneous velocities and the mean velocities for each ensemble. The resulting ensemble of velocity fluctuations is then sorted sequentially by placing each fluctuation into a quadrant on a (u',v') scatter plot (see Herrin and Dutton, 1995). For example, a velocity fluctuation obtained from a slower moving (u' < 0), upward oriented (v' > 0) fluid element would be categorized as a "quadrant two" event which, hereafter, will

6

be labeled Q2. Conversely, a faster moving (u' > 0) downward oriented (v' < 0) fluid element would be labeled a Q4 event. By investigating the probabilities of velocity fluctuations occurring in each quadrant, one can qualitatively identify the relative importance of each type of dynamic event. After sorting the velocity fluctuation data into quadrants, it is also possible to determine the quadrant contributions to the total shear stress <u'v'> by averaging the instantaneous (u'v') products in each quadrant. Quadrants 2 and 4 will provide negative shear stress contributions while positive contributions will come from quadrants 1 and 3; the arithmetic sum of all four quadrants will equal the total shear stress, <u'v'>, which is the quantity shown in Fig. 4.

In an attempt to better understand the organization (coherency) of the large scale, energy-containing eddies in the reattachment region, an instantaneous shear angle, Ψ, is defined:

$$\Psi = \tan^{-1}(v'/u') \qquad (3)$$

As this equation indicates, the shear angle is essentially the angle between the fluctuating velocity vector and the axial direction (assuming the swirl component of velocity is negligible). At each spatial location where LDV data were obtained, an ensemble of shear angles $\{\Psi_i\}$ is determined. From this ensemble, discrete probability density functions (pdfs) can be generated which indicate the relative probability of Ψ_i falling within a range of angles, $\Psi_1 < \Psi_i \leq \Psi_1 + \Delta\Psi$, where $\Delta\Psi$ is the bin width of the pdf (taken as 4 degrees in the present study). Figure 10 shows representative shear angle pdfs in the reattachment region of the present flow. Note that the shear angles in Fig. 10 are restricted to $-90° < \Psi_i < 90°$ to more clearly document pdfs with the limited size of each ensemble (i.e., ensembles much larger than the present 4000 realizations would be needed to obtain smooth pdfs over the entire 360 degree range). In the shear layer upstream of reattachment (Fig. 10a), a well defined peak in the shear angle pdf is shown, which indicates a consistent orientation for the velocity fluctuations about the mean flow. This organization in the shear layer turbulence field is consistent with previous observations of large scale turbulent structures in compressible shear layers, and is similar to that found in the present flowfield near the shear layer origin (Herrin and Dutton, 1995). Note that the overwhelming majority of the velocity fluctuations yield negative shear angles which is indicative of Q2 and Q4 events. Through the reattachment region, the organization of the turbulence field diminishes as indicated by the pdfs at the reattachment point (Fig. 10b) and downstream of reattachment (Fig. 10c). Although, the shape of the pdf at the last measurement station still resembles that upstream of recompression, the dominance of the peak at negative angles is no longer as strong. This behavior is consistent with the previous observation of significant reductions in the shear stress magnitude and

correlation coefficient through the reattachment region as indicated in Figs. 5 and 9, respectively. Clearly, the large scale structures present at the onset of recompression can negotiate the adverse pressure gradient associated with reattachment, but as a whole they lose strength and organization in the process.

Due to space limitations, pdfs at only three spatial locations for the reattaching shear layer are shown in Fig. 10 (the radial locations correspond to those of peak shear stress for each axial location). Shear angle pdfs were also computed for several other locations in the shear layer along radial traverses at the same axial stations as the data in Fig. 10. By assuming that the overall degree of turbulence organization at any location is proportional to the peak value of the pdf, it is possible to make a two-dimensional comparison (axial and radial) of the overall effect of the reattachment process on the turbulence structure. Figure 11 makes such a comparison between the data upstream of reattachment ($x/x_R = 0.56$) and that obtained downstream of reattachment ($x/x_R = 1.46$). Radial profiles of the peak probability (in percent) of the pdf at each station are shown for each axial station. In addition, the radial location of the local maximum total shear stress <u'v'> is also indicated for each profile. By comparing the two profiles in Fig. 11, it is apparent that the turbulence field upstream of reattachment is more organized over a large portion of the shear layer than that in the developing wake. Note that in the shear layer, the probability profile forms a definite peak similar to that shown in Fig. 4 for the approach shear stress profile and, as expected, is a maximum near the peak shear stress location. Not only is the probability profile downstream of the reattachment region of smaller magnitude than the peak levels in the upstream shear layer, but the peak probability also decreases in magnitude as the axis of symmetry is approached. Although somewhat inconclusive, due to limited data, it appears that the peak probabilities occur at radial distances beyond the peak shear stress location in the wake. The physical reasoning for this observation is not clear, although it suggests that the large scale structures present in the wake flow, although weakened and less organized as a result of the reattachment process, are still present across a majority of the wake and play an important role in its subsequent development. Of course, as the mean shear rate ($\partial U/\partial r$) decays with downstream distance, one would expect the large scale structures to continually weaken.

The shear angle analysis presented above considers only the angular orientation of the velocity fluctuations and, therefore, no information about the strength (magnitude) of the fluctuations at different stages in the reattachment process is provided. For this reason, a conditional quadrant sorting technique (sometimes referred to as a hole analysis) is utilized here to provide detailed information about the dynamic events that contribute most to the total shear stress magnitude. In this technique, the magnitude of the instantaneous product

7

(u'v') is compared to a preset threshold and subsequently sorted into a particular class of events. The sorting algorithm can be symbolically represented as follows:

$$\text{if } |u'v'| \leq H \, |<u'v'>| \rightarrow \text{hole} \qquad (4)$$

$$\text{if } |u'v'| > H \, |<u'v'>| \rightarrow Q1, Q2, Q3, \text{ or } Q4$$

which indicates that (u'v') realizations are placed in their respective quadrants if their magnitude exceeds the threshold, otherwise they are placed in a fifth category called the *hole* which contains all of the "weak" velocity fluctuation products. The threshold for this sorting process is the product of the hole size (H) and the magnitude of the total, ensemble-averaged shear stress. The hole size is altered parametrically in the sorting process in order to determine which quadrant contains the strongest dynamic events in the flowfield. Figure 12 is a sketch of the hole region on a (u',v') velocity fluctuation scatter plot where the H = 3 threshold is essentially a line of constant (u'v') with a magnitude three times the value of the ensemble-averaged shear stress, <u'v'>. After sorting each velocity realization according to the algorithm in Eq. 4, the categories are averaged (including the hole) in order to identify the quadrant (and hole) contributions to the total shear stress. The quadrant averages are computed by the following equation:

$$<u'v'>_n = \frac{\sum (u'v')_n}{N_{tot}} \qquad (5)$$

where $(u'v')_n$ is a realization falling in quadrant n and N_{tot} is the total number of realizations in the entire ensemble. In this manner, the sum of the quadrant and hole averages will identically equal the total, ensemble-averaged shear stress, <u'v'>.

Representative hole diagrams upstream (x/x_R = 0.56), at (x/x_R = 1.01), and after (x/x_R = 1.46) reattachment are shown in Fig. 13 for data at the local peak shear stress radial location. Note that the independent variable in these diagrams is the hole size (H) and the plotted variable is the percentage contribution of each quadrant and the hole region to the total shear stress. The quadrant values for H = 0 correspond to shear stress contributions in the absence of conditional sorting (i.e., vanishing hole region). Upstream of reattachment (Fig. 13a), large and approximately equal contributions to the shear stress are indicated for Q2 and Q4 events with large instantaneous fluctuations of (u'v') up to five times the ensemble-averaged value (i.e., H = 5). Also, Q1 and Q3 events are shown to contribute very little to the total shear stress magnitude. The distributions shown in Fig. 13a are very similar to those shown previously (Herrin and Dutton, 1995) for the same shear layer near its origin (boundary layer separation point). As the shear layer enters the reattachment region, however, the contribution from Q2 events begins to exceed those from Q4 events and, in fact, at the end of reattachment a significant difference between the Q2 and Q4 contributions exists.

By comparing all three plots in Fig. 13, it is apparent that the percentage contributions from Q4 events remain relatively constant throughout the reattachment process. It has been shown (Fig. 5) that the peak ensemble-averaged shear stress magnitude decreases sharply through reattachment (the conventionally-averaged total shear stress for the data in Fig. 13c is at least three times smaller than that in Fig. 13a). Therefore, Fig. 13 suggests that since the total contributions from Q4 events decrease at a rate nearly identical to that for the total shear stress, it is the attenuation of these events that plays a large role in the overall decrease of the Reynolds shear stress through reattachment. In contrast, the shear stress contribution from Q2 events increases in percentage terms through reattachment which implies a persistence of these events throughout the reattachment process. Notice that in the developing wake (Fig. 13c), large instantaneous Q2 fluctuations over ten times greater than the ensemble-averaged shear stress have been measured.

The obvious question that comes to mind after the preceding discussion is what exactly are instantaneous Q2 and Q4 events in the shear layer and how are they related to the passage of large scale turbulent structures? From the signs of the velocity fluctuations, a Q4 event corresponds to a faster moving (u' > 0), downward oriented (v' < 0) fluid element relative to the mean flow at a particular spatial location. Considering the evolution of large scale turbulent structures, this orientation is consistent with the influx (entrainment) of freestream fluid into the shear layer or wake as part of a clockwise eddy rollover process in the convective frame of reference. Conversely, a Q2 event (u' < 0, v' > 0) could correspond to the backside of a "typical" clockwise eddy that carries low speed, turbulent fluid away from the centerline. It is understood that this description of Q2 and Q4 events is necessarily simplistic due to the complicating differences between incompressible planar mixing layers (where the dynamics of large scale structures are better understood) and the current reattaching shear layer. However, by using these simplified descriptions, it is found that the decay in Q4 events relative to Q2 events through the reattachment region is consistent with a reduction in the entrainment of mass at the outside edge of the wake. In fact, the <u'u'v'> triple product profiles in Fig. 6 confirm the suspected loss in the transport of turbulence energy toward the axis of symmetry in the wake region (axisymmetric containment effect), especially compared to that in the shear layer approaching reattachment. In addition, the last axial station shown in Fig. 6 indicates that the overwhelming majority of the radial transport of turbulence energy in the wake is *away* from the axis, which is consistent with the quadrant decomposition analysis results discussed above.

SUMMARY AND CONCLUSIONS

Experimental data on the turbulence structure of a reattaching supersonic axisymmetric shear layer have been presented. In contrast to the popular solid wall

8

reattachment problem, the present work investigates reattachment onto the compliant boundary (i.e., no solid wall) along the axis of symmetry. Detailed mean velocity and turbulence measurements have been made throughout the reattachment region to document the overall effect of the many "extra" strain rates including bulk compression, concave streamline curvature, and lateral streamline convergence. From these data, the following conclusions can be drawn:

(1) The Reynolds stress field throughout the reattachment zone is far different than that found in solid wall reattachment studies. In the present case, immediate reductions in the axial normal stress and primary shear stress are discernible at the onset of the adverse pressure gradient associated with reattachment. Downstream of the reattachment point, all Reynolds stresses decay as the mean shear rate decreases with downstream distance. These findings also indicate a significant difference between axisymmetric and two-dimensional reattachment flowfields apparently caused by the substantial effect of lateral streamline convergence near the axis of symmetry.

(2) The velocity triple products through the reattachment region indicate a containment of large scale eddies along the centerline similar to that observed in subsonic, solid wall reattachment studies. This results in a relative decrease in the transport of turbulence energy toward the centerline downstream of reattachment. The reattachment effect on the streamwise transport of turbulence energy was minimal compared to the radial component.

(3) The axial-to-radial normal stress anisotropy ratio was strongly affected by the initial stages of the reattachment process, although shortly downstream of reattachment, relatively constant values were maintained. Throughout reattachment, the two secondary normal stresses (radial and tangential) maintained essentially equal magnitudes. Other turbulence structure parameters ($<u'v'>/k$ and R_{uv}) show significant reductions through reattachment which suggests a loss of organization of the large scale, shear stress-producing structures.

(4) The results of a quadrant decomposition analysis of the turbulence data support the notion of decaying turbulent structures through the reattachment region. The overall organization of the velocity fluctuations is reduced in the wake relative to that in the shear layer approaching reattachment. In addition, a reduction in the strength of Q4 events ($u' > 0$, $v' < 0$) suggests reduced turbulence transport toward the axis relative to that away from the axis in the developing wake, similar to that observed in the velocity triple product profiles.

ACKNOWLEDGMENTS

REFERENCES

Abu-Hijleh, B. and Samimy, M. (1989), "An Experimental Study of a Reattaching Supersonic Shear Layer," AIAA Paper 89-1801.

Amatucci, V.A. (1990), "An Experimental Investigation of the Two-Stream, Supersonic, Near-Wake Flowfield Behind a Finite-Thickness Base," Ph.D. Thesis, Dept. of Mechanical and Industrial Engineering, Univ. of Illinois at Urbana-Champaign, Urbana, Illinois.

Amatucci, V.A., Dutton, J.C., Kuntz, D.W., and Addy, A.L. (1992), "Two-Stream, Supersonic, Wake Flowfield Behind a Thick Base, Part 1: General Features," AIAA Journal, Vol. 30, No. 8, pp. 2039-2046.

Bloomberg, J.E. (1989), "An Investigation of Particle Dynamics Effects Related to LDV Measurements in Compressible Flows," M.S. Thesis, Dept. of Mechanical and Industrial Engineering, Univ. of Illinois at Urbana-Champaign, Urbana, Illinois.

Bradshaw, P. (1973), "Effects of Streamline Curvature on Turbulent Flow," NATO AGARDograph No. 169.

Bradshaw, P. (1974), "The Effect of Mean Compression or Dilatation on the Turbulence Structure of Supersonic Boundary Layers," Journal of Fluid Mechanics, Vol. 63, Part 3, pp. 449-464.

Chandrsuda, C. and Bradshaw, P. (1981), "Turbulence Structure of a Reattaching Mixing Layer," Journal of Fluid Mechanics, Vol. 110, pp. 171-194.

Eaton, J.K. and Johnston, J.P. (1981), "A Review of Research on Subsonic Turbulent Flow Reattachment," AIAA Journal, Vol. 19, No. 9, pp. 1093-1100.

Goebel, S.G. (1990), "An Experimental Investigation of Compressible Turbulent Mixing Layers," Ph.D. Thesis, Dept. of Mechanical and Industrial Engineering, Univ. of Illinois at Urbana-Champaign, Urbana, Illinois.

Harsha, P.T. and Lee, S.C. (1970), "Correlation Between Turbulent Shear Stress and Turbulent Kinetic Energy," AIAA Journal, Vol. 8, No. 8, pp. 1508-1510.

Hayakawa, K., Smits, A.J., and Bogdonoff, S.M. (1984), "Turbulence Measurements in a Compressible Reattaching Shear Layer," AIAA Journal, Vol. 22, No. 7, pp. 889-895.

Herrin, J.L. (1993), "An Experimental Investigation of Supersonic Axisymmetric Base Flows Including the Effects of Afterbody Boattailing," Ph.D. Thesis, Dept. of Mechanical and Industrial Engineering, Univ. of Illinois at Urbana-Champaign, Urbana, Illinois.

Herrin, J.L. and Dutton, J.C. (1993), "An Investigation of LDV Velocity Bias Correction Techniques for High-Speed Separated Flows," Experiments in Fluids, Vol. 15, No. 4/5, pp. 354-363.

Herrin, J.L. and Dutton, J.C. (1994), "Supersonic Near-Wake Afterbody Boattailing Effects on Axisymmetric Bodies," Journal of Spacecraft and Rockets, Vol. 31, No. 6, pp. 1021-1028.

Herrin, J.L. and Dutton, J.C. (1995), "Effect of a Rapid Expansion on the Development of Compressible Free Shear Layers," Physics of Fluids, Vol. 7, No. 1, pp. 159-171.

Hohler, V. and Stilp, A. (1990), "Penetration Performance of Segmented Rods at Different Spacing - Comparison with Homogeneous Rods at 2.5 - 3.5 km/s," Proceedings of the 12th International Symposium on Ballistics, Vol. III, San Antonio, Texas, pp. 178-187.

Korst, H.H. (1956), "A Theory for Base Pressures in Transonic and Supersonic Flow," Journal of Applied Mechanics, Vol. 78, No. 12, pp. 593-600.

Lu, S.S. and Willmarth, W.W. (1973), "Measurements of the Structure of the Reynolds Stress in a Turbulent Boundary Layer," Journal of Fluid Mechanics, Vol. 60, pp. 481-511.

Samimy, M. and Addy, A.L. (1986), "Interaction Between Two Compressible, Turbulent Free Shear Layers," AIAA Journal, Vol. 24, No. 12, pp. 1918-1923.

Samimy, M. and Lele, S.K. (1991), "Particle-Laden Compressible Free Shear Layers," Physics of Fluids-A, Vol. 3, No. 8, pp. 1915-1923.

Samimy, M., Petrie, H.L., and Addy, A.L. (1986), "A Study of Compressible Turbulent Reattaching Free Shear Layers," AIAA Journal, Vol. 24, No. 2, pp. 261-267.

Shen, Z.H., Smith, D.R., and Smits, A.J. (1993), "Wall Pressure Fluctuations in the Reattachment Region of a Supersonic Free Shear Layer," Experiments in Fluids, Vol. 14, No. 1/2, pp. 10-16.

Smith, K.M. and Dutton, J.C. (1995), "Large-Scale Structures in Supersonic Reattaching Shear Flows," AIAA Paper 95-2251.

Smits, A.J., Young, S.T.B., and Bradshaw, P. (1979a), "The Effect of Short Regions of High Surface Curvature on Turbulent Boundary Layers," Journal of Fluid Mechanics, Vol. 94, Part 2, pp. 209-242.

Smits, A.J., Eaton, J.A., and Bradshaw, P. (1979b), "The Response of a Turbulent Boundary Layer to Lateral Divergence," Journal of Fluid Mechanics, Vol. 94, Part 2, pp. 243-268.

Smits, A.J. and Wood, D.H. (1985), "The Response of Turbulent Boundary Layers to Sudden Perturbations," Annual Review of Fluid Mechanics, Vol. 17, pp. 321-358.

Wallace, J.M., Eckelmann, H., and Brodkey, R.S. (1972), "The Wall Region in Turbulent Shear Flow," Journal of Fluid Mechanics, Vol. 54, pp. 39-48.

Willmarth, W.W. and Lu, S.S. (1972), "Structure of the Reynolds Stress Near the Wall," Journal of Fluid Mechanics, Vol. 55, pp. 65-92.
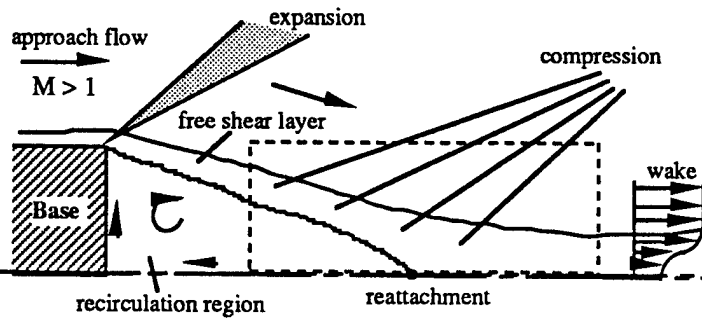
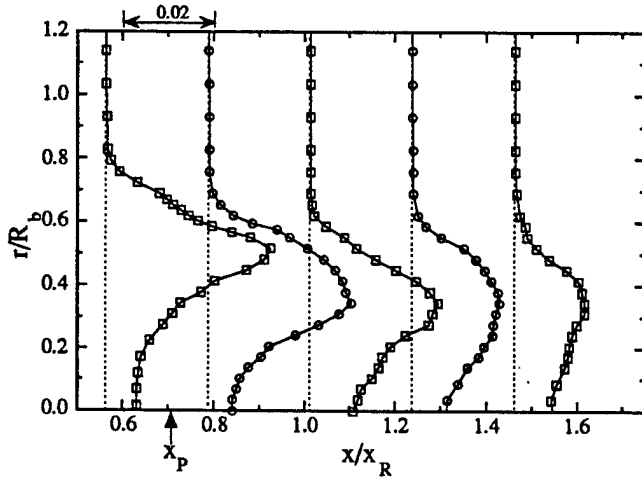Fig. 1 Sketch of entire near-wake flowfield and region of interest
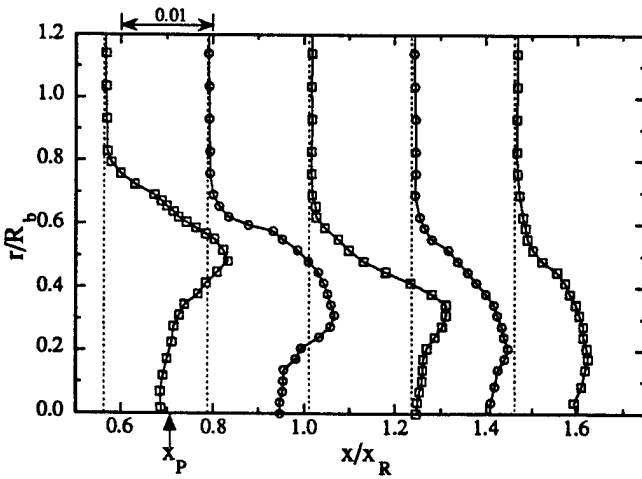

Fig. 4 Primary Reynolds shear stress profiles, $-\langle u'v'\rangle/U_{ref}^2$

Fig. 2 Axial Reynolds stress profiles, $(\sigma_u/U_{ref})^2$
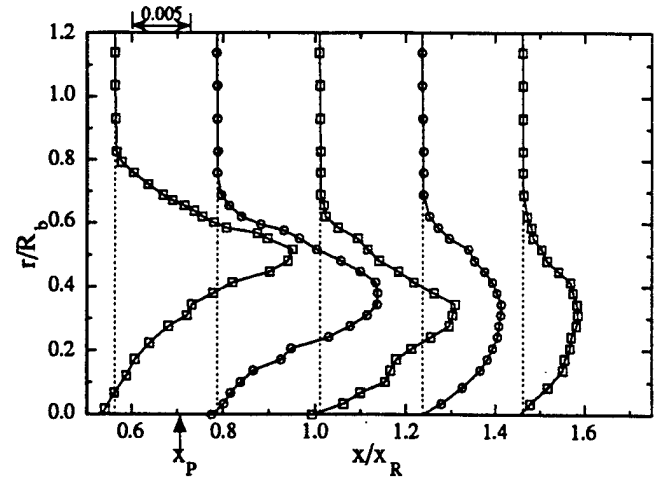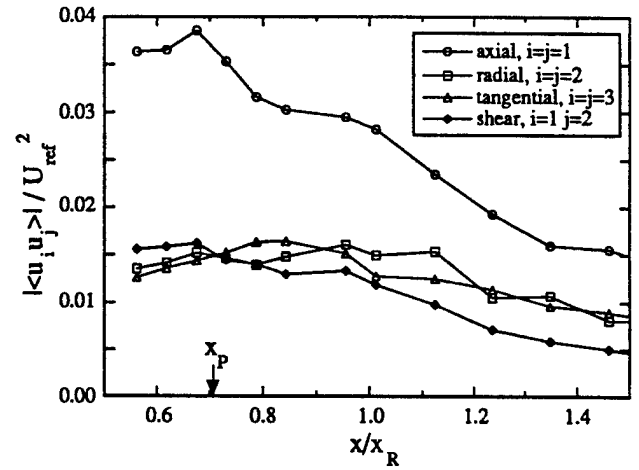
Fig. 5 Peak Reynolds stress magnitudes through reattachment

Fig. 3 Radial Reynolds stress profiles, $(\sigma_v/U_{ref})^2$
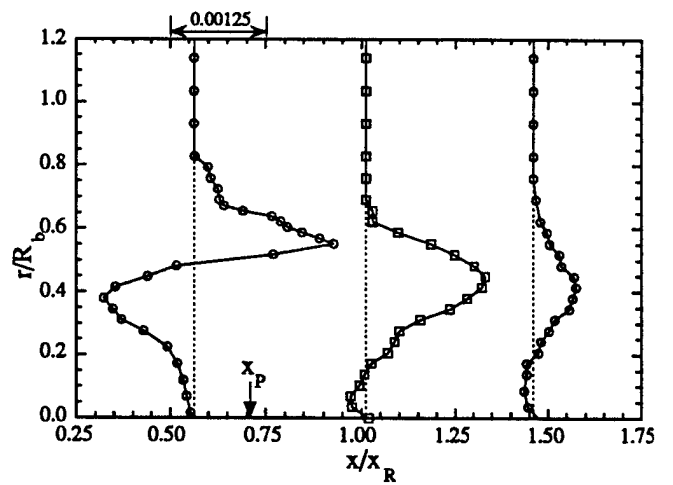
Fig. 6 Velocity triple product profiles, $\langle u'u'v'\rangle/U_{ref}^3$

11
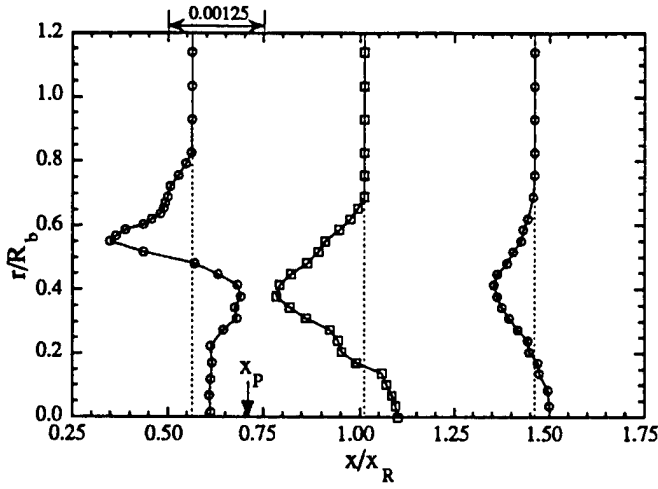
Fig. 7 Velocity triple product profiles, $\langle u'v'v'\rangle/U_{ref}^3$
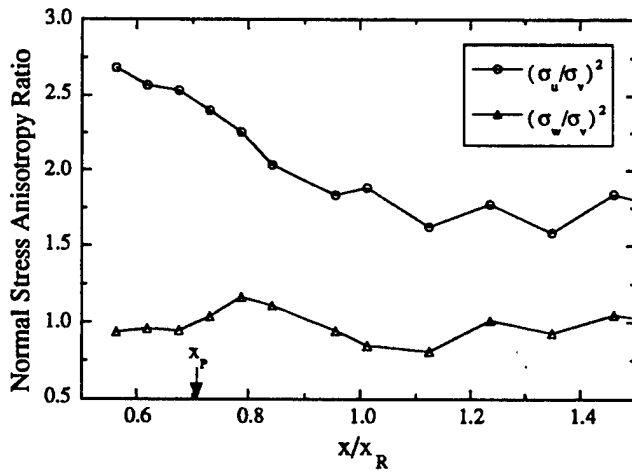
Fig. 8 Normal stress anisotropy ratios at the peak shear stress locations
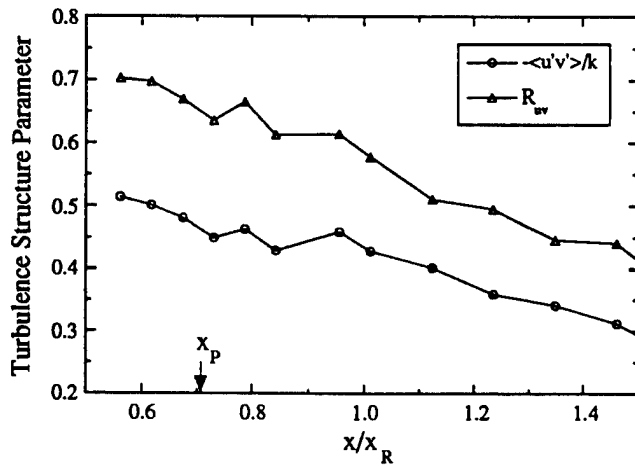

Fig. 9 Turbulence structure parameters at the peak shear stress locations
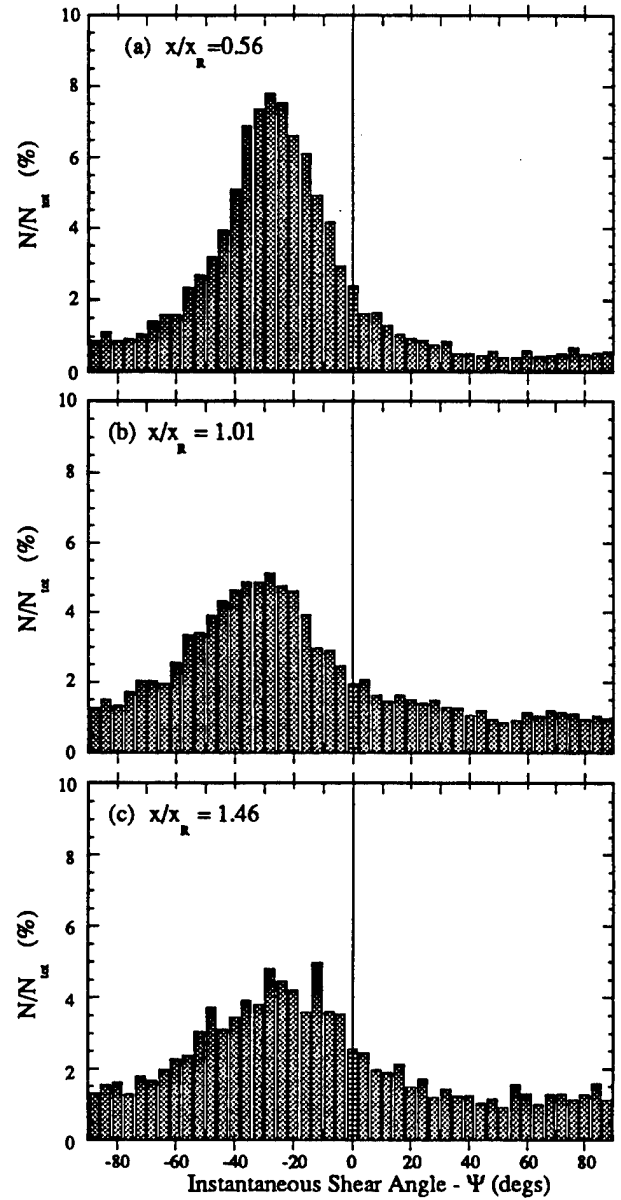

Fig. 10 Shear angle histograms near reattachment: (a) $x/x_R = 0.56$, (b) $x/x_R = 1.01$, (c) $x/x_R = 1.46$
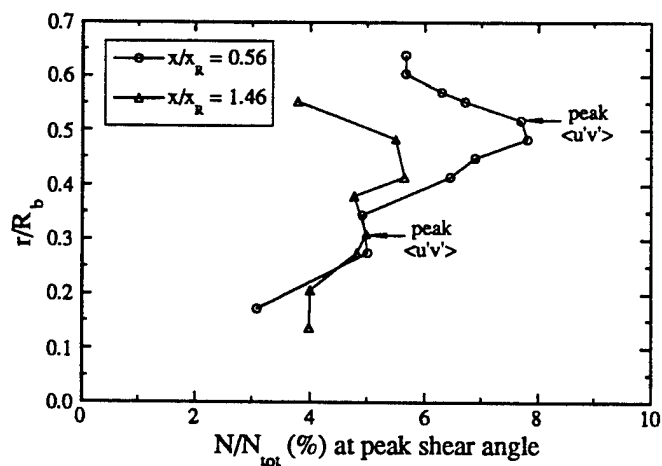
Fig. 11 Shear angle probability distributions upstream and downstream of reattachment
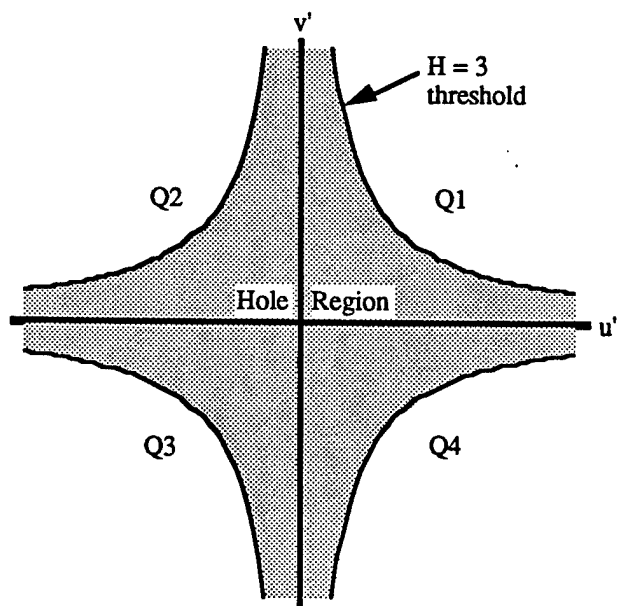

Fig. 12 Sketch of hole region in conditional quadrant analysis technique
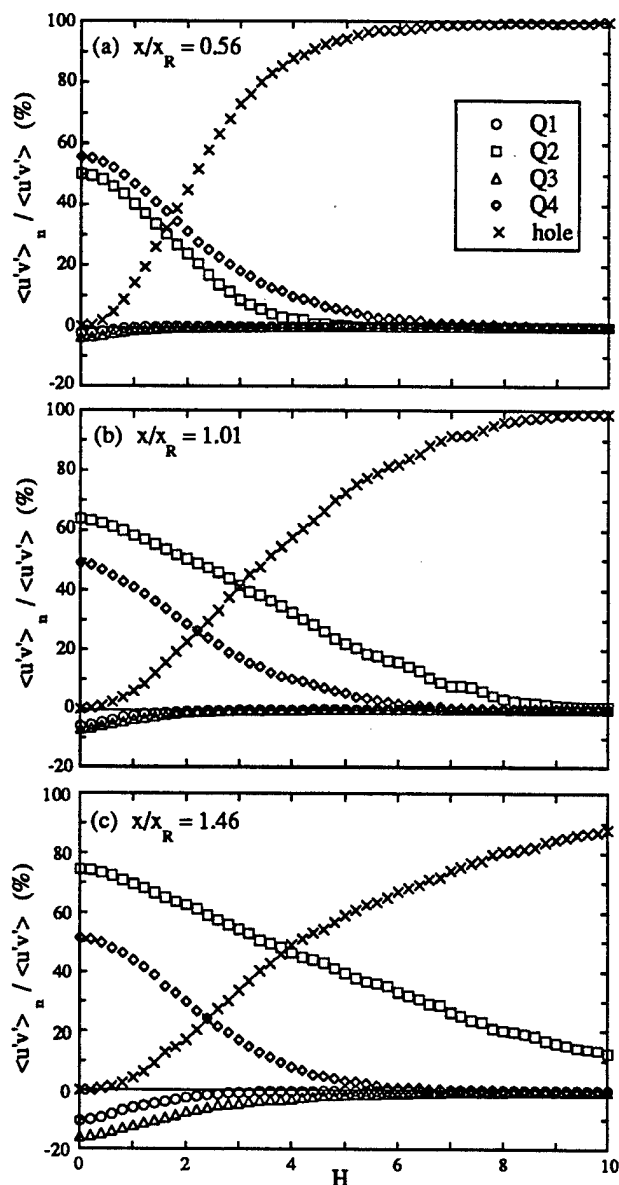

Fig. 13 Quadrant contributions to the total shear stress: (a) $x/x_R = 0.56$, (b) $x/x_R = 1.01$, (c) $x/x_R = 1.46$

13

APPENDIX A.20

VELOCITY AND TURBULENCE MEASUREMENTS IN A SUPERSONIC BASE FLOW WITH MASS BLEED

by

T. Mathur and J. C. Dutton

AIAA 96-0456

Velocity and Turbulence Measurements in a Supersonic Base Flow with Mass Bleed

T. Mathur and J.C. Dutton
Department of Mechanical and Industrial Engineering
University of Illinois at Urbana-Champaign
Urbana, Illinois 61801

34th Aerospace Sciences
Meeting & Exhibit
January 15-18, 1996 / Reno, NV

VELOCITY AND TURBULENCE MEASUREMENTS IN A SUPERSONIC BASE FLOW WITH MASS BLEED

T. Mathur[*] and J.C. Dutton[†]
Department of Mechanical and Industrial Engineering
University of Illinois at Urbana-Champaign
Urbana, Illinois 61801

ABSTRACT

Two-component laser Doppler velocimetry was used to obtain detailed mean velocity and turbulence measurements in the near-wake of a cylindrical afterbody with base bleed in a Mach 2.5 flow. The bleed flow provides at least some of the fluid required for shear layer entrainment and shields the base annulus from the outer shear layer and the primary recirculation region, leading to an increase in base pressure. There is an overall reduction in turbulence levels throughout the base bleed flowfields relative to the near-wake flowfields of blunt-based and boattailed afterbodies. With increasing bleed, the formation of a strong bleed jet shear layer and secondary recirculation region near the base annulus offsets the benefits of base bleed, leading to a drop in the base pressure. The net benefits of base bleed are maximized at the optimum bleed condition, which corresponds to the highest base pressure, the disappearance of the primary recirculation region, and the lowest turbulence levels in the near-wake flowfield. Increased benefits from base bleed could be achieved by injecting the bleed fluid at the lowest possible velocity through the use of larger bleed orifices, porous bases, or bleed orifices located along the outer base annulus.

NOMENCLATURE

A_b = base area, πR_o^2

I = injection parameter, $\dfrac{\dot{m}_{bleed}}{\rho_1 U_1 A_b}$

k = turbulent kinetic energy, m^2/s^2

$\dot{m}_{bleed}$ = bleed mass flow rate, kg/s

M = Mach number

P = pressure, kPa

r = radial coordinate, mm

R_{jet} = bleed jet radius, mm

R_o = afterbody radius, mm

S = stagnation point (location of U = 0 along the axis of symmetry)

T_o = wind tunnel stagnation temperature, K

U = mean axial velocity, m/s

U_1 = freestream approach velocity, m/s

u' = instantaneous axial velocity fluctuation, m/s

V_r = mean radial velocity, m/s

v_r' = instantaneous radial velocity fluctuation, m/s

V_t = mean tangential velocity, m/s

v_t' = instantaneous tangential velocity fluctuation, m/s

x = axial (streamwise) position relative to the base plane, mm

ρ = density, kg/m^3

σ_U = axial rms velocity fluctuation, m/s

σ_{Vr} = radial rms velocity fluctuation, m/s

σ_{Vt} = tangential rms velocity fluctuation, m/s

$<>$ = ensemble-averaged value

Subscripts

b = base

f = forward

o = stagnation or afterbody

r = radial component or rear

t = tangential (swirl) component

1 = freestream approach conditions

INTRODUCTION

Aerodynamic vehicles such as missiles, rockets, and projectiles suffer significant base drag due to flow separation at the base corner and the formation of a low-pressure, low-speed recirculation region near the base. Due to a lack of understanding of the fluid dynamic interactions occurring in the near-wake base region, drag-reducing techniques such as boattailing, base burning, and base bleed have traditionally been applied in an empirical manner to improve flight performance. The advent of laser-based optical flow diagnostic techniques in recent years has provided non-intrusive means to gain deeper insight into these complex flowfields. A detailed investigation of supersonic axisymmetric base flows including the effects of afterbody boattailing was completed recently,[1,2] and a study of the effects of base bleed has been initiated by the present authors as a logical extension.[3]

[*]Graduate Research Assistant, Student Member AIAA.
[†]Professor, Associate Fellow AIAA.

Figure 1 is a schematic of a blunt cylindrical body with base bleed, aligned in a supersonic flow. The supersonic freestream flow expands at the base corner and the turbulent boundary layer separates and forms a free shear layer which eventually undergoes recompression, realignment, and redevelopment in the wake of the afterbody. The primary recirculation region (PRR) is formed as the fluid from the region adjacent to the base is entrained and accelerated by the outer shear layer and subsequently returned to the base region by a recompression shock system. With base bleed, low-speed fluid is introduced into the base region causing a downstream displacement of the PRR, and the appearance of a forward stagnation point whose location depends on the relative strengths of the bleed jet and the recirculating fluid. The non-dimensional injection parameter, I, defined as the bleed mass flow rate normalized by the product of the freestream mass flux and base area, is used to quantify the amount of base bleed in the current study, and in most other experimental studies. It should be noted that unlike the generalized injection coefficient,[4] the injection parameter I does not account for the approach boundary layer thickness and the bleed flow momentum, both of which have been theorized to affect the base pressure in a manner analogous to base bleed.

Experiments performed by several researchers[5-9] to study the effect of bleed mass flow rate on the base pressure ratio (P_b/P_1) exhibit certain common characteristics and indicate three distinct operating regimes based on the quantity of bleed fluid injected. At low values of I (regime 1), the base pressure ratio increases fairly linearly with bleed rate. A peak in the base pressure ratio is observed at an intermediate value of I (near I = 0.01 for air). Increases in base pressure ratio (relative to the no-bleed case) from 10 to 90% have been reported for the optimum bleed condition, which depends on factors such as the freestream Mach number and the size and geometry of the bleed orifice. Past the optimum value (regime 2), the base pressure ratio decreases with increasing bleed rate until it reaches a relative minimum. Further increase in the bleed flow leads to an increase in base pressure ratio (regime 3) due to the onset of power-on flow conditions.

Over the past few decades, the effects on base pressure ratio of other bleed parameters such as the bleed jet exit area,[5,6,8-10] bleed gas molecular weight[10,11] (relative to the freestream gas), and bleed gas temperature[12] have also been investigated. Key results from these investigations have been summarized in Ref. 3. Most of the above experimental investigations were carried out prior to the development of reliable non-intrusive diagnostic methods, and their

scope was primarily limited to determining the global influence of various bleed parameters on base pressure. Therefore, while the effectiveness of base bleed as a drag-reducing technique is well known, the details of the fluid dynamic interactions caused by base bleed are not clearly understood due to a lack of detailed flowfield data.

Analytical models based on an empirical component-type approach[13] have been fairly successful in predicting the qualitative effects of mass bleed on base pressure.[14,15] One of the drawbacks of these models is that they only represent the base bleed flowfield in a time-mean sense, and can not account for its instantaneous turbulent nature. Computations of the base bleed flowfield[16-21] using the Reynolds-averaged Navier-Stokes equations have also had some degree of success in predicting qualitative base pressure trends and in capturing flowfield structure details. Numerical techniques, however, are currently limited by turbulence modeling issues, insufficient grid resolution, and lack of detailed experimental data for validation.[22]

As shown in Fig. 2, preliminary experiments with base bleed by the current authors[3] have confirmed the base pressure ratio variation with bleed mass flow rate (as discussed earlier) in regimes 1 and 2, indicating a peak base pressure ratio at an injection parameter value of I = 0.0148. The peak area-averaged base pressure ratio at this optimum bleed rate was 18.5% higher than the average base pressure ratio of a blunt-based afterbody.[1] Qualitative flowfield features such as flattening of the shear layer angle, widening of the wake, and weakening of the base corner expansion with increasing bleed rate in regime 1 were confirmed using schlieren and shadowgraph photography. Axial traverses along the near-wake centerline using two-component laser Doppler velocimetry (LDV) at several bleed rates show the PRR decreasing in size with increasing bleed rate, and nearly disappearing at the optimum bleed rate. Peaks in the turbulent kinetic energy (and the individual axial and radial turbulence intensities) were observed at the forward and rear stagnation point locations along the centerline, with the magnitudes of the peaks decreasing with increasing bleed rate.

The primary objectives of the research presented here are to obtain detailed mean velocity and turbulence field data in the entire near-wake region of a cylindrical afterbody with base bleed in supersonic flow, and to identify the dominant fluid dynamic mechanisms inherent in this complex flow. Since no known detailed measurements of the base bleed flowfield have been made prior to these, the measurements described here provide benchmark data that will enhance the overall understanding of base flow

phenomena and will also serve to validate modeling and computational efforts in this field.

EXPERIMENTAL FACILITIES AND PROCEDURES

The experiments described here were conducted in a supersonic, blow-down type wind tunnel at the University of Illinois Gas Dynamics Laboratory designed solely for the study of axisymmetric base flows. The mean Mach number approaching the afterbody is 2.47, the unit Reynolds number is 45 (10^6) m^{-1}, and the freestream turbulence intensity is less than 1%. The afterbody model is mounted at the end of a hollow sting, which is supported at two points upstream of the nozzle entrance to avoid support disturbances in the flowfield. A detailed description of the wind tunnel design is provided in Ref. 23. The 63.5 mm diameter cylindrical afterbody contains a 0.4 caliber bleed orifice preceded by an elliptically contoured section to ensure a uniform velocity profile for the bleed flow exiting the base. A stainless steel bleed line constructed with 50.8 mm diameter pipe sections, a contoured inlet and screen, an electronic flowmeter, and valves facilitates conditioning, measurement, and control of the bleed flow. Since the base pressure is significantly sub-atmospheric, ambient air is an adequate source for the bleed air supply. Details of the base bleed afterbody and the bleed line design are provided in Ref. 3.

The two-component LDV system used for the current experiments is identical to the setup used in earlier experiments.[3] The measurement volume diameter and effective length are 120 μm and 730 μm, respectively. Due to the axisymmetric nature of the flowfield, radial traverses in two perpendicular planes (vertical and horizontal) passing through the axis of symmetry were used to measure the three mean velocity components (U, V_r, and V_t), the three Reynolds normal stresses (σ_U^2, $\sigma_{V_r}^2$, and $\sigma_{V_t}^2$), and two of the three Reynolds shear stresses (<$u'v_r'$> and <$u'v_t'$>). Figure 3 shows a typical LDV measurement grid consisting of approximately 1200 spatial locations. An error analysis of the LDV measurements[23] has estimated the worst-case uncertainties in the mean velocity and the rms velocity fluctuations to be 1.2% and 2.3% of U_1, respectively (U_1 = 574 m/s in the current experiments).

RESULTS

The experimental flow conditions and geometry are listed in Table 1. Earlier experiments[3] indicate uniform flow conditions at the wind tunnel nozzle exit and at the exit of the bleed jet at various bleed rates. For the detailed measurements described in

this paper, three bleed flow rates with injection parameter values of I = 0.0038 (case A), 0.0113 (case B), and 0.0226 (case C) were selected to investigate the entire near-wake flowfield under low bleed, slightly sub-optimal bleed, and slightly post-optimal bleed conditions, respectively (see Fig. 2). The optimum bleed rate was not chosen because the near disappearance of the PRR at this bleed rate (as indicated by prior measurements[3]) could make spatial resolution in that part of the flowfield difficult. The sub-optimal bleed rates spanned by cases A and B represent the operating range of most practical base bleed projectiles.

It should be noted that the injection parameter values used here are based on the direct output from the electronic mass flowmeter, and do not account for the following: (a) the carrier air with the LDV seed particles in the bleed line, injected downstream of the flowmeter, adds an estimated I = 0.0004 to the measured primary bleed flow; (b) no attempt was made to correct for the drift in the flowmeter calibration (estimated to be a maximum of 10%) due to gradual sensor degradation over the two-year span of the base bleed experiments. The effect of this drift was considered negligible because the mean flow and turbulence data from the centerline measurements[3] made nearly one year previously were found to be virtually identical to the current detailed measurements at r = 0 for the same injection parameter values. The following sections briefly describe the key results obtained from the near-wake LDV measurements.

Near-Wake Mean Velocity Measurements

Figure 4 shows the mean velocity vector fields in the near-wake region of the flowfield. In this figure and in all subsequent figures, the vertical scale has been expanded by 42% (relative to the horizontal scale) to display the flowfield features clearly. The data from the non-uniform measurement grids have been transformed to uniform grids with resolution equal to the minimum spacings of the corresponding experimental grids in each direction. The uniform grids are then filled by linear interpolation between the experimental values and are subsequently used to generate the vector and contour plots shown here.

The main features of the flowfield [the turning of the flow through the base corner expansion, the PRR (cases A and B), the bleed jet, and the secondary recirculation region (SRR) between the bleed jet and the outer shear layer (cases B and C)] are clearly visible in Fig. 4. The mean freestream flow angles downstream of the base corner for each case are consistent with the Prandtl-Meyer turning angle based on the measured base pressure ratio and the approach freestream Mach number of 2.47.

With increasing bleed flow the size and strength of the PRR (bounded in the axial direction by the forward and rear stagnation points S_f and S_r, respectively) decrease (case A to B) until it finally disappears (case C) as the bleed flow penetrates the outer shear layer reattachment region. In addition, the forward stagnation point is displaced progressively downstream of the base plane and the radial extent of the forward portion of the PRR decreases (case A to B). These observations confirm earlier predictions based on near-wake centerline measurements[3]. With increasing bleed, the SRR near the base annulus becomes more evident. Much of the reverse flow in the PRR is oriented parallel to the axis of symmetry (cases A and B). This is in contrast to the blunt base[1] and boattailed[2] afterbody cases where much of the recirculating flow is directed towards the point of separation (the base corner), similar to the SRR in the current cases. The downstream shift of the rear stagnation point locations (S_r at $x/R_0 = 2.65$, 3.08, and 3.25 for the blunt base,[1] case A, and case B, respectively) is consistent with the increase in base pressure with base bleed.

The vector plots in Fig. 4 show that the bleed flow provides at least a portion of the fluid required for entrainment by the outer shear layer and shields the base annulus from the shear layer and the PRR, resulting in increased base pressures. However, the increased strength of the SRR near the base annulus and the increased entrainment by the inner bleed jet shear layer at higher bleed rates offsets the aforementioned benefits. As shown in Fig. 2, at the low bleed conditions corresponding to case A, the rate of pressure increase is very high. As the bleed rate is increased, the detrimental effects of the low pressure SRR and entrainment by the inner shear layer become stronger, and the rate of pressure rise decreases. This trend continues until the optimum bleed condition is reached where the maximum net benefits of base bleed are achieved. As the bleed rate increases past the optimum value, the base pressure starts decreasing due to the overwhelming influence of the bleed jet shear layer and the SRR.

Mean axial velocity contours are shown in Fig. 5. The rapid growth of the outer shear layer is evident from the divergence of the contour lines with downstream distance from the base corner. Due to the presence of the bleed jet and the accompanying SRR, the mean axial velocity fields are quite different from the blunt base flowfield.[1] In cases B and C, the bleed jet velocity profiles remain uniform through a significant axial extent downstream of the base plane. The shear layer growth at the outer bleed jet boundary with increasing bleed rate is also apparent in Fig. 5.

Contours of the mean radial velocity component for case B are shown in Fig. 6. The small magnitudes relative to the mean axial approach velocity show the dominance of the axial component in the near-wake flowfield. The base corner expansion fan appears to be fairly well centered at the base corner. Peak magnitudes of radial velocity appear in the freestream downstream of the expansion where the mean flow is turned radially inward after separation. Positive values of radial velocity appear between the base plane and the forward stagnation point where entrainment into the outer shear layer causes a portion of the bleed flow to turn radially outward [see Fig. 4(b)]. Radial velocity contours for cases A and C (not presented here for brevity) are similar to the ones shown for case B. In both cases A and C, the peak magnitudes of inward radial velocity are higher (and occur at locations upstream) relative to case B, due to their lower base pressures and stronger base corner expansions. In case A, the peak positive radial velocities near the base are slightly larger in magnitude than case B, and are confined to the region $x/R_0 \leq 1.5$ due to the strong PRR [see Fig. 4(a)]. Since the bleed flow penetrates the shear layer recompression region in case C [see Fig. 4(c)], the peak positive radial velocities are lower than in case B, and have a larger axial extent (approx. $x/R_0 = 3$). The tangential component of mean velocity was also measured (for case B only) and, as expected, the magnitudes of this component were negligible due to the axisymmetric nature of the flow.

Near-Wake Turbulence Measurements

The axial turbulence intensity distribution in the near-wake for case B is shown in Fig. 7. After the base corner expansion, the axial turbulence intensity in the outer shear layer increases to a global peak of approximately $\sigma_U/U_1 = 0.151$ at $x/R_0 = 1.37$ downstream of the base corner. This peak is smaller in magnitude and occurs at an upstream location relative to the maximum axial turbulence intensity in the blunt base flowfield[1] ($\sigma_U/U_1 = 0.220$ at $x/R_0 = 2.20$), indicating a significant decrease in the outer shear layer's entrainment potential resulting from base bleed. It is also evident from Table 2 that the peak axial turbulence intensity at the slightly pre-optimum case B is lower than in cases A and C. Beyond the peak location, the axial turbulence intensity magnitude decreases with downstream distance from the base. Local peaks in axial turbulence intensity occur in the SRR, the reattachment region, and near the forward stagnation point. The low axial turbulence intensity levels in the exiting bleed jet core are also evident from the figure. In case C (not shown), the local peak axial turbulence intensity level in the low-speed portion of

4

the bleed jet shear layer is equal to the global peak value in the outer shear layer due to the increased mean jet shear at the high bleed rate.

Figure 8 shows the near-wake radial turbulence intensity levels for case B. Downstream of the base corner, the radial turbulence intensity increases to a peak of $\sigma_{V_r}/U_1 = 0.112$ at $x/R_0 = 1.35$, the same location as for the peak axial turbulence intensity. The corresponding peak radial turbulence intensity magnitude in the blunt base study[1] was found to be $\sigma_{V_r}/U_1 = 0.156$ at $x/R_0 = 2.20$. The local peaks in radial turbulence intensity near the forward and rear stagnation points are not particularly distinct due to the dominance of flow mechanisms in the axial direction at these points. Downstream of the peak levels in the shear layer, the radial turbulence intensity decays through the reattachment region and the developing wake. Once again, Table 2 shows that the peak radial turbulence intensity at the slightly pre-optimum case B is lower than in cases A and C. The tangential turbulence intensity was also measured for case B, and the distribution (not shown for brevity) was found to be similar in magnitude and distribution to the radial turbulence intensity field. The relative ordering of the turbulence intensities ($\sigma_U > \sigma_{V_r} \approx \sigma_{V_t}$) indicates the level of anisotropy of the normal stresses in the near-wake base bleed flowfield.

The turbulent kinetic energy (k) for case B is determined from the measured Reynolds normal stresses using the relation:

$$k = \frac{1}{2}\left(\sigma_U^2 + \sigma_{V_r}^2 + \sigma_{V_t}^2\right) \tag{1}$$

The nondimensional turbulent kinetic energy (k/U_1^2) distributions shown in Fig. 9 for all three cases are quite similar to the corresponding axial turbulence intensity distributions which dominate the near-wake turbulence field. The low turbulent kinetic energy (TKE) levels in the bleed jet and in the redeveloping flow downstream of reattachment are also evident from the figure. Due to the similarity of the radial and tangential normal stress fields observed in case B and in the boattail study (and, to a lesser extent, in the blunt base case), the tangential turbulence intensity was not measured for cases A and C, and the TKE for these cases was estimated by substituting the measured radial normal stress value for the tangential term in Eq. (1). The estimated TKE field obtained by applying this procedure to case B was nearly identical to the measured values shown in Fig. 9(b), indicating the validity of the substitution. From Table 2, it can be seen that the peak TKE levels in all of the bleed cases are lower than the blunt base and boattail values. The peak levels for case B are the lowest of all, indicating reduced entrainment capability

for the outer shear layer at the near-optimum bleed condition. Figure 9(c) also shows that the increased velocity and mean shear of the bleed jet in the post-optimum case C leads to high TKE levels in the bleed jet shear layer, which in turn causes the base pressure to decrease.

The primary axial-radial Reynolds shear stress $\langle u'v_r'\rangle$ shown in Fig. 10 exhibits trends similar to those of the TKE with global peak magnitudes occurring near the corresponding peak TKE locations, followed by a decay to lower levels in the redeveloping wake. Once again, as shown in Table 2, the peak magnitudes for the bleed cases are lower than those found in the blunt base and boattail studies. The lowest peak magnitude in the outer shear layer is found in case B, indicating highly reduced entrainment by the outer shear layer for the near-optimum bleed condition. The positive $\langle u'v_r'\rangle$ values at the edge of the bleed jet indicate the presence of large turbulent structures in the shear layer formed by the bleed jet, and their subsequent entrainment of fluid from the SRR. With increasing bleed, the increase in the magnitude of these positive $\langle u'v_r'\rangle$ values and their spatial extent is in accordance with the increased strength of the SRR and entrainment by the bleed jet shear layer, and their detrimental base pressure-reducing effects. The axial-tangential Reynolds shear stress $\langle u'v_t'\rangle$ was also measured for case B, and, as expected, the magnitudes were negligible compared to the primary shear stress for this case.

Based on the above findings, in order to achieve the maximum benefits of base bleed without the detrimental side-effects of the strong bleed jet and SRR, the bleed mass should be injected into the near-wake at very low velocities. This is consistent with earlier observations based on parametric global base pressure measurements which suggest the use of a larger bleed orifice relative to the base area[5,6,8-10] or a porous base.[9] The formation of the undesirable secondary recirculation region could also be avoided by locating the bleed orifice (holes or slots) along the outer annular periphery of the base. This configuration has been found to reduce base drag in the case of axisymmetric bodies in subsonic flow[24]; however no known experiments with this configuration have been reported for the supersonic case.

SUMMARY AND CONCLUSIONS

Detailed mean velocity and turbulence measurements have been obtained in the near-wake of a cylindrical afterbody with base bleed in a Mach 2.5 flow using two-component laser Doppler velocimetry. The three cases studied provide insight into the near-wake fluid dynamic interactions produced by incipient bleed, slightly pre-optimal bleed, and slightly post-

optimal bleed conditions. The bleed flow displaces the primary recirculation region downstream of the base plane, and reduces its size and strength by providing most of the fluid required for shear layer entrainment. The bleed fluid also shields the base annulus from the outer shear layer and the primary recirculation region, leading to an increase in base pressure. There is an overall reduction in turbulence levels throughout the base bleed flowfields relative to the near-wake flowfields of blunt-based and boattailed afterbodies. A pair of secondary recirculation regions is formed near the base annulus due to the interaction of the bleed jet and the outer shear layer. With increasing bleed, the increased strength of the secondary recirculation region and bleed jet shear layer offsets the benefits of base bleed leading to a drop in the base pressure. The net benefits of base bleed are maximized at the optimum bleed condition, which corresponds to the highest base pressure, the disappearance of the primary recirculation region, and the lowest turbulence levels in the near-wake flowfield. The use of larger bleed orifices, porous bases, or bleed orifices located along the outer base annulus is suggested for maximizing the benefits from base bleed.

ACKNOWLEDGMENTS

REFERENCES

[1]Herrin, J.L. and Dutton, J.C., "Supersonic Base Flow Experiments in the Near Wake of a Cylindrical Afterbody," *AIAA Journal*, Vol. 32, No. 1, 1994, pp. 77-83.

[2]Herrin, J.L. and Dutton, J.C., "Supersonic Near-Wake Afterbody Boattailing Effects on Axisymmetric Bodies," *Journal of Spacecraft and Rockets*, Vol. 31, No. 6, 1994, pp. 1021-1028.

[3]Mathur, T. and Dutton, J.C., "Base Bleed Experiments with a Cylindrical Afterbody in Supersonic Flow," AIAA Paper 95-0062, January 1995.

[4]Delery, J. and Lacau, R.G., "Prediction of Base Flows," AGARD Report R-754, 1987.

[5]Cortright, E.M. and Schroeder, A.H., "Preliminary Investigation of Effectiveness of Base Bleed in Reducing Drag of Blunt-Base Bodies in Supersonic Stream," NACA RM E51A26, March 1951.

[6]Reid, J. and Hastings, R.C., "The Effect of a Central Jet on the Base Pressure of a Cylindrical Afterbody in a Supersonic Stream," Aeronautical

Research Council (Great Britain), Reports and Memoranda No. 3224, December 1959.

[7]Badrinarayanan, M.A., "An Experimental Investigation of Base Flows at Supersonic Speeds," *Journal of the Royal Aeronautical Society*, Vol. 65, 1961, pp. 475-482.

[8]Bowman, J.E. and Clayden, W.A., "Cylindrical Afterbodies in Supersonic Flow with Gas Ejection," *AIAA Journal*, Vol. 5, No. 6, 1967, pp. 1524-1525.

[9]Valentine, D.T. and Przirembel, C.E.G., "Turbulent Axisymmetric Near-Wake at Mach Four with Base Injection," *AIAA Journal*, Vol. 8, No. 12, 1970, pp. 2279-2280.

[10]Zakkay, V. and Sinha, R., "An Experimental Investigation of the Near Wake in an Axisymmetric Supersonic Flow with and without Base Injection," *Israel Journal of Technology*, Vol. 7, No. 1-2, 1969, pp. 43-53.

[11]Hubbartt, J.E., Strahle, W.C., and Neale, D.H., "Mach 3 Hydrogen External/Base Burning," *AIAA Journal*, Vol. 19, No. 6, 1981, pp. 745-749.

[12]Clayden, W.A. and Bowman, J.E., "Cylindrical Afterbodies at M = 2 with Hot Gas Ejection," *AIAA Journal*, Vol. 6, No. 12, 1968, pp. 2429-2431.

[13]Korst, H.H., "A Theory for Base Pressures in Transonic and Supersonic Flows," *Journal of Applied Mechanics*, Vol. 23, No. 4, 1956, pp. 593-600.

[14]Korst, H.H., Chow, W.L., and Zumwalt, G.W., "Research on Transonic and Supersonic Flow of a Real Fluid at Abrupt Increases in Cross Section (With Special Consideration of Base Drag Problems)," Engineering Experiment Station, Mechanical Engineering Department, University of Illinois, ME Technical Report 392-5, October 1964.

[15]Reijasse, P., Benay, R., Delery, J., and Lacau, R.G., "Prediction of Powered Missile or Projectile Base Flows by Multicomponent Methods," *La Recherche Aerospatiale*, Vol. 1989-4, 1989, pp. 15-32.

[16]Sahu, J., Nietubicz, C.J., and Steger, J.L., "Navier-Stokes Computations of Projectile Base Flow with and without Mass Injection," *AIAA Journal*, Vol. 23, No. 9, 1985, pp. 1348-1355.

[17]Sahu, J., "Supersonic Flow Over Cylindrical Afterbodies with Base Bleed," AIAA Paper 86-0487, January 1986.

[18]Danberg, J.E. and Nietubicz, C.J., "Predicted Flight Performance of Base Bleed Projectiles," AIAA Paper 90-2069, July 1990.

[19]Nietubicz, C.J. and Sahu, J., "Navier-Stokes Computations of Base Bleed Projectiles," in *Base Bleed: First International Symposium on Special Topics in Chemical Propulsion,* ed. K.K. Kuo and J.N.

Fleming, Hemisphere Publishing Corp., 1991, pp. 93-106.

[20]Nietubicz, C.J. and Gibeling, H.J., "Navier-Stokes Computations for a Reacting, M864 Base Bleed Projectile," AIAA Paper 93-0504, January 1993.

[21]Sahu, J. and Heavey, K.R., "Numerical Investigation of Supersonic Base Flow with Base Bleed," AIAA Paper 95-3459, August 1995.

[22]Dutton, J.C., Herrin, J.L., Molezzi, M.J., Mathur, T., and Smith, K.M., "Recent Progress on High-Speed Separated Base Flows," AIAA Paper 95-0472, January 1995.

[23]Herrin, J.L., "An Experimental Investigation of Supersonic Axisymmetric Base Flow Including the Effects of Afterbody Boattailing," Ph.D. Thesis, University of Illinois at Urbana-Champaign, July 1993.

[24]Freund, J.B. and Mungal, M.G., "Drag and Wake Modification of Axisymmetric Bluff Bodies Using Coanda Blowing," *Journal of Aircraft*, Vol. 31, No. 3, 1994, pp. 572-578.

Table 1 Experimental flow conditions and geometry

Tunnel stagnation pressure (P_0)	470.8 kPa $\pm$ 0.4%
Freestream static pressure (P_1)	28.76 kPa $\pm$ 0.4%
Approach Mach number based on pressure data	2.47 $\pm$ 0.1%
Tunnel stagnation temperature (T_0)	300.4 K $\pm$ 0.2%
Approach velocity measured with LDV (U_1)	574 m/s $\pm$ 0.3%
Approach Mach number based on T_0 & U_1	2.45 $\pm$ 0.4%
Freestream unit Reynolds number	44.88 (10^6) m^{-1} $\pm$ 0.8%
Bleed flow stagnation temperature ($T_{0,bleed}$)	293 K $\pm$ 0.4%
Base radius (R_0)	31.75 mm
Bleed orifice radius (R_{jet})	12.7 mm

Table 2 Peak magnitudes of turbulence quantities

	Blunt Base[1]	Boattail[2]	Base Bleed I = 0.0038	Base Bleed I = 0.0113	Base Bleed I = 0.0226
σ_U/U_1	0.220	0.203	0.159	0.151	0.179
σ_{Vr}/U_1	0.156	0.129	0.119	0.112	0.126
σ_{Vt}/U_1	0.135	0.133	–'	0.117	–
k/U_1^2	0.0440	0.0359	0.0268*	0.0245	0.0298*
$<u'v_r'>/U_1^2$	-0.0190	-0.0175	-0.0122 & 0.00208	-0.0106 & 0.00367	-0.0126 & 0.0119

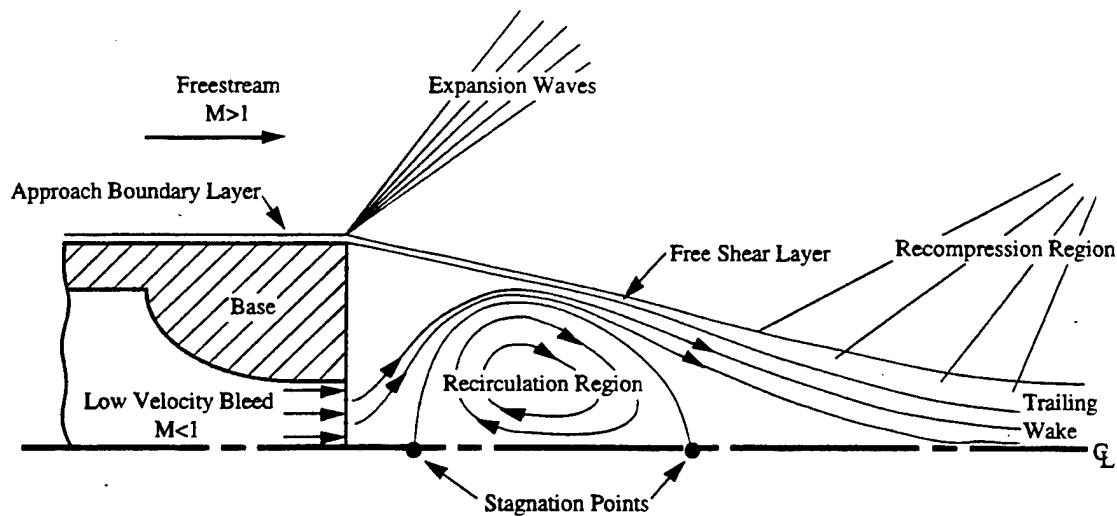* estimated using $\sigma_{Vt} = \sigma_{Vr}$
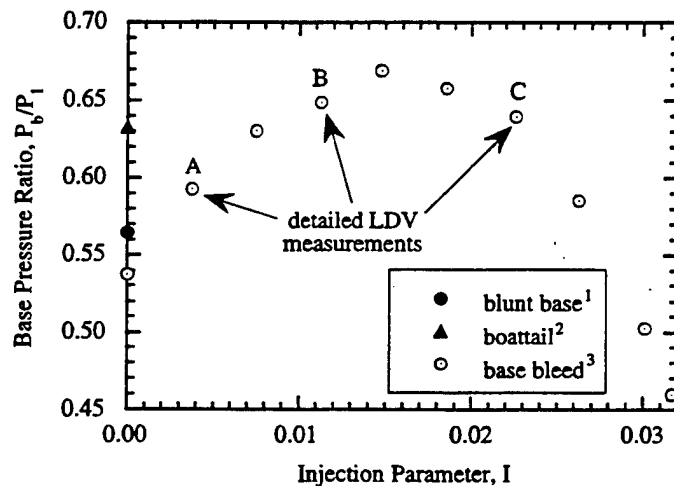
Fig.1 Schematic of the near-wake flowfield with base bleed

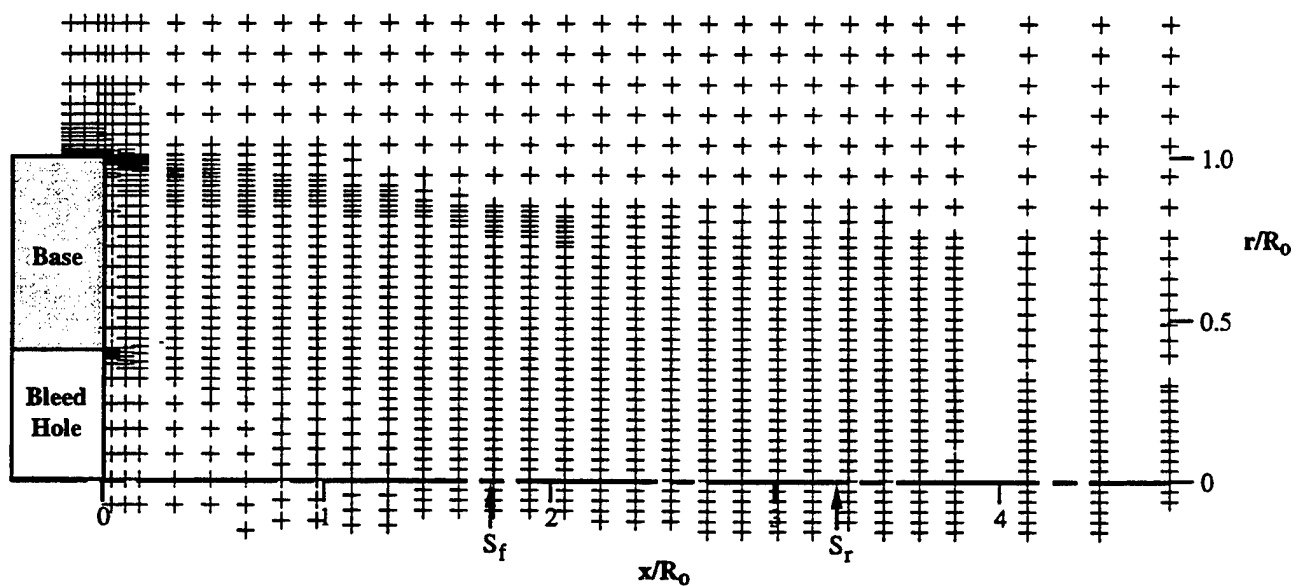Fig. 2 Effect of base bleed on area-averaged base pressure ratio
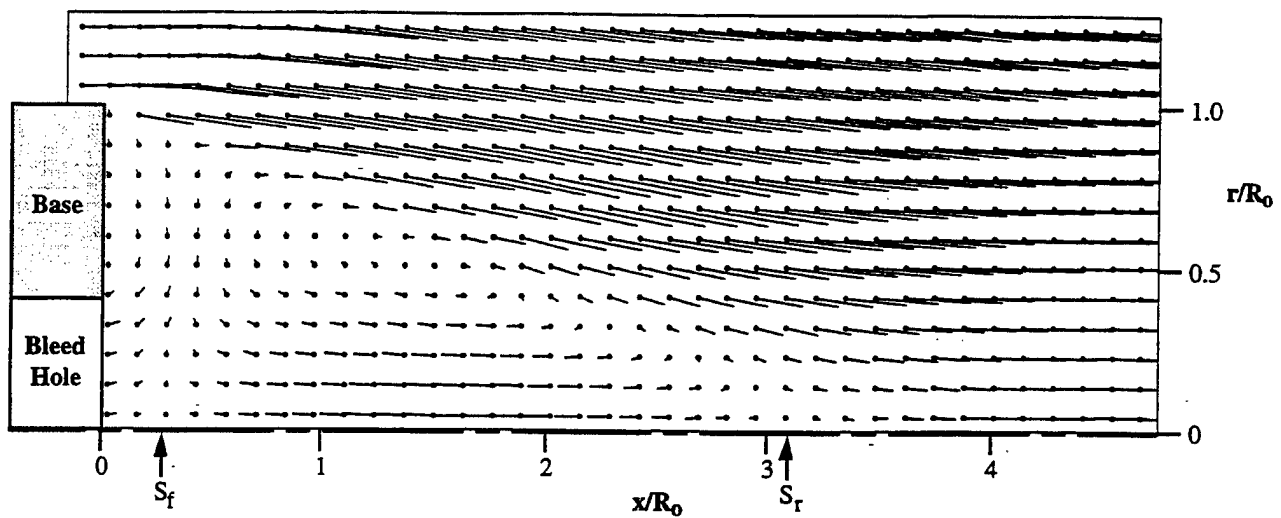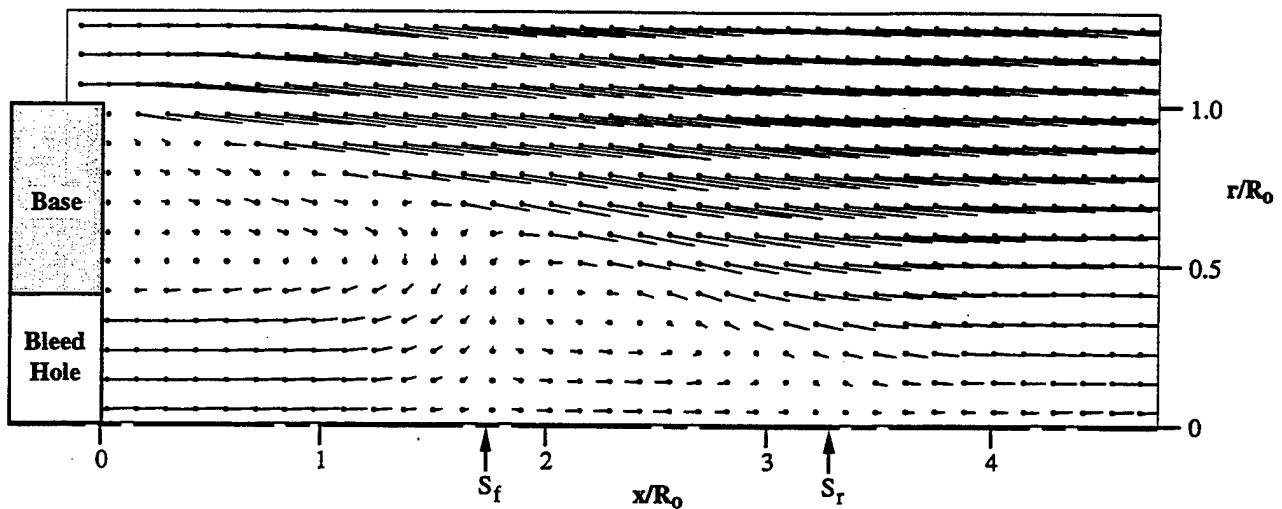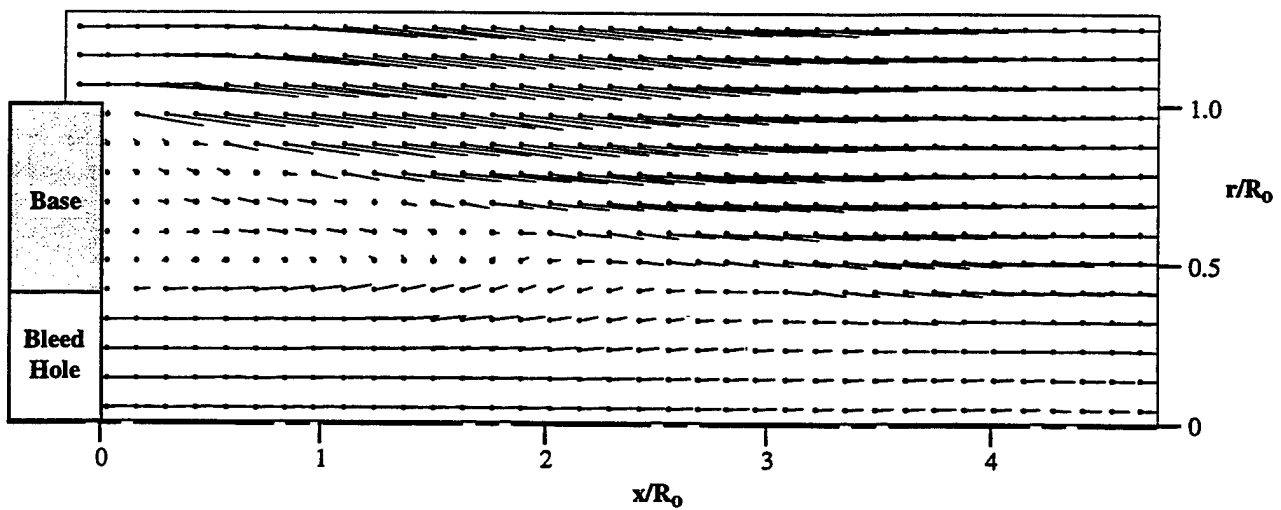

Fig. 3 LDV measurement locations, I = 0.0113

(a) I = 0.0038
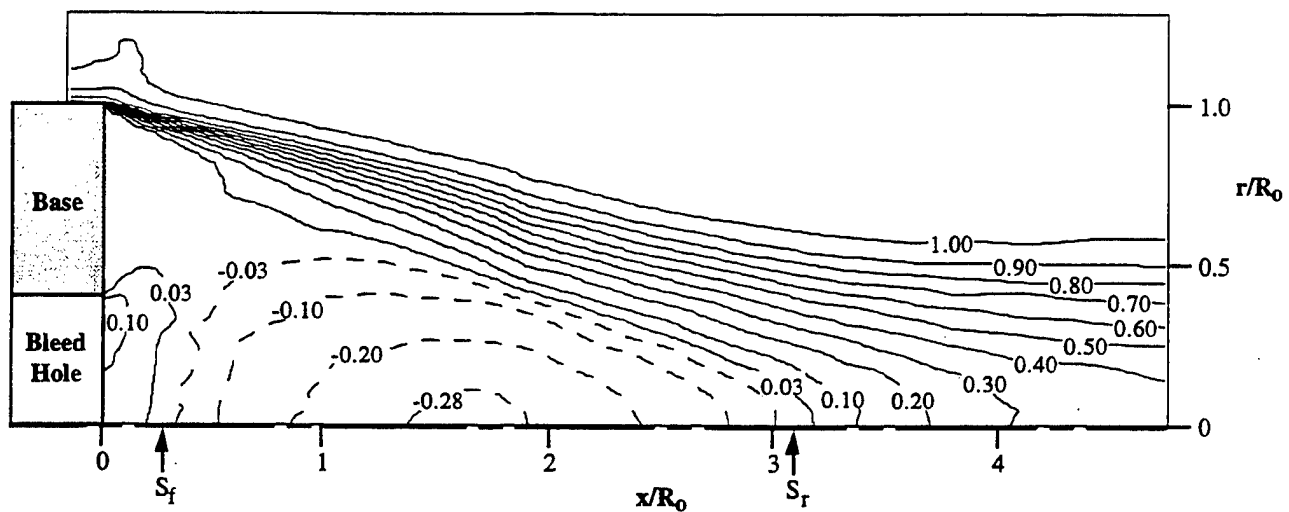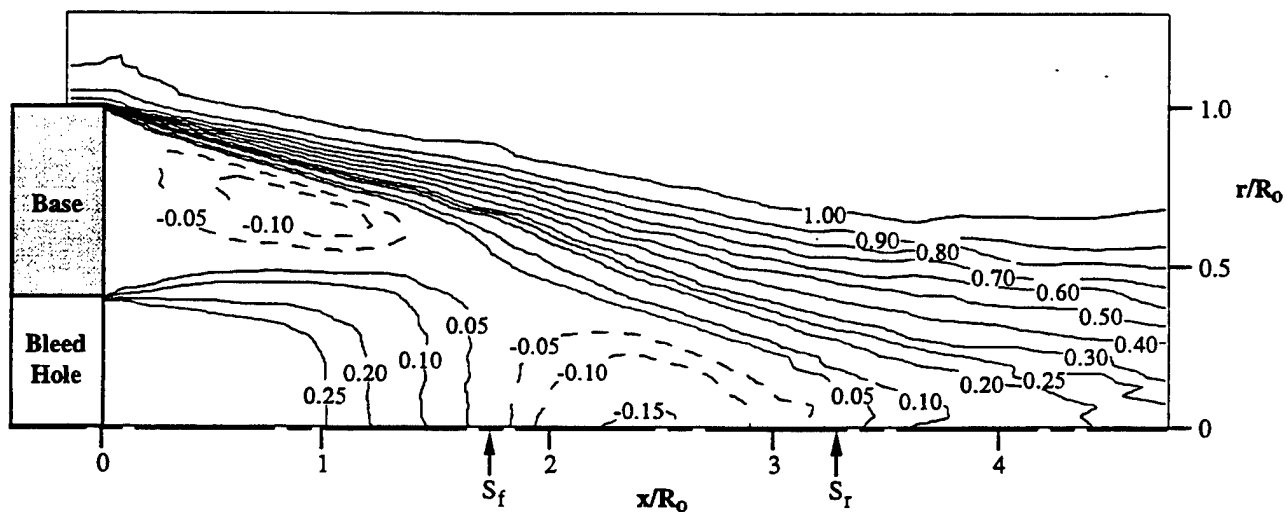
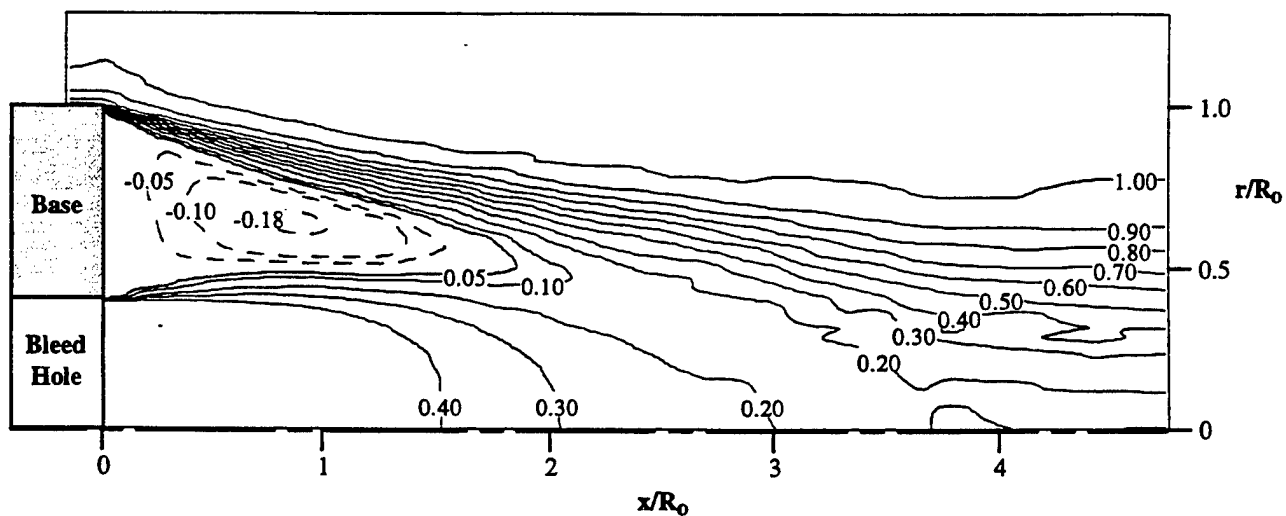(b) I = 0.0113

(c) I = 0.0226

• ———— 574 m/s

Fig. 4 Mean velocity vector field

(a) I = 0.0038

(b) I = 0.0113

(c) I = 0.0226

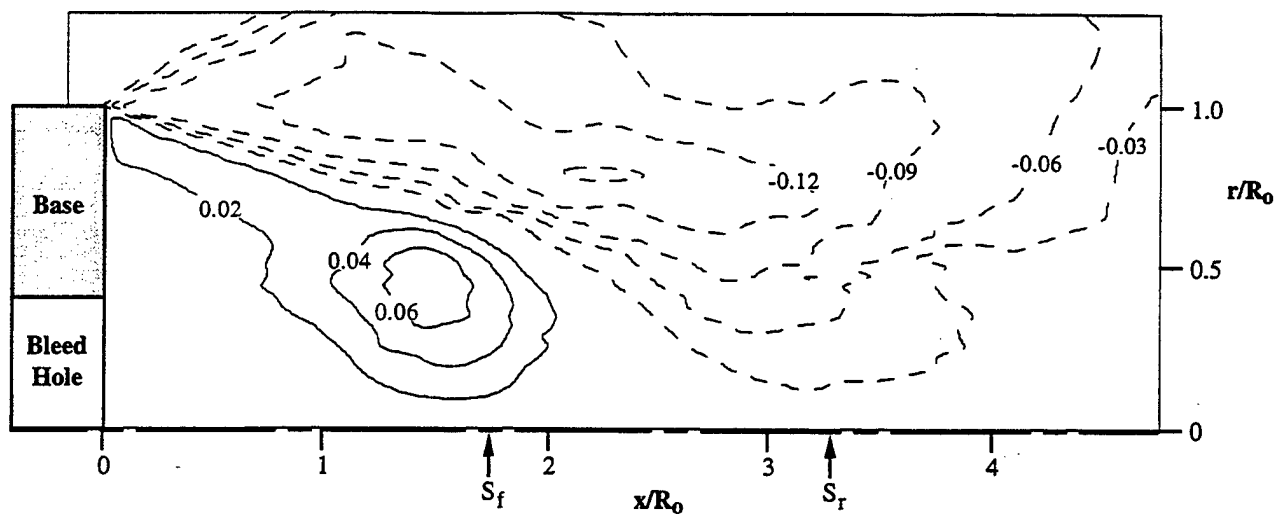Fig. 5 Mean axial velocity field - U/U$_1$

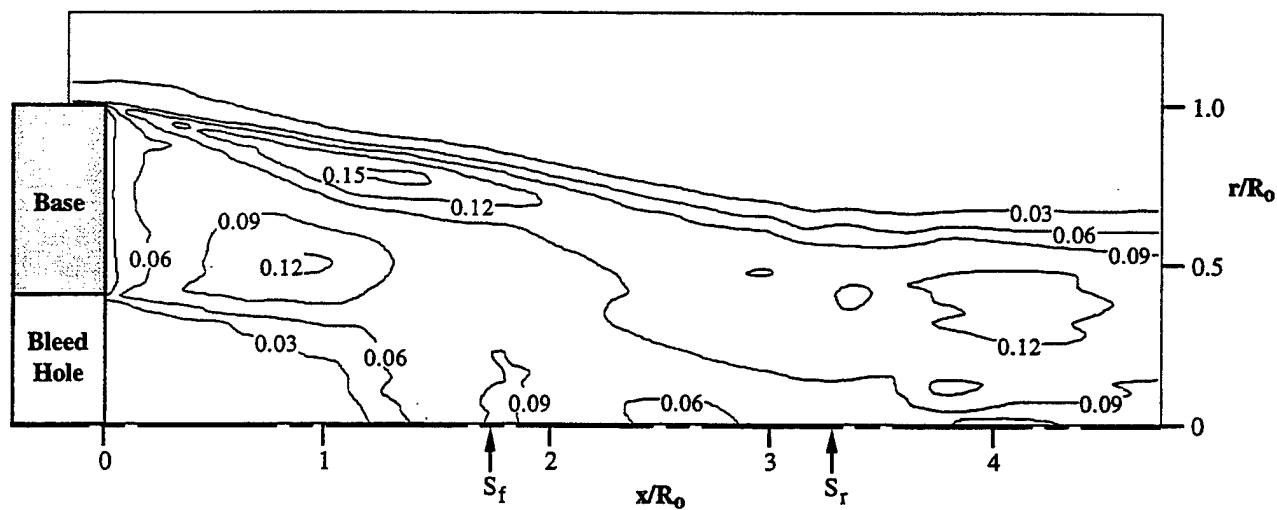Fig. 6 Mean radial velocity field at $I = 0.0113 - V_r/U_1$

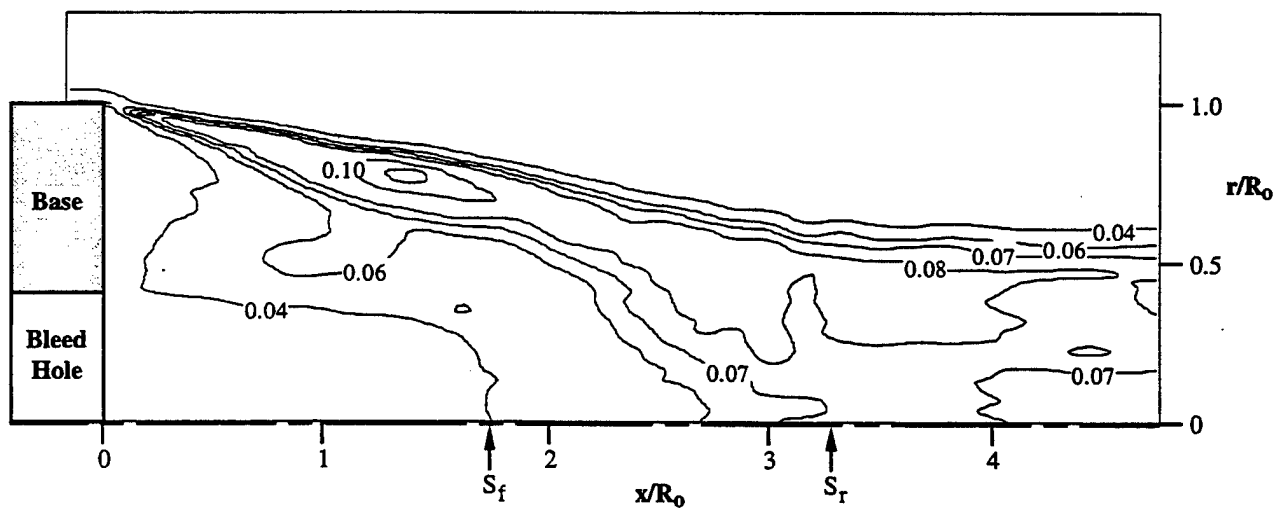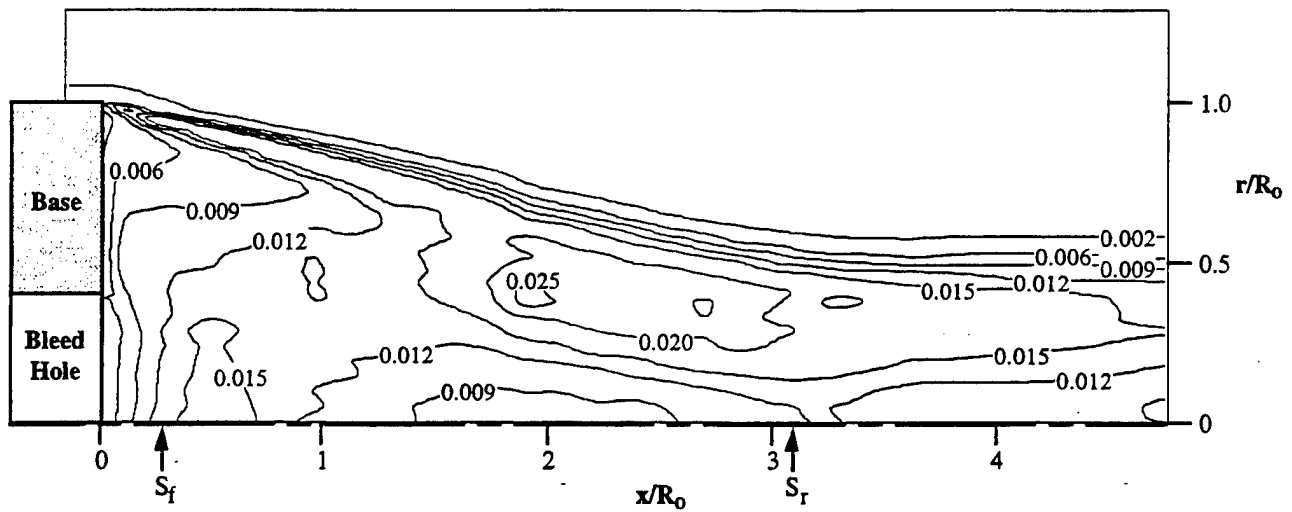Fig. 7 Axial turbulence intensity contours at $I = 0.0113 - \sigma_U/U_1$

Fig. 8 Radial turbulence intensity contours at $I = 0.0113 - \sigma_{V_r}/U_1$

(a) I = 0.0038 (estimated TKE)
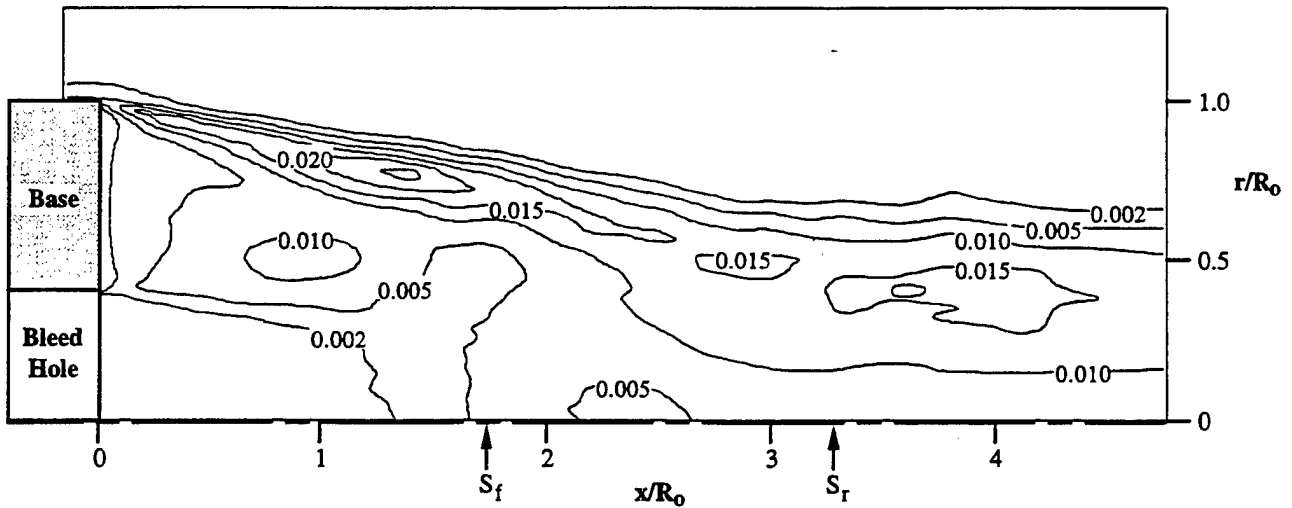
(b) I = 0.0113
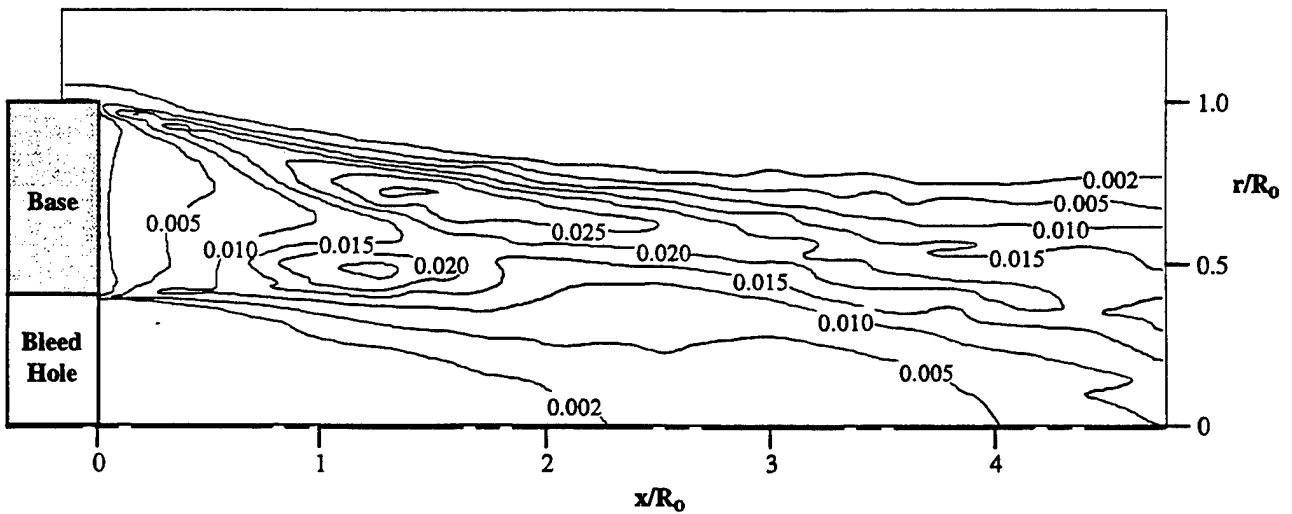
(c) I = 0.0226 (estimated TKE)

Fig. 9 Turbulent kinetic energy contours - k/U_1^2

(a) I = 0.0038

(b) I = 0.0113

(c) I = 0.0226

Fig. 10 Reynolds shear stress (axial-radial) contours - $<u'v_r'>/U_1^2$

13
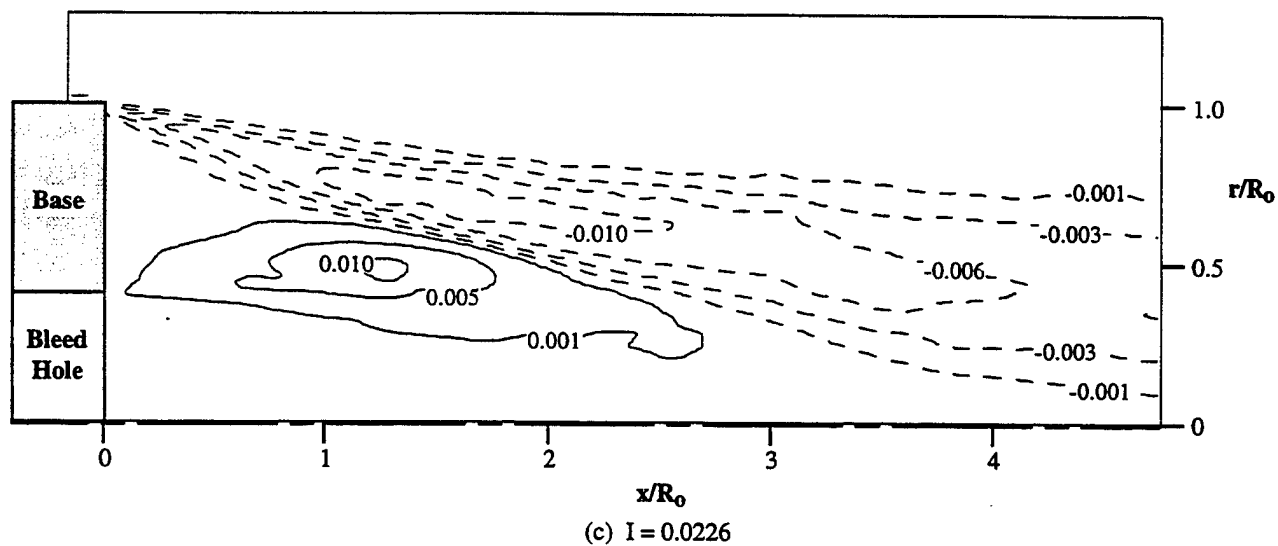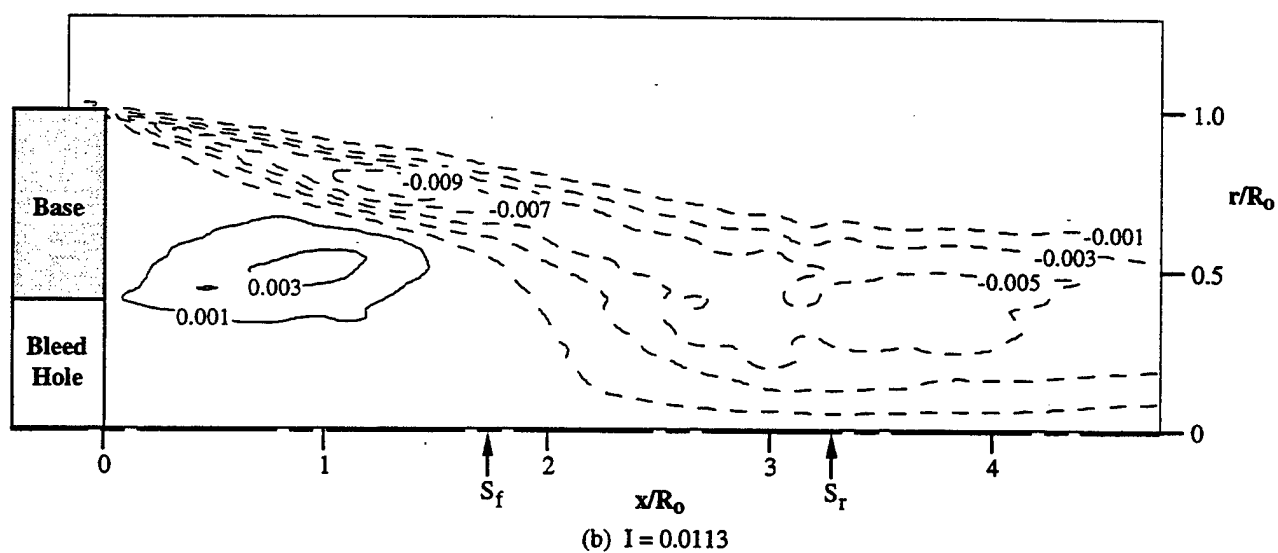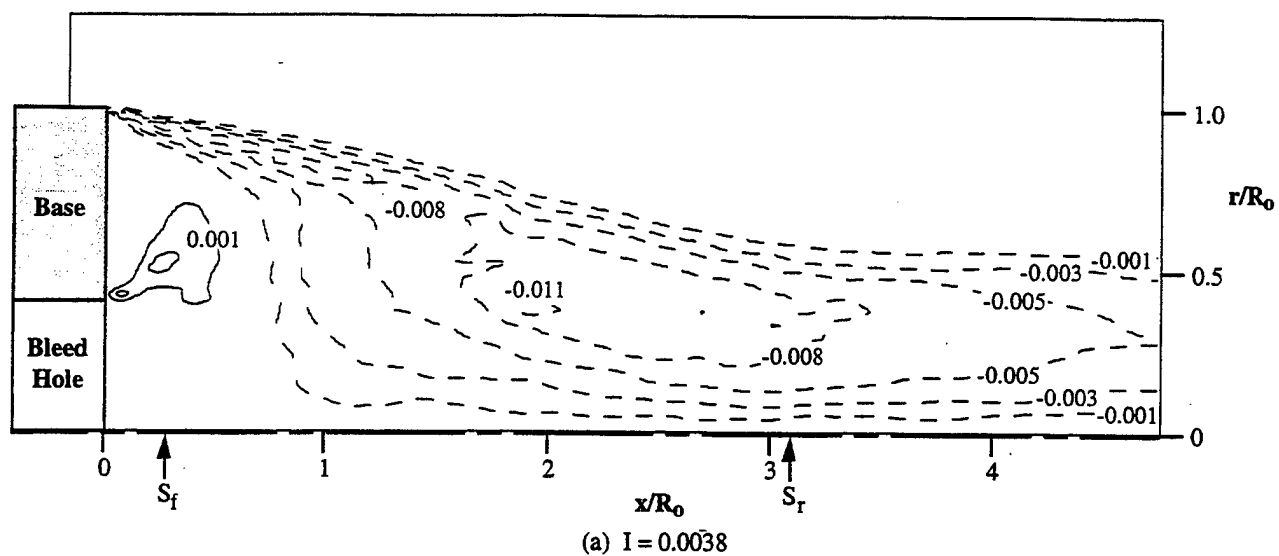
APPENDIX A.21

A METHOD FOR SEPARATING SHOCK WAVE MOTION AND TURBULENCE IN LDV MEASUREMENTS

AIAA Paper No. 97-1919

Presented at the *28th AIAA Fluid Dynamics Conference*

Snowmass, Colorado

June-July 1997

by

C. W. Palko and J. C. Dutton

AIAA 97-1919

A Method for Separating Shock Wave Motion and Turbulence in LDV Measurements

C. W. Palko and J. C. Dutton
University of Illinois at Urbana-Champaign
Urbana, IL

28th AIAA Fluid Dynamics Conference
4th AIAA Shear Flow Control Conference
June 29 - July 2, 1997
Snowmass Village, CO

A METHOD FOR SEPARATING SHOCK WAVE MOTION AND TURBULENCE IN LDV MEASUREMENTS

C. W. Palko[*] and J.C. Dutton[†]
Department of Mechanical and Industrial Engineering
University of Illinois at Urbana-Champaign
Urbana, Illinois 61801

ABSTRACT
Two-component laser Doppler velocimetry (LDV) measurements were made in a planar, two-dimensional flow containing an unsteady oblique shock wave formed by the convergence of two supersonic streams past a thick plate. Wall pressure measurements have been used to locate the shock wave and consequently separate the shock wave motion from the turbulence fluctuations in the LDV measurements of the shock-separated free shear layer. The primary result of isolating the large-scale changes in the position of the shock from the turbulence is a reduction in the experimental scatter rather than significant changes in the shape or magnitudes of the turbulent stress profiles. The overall effects of the changes in shock position on the turbulence were found to be small and do not significantly change the overall trends in the turbulence data. Velocity data were also analyzed to determine the effect of changes in the direction of shock motion rather than shock position. Shock motion direction was found to have a greater effect on the turbulence measurements than shock position. Like changes in the shock position, changes in the direction of shock motion did not significantly change the mean velocity. However, changes in the direction of the shock motion may either increase or decrease the turbulent stresses depending on the portion of the shear layer in question.

INTRODUCTION
A supersonic plume-induced boundary layer separated (PIBLS) flowfield is caused by the interaction of the exhaust plume from an underexpanded jet with the boundary layer on the afterbody surface of a rocket or missile. As the flow around the vehicle encounters the blockage caused by the exhaust plume, an oblique shock is formed. This shock imposes an adverse pressure gradient on the afterbody boundary layer and, if strong enough, will cause separation. This separation process is unsteady

due to the oscillatory motion of the shock wave in the streamwise direction. This unsteadiness complicates both prediction and measurement of PIBLS flowfields.

Although shock-induced shear layer formation in front of solid objects, such as in unswept compression corner flows, has been extensively investigated,[1,2] only four studies of turbulence in such flows exist to our knowledge.[3-6] However, no accurate published investigations exist of turbulence in a shock-induced separation caused by a second fluid stream. Also, current computational models are unable to accurately predict flowfields containing shock-induced separation, and detailed experimental data are needed to allow verification of improved numerical solutions, including improved turbulence models for these flows.[7]

All four of the previously mentioned turbulence studies in compression corners noticed shock wave unsteadiness (i.e., streamwise translation), but did not use any conditional sampling technique to isolate its effects. Whether the increased turbulence levels measured by the four studies were due to actual turbulent velocity fluctuations or by the shock wave unsteadiness is unclear. The measured turbulence levels may be inaccurate due to the motion of the shear layer across the measurement region. In a recent review, Dussauge and Dupont[7] conclude that, to date, no measurements exist concerning the impact of shock motion on the downstream level of turbulence. Selig and Smits[8] did, however, examine the effect of periodic blowing (inside the separated region) on the shock wave unsteadiness in a separated compression corner flow. Selig and Smits succeeded in changing the shock wave oscillation frequency, but did not observe any difference in the level of turbulence amplification due to the presence of blowing. These investigators concluded that the shock motion was not responsible for the turbulence amplification. Although Dussauge and Dupont[7] cite Selig and Smits'[8] study, they do not apparently consider it as conclusive evidence of the effect of shock motion on turbulence.

Several facts concerning shock wave unsteadiness in compression corners are now known. Erengil and Dolling[9,10] concluded from wall

---

[*] Research Assistant, Department of Mechanical and Industrial Engineering. Student Member AIAA.

[†] Professor, Department of Mechanical and Industrial Engineering, Associate Fellow AIAA.

1

pressure measurements in compression corners that the high-frequency "jitter" of the shock wave position is caused by the convection of large-scale turbulent structures in the boundary layer through the interaction. The low-frequency (< 1 kHz), large-scale "sweeps" of the shock wave are most probably caused by pressure fluctuations inside the separation bubble. Erengil and Dolling also found that the separation bubble "expands and contracts like a balloon." This is believed to correspond to pressure fluctuations inside the separated region, and may cause the shock to rotate about its foot. The separation shock is followed by a series of compression waves and is not simply a single shock as some previous researchers have suggested.[9-11]

Conditional analysis has been successfully used with LDV in periodic flows for the past 15 years, but usually the flowfield has a single predictable frequency, such as in turbomachinery flows. For example, in an internal combustion engine the LDV measurements can be encoded with the instantaneous crank angle to allow conditional averages to be formed from measurements taken at a particular crank angle (i.e., cylinder position). In the current study, however, the shock motion is a normally distributed random process with a broad range of frequency components.

The one previous study using a similar type of conditional analysis for a shock wave-boundary layer interaction was the study by Kussoy et al.[12] In this study, Kussoy et al. used two-component LDV to investigate a Mach 2.85 flow past a flared cylinder. To increase the three-dimensionality of the flowfield, the flare was swept with respect to the cylinder axis. The shock wave position was determined using high-speed shadowgraph movies and six pressure transducers placed 5 mm apart along the cylinder centerline upstream of the flare. These were differential pressure transducers using the undisturbed wall pressure upstream of the separation shock wave as a reference pressure (as in the current study). Shock positions determined with the shadowgraph visualizations and the pressure transducers were well correlated. This indicates that differential surface pressure measurements can be used to accurately determine shock positions. Kussoy et al. used the following conditional analysis algorithm to divide the shock positions into two states: "shock forward" and "shock back." The shadowgraph movies were first used to determine which transducer was beneath the mean shock wave position. The velocity realizations were then sorted according to the instantaneous pressure level at this transducer. Those with pressures greater than one

standard deviation above the mean pressure were considered the "shock forward" data set. Those with pressures less than one-half standard deviation below the mean pressure were considered the "shock back" data set.[13]

The primary objective of this study is to demonstrate a technique to allow the characterization of the development of a shock-separated shear layer while also isolating the effects of shock unsteadiness from the turbulent velocity fluctuations. To demonstrate this technique, conditionally analyzed LDV measurements have been made along the spanwise center plane in a PIBLS flowfield to obtain the mean velocity components and normal stresses in both the streamwise and transverse directions as well as the <u'v'> primary Reynolds shear stress.

EQUIPMENT

Wind Tunnel

Figure 1 shows the blow-down type supersonic wind tunnel used in this study. The tunnel supply air is provided by a 146 m^3 tank farm which is at 892 kPa prior to each tunnel run. The tank farm is connected to Ingersoll-Rand and Gardner-Denver air compressors which provide 0.68 kg/s at 892 kPa and 0.33 kg/s at 789 kPa of dry air, respectively. This air supply system provides a tunnel run time of about 5 minutes at the operating point used for this experiment. Shaw[14] gives a detailed description of the tunnel design and testing.

For this study, absolute stagnation pressures of 506 kPa and 251 kPa are used for the upper and lower streams, respectively. These stagnation pressures are measured with pitot tubes located just upstream of each converging-diverging nozzle. A globe valve in the lower inlet pipe is used to throttle the lower stream to various stagnation pressures, which changes the static pressure ratio between the two streams. An iron-constantan thermocouple is used to measure the plenum chamber stagnation temperature during each tunnel run. Honeycombs and fine mesh screens are used in both streams to reduce turbulence in the incoming flow. (The lower stream's flow conditioning module is inside the tunnel and is not shown in Figure 1.)

Flowfield

Figure 2 shows a schematic of the planar, two-dimensional flowfield investigated in this study. The flowfield consists of an upper Mach 2.5 stream (unit Reynolds number, Re=48.9x10^6 m^{-1}) and a lower Mach 1.5 stream (Re=36.2x10^6 m^{-1}) converging at a 40° angle past a 12.7 mm high base plane. The static pressure ratio of the lower to the

2

upper streams is $P_2/P_1 = 2.27$. The spanwise width of the flowfield and the height of the upper stream are both 50.8 mm. Surface oil flow visualization shows that the center 32 mm (63%) of the flowfield is free from sidewall effects and is, consequently, two-dimensional in this region. The upper stream is analogous to the supersonic freestream surrounding a rocket afterbody, while the lower stream is analogous to an underexpanded exhaust plume.

The primary subject of this study is the behavior of the boundary layer ($\delta_0 = 3$ mm) and separated free shear layer of the upper stream. This boundary layer intercepts the separation shock, consequently separates, and forms a free shear layer, as shown in Figure 2. This shear layer then reattaches with the shear layer formed by the separation (at near zero pressure gradient) of the boundary layer of the lower stream. These two shear layers enclose a recirculating region behind the base, and their reattachment generates a recompression shock system and the resulting trailing wake. Figure 3 is a shadowgraph taken of the flowfield showing the separation shock, the incoming boundary layers of both streams bordering the base, the recirculation region behind the base plane, and the developing free shear layers, along with their reattachment and the accompanying system of recompression shocks. The shadowgraph shown in Figure 3 was produced using a 25 ns pulse from a Xenon model 437B Nanopulser at a jet static pressure ratio of $P_2/P_1 = 2.35$ between the two streams.[14]

Pressure Data Acquisition System

The pressure data acquisition system consists of two Kulite model XCS-062-15G piezoresistive differential pressure transducers flush-mounted (in the spanwise center plane) along the bottom wall of the upper stream. Figure 2 shows the positions of the two pressure transducers located at 19.05 and 16.51 mm upstream of the base plane. Each transducer has a full scale of 103 kPa, an active element diameter of 1.6 mm, and uses the static pressure upstream of the separated region as a reference pressure. This reference pressure is measured through a port in the bottom wall of the upper stream located 65 mm upstream of the base plane.[14]

The transducers are powered by two Measurements Group Inc. Model 2311 signal conditioning amplifiers that also provide an adjustable DC offset and gain to the output signals. The output from each amplifier is routed through a low pass, active Butterworth filter with a -3 dB cutoff frequency of 50 kHz. This cutoff frequency is less than any inherent frequency limitations in the rest of the pressure acquisition system.

Laser Doppler Velocimetry System

A schematic of the two-component LDV system, a TSI model 9100-7, used for the mean velocity and turbulence measurements, is shown in Figure 4. The system utilizes the 488 nm and 514.5 nm lines of a 5 watt Spectra-Physics argon-ion laser. A 40 MHz shift is added to one beam of each color to allow discrimination of negative velocities and to minimize fringe biasing. To further reduce fringe biasing and fringe blindness, the green and blue beam pairs are oriented at approximately $+45°$ and $-45°$, respectively, to the mean flow direction of the upper stream. The 13 mm beam spacing and 250 mm focal length transmitting lens result in a measurement volume diameter of 0.127 mm.

Separate TSI model 9306 six-jet atomizers are used to inject 50 centistoke, silicone oil from Dow Corning into each stream. The oil droplets are injected downstream of all flow-conditioning modules and upstream of the nozzle blocks through small stainless steel tubes. Bloomberg[15] demonstrated that these six-jet atomizers produce a mean droplet diameter of 0.8 microns when using this fluid. The scattered light from the silicone oil droplets is collected in forward scatter with a 250 mm focal length lens at an off-axis collection angle of $10°$. This results in an effective measurement volume length of 1.5 mm. A TSI IFA 750 digital burst correlator operating in coincident mode determines the Doppler frequencies. Jenson[16] gives a detailed discussion of the IFA 750 operation. A discussion of the accuracy of the LDV system is presented in Appendix A.

EXPERIMENTAL TECHNIQUE

In the current study, the shock motion spans a streamwise distance of $4.7\delta_0$ or 14 mm, contains frequencies as large as 10 kHz, and is captured by sampling each pressure transducer at 20 kHz. The Nyquist criterion was used to select the sampling frequency of 20 kHz. Since the boundary layer separation point oscillates in the streamwise direction with the shock wave, the shear layer will also oscillate and cause biasing of unconditionally averaged velocity data. Consequently, a method is needed to minimize the bias in the velocity measurements of the developing shear layer due to the shock wave unsteadiness. This is provided by the following procedure.

3

Acquisition Timing

At the beginning of each tunnel run, a timing pulse initiates pressure measurements using the two transducers that are flush-mounted in the bottom wall of the upper stream (i.e., beneath the separation shock wave). The algorithm described below uses these wall pressure measurements to determine the shock position. This same timing pulse also produces a timing marker in the velocity data that provides a common time origin for both the pressure and velocity measurements. This allows the time histories of the pressure and velocity data to be merged. While the pressure is sampled at regular intervals, the velocity data are collected at random times (i.e., whenever an oil droplet produces a valid Doppler burst on both velocity channels). The IFA 750 Digital Burst Correlator, used to collect the velocity data, has a temporal resolution of ± 1 μsec. This is the limiting temporal resolution of the combined pressure/velocity data acquisition system.

TTMBCC Algorithm

The pressure time history for each of the two channels is analyzed using the two-threshold method boxcar conversion (TTMBCC) algorithm developed by Prof. D. S. Dolling and co-workers at the University of Texas-Austin.[17] The TTMBCC algorithm isolates the pressure fluctuations due to the shock motion from those present in the incoming turbulent boundary layer and in the separated region behind the shock. This results in a boxcar time history (i.e., a binary representation of upstream and downstream shock positions) for each channel (see Figure 5). The TTMBCC algorithm has been used extensively in studies of shock motion in unswept compression corner flows.[9,10,17,18]

Each channel's boxcar history is described by the time at which each rise or fall in pressure associated with a shock crossing occurs. The boxcar history is formed by first setting thresholds of 3σ and 6σ above the mean pressure in the incoming boundary layer (where σ is the standard deviation of the pressure fluctuations in the incoming boundary layer). Shaw[14] describes in detail the criteria for picking the two thresholds used in this study. For a rise event to register (i.e., the shock moves upstream of the transducer), the pressure must initially be less than the lower threshold and must rise past the upper threshold. For a fall event to register (i.e., the shock moves downstream of the transducer), the pressure must initially be greater than the upper threshold and must fall past the lower threshold. The TTMBCC algorithm prevents the mistake of interpreting oscillations about the lower threshold prior to a rise

event and oscillations about the upper threshold prior to a fall event as shock motions. The occurrence time of either a rise or fall event is defined as the time when the first pressure sample is taken after the upper threshold is crossed.

Both thresholds are used to determine if a pressure change represents a shock motion, but only the upper threshold is used to determine the occurrence time of a shock motion. This ensures that the position of the shock wave relative to the pressure transducer will be the same for both upstream and downstream shock crossings. Since the separation distance between the transducers (2.54 mm) is less than the length of the shock foot (3 mm), the TTMBCC algorithm used in conjunction with this pressure acquisition system is capable of resolving the shock position to within ± 1.6 mm (the active element diameter of a single transducer).

Conditional Analysis

A second algorithm is used to determine the position of the shock wave corresponding to each velocity realization. Figure 5 illustrates this process. The shock wave positions are defined using the numbers 1, 2, or 3, depending on whether the shock wave is upstream, between, or downstream of the two transducers, respectively. Additional categories are defined for various shock position transitions and error cases, which represent less than 1% of the acquired data. This small percentage of transitional cases indicates that the shock motion is accurately captured using this method.

Each velocity realization is matched to the corresponding point in the boxcar history of the pressure data, and the shock wave position for that realization is determined. Then the velocity measurement is saved with the corresponding shock wave position. Finally, conditional averages are formed from the velocity realizations corresponding to shock wave position 2 (between the two transducers), thereby effectively "freezing" the shock position at this location. This conditional average retains only approximately 25% of the velocity data and therefore necessitates collecting very large data sets to obtain adequate statistical certainty from the ensemble averages.

The algorithm used for the current study has two advantages over that used by Kussoy et al.[12] First, by using two transducers instead of only one, it is possible to form velocity data ensembles with the shock wave in a single position, region 2, instead of for only a range of positions, i.e., shock forward or shock back. Second, this technique uses only pressure measurements and consequently eliminates

4

the subjective process of inspecting shadowgraph movies for the mean shock positions.

Since the transducers are placed at 19.0 and 16.5 mm upstream of the base plane, the shock foot position (i.e., the boundary layer separation point) for the region 2 data set is 17.75±1.6 mm upstream of the base plane. Increases in the jet-to-freestream static pressure ratio (JSPR) between the two streams shift the region of shock oscillation upstream, away from the base corner. As this shift occurs, the intermittency (i.e., the proportion of time spent by the shock upstream of a given transducer) increases for both transducers. However, the time spent by the shock between the two transducers (in region 2) at first increases, peaks at near 25%, and then decreases. The JSPR of 2.27 for this study was selected to maximize the time spent by the shock in region 2 (between the transducers) and thereby to maximize the amount of data obtained from the conditional analysis.

RESULTS

This section presents data obtained using the technique described above. A complete mapping of the plume-induced separated flowfield has recently been completed and will be, along with a detailed discussion of the flowfield features and trends, the subject of a future paper.[19] Therefore, this discussion will concentrate on the effects of changes in the shock position and in the direction of shock motion on the velocity statistics. This section presents conditionally and unconditionally averaged data at four streamwise stations. The four stations A, B, C, and D are located at x=-25, 0, +15, and +30 mm from the base plane, respectively (see Figure 2). These positions lie in the approach boundary layer upstream of the separation shock, at the base plane, just before reattachment, and in the developing wake, respectively. Station A lies at the limit of optical access in the upstream direction.

All traverses are limited to 25 mm above the bottom wall (i.e., the bottom half of the upper stream); all flowfield features of interest are contained within this region. The laser beams become clipped at positions closer than 1 mm from the wall; therefore, each traverse begins at y=1 mm. Due to their inertia, LDV seed particles can produce curved pathlines behind an oblique shock wave instead of following the fluid streamlines that bend sharply at the shock front. This difference in the particle and fluid responses to shocks can introduce particle dynamics errors. The effects of particle dynamics in the current flowfield are negligibly small outside the region immediately downstream of the

shock wave (1.4 mm normal to the shock or 2.8 mm in the streamwise direction). While stations B and C cross the separation shock wave, the shear layer at both of these locations lies below the region of significant particle lag.

Effects of Shock Position

The primary motivation for the conditional averaging technique described earlier is to precisely locate the separation shock wave between the two flush-mounted pressure transducers at the instant in time at which a velocity measurement is made. This allows the effects of changes in shock position on the velocity field to be distinguished from the inherent turbulence in the velocity field. The effects of shock position on the flowfield may be discerned by comparing LDV data acquired when the shock was between the two transducers (in region 2) to LDV data acquired without accounting for shock position. Region 2 was chosen because it is the smallest region (only 2.5 mm in streamwise extent) in which the shock could be located.

To equalize the random error in the velocity measurements, which depends on the ensemble size (see Appendix A), both the unconditional (total data) and conditional (region 2) averages use an ensemble size of 4096 realizations. The systematic error or bias error in the LDV data is identical for the two sets. Any differences between the two sets are, therefore, due only to the shock motion or to random errors in the LDV data.

Figure 6 shows the dimensionless mean streamwise velocity (nondimensionalized by the freestream velocity, U_∞=590 m/s) for each station. Several features of Figure 6 should be noted. First, the "all data" and "region 2" profiles are very similar at all four stations. This shows that the mean velocity is unaffected by changes in the shock position. In addition, the inclination of the shear layer is apparent, since the noticeable trough in the velocity profiles (which is in the recirculation region) occurs at increasing heights above the base for each successive station. The smoothness of the profiles also indicates that the random LDV errors are small. Finally, the slight variation (less than 2%) in the freestream mean velocity profile at station A may be due to a slight wake from the seed injection tube which is upstream of the converging-diverging freestream nozzle.

Figure 7 presents the dimensionless streamwise normal stress profiles for each station. As with the mean velocity data, the streamwise normal stress profiles for the unconditional and conditional data sets are nearly identical at stations B, C, and D. There are some differences between the

peak values of the "all data" or "region 2" profiles at these downstream stations, but these differences are not substantially larger than the measurement uncertainties at these locations. However, some significant differences are apparent near the wall at station A. In particular, the "region 2" profile appears to be much smoother than that of the "all data" profile. This difference between data sets seems to indicate that shock motion does increase the apparent normal stress inside the boundary layer. Although taken as far upstream as optical access allowed, Station A lies just within the region of oscillation of the separation shock wave. Consequently, the shock wave makes infrequent excursions upstream of station A. These excursions, however, occur during only a small fraction of the time during data collection. The result is increased random error in the resulting turbulence quantities in this region.

The streamwise stress profiles obtained downstream of separation (B, C, D) show much less deviation between the "all data" and "region 2" data sets. This is expected since the effects of shock wave unsteadiness should be greatly diminished at these downstream locations. Comparing station A with stations B and C shows that the shock-induced separation process greatly increases the streamwise normal stress. Comparing stations C and D shows the dramatic decrease in the peak streamwise normal stress through reattachment. As with the mean velocity profiles, the inclination of the shear layer above the wall is apparent since the dominant peak in the streamwise normal stress profiles occurs at increasing heights above the wall for each successive station.

The dimensionless transverse normal stress profiles for each station are presented in Figure 8. As in Figure 7 for the streamwise component, the "all data" and "region 2" data sets show close agreement at all stations except within the boundary layer at station A. At station A, the transverse normal stress profile shows the same characteristics as that of the streamwise normal stress in that the "region 2" profile is notably smoother than the "all data" profile.

Similar to Figure 7 for the streamwise normal stress, the dimensionless transverse normal stress is greatly increased by the shock-induced separation. The asymmetry of the main peak in the transverse normal stress at station C is due to the effects of the lower shear layer. Since this lower shear layer is inclined at 40° with respect to the x-axis, the turbulence in the lower shear layer has a large transverse component. The small secondary peaks in the transverse normal stress at stations B and

C coincide with the location of the separation shock. This slight increase in turbulence is due to either small-scale shock unsteadiness that is below the resolution limit of the conditional averaging technique or to particle lag.

Comparing Figures 7 and 8, it is apparent that the freestream turbulence is isotropic while the boundary layer and free shear layer turbulence is anisotropic. The peak normal stress anisotropy ratio, $<u'^2>/<v'^2>$, in the shear layer at stations B, C, and D is approximately 13, 9.5, and 5.6, respectively. The peak normal stress anisotropy in the approaching boundary layer at station A is difficult to estimate with certainty since the transverse normal stress may only be measured at positions above $y=1$ mm. However, over the outer portion of the boundary layer that has been probed, the anisotropy increases and levels off at approximately 3 as the wall is approached. This gives evidence of the much stronger amplification of the streamwise normal stress by the shock interaction than the amplification of the transverse normal stress. As the shear layer moves downstream from separation, there is a strong reorganization of the turbulence and a shift in the turbulent kinetic energy from the streamwise to the transverse direction. This occurs both during shear layer development and through reattachment.

The Reynolds shear stress profiles for each station are shown in Figure 9 where, following convention, the negative of the shear stress, $-<u'v'>/U_\infty^2$, is plotted. As in Figures 6-8, the profiles for the "all data" and "region 2" data sets agree closely at each station with the noticeable exception of the boundary layer at station A. At station A the "region 2" profile is again much smoother than the "all data" profile. As expected, the Reynolds shear stress inside the boundary layer is negative. Also interesting is the near zero value of the Reynolds shear stress in the freestream at all four stations, as is expected. The uppermost positive peak in the shear stress profiles at stations B and C coincides with the location of the separation shock. Like the secondary peaks in the transverse normal stress, this is an artifact of either small-scale shock motion or particle lag.

Figure 10 shows the nondimensional turbulent kinetic energy profiles. Previous LDV measurements in related 2-D flows[20] show that the spanwise turbulence intensities are approximately equal to the transverse turbulence intensities in compressible shear layers. Therefore, the turbulent kinetic energy in this study is approximated as

$$TKE = \frac{1}{2}\left(u'^2 + 2v'^2\right) \qquad (1)$$

where the spanwise normal stress is approximated as equal to the transverse normal stress, and u'^2 and v'^2 are the streamwise and transverse normal stresses, respectively. This definition is slightly different than that used by some previous researchers such as Kuntz,[4] where the spanwise normal stress is approximated as the arithmetic average of the streamwise and transverse normal stresses. This average definition has the effect of overestimating both the spanwise turbulence and, consequently, the turbulent kinetic energy.

The most obvious feature of the turbulent kinetic energy profiles in Figure 10 is the close similarity to the streamwise normal stress. The streamwise normal stress is much larger than the transverse normal stress over most of the flowfield and so dominates the turbulent kinetic energy. Like the streamwise and transverse normal stresses, the turbulent kinetic energy profiles show very little variation with changes in shock position, except in the approaching boundary layer.

It is not surprising that Kussoy et al.'s[12] turbulent kinetic energy data showed a greater variation based on shock position than the data presented here. As described previously, Kussoy et al.'s algorithm formed data sets only for shock positions ahead of or behind a given transducer. This results in forward- and rearward-biased data sets, and a total data set of unknown bias. In the current study, which uses an algorithm utilizing two transducers, the data may be formed into a single data set of minimal bias (region 2 data). Based on the results of this study, it is apparent that a conditional analysis technique such as Kussoy's can overstate the effect of shock wave unsteadiness on the measured turbulence quantities.

Effects of Shock Motion Direction

The conditional averaging algorithm described earlier may be modified to isolate the effects of the *direction* of the shock motion rather than the effects of the shock *position* on the velocity field. As mentioned earlier, LDV data are acquired at random times (whenever a seed particle passes through the measurement volume), while the pressure data (used to determine the shock position) are acquired at regular intervals. Therefore, each LDV point occurs within a time interval bounded by pressure samples. If the shock position at the beginning and the end of an interval containing an LDV data point are the same, the shock position is

known for that LDV data point and the corresponding shock region is assigned to that point. However, if the shock position at the beginning and end of an interval containing an LDV data point are not the same, the shock wave must have transitioned between the two regions during the time interval in question. Inspection of typical data ensembles for this flow shows that these shock transitions occur in less than 1% of the sample intervals. The exact shock position is not known for LDV data points occurring during these transition intervals and so, instead, a classification number corresponding to the particular type of shock transition is assigned to each such LDV data point.

There are three such transition cases in each of the upstream and downstream directions. In the downstream direction, these correspond to transitions from upstream of both to between the two transducers (transition from region 1 to region 2), from between the two transducers to downstream of both (transition from region 2 to region 3), or from upstream of both to downstream of both transducers (transition from region 1 to region 3). In the upstream direction, these correspond to transitions from downstream of both to between the two transducers (transition from region 3 to region 2), from between the two transducers to upstream of both (transition from region 2 to region 1), or from downstream of both to upstream of both transducers (transition from region 3 to region 1).

For this study of the effects of the direction of shock motion, only the transitions beginning or ending in region 2 (between the transducers) are considered. The transitions across both transducers are excluded due to their increased shock position uncertainty at *both* endpoints of the motion. Due to the low LDV data rates, the short tunnel run times, and the small number of transition cases (less than 1% of all acquired data in this flowfield) the directionally conditional ensemble size was limited to 1100 velocity realizations for each direction, requiring acquisition of 196,608 velocity realizations per spatial location. This is considerably smaller than the 4096 realization ensembles used in all other data presented in this study, which substantially increases the random error in the resulting mean velocity and turbulent stresses (see Appendix A).

Because of the large number of velocity realizations required for statistically significant ensembles, direction conditional ensembles were obtained only within the shear layer at station B, the base plane (see Figure 2). This position was selected because of its proximity to the separation point and the presence of the recirculation zone. The traverse

7

was limited to below y=8.5 mm, so as to lie beneath the region of particle lag lying downstream of the separation shock wave. To equalize the random error, which depends on the ensemble size, all of the conditional (upstream, downstream, and region 2) averages for the data presented in this portion of the study use an ensemble size of 1100 realizations. The systematic error or bias error in the LDV data is identical for the three sets. Any differences between the two sets are, therefore, due only to changes in the direction of the shock motion or to random errors in the LDV data.

The profiles in Figure 11 for the streamwise mean velocity and turbulent stresses show the effects of changes in the direction of shock motion. As can be seen from Figure 11, no significant effect of the direction of shock motion can be separated from the direction-independent but position-conditioned (region 2) data for the mean streamwise velocity. As just discussed, the increased experimental scatter in these profiles is due to the reduced ensemble size compared to that in Figures 6-10. Interestingly, even with equal ensemble sizes, the downstream data set, rather than the region 2 data set, displays the most experimental scatter of the three conditional averages. This provides some evidence that the direction of the shock motion may have a more important effect on the velocity statistics than the position of the shock. For all four plotted quantities, the upstream and region 2 profiles in Figure 11 agree fairly closely, especially in the mean streamwise velocity and transverse normal stress. However, for the streamwise normal stress the upstream data set exhibits less scatter than the region 2 profile. Also interesting is the agreement in the peak magnitude of the streamwise normal stress for the downstream and region 2 data sets. Comparing this peak value with that found in Figure 7 for the same location, but with a larger ensemble size (i.e., smaller random error), the values are found to agree. The peak streamwise normal stress for the upstream data profile, however, displays a smaller peak. This difference is well outside the 9% error bars at this location.

Examining the transverse normal stress and Reynolds shear stress profiles in Figure 11 reveals two other statistically significant trends. First, the transverse normal stress profile for the downstream data set deviates significantly from the upstream and region 2 profiles over the region 2 mm<y<5 mm. This deviation is also larger than the measurement uncertainties at these locations. Most noticeable in the downstream transverse normal stress profile is the presence of a distinct and large trough and peak in this region. The midpoint between these two features

also coincides with the location of the peak streamwise normal stress (i.e., the center of the shear layer). The last noteworthy feature of Figure 11 is the greatly increased peak positive shear stress value displayed (note by convention the negative of the shear stress has been plotted) by the downstream data profile. This peak value of approximately −0.0095 is almost twice the value of approximately −0.005 peak exhibited by both the upstream and region 2 data profiles. Interestingly, comparing the region 2 shear stress profile in Figure 11 to those found in Figure 9 at the same streamwise location reveals that the use of a larger ensemble size for the region 2 data does not change the peak value from that present in the upstream and region 2 profiles of Figure 11. The positive shear stress peak in Figure 9 does, however, occur closer to the wall than the positive shear stress peak of the downstream profile in Figure 11.

SUMMARY AND CONCLUSIONS

The technique described for separating shock motion from turbulence in LDV measurements has been successfully demonstrated. Data have been presented for streamwise locations upstream of mean separation, in the separated shear layer, and through the reattachment region. The shock motion has been shown to have a significant effect on the measured turbulence within the boundary layer upstream of the mean separation location, and a much smaller effect through the separated shear layer and reattachment regions. This study has shown that changes in shock wave position do not have a significant effect on measured mean velocities or turbulence quantities downstream of separation.

This study indicates, however, that changes in the direction of shock wave motion do significantly alter the measured levels of downstream turbulence, although the mean velocity is still unaltered. Specifically, upstream shock motion decreases the apparent peak streamwise normal stress, but does not change the peak transverse normal stress or the Reynolds shear stress. Downstream shock motion increases the peak positive shear stress and shifts the location of this peak further from the wall. Downstream shock motion also does not appreciably change the streamwise normal stress. Downstream shock motion decreases the transverse normal stress over a portion of the top of the shear layer, while increasing the transverse normal stress over a portion of the bottom of the shear layer. Taken together this indicates that there may be changes in the underlying turbulent structures inside the shear layer that correspond to changes in the direction of the shock motion. For

8

example, the separation shock may rotate about its foot as it translates in the streamwise direction. This rotation would correspond to a varying shock strength and a varying adverse pressure gradient being imposed on the shear layer. This variation could alter the turbulent structures inside the shear layer, and therefore, alter the velocity statistics.

The results of this study are intriguing and may serve as encouragement for further investigations. Such changes in turbulent structure are difficult, but not impossible, to detect. Future laser sheet visualizations may reveal the nature of such changes. Unsteady shock-separated flows such as this represent some of the most challenging flowfields to investigate either experimentally or numerically. In general, LDV, as a non-intrusive technique capable of measuring velocity independent of the pressure and density fluctuations inherent in such flows, is more accurate than hot-wires in these flows. However, the random nature of LDV data acquistion times in supersonic flows (due to low seeding levels) makes synchronization with shock motion difficult and requires discarding large amounts of data. Despite these difficulties, this study has shown that LDV can be used to obtain accurate velocity statistics with minimal bias in flows containing unsteady shock waves.

APPENDIX A

Experimental Uncertainty

A detailed error analysis has been performed[21] for this experiment. The relative systematic or bias error in the mean velocity and normal stresses for both the streamwise and transverse velocity components was estimated to be no larger than 2% and is primarily due to uncertainty in the measurement of the LDV fringe spacing. Due to the careful choice of seeding levels, seed material, and beam angles. and from the use of both frequency shifting and interarrival time velocity debiasing,[22] the effects of fringe bias, velocity gradient bias, velocity bias, particle concentration bias, and particle lag were estimated to be negligibly small. As noted previously, particle lag is estimated to be significant only in the region immediately downstream of the shock wave, which is outside the region of interest.

The overall random or precision errors in both the mean and variance of the velocities are given by 95% confidence intervals (assuming a normal distribution of velocities). The limits of these confidence intervals depend both on the ensemble size[23] and on the standard deviation of the velocity distribution, i.e., the rms velocity fluctuation. Equations 2-5 below give the random error in the

mean and variance estimates at 95% confidence, where M, μ, s, N, and σ are the estimate of the mean velocity, the actual mean velocity, the estimate of the rms velocity, the ensemble size, and the actual rms velocity, respectively. Please note that these equations apply to both the streamwise and transverse velocities.

Specifically, for N=4096:

$$M - 0.031s \leq \mu < M + 0.031s \qquad (2)$$

$$0.957s^2 \leq \sigma^2 < 1.046s^2 \qquad (3)$$

and for N=1100:

$$M - 0.060s \leq \mu < M + 0.060s \qquad (4)$$

$$0.920s^2 \leq \sigma^2 < 1.091s^2 \qquad (5)$$

The random error in the estimate of the mean at any given point in the flow is directly proportional to the rms velocity at that point. However, the random error in the estimate of the variance of the velocity is independent of the mean velocity. For a fixed sample size, the random error in the velocity variance estimate is simply a fixed percentage of the velocity variance at each point.

The maximum measured streamwise rms velocity, or the square root of the streamwise normal stress, in the present study is $0.32U_\infty$ or 189 m/s and occurs just upstream of reattachment. This maximum rms velocity yields a random error in the streamwise mean velocity of 5.9 m/s or $0.01U_\infty$ for the data with ensemble sizes of 4096 points (i.e., Figures 6-10). The maximum measured transverse rms velocity, or the square root of the transverse normal stress, in the present study is $0.12U_\infty$ or 71 m/s and occurs just upstream of reattachment. This maximum rms velocity yields a random error in the streamwise mean velocity of 2.25 m/s or $0.0038U_\infty$ for data in Figures 6-10. The maximum random error in the two normal stresses is 4.6% for data in Figures 6-10.

Almost all of the data presented in this study use an ensemble size of 4096 points. However, for the shock transition conditional averages, the ensemble size was limited to 1100 points. For these transition conditional averages, the maximum rms velocities are $0.28U_\infty$ or 165 m/s and $0.11U_\infty$ or 65 m/s for the streamwise and transverse directions, respectively. The resulting maximum random errors in the mean velocity estimates are 9.9 m/s ($0.017U_\infty$) and 3.8 m/s ($0.0064U_\infty$) for the streamwise and transverse directions, respectively. The maximum

9

random error in the two normal stresses for the transition data sets is 9.1%.

REFERENCES

[1] Adamson, T.C., Jr. and A.F. Messiter, "Analysis of Two-Dimensional Interactions Between Shock Waves and Boundary Layers," *Annual Review of Fluid Mechanics*, Vol. 12, 1980, pp. 103-138.

[2] Green, J.E., "Interactions Between Shock Waves and Turbulent Boundary Layers," *Progress in Aerospace Sciences*, Vol. 11, 1970, pp. 235-340.

[3] Ardonceau, P.L., "The Structure of Turbulence in a Supersonic Shock-Wave/Boundary-Layer Interaction," *AIAA Journal*, Vol. 22, No. 9, 1984, pp. 1254-62.

[4] Kuntz, D.W., "An Experimental Investigation of the Shock Wave-Turbulent Boundary Layer Interaction," Ph.D. Thesis, University of Illinois at Urbana-Champaign, 1985.

[5] Smits, A.J. and K.C. Muck, "Experimental Study of Three Shock Wave/Turbulent Boundary Layer Interactions," *Journal of Fluid Mechanics*, Vol. 182, 1987, pp. 291-314.

[6] Selig, M.S., J. Andreopoulos, K.C. Muck, J.P. Dussauge, and A.J. Smits, "Turbulence Structure in a Shock Wave/Turbulent Boundary Layer Interaction," *AIAA Journal*, Vol. 27, No. 7, 1989, pp. 862-869.

[7] Dussauge, J.P. and P. Dupont, "Experimental Evidences of Compressibility Effects on Turbulence in High Speed Flows," in *Transitional and Turbulent Compressible Flows*, L.D. Kral, E.F. Spina, and C. Arakawa, eds., ASME, 1995, pp. 185-192.

[8] Selig, M.S. and A.J. Smits, "Effect of Periodic Blowing on Attached and Separated Supersonic Turbulent Boundary Layers," *AIAA Journal*, Vol. 29, No. 10, 1991, pp. 1651-1658.

[9] Erengil, M.E. and D.S. Dolling, "Unsteady Wave Structure near Separation in a Mach 5 Compression Ramp Interaction," *AIAA Journal*, Vol. 29, No. 5, 1991, pp. 728-735.

[10] Erengil, M.E. and D.S. Dolling, "Correlation of Separation Shock Motion with Pressure Fluctuations in the Incoming Boundary Layer," *AIAA Journal*, Vol. 29, No. 11, 1991, pp. 1868-77.

[11] Dolling, D.S. and M.T. Murphy, "Unsteadiness of the Separation Shock Wave Structure in a Supersonic Compression Ramp Flowfield," *AIAA Journal*, Vol. 21, No. 12, 1983, pp. 1628-1634.

[12] Kussoy, M.I., J.D. Brown, J.L. Brown, W.K. Lockman, and C.C. Horstman, "Fluctuations and Massive Separation in Three-Dimensional Shock Wave/Boundary Layer Interactions," in *Transport Phenomena in Turbulent Flows: Theory, Experiment, and Numerical Simulation*, M. Hirata and N. Kasagi, eds., Hemisphere, New York, 1988, pp. 875-887.

[13] Brown, J.D., J.L. Brown, M.I. Kussoy, M. Holt, and C.C. Horstman, "Two-Component LDV Investigation of Three-Dimensional Shock/Turbulent Boundary Layer Interactions," AIAA Paper 87-0553, 1987.

[14] Shaw, R.J., "An Experimental Investigation of Unsteady Separation Shock Wave Motion in a Plume-Induced, Separated Flowfield," Ph.D. Thesis, University of Illinois at Urbana-Champaign, 1995.

[15] Bloomberg, J.E., "An Investigation of Particle Dynamics Effects Related to LDV Measurements in Compressible Flows," M.S. Thesis, University of Illinois at Urbana-Champaign, 1989.

[16] Jenson, L., "Automatic Digital Signal Processing for LDV," *Proceedings of the 4th International Conference on Laser Anemometry Advances and Applications*, Vol. 2, Cleveland, Ohio, pp. 617-628, 1991.

[17]Dolling, D.S. and L. Brusniak, "Separation Shock Motion in Fin, Cylinder, and Compression Ramp--Induced Turbulent Interactions," *AIAA Journal*, Vol. 27, No. 6, 1989, pp. 734-742.

[18]Brusniak, L., "Evaluation of Conditional Sampling Methods for Analysing Separation Shock Motion," AIAA Paper 88-0091, 1988.

[19]Palko, C.W. and J.C. Dutton, "Velocity Measurements in a Shock-Sparated Free Shear Layer," abstract submitted for presentation at AIAA Aerospace Sciences Meeting, Jan 1998.

[20]Herrin, J.L. and J.C. Dutton, "The Turbulence Structure of a Reattaching Axisymmetric Supersonic Free Shear Layer," AIAA Paper 95-2250, 1995.

[21]Palko, C.W., "Velocity Measurements in a Shock-Separated Free Shear Layer," Ph.D. Thesis, University of Illinois at Urbana-Champaign, 1997.

[22]Herrin, J.L. and J.C. Dutton, "An Investigation of LDV Velocity Bias Correction Techniques for High-Speed Separated Flows," *Experiments in Fluids*, Vol. 15, No. 4/5, 1993, pp. 354-363.

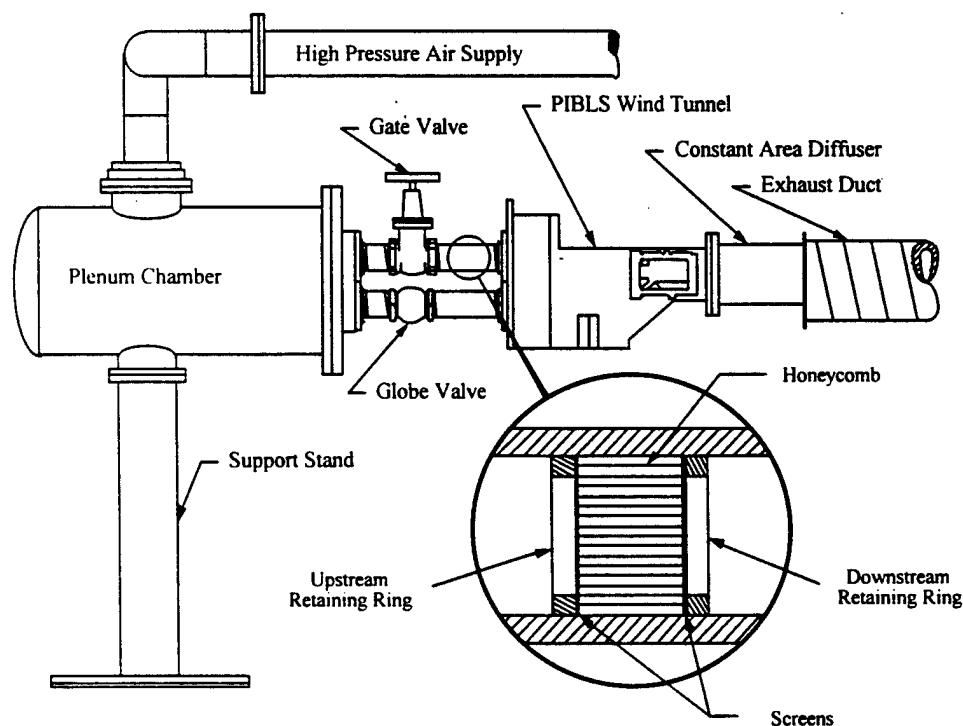[23]Bendat, J.S. and A.G. Piersol, *Random Data*, Wiley-Interscience, New York, 1986.
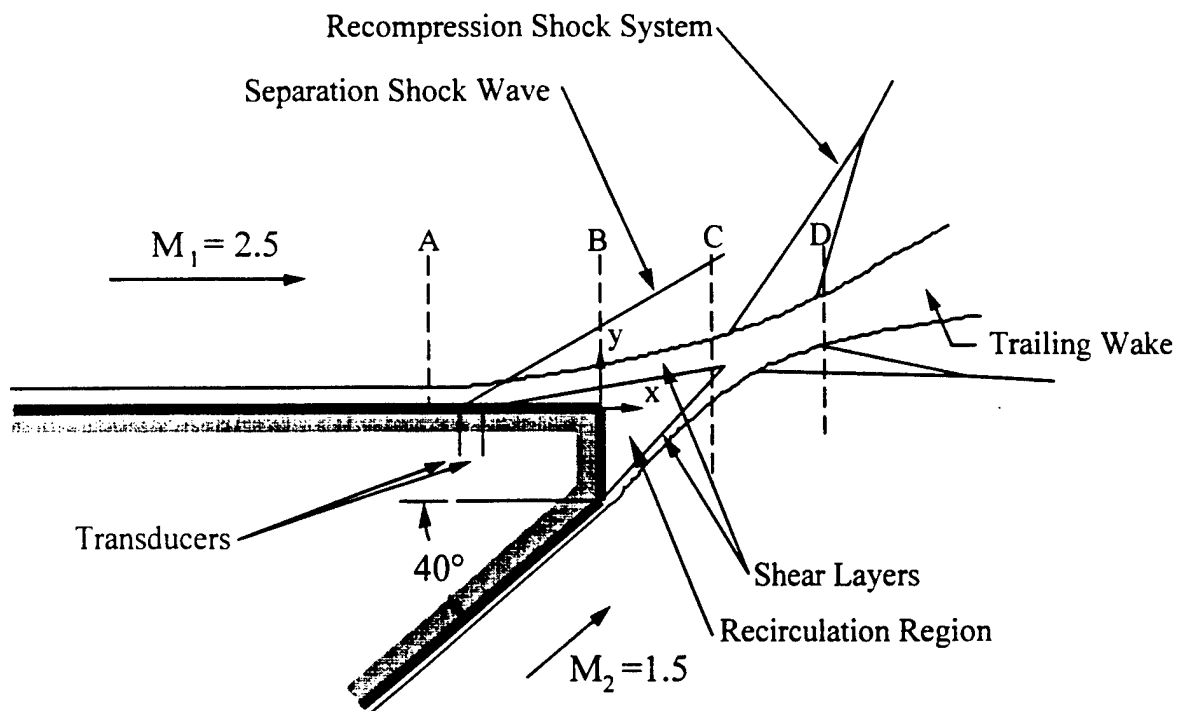
Figure 1 PIBLS tunnel schematic[14]

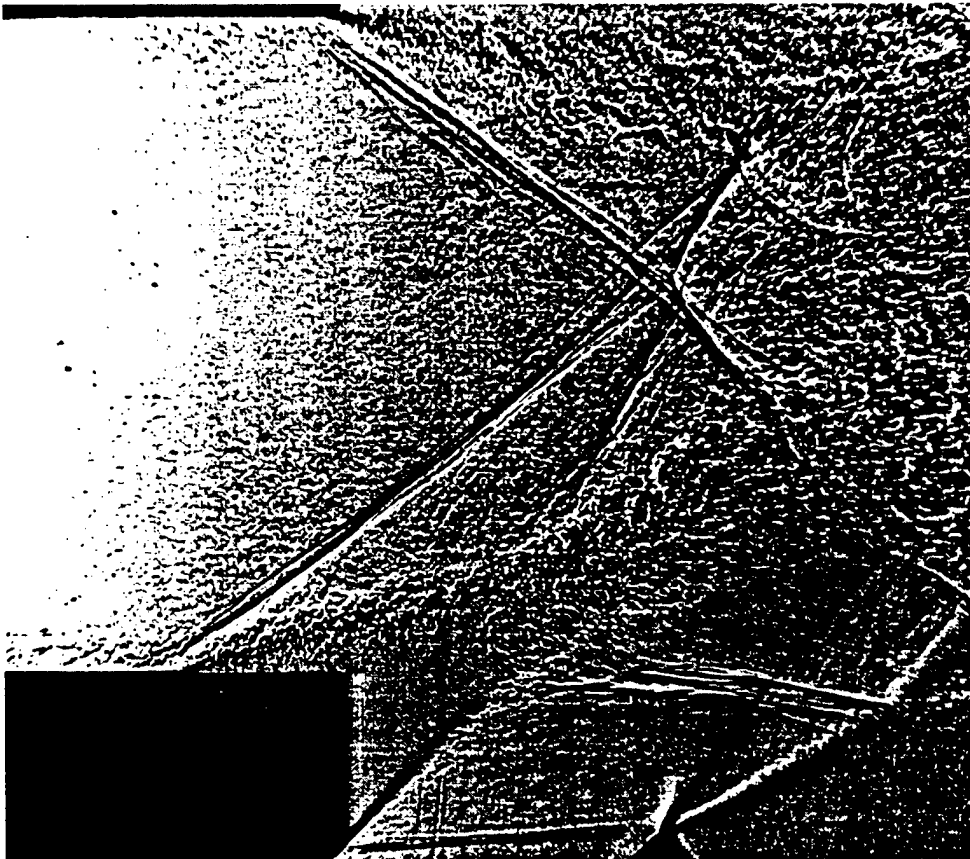Figure 2 Flowfield schematic

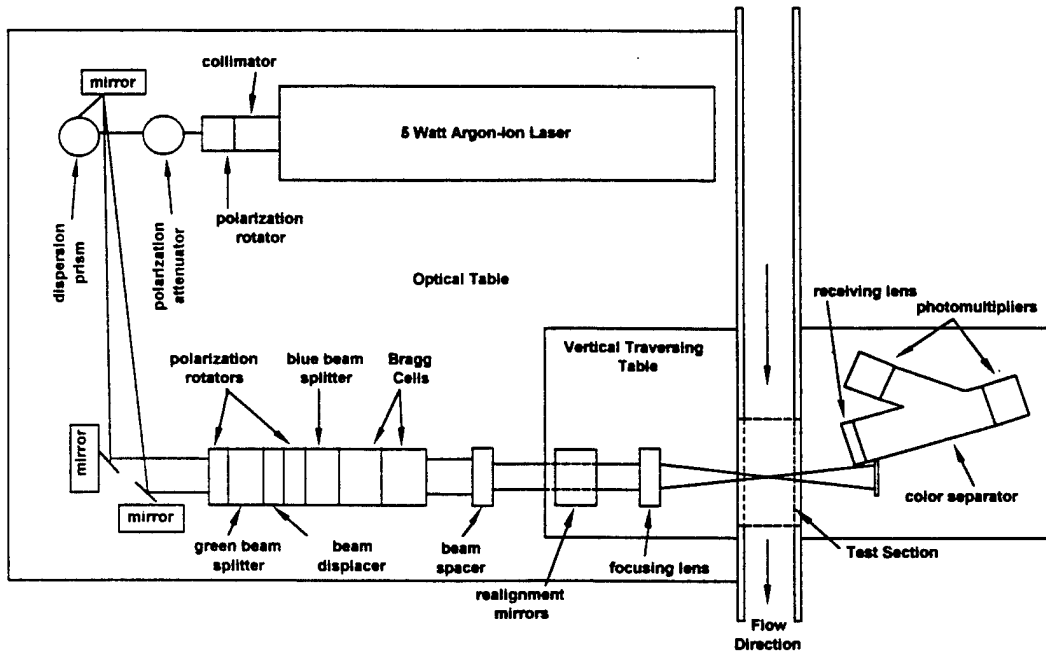

Figure 3 Flowfield shadowgraph[14]

Figure 4 Laser Doppler velocimetry (LDV) system
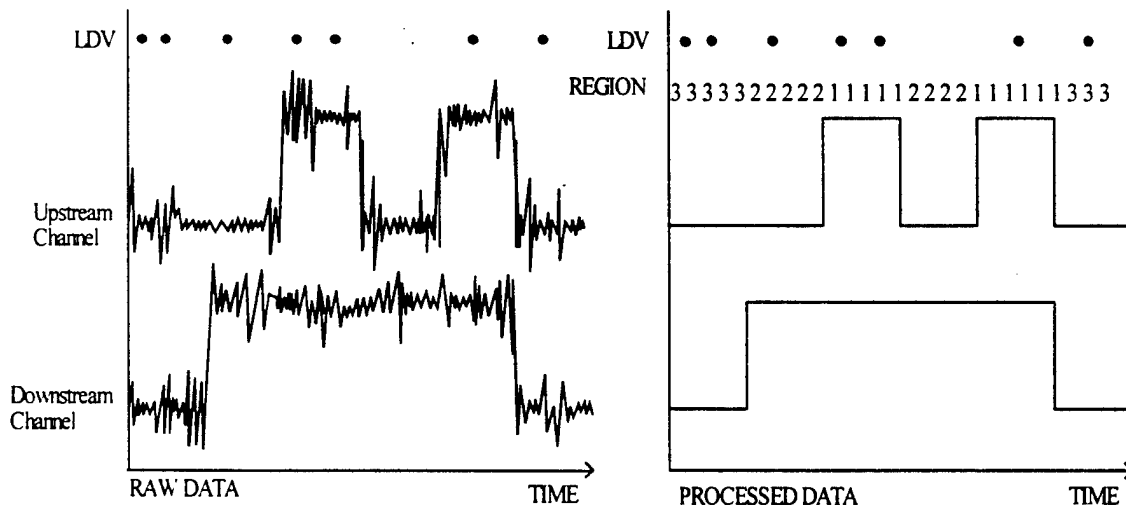

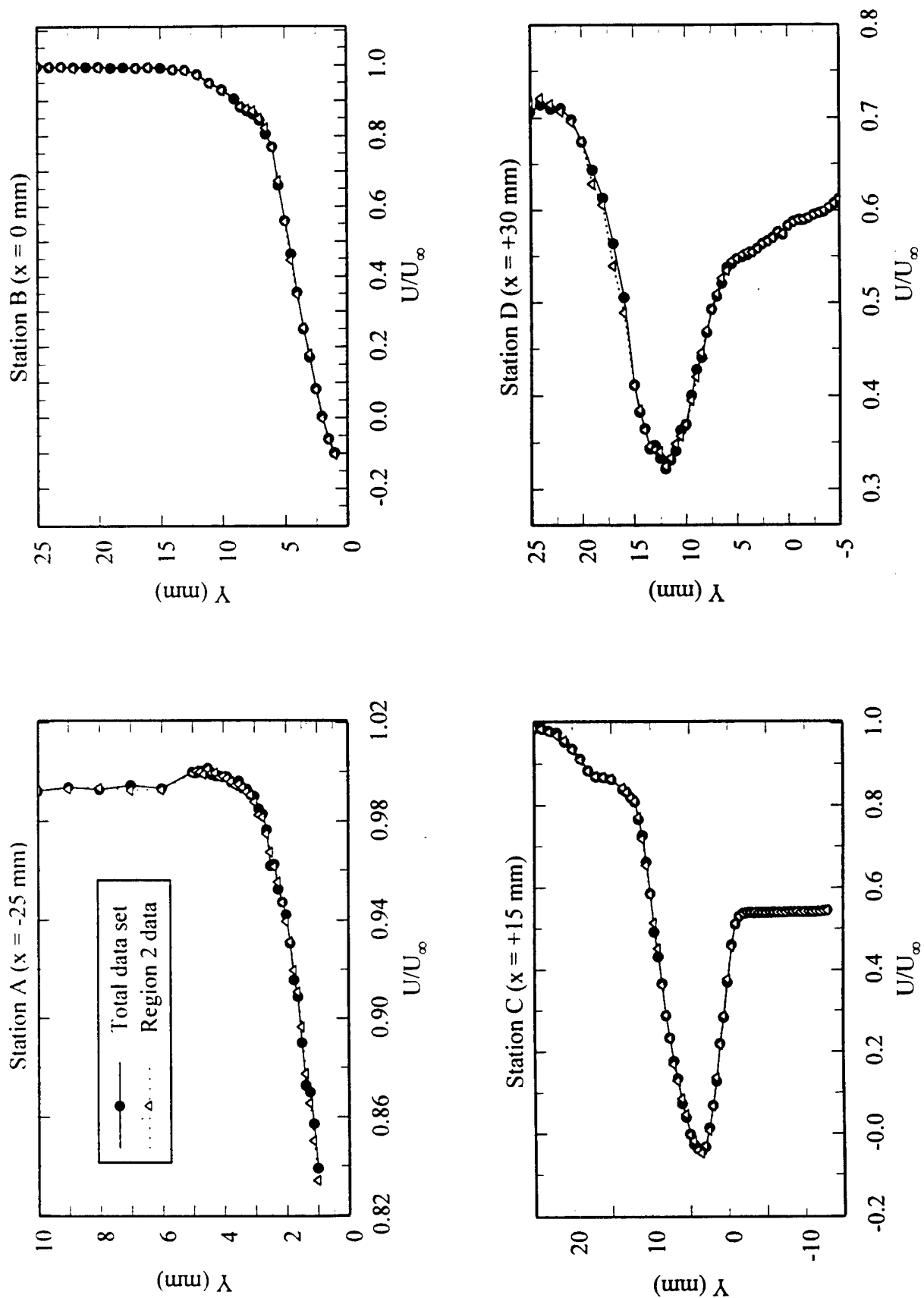Figure 5 Conditional analysis algorithm

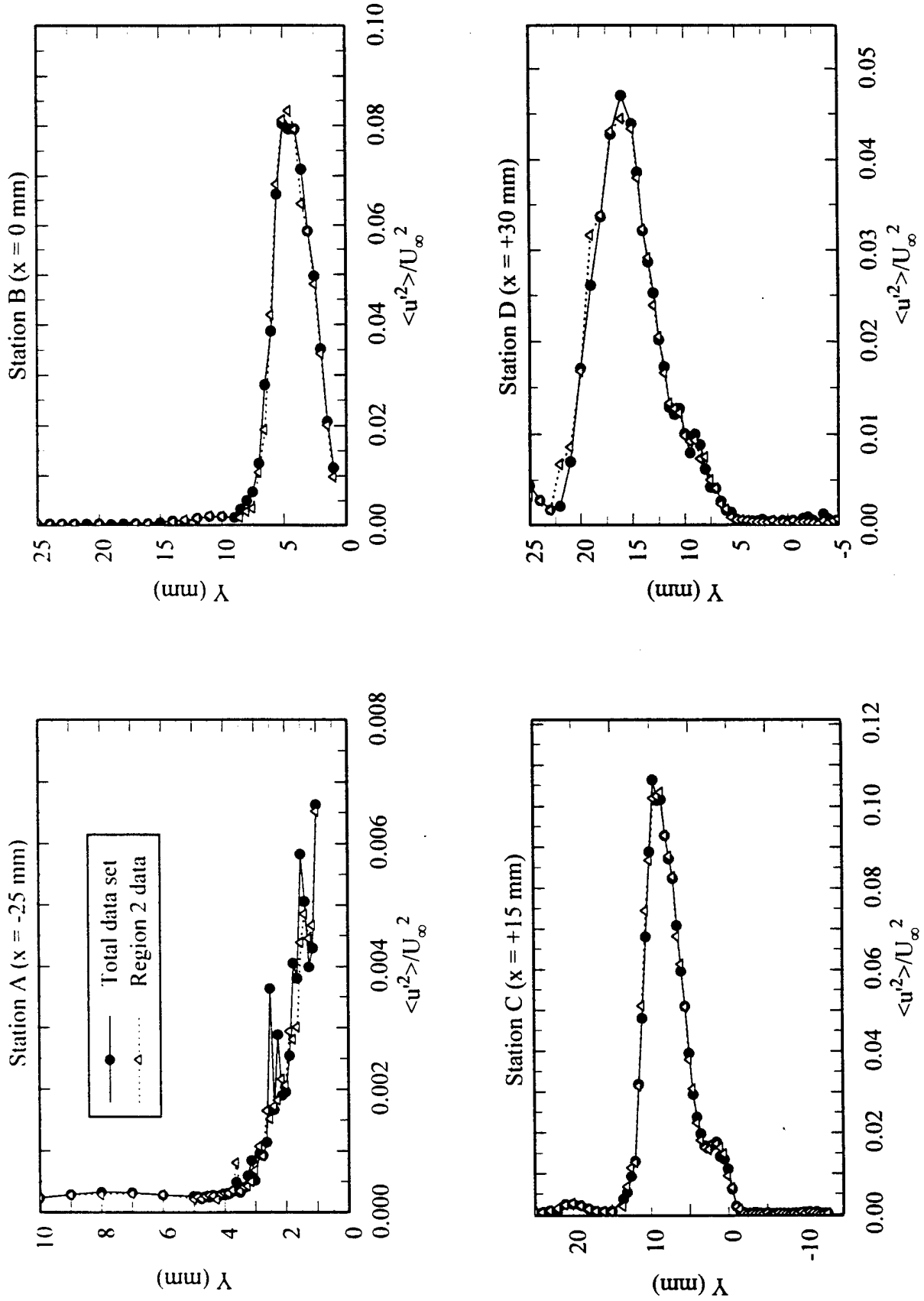Figure 6 Dimensionless mean streamwise velocity, U/U_∞

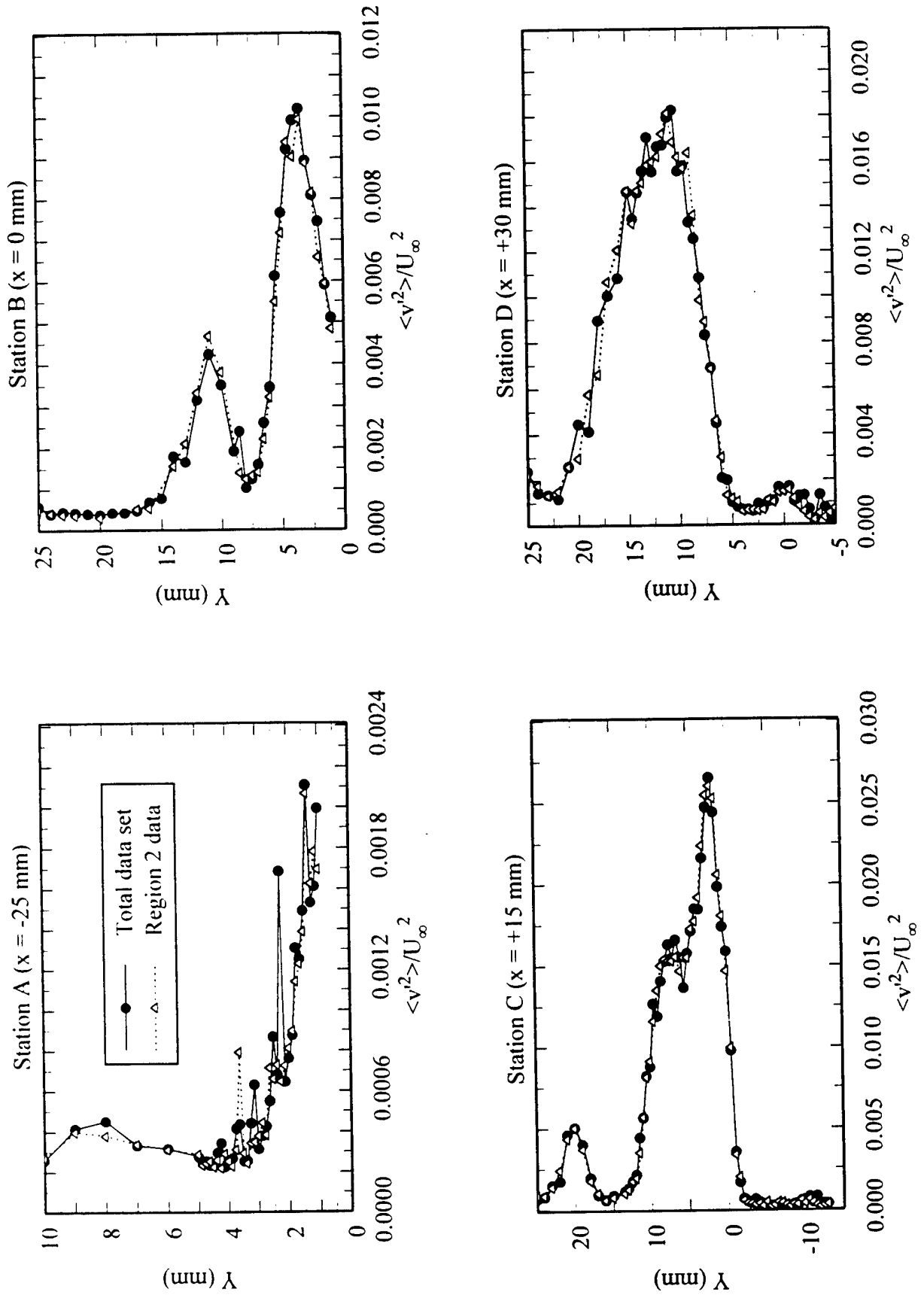Figure 7 Dimensionless streamwise normal stress, $\langle u'^2 \rangle / U_\infty^2$

15

Figure 8 Dimensionless transverse normal stress, $\langle v'^2 \rangle / U_\infty^2$

16

Figure 9 Dimensionless Reynolds shear stress, $-\langle u'v'\rangle/U_\infty^2$

17

Figure 10 Dimensionless turbulent kinetic energy, $(\langle u'^2 \rangle + 2\langle v'^2 \rangle)/2U_\infty^2$

18
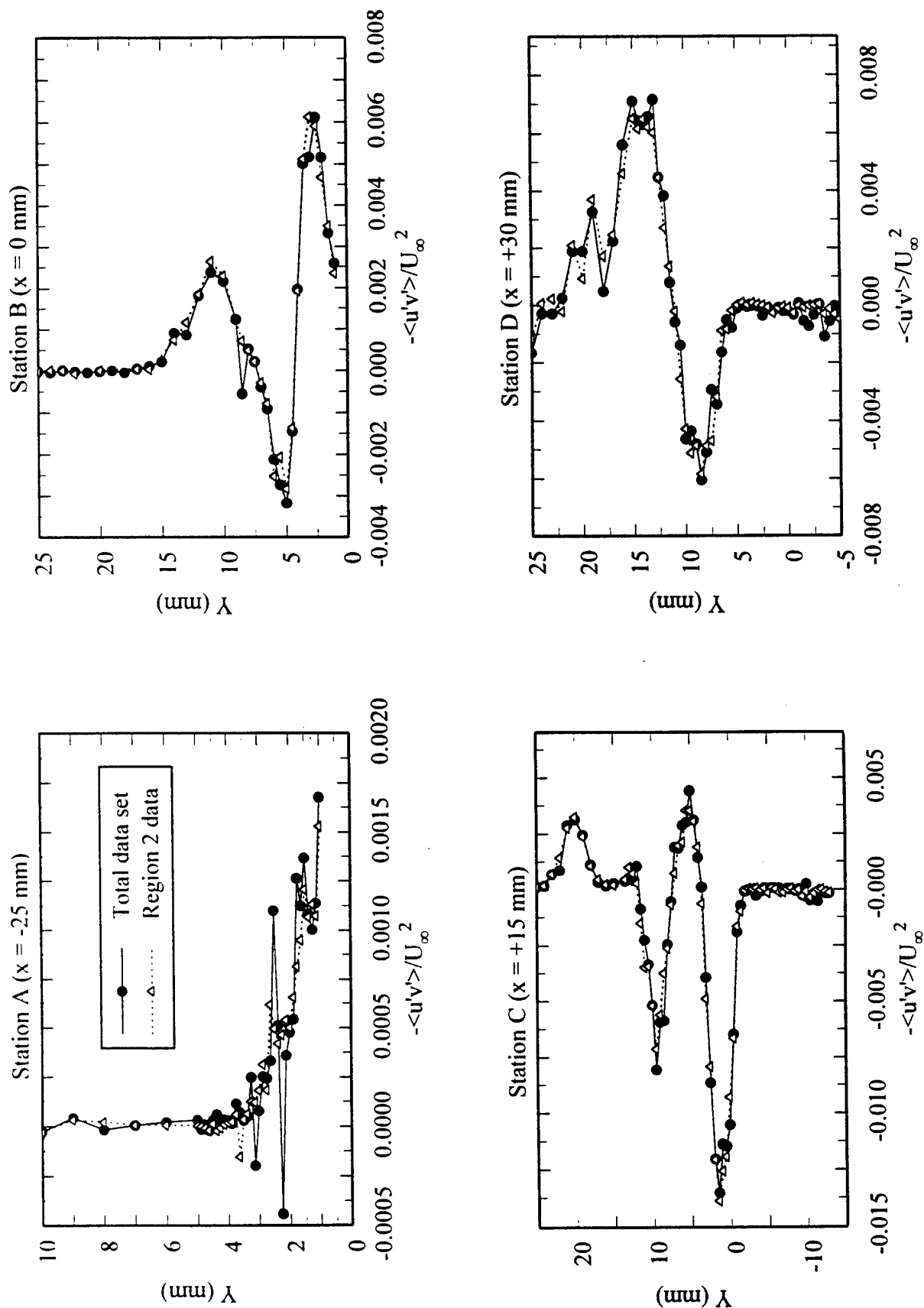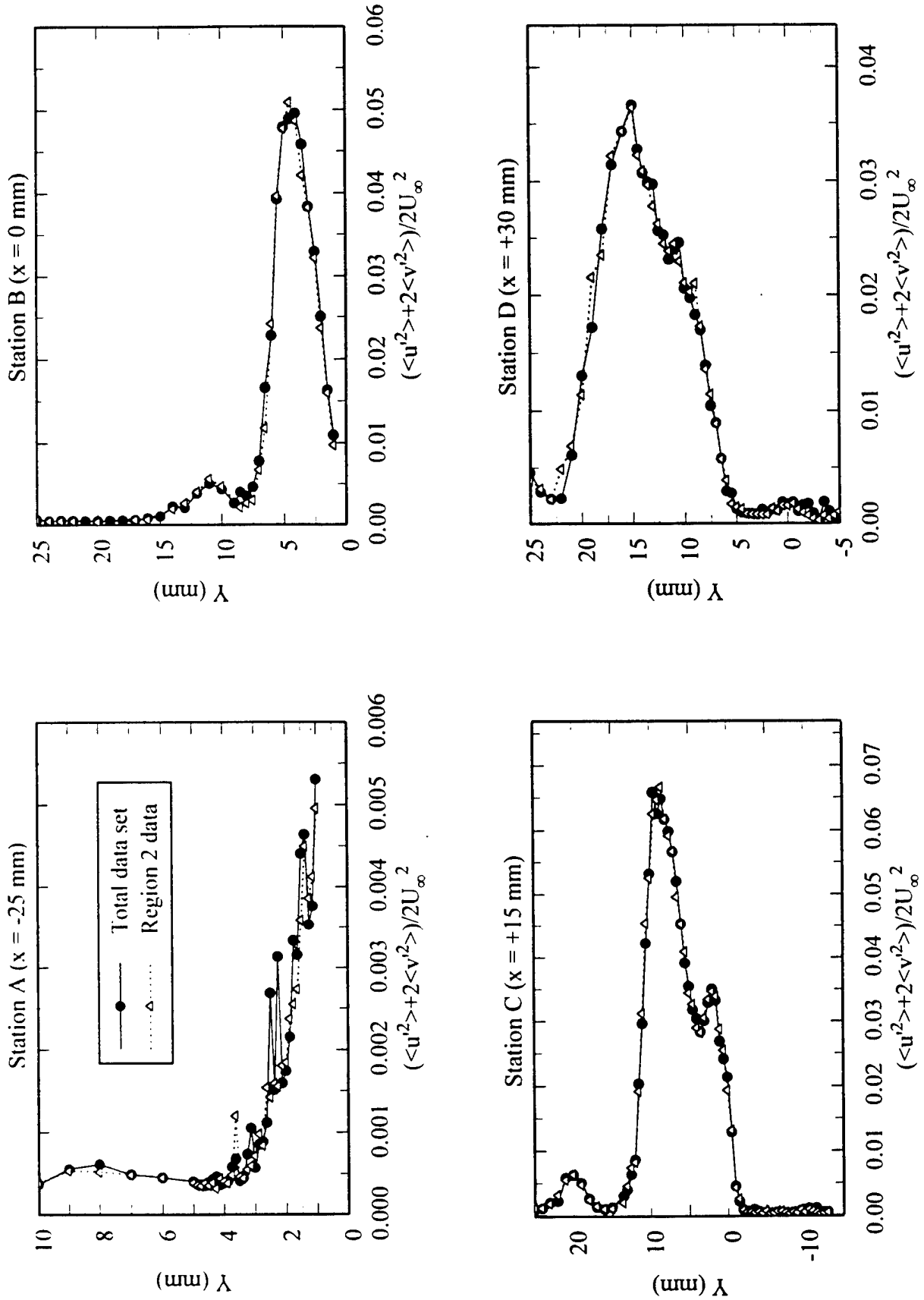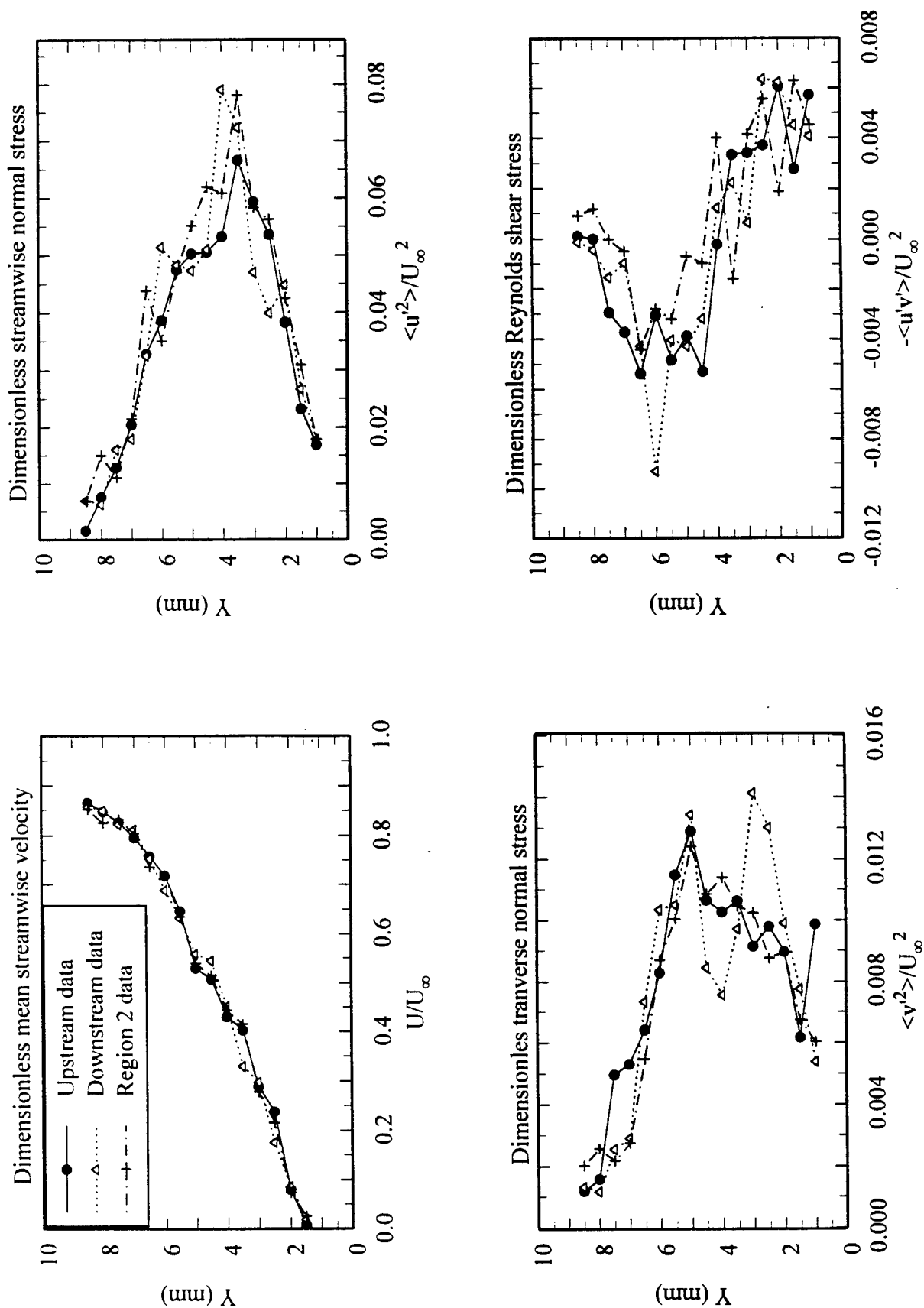
Figure 11 Shock direction results at station B (x = 0 mm)

APPENDIX A.22

VELOCITY MEASUREMENTS IN A SHOCK-SEPARATED FREE SHEAR LAYER

AIAA Paper No. 98-0698

Presented at the *36th AIAA Aerospace Sciences Meeting*

Reno, Nevada

January 1998

by

C. W. Palko and J. C. Dutton

AIAA 98-0698

Velocity Measurements in a Shock-Separated Free Shear Layer

C. W. Palko
The Aerospace Corporation
El Segundo, CA

J. C. Dutton
University of Illinois at Urbana-Champaign
Urbana, IL

36th Aerospace Sciences Meeting & Exhibit
January 12–15, 1998 / Reno, NV

VELOCITY MEASUREMENTS IN A SHOCK-SEPARATED FREE SHEAR LAYER

C. W. Palko*
Propulsion Department
The Aerospace Corporation
El Segundo, California 90245

J.C. Dutton[†]
Dept. of Mechanical and Industrial Engineering
Univ. of Illinois at Urbana-Champaign
Urbana, Illinois 61801

ABSTRACT

Two-component laser Doppler velocimetry (LDV) measurements were made in a planar, shock-separated free shear layer formed by the convergence of two supersonic streams past a thick plate. High-speed wall pressure measurements locate the unsteady shock wave formed by this interaction and, consequently, allow separation of the effects of shock motion from the turbulence fluctuations in the velocity measurements of the shear layer. Shock-induced separation dramatically increases the normal stresses and shear stress. The shock-separated shear layer displays a positive shear stress region between separation and reattachment. Reattachment produces a shift in turbulent kinetic energy from the streamwise component to the transverse component. The region of shock motion has a relatively constant width irrespective of distance from the wall.

INTRODUCTION

While shock-induced boundary layer separation caused by a second fluid stream has been investigated over the last 40 years, there are no known turbulence measurements in such a flow. However, shock-induced shear layer formation in front of solid objects has been investigated.[1-3] Among these geometries, unswept compression corner flows provide the closest analogy to the current study.

To date only four studies of turbulence in unswept compression corners have been performed: Ardonceau;[4] Kuntz;[5] Smits and Muck;[6] and Selig et al.[7] All of the studies, except for that of Selig et al., considered a series of corner angles resulting in both unseparated and separated

---

* Member of the Technical Staff. The research and preparation of this report were completed prior to Dr. Palko becoming a Member of the Technical Staff. Dr. Palko is a member of the AIAA.

[†] W. Grafton and Lillian B. Wilkins Professor, Associate Fellow AIAA.

flows. Unlike the other studies, Selig et al. investigated a flowfield with active forcing (by mass addition). All of Kuntz's data and some of Ardonceau's were obtained using two-component LDV. The remaining studies, including a portion of Ardonceau's, used constant temperature hot-wire anemometry. The Mach numbers for the studies by Ardonceau, Kuntz, Smits and Muck, and Selig et al. were 2.25, 2.94, 2.90, and 2.84, respectively. All of these studies noted large increases in turbulence through the shock interaction and unsteady shock motion. However, none of these studies used any conditional analysis to separate velocity fluctuations due to the motion of the shock from those due to turbulence. Palko and Dutton[8] have demonstrated a technique for separating the fluctuation contributions from these two sources; this method is used in the measurements reported here.

Several mechanisms have been proposed to explain the turbulence amplification in shock wave-boundary layer interactions. A nonlinear coupling of entropy, pressure, and vorticity fluctuations involving the Rankine-Hugoniot jump conditions at the shock has been proposed by Anyiwo and Bushnell.[9] Turbulence amplification as a direct result of shock wave unsteadiness[10,11] is also widely cited. Finally, both bulk compression and concave streamline curvature present in shock wave-boundary layer interactions are known to be destabilizing and, therefore, turbulence enhancing.[12] All four of these mechanisms become more significant as the corner angle is increased, thereby increasing the shock strength and the range of shock motion. Another mechanism that is not often cited is the effect of separation itself.

The studies of Ardonceau, Kuntz, Selig et al. and Smits and Muck all involved relatively thick boundary layers (8, 8, 26, and 26 mm, respectively) and very small separated regions. The current study involves an approximately 3 mm thick turbulent incoming boundary layer and a large separated flow region. This separation bubble serves as a reservoir of low momentum

fluid that may be entrained by turbulent structures within the free shear layer. Unfortunately, the lack of prior studies involving a large separated region makes the effects of separation caused by a second fluid stream rather than by a solid ramp face difficult to determine.

In contrast to the case of shock-separated free shear layers are expansion-separated shear layers. To help understand the flow physics of the shock-separated case, this paper will make comparisons with the work of Amatucci[13] and Herrin,[14] which represent comprehensive LDV investigations of the mean flow and turbulence in planar and axisymmetric expansion-separated shear layers, respectively. Herrin investigated a single $M = 2.5$ (before separation) shear layer while Amatucci studied both $M = 2.56$ and $M = 2.05$ shear layers. Like the current study, both Amatucci's and Herrin's flows involved relatively thin incoming boundary layers and a large separated flow region.

FLOW FACILITY

A schematic of the test section and flowfield features investigated in this study is shown in Figure 1. The upper Mach 2.5 stream (unit Reynolds number, Re=48.9x10^6 m^{-1}) and the lower Mach 1.5 stream (Re=36.2x10^6 m^{-1}) converge at a 40° angle past a 12.7 mm high base plane. The boundary layer of the upper stream intercepts the oblique separation shock, consequently separates, and forms a free shear layer, as shown in Figure 1. This shear layer then reattaches with the shear layer formed by the separation (at near zero pressure gradient) of the boundary layer of the lower stream, thereby enclosing a recirculating region behind the base. The reattachment of the shear layers generates a recompression shock system and the resulting trailing wake.

The upper and lower streams have absolute stagnation pressures of 506 kPa and 251 kPa, respectively, resulting in a static pressure ratio of the lower to the upper streams of P_2/P_1=2.27. Surface oil flow visualization shows that the center 32 mm (63%) of the flowfield is free from sidewall effects and is, consequently, two-dimensional in this region. The blowdown-type supersonic wind tunnel used to produce this flowfield is described briefly in Palko and Dutton[8] and comprehensively in Palko[15] and Shaw.[16]

EQUIPMENT

A two-component laser Doppler velocimetry (LDV) system, with a TSI IFA 750 digital burst correlator operating in coincident mode, was used for the mean velocity and turbulence measurements. A detailed discussion of the IFA 750 operation is given by Jenson.[17] One beam of each color is shifted by 40 MHz to minimize fringe biasing and to allow discrimination of negative velocities. The blue and green beam pairs are also oriented at approximately +45° and −45°, respectively, to the mean flow direction of the upper stream to minimize fringe blindness.

Separate TSI model 9306 six-jet atomizers introduce silicone oil droplets with a mean diameter of approximately 0.8 μm into each stream.[18] The oil droplets are injected downstream of all flow-conditioning modules and upstream of the nozzle blocks through small stainless steel tubes. The scattered light from the droplets is collected in forward scatter at an off-axis collection angle of 10°, resulting in an effective measurement volume length of 1.5 mm. The 13 mm beam spacing and 250 mm focal length transmitting lens result in a measurement volume diameter of 0.127 mm (the spatial resolution in the two velocity measurement directions).

Due to their significant inertia, seed particles produce curved pathlines behind an oblique shock wave instead of following the fluid streamlines that bend discontinuously at the shock front. Using the Carlson-Hoglund[19] empirical drag law, significant particle lag effects in this study were estimated to be limited to a region extending 2.8 mm in the streamwise (x) direction downstream of the shock wave (i.e., 1.4 mm normal to the shock). This oblique shock wave represents by far the largest velocity gradient in the present flowfield. A detailed uncertainty analysis of the velocity measurements[15] predicts a maximum uncertainty outside the region of significant particle lag of ±3.1% for the mean velocity and ±4.6% for the turbulent stresses.

Since the boundary layer separation point oscillates in the streamwise direction with the shock wave, the shear layer will also oscillate and cause biasing of unconditionally averaged velocity data. Palko and Dutton[8] and Palko[15] describe in detail the conditional analysis technique used in the current study to minimize bias in the velocity measurements due to shock wave unsteadiness.

This technique allows the shock position (upstream, between, or downstream of the two transducers) to be determined for each velocity realization. By ensemble-averaging realizations that are obtained only when the shock is between the transducers, this procedure effectively "freezes" the shock in this position and minimizes the velocity fluctuations that would otherwise be recorded due to the shock motion. However, large data sets must be obtained to ensure adequate statistical certainty from the ensemble averages. Since the transducers are placed at 19.0 and 16.5 mm upstream of the base plane (Figure 1), the mean shock foot position (i.e., the boundary layer separation point) for the conditionally analyzed data set is 17.75±1.6 mm upstream of the base. Palko[15] describes in detail the entire pressure data acquisition system.

RESULTS

This paper presents data obtained at approximately 1500 spatial locations along the spanwise centerplane of the flowfield. The origin of the measurement grid is the upper base corner with the x-axis aligned parallel to the wall (Figure 1). The streamwise spacing of the measurement locations is a uniform 2.5 mm, but the transverse spacing varies from 0.125 mm in high-gradient regions to 1.0 mm in the almost uniform freestreams. Two-component velocity measurements are limited to y > 1 mm due to beam clipping at the wall below this point. The entire measurement grid has an *absolute* positional uncertainty (systematic error) in the streamwise and transverse directions of ±250 μm with respect to the base, but the *relative* positional uncertainty (random error) of each point with respect to each other within the measurement grid is only ±0.5 μm.

Previously, Palko and Dutton[8] presented selected profiles obtained with and without conditional analysis to illustrate the effects of shock motion on the turbulence. This paper instead analyzes *global flowfield features* by presenting results (using 4096 instantaneous velocity realizations at each spatial location) obtained only when the shock was between the two transducers. The contour levels in the data plots do not represent regular intervals in the data, but instead were chosen to clearly illustrate the features of the flowfield. Furthermore, the mean velocities and Reynolds stresses have been non-dimensionalized using the freestream velocity in the upper stream,

U_∞ = 590 m/s. Finally, all contour and line plots presented in this study are unsmoothed, and the data have been velocity debiased using the interarrival time weighting method shown by Herrin and Dutton[20] to be the most accurate debiasing method in this type of flow.

Mean Flow

Table 1 lists various properties of the incoming boundary layer of the upper stream. These properties were determined by applying a curve-fit for compressible, turbulent boundary layers[21] to the experimentally obtained boundary layer profile. The best curve-fit was found by varying the boundary layer thickness, δ, and the skin friction coefficient, C_f, until the mean square deviation between the curve-fit and the experimental data was minimized. The resulting profile equation was then numerically integrated to yield the boundary layer integral parameters listed in Table 1. The Reynolds number based on the various thicknesses may be estimated as Re_δ = 120,000, Re_{δ^*} = 28,000, and Re_θ = 7600.

Figure 2 presents a contour plot of the normalized mean streamwise velocity component, U/U_∞. These results clearly indicate the approach boundary layer, the two shear layers, the recirculation region behind the base (denoted by negative values of U/U_∞), the separation shock, the upper system of recompression waves, and the trailing wake. The two shear layers reattach at approximately 16.25 mm downstream of the base. (Due to the dominance of the streamwise velocity component, reattachment is defined here as the point of zero U/U_∞.) The reattachment point is noted by a small plus sign in Figure 2 and all subsequent contour plots. Also interesting is the sudden, almost discontinuous decrease in the streamwise mean velocity and subsequent thickening of the boundary layer at the shock foot location (x = -17.75 mm). The presence of this discontinuity at the expected location between the two transducers indicates that the shock position is being accurately "frozen" by the conditional analysis algorithm.

The combined mean velocity field (streamwise and transverse components) is presented as a vector plot in Figure 3. This figure clearly shows the uniform flow in each freestream approaching the base, the two shear layers, the separation shock, the reattachment point at x = +16.25 mm, and the wake development. The

3

thickening of the upper boundary layer as the base plane is approached is also apparent in Figure 3. The inflection points in the velocity profiles immediately upstream of the base are expected since the flow is separated at these locations. To allow closer examination of the recirculation region, a vector plot of only the base region is presented in Figure 4. The two distinct recirculating eddies within the region of separated flow may be clearly seen in Figure 4 as well as the recirculating flow near the wall at the base plane below the upper shear layer. The reattachment of the two shear layers in the neighborhood of x = +16 mm is also more apparent in this expanded view.

An equivalent "ramp corner angle" may be defined for the current flow as the angle between the mean reattached wake direction (inviscid slip line) and the x-axis. This inviscid slip line is, of course, a compliant boundary rather than a rigid boundary such as the downstream ramp surface in a compression corner. By using a linear regression through the points of minimum streamwise velocity at all measured streamwise locations downstream of reattachment, this equivalent corner angle is estimated to be 28°.

Figure 5 presents the mean Mach number distribution throughout the flowfield. The Mach number was obtained by measuring the stagnation temperature inside the plenum chamber of the wind tunnel and applying the assumption of adiabatic flow to extract the static temperature and speed of sound throughout the flowfield. Figure 5 clearly reveals the separation shock, the recompression wave systems, and the large subsonic region downstream of the base. The dramatic change in compressibility across the upper shear layer is indicated by the highly compressible freestream on the outside (M > 2.0) and the large region of nearly incompressible flow near the base on the inside of this thin layer (M < 0.3).

To quantify the compressibility of the shock-separated shear layer, one may use the mean velocity data to determine a convective Mach number, M_C.[22,23] The convective Mach number is the Mach number of each freestream relative to the large-scale turbulent structures in the free shear layer. For cases in which the freestream gases on each side of the shear layer are the same and stream 1 is the high-speed stream, the convective Mach number can be computed as:

$$M_C = \frac{U_1 - U_2}{a_1 + a_2} \qquad (1)$$

For the upper shear layer in this study, the convective Mach number is approximately 1.4, which indicates very strong effects of compressibility. This value of M_C is also approximately equal to those of the planar and axisymmetric expansion-separated free shear layers in the studies of Amatucci[13] and Herrin,[14] respectively.

Reynolds Normal Stresses

The dimensionless streamwise normal stress distribution is displayed in Figure 6. Clearly, the turbulence in both freestreams is very small. The shock-induced separation process dramatically increases the streamwise normal stress, and the reattachment process and wake development dramatically decrease it in the upper shear layer. The shock interaction increases the streamwise normal stress by a factor of about 5.5 times the peak measured value in the incoming boundary layer of $0.02U_\infty^2$. The maximum streamwise normal stress value of $0.11U_\infty^2$ occurs immediately upstream of reattachment.

The increased streamwise turbulence levels in the current study match closely those cited by Ardonceau[4] in his separated, 18° compression corner flow, but exceed those cited in the other shock interaction studies. These differences could be attributable to possible difficulties in interpreting hot-wire measurements made in supersonic flows[6] and the lack of LDV data immediately downstream of the interaction in Kuntz's[5] study. The peak streamwise turbulence levels in the present study exceed those of both Herrin and Amatucci. This difference is due to the presence of the adverse pressure gradient, bulk compression, and concave streamline curvature at separation for the current shock-separated shear layer, as compared to the expansion-separated cases.

The transverse normal stress distribution is displayed in Figure 7. Separation of the upper shear layer dramatically increases the transverse normal stress by a factor of 5 over that in the incoming boundary layer. The lower shear layer displays large values of transverse normal stress, but this is primarily due to the inclination of the lower shear layer with respect to the x-axis. Because of this, velocity fluctuations within the

4

lower shear layer have a large transverse component.

While the transverse normal stress in the lower shear layer (and for the entire flowfield) peaks before reattachment (at x = +12.5 mm), the transverse normal stress in the upper shear layer increases throughout the recompression region and through reattachment. In general the developing wake exhibits decreasing turbulence levels, but large values ($> 0.018U_\infty^2$) of transverse normal stress persist for over 12.5 mm downstream of reattachment (to x = +28.75 mm). The far wake is characterized by decreasing transverse normal stress, but at the downstream limit of the measurement region (x = +40 mm), the values are still greater than $0.010U_\infty^2$ (which is equal to the value immediately after separation). This delayed decrease in the transverse normal stress may be indicative of a shift in turbulent energy with recompression and reattachment from the streamwise normal stress to the transverse and spanwise normal stresses. Herrin and Dutton[24] also note increasing normal stress isotropy through reattachment of an axisymmetric shear layer that is indicative of such a shift in turbulent energy. This delayed decrease may also be due to the large transverse normal stress in the lower shear layer that comes primarily from the inclination of the lower shear layer with respect to the x-axis.

The streamwise normal stress in the current study peaks immediately before reattachment. This feature is common to compressible free shear layers formed through both planar rapid expansions[13] and planar shock-induced separation, but contrasts with the decreasing turbulence levels through recompression and reattachment in axisymmetric geometries.[24] This provides evidence of the stabilizing (i.e., turbulence-reducing) effect of lateral streamline convergence that occurs for the axisymmetric case, but not for the planar.

Turbulence Amplification

Turbulence amplification has been documented in many types of shock wave-boundary layer interactions. Smits and Muck[6] reported in their 8°, 16°, and 20° compression corner studies normal stress amplification factors of up to 14 times the incoming boundary layer values, with the larger corner angles (i.e., stronger shocks) exhibiting the larger turbulence amplification. Smits and Muck used the "Strong

Reynolds Analogy" (SRA) to extract the kinematic turbulent stresses from the mass-weighted hot-wire measurements. However, the SRA assumes that pressure fluctuations are negligible, which is not true downstream of unsteady shock waves and therefore complicates the interpretation of hot-wire measurements in such flows. Kuntz[5] reported peak streamwise normal stress levels in the *reattached* boundary layer of between 2 and 10 times the levels in the approaching boundary layer, for his 8°, 12°, 16°, 20°, and 24° compression corners, respectively. Larger turbulence amplification factors may well have occurred in Kuntz's flow upstream of reattachment, but were not measured. By comparison, the streamwise normal stress in the present study peaks *upstream* of reattachment. In his 18° compression corner, Ardonceau[4] reports a peak streamwise normal stress value just below the center of his shear layer prior to reattachment of $0.114U_\infty^2$, an increase of a factor of 4.3 over the approaching boundary layer values. This agrees well with the peak value in the present study. The normal stress amplification ratios quoted for Kuntz and Ardonceau are estimated from turbulence intensity profiles and consequently have large uncertainties.

Ardonceau[4], Kuntz[5], and Smits and Muck[6] examined a range of compression corner angles. All these studies found increasing turbulence amplification with increasing corner angle and attributed it to increasing shock strength, bulk compression, and concave streamline curvature. Both Ardonceau and Kuntz found no dramatic difference between separated (larger angles) and unseparated (smaller angles) corner flows, indicating that separation has little effect on turbulence amplification. Smits and Muck[6] concluded that for weak shocks turbulence amplification is primarily due to the effects of bulk compression, adverse pressure gradient, and concave streamline curvature. Smits and Muck assert that the turbulence amplification depends more on the overall pressure rise through the interaction than on the presence of a shock wave. They also proposed that shock wave oscillation becomes an important mechanism for stronger shocks.

Selig and Smits,[11] however, in a separated 24° compression corner study, concluded that shock unsteadiness is not an important mechanism, since the downstream turbulence showed no change when the shock wave was

driven at a particular frequency. The shock wave was forced in this flow by periodic blowing into the separated region and, unlike the present study, no conditional analysis was used to isolate either shock position or shock motion direction from the turbulent fluctuations. In contrast, Palko and Dutton[8] found that shock motion direction does have a significant effect on downstream turbulence levels as well as on the organization of the turbulence.

Amatucci[13] and Herrin[14] also report turbulence increases smaller than the above-cited levels for their planar and axisymmetric base flows, respectively. Both researchers found that, despite the stabilizing influences of a favorable pressure gradient, bulk expansion, and convex streamline curvature, the turbulence at the inner (low-speed) edge of the free shear layer increases dramatically over its levels in the approaching boundary layer in response to the expansion at separation. In particular, Herrin found that the turbulence levels in the outer portion of his free shear layer formed through a rapid expansion were "frozen" at or below the upstream levels, while the inner edge experienced streamwise normal stress increases of approximately 9 times the levels in the approaching boundary layer.

Ardonceau[4] and Kuntz[5] report increases of 9 and 20, respectively, over the peak transverse normal stress levels in their approaching boundary layers for their compression corner flows. Herrin[14] reports a peak transverse normal stress value of $0.024U_\infty^2$ for his rapidly expanded axisymmetric free shear layer. The data of Herrin reflect an increase of 3 over the transverse normal stress level in his approaching boundary layer. Amatucci's[13] data display amplifications of roughly 3 and 8 times the peak transverse normal stress levels in the approaching boundary layers for his upper (Mach 2.56) and lower (Mach 2.05) rapidly expanded planar shear layers, respectively. The peak transverse normal stress amplification factor in the present study lies within the range cited above.

Turbulent Kinetic Energy

The turbulent kinetic energy, TKE, distribution (where the spanwise normal stress is assumed equal to the transverse normal stress) is displayed in Figure 8. The turbulent kinetic energy contours resemble closely the streamwise normal stress contours, Figure 6. The streamwise normal

stress is much larger than its transverse counterpart over most of the flowfield and so dominates the turbulent kinetic energy. Therefore, like the streamwise normal stress, the turbulent kinetic energy is much larger in the upper shear layer than in the lower shear layer and peaks near reattachment.

Unlike the present study, both Kuntz and Amatucci approximated the spanwise normal stress as the average of the streamwise and transverse normal stresses. This average definition may overstate the actual value of the TKE. Herrin,[14] however, was able to measure all three velocity components and, therefore, determined the TKE without any approximations. The maximum TKE in the present study, $0.07U_\infty^2$, exceeds the maximum value of $0.042U_\infty^2$ Herrin found upstream of reattachment for his axisymmetric expansion-induced free shear layer. The reasons for the difference in the TKE values in the present study and those of Herrin are the additional mechanisms discussed earlier for turbulence production present in shock wave-boundary layer interactions that are not present in rapidly expanded compressible shear layers.

The maximum TKE value in the current study is also larger than the $0.05U_\infty^2$ maximum TKE value reported by Kuntz[5] after reattachment in his 24° compression corner (the largest ramp angle tested and largest TKE value reported). The larger equivalent corner angle (28°) in the present study than the actual corner angle of Kuntz's flow may also explain the larger TKE level of the present study. In addition a larger peak may have occurred near reattachment but upstream of the region of measurement in Kuntz's study. Amatucci[13], however, reports maximum TKE values occurring close to reattachment of approximately $0.06U_\infty^2$ and $0.07U_\infty^2$ for his upper (Mach 2.56 freestream) and lower (Mach 2.05 freestream) expansion-induced planar free shear layers, respectively. Both of these peak values are close to the peak value observed in the current study.

Residual Shock Motion

The transverse normal stress contour plot, Figure 7, indicates a narrow band of increased turbulence that lies well above the upper shear layer. By comparing the location of this band to the contour plot of mean streamwise velocity, Figure 2, this region is seen to correspond to the

location of the separation shock wave. This increase in apparent transverse normal stress immediately downstream of the shock wave may be due to one of three factors: (1) small-scale shock unsteadiness that is below the resolution limit of the conditional analysis technique (± 1.6 mm); (2) particle lag downstream of the shock due to the finite sized LDV seed particles (2.8 mm extent in the streamwise direction); or (3) the slight polydisperse size distribution of seed particles.

Bloomberg[18] compared LDV data acquired using the same seeder and silicone oil used in this study with data acquired using monodisperse polystyrene latex particles behind an oblique shock wave slightly stronger than the separation shock in the current study. Bloomberg concluded that false turbulence due to the slight polydispersion of silicone oil droplet sizes was small compared to the overall turbulence levels in his flowfield. For this reason, the small increase in turbulence downstream of the separation shock wave in the current experiment is most probably not due to a polydisperse size distribution of seed particles.

Across an oblique shock wave, the tangential velocity component (relative to the shock front) is unaltered, but the normal velocity component is dramatically decreased. One may then expect that small-scale shock motion below the resolution limit of the conditional analysis technique would result in bimodal distributions in the velocity component normal to the shock at locations near the mean shock location (depending on whether the instantaneous shock location is ahead of or behind the measurement location). Figure 9 presents velocity histograms from the green LDV channel obtained at six different transverse (y) locations near the separation shock. The data in Figure 9 have been conditionally analyzed to contain only velocity realizations occurring when the shock foot was between the two pressure transducers, but have not been velocity debiased.

For these particular measurements the green LDV channel was aligned at 44° clockwise from the x-axis and the separation shock wave is inclined at a 32° angle counter-clockwise from the x-axis. (Two slightly different alignments were used during the data collection for this study, but as noted in the equipment section both were approximately $\pm 45°$ to the x-axis.) This particular

alignment results in the green LDV channel being aligned at 76° to the separation shock (a perfect 90° alignment would simply further accentuate the observed bimodal nature of the velocity histograms). Figure 9 clearly shows that, at locations above (y = +18 mm) and below (y = +13 mm) the shock, a roughly unimodal velocity distribution occurs. As the mean shock location is approached from either above or below, however, the velocity distribution becomes increasingly bimodal with maximum bi-modality occurring at y = +15 mm.

One may estimate from the histograms shown in Figure 9 that significant bimodality exists over a transverse region of approximately 3 mm (y = +14 mm to y = +17 mm). This equates to a streamwise shock motion distance of 4.8 mm. Together, the resolution limit of the conditional analysis algorithm and particle lag are conservatively estimated to produce significant uncertainty over a streamwise region of roughly 6.0 mm. This length scale agrees with the length scales estimated from the velocity histograms in Figure 9 and from the relatively constant width band of increased apparent transverse normal stress near the shock location in Figure 7. Smits and Muck[6] also noted small peaks at the shock location in profiles of mass-weighted streamwise normal stress obtained with hot-wires in their compression corner flows without conditional analysis. Smits and Muck concluded that, like this study, the region of shock motion has an approximately constant length, independent of distance from the wall.

Reynolds Shear Stress

The dimensionless primary Reynolds shear stress distribution, $-\langle u'v' \rangle / U_\infty^2$, is displayed in Figures 10 and 11. Since the primary Reynolds shear stress is negative in boundary layers, the negative of the shear stress is often presented, i.e. $-\langle u'v' \rangle$. This study follows this convention in all shear stress plots. As can be seen from Figures 10 and 11, the shock-induced separation increases the magnitude of the primary shear stress. Figure 10 also indicates a significant region of positive shear stress in the shock-separated free shear layer. In their compression corner experiment, Smits and Muck[6] reported only negative values of $\langle u'v' \rangle$ and increases in the peak magnitude of the shear stress of up to 13 times the peak level in the approaching boundary layer. In the current experiment, a band

of negative shear stress may be seen lying above the shear layer in Figure 10. By comparing Figure 10 with the contour plot of the streamwise mean velocity (Figure 2), this band of negative shear stress is again seen to coincide with the separation shock wave and is most likely due to particle dynamics and shock wave motion below the resolution limit of the conditional analysis technique.

The compression corner studies of Ardonceau,[4] Kuntz,[5] Smits and Muck,[6] and the expansion-induced separation studies of Amatucci[13] and Herrin[14] contain peak negative shear stress values of $-0.002U_\infty^2$, $-0.018U_\infty^2$, $-0.006U_\infty^2$, $-0.042U_\infty^2$, and $-0.012U_\infty^2$, respectively. The peak positive and negative shear stress values of $+0.007U_\infty^2$ and $-0.007U_\infty^2$, respectively, that are found inside the shock-induced shear layer of the present study exceed the peak values recorded in the separated compression corners of Ardonceau and Smits and Muck, but lie well below the value reported by Kuntz for his compression corner flows after reattachment. We believe that the scale of the shear stress plots in Ardonceau's article may be in error and that the true peak shear stress in this work may actually be an order of magnitude larger than the value cited above. The values of both Amatucci and Herrin in expansion-induced shear layers lie well above those of the present study, and indicate that the underlying turbulent structures in rapidly expanded compressible free shear layers differ from those in shock wave-boundary layer interactions.

Figure 11 clearly shows both the positive and negative shear stress peaks at the $x = 0$ and $x = +12.5$ mm locations (the two plotted profiles through the free shear layer). The top negative peak in $<u'v'>$ in the $x = 0$ and $x = +12.5$ mm profiles is due to residual shock motion. The $x = +12.5$ mm profile shows a second large positive shear stress peak coinciding with the lower shear layer. This positive peak is expected, since the mean velocity profile has a negative slope inside the lower shear layer. Examining Figure 10, one sees that the region of positive shear stress within the shock-induced free shear layer only exists between separation and reattachment. Examining the $x = +30$ mm profile in Figure 11, one sees that single negative and positive peaks appear symmetrically across the wake. This is expected due to the deficit in the mean velocity

profiles inside the wake, and matches the shear stress profiles found in other wake studies.

Can a Positive Shear Stress Exist?

The region of positive shear stress in the upper-half (high-speed side) of the shock-separated shear layer is not expected since the slope of the mean velocity profile there is positive. If a fluid element moves up or down between the high-speed and low-speed regions inside a shear layer with a positively sloped mean velocity profile, then the instantaneous shear stress, $u'v'$, for the fluid element is expected to be negative. This argument, however, neglects the potential effects of coherent turbulent structures in the shear layer which physically allow a region of positive $<u'v'>$ to exist.

The separated compression corner studies of Ardonceau[4] and Smits and Muck[6] include measurements of the free shear layer prior to reattachment, but did not indicate a positive shear stress region. This absence may be due to the difference in incoming boundary layer thickness relative to the size of the separated region or to the presence of a rigid downstream boundary rather than a second fluid stream as in the present study. The absence of a positive shear stress region in the data of Ardonceau and Smits and Muck may also be due to the larger equivalent corner angle (28°) of the present flow than the corner angles in their two studies.

The disappearance of the positive shear stress region in the outer portion of the upper shear layer at reattachment may explain why Kuntz,[5] who made no measurements upstream of reattachment, did not measure a positive shear stress region in any of the compression corners he investigated. Similarly, the additional mechanisms for turbulence amplification and alteration present in shock wave-boundary layer interactions may explain why the expansion-induced free shear layer studies of Amatucci[13] and Herrin[14] include only a negative shear stress region.

A positive shear stress peak occurs at all but one of the 13 streamwise traverse locations in the shock-induced free shear layer of the current study. The locations of these positive peaks form a straight line along this free shear layer. Furthermore, these shear stress measurements (like the rest of the data presented in this study) are repeatable over a period of several months. Finally, other turbulence quantities, including

higher order statistical moments such as the <u'u'u'> triple product extracted from the same velocity ensembles used to calculate the shear stress, display the expected trends. This persistence and uniformity of these shear stress data, combined with the presence of expected trends in other quantities, provide evidence that the positive shear stress regions inside the upper shear layer are a true physical phenomenon and not an artifact of the measurement technique. However, if the instantaneous velocity data are rotated to coordinates parallel and perpendicular to the local shear layer direction, rather than the tunnel coordinates (Figure 1) used in this paper, the positive shear stress values might disappear. This will be the subject of future work, but preliminary analysis indicates that this would cause the shear stress values to approach small positive values rather than significant negative values.

Counter-rotating vortex pairs oriented in the streamwise direction may exist inside the shock-separated free shear layer of the present study. These vortex pairs are similar to the Taylor-Görtler vortices that are known to form in boundary layers on walls with concave curvature. The shock-separated shear layer in the present study also displays a concave curvature, so an instability mode similar to the Taylor-Görtler mode may be expected. These vortex pairs are believed to produce powerful ejections of fluid (Quadrant I: $u' > 0$, $v' > 0$) that result in the observed region of positive shear stress. This vortex theory was first proposed by Palko[15] in conjunction with a further detailed analysis and discussion of the shock-separated shear layer turbulence structure that provides additional evidence of such vortex pairs. This analysis will be the subject of a future paper.

CONCLUSIONS

This study presents to our knowledge the first turbulence measurements obtained in a shock-separated shear layer and the first turbulence measurements in any two-dimensional, shock-separated free shear layer to account directly for shock wave unsteadiness.[25] Detailed experimental data are presented to allow verification of improved numerical solutions, including improved turbulence models for shock wave-boundary layer interactions. The results show that shock-induced separation dramatically increases the Reynolds normal stresses in the upper shear layer. The streamwise normal stress is much larger than the transverse normal stress and, consequently, dominates the turbulent kinetic energy through most of the flowfield (assuming that the transverse and spanwise normal stress magnitudes are similar, as has been found in previous related studies).

The subsequent reattachment of the two shear layers dramatically decreases the turbulence levels. The developing wake is dominated by a further reduction in all turbulent stresses. However, large values of the transverse normal stress are seen to persist well downstream of reattachment, possibly indicating a shift in turbulent energy from the streamwise component to the transverse (and presumably spanwise) components through recompression and reattachment. As in expansion-separated planar shear layers, the streamwise normal stress is seen to peak at reattachment rather than upstream of reattachment as in axisymmetric expansion-induced shear layers. This provides further evidence of the stabilizing effects of lateral streamline convergence on the turbulent flowfield for the axisymmetric case. Interestingly, regions of both positive and negative Reynolds shear stress exist inside the shock-separated shear layer. The positive shear stress region is formed at separation and disappears at reattachment, and may be explained by the presence of streamwise-oriented counter-rotating vortex pairs similar in nature to Taylor-Görtler vortices. Finally, velocity histograms obtained in the immediate neighborhood of the shock indicate that the range of unsteady shock motion has a relatively constant width irrespective of distance from the wall.

ACKNOWLEDGMENTS

REFERENCES

[1]Adamson, T.C., Jr. and A.F. Messiter, "Analysis of Two-Dimensional Interactions Between Shock Waves and Boundary Layers," *Annual Review of Fluid Mechanics*, Vol. 12, 1980, pp. 103-138.

[2]Green, J.E., "Interactions Between Shock Waves and Turbulent Boundary Layers," *Progress in Aerospace Sciences*, Vol. 11, 1970, pp. 235-340.

[3]Dolling, D.S., "Fluctuating Loads in Shock Wave/Turbulent Boundary Layer Interaction: Tutorial and Update," AIAA Paper 93-0284, 1993.

[4]Ardonceau, P.L., "The Structure of Turbulence in a Supersonic Shock-Wave/Boundary-Layer Interaction," *AIAA Journal*, Vol. 22, No. 9, 1984, pp. 1254-62.

[5]Kuntz, D.W., "An Experimental Investigation of the Shock Wave-Turbulent Boundary Layer Interaction," Ph.D. Thesis, University of Illinois at Urbana-Champaign, 1985.

[6]Smits, A.J. and K.C. Muck, "Experimental Study of Three Shock Wave/Turbulent Boundary Layer Interactions," *Journal of Fluid Mechanics*, Vol. 182, 1987, pp. 291-314.

[7]Selig, M.S., J. Andreopoulos, K.C. Muck, J.P. Dussauge, and A.J. Smits, "Turbulence Structure in a Shock Wave/Turbulent Boundary Layer Interaction," *AIAA Journal*, Vol. 27, No. 7, 1989, pp. 862-869.

[8]Palko, C.W. and J.C. Dutton, "A Method for Separating Shock Wave Motion and Turbulence in LDV Measurements," AIAA Paper 97-1919, 1997.

[9]Anyiwo, J.C. and D.M. Bushnell, "Turbulence Amplification in Shock Wave/Boundary Layer Interaction," *AIAA Journal*, Vol. 20, 1982, pp. 893-899.

[10]Hussaini, M.Y., F. Collier, and D.M. Bushnell, "Turbulence Alteration Due to Shock Motion," *IUTAM Symposium on Turbulent Shear Layer/Shock Wave Interaction*, Palaiseau, France, pp. 371-382, 1985.

[11]Selig, M.S. and A.J. Smits, "Effect of Periodic Blowing on Attached and Separated Supersonic Turbulent Boundary Layers," *AIAA Journal*, Vol. 29, No. 10, 1991, pp. 1651-1658.

[12]Bradshaw, P., "The Effect of Mean Compression or Dilatation on the Turbulent Structure of Supersonic Boundary Layers," *Journal of Fluid Mechanics*, Vol. 63, No. 3, 1974, pp. 449-464.

[13]Amatucci, V.A., "An Experimental Investigation of the Two-Stream, Supersonic, Near-Wake Flowfield Behind a Finite-Thickness Base," Ph.D. Thesis, University of Illinois at Urbana-Champaign, 1990.

[14]Herrin, J.L., "An Experimental Investigation of Supersonic Axisymmetric Base Flow Including the Effects of Afterbody Boattailing," Ph.D. Thesis, University of Illinois at Urbana-Champaign, 1993.

[15]Palko, C.W., "Conditionally Analyzed Mean Velocity and Turbulence Measurements in a Plume-Induced Boundary Layer Separated Flowfield," Ph.D. Thesis, University of Illinois at Urbana-Champaign, 1998.

[16]Shaw, R.J., "An Experimental Investigation of Unsteady Separation Shock Wave Motion in a Plume-Induced, Separated Flowfield," Ph.D. Thesis, University of Illinois at Urbana-Champaign, 1995.

[17]Jenson, L., "Automatic Digital Signal Processing for LDV," in *Proceedings of the 4th International Conference on Laser Anemometry Advances and Applications*, Cleveland, Ohio, 1991, pp. 517-628.

[18]Bloomberg, J.E., "An Investigation of Particle Dynamics Effects Related to LDV Measurements in Compressible Flows," M.S. Thesis, University of Illinois at Urbana-Champaign, 1989.

[19]Carlson, D.J. and R.F. Hoglund, "Particle Drag and Heat Transfer in Rocket Nozzles," *AIAA Journal*, Vol. 2, No. 11, 1964, pp. 1980-1984.

[20]Herrin, J.L. and J.C. Dutton, "An Investigation of LDV Velocity Bias Correction Techniques for High-Speed Separated Flows," *Experiments in Fluids*, Vol. 15, No. 4/5, 1993, pp. 354-363.

[21]Sun, C.C. and M.E. Childs, "A Modified Wall Wake Velocity Profile for Turbulent Compressible Boundary Layers," *Journal of Aircraft*, Vol. 10, No. 6, 1973, pp. 381-383.

[22]Bogdanoff, D.W., "Compressibility Effects in Turbulent Shear Layers," *AIAA Journal*, Vol. 21, No. 6, 1983, pp. 926-927.

[23]Papamoschou, D. and A. Roshko, "The Compressible Turbulent Shear Layer: An Experimental Study," *Journal of Fluid Mechanics*, Vol. 197, 1988, pp. 453-477.

[24]Herrin, J.L. and J.C. Dutton, "The Turbulence Structure of a Reattaching Axisymmetric Compressible Free Shear Layer," *Physics of Fluids*, Vol. 9, 1997, pp. 3502-3512.

[25]Dussauge, J.P. and P. Dupont, "Experimental Evidences of Compressibility Effects on Turbulence in High Speed Flows," in *Transitional and Turbulent Compressible Flows*, L.D. Kral, E.F. Spina, and C. Arakawa, eds., ASME FED-Vol. 224, 1995, pp. 185-192.

Table 1 Approach boundary layer properties

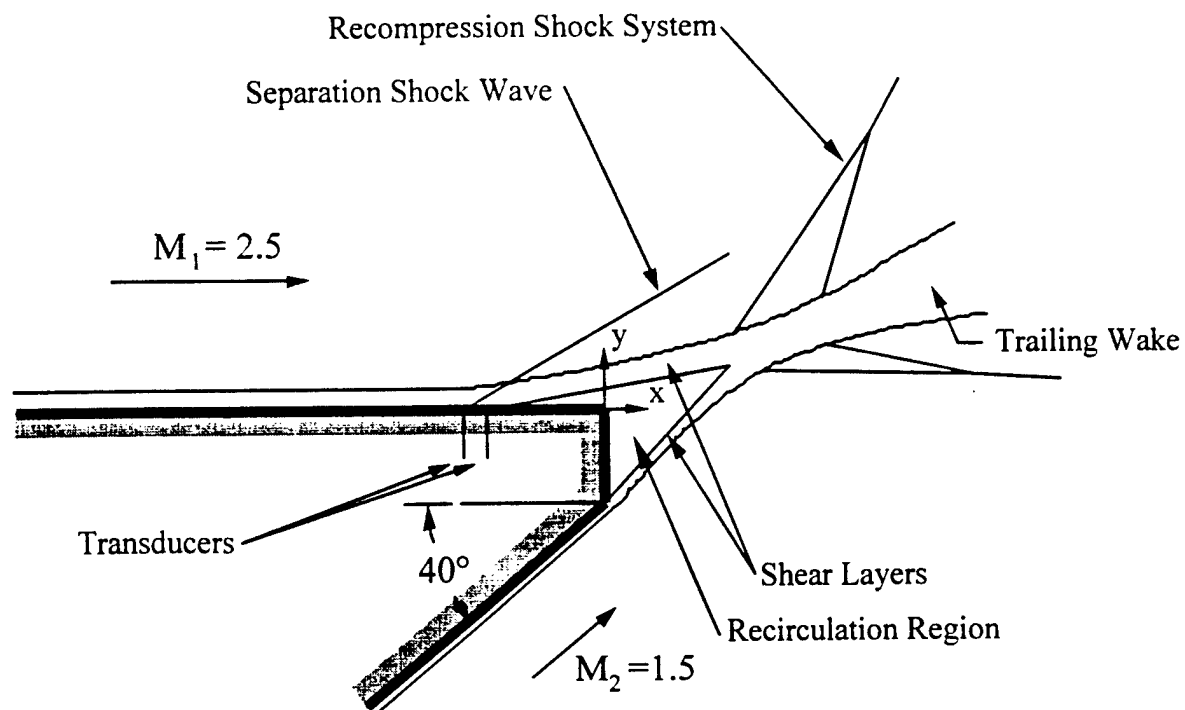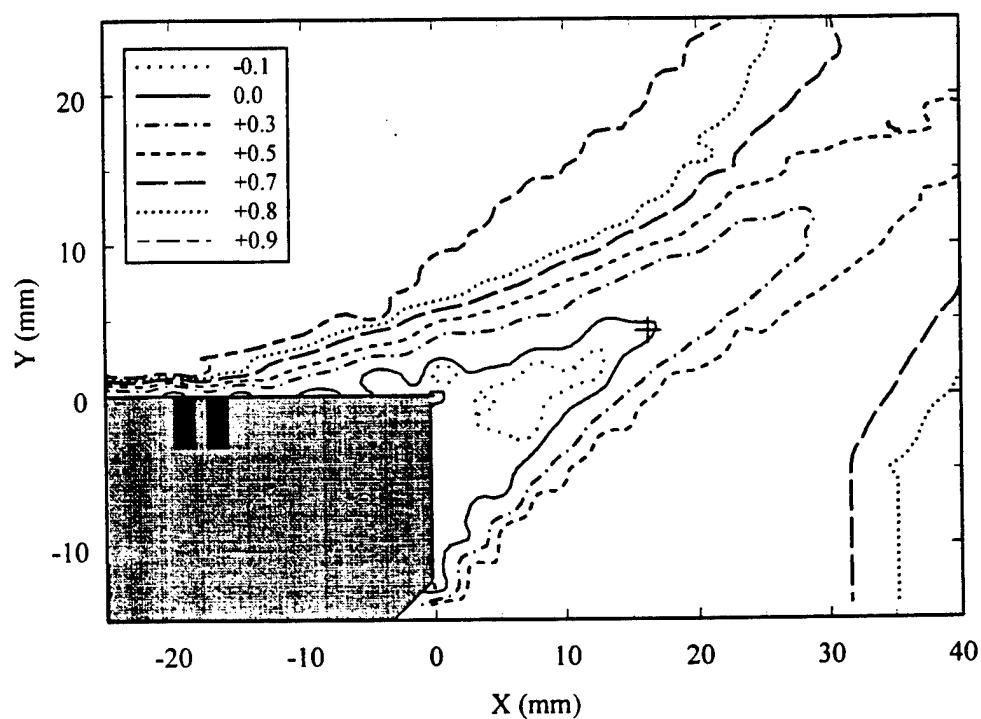|	
Boundary layer thickness, δ (mm)	3.2
Displacement thickness, δ^* (mm)	0.78
Momentum thickness, θ (mm)	0.21
Shape factor, $H = \delta^*/\theta$	3.7
Wake strength factor, Π	0.86
Skin friction coefficient, C_f	0.0016
Friction velocity, u_τ (m/s)	23.6

Figure 1 Flowfield schematic

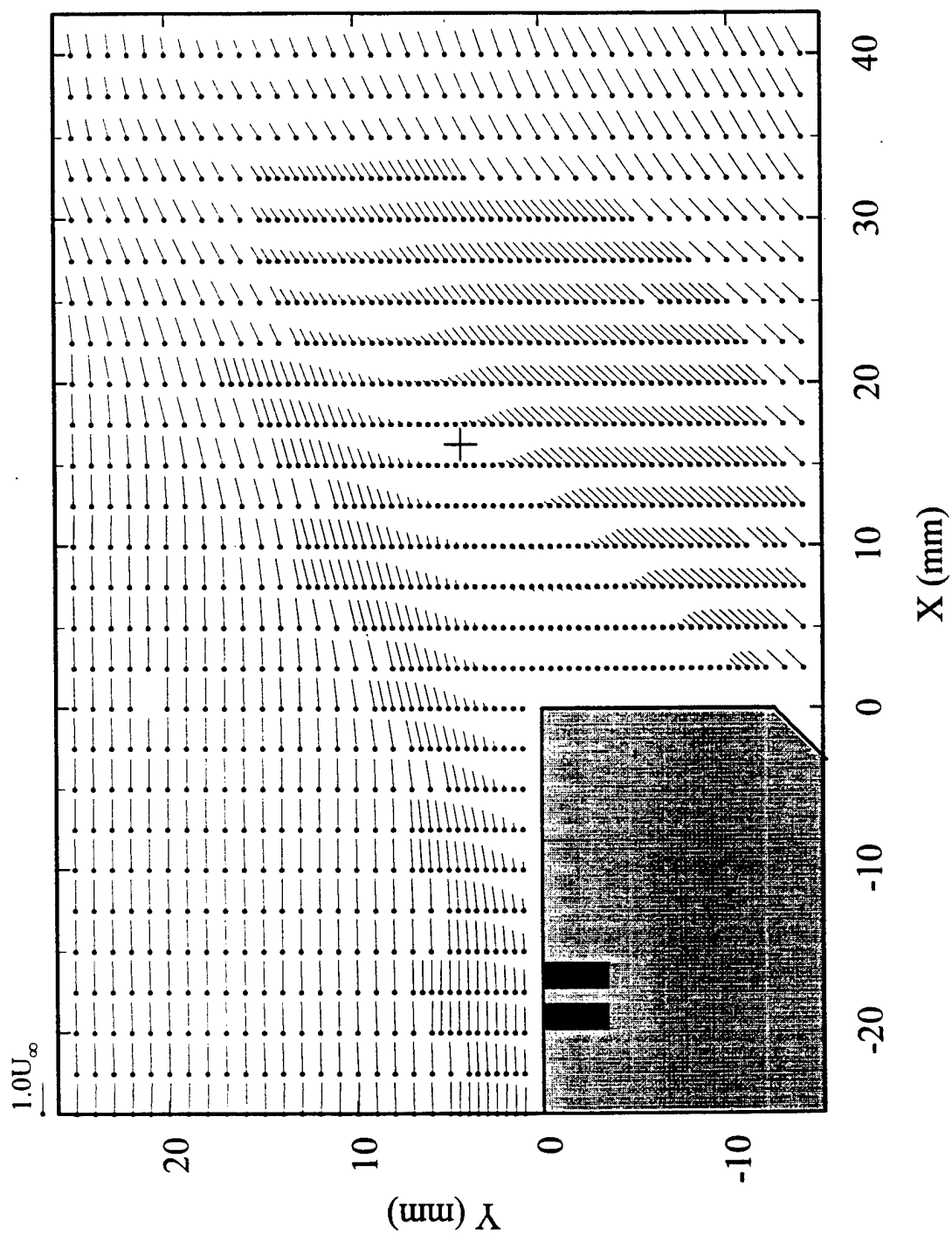**Figure 2 Mean streamwise velocity field, U/U∞**
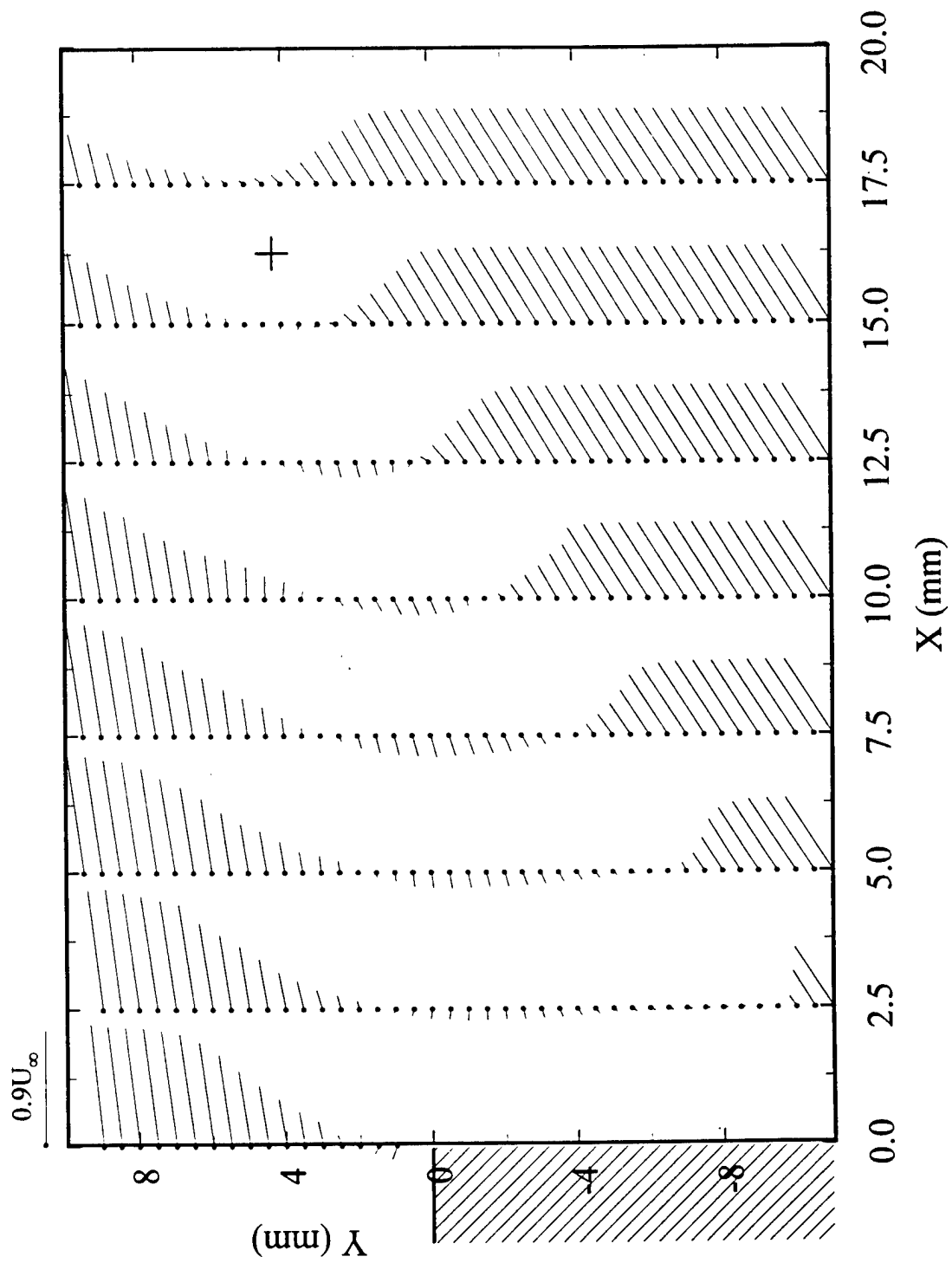
Figure 3 Mean velocity vector field

13
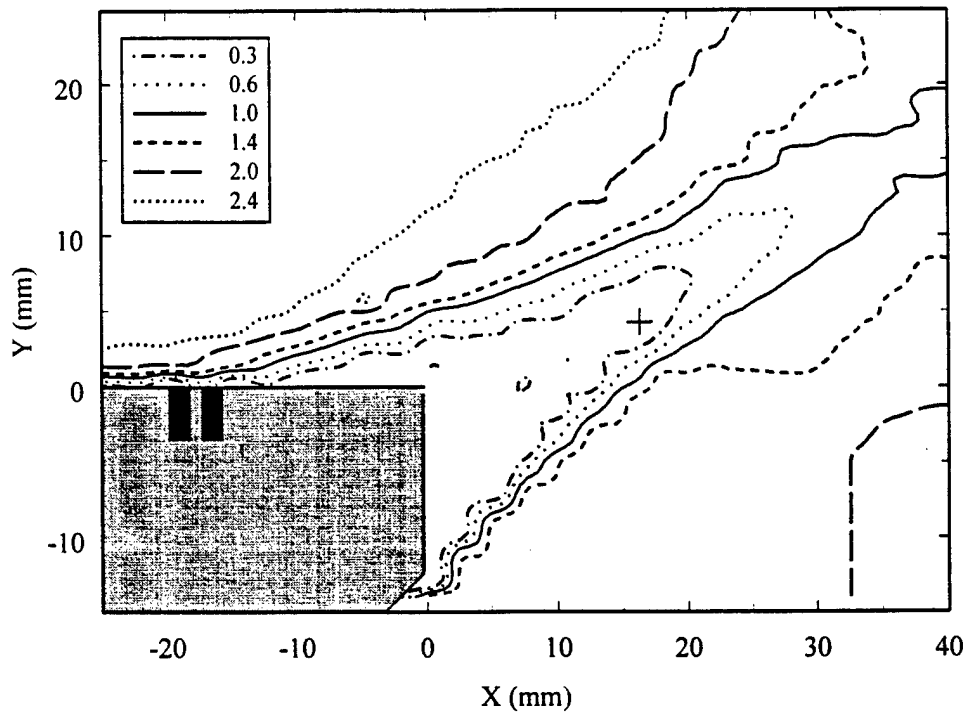
Figure 4 Base region mean velocity vector field

14

Figure 5 Mean Mach number field

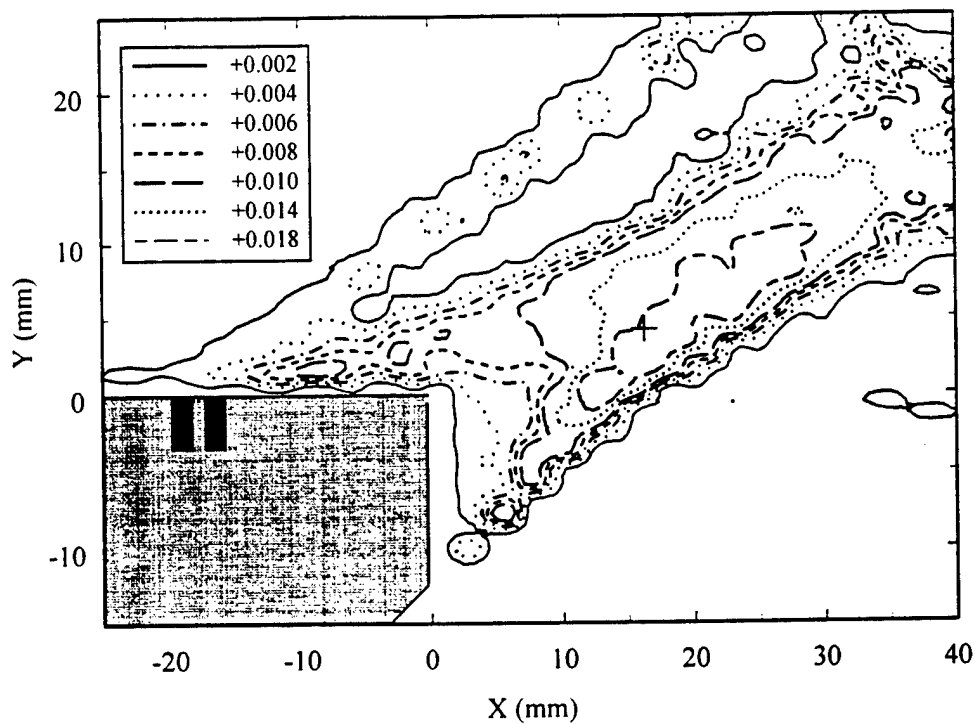**Figure 6 Streamwise normal stress field, $<u'^2>/U_\infty^2$**

Figure 7 Transverse normal stress field, $<v'^2>/U_\infty^2$

Figure 8 Turbulent kinetic energy (TKE) field, $(<u'^2>+2<v'^2>)/2U_\infty^2$
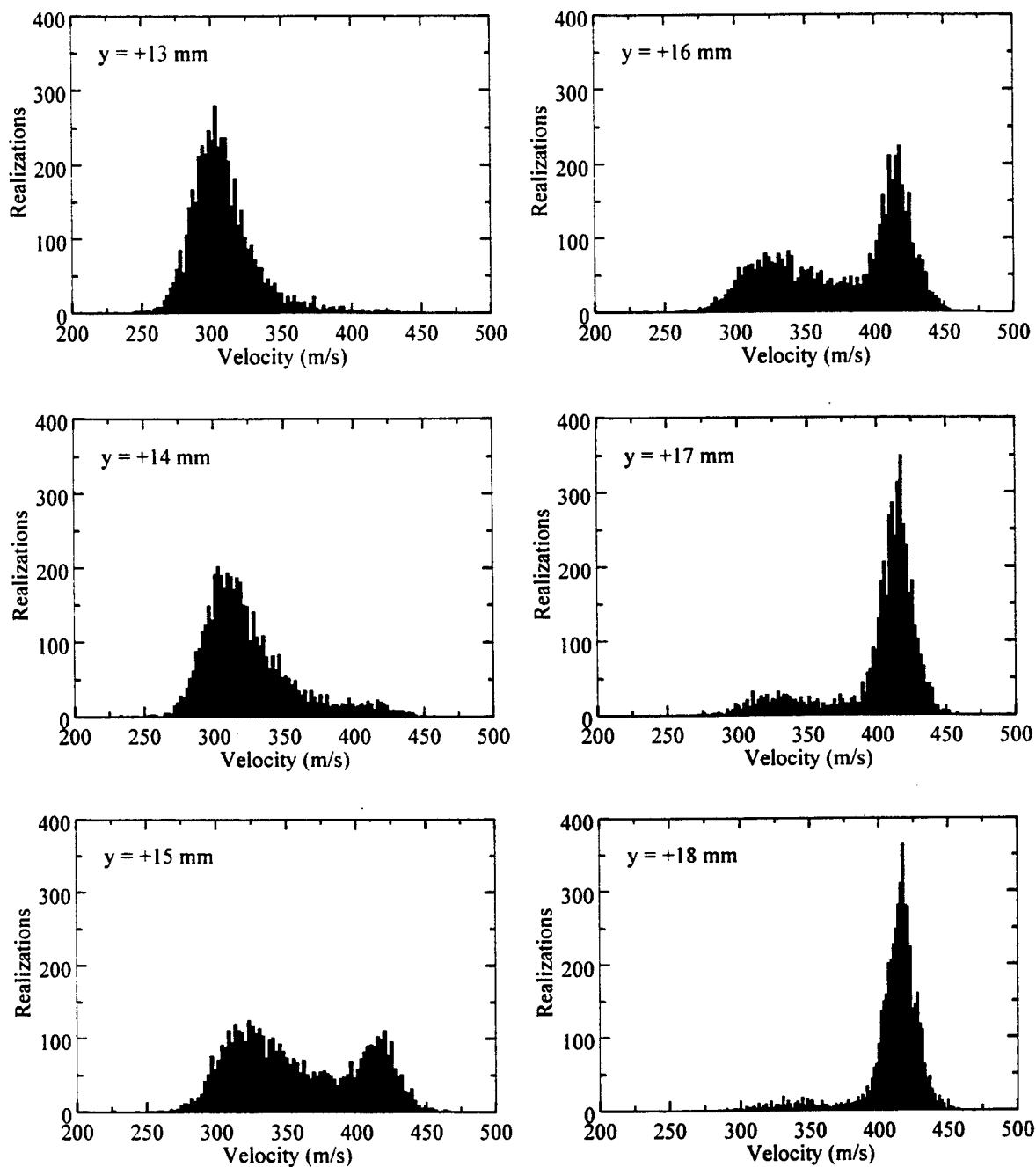
Figure 9 Green LDV channel velocity histograms near shock location (x=+7.5 mm)

Figure 10 Reynolds shear stress field, $-<u'v'>/U_\infty^2$

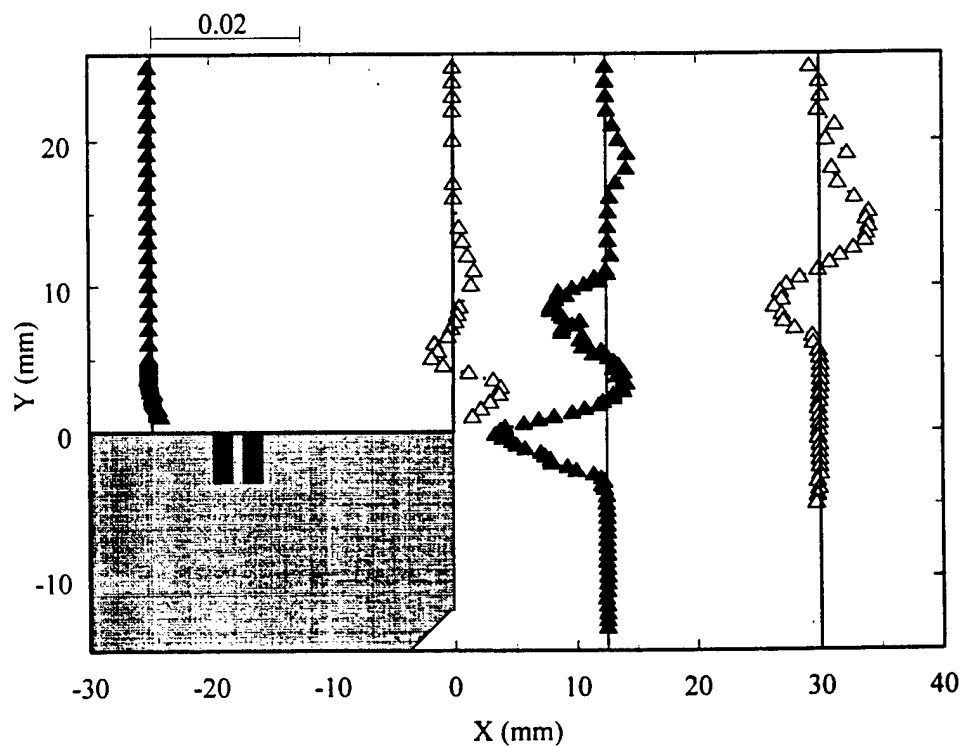**Figure 11 Reynolds shear stress profiles, $-<u'v'>/U_\infty^2$**

18

APPENDIX A.23

AN EXPERIMENTAL INVESTIGATION OF SUPERSONIC AXISYMMETRIC BASE FLOWS INCLUDING THE EFFECTS OF AFTERBODY BOATTAILING

Ph.D. Thesis

Department of Mechanical and Industrial Engineering

University of Illinois at Urbana-Champaign

July 1993

by

J. L. Herrin

AN EXPERIMENTAL INVESTIGATION OF SUPERSONIC AXISYMMETRIC BASE FLOWS INCLUDING THE EFFECTS OF AFTERBODY BOATTAILING

J. L. Herrin, Ph.D. Thesis
Department of Mechanical and Industrial Engineering
University of Illinois at Urbana-Champaign

ABSTRACT

An experimental investigation of the near-wake flowfield downstream of blunt-based axisymmetric bodies in supersonic flow has been conducted. Using a blowdown-type wind tunnel designed specifically for this purpose, experiments were conducted at a nominal approach Mach number of 2.5 and a unit Reynolds number of 51 (10^6) per meter. Two different axisymmetric afterbodies were examined in the study: a circular cylinder was used as a baseline configuration, and a conical boattailed afterbody with a boattail angle of five degrees and a boattail length of one afterbody radius was used to investigate the effects of afterbody boattailing on the fluid dynamic processes in the near-wake. Neither afterbody contained a central jet so that the base flowfield in unpowered, supersonic flight was simulated. The primary objective of the research program was to enhance the understanding of the fluid dynamic processes inherent to axisymmetric base flows by obtaining and analyzing detailed, non-intrusive experimental data including flow visualization photographs, static pressure measurements, and mean velocity and turbulence data throughout the near-wake. Of special significance in the current research is the detailed turbulence information obtained with laser Doppler velocimetry (LDV) since these data are virtually nonexistent in supersonic base flows and provide new insight into the physics of these complex flows. In addition, the present data form a substantial data base which can be used to advance and improve theoretical and numerical base flow modeling techniques.

The static pressure measurements on the base and afterbody of each model indicate a relatively constant pressure across the base with the addition of the boattail resulting in a decrease in the base drag coefficient of 16% from the baseline cylindrical afterbody. The net afterbody drag coefficient (boattail + base contributions) was reduced by 21% which shows the usefulness of

afterbody boattailing as a practical method to reduce afterbody drag in supersonic, axisymmetric flow. The mean velocity and turbulence fields in the near-wake of each afterbody were investigated with LDV. In general, the near-wake flowfield can be characterized by large turbulence levels in the separated shear layer, relatively large reverse velocities in the recirculation region, and gradual recompression/realignment processes as the shear layer converges on the axis of symmetry. The shear layer development was found to be dependent on the conditions immediately downstream of the base corner separation point (upstream history effect). Furthermore, the centered expansion at the base corner reduced the turbulence levels in the outer region of the shear layer relative to the approach boundary layer but enhanced the mixing and entrainment along the fluid-fluid interface between the shear layer and the recirculating region which results in large turbulence levels along the inner edge of the shear layer. The shear layer growth rate is initially large due to substantial mass entrainment from the recirculation region near the inner edge, but further downstream, a self-similar state is reached where growth rates are significantly reduced. In general, the effects of afterbody boattailing on the near-wake flowfield include a weaker expansion at the base corner separation point (less distortion of the shear layer and reduced turbulence production near the inner edge), reduced turbulence intensity and Reynolds shear stress levels throughout the near-wake (reduced mass entrainment along the length of the shear layer resulting in a higher base pressure), and a mean velocity field which is qualitatively similar to that of the cylindrical afterbody.

APPENDIX A.24

AN EXPERIMENTAL INVESTIGATION OF UNSTEADY SEPARATION SHOCK WAVE MOTION IN A PLUME-INDUCED, SEPARATED FLOWFIELD

Ph.D. Thesis

Department of Mechanical and Industrial Engineering

University of Illinois at Urbana-Champaign

August 1995

by

R. J. Shaw

AN EXPERIMENTAL INVESTIGATION OF UNSTEADY SEPARATION SHOCK WAVE MOTION IN A PLUME-INDUCED, SEPARATED FLOWFIELD

R. J. Shaw, Ph.D. Thesis
Department of Mechanical and Industrial Engineering
University of Illinois at Urbana-Champaign

ABSTRACT

An experimental investigation of the unsteady separation shock wave motion in plume-induced, boundary layer separated (PIBLS) flowfields has been conducted. The PIBLS flowfields were created in a blowdown-type wind tunnel designed specifically to produce PIBLS in a planar, two-stream, supersonic flow. In this unique wind tunnel, separation of the freestream boundary layer upstream of the base plane was accomplished by utilizing an angle-induced separation geometry in the wind tunnel design in addition to operating the wind tunnel at jet-to-freestream static pressure ratios (JSPRs) greater than unity. In essence, the wind tunnel design consisted of a Mach 1.5 inner-jet flow angled at 40 degrees with respect to a Mach 2.5 freestream flow in the presence of a 0.5-inch thick base height. By throttling the stagnation pressure of the inner-jet flow, PIBLS flowfields, with nominal separation point locations ranging from two (JSPR≈1.7) to six (JSPR≈2.3) or more boundary layer thicknesses upstream of the base plane, were produced in the wind tunnel. The separation process associated with all of these PIBLS flowfields was observed by flow visualization techniques to be unsteady, and the separation shock wave that accompanied the separation process was found to exhibit large-scale (on the order of the incoming boundary layer thickness) motion in the streamwise direction.

The primary objective of the current research program was to understand the unsteady characteristics of the separation shock wave motion present in the PIBLS flowfields by obtaining and analyzing detailed, non-intrusive experimental data including flow visualization photographs, surface flow visualization patterns, mean static pressure measurements, and instantaneous pressure fluctuation measurements throughout the region of shock wave motion (called the intermittent region). Since the vast majority of the statistical properties of the shock wave motion were

computed from the fast-response pressure transducer measurements, the instantaneous pressure fluctuation measurements were of primary importance in the study. In recent years, similar measurements have been used to characterize the unsteady separation shock wave motion in shock wave/boundary layer interactions (SWBLIs) produced by solid boundary protuberances (i.e., compression ramps, circular cylinders, sharp- and blunt-edged fins, etc.). However, such data are virtually nonexistent in a plume-induced interaction and, therefore, the current data are quite unique.

From standard time series and conditional analysis methods applied to the pressure fluctuation measurements, the statistical properties of the shock wave motion were determined over the intermittent region. In general, most (70% to 80%) of the energy contained in the pressure fluctuations caused by the shock wave motion was distributed over the frequency range below 1 kHz, the mean frequency of the shock wave motion ranged between 1.3-1.5 kHz, and the most probable shock wave frequency occurred between approximately 1-4 kHz over the intermittent region. The mean shock wave velocities, when normalized by the freestream velocity, were found to be 0.034-0.035 over the intermittent region in the PIBLS flowfields. In general, the length scale of the intermittent region increased as the JSPR increased, varying from 0.32-0.37 inches (2.6δ to 3.0δ) at a JSPR of 1.95 to 0.68-0.69 inches (5.4δ to 5.5δ) at a JSPR of 2.41. The maximum zero-crossing frequency (the average number of shock wave crossings per second) of the shock wave motion was approximately 500-600 Hz, depending upon the JSPR, and occurred near the middle of the intermittent region.

The shock wave motion was found to be responsible for producing large pressure fluctuations over the intermittent region in these PIBLS flowfields. The standard deviation of the pressure fluctuations, when nondimensionalized by the local mean pressure, reached a maximum value of 0.22 near the middle of the intermittent region. The strength of the unsteady shock wave motion, determined as the ratio of the maximum standard deviation of the pressure fluctuations over the intermittent region to the mean pressure difference across the intermittent region, was calculated to be 0.43 for the current PIBLS flowfields. Both of these quantities demonstrate that

the unsteady pressure loading caused by the shock wave motion has essentially the same magnitude in plume-induced separated flowfields as in SWBLI flowfields produced by solid boundary protuberances.

APPENDIX A.25

AN EXPERIMENTAL INVESTIGATION OF THE EFFECTS OF BASE BLEED
IN AXISYMMETRIC SUPERSONIC FLOW

Ph.D. Thesis

Department of Mechanical and Industrial Engineering

University of Illinois at Urbana-Champaign

July 1996

by

T. Mathur

AN EXPERIMENTAL INVESTIGATION OF THE EFFECTS OF BASE BLEED IN AXISYMMETRIC SUPERSONIC FLOW

T. Mathur, Ph.D. Thesis
Department of Mechanical and Industrial Engineering
University of Illinois at Urbana-Champaign

ABSTRACT

Base bleed is a technique wherein a small quantity of fluid is injected into the base region of a projectile to reduce the base drag. The effects of base bleed on the near-wake flowfield of a cylindrical afterbody in a Mach 2.5 flow have been investigated in the present study. This experimental study is aimed at better understanding the complex fluid dynamic interactions occurring in the near-wake due to base bleed and is motivated by the lack of detailed velocity and turbulence data in this flowfield. The experimental techniques used include static pressure measurements, schlieren and shadowgraph photography, and two-component laser Doppler velocimetry (LDV). The comprehensive LDV mean velocity and turbulence measurements obtained during this study provide valuable insight into the physics of the base bleed mechanism and constitute a benchmark data set to aid analytical and computational efforts in modeling and predicting supersonic base flows.

Static pressure measurements show that with increasing bleed flow rate, the average base pressure increases initially, attains a peak value near an injection parameter of $I = 0.0148$, and then decreases with further increase in I. The peak base pressure ratio at the optimum bleed condition is 18.5% higher than the blunt base case and 5.7% higher than for a 5 degree boattailed afterbody. Axial LDV traverses show peaks in turbulent kinetic energy along the centerline at the forward and rear stagnation point locations. Centerline measurements also indicate the near-disappearance of the primary recirculation region near the optimum bleed condition. Detailed mean velocity and turbulence data were obtained in the entire near-wake flowfield for three different bleed cases corresponding to low bleed, slightly pre-optimal bleed, and slightly post-optimal bleed conditions. These measurements indicate that the bleed flow provides at least some of the fluid

required for shear layer entrainment and shields the base annulus from the outer shear layer and the primary recirculation region, leading to an increase in base pressure. There is an overall reduction in turbulence levels throughout the base bleed flowfields relative to the near-wake flowfields of blunt-based and boattailed afterbodies. With increasing bleed, the formation of a strong bleed jet shear layer and secondary recirculation region near the base annulus offsets the benefits of base bleed, leading to a drop in the base pressure. At all bleed conditions, the Reynolds normal stress distribution is highly anisotropic with the axial component dominating the near-wake turbulence field. The net benefits of base bleed are maximized at the optimum bleed condition, which corresponds to the highest base pressure, the disappearance of the primary recirculation region, and the lowest turbulence and entrainment levels in the near-wake flowfield.

APPENDIX A.26

CONDITIONALLY ANALYZED MEAN VELOCITY AND TURBULENCE MEASUREMENTS IN A PLUME-INDUCED BOUNDARY LAYER SEPARATED FLOWFIELD

Ph.D. Thesis

Department of Mechanical and Industrial Engineering

University of Illinois at Urbana-Champaign

October 1997

by

C. W. Palko

CONDITIONALLY ANALYZED MEAN VELOCITY AND TURBULENCE MEASUREMENTS IN A PLUME-INDUCED BOUNDARY LAYER SEPARATED FLOWFIELD

C. W. Palko, Ph.D. Thesis
Department of Mechanical and Industrial Engineering
University of Illinois at Urbana-Champaign

ABSTRACT

A supersonic plume-induced boundary layer separated (PIBLS) flowfield occurs when an underexpanded exhaust plume obstructs the flow around a rocket causing an oblique shock wave to form on the afterbody. The shock oscillates randomly in the streamwise direction causing an unsteady boundary layer separation that complicates prediction and measurement of PIBLS flowfields. This study provides the first turbulence measurements in a PIBLS flowfield and, consequently, the first benchmark data for evaluating future computational models for such flows.

Conditionally analyzed two-component laser Doppler velocimetry (LDV) measurements were made in a planar, two-dimensional PIBLS flow containing an unsteady oblique shock wave formed by the convergence of two supersonic streams past a thick plate. High-speed wall pressure measurements were used to locate the shock wave and, consequently, allow separation of the effects of shock wave motion from the turbulence fluctuations in the velocity measurements of a shock-separated free shear layer. It was found that isolating the large-scale changes in the shock position from the turbulence reduces the experimental scatter rather than substantially changing the shapes or magnitudes of the turbulent stress profiles. Changes in shock motion direction, however, do significantly alter the turbulent stresses. This is the first direct evidence of the effects of changes in shock wave position on turbulence amplification.

The shock-induced separation process was found to dramatically increase the streamwise and transverse Reynolds normal stresses (which both peak near reattachment), the primary shear stress, and the normal stress anisotropy. The shock-separated shear layer consists of only a single layer with a large initial growth rate followed by a much smaller growth rate, instead of the two layers found in rapidly expanded shear layers. The large-scale structures in the shock-separated

shear layer span the shear layer width and exhibit a uniform transverse size. These structures display positive and negative shear stresses on their upper and lower edges, respectively, and are greatly altered by reattachment. All turbulent stresses decrease and the normal stress isotropy increases in the developing wake.